

Applied **SEISMOLOGY**

A Comprehensive Guide to Seismic Theory and Application

By

Mamdouh R. Gadallah

and

Ray L. Fisher



Copyright © 2005
by PennWell Corporation
1421 South Sheridan/P.O. Box 1260
Tulsa, Oklahoma 74112/74101

800.752.9764
+1918.831.9242
sales@pennwell.com
www.pennwellbooks.com
www.pennwell.com

Managing Editor: Marla Patterson
Production Editor: Sue Rhodes Dodd
Book and Cover Designer: Clark Bell

Library of Congress Cataloging in Publication Data

Gadallah, Mamdouh R.

Applied seismology : a comprehensive guide to seismic theory and application / by Mamdouh R. Gadallah, Ray L. Fisher.--1st American ed.

p. cm.

Includes bibliographical references.

ISBN 1-59370-022-9

1. Seismic prospecting. 2. Seismic reflection method--Data processing 3. Seismic refraction method--Data processing. 4. Seismology. 5. Geophysics--Mathematics. I. Fisher, Ray L. II. Title.

TN269.8.G32 2004

622'.1592--dc22

2004009843

All rights reserved. No part of this book may be reproduced, stored in a retrieval system, or transcribed in any form or by any means, electronic or mechanical, including photocopying and recording, without the prior written permission of the publisher.

Printed in the United States of America

1 2 3 4 5 09 08 07 06 05

Preface

After spending many years working in the earth sciences, we became aware that there was no single book that covered all aspects of petroleum exploration, development, and exploitation. It is the aim of this book to fill that perceived need.

The downturn of the industry over the past two decades, the reduction of the work force, and the drop in earth science--student enrollments in colleges and universities have produced a gap between experienced and inexperienced professionals. We know from the history of the petroleum industry that there can be a sudden increase in the need for professionals in our industry. In such an event, there will be a need to rapidly train and upgrade the professional level of geophysicists, geologists, engineers, managers, and others in our industry.

We also see a need for a book that is practical as well as theoretical, easily understood, and comprehensive. We see the inclusion of workshops as another positive of this book. These allow the students to review and reinforce the concepts, theory and practical applications provided in the book.

Mamdouh R. Gadallah

Ray L. Fisher

Houston, Texas



1

Overview and Summary

Introduction

Until 1859, petroleum exploration was a rather simple and straightforward procedure. One simply looked for oil seepage at the surface—particularly near streams and from oil springs. Petroleum was used principally for medicinal purposes at that time, so the approach yielded a sufficient supply to meet demands.

In 1859, Colonel E. L. Drake completed the first successful well, drilled specifically for oil (although wells drilled earlier for other purposes had yielded oil). Actually, Drake used the early method of petroleum exploration since his well was located near a known oil seep along Oil Creek in western Pennsylvania. Soon, there were many wells being drilled up and down Oil Creek.

These early successes led to an exploration method often called *creekology* in which accumulations of oil were associated with low spots along and near streams. Hills and plateaus were not considered suitable drilling sites.

Trendology was another early exploration method arising from the observation that oil pools and fields frequently occurred along almost straight lines for many miles. In other words, after early discovery of two or more fields, lines connecting these were extended in both directions and wells located along the line. Actually, this is a relatively sound procedure, which is still used under certain conditions. Locating wells near oil seeps is also a good method.

As more data accumulated, geologists were able to develop scientific theories concerning oil and gas accumulation. These theories led to practical application and discovery of petroleum deposits from observations of surface geology. Observations of surface rocks and landforms enabled trained geologists to infer whether proper conditions for petroleum accumulation existed at depths of hundreds or thousands of feet.

The invention of the internal combustion engine near the beginning of the 20th century greatly increased the demand for petroleum. Likewise, drilling activity increased and was extended to a wider geographic area and to greater depths. As a result, surface geology in many cases was no longer a reliable guide to the location of drilling sites.

A number of scientifically based petroleum exploration methods have been developed over the years. Where drilled wells are available, various kinds of well surveys are made by lowering instruments into the borehole to obtain directly measured data for analysis to determine the kinds of subsurface rocks present and to identify their various properties.

Other methods yield data useful in assessing the probability of petroleum accumulation without the necessity of drilling to very great depths. Among these are observations of magnetic anomalies caused by local variations in magnetic properties of subsurface rocks, observations of anomalies in gravitational attraction due to variations in rock densities, and observations of seismic waves (earth vibrations or earthquake waves) that propagate through subsurface rocks and return to the surface.

The seismic method, particularly the form called *seismic reflection*, usually yields the most precise and accurate results. It is by far the most popular geophysical exploration method and the one this book will investigate.

Seismic Refraction Exploration Overview

By the end of the 19th century, earthquake seismologists brought seismic theory to a high degree of development. Studies of earthquake waves led to a very good understanding of the internal structure of the earth as a whole, and a rather detailed model of the crust in Europe resulted from study of refracted arrivals from earthquakes. Interest in finding new deposits of petroleum resulted in application of seismic refraction techniques to the problem.

The refraction method was quite successful in locating salt domes, first along the Baltic coast of Germany and later along the Gulf of Mexico coastal regions in the United States. Very large charges of dynamite were used to generate the seismic waves over rather long distances with adequate amplitudes to be recorded by the primitive instruments of the day.

Although refraction data can be analyzed and interpreted rather easily, it has a fatal flaw—it cannot give accurate results unless the seismic velocity in each rock layer is higher than the one above it. An exception to this situation, a *velocity inversion*, causes incorrect layer velocities and thicknesses to be calculated.

Seismic Reflection Exploration Overview

During World War I, the Germans had a huge cannon (nicknamed Big Bertha) capable of firing shells from Germany to Paris, France. When the cannon was fired, its recoil was so intense that it produced seismic waves that could be recorded in Paris. Since the seismic waves traveled faster than the cannon shells, the French were able to warn Paris residents before the shell arrived (Fig. 1–1).

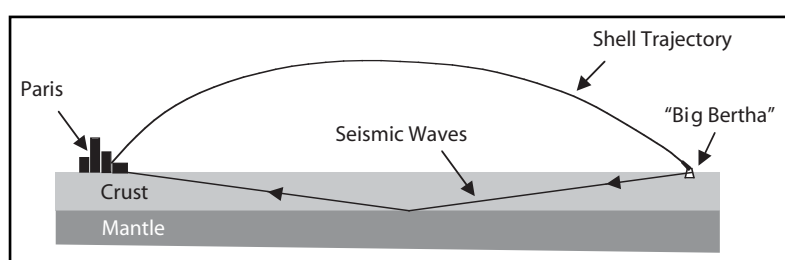


Fig. 1–1 Seismic Waves from Big Bertha's Firing

Dr. Clarence Karcher was stationed in France during this time and was intrigued by this application of seismic wave recording. After the war, Dr. Karcher began experimenting with reflected seismic waves when he was a professor of physics at the University of Oklahoma. His experiments demonstrated that

- seismic waves reflected from interfaces between rock layers could be recorded
- the times it took for these seismic waves to return to the surface after reflection could be used to determine their depths and attitudes

Dr. Karcher later formed the first seismic reflection exploration company, Geophysical Research Corporation, which became a training ground for the industry.

The seismic reflection method is quite simple in concept. It requires

- a source to generate seismic waves (explosives only until around 1950)
- seismic receivers to detect seismic waves and convert them to electrical signals (seismometers or geophones)
- instruments to record amplitude and elapsed time between firing the source and arrival of the reflection

Many things have changed over the years since Dr. Karcher's pioneering work.

- Explosives are no longer the only choice for the energy sources. Vibrators are most often used on land and airguns for marine surveys.
- Detectors (geophones on land, hydrophones for marine) have become smaller and more powerful.
- Recording has progressed from analog recording on photographic paper to digital recording on magnetic tape.
- Processing has evolved from a few manual operations to sophisticated software applications on computers.

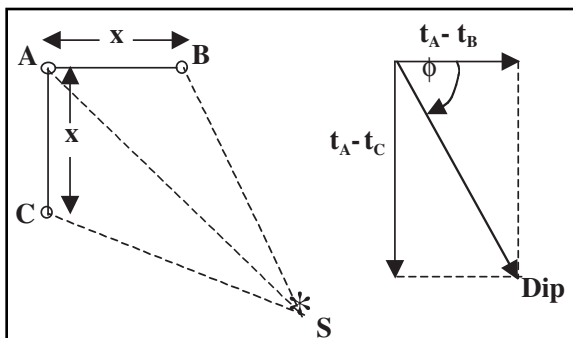


Fig. 1-2 Dip Shooting

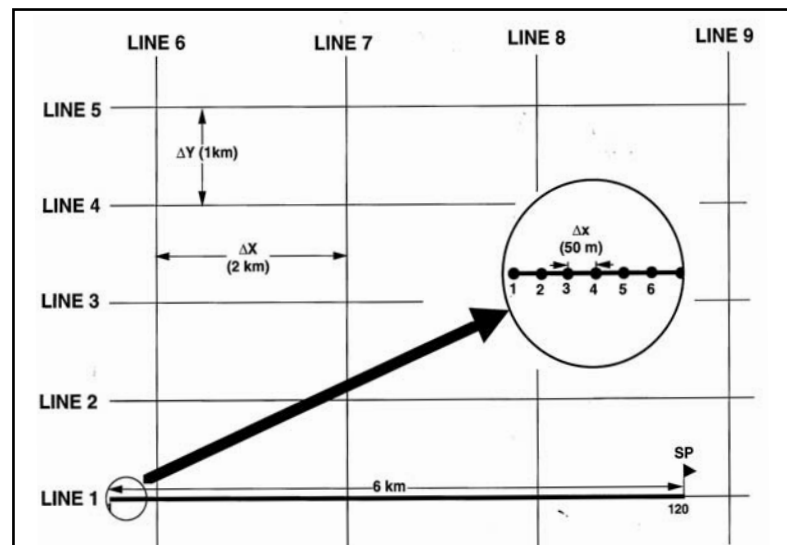


Fig. 1-3 Typical 2-D Seismic Geometry

Seismic acquisition techniques have also undergone many changes. The earliest technique was called *dip shooting*. Detectors were laid out in an L-shaped pattern with receivers at A, B, and C and a source at S (Fig. 1-2). Reflection times at each location; $t_A < t_B$, and were then plotted. Their vector sum gave dip, in seconds (sec) or milliseconds (ms), and dip direction, ϕ .

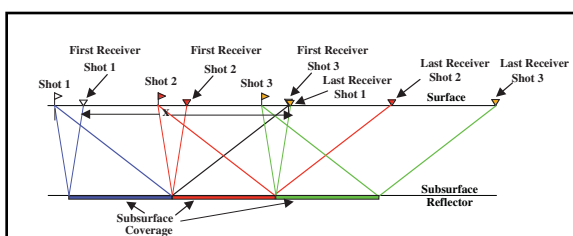


Fig. 1-4 Continuous or Single-fold Subsurface Coverage

t_C , were measured time differences $t_A - t_B$ and $t_A - t_C$ in milliseconds (ms), and dip direction, ϕ .

Dip shooting gave way to continuous (or single-fold) coverage in which receivers were laid out along intersecting lines (Fig. 1-3). For a given shot, receivers were laid out over a distance x that gave subsurface coverage of $x/2$. For the next shot, source point and receivers were moved a distance $x/2$ along the line (Fig. 1-4).

Moving the *spread* (source plus receivers) one-half spread length between shots produced continuous subsurface coverage whereas dip shooting left gaps in subsurface coverage. Later, a method called multi-fold or *common mid-point* (CMP) shooting was developed. In this method, the spread is moved less than one-half spread length resulting in overlap of subsurface coverage. Moving one-fourth spread length means that the same reflections are recorded by two different shots at two different receivers at two different shot-to-receiver distances but the midpoint between shots and receivers is the same! This is called *2-fold shooting*. Increasing the overlap increases the fold as shown in the following examples:

- move-up of 1/6 spread gives 3-fold
- move-up of 1/8 spread gives 4-fold
- move-up of 1/12 spread gives 6-fold

CMP shooting was not really practical at the time it was introduced because analog recording was still being used. Figures 1-5 and 1-6 illustrate CMP shooting.

The method described to this point is now called 2-D shooting. In 2-D shooting, one is forced to assume that all reflections are recorded in a vertical plane below the surface spread, which often is not true. The rather coarse sampling of the subsurface limits the ability to detect and correctly map subsurface features. Figure 1-7 gives an example of a subsurface feature that is very difficult to accurately map with 2-D data but can be with 3-D data.

3-D shooting gives much finer sampling of the subsurface by placing receiver lines much closer together and by having sources that are not generally in line with the receivers. (Fig. 1-8).

Similar advances occurred in marine shooting where, instead of a single streamer being towed, as many as 12 have been used.

Project coordination. On large jobs, it is advisable to have one overall project manager/supervisor who is responsible for the following:

- technical/geophysical coordination
- operational coordination
- client contacts/communications
- planning

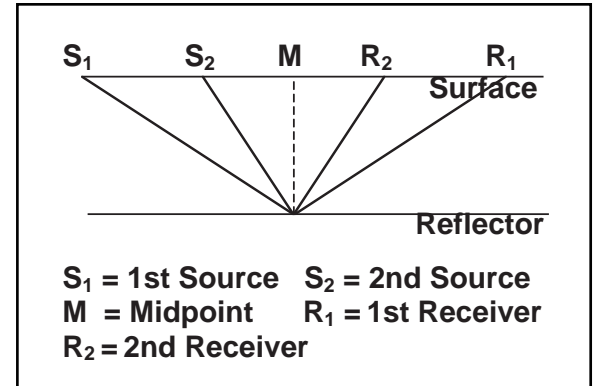


Fig. 1-5 CMP Shooting

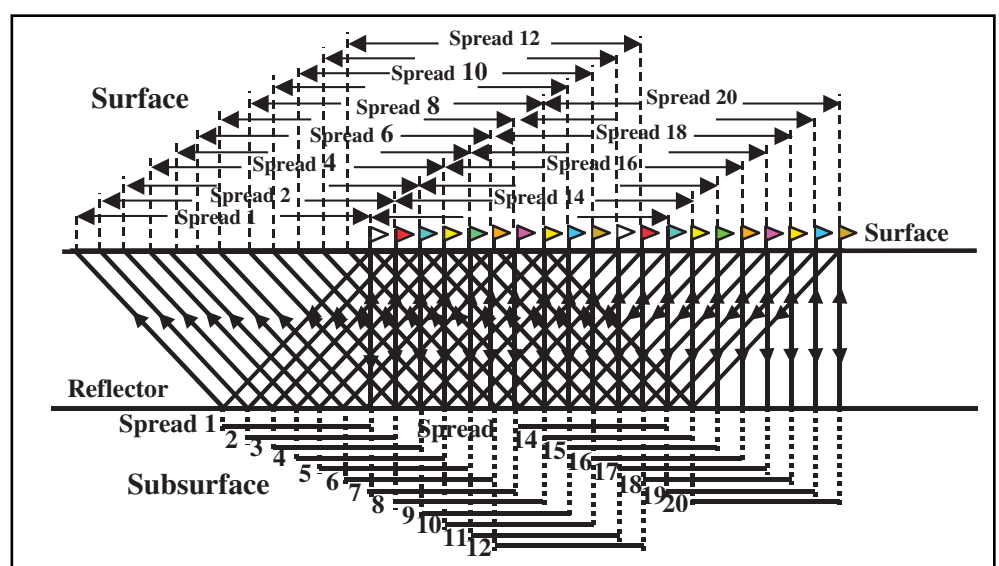


Fig. 1-6 Multi-fold Shooting

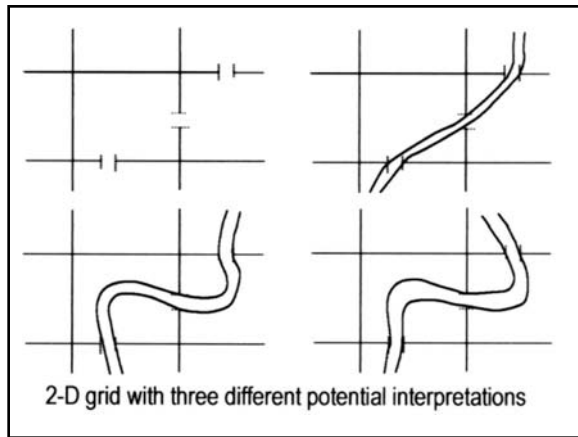


Fig. 1-7 Meandering Stream Channel

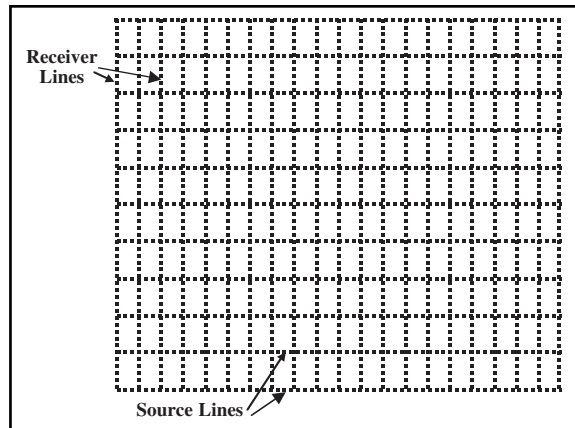


Fig. 1-8 3-D Prospect Layout

This person should be involved from the start of the job. Survey designs are normally completely specified long before recording starts, but operational factors (weather and other considerations) may change. Technical and/or cost improvements can frequently be made by intelligent personnel scheduling, equipment use, helicopter flight and load scheduling, and recovery shot planning. Major steps in seismic reflection exploration include

- pre-planning
- data acquisition
- data processing
- interpretation

Pre-planning. The objective here is to determine the economic viability of the proposed project and, if viable, design the best survey possible with available funds to satisfy the geologic and geophysical requirements. Another purpose is to anticipate problems and develop solutions for them, before work has started.

Steps in the preplanning stage include the following:

- select primary and secondary targets
- estimate their potential return
- determine survey main objectives
- establish priorities for all objectives
- document both objectives and priorities.
- allocate acquisition and processing budgets based on
 - data quantity and quality specifications
 - reasonable schedules and deadlines
- locate and modify lines of survey as required by
 - natural and man-made obstructions
 - environmental and permit restrictions
- specify acquisition methods and equipment types
- determine acquisition parameters

Geologic objective. The geologic objective must be described with regard to trap type (structural, stratigraphic, or combination); depth, thickness, and areal extent; and maximum dip expected. In addition, regional dip needs to be specified.

Acquisition parameters. Parameters that must be defined include the following:

- spacing of receiver groups
- number of receiver groups
- line spacing
- number of lines
- maximum and minimum source-to-receiver distances (offsets)
- source spacing
- source type
- recording geometry

Data acquisition functions include the following:

- permitting
 - permission must be obtained from all owners or authorities prior to entering and working in the area
- positioning
 - precise locations of source and receiver positions must be known
- signal generation
 - seismic waves having appropriate amplitudes and frequency spectra must be generated
- recording
 - seismic waves must be detected and converted to electrical signals
 - electrical signals must be transmitted to the recording system with minimum attenuation and distortion
 - signals must be recorded in a form that provides easy retrieval while preserving as much of the information contained in the original signal as possible

Data processing. The objective of seismic data processing is to produce an as accurate as possible image of the subsurface target. Inputs are field records on magnetic tape, survey/navigation data on magnetic tape, reports, maps, and other items on a variety of media. Outputs are seismic (cross) sections, horizontal sections (3-D), and various special displays.

The same basic processes are applied to both 2-D and 3-D data but the nature of the 3-D data volume is such that some different processes are applied and others are applied quite differently.

Data interpretation. The objective of seismic data interpretation is to convert the *geophysical image* of the subsurface (output of seismic data processing) into a *geologic image* or model of the subsurface. Approaches to the problem include: *modeling*, *inversion*, and *amplitude versus offset studies* (AVO). *Vertical seismic profiling* (VSP) and *seismic stratigraphy* have also been found to be useful tools.



2

Geological Background

Introduction

Geology as a science can really be traced to one man, James Hutton (1726–1797), who promulgated the three basic laws of geology.

Uniformitarianism

- The processes that formed rocks throughout geological time are the same that form rocks today—the present is the key to the past.
- Sandstone is formed from sand deposited as beaches, in rivers, as dunes, etc.
- Limestone is formed in reefs as carbonate banks resulting from calcite coming out of solution.
- Present environments of deposition infer conditions under which material comprising ancient rocks was deposited.

Law of Superposition

- The oldest rocks are usually at the bottom of a sequence of rocks.
- Youngest rocks are at the top of such a sequence.
- Structural deformation may alter this relationship and the resultant change can be used to interpret deformation events.

Law of Horizontality

- Sedimentary rocks are formed from material usually deposited in layers that are nearly flat or have very small slope.
- Subsequent structural deformations may result in steep slopes in rock layers.
- Stratification, bedding or layering is usually observed in sedimentary rocks.
- Variations in sediment deposition may be seasonal or caused by climatic changes, change in sediment source, or structural deformation.

Geology has many subdivisions or specialties. This text discusses a few of these.

- **Historical Geology** – Studies dealing with changes in geology with time. This owes much to the theory of evolution that was originated by Charles Darwin.
- **Structural Geology** – The study of rock deformations and shapes of geologic features.
- **Petroleum Geology** – Studies dealing with the origin, composition, and accumulation of oil and natural gas.

Geologic Time Scale

The Earth is approximately 4.6 billion (4.6×10^9) years old. The geologic record, however, does not extend back that far. The oldest rocks found on continents are about 3.3 billion years old. Rocks along continental margins tend to be much younger than near centers of continents. Most current land surfaces have been alternately covered by shallow seas then uplifted above sea level.

Deposition of rock-forming sediments has occurred along shorelines and ocean bottoms for more than 3.3 billion years. This deposition has covered much of the Earth's surface. Evidence of ancient life forms is included with the sediments, as fossils. Fossils in older rocks are of simpler, more primitive life forms. This suggests that physical changes in the Earth can be correlated with evolution of plants and animals.

Relative time dates rocks and rock groups as older or younger than others, primarily based on fossil evidence. Radioactive dating provides absolute times. Geologic time divisions (see Table 2–1) are not uniform, as they are based on large-scale geologic events, called *orogenies*. The largest time divisions, called *eras*, are based on worldwide orogenies.

Table 2–1 Divisions of Geologic Time

Era	Period	Epoch	Absolute Age (millions of years)
Cenozoic	Quaternary	Holocene	0.01
		Pleistocene	2
	Tertiary	Pliocene	5.
		Miocene	38
		Eocene	55
		Paleocene	65
Mesozoic	Cretaceous		140
	Jurassic		200
	Triassic		250
Paleozoic	Permian		290
	Pennsylvanian		320
	Mississippian		365
	Devonian		405
	Silurian		445
	Ordovician		500
Cambrian			570
Precambrian			4500

Eras are subdivided into *periods*, whose boundaries are marked by less intense but worldwide (or nearly so) orogenies. Periods are subdivided into *epochs* and epochs into *ages*. Boundaries of the latter two subdivisions are not usually found to agree worldwide.

Rock groups are also identified by their ages. *Time rock groups* are subdivided into eras, systems, series, and stages in decreasing order. Charts later in this chapter provide details on the geologic time scale and time rock groups.

Paleontology—paleo for short—is the branch of geology that deals with the age of rocks. It uses the preserved remains of plants and animals in sedimentary rocks, called *fossils*. The age of fossils is based on the theory of evolution that assumes that there was a continuous change and extinction of plants and animals through geologic time.

Fossils are used to date rock layers by invoking the geologic Law of Superposition. Figure 2–1 shows a fossil sequence and from the Law of Superposition. We infer that the fossil at the top of the sequence is the youngest (most recent) and the one at the bottom is the oldest.

The age of fossils in rock can be used to fix location in the subsurface (Fig. 2–2). The wellsite geologist looks at fossils in the rock material, called *cuttings*, that are flushed to the surface while drilling wells. Since the drilling process destroys large fossils, small microfossils are the most useful in wells because the drilling does not destroy them. These fossils are the remains of small plants and animals that lived primarily in the ocean.

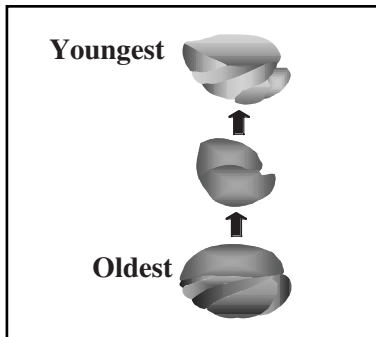


Fig. 2–1 A Fossil Sequence

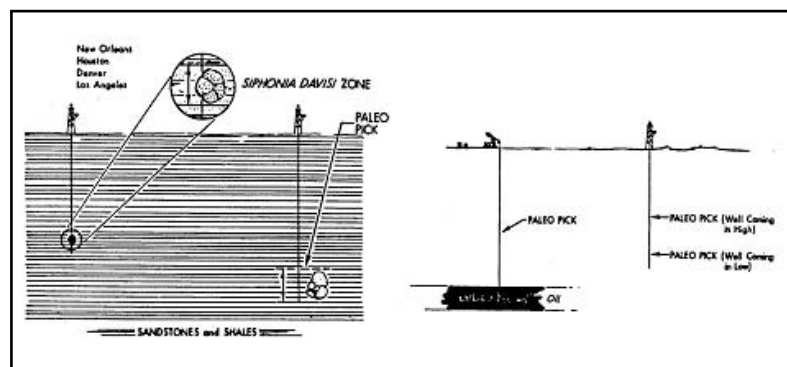


Fig. 2–2 Dating Rocks from Fossils

Internal Structure of the Earth

Structurally, the Earth has three main parts (Fig. 2–3). At the center is the *core*, composed mostly of nickel and iron. The inner core, with a radius of about 1230 kilometers (km) appears to be a solid. The outer core, with a thickness of 2220 km, behaves as a liquid. Because of its core, the Earth has electric and magnetic fields. The interaction of the Earth's magnetic field with the solar wind gives rise to the northern lights and also helps protect us from harmful radiation.

Outside the core is the *mantle*, rich in silicates and other rock-forming minerals. The mantle also has two parts. The inner mantle has a thickness of about 1900 km. The outer mantle's thickness is about 970 km. It is thought that the difference between the inner and outer mantle is physical rather than chemical—caused by the increase in temperature and pressure.

The outermost part of the Earth is called the *crust*. The thickness of the crust is highly variable, ranging from as little as 5 km at a few points in the oceans to about 70 km beneath the highest mountain ranges.

There are two types of crust—*oceanic* and *continental*. The oceanic crust has a single layer composed of basalts. The continental crust has two layers—a granitic layer and a basaltic layer. There are also transition zones at continental margins. There is a very distinct boundary between the crust and the mantle where seismic wave propagation velocities become appreciably and abruptly faster in the mantle. This boundary is called the *Mohorovicic discontinuity* or more informally as the *Moho*.

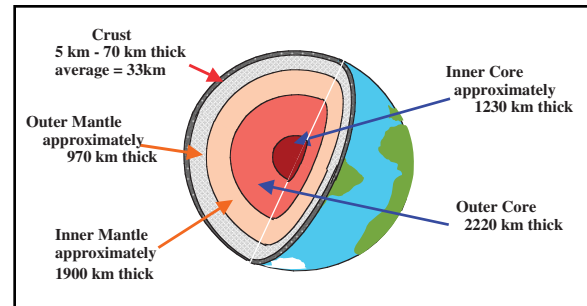


Fig. 2–3 Internal Structure of the Earth

The upper mantle, just below the Moho, is quite complex. There is a concentration of radioactive elements in this zone, and their decay causes heating of the upper mantle, resulting in a narrow zone of variable thickness that behaves as a viscous liquid. This is called the *asthenosphere*. The *lithosphere* includes the uppermost part of the mantle down to just below the asthenosphere and the crust (Fig. 2-4).

Numerous theories to explain the distribution of continents, mountain chains, and oceanic ridges and trenches have been proposed (Fig. 2-5). Some early geologists attempted to explain these by assuming the Earth was shrinking. It was shown that this could not account for all the distributions. Others proposed the opposite—an expanding Earth! This could not explain the distribution satisfactorily either.

In the mid-1950s, a startling discovery was made. Rocks on the seafloor near the Mid-Atlantic Ridge were very young. There were no signs of older rocks there but progressively older rocks were found on the seafloors in both directions away from the ridge. The Atlantic Ocean floor was getting larger!

Sampling the seafloors all over the world found similar patterns. The conclusion reached was that new oceanic crust was being formed at the oceanic ridges. This led to the *Seafloor Spreading Theory* illustrated in Figure 2-6. Magma, molten mantle material, is forced upward through the top of the ridge system. It then flows downward, pushing the older crustal material away from the ridge and creating new crust.

Studies of magnetic polarization in seafloor rocks corroborated this conclusion. It is known

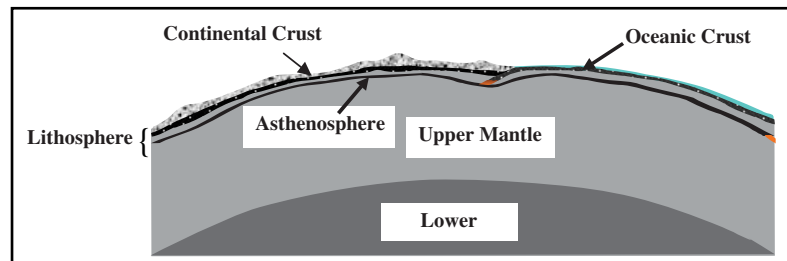


Fig. 2-4 The Lithosphere

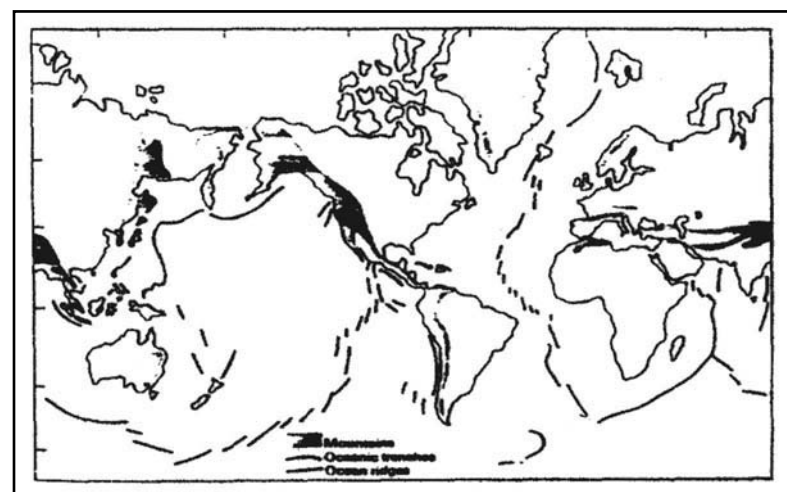


Fig. 2-5 Mountains, Ridges, and Rises of the World

that the Earth's magnetic poles have switched between north and south many times in the past. Magnetic particles in magma are polarized in the direction of the Earth's magnetic field as they cool, and they retain this polarity even though the Earth's field reverses. It was found that all across the floor of the Atlantic Ocean, paralleling the ridge, there are strips of alternating magnetic polarity. This can be explained by the seafloor spreading theory.

These findings led to the resurrection of an old idea—*continental drift*. Many people had noted that the east coast of South America and the west coast of Africa could be fitted together quite nicely. North America and Europe also could be fitted together with a few shifts. A comprehensive theory of continental drift was proposed by Alfred Wegener in papers published in 1912 and 1924. Unfortunately, the theory lacked a convincing mechanism to drive this drift. Seafloor spreading coupled with the idea of upper mantle convection currents provided the mechanism (Fig. 2-7).

Continental drift was reborn and expanded by the *Tectonic Plate Theory*. According to this theory, the lithosphere is not continuous but instead composed of separate pieces called *tectonic plates* that move over the Earth's surface relative to one another in a variety of ways. The upper

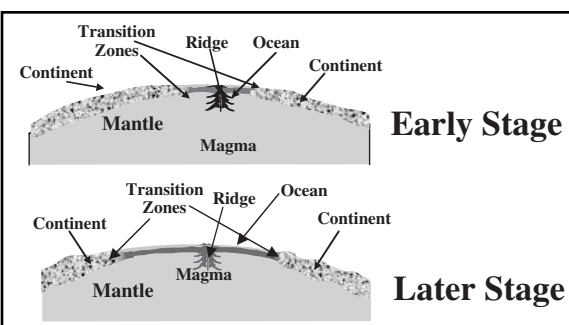


Fig. 2-6 Seafloor Spreading

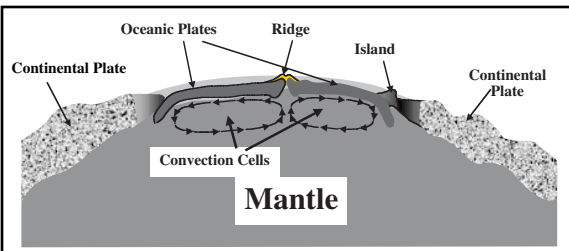


Fig. 2-7 Mantle Convection Current

mantle, as previously noted, behaves as a viscous liquid. Because of differential heating, convection cells develop with hotter material rising toward the surface, cooling, and sinking back down. Because of its viscosity, the mantle material drags the oceanic plates with it away from the oceanic ridges toward the continental plates. The oceanic plates, being heavier than continental plates, dive down under the continental plates and are consumed into the mantle.

The lithosphere is divided into many tectonic plates. Figure 2–8 shows the plates and their boundaries. Note that there are three different types of plate boundaries—consuming (where one plate dives below another and is consumed in the mantle), extensional (plates pull apart as along the Mid-Atlantic Ridge), and transform (where plates move horizontally past one another, as along the San Andreas Fault of California). Figure 2–9 shows the plate boundary types in more detail with a tectonic plate model.

Zones of intense earthquake activity exist along the west coast of South America and along the island arcs of the western Pacific ocean. In these regions, earthquake foci show a pattern of increasing depth as one moves from the ocean toward the continents or across the island arcs. These patterns of earthquake occurrence are explained by the Pacific and Nazca plates plunging under the American, Eurasian, and Indian plates.

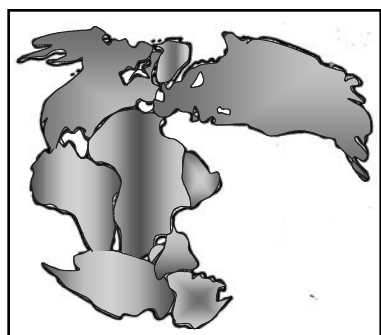


Fig. 2–10 *Pangea, the Universal Continent, about 200 Million Years Ago*

Another part of the tectonic plate theory is that about 200 million years ago, there was only one continent (given the name *Pangea*) as shown in Figure 2–10. The fit of the continents is based not on just shapes of continental margins but also on similarity of fossils, rocks, and geological features.

The continents are still moving. Figure 2–11 shows the continents in their present position and their projected positions 50 million years from now.

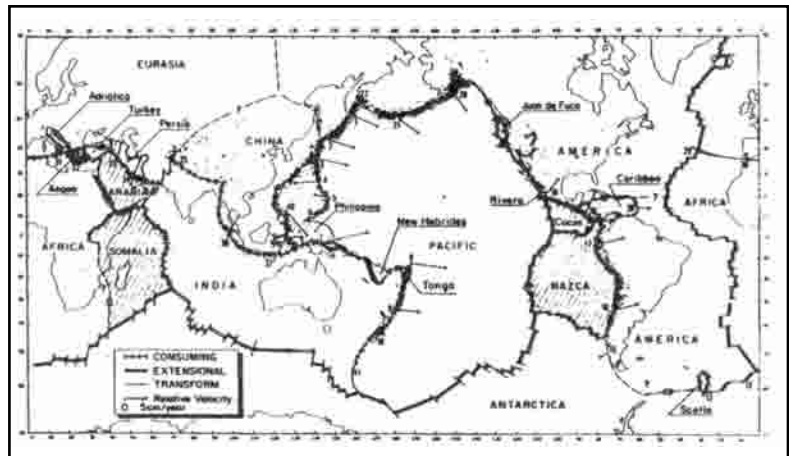


Fig. 2–8 *Tectonic Plate Boundaries*

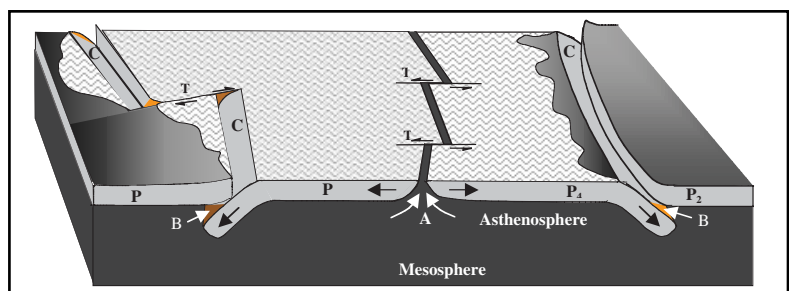


Fig. 2–9 *Tectonic Plate Model*

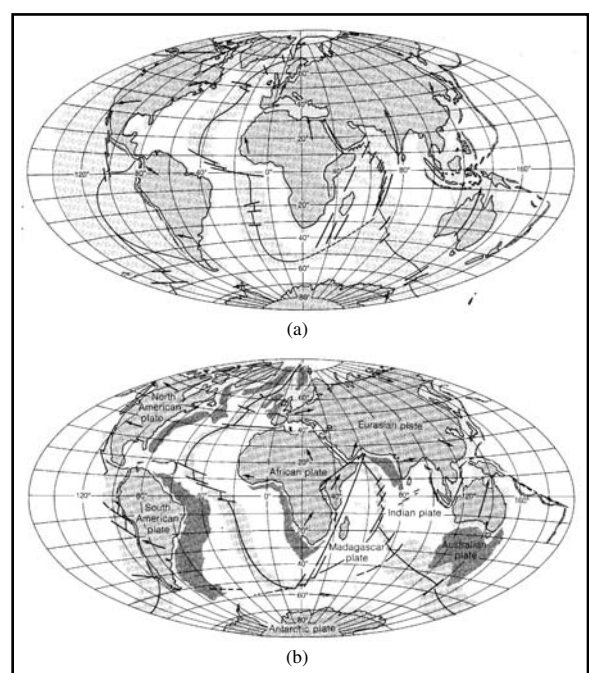


Fig. 2–11 *The Continents in Their Present Positions and Their Projected Positions 50 Million Years from Now*

Rocks in the Earth's Crust

To this point, we have discussed only the large-scale features and structures of the Earth. Our real interest, however, is centered on the uppermost parts of the Earth's crust. This is shown in Figure 2-12.

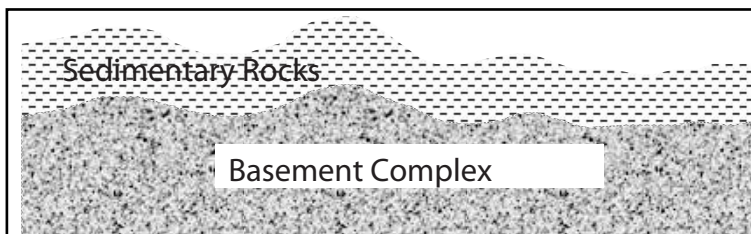


Fig. 2-12 Top Part of the Earth's Crust

Rocks and soils of the Earth's crust are aggregates of mineral grains. Minerals are naturally occurring chemical compounds. Two of the more common minerals are quartz (SiO_2) and calcite (CaCO_3). Some rocks are composed of many different minerals. For example, granite contains black mica, feldspar, and quartz. Other rocks, such as limestone, are composed of only one mineral—calcite in the case of limestone.

There are three classes of crustal rocks—*igneous*, *sedimentary*, and *metamorphic*.

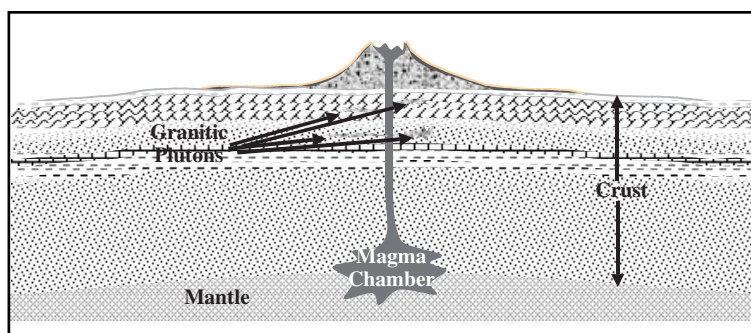


Fig. 2-13 Formation of Igneous Rocks

Igneous rocks are created when cooling from a molten state, and are subdivided into two types. *Volcanic* (basaltic or extrusive) igneous rocks form through quick cooling of lava flows. They are glassy or fine-grained crystalline rocks. *Plutonic* (granitic or intrusive) igneous rocks result from the slow cooling of magma beneath the surface. They are coarse-grained crystalline rocks.

Igneous rocks are associated with zones of weakness in the Earth's crust, such as an island arc or crest of an oceanic ridge (Fig. 2-13).

Sedimentary rocks are formed in layers from sediments transported from one place and deposited in another. There are three types of sedimentary rocks.

- *Clastic* rocks are compacted and cemented rock fragments eroded from pre-existing rocks. Examples include sandstone and shale.
- *Chemical* rocks are precipitated from solution. They include carbonates, salts, and sulfates.
- *Organic* rocks are composed of the remains of plants and animals. Coal is an example of an organic rock.

Metamorphic rocks are formed from rocks altered by high temperature and/or pressure but without melting. Limestone, a sedimentary rock, can be changed into marble, a metamorphic rock. Shale, also a sedimentary rock, can be changed into slate, a metamorphic rock. Metamorphic rocks are associated with mountains and the basement complex. As shown in Figure 2-14, any of the three rock classes can be changed into either of the other two.

The processes of *weathering*, *erosion* and *deposition* form clastic sedimentary rocks. Weathering is the process in which physical, chemical, and biologic agents that break the rocks down into smaller pieces or chemical components act upon exposed rocks. In erosion, products of weathering are transported from their place of origin to another site. Deposition is when eroded rock fragments settle to the bottom of a stream, ocean, etc.

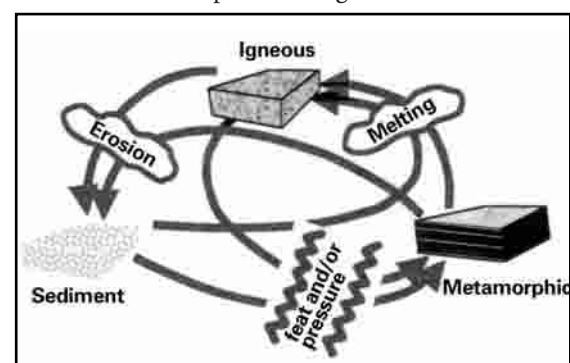


Fig. 2-14 The Rock Cycle

Clastic sedimentary rocks are formed when grains resulting from erosion of existing rocks are transported by gravity, wind, and water to an area of deposition. The area of deposition may be a topographic low or depression such as a lake, sea, or ocean. The rocks tend to form as relatively flat, parallel layers or strata in a marine environment. The greatest thicknesses of sedimentary rocks are found in *sedimentary basins*. These were once oceans or seas that received sediments from rivers that drained large land areas.

Sediments tend to have a high (15 to 45%) *porosity* immediately after deposition. Porosity is the percent of rock volume made up of pores or open spaces. Porosity may be subsequently decreased by *cementation* and *compaction*. Cementation is the precipitation of salts and minerals such as calcite, sulfates, quartz, and salts between loose grains. Compaction is the compression of rock material by weight of sediments deposited on it.

Permeability, the rate of fluid flow through a rock, tends to vary with uniformity in the size in grains deposited. Compaction and cementation tend to decrease permeability. Rocks in the subsurface are usually full of fluid, and subsurface water or other fluids can flow through permeable rocks.

Water flowing through rock can cause cementation or *leaching*—dissolving of rock material. Leaching may be selective, dissolving only certain grain types, but it can also improve porosity and permeability of rocks. Primary porosity results from original holes between fragments. Secondary porosity results from leaching of rock material.

Grain size is important to porosity and permeability. Consequently, geologists have created a nomenclature to describe grain size as shown in Table 2-2.

Table 2-2 Clastic Grain Size Classification

Class	Diameter (mm)
Boulders	>256
Cobbles	64 to 256
Pebbles	4 to 64
Granules	2 to 4
Sand	1/16 to 2
Silt	1/256 to 1/16
Clay	< 1/256

The depositional environment can be inferred from the interpretation of sedimentary rocks based on preserved clues such as ripple marks, mud cracks, fossils (evidence of ancient animals and plants), and on environmental types as follows:

- alluvial—seasonal water flow or landslides
- fluvial—river deposits
- glacial
- marine

Sorting describes the size distribution of rock grains. Well-sorted means that all grains are approximately the same size, e.g. clean sands. Poorly sorted means that there is a wide range of intermixed grain sizes, e.g. dirty sands that contain sand plus finer material. In graded sorting, grain sizes vary linearly with depth in a rock segment (Fig. 2-15).

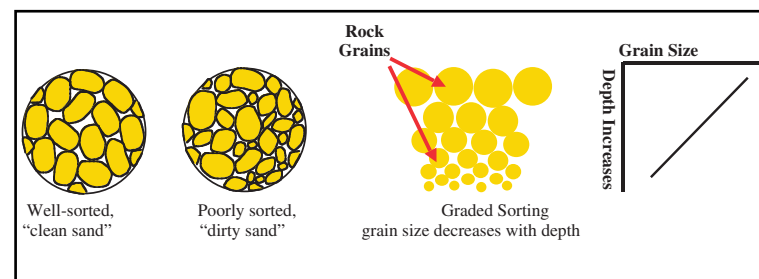


Fig. 2-15 Sorting

Interpretation of sedimentary rocks is also based on rock type—clastic or carbonate—and fluid content—fresh water, brine, oil, or gas.

The most prevalent sedimentary rock types are shale, sandstone, and limestone. They comprise 99% of the Earth's sedimentary rocks. Shale has a small grain size and a high organic content. This is important to petroleum formation. Sandstone has a larger grain size than shale, and its grains are predominately silica fragments. Sandstone has high porosity and permeability in many cases. Limestone is either chemically precipitated calcite or built up from skeletal remains of animals. It is of oceanic (marine) origin. Limestone may be chemically altered to dolomite. More petroleum has been found in limestone and dolomite than any other rock type.

Limestone, sandstone, and shale are not always found in pure forms but frequently grade from one to another as shown in Figure 2-16.

Petroleum is found within porous and permeable rocks. Pores are needed to store the petroleum. Permeability is necessary for petroleum to enter rocks. Porosity is the percentage of rock volume made up of pores or openings between fragments. Porosity in rocks ranges from 1 to 45%. Porosity is classified as follows:

- poor, 1–8%
- fair, 9–15%
- good, 16–25%
- excellent, more than 25%

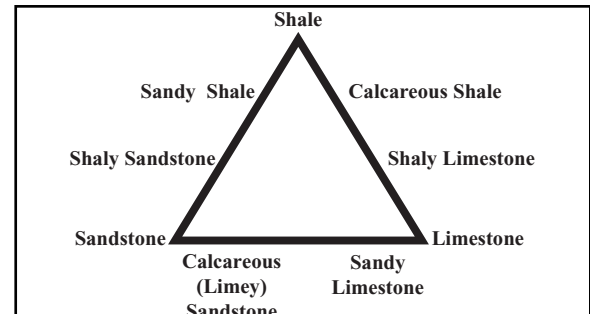


Fig. 2-16 Prevalent Sedimentary Rock Types

Permeability is a measure of fluid flow and depends on interconnection of pores. The *darcy* is the unit of permeability measurement, but because this is such a large unit, *millidarcies* ($md = .001$ darcies) are most often used. Permeability can be measured in the laboratory by determining the rate of hydrogen flow through a rock under a standard pressure. Adjustments are made to correct from gas to liquid flow. Relative permeability measurements are

- poor, 0.1–50 md
- fair, 50–250 md
- good, 250–1000 md
- excellent, more than 1000 md

Clastic sedimentary rocks are most likely to be porous and permeable since they consist of fragments eroded from other rocks. Carbonate rocks (banks and reefs) may also be porous and permeable. Igneous and metamorphic rocks can be of interest if they have sufficient cracks (fractures) to produce porosity and permeability. Fractured igneous and metamorphic rocks can have high permeability but usually have low porosity, limiting the amount of petroleum they can hold.

Deformation of Crustal Rocks

Weathering breaks down rocks at the Earth's surface into smaller pieces or fragments called *sediments*. The breakdown can be by mechanical means (a physical break in the rock) or chemical (dissolution of parts of the rock by groundwater or other liquids such as dilute acids).

Erosion is the transportation of sediments from their site of origin. Gravity, in the form of landslides or rock fragments simply rolling down slope, can be a cause of erosion. Wind picks up smaller sediments and drops them at various distances from their original position. Glaciers slowly move downhill, and, as they move, pick up sediments beneath them. Later, melting allows these sediments to be deposited elsewhere. Moving water—waves or currents in rivers and oceans—is perhaps the most active agent of erosion. Most sediments are deposited at the bottom of oceans or other bodies of water.

Unconformities are surfaces of erosion or non-deposition. Of particular interest to petroleum exploration are *angular unconformities*. In angular unconformities, rock layers below the erosional surface are tilted at an angle while layers above the erosional surface are more nearly horizontal. An unconformity represents a period of major mountain building and subsequent erosion. Angular unconformities can form giant hydrocarbon traps as seen in the East Texas and Prudhoe Bay Fields. The East Texas field is shown in Figure 2-17.

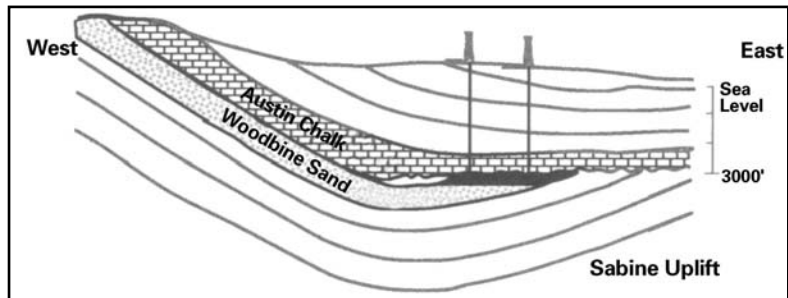


Fig. 2-17 The East Texas Oil Field

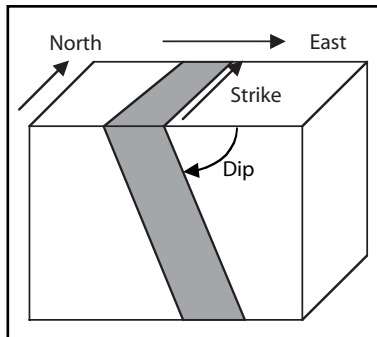


Fig. 2-18 Strike and Dip

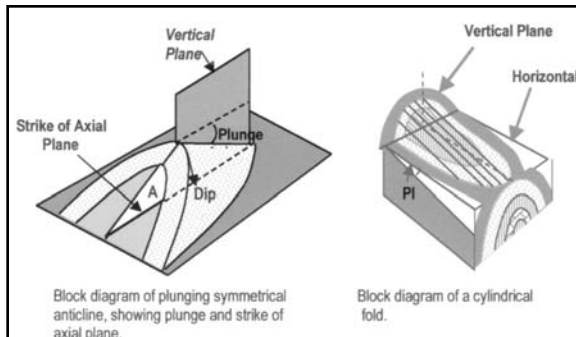


Fig. 2-19 Strike, Dip, and Plunge

Structural position of tilted, sedimentary layers is described using *strike* and *dip*. *Strike* is the direction relative to north of the line formed by the intersection of the top (or bottom) of a layer with a horizontal plane. *Dip* is the angle that a plane surface (layer or bedding) makes with a horizontal plane. Both the dip and strike are usually specified for a dipping layer. In Figure 2-18 the strike is 0° , which is due north. Some structures require another parameter, *plunge*, to describe their positions. This is shown in Figure 2-19.

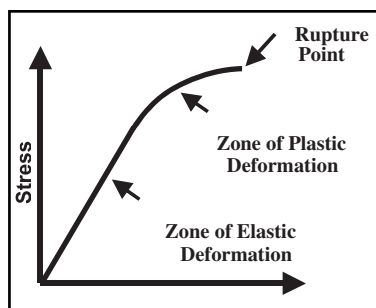


Fig. 2-20 Stress-Strain Relationship

Crustal layers are deformed by stresses (force per unit area) caused by

- collision of tectonic plates at plate boundaries
- weight of overlying rock layers (overburden)
- *isostasy*, or buoyancy of lithospheric units in underlying mantle

Layer deformation is a function of the size of the applied stress and the physical properties of the layer. Figure 2-20 is a plot of stress and strain. If the stress is within elastic limits of a given layer, then an applied stress results in a *strain* (the relative change in dimensions or shape) directly proportional to the stress. When stress exceeds the elastic limit, the strain is no longer proportional to the stress and there is a zone of plastic deformation, called *folding*. At the upper limit of plastic deformation the layer ruptures, fracturing into separate layers with relative movement between them. This is called *faulting*.

There are three general types of deforming stresses: *compressive*, collinear forces (F) that push rocks together; *extensional*, which are also collinear but pull rocks apart; and *shear*, in which forces are offset from one another causing one face of a rock to slide past the opposite one. These stresses are illustrated in Figure 2-21.

Folding of crustal rocks. Folds (Fig. 2-22) occur when horizontal sedimentary layers are subjected to a compressive stress but the plastic limit is not exceeded. *Deformation* is the bending of the rock layers. Bends in rock layers are called folds. Ruptures of the rock layers occur when the plastic limit is exceeded. Ruptures are called faults.

Mountain building involves intense, large-scale folding and it is very common to have both folding and faulting. Folds tend to remain even after faulting occurs. Folds in the Earth's crustal layers are excellent places for hydrocarbons to be found. Early geologists and geophysicists worked to find folds in rocks.

Fig. 2-21 Types of Stress

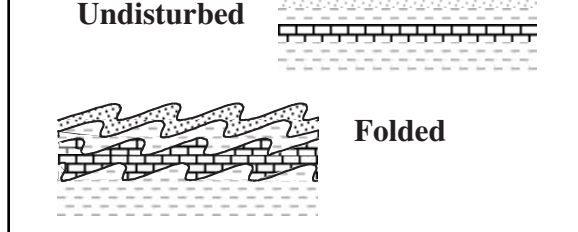


Fig. 2-22 Folding of Rocks

There are many kinds or classes of folds. A *monocline* is when rock layers are tilted (dip) in one direction. Note that the dip can vary in a monocline, but the dip direction stays the same. A *syncline* is when rock layers are folded down into a depression. An *anticline* is when rock layers are folded up into an arch.

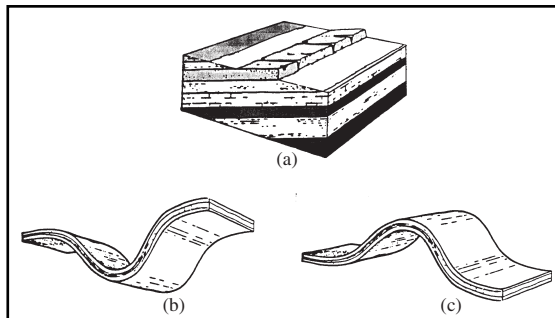


Fig. 2-23 Monoclines, Synclines, and Anticlines

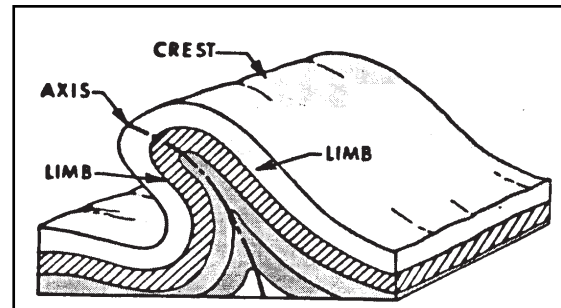


Fig. 2-24 Terms Describing Anticlines

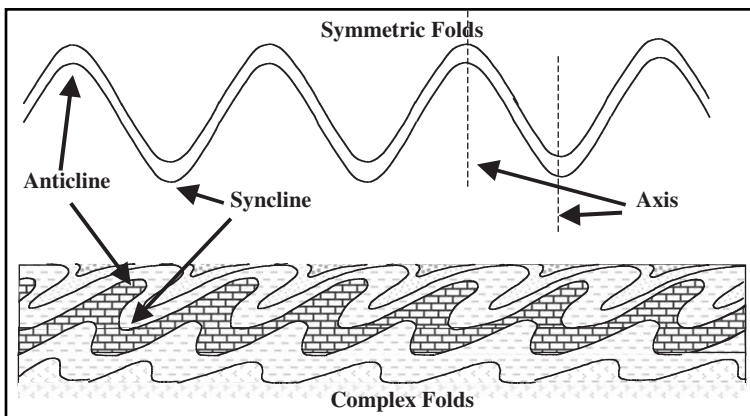


Figure 2-25 Symmetric and Asymmetric Folds

Anticlines make excellent hydrocarbon traps. Figure 2-23 shows monoclines, synclines, and anticlines.

Figure 2-24 illustrates some terms used to describe anticlines. The *crest* is simply the highest point on the anticline. The *axis* is an imaginary line or surface about which the folding takes place. The *limbs* are the parts of the fold that slope down on each side of the crest. It is not unusual to have a series of folds with anticlines and synclines in succession.

A *symmetric anticline* is one with limbs dipping down from the crest at the same angle but in opposite directions. Symmetric synclines have limbs that dip up from the trough (low) at the same angle but in opposite directions. Limbs of asymmetric anticlines and synclines have different dips on each limb. Usually one has a much steeper dip than the other. See Figure 2-25.

A *dome* is a circular or elliptical anticline. It makes a perfect hydrocarbon trap. Figure 2-26 illustrates the features of a dome.

Young folds are ridges or valleys that have not been extensively eroded. *Old folds* have been eroded flat (*planeplaned*). The surface pattern of an eroded cylindrical fold is symmetrical stripes. An anticline has the oldest rocks in the center. A syncline has the youngest rocks in center as seen in Figure 2-27. The surface erosion pattern of any anticline is for the oldest rocks to be in the center.

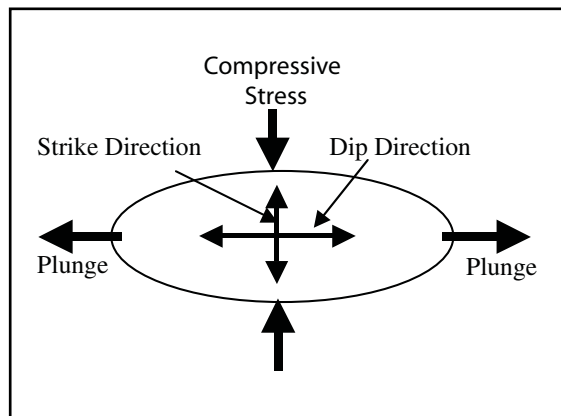


Fig. 2-26 Anticlinal Dome, Overhead View

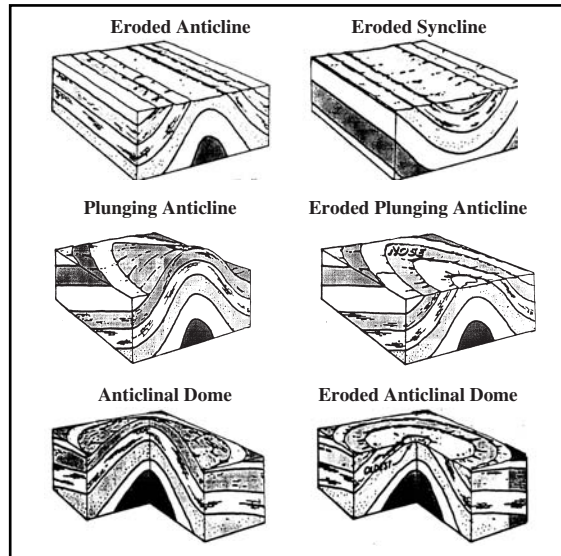


Fig. 2-27 Eroded Folds

In a *plunging fold*, the axis is not level. The surface pattern of an eroded, plunging fold is called a *nose*. Plunging anticlines and plunging synclines are most common. A plunging anticline has the oldest rocks in the center. A plunging syncline has the youngest rocks in the center.

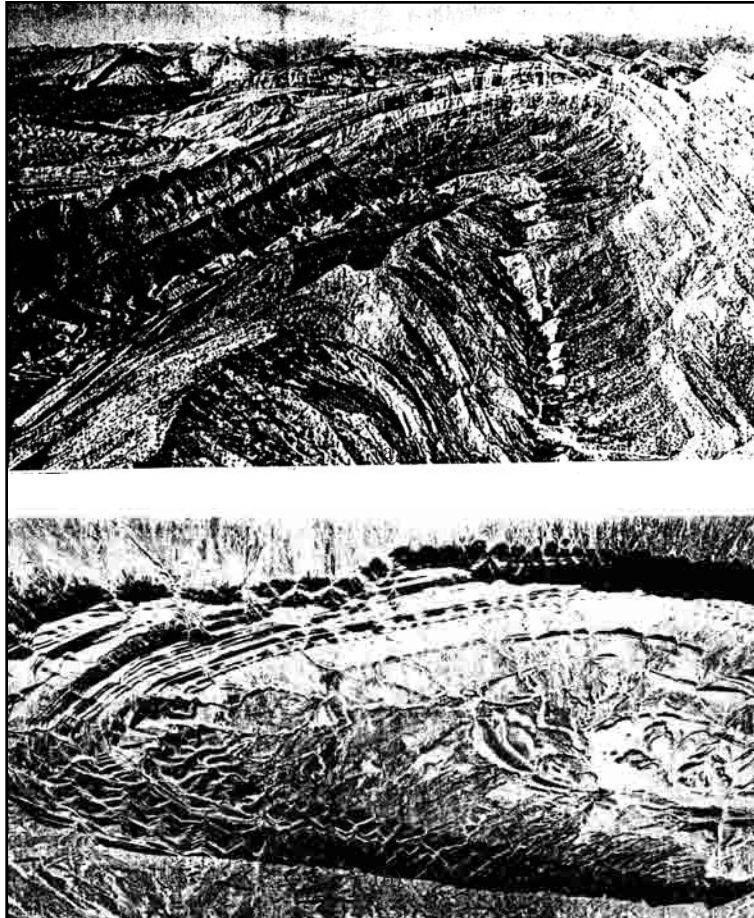


Fig. 2-28 An Eroded, Plunging Syncline in Northwest Africa and an Eroded, Plunging Anticline in the Zagros Mountains of Iran

Such faults are classified as *normal* and *reverse*, depending on which fault block appears to have moved up. In *strike slip*, movement is strictly horizontal. *Oblique slip* is a combination of dip slip and strike slip motion. Fault motion is illustrated in Figure 2-30.

Figure 2-31(a) shows a type of dip slip fault called a normal or *gravity* fault. Also shown in the figure are some terms used to describe faults. The *fault plane* is the surface along which the two blocks created by the fault move. The *footwall* is the block below the fault plane. The *hanging wall* is the block above the fault plane. *Heave* is the amount of horizontal movement between the two fault blocks, and *throw* is the amount of vertical movement between the two fault blocks. A normal fault is one where the hanging wall has moved down relative to the footwall. Note that this is relative motion. The footwall could have moved up or the hanging wall down or a combination of the two.

Figure 2-28 shows photographs of a real eroded anticline and eroded syncline. Without knowledge of rock ages, it would be impossible to tell the anticline from the syncline.

Joints are natural fractures in rocks. They are caused by compressive or tensional stress. The applied stress exceeds the plastic limit of a rock, causing rupturing or fracturing. However, there is no relative movement of one side of fracture relative to the other. Joints usually occur as relatively evenly spaced sets with the same general orientation throughout an area. Homogeneous rocks exhibit fairly uniform fracture patterns (Fig. 2-29).

Joints enhance porosity with more space to store fluids and permeability by providing fluid flow paths in subsurface rocks. Joints also increase the surface area exposed to water and ice, thus weathering and erosion of rocks with joint patterns is enhanced.

Faults are fractures in rock layers accompanied by relative motion between the resulting faults. Movement on one side of a fracture relative to the other side can be of three different types. In *dip slip*, movement is up and down along the fault plane.

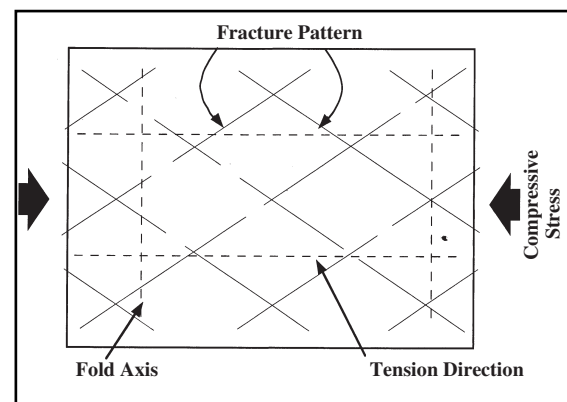


Fig. 2-29 Joints

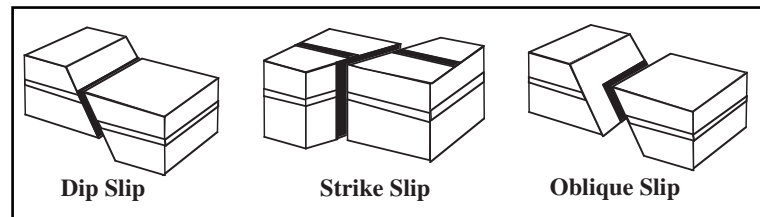


Fig. 2-30 Fault Motion

Figure 2–31(b) shows a reverse fault. In this case, the hanging wall has moved up relative to the footwall. If the fault motion is the same but the dip of the fault plane is less than 45° , then it is called a *thrust* fault.

The stress causing a normal fault is tension that pulls the two blocks apart. The weight of the hanging wall causes it to fall. In a well cutting a normal fault there will be a missing section—layers that are present in Earth's section are not penetrated by the well bore. The stress causing a reverse or thrust fault is compression. A well cutting a reverse fault will have a repeat section—a particular layer is present twice in a well bore (Fig. 2–32).

In strike slip faults, the stress applied to the beds is shear. Motion of the fault blocks is horizontal along the strike of the fault plane. Displacements can be very large like those along the San Andreas Fault of California or the Great Glen Fault of Scotland (Fig. 2–33). Dip slip and strike slip faults are both important to exploration for hydrocarbons (oil and gas). Many anticlinal traps worldwide are related to normal and reverse faults. California's oil production along the Pacific Ocean coast is directly related to the strike slip motion of the San Andreas Fault.

Horsts and *grabens* (Fig. 2–34) are formed by parallel normal faults. The graben is the down dropped block and the horst is the ridge between grabens.

Growth faults are a type of normal fault formed in river deltas and coastal plains (depositional basins). Large volumes of loose sediments are rapidly deposited. Movement along the fault occurs at the same time as sediment deposition, providing accommodation space for more sediment. Movement is caused by the weight of the water and saturated sediments. The fault plane is arcuate, concave toward the basin. It is steep at the ground surface and becomes less steep at depth. It *soles* out at depth—becomes parallel to layers at depth.

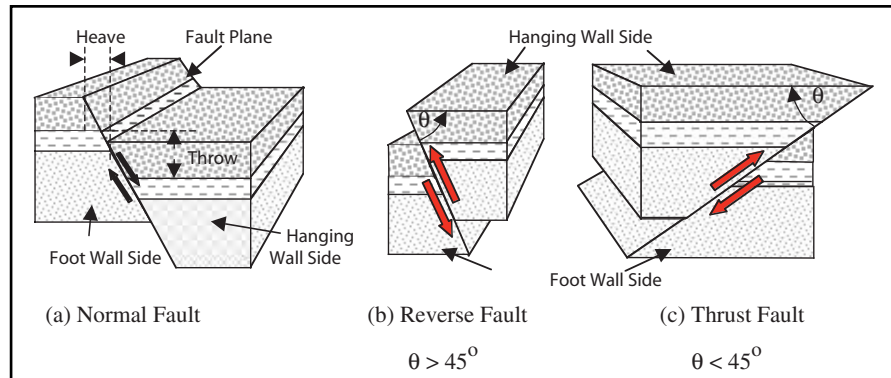


Fig. 2-31 Dip Slip Faults

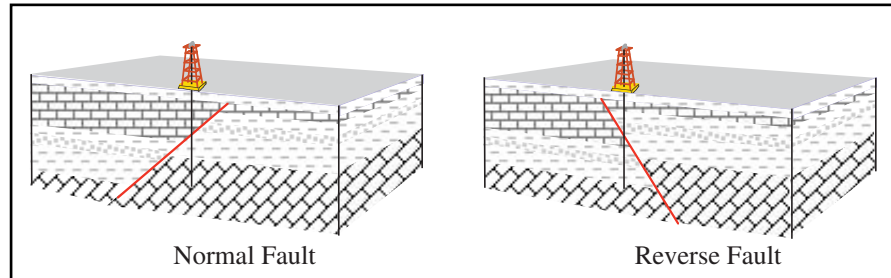


Fig. 2-32 Well Bores through Normal and Reverse Faults

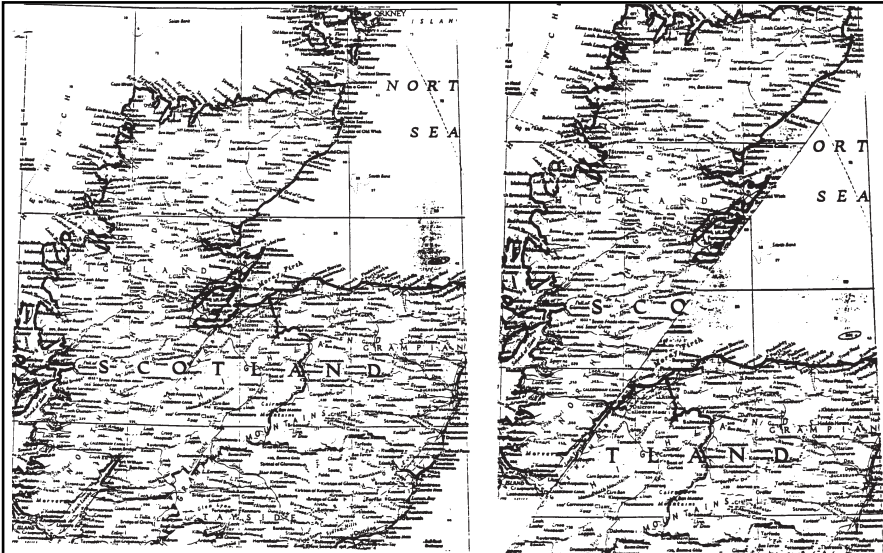


Fig. 2-33 Fault Displacement along the Great Glen Fault

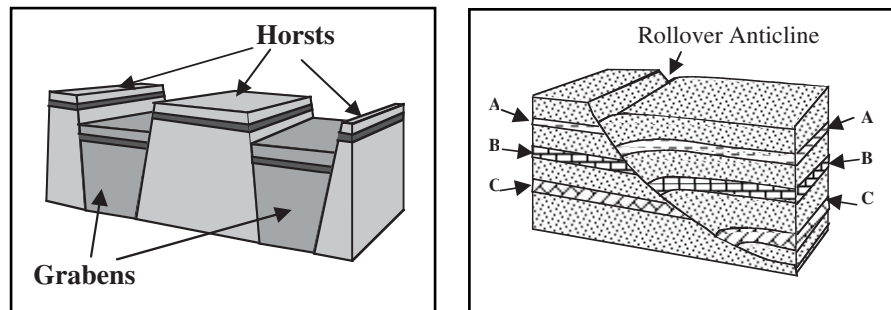


Fig. 2-34 Horsts and Grabens

Fig. 2-35 Rollover Anticline



3 Geophysical and Mathematical Background

Basic Geophysical Theory

The theory upon which seismic exploration for oil is based comes from a branch of physics called *classical mechanics* that was developed by the late 17th to the early 18th century. Of particular interest to us is the development of the *wave equation*. The wave equation is applicable to virtually any kind of wave motion—mechanical or electromagnetic. The wave equation can be written as:

$$\nabla^2 u = \frac{1}{V^2} \frac{\partial^2 u}{\partial t^2} \quad \text{or} \quad \frac{\partial^2 u}{\partial x^2} + \frac{\partial^2 u}{\partial y^2} + \frac{\partial^2 u}{\partial z^2} = \frac{1}{V^2} \frac{\partial^2 u}{\partial t^2}$$

Where u is the wavefield; x , y , and z are the three coordinates of a three-dimensional coordinate system (for example, x may be distance along some particular direction, y is distance at right angles to x , and z is vertical depth or altitude); t is time; and V is propagation velocity or rate at which the wave progresses.

Seismic waves are mechanical waves in the solid earth. Solutions of the wave equation are facilitated if certain simplifying assumptions are made about the medium through which the seismic waves are propagating. These assumptions usually are that the medium is perfectly *elastic*, *homogeneous*, and *isotropic*.

An elastic solid is one in which *stress* is proportional to *strain*. Stress is a force applied perpendicular or parallel to a surface of a body divided by the area of that surface. Strain is the ratio of change in dimension(s) caused by an applied stress to the original dimension(s). Different constants of proportionality are used depending on the type of stress applied.

Young's modulus (E) is the constant for linear stress as seen in Figure 3-1a. It is defined as the force per unit area divided by the ratio of change in length to original length. Young's modulus ignores the effect of applying a linear stress to a body. The applied stress does cause a strain in the direction of the applied stress, but it also causes a strain in the orthogonal directions. Figure 3-1b shows the **bulk modulus (k)** that is used to relate stress to volumetric strain. Bulk modulus is defined as the force per unit area acting on a surface divided by the ratio of change in volume to the original volume. In Figure 3-1b, it can be seen that a stress applied vertically changes the vertical dimension of a cube from d to $(d - \Delta h)$, but the two horizontal dimensions are changed from d to $(d + \Delta d)$. Thus, a stress applied in one direction results in strains not only in the direction of the stress but in the orthogonal direction as well. It can be seen that the compression in the vertical direction decreases the vertical dimension while increasing the horizontal dimensions.

The ratio of the strain in an orthogonal direction to the strain collinear with the stress is called **Poisson's ratio (σ)** and can be seen in Figure 3-1c. Poisson's ratio varies from 0 to 0.5. The drawing in Figure 3-1d illustrates the **shear modulus (μ)**. The stress in this case is across, rather than perpendicular to, the surface on which it acts. The deformation is in shape rather than volume or linear dimension. Shear modulus is defined as the force per unit area acting on a surface divided by the angle through which one dimension is rotated.

A homogeneous body is identical throughout. If a homogeneous body were divided into pieces, then every piece would be chemically and physically identical, no matter how small the pieces. This, of course, cannot be realized in the rocks through which seismic waves propagate. Rocks are usually made of fragments or interlocking crystals. If such rocks were cut into very small pieces, differences in pieces would be observed. Thus, rocks are *inhomogeneous*—not homogenous.

An isotropic medium has the same physical properties in all directions. Of particular concern are the propagation velocities of the medium—the time rate at which seismic waves travel through the medium. In an *anisotropic* (not isotropic) medium, propagation velocity does depend on direction of propagation. There are many types of anisotropy. One type, called *transverse isotropy*, behaves as though it were composed of thin isotropic layers. As a result, there is a difference between horizontal and vertical propagation velocities. Another type of anisotropy is found in rocks that have cracks running through them. In such cases, the velocity parallel to the cracks differs from velocity orthogonal to the cracks.

Wave propagation

Solutions of the wave equation for perfectly elastic, homogenous and isotropic media describe four different types of waves. Two of these propagate through the body of the medium and are called *body waves*. One is called a *P-wave* and the other is called an *S-wave*. Both are shown in Figure 3-2.

A P-wave is, basically, a sound wave or pressure wave. The name, however, comes from *primus* or *first* because the P-wave is always the first-arriving seismic wave. Rock particles are alternately compressed and pulled apart as the wave passes by. Also shown in Figure 3-2 is *wavelength (λ)*. The wavelength is the distance over which all possible amplitudes are reached. It can be measured from peak (maximum amplitude) to peak or from trough (minimum or maximum negative amplitude) to trough. P-wave particle motion is in the direction of propagation. P-wave velocity in a particular medium is the fastest of all seismic waves. If the elastic moduli and *bulk density (ρ)* are known, P-wave velocity can be calculated using the following equations.

$$V_p = \sqrt{\frac{k + \frac{4}{3}\mu}{\rho}} \quad (3.1)$$

$$V_p = \sqrt{\frac{E(1+\sigma)(1-2\sigma)}{\rho(1-\sigma)}} \quad (3.2)$$

or

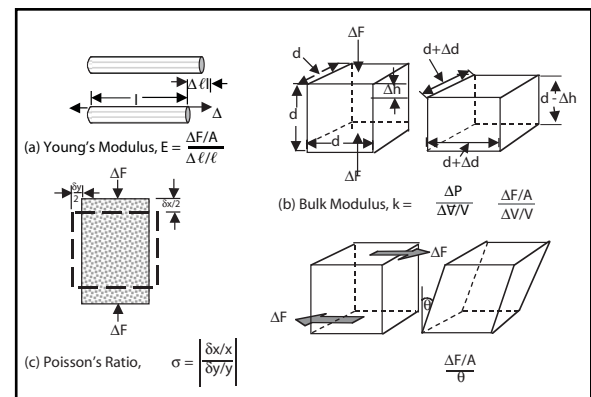


Fig. 3-1 Basic Elastic Moduli and Poisson's Ratio

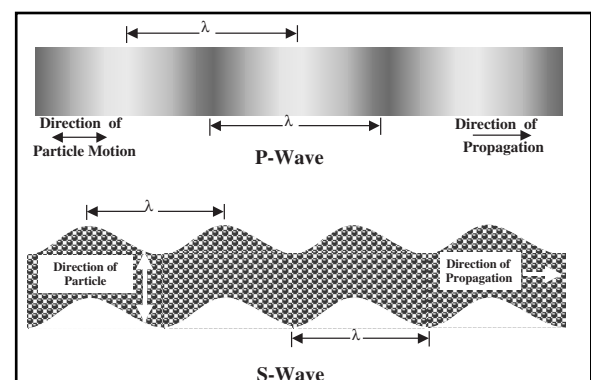


Fig. 3-2 P- and S-waves

If the elastic moduli and *bulk density (ρ)* are known, P-wave velocity can be calculated using

S-waves, also called *shear* waves, are the second type of body wave. On earthquake seismograms, they are the second-arriving wave packets, hence the designation S-wave. While P-waves can propagate in solids or fluids, S-waves can propagate in solids only. S-wave velocity can be calculated from the following equations.

$$V_s = \sqrt{\frac{\mu}{\rho}} \quad (3.3)$$

or

$$V_s = \sqrt{\frac{E}{2\rho(1+\sigma)}} \quad (3.4)$$

P-wave velocity is always faster than S-wave velocity. Dividing Equation 3.2 by Equation 3.4 gives the P- to S-wave velocity ratio as:

$$\frac{V_p}{V_s} = \sqrt{\frac{2(1-\sigma)}{1-2\sigma}} \quad (3.5)$$

$$0 \leq \sigma \leq 0.5, \frac{V_p}{V_s} \geq \sqrt{2}$$

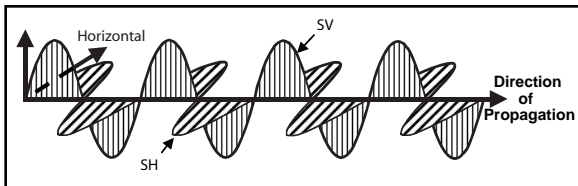


Fig. 3-3 SV- and SH-waves

S-wave motion can be resolved onto vertical and horizontal components, called SV and SH. In some anisotropic media, the S-wave train becomes separated into separate SV and SH wave trains because the two have different propagation velocities. Figure 3-3 illustrates SV- and SH-wave motion.

The other two solutions of the wave equation are called *surface waves*. These are restricted to the surface of solid media. There are two kinds of surface waves. One is called a *Rayleigh wave*, in honor of Lord Rayleigh, a 19th century British natural scientist who first developed the theory. Rayleigh wave motion is described as retrograde elliptical. That is, as the wave passes, a ground particle describes an ellipse, starting at point A in Figure 3-4. This is actually a combination of vertical and radial motion. Radial is horizontal motion in the direction of propagation.

Figure 3-4 shows Rayleigh wave motion. Rayleigh wave propagation velocity is about 92% of S-wave velocity.

Ground roll, a frequently encountered type of noise observed on exploration seismic records, is a Rayleigh wave. Ground roll can be the largest amplitude event on a seismic record and mask the reflected events that are desired.

The second type of surface wave is called a *Love wave*. Love waves are also named for a British scientist who developed the theory for them. As shown in Figure 3-5, Love wave motion is essentially SH motion but is restricted to the surface of the medium. Love wave propagation velocity is slightly slower than Rayleigh wave velocity.

Love waves are not usually a problem on exploration seismic records. However, if special energy sources are used to generate SH-waves, Love waves can be a severe problem because of their high amplitudes.

Fig. 3-4 Rayleigh Waves

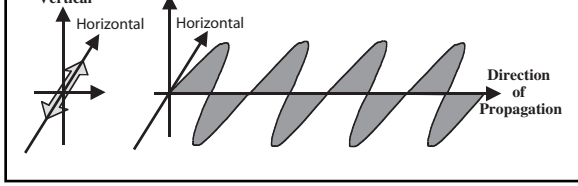


Fig. 3-5 Love Waves

motion but is restricted to the surface of the medium. Love wave propagation velocity is slightly slower than Rayleigh wave velocity.

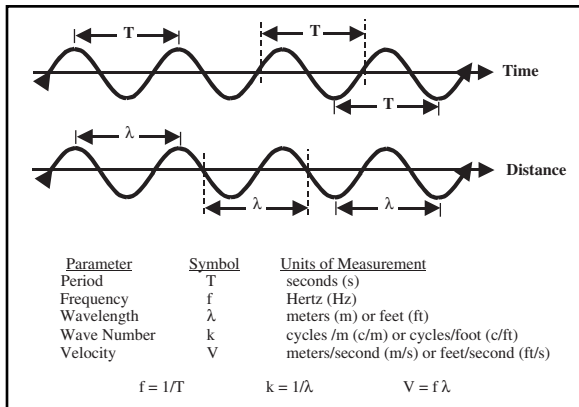


Fig. 3-6 Basic Wave Parameters

$\psi(t,x)$ = the wave field

A = amplitude

t = time

x = distance

ϕ = phase

Figure 3-6 illustrates and defines some basic wave parameters. Two sinusoids are shown in Figure 3-6. The top one is a function of time and the bottom one is a function of distance. A *cycle* is defined as the interval over which all possible amplitudes occur. A *period* is the time, in seconds, required to complete one cycle. *Frequency*, the reciprocal of period, is the number of cycles per unit of time. Frequency is measured in Hertz (Hz), where 1 Hz equals one cycle/second.

A *wavelength* is the distance over which one cycle is completed. The reciprocal of wavelength is *wave number* (sometimes called spatial frequency). A sinusoidal wave is described by the mathematical expression

$$\psi(t,x) = A \cos[2\pi(f t - kx) + \phi] \quad (3.6)$$

where

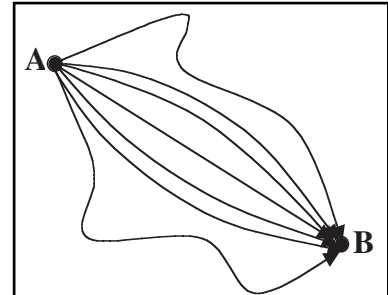


Fig. 3-7 Fermat's Principle

Amplitude is usually defined as the maximum deflection from the rest position (zero to peak) but is sometimes measured from peak to trough (peak-to-trough amplitude). Phase is an angular quantity that is usually measured in radians or degrees. Phase indicates the initial position of the wave in a cycle.

Much theoretical work in, or applicable to, seismic exploration is based on ray theory. Rays are simply lines (not necessarily straight) that show the paths waves take between two points. A very important concept in ray theory is *Fermat's Principle* (Fig. 3-7). This principle can be stated many ways. In Sheriff's *Encyclopedic Dictionary of Exploration Geophysics*, the first statement is, "The seismic raypath between two points is that for which the first-order variation of travel time with respect to all neighboring paths is zero." Further on, Sheriff states, "If the intervening media have different speeds, the path will not be straight but will be such that the overall travel-time is minimized (usually)." The resulting raypath is also called the *least time path* or *brachistochrone*.

Seismic exploration is normally conducted in areas called *sedimentary basins*. There, rocks exist as thick sequences called strata. Strata differ not only in rock type but also in geophysical parameters such as propagation velocity and bulk density. When a seismic wave is incident on the boundary between two strata or layers, the normal circumstance is that some of the incident energy is reflected in the first layer and some is transmitted into the second layer. Whether a P-wave or an SV-wave is incident on the boundary, there will usually be reflected P- and S-waves and transmitted P- and S-waves. *Snell's Law* (Fig. 3-8) predicts the resulting ray paths for the waves generated at the interface. In each of the four cases, a P-wave is incident on the interface at an angle θ_0 —the angle between the ray and perpendicular to the boundary. P- and S-wave velocities in layer 1 are V_{P1} and V_{S1} , respectively. P- and S-wave velocities in layer 2 are V_{P2} and V_{S2} , respectively.

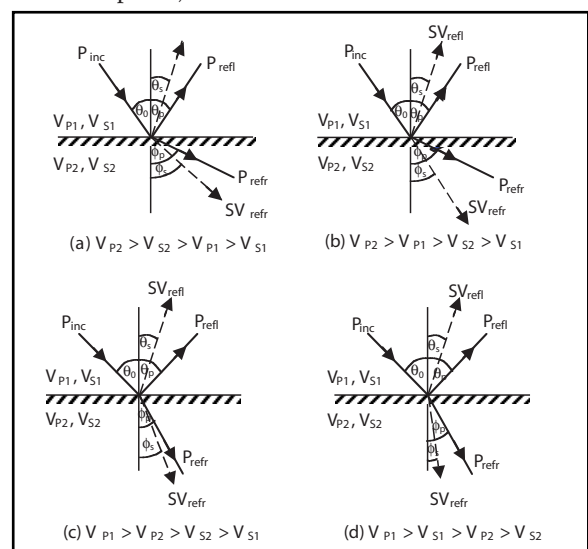


Fig. 3-8 Snell's Law

In Figure 3–8a, the P-wave and S-wave velocities in the second layer are faster than the P-wave velocity in the first layer. Consequently, the transmitted P- and SV-waves are bent, or refracted, at angles greater than the incident angle. That is, they are bent toward the horizontal. In the first layer, the angle of reflection for the P-wave equals the incident angle, but the angle of reflection for the reflected SV-wave is smaller. This is because the S-wave velocity is slower than the P-wave velocity. The refraction angle of the SV-wave in the second layer is also smaller than that of the refracted P-wave.

In Figure 3–8b, the P-wave velocity in the second layer is still the fastest but the S-wave velocity in the second layer is slower than the P-wave velocity in the first layer. Thus, the angle of refraction for the SV-wave is now smaller than the angle of incidence.

In Figure 3–8c, the P-wave velocity in the first layer is faster than the P-wave velocity in the second layer so the angle of refraction for the P-wave is less than the angle of incidence—bent toward the vertical). Since the S-wave velocity in layer 2 is faster than the S-wave velocity in layer 1, the angle of refraction for the SV-wave is greater than the angle of reflection for the SV-wave.

In Figure 3–8d, the P-wave velocity in the first layer is faster than the P-wave velocity in the second layer and the S-wave velocity in the first layer is also faster than the S-wave velocity in the second layer. As a result, the angle of refraction for the P-wave is less than the angle of incidence, and the angle of refraction for the SV-wave is less than the angle of reflection for the SV-wave.

The following summarizes Snell's law:

$$\frac{\sin\vartheta_o}{V_{P1}} = \frac{\sin\vartheta_P}{V_{P1}} = \frac{\sin\vartheta_S}{V_{S1}} = \frac{\sin\phi_P}{V_{P2}} = \frac{\sin\phi_S}{V_{S2}} = p \quad (3.7)$$

where

p is the ray constant

The first two terms of Equation 3.7 correspond to reflection in the upper layer and since the velocities are the same, $\sin\vartheta_p = \sin\vartheta_0$. This is the *Law of Reflection*. Generalizing from the first, fourth, and fifth terms, the *Law of Refraction* can be written as $\sin\vartheta_2 = \frac{v_2}{v_1} \sin \vartheta_1$, where ϑ_2 is the angle of refraction, v_2 is velocity in the lower layer for the refracted wave, ϑ_1 is the angle of incidence, and V_1 is velocity in the upper layer for the incident wave.

There are two exceptions to the preceding discussion. The first is the case of an incident SH-wave. In this case, no P-waves or SV-waves are generated so only reflected and refracted SH-waves result.

$$\frac{\sin\theta_0}{V_{S1}} = \frac{\sin\theta_S}{V_{S1}} = \frac{\sin\phi_S}{V_{S2}} \quad (3.8)$$

The second exception is when the angle of incidence exceeds the critical angle. The critical angle is the angle of incidence at which the angle of refraction is 90° . Actually, there are two critical angles, one for P-waves and one for S-waves. In the first case:

$$\frac{\sin\theta_{cp}}{V_{P1}} = \frac{\sin 90^\circ}{V_{S2}} = \frac{1}{V_{S2}} \text{ so } \sin\theta_{cp} = \frac{V_{P1}}{V_{S2}} \quad (3.9)$$

Similarly, for the SV:

$$\frac{\sin\theta_{cs}}{V_{P1}} = \frac{\sin 90^\circ}{V_{S2}} = \frac{1}{V_{S2}} \text{ so } \sin\theta_{cs} = \frac{V_{P1}}{V_{S2}} \quad (3.10)$$

The existence of a critical angle requires that the layer into which transmission occurs have a higher velocity than in the incident layer. That is, $V_{P2} > V_{P1}$ for critical P-waves and $V_{S2} > V_{P1}$ for critical S-waves. If the angle of incidence is larger than the critical angle, then no energy is transmitted into the lower layer.

From the ray theory point of view, a critically refracted wave travels along the interface between layers and is refracted back into the upper layer at the critical angle, as shown in Figure 3-9. The waves refracted back into the upper layer are called *head waves* or sometimes *first-break refractions* because at certain distances from a source they are the first-arriving energy.

The problem with ray theory is that a ray is one dimensional, showing only direction and only an infinitesimal amount of energy can be transmitted along a ray. To explain phenomena involving finite amounts of energy requires use of *wavefronts*.

A wave front can be defined as the locus of all points reached at the same time by a wave. It turns out that rays intersect wavefronts at right angles. Figure 3-10 illustrates the relationship between wavefronts and rays.

Figure 3-11 shows wavefronts corresponding to the time required for energy to be reflected from the bottom of the first layer and return to the surface at the energy source point. Since a constant velocity is assumed, the direct and reflected wavefronts are spherical. The refracted wavefront, however, is not spherical because it does not come from a single point. The figure also shows that the head wave energy does not penetrate the lower layer. Its wavefront, which has the shape of a truncated cone, results from a coupling between the reflected and refracted wavefronts.

Huygen's Principle (Fig. 3-12) is very important to studies of seismic wave propagation. Its definition from Sheriff's *Encyclopedic Dictionary of Exploration Geophysics* is, "The concept that every point on an advancing wavefront can be regarded as the source of a secondary wave and the later wavefront is the envelope tangent to all the secondary waves."

Seismic amplitudes

To this point, no mention has been made of the amplitudes of reflected and refracted seismic waves. Zoeppritz derived a relationship governing the reflection and transmission coefficients for plane waves as a function of angle of incidence and six parameters, three on either side of the reflecting interface. These are V_p , V_s , and density. The equation is complex, and its solution is laborious. Figure 3-13 is representative of P- and SV-wave reflection coefficients derived from the Zoeppritz equations.

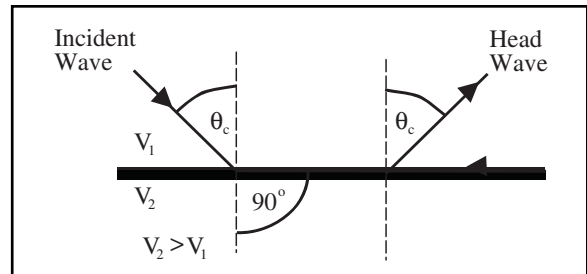


Fig. 3-9 Critical Refraction and Head Waves

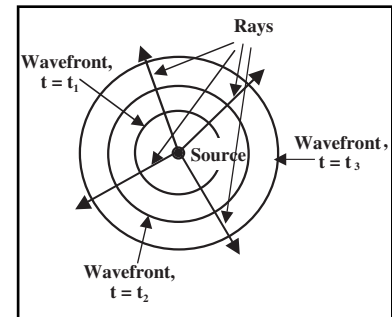


Fig. 3-10 Wavefronts and Rays

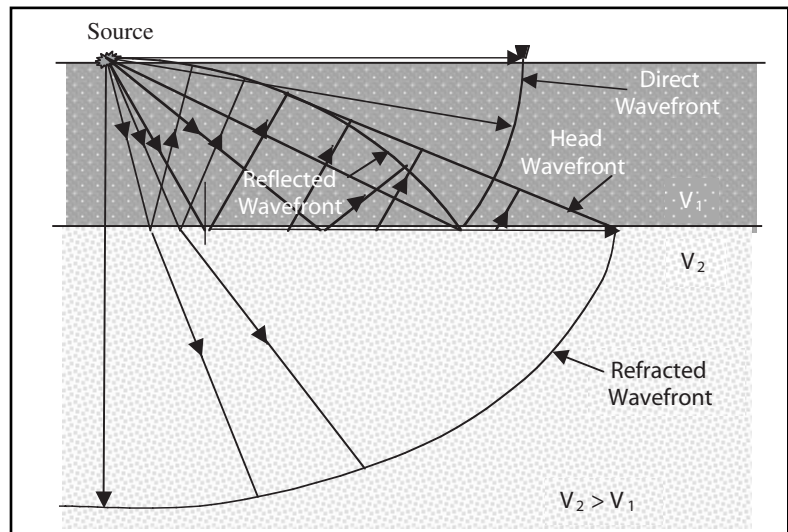


Fig. 3-11 Wavefronts from a Point Energy Source

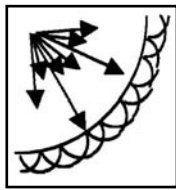


Fig. 3-12
Huygen's
Principle

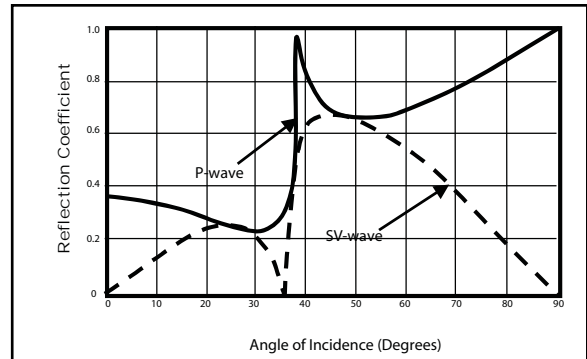


Fig. 3-13 P- and SV-wave Reflection Coefficients

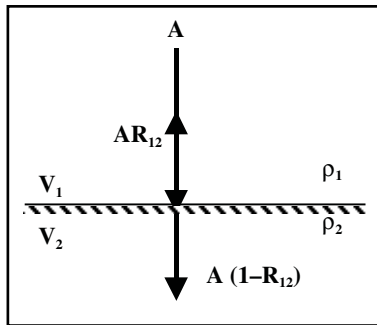


Fig. 3-14 P-wave Normal Incidence Reflection and Transmission

At normal incidence (angle of incidence equals 0°) of a P-wave, no reflected or refracted SV-wave is generated. (Fig. 3-14)

As a result, a simplified expression for P-wave *reflection* and *transmission coefficients* at normal incidence can be developed. These are:

$$R_{12} = \frac{\rho_2 V_2 - \rho_1 V_1}{\rho_2 V_2 + \rho_1 V_1} \quad (3.11)$$

and

$$T_{12} = 1 - R_{12} = \frac{2\rho_1 V_1}{\rho_2 V_2 + \rho_1 V_1} \quad (3.12)$$

where

R_{12} = P-wave normal incidence reflection coefficient at the interface separating layers 1 and 2

T_{12} = P-wave normal incidence transmission coefficient at the interface separating layers 1 and 2

ρ_1, ρ_2 = Bulk density of layers 1 and 2, respectively

V_1, V_2 = P-wave velocities of layers 1 and 2, respectively

Introducing the concept of *acoustic (or seismic) impedance*, $Z = \rho V$, the reflection and transmission coefficients can be written as:

$$R_{12} = \frac{Z_2 - Z_1}{Z_2 + Z_1} \quad (3.13)$$

and

$$T_{12} = \frac{2Z_1}{Z_2 + Z_1} \quad (3.14)$$

where

Z_1, Z_2 = acoustic impedance of layers 1 and 2, respectively

The seismic record

The objective of seismic data acquisition is to obtain data that can be related to subsurface geology. At various points on or near the Earth's surface, an energy source is used to generate seismic waves that travel downward and are reflected at interfaces between geologic strata that differ in acoustic impedance. The reflected energy returns to the surface where it is detected and recorded. This reflected energy is called *signal* or *primary reflections*. From the times at which the primary reflections were recorded and their amplitudes, it is desired to obtain the Earth's *reflectivity function*. This is a set of impulses with amplitudes

proportional to the reflection coefficient of each interface and time of occurrence equal to the *two-way reflection time*. The impulse response can then be related to the geologic section from which data were acquired (Fig. 3-15).

Unfortunately, the primary reflection impulse response cannot be recorded directly. It is impossible to record impulses; instead reflections are recorded as *wavelets* whose shapes depend upon the energy source used and transmission losses along the reflection path, as seen in Figure 3-16. For that matter, a seismic record cannot be constrained to record signal only.

Anything on a seismic record other than primary reflections is called *noise*. There are several kinds of noise, but all can be placed in two categories—*source-generated* and *ambient noise*. Table 3-1 summarizes source-generated noise observed on seismic records.

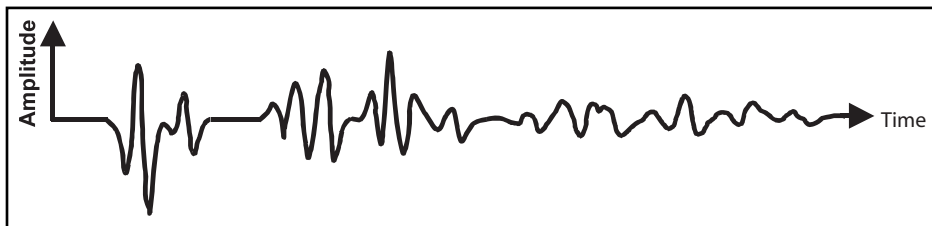


Fig. 3-16 Noise-free Seismic Trace Derived from Earth Reflectivity Function

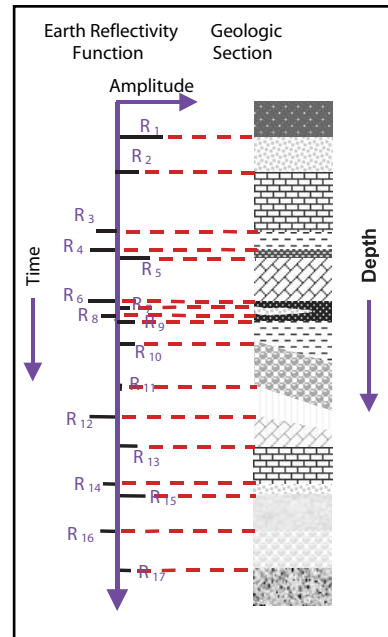


Fig. 3-15 Earth Reflectivity Function

Table 3-1 Source-generated Noise

Type	Description	Appearance on Seismogram
Direct Waves	Waves propagating directly from shot	High amplitude first events on near traces
Ground roll	Wave propagation along ground surface	Usually low frequency and low apparent velocity
Air waves	Sound waves from shot	Very low apparent velocity (1100 ft/sec)
Shallow refraction	Near-surface refracted wave	High amplitude, often first events on far traces
Reverberations	Ghosts; tails on shot pulse	Tails on reflected events
Multiples (long period)	Repeated reflection	Reflections at even time intervals after the primary reflection
Guided waves	Multiples of direct wave and shallow refractions	Events paralleling first breaks
Diffractions	Wave energy propagated in all directions from a point such as a fault interface	Coherent hyperbolic events

Either the direct arrivals or the shallow refraction (head wave) are the first events seen on seismic records are either direct arrivals or refractions. Direct arrivals travel a direct path from source to the nearest receivers. Refractions, or head waves (Fig. 3-17), travel from source down to the base of near-surface layer, then more or less horizontally, and, finally, back up to the farther receivers.

As previously discussed, ground roll is really a Rayleigh wave. The heterogeneity of the surface layer distorts the retrograde elliptical particle motion somewhat. Velocity increases with depth in the surface layer. The longer wavelength components of the ground roll penetrate more deeply in the surface layer than the shorter wavelengths and thus see higher velocities. Longer wavelength means lower frequency since $f = V/\lambda$ (Fig. 3-6). Ground roll occurs as a set of dispersed wave trains with the lower frequency, longer wavelength components arriving first.

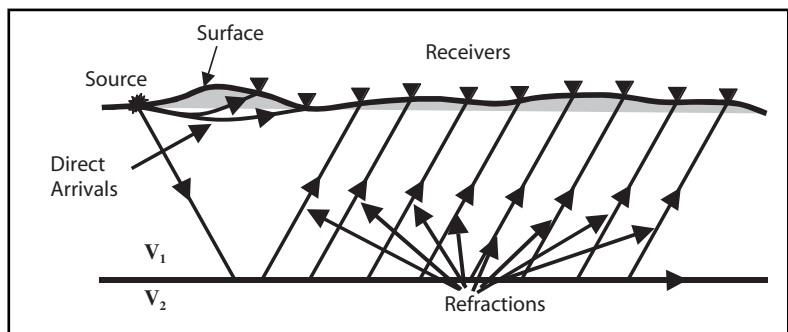


Fig. 3-17 Direct Waves and Shallow Reflections

Airwaves are simply sound generated by the source traveling through the air.

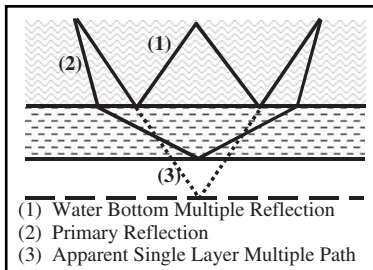


Fig. 3-18 Reverberations or Water Bottom Multiple Reflections

Multiple reflections are of three types.

- *Simple multiples* or *reverberations* (multiple reflections in a water layer) simply repeat the primary reflection raypath as seen in Figure 3-18. Simple multiples are not restricted to the water layer.
- *Peg-leg multiples* add a reflection in the surface layer to the primary reflection raypath.
- *Interbed multiples* have a repeat reflection within a layer.

Figure 3-19 illustrates peg leg and interbed multiples.

Guided waves are trapped energy in surface layers—reflected refractions that appear to be multiples of first break refractions. Figure 3-20 illustrates guided wave raypaths.

Diffractions are scattered energy from a subsurface point, such as the truncation of a reflector caused by a fault. Figure 3-21 illustrates diffractions.

The second type of noise, or unwanted recording, is called ambient noise. Perhaps the best way to describe ambient noise is that it is what would be recorded if a seismic record were made without an energy source being fired. Table 3-2 lists various types of ambient noise.

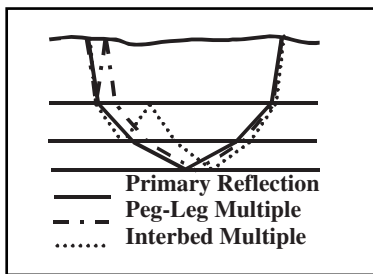


Fig. 3-19 Multiple Reflections

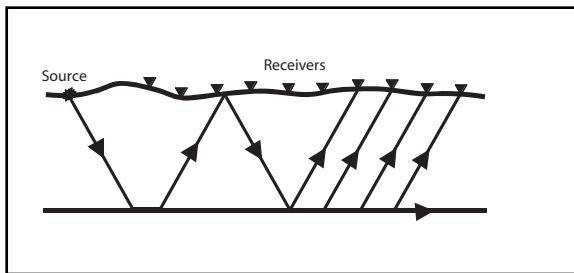


Fig. 3-20 Guided Waves

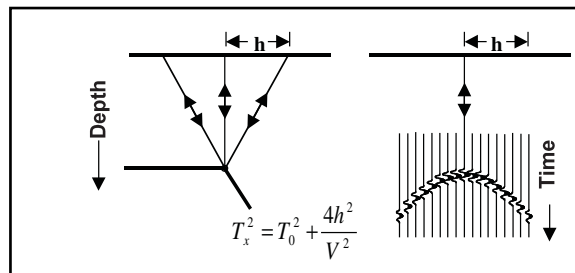


Fig. 3-21 Diffractions

Table 3-2 Ambient Noise

Type	Description	Appearance on Seismogram
Traffic	Cars, animals, people	Often seen as spikes
Wind	Air currents	High frequency
Earthquakes	Any motion produced from within the earth by other than the seismic source	Usually very low frequency
Highline noise	Induced noise from nearby power lines	50 or 60 Hz
Shot hole	Debris falling from the blown shot hole	Both high and low frequency, fanning from the source point
Instrument	From recording instruments	Usually high frequency, noise should be very low level

Figure 3-22a is the noise-free trace of Figure 3-16 and Figure 3-22b shows the same trace with the addition of ambient noise.

A seismic shot record is a set of seismic traces recorded at one time from a single source. The number of traces on a record varies considerably, sometimes more than a thousand traces per record. Figure 3-23, a schematic land seismic record, shows the different kinds of events recorded on a seismic record. Figure 3-24 shows a real seismic shot record.

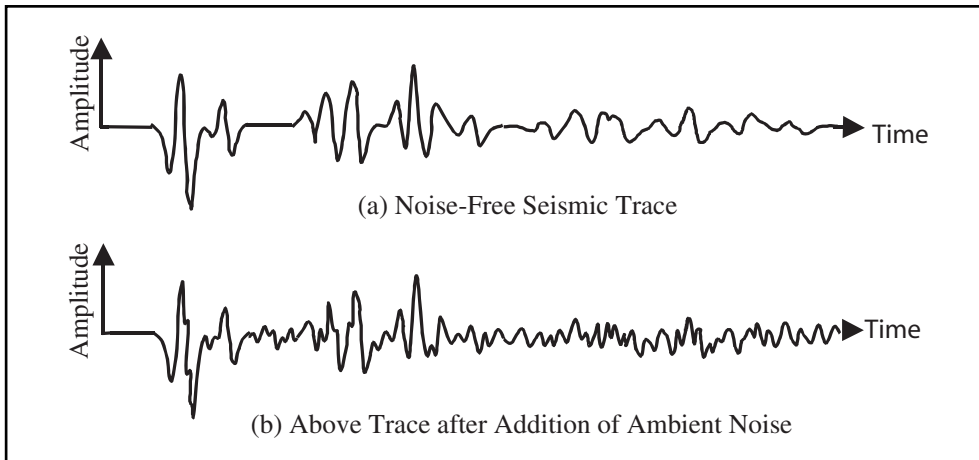


Fig. 3-22 Effect of Ambient Noise on Seismic Trace

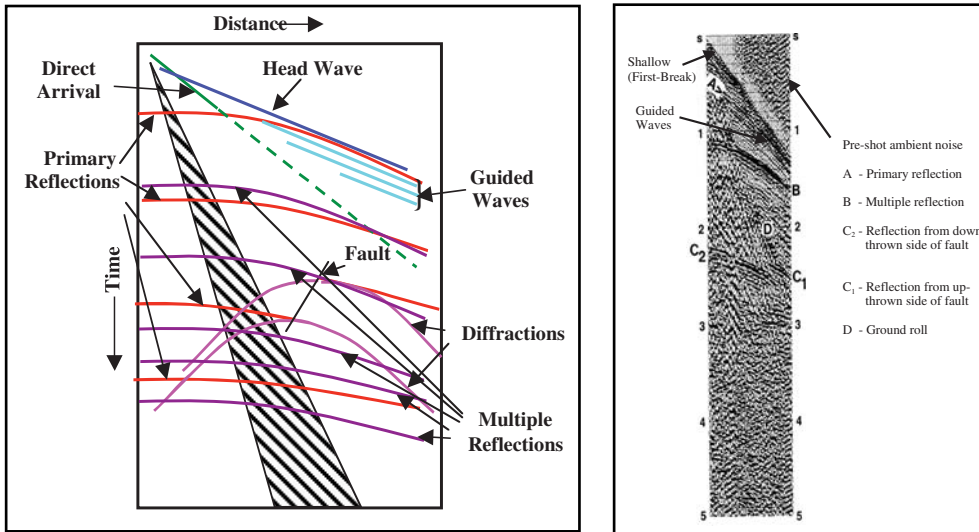


Fig. 3-23 Schematic Land Seismic Record

Fig. 3-24 A Seismic Shot Record

Mathematical Theory and Concepts

As with any scientific-based discipline, seismic exploration makes considerable use of mathematics. Much of seismic data processing is based on a branch of mathematics called *Statistical Communication Theory*. Details of that theory are beyond the scope of this text but some of the basic concepts and applications of it will be presented. One aspect of modern seismic exploration methods results in a simplification of mathematical tools required. Since seismic data are recorded as *sampled* data, integration reduces to summation and differentiation to subtraction.

Sampled data

In the early days of seismic exploration, data were recorded in analog form. That is, there was a representation of every change in the wavefield. At first, seismic data were recorded optically (light on photographic paper). Later, analog magnetic tape was used. In this case, the amplitude of the seismic data was represented by a continuously varying magnetic intensity. Since the late 1960s, digital recording has been used. Digital recording samples the incoming analog signal at regular time intervals and records the data as a binary number representing the voltages of the samples. A continuous signal is input to the sampler and a set of numbers or time series is output. Figure 3-25 illustrates sampling and reconstruction of the sampled data to analog form.

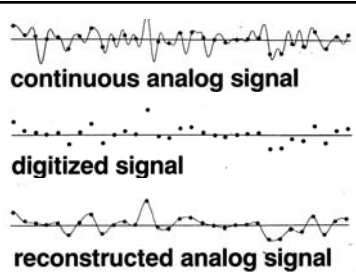


Fig. 3-25 Digital Recording

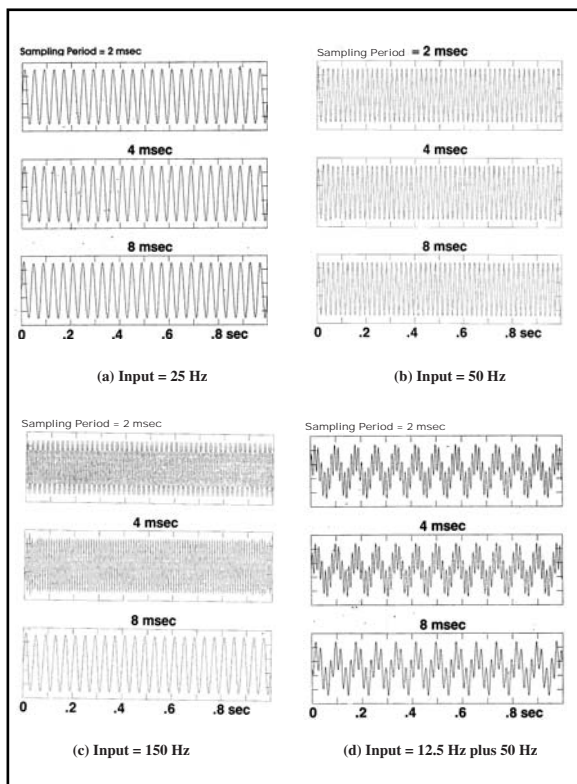


Fig. 3-26 Effect of Sample Period

Analyzing the data of Figure 3-26, it can be seen that the 25-Hz sinusoid is below Nyquist for all three sample periods. The 75-Hz signal is lower than f_N for 2 and 4 ms sampling but above f_N for 8 ms sampling. From Table 3-3, the Nyquist frequency for 8 ms is 62.5 Hz and 75 Hz is 12.5 Hz more than f_N . The output frequency f_o is 50 Hz or 12.5 Hz less than f_N .

Table 3-3 Nyquist Frequency

DT (ms)	f_N (Hz)
0.5	1000
1	500
2	250
4	125
8	62.5

In most cases, the ability to correctly reconstruct a digital signal depends upon the frequency content of the signal and the sampling increment.

Figure 3-26 shows the effect of sampling at different *sample increments* or *sample periods*. In Figure 3-26a, the input is a 25-Hz sinusoid. The reconstructions of the outputs sampled at 2 ms, 4 ms, and 8 ms are the same as the input. In Figure 3-26b, the input is a 75-Hz sinusoid. The reconstructions of the outputs sampled at 2 ms and 4 ms are the same as the input, but the output sampled at 8 ms is a 25-Hz sinusoid! In Figure 3-26c the input is a 150-Hz sinusoid. The reconstruction of the output sampled at 2 ms is the same as the input, but the 4 ms output is a 100-Hz sinusoid and the 8 ms output is a 25-Hz sinusoid!

In Figure 3-26d, the input is the sum of 12.5-Hz and 75-Hz sinusoids but the reconstructed output is the sum of 12.5 and 25-Hz sinusoids. What is being demonstrated here is the phenomenon called *aliasing*.

The *Sampling Theorem* can be stated as follows:

An analog signal which is band-limited to frequencies less than f_o is completely described by samples taken at intervals of time Δt , where $\Delta t < 1/2f_o$. Conversely, then, an analog signal band-limited to signals less than f_o can be completely recovered from samples taken at intervals of time Δt , if $f_o < 1/2\Delta t$. If, however, a signal sampled at a sample interval Δt contains frequencies higher than $f_N = 1/2\Delta t$, where f_N is the Nyquist or alias frequency, it cannot be correctly recovered (using conventional processing techniques) because of a distortion called aliasing.

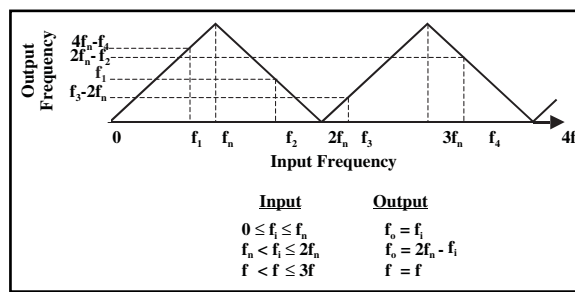


Fig. 3-27 Aliasing

At 4 ms sampling, the 150-Hz sinusoid is 25 Hz above f_N and its output of 100 Hz is 25 Hz below f_N . At 8 ms sampling, the 150-Hz sinusoid is 87.5 Hz above f_N or and 25 Hz above $2f_N$. Its output of 25 Hz is equal to the difference between the input and $2f_N$. Figure 3-27 is a chart for calculating output frequencies relative to input and multiples of f_N .

To prevent aliasing, a filter must be applied before sampling or resampling to a larger sample period, and a filter must be applied to limit frequencies to below Nyquist.

Convolution and correlation

Earlier in this chapter, the concept of the earth reflectivity function was introduced. This is a special kind of *impulse response*. An impulse response is measured by inputting a unit impulse (spike or Dirac delta function) into the system and recording the system output. Figure 3–28 illustrates this by considering the earth to be a system. Each reflecting horizon produces an impulse with amplitude equal to its vertical reflection coefficient and a time delay equal to the two-way reflection time to the horizon.

Figure 3–16 presents a noise-free seismic trace derived from an earth impulse response but does not explain how it was derived. The method used is called *convolution*. Given the impulse response of a system, $e(t)$ is the output of the system, $o(t)$ an arbitrary input, and $w(t)$ is given by the convolution of the input and the system impulse response. Expressed mathematically, this is:

$$o(t) = w(t)^* e(t)$$

where convolution is symbolized by the asterisk *

For sampled data, convolution of the sampled set $\{x_n\}$ with sampled set $\{y_m\}$ is calculated from:

$$w_n = \sum_{i=0}^m x_i y_{i-n} = \sum_{j=0}^p x_{j-n} y_j \quad (3.15)$$

where

- $\{x_m\}$ = the $m+1$ sample values of the input $x(t) = \{x_0, x_1, x_2, \dots, x_m\}$
- $\{y_p\}$ = the $p+1$ sample values of the input $y(t) = \{y_0, y_1, y_2, \dots, y_p\}$

The convolution of $\{x_m\}$ and $\{y_p\}$ can be calculated by performing the following steps:

1. Time reverse either $\{x_m\}$ or $\{y_p\}$.
2. Shift the reversed series to the left until only one sample of $\{x_m\}$ and $\{y_p\}$ or $\{x_m\}$ and $\{y_p\}$ are aligned in time.
3. Multiply the aligned x and y values. This is the first output.
4. Shift the reversed series one sample to the right.
5. Multiply the aligned x and y values and sum the products. This is the next output.
6. Repeat steps 4 and 5 until no samples are aligned.

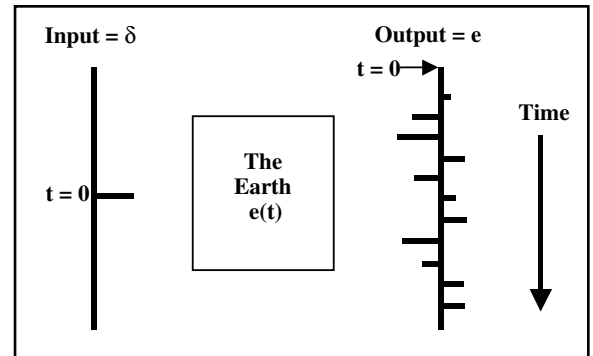


Fig. 3–28 Measuring the Earth's Impulse Response

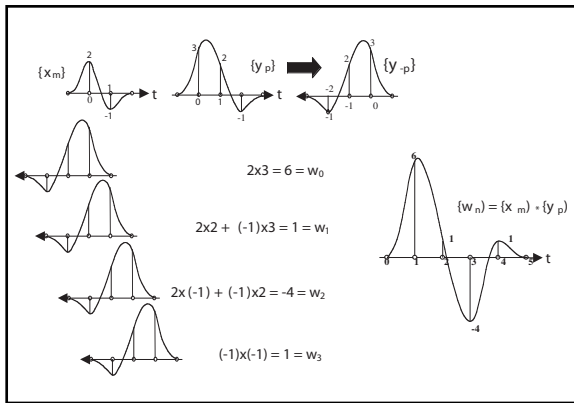


Fig. 3-29 Convolution

Figure 3-29 illustrates convolution using $\{x_m\} = \{2, -1\}$ and $\{y_p\} = \{3, 2, -1\}$.

Convolution is an operation describing the interaction between an input and a system of some sort. Computationally, the outcome of the operation is the same whichever time series is time reversed. Also, note that the convolution of any time series with a unit impulse is simply the input time series. Convolution with a time-delayed unit impulse gives a time-delayed version of the input time series.

Cross-correlation is a process or procedure for measuring the similarity of one time series to another. Computationally, correlation and convolution appear similar. For sampled data, the cross-correlation of $\{x_m\}$ with $\{y_p\}$ is:

$$\varphi_{\lambda}^{xy} = \sum_{i=0}^m x_i y_{i-\lambda} \quad (3.16)$$

The steps taken to crosscorrelate $\{y_p\}$ onto $\{x_m\}$ follow.

1. Shift $\{y_p\}$ to the left until only one sample of the two time series is aligned.
2. Cross multiply the two aligned values. This is the cross-correlation for the $-n^{th}$ lag, where n is the number of sample periods $\{y_p\}$ was shifted left.
3. Shift $\{y_p\}$ to the right one sample period and cross multiply the two aligned value.
4. Sum the cross products. This is the cross-correlation for the $-(n-1)^{th}$ lag
5. Repeat steps 3 and 4 until only one sample of each time series are aligned. The output lag value increments by +1 for each shift to the right.

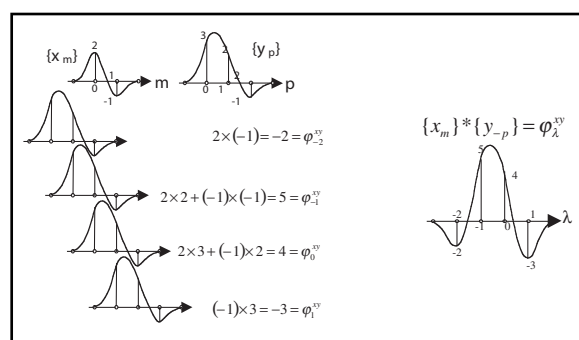
Fig. 3-30 Cross-correlation of $\{y_p\}$ onto $\{x_m\}$

Figure 3-30 uses the same two time series that were convolved together to demonstrate cross-correlation. Note how different the cross-correlation is from the convolution of these two wavelets. Also, it can be seen that the two wavelets are most similar at a lag of -1 . Since convolution requires that one time series be time reversed but cross-correlation does not, it can be seen that convolution of a time-reversed time series with another is equivalent to cross-correlation — $\{x_m\} * \{y_p\} = \varphi_{\lambda}^{xy}$.

Another difference between cross-correlation and convolution is that the output *does* depend upon which of the time series is shifted past the other. Figure 3-31 demonstrates this by crosscorrelating $\{x_m\}$ onto $\{y_p\}$, i.e. $-\varphi_{\lambda}^{yx}$. Comparing the two cross-correlations shows that one is the time reversed version of the other, that is $\varphi_{\lambda}^{yx} = \varphi_{-\lambda}^{xy}$.

Autocorrelation is simply the cross-correlation of one time series with itself. Mathematically

$$\varphi_{\lambda}^{xx} = \sum_{i=0}^m x_i x_{i-\lambda} \quad (3.17)$$

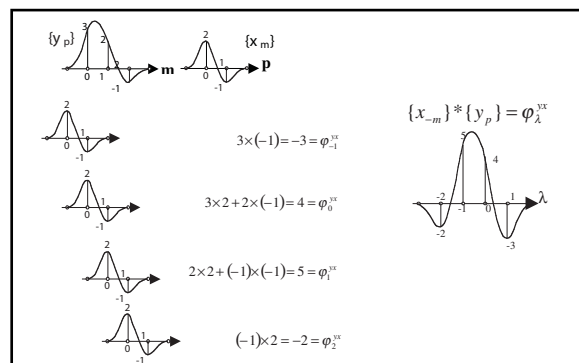
Fig. 3-31 Cross-correlation of $\{x_m\}$ onto $\{y_p\}$

Figure 3–32 illustrates the autocorrelation of $\{x_m\}$. Note that the autocorrelation is symmetrical about $\lambda = 0$. This means that the autocorrelation is an even function. Note also that the maximum value of the autocorrelation is at $\lambda = 0$, and this value equal to the sum of the squares of all the amplitudes in the time series. This is the *power* of the series or wavelet.

Time and frequency domains

To this point, only time series and wavelets defined in terms of amplitudes as functions of time have been discussed. That is, only the *time domain* has been used. In the time domain, a signal is described as having certain amplitudes at certain times. Most signals, traces, etc. can be described in the *frequency domain*.

In the frequency domain, data are described in terms of amplitudes and phases at certain frequencies. The simplest example to illustrate this is a single-frequency sinusoid, illustrated in Figure 3–33. On the right of the figure, a mass is shown suspended from a spring and a light source is attached to the mass. The light shines on photographic film that moves from right to left. When the film is developed, a picture such as that shown at the top or bottom of Figure 3–33 will be seen.

The trace seen on the developed film can be described by

$$y(t) = A \cos(2\pi t/T + \phi)$$

where

T is the period of time for the suspended mass to complete one cycle of its motion (from its highest to lowest position and back)

ϕ is the phase added to indicate the position of the mass in its cycle relative to the rest position (one cycle corresponds to 2π radians or 360°)

Alternatively, the trace can be described by:

$$y(t) = A \cos(2\pi f t + \phi)$$

where

$$f = \text{frequency} = 1/T$$

The latter of these expressions is the usual time domain description of a single-frequency sinusoid.

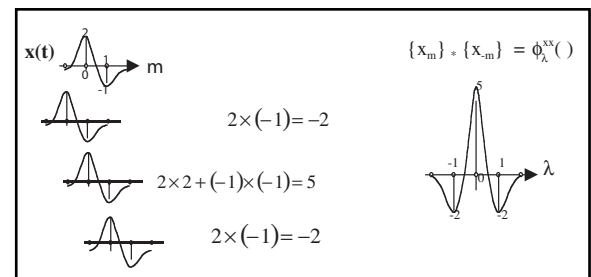


Fig. 3-32 Autocorrelation of $\{x_m\}$

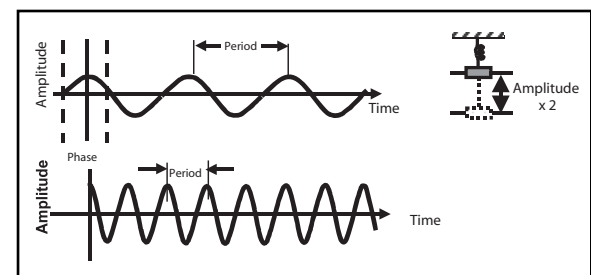


Fig. 3-33 Single Frequency Sinusoids

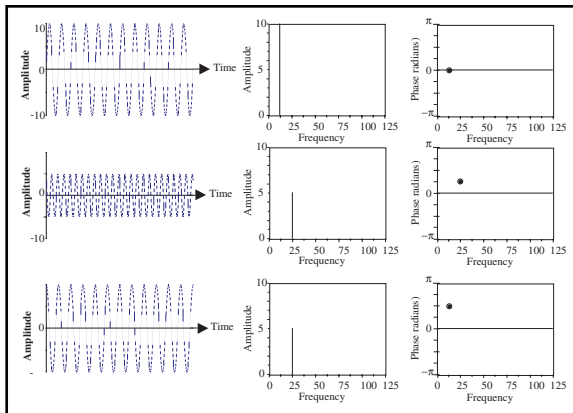


Fig. 3-34 Amplitude and Phase Spectra for Single-frequency Sinusoids

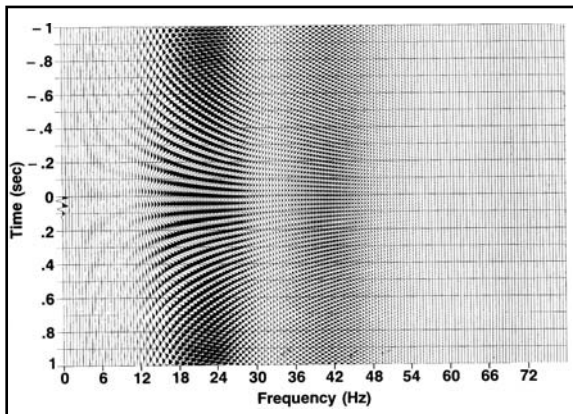


Fig. 3-35 Signal Synthesis and Decomposition

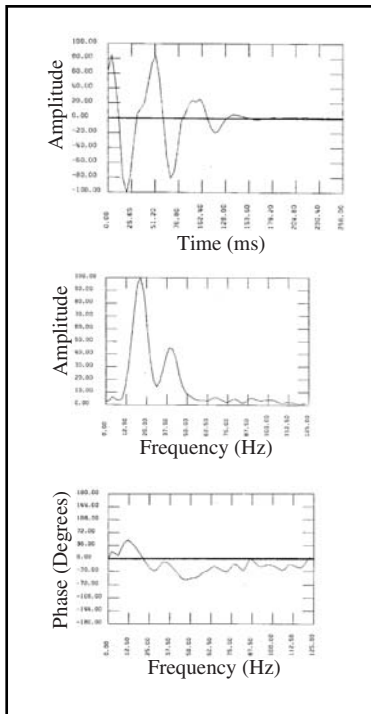


Fig. 3-36 Time and Frequency Domains

To describe something in the frequency domain requires both an *amplitude spectrum* and a *phase spectrum*. The amplitude spectrum simply gives an amplitude at each frequency. The phase spectrum similarly gives the phase at each frequency. A single frequency sinusoid has only one amplitude and one phase value, as shown in Figure 3-34. The top and bottom sinusoids have the same frequency and amplitude but different phase. The top and middle sinusoids differ in frequency, amplitude, and phase.

By combining many sinusoids having different amplitudes, phases, and frequencies, complex signals can be synthesized. Conversely, many complex signals can be decomposed into constituent sinusoids having different amplitudes, phases, and frequencies. An example is shown in Figure 3-35.

On the far left of Figure 3-35 is a time domain signal or wavelet similar in appearance to many seismic wavelets. To the right of the wavelet is a set of single frequency sinusoids, with frequencies ranging from 0.5 Hz to 78 Hz. The wavelet is synthesized by summing all these sinusoids. On the other hand, the wavelet can be decomposed into these wavelets.

A plot of each sinusoid's amplitude against its frequency yields an amplitude spectrum. A plot of each sinusoid's phase against its frequency yields a phase spectrum. These are shown in Figure 3-36 for the data of Figure 3-35. Also shown in Figure 3-36 is the time domain wavelet. The amplitude and phase spectra describe the sinusoids that can be summed to synthesize the time domain wavelet. Thus, it can be seen that the time and frequency domain descriptions are equivalent.

The mechanism that allows transformation from the time to the frequency domain is the *Fourier Transform* and the *Inverse Fourier Transform* is used to transform from the frequency domain to the time domain. For sampled data, the Fourier Transform of the time series $\{g_n\}$ is given by:

$$F\{g(\Delta T)\} = G(m\Delta f) \sum_{n=0}^N g_n e^{-j2\pi mn\Delta f \Delta T}, \quad m=0, 1, 2, \dots, M \quad (3.18)$$

where

$F\{g(\Delta T)\}$ = Fourier Transform of $\{g(\Delta T)\}$

$G(m\Delta f)$ = frequency spectrum of the time series $\{g_n\}$ at the frequency $m\Delta f$

g_n = n^{th} amplitude of the time series $\{g_n\}$, $n=0, 1, 2, \dots, N$

Δf = frequency increment $= f_n/M\Delta T$ = sample period

$i = \sqrt{-1}$

Taking advantage of the relationship, $e^{-j\theta} = \cos\theta + j\sin\theta$, Equation 3.18 can be written as:

$$G(m\Delta f) = \sum_{n=0}^N \{g(\Delta T)\} [\cos(2\pi mn\Delta f \Delta T) - j \sin(2\pi mn\Delta f \Delta T)] \quad (3.19)$$

It can be seen that, in the general case, the frequency spectrum is complex. Thus, it can be written as:

$$G(m\Delta f) = \text{Re}[G(m\Delta f)] + \text{Im}[G(m\Delta f)]$$

where

$$\text{Re}[G(m\Delta f)] = \sum_{n=0}^N g_n \cos(2\pi mn\Delta f \Delta T), \quad (3.20a)$$

$$\text{Im}[G(m\Delta f)] = \sum_{n=0}^N g_n \sin(2\pi mn\Delta f \Delta T) \quad (3.20b)$$

The amplitude spectrum $A(m\Delta f)$ is given by the absolute value of the frequency spectrum.

$$A(m\Delta f) = |G(m\Delta f)| = \sqrt{\text{Re}[G(m\Delta f)]^2 + \text{Im}[G(m\Delta f)]^2} \quad (3.21a)$$

The phase spectrum $\phi(m\Delta f)$ is given by:

$$\phi(m\Delta f) = -\tan^{-1} \left(\frac{\text{Im}[G(m\Delta f)]}{\text{Re}[G(m\Delta f)]} \right) \quad (3.21b)$$

From the preceding, an alternate way of writing the frequency spectrum is:

$$G(m\Delta f) = A(f) e^{i\phi(f)} \quad (3.22)$$

To completely describe something in the frequency domain requires both an amplitude and a phase spectrum.

The inverse Fourier Transform is calculated from:

$$F^{-1}[G(m\Delta f)] = g(nDT) = \sum_{m=0}^M G(m\Delta f) e^{i2\pi mn\Delta f \Delta T}, \quad n = 0, 1, 2, \dots, N \quad (3.23)$$

where

$$F^{-1}[G(m\Delta f)] = \text{inverse Fourier Transform of } G(m\Delta f)$$

As the length of the time series increases, the computer time required to transform from the time to the frequency domain (or vice versa) increases very rapidly. Consider a 5 s trace, sampled at 2 ms. There are $(5/0.002 + 1) = 2501$ samples in the trace. A modern seismic record usually has hundreds of traces per record and thousands of records in the total data volume. Transforming this quantity of data into the frequency domain would be prohibitively expensive using Equation 3.18 or 3.19. Fortunately, an algorithm (actually, a family of algorithms) has been developed that speeds up the process sufficiently to allow transformation back and forth between time and frequency domains to be quite economical. The algorithm to transform from the time domain to the frequency domain is called the Fast (or Finite) Fourier Transform (FFT), and the algorithm for transforming from the frequency domain to the time domain is the inverse FFT or IFFT.

The Fourier Transform has many interesting properties. For example, it is linear. This means, for example, that if $F\{x_m\} = X(m\Delta f)$ and $F\{y_n\} = Y(m\Delta f)$, then

$$F[ax_m + b y_n] = aX(m\Delta f) + bY(m\Delta f) \quad (3.24)$$

Reversing a wavelet in time is equivalent to changing the polarity of its phase spectrum but the amplitude spectrum stays the same (Fig. 3-37).

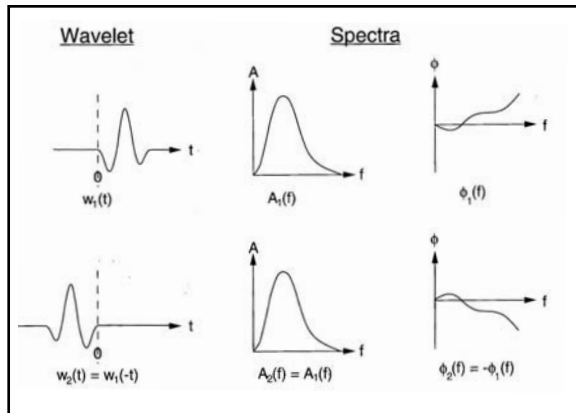


Fig. 3-37 Effect of Time Reversal

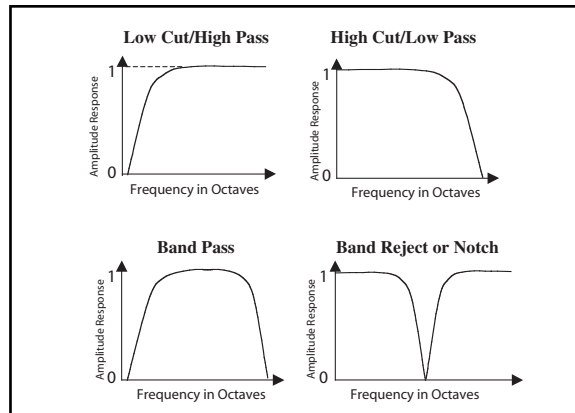


Fig. 3-38 Frequency Filter Types

Convolution in the time domain is equivalent to multiplying in the frequency domain and this is equivalent to multiplying amplitude spectra and summing phase spectra.

$$F[\{x_m\} * \{y_n\}] = [A_x(f)e^{i\phi_x(f)}] \times [A_y(f)e^{i\phi_y(f)}] = A_x(f)A_y(f)e^{i[\phi_x(f)+\phi_y(f)]} \quad (3.25)$$

Multiplication in the time domain is equivalent to convolving frequency spectra in the frequency domain. Cross-correlation in the time domain is equivalent to multiplying amplitude spectra and subtracting phase spectra in the frequency domain. To see this, recall that cross-correlation is equivalent to convolving one time series with another time-reversed time series.

$$\begin{aligned} F[\{\phi_{xy}\}] &= F[\{x_m\} * \{y_{-n}\}] \\ &= [A_x(f)e^{i\phi_x(f)}] \cdot [A_y(f)e^{i\phi_y(f)}] = A_y(f)e^{i[\phi_x(f)-\phi_y(f)]} \end{aligned} \quad (3.26)$$

Autocorrelation in the time domain is equivalent to squaring the amplitude spectrum in the frequency domain the phase spectrum is always zero. Since autocorrelation is the cross-correlation of a time series with itself, it follows from Equation 3.26 that:

$$F[\{\phi_{xx}\}] = F[\{x_m\} * \{x_{-m}\}] = A_x(f)A_x(f)e^{i[\phi_x(f)-\phi_x(f)]} = [A_x(f)]^2 \quad (3.27)$$

When the term filtering is used alone, it usually means frequency filtering. There are four types of filters, based on what they do. These are illustrated by amplitude responses of Figure 3-38.

Filters are defined by parameters called *cutoff frequency* and *attenuation rate*. Before defining these, definitions of two terms, *decibels* (dB) and *octaves* need to be provided. Decibels are a logarithmic measure of relative amplitude. They are calculated from:

$$A_{dB} = 20 \log \left(\frac{A}{A_0} \right) \quad (3.28)$$

where A_0 is the normalization amplitude (often the largest amplitude for a time series, trace, etc.)

Octaves are a measure of relative frequency or frequency range. If frequency f_2 equals $2f_1$, then f_2 is one octave above f_1 . If frequency f_2 equals $4f_1$, then f_2 is two octaves above f_1 . If frequency f_2 equals f_1 , then f_2 is one octave below f_1 . In the general case, the number of octaves, n , between frequencies f_2 and f_1 is given by:

$$n = \frac{\log \left(f_2 / f_1 \right)}{\log 2} \quad (3.29)$$

The cutoff frequency f_{c0} is the frequency at which the response is -3dB. The attenuation rate is usually stated as the number of dB/octave the filter amplitude response decreases beyond the cutoff frequency.

When data are filtered, the input amplitude spectrum is multiplied by the filter amplitude response. At frequencies where the filter amplitude response is less than one, attenuation takes place as seen in Figure 3-39. Thus the idea of filtering is to reduce or attenuate frequency components where noise dominates over signal. A low cut (high pass) filter attenuates frequencies less than the cutoff frequency. A high cut (low pass) filter attenuates frequencies above the cutoff. A bandpass filter attenuates frequencies below its low cutoff frequency and above its high cutoff frequency. (The difference between these two cutoff frequencies is the pass band.) A band reject filter attenuates frequencies between its low and high cutoff frequencies.

Figure 3-40 illustrates a special kind of high cut filter—an *anti-alias filter*. If the sampled input contains frequency components greater than $1/2\Delta T$ where ΔT is the sample period, then aliasing occurs. To avoid this, an anti-alias filter is usually applied. In Figure 3-40, the input data were filtered with the filters whose amplitude responses are shown on the far right before sampling.

Filters have phase responses as well as amplitude responses. When a filter is applied to input data, the output phase spectrum is the sum of the filter phase response and the input phase spectrum. Thus, filtering is the frequency domain equivalent of convolving an input time series with a filter impulse response.

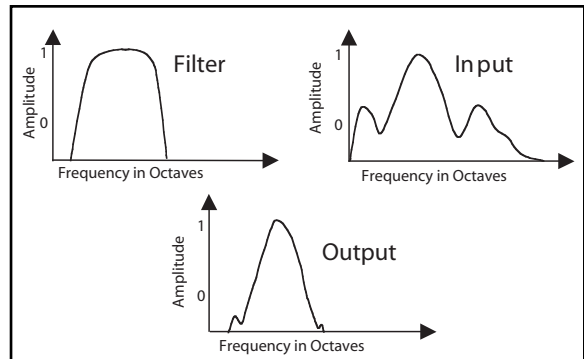


Fig. 3-39 Bandpass Filtering

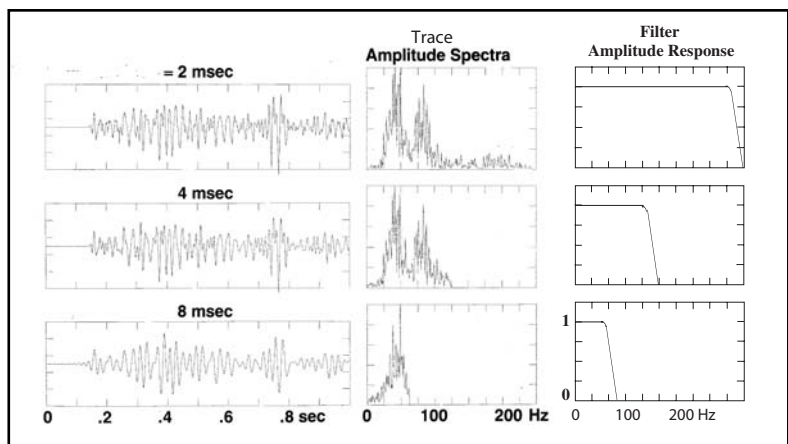


Fig. 3-40 Anti-alias Filters

Phase and its effect on waveforms

As previously stated, phase is an angular measurement of position of a sinusoid at the time observation begins. The terms phase *lead* and *lag* are also used. Figure 3-41 defines these terms and the method of phase measurement. Note that the cosine wave is the sinusoid of reference since it is a maximum at time zero and is an even or symmetrical waveform. It is also zero phase.

A wavelet can be zero phase only if all its constituent frequency components are zero phase. Such a wavelet is shown in Figure 3-42a. Figure 3-42b shows the effect of adding 90° to the phase of every frequency component. The amplitude spectrum has not been changed, but simply adding 90° to the phase spectrum makes a drastic change in the waveform. Figure 3-43 shows the changes in waveform as the phase spectrum is modified by successive additions in 90° increments.

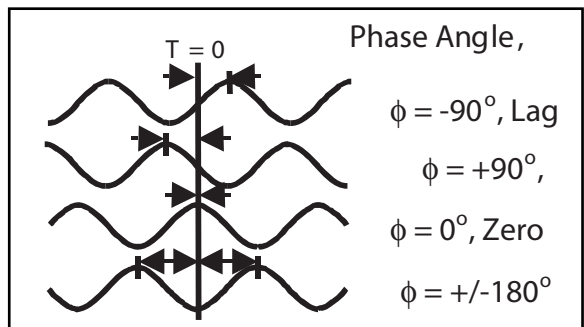


Fig. 3-41 Phase Definitions

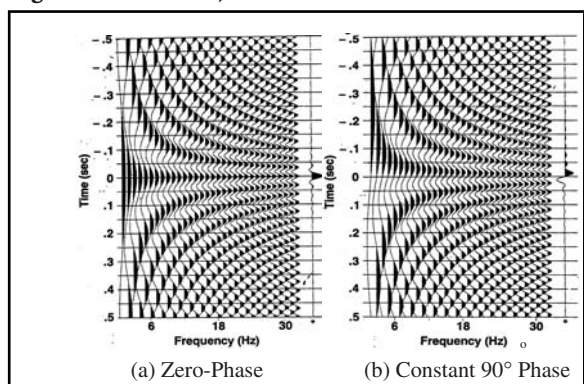


Fig. 3-42 Effect of Adding 90° to Phase Spectrum

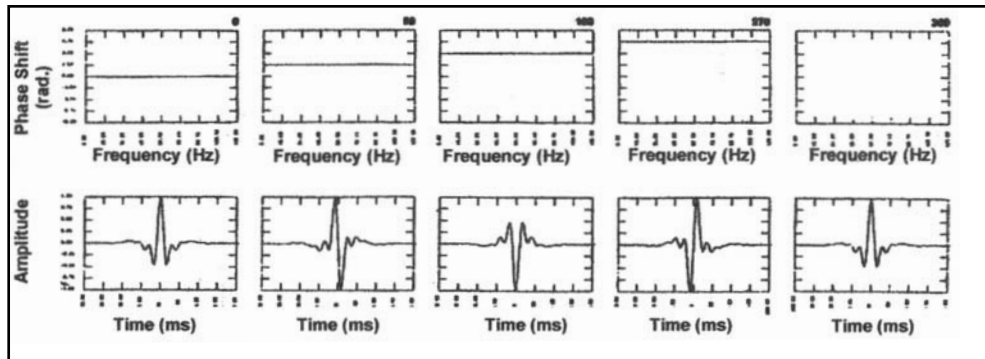


Fig. 3-43 Changes in Waveform with Successive Additions of 90° Phase

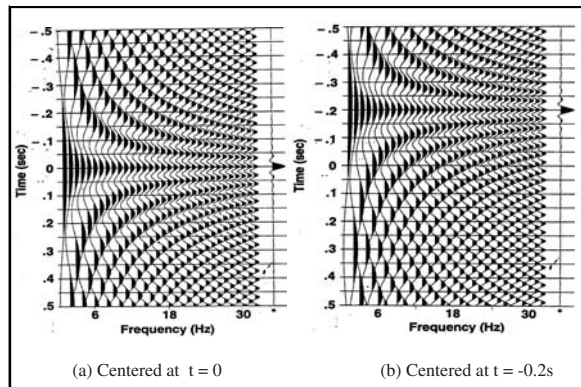


Fig. 3-44 Effect of Adding Linear Phase-to-phase Spectrum

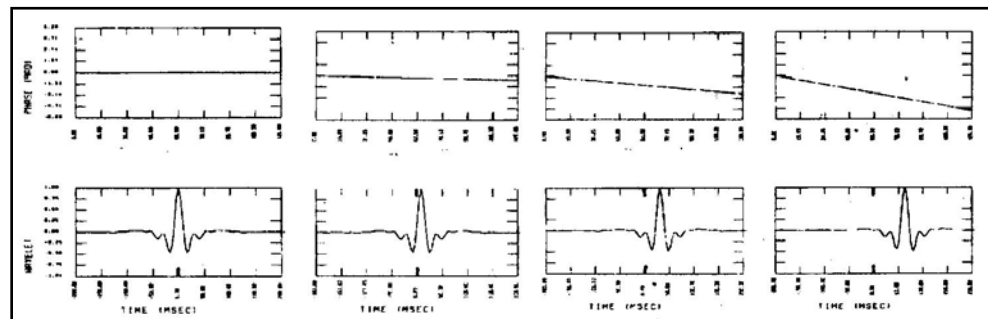


Fig. 3-45 Linear Phase Slope and Time Shift

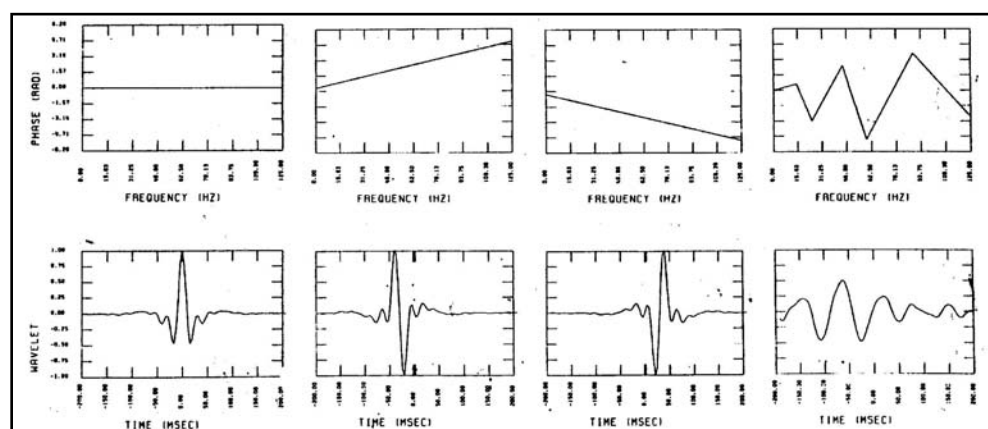


Fig. 3-46 Phase and Wavelet Shape

If a linear phase, i.e. phase proportional to the magnitude of frequency, is added to each frequency component, the effect is quite different. The waveform is unchanged but it is shifted in time. A wavelet can be truly zero phase only if it is centered at time zero. If a zero-phase wavelet is shifted in time, it becomes a linear-phase wavelet (Fig. 3-44).

A linear phase spectrum is a straight line with nonzero slope. A negative slope corresponds to a delay (wavelet is shifted toward a later time). The greater the slope, the larger the time delay (Fig. 3-45). A positive slope corresponds to a negative shift or to an earlier time.

Any phase shift other than linear causes a change in wavelet shape. This is shown in Figure 3-46. From left to right in this figure are a zero-phase wavelet, a constant -90° wavelet advanced 25 ms in time, a constant $+90^\circ$ wavelet delayed 25 ms in time, and a wavelet with an arbitrary phase spectrum. Note that all wavelets shown in this figure have the same amplitude spectrum.

As has been shown, there can be a family of wavelets having the same amplitude spectrum but different phase spectra. One of these wavelets has the smallest phase spectrum. This is the *minimum-phase* or *minimum-delay* wavelet. A minimum-phase wavelet also has the greatest amount of its energy at the beginning of the wavelet as possible. Another wavelet out of this family has the largest phase spectrum. This is called the *maximum-phase* or *maximum-delay* wavelet. All other wavelets in the family are called *mixed-phase* wavelets. See Figure 3-47.

See Figure 3-47.

The time series $\{x_n\} = \{x_0, x_1, x_2, \dots, x_N\}$ can be expressed as the convolution of $(N+1)/2$, two-point wavelets or doublets:

$$\{x_n\} = \{x_0, x_1, x_2, \dots, x_N\} = \{a_1, b_1\} * \{a_2, b_2\} * \{a_3, b_3\} * \dots * \{a_M, b_M\}$$

where

$$M = (N+1)/2$$

If $|a_m| > |b_m|$ for $m = 1, 2, 3, \dots, M$, then $\{x_n\}$ is minimum phase. If $|a_m| < |b_m|$ for $m = 1, 2, 3, \dots, M$, $\{x_n\}$ is maximum phase.

If $|a_m| > |b_m|$ for some values of m and $|a_m| < |b_m|$ for the other values of m , then $\{x_n\}$ is mixed phase. A zero-phase wavelet is a special kind of mixed-phase wavelet. To see this, let $\{a, b\}$ be a minimum-phase doublet where a is the value at $t = 0$ and b is the value at $t = \Delta T$. The time reversed version of this wavelet is $\{b, a\}$ where b is the value at $t = -\Delta T$ and a is the value at $t = 0$. Convoluting these two wavelets gives $\{b, a\} * \{a, b\} = \{ab, a+b, ab\}$. In the resulting wavelet the values at $t = -\Delta T$ and $t = \Delta T$ are equal making the wavelet symmetrical about $t = 0$ and, thus, a zero-phase wavelet. But if $\{a, b\}$ is minimum phase, then $\{b, a\}$ must be maximum phase and $\{ab, a+b, ab\}$ is mixed phase.

Effect of bandwidth

In the discussion of bandpass filters, the passband was defined as the frequency difference between the low and high cutoff frequencies or -3 dB points. Similarly, the bandwidth of an amplitude spectrum is defined as the frequency difference between the -3 dB points. While bandwidth can be expressed in Hz or octaves, the latter is usually more important.

Figure 3-48 illustrates the effect of bandwidth by showing eight zero-phase wavelets and their constituent frequency components. At the top left is the wavelet obtained by summing 1-Hz and 2-Hz cosine waves, giving a bandwidth of one octave. At the bottom is the wavelet obtained by summing 1-Hz through 123-Hz cosine waves (6.94 octaves). There is a steady decrease in wavelet duration or increase in wavelet sharpness. If the bandwidth is increased without limit, then the unit impulse is obtained, as it has an infinite bandwidth.

A wide bandwidth is desirable in many regards. For example, the wider the bandwidth the better one can image the subsurface. Another important aspect of bandwidth is its effect on *resolution*. *Vertical resolution* is defined as the ability to detect two closely spaced reflectors in the subsurface. It has been found that the limit of vertical resolution is $1/4$ of the dominant wavelength. Since $V = f\lambda$, then $\lambda/4 = V/4f$ where λ = wavelength, V = velocity between the two reflectors, and f is the dominant frequency. Table 3-4 shows how resolution gets worse as velocity increases and frequency decreases. Velocity tends to increase and frequency to decrease with depth. Thus, resolution usually gets worse with depth.

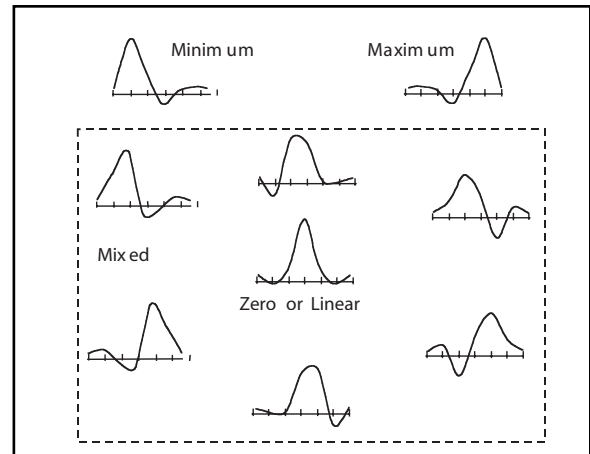


Fig. 3-47 Minimum-, Maximum-, and Mixed-phase Wavelets

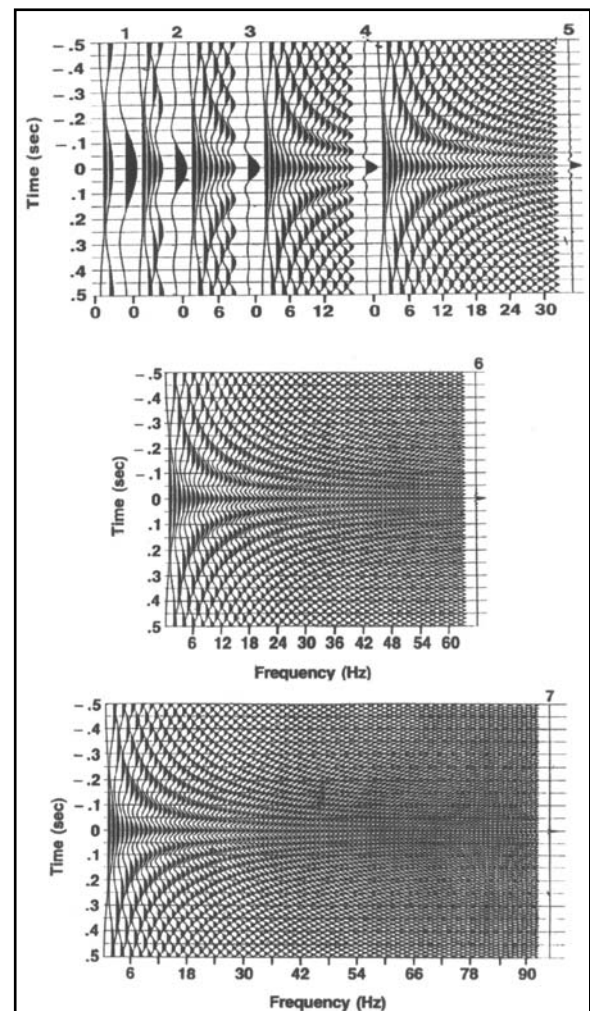
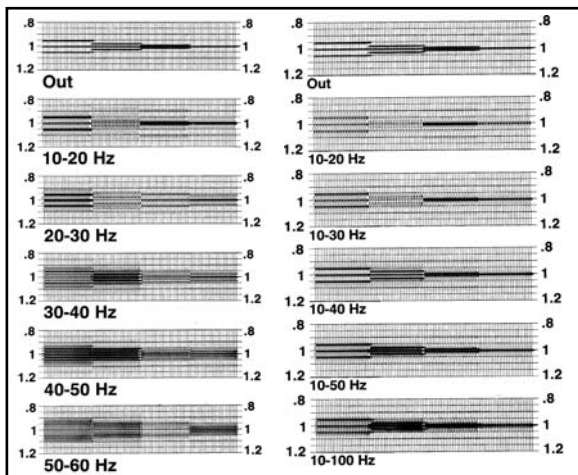
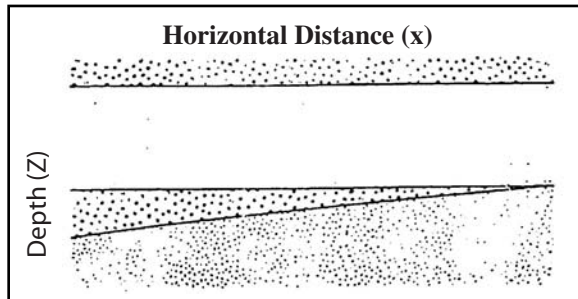
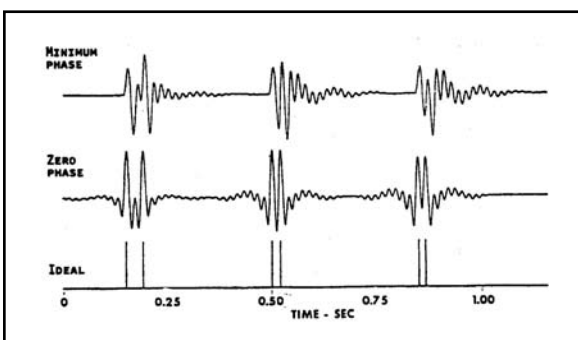


Fig. 3-48 Effect of Bandwidth

Table 3-4 Vertical Resolution

V (m/sec)	f (Hz)	$\lambda/4$ (m)
2000	50	10
3000	40	18
4000	30	33
5000	20	62

**Fig. 3-49 Bandwidth and Vertical Resolution****Fig. 3-50 A Wedge or Pinchout****Fig. 3-51 Phase and Resolution**

side later in time than the other. In Figure 3-53, the actual subsurface displacement ranges from $1/16$ to $1/2$ of a wavelength. For displacements less than $1/4$ wavelength, the fault cannot be discerned.

Figure 3-49 shows the effect of bandwidth on vertical resolution. There are four sets of three reflectors. The first set is 50 ms apart, the second 25 ms apart, the third 12.5 ms apart, and the fourth 6.25 ms apart. With the maximum bandwidth (filters out), the individual reflections can be seen for the first two sets and just barely seen in the third set. Individual reflections cannot be seen with just 6.25 ms separation. On the left, starting with the second from the top, the bandwidth has been limited to 10 Hz. On the 10 Hz to 20 Hz (one octave), the reflections at 12.5 ms separation seem to have blended into one long event. Below this, as the 10 Hz bandwidth moves to higher frequencies, the ability to detect separate reflections becomes progressively more difficult. Note, also, that the bandwidth in octaves has shrunk from 1.0 to 0.26. So, even though the bandwidth has remained a constant 10 Hz and become higher frequency, vertical resolution has become worse. The right side of Figure 3-49 shows the improvement in vertical resolution as the bandwidth increases from one octave (10 to 20 Hz) to 3.32 octaves (10 to 100 Hz). Thus, good vertical resolution requires a large bandwidth. Figure 3-49 is used courtesy of WesternGeco.

Figure 3-50 shows a geologic situation where good vertical resolution is needed to detect the termination of the pinchout. This could be very important in deciding the location of a well.

Figure 3-51 illustrates another important aspect of resolution—the wavelet type. In this figure, three pairs of reflections are shown with separations of about 40 ms, 20 ms, and 10 ms. At the bottom, the reflection waveform is a spike. At the top, the waveform is minimum phase and in the center the waveform is zero phase. Separate reflections can be seen for all three separations in the case of the spikes and the zero-phase wavelets but it is difficult to identify the time of the second reflection at 20 ms and 10 ms separation for the minimum-phase wavelet.

Reflection time for a minimum-phase wavelet is measured at the start of the wavelet where the trace first breaks down or up. When two minimum-phase wavelets overlap, it makes picking the second reflection difficult unless the wavelet duration is on the order of the reflection separation. Reflection time, for a zero-phase wavelet, is at the central peak, or trough, so picking reflection times is much easier and accurate for zero-phase wavelets. This is one reason why zero-phase wavelets are usually output in seismic data processing.

Reflection time for a zero-phase wavelet is at the central peak, or trough, so picking reflection times is much easier and accurate for zero-phase wavelets. This is one reason why zero-phase wavelets are usually output in seismic data processing.

Horizontal resolution. This describes the ability to detect the position of reflector terminations. An example is shown in Figure 3-52. A fault is indicated when a reflection horizon is broken with one

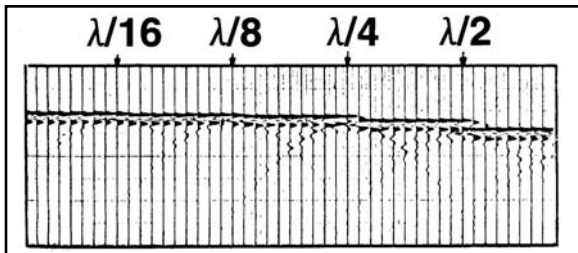


Fig. 3-52 Horizontal Resolution and Fault Displacement

Horizontal resolution is related to the *Fresnel Zone*. The Fresnel Zone is a phenomenon observed for many kinds of wave propagation and was first observed in studies of light. Consider the setup in Figure 3-53a. A light source shines through a pinhole onto a screen in a darkened room. Instead of seeing only a circle of light on the screen, there is a central circle of light surrounded by light and dark bands. This is a result of diffraction of light through the pinhole. The central circle of light is the first Fresnel Zone. It is the only part of the screen that is fully illuminated. Subsequent circular bands of light and dark are the second, third, fourth, etc. Fresnel Zones.

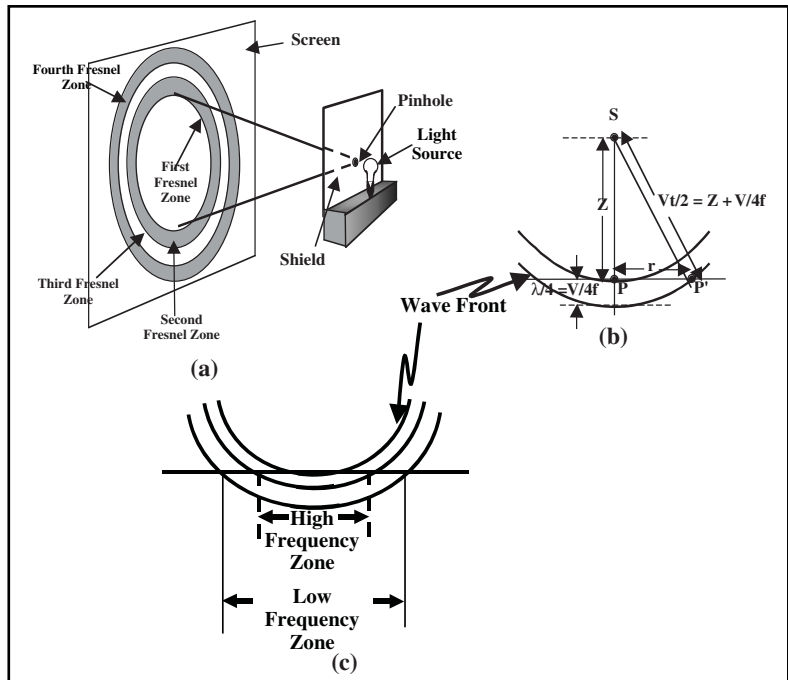


Fig. 3-53 The Fresnel Zone

Diffraction also occurs in propagation of seismic waves. In Figure 3-53b, a horizontal reflector is located a depth Z vertically below a seismic energy source at point S . A wavefront reaches the reflector at point P . After traveling $\frac{1}{4}$ wavelength farther, the wavefront is at point P^1 , a horizontal distance r from P . The distance r is the radius of the first Fresnel Zone. Since SPP^1 is a right triangle, the radius of the first Fresnel Zone in terms of velocity V , reflection time t , and frequency f , can be determined.

$$\begin{aligned} \left(\frac{Vt}{2}\right)^2 &= Z^2 + r^2 = \left(\frac{Vt}{2} - \frac{V}{4f}\right)^2 + r^2 \\ r^2 &= \left(\frac{Vt}{2}\right)^2 - \left(\frac{Vt}{2} - \frac{V}{4f}\right)^2 \\ r &= \sqrt{\left(\frac{Vt}{2}\right)^2 - \left(\frac{Vt}{2} - \frac{V}{4f}\right)^2} = \frac{V}{2} \sqrt{r^2 - \left(t - \frac{1}{2f}\right)^2} \approx \frac{V}{2} \sqrt{\frac{t}{f}} \end{aligned} \quad (3.30)$$

By analogy with optics, it can be seen that the only the first Fresnel Zone is fully illuminated and, thus, its radius defines horizontal resolution. Figure 3-53c shows that higher frequencies have smaller Fresnel zones than lower frequencies. Table 3-5 also illustrates this and the variation with time. Note that frequency usually decreases with time so the lower frequency values in Table 3-5 are more realistic at the later times.

Table 3-5 Variation of the Fresnel Zone with Time and Frequency

$r = (zl/2)1/2 = (V/2)(t/f)1/2$					
$V = 3000 \text{ m/s}$					
Fresnel Zone (m)					
$t(s)$	10	20	30	40	50
1	474	335	273	237	212
2	670	474	387	336	300
3	821	580	474	410	367
4	948	670	547	474	424

The F-K domain

In seismic exploration detectors are placed at discrete locations and the reflected wavefields recorded at those points (Fig. 3-54). So, in seismic exploration, sampling is done in space as well as time.

Just as the Fourier Transform can be used to transform a function of time to a function of frequency, so can it be used to transform a function of space x to a function of wave-number k and vice versa.

$$y(x) \Leftrightarrow Y(k)$$

where

Wavenumber is the reciprocal of wavelength λ

$$k = 1/\lambda = f/V$$

f = frequency

V = velocity

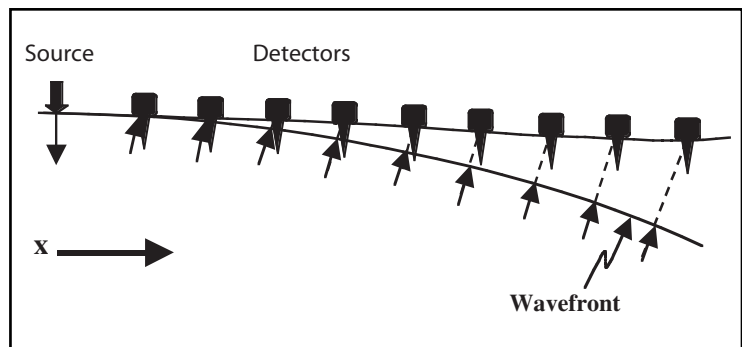


Fig. 3-54 Spatial Sampling

If $\{g(n\Delta x)\}$ is the series of amplitudes obtained by sampling, then the wavefield at discrete spatial locations, spaced Δx apart is as follows:

$$F\{g(n\Delta x)\} = G(m\Delta k) = \sum_{n=0}^N g(n\Delta x) e^{-i2\pi mn\Delta k\Delta x}, m = 0, 1, 2, \dots, M \quad (3.31)$$

$$F^{-1}\{G(m\Delta k)\} = \sum_{m=0}^M G(m\Delta k) e^{i2\pi mn\Delta k\Delta x}, n = 0, 1, 2, \dots, N \quad (3.32)$$

Just as in temporal sampling, sampling at too large an interval results in aliasing. The aliasing, or Nyquist, wavenumber is:

$$k_n = \frac{1}{2\Delta x}$$

		$x \longrightarrow$						
		$g_{1,0}$	$g_{2,0}$	$g_{3,0}$	$g_{4,0}$	$g_{5,0}$	\dots	$g_{P,0}$
T		$g_{1,1}$	$g_{2,1}$	$g_{3,1}$	$g_{4,1}$	$g_{5,1}$	\dots	$g_{P,1}$
		$g_{1,2}$	$g_{2,2}$	$g_{3,2}$	$g_{4,2}$	$g_{5,2}$	\dots	$g_{P,2}$
		$g_{1,3}$	$g_{2,3}$	$g_{3,3}$	$g_{4,3}$	$g_{5,3}$	\dots	$g_{P,3}$
		⋮	⋮	⋮	⋮	⋮	⋮	⋮
		$g_{1,N}$	$g_{2,N}$	$g_{3,N}$	$g_{4,N}$	$g_{5,N}$	\dots	$g_{P,N}$

Since the record is sampled in time and space, it can be represented by a two-dimensional array of numbers $\{g(n\Delta T, m\Delta x)\}$. (Fig. 3-55) A two-dimensional Fourier Transform is used to transform the record into $\{G(n\Delta T, m\Delta k)\}$. This transforms the data from the T - X domain into the F - K domain. A two-dimensional Fourier Transform changes from the F - K domain into the T - X domain.

Fig. 3-55 A Seismic Record as a Two-dimensional Array

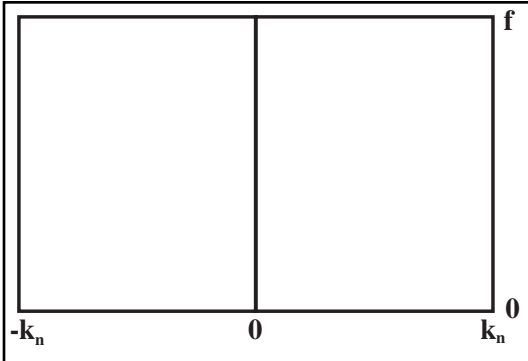


Fig. 3-56 The F-K Plane

Figure 3-57 shows a noise record (one shot to identify all source-generated noises) in both the T - X and F - K domains. Note that linear events in T - X are linear events in F - K . However, a steeply dipping event in T - X appears to have low dip in F - K , and vice versa.

Noise such as ground roll and air waves propagate more or less horizontally, as do direct arrivals, first break refractions, and guided waves. These are called linear events because their propagation velocities can be determined from $V = \Delta x \Delta t$, where Δx is a distance increment and t is the corresponding time increment measured on the record. Primary reflections, multiple reflections, and diffractions do not propagate horizontally, but these events appear in the F - K plane in terms of an apparent horizontal velocity. This is illustrated in Figure 3-58.

In Figure 3-58, a plane reflected wavefront (line AB) is incident on the surface at an angle of emergence of θ . The wavefront arrives at the n^{th} receiver group at an offset x_n at time t . It arrives at the $(n+1)^{th}$ group at an offset $x + \Delta x$ at time $t + \Delta t$. Thus, in the time interval Δt , the wavefront travels the distance BB^1 . From the right triangle ABB^1 , the distance $BB^1 = \Delta x \sin \theta$. But since the propagation velocity is V , then $BB^1 = V\Delta t$ also. So, $V\Delta t = \Delta x \sin \theta$, and with a little algebraic manipulation:

$$\frac{\Delta x}{\Delta t} = \frac{V}{\sin \theta} = V_{app} \quad (3.33)$$

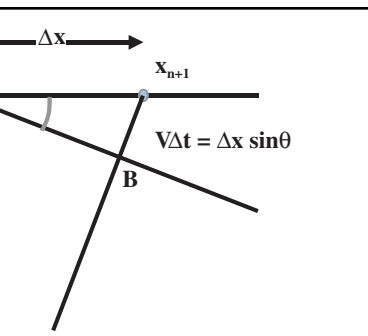


Fig. 3-58 Plane Wave Incident on Surface

Because data are sampled in both time and space, data outside a plane that is between $-k_n$ and $+k_n$ in the wavenumber direction and between zero and f_n in the frequency direction is called the F - K plane. Thus, the F - K plane for data display is as shown in Figure 3-56.

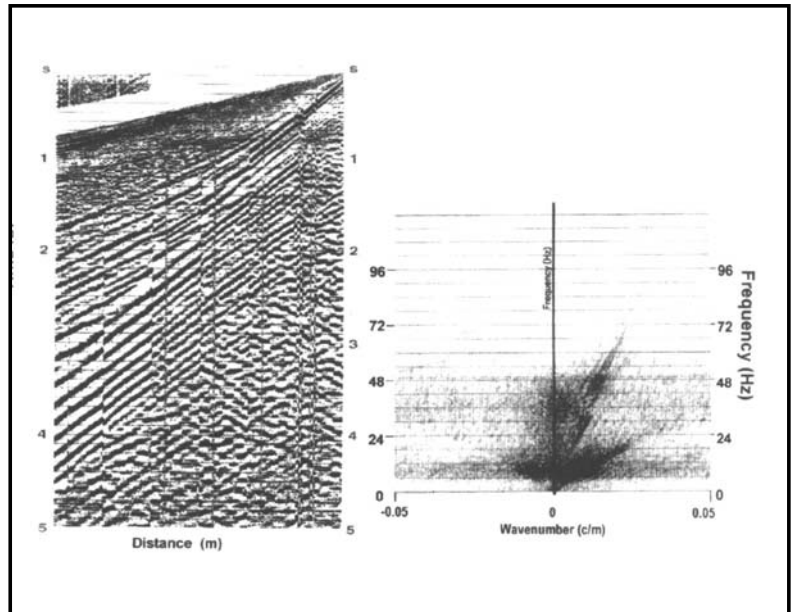


Fig. 3-57 Noise Record in T - X and F - K Domains

where

V_{app} is the apparent horizontal velocity

When $\theta = 90^\circ$, (horizontal propagation) $V_{app} = V$

When $\theta = 0^\circ$, $V = \infty$

At any angle of emergence other than 90° , $V_{app} > V$

If a plane wave is reflected from a reflector that is dipping at an angle θ , then the effect will be as described in the previous section. There is, however, another way to look at this. The reciprocal of apparent velocity is dip.

$$\text{dip} = \frac{\Delta x}{\Delta t} = \frac{1}{V_{app}} \quad (3.34)$$

When dip is measured from a seismic record or vertical section, it is usually measured in msec/trace. Since two adjacent traces correspond to a distance Δx , and $1\text{s} = 1000 \text{ msec}$, the dip in msec/trace, D , can be related to apparent velocity by:

$$k = \frac{fk_N}{500} D \quad (3.36)$$

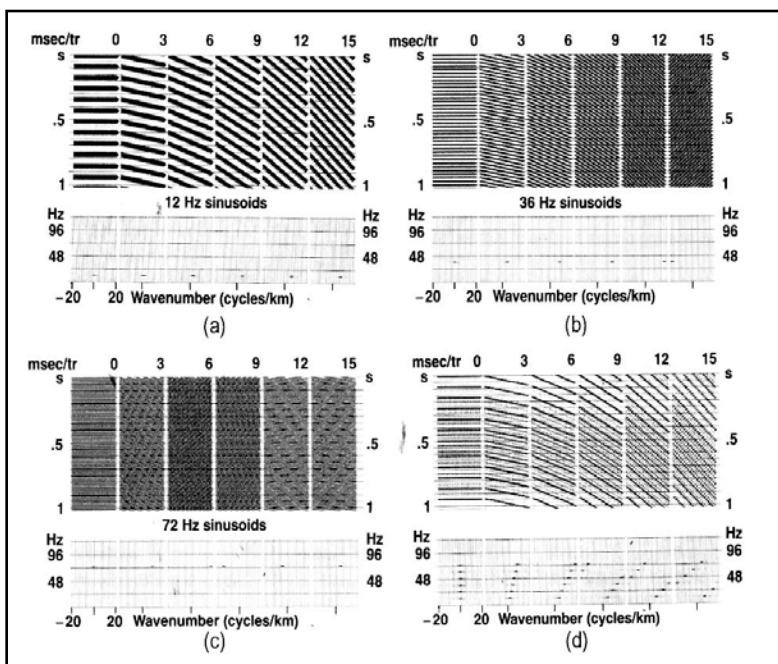


Fig. 3-59 Spatial Aliasing as a Function of Dip and Frequency

single linear event. This is also a linear event in the $F-K$ domain, where it can be seen that the signal waveform is band-limited to about 6–48 Hz. Figure 3-60b shows, in the $T-X$ domain, a set of parallel linear events with the same signal as in Figure 3-60a. In the $F-K$ domain, however, only one event can be seen. Thus, *all events with same dip plot in the same part of the F-K plane*.

Spatial aliasing occurs when $k > k_N$, and from Equation 3.36, this depends on both frequency and dip. This is shown in Figure 3-59. Single frequency sinusoids at 12, 36, and 72 Hz are shown in Figure 3-59 sections a, b, and c, respectively. Figure 3-59d shows a combination of 12, 24, 36, 48, and 72 Hz sinusoids. In each case, they are shown at dips of 0 through 15 msec/trace in 3 msec/trace increments. No aliasing occurs at any dip in the 12 Hz case. In Figure 3-59b, the 36 Hz sinusoid aliases at a dip of 15 msec/trace ($15 \times 36/500 > 1$). In the $T-X$ domain, the dip aliases to -15 msec/trace. In the $F-K$ domain, the wave number aliases to -18.6 c/km.

In Figure 3-59c, the 72 Hz sinusoid aliases at dips of 9, 12, and 15 msec/trace. In Figure 3-59d, the 72 Hz sinusoid first aliases at a dip of 9 msec/trace. At 12 msec/trace, dip both the 72 and 60 Hz sinusoids alias. At 15 msec/trace dip, only the 12 and 24 Hz sinusoids are not aliased. Thus, spatial aliasing increases as dip and frequency increase.

Figure 3-60a shows, in the $T-X$ domain, a single linear event. This is also a linear event in the $F-K$ domain, where it can be seen that the signal waveform is band-limited to about 6–48 Hz. Figure 3-60b shows, in the $T-X$ domain, a set of parallel linear events with the same signal as in Figure 3-60a. In the $F-K$ domain, however, only one event can be seen. Thus, *all events with same dip plot in the same part of the F-K plane*.

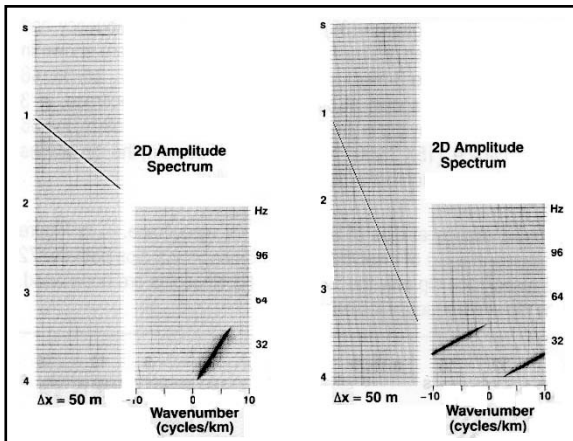


Figure 3-60 Linear Events in T-X and F-K

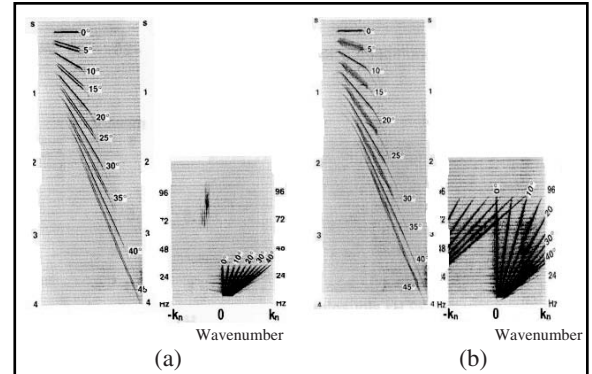


Fig. 3-61 Linear Dipping Events

None of the events shown in Figure 3-60 alias because the highest frequency present is 48 Hz. In Figure 3-61a, linear events with dips from 0° to 45° in 5° increments are shown. Signal is band limited from 6 to 36 Hz and no aliasing occurs. Figure 3-61b has linear events with the same dips, but the upper frequency limit has been raised to 90 Hz. As a result, aliasing occurs for dips of 20° and steeper.

It appears that spatial aliasing can be avoided by limiting dips or by limiting bandwidth—neither of which is desirable in most cases. There is, however, an alternative. As shown in Figure 3-62, the smaller the group interval, the higher the frequency that signal can contain without aliasing. That is why the highest frequency required to properly image the exploration objective is an important parameter in designing data acquisition programs.

The great advantage of transformation from the T - X domain into the F - K domain is that noise, such as ground roll, that crosses through signal in T - X can be separated from signal in F - K . This is illustrated in Figure 3-63. As shown, signal is usually located near $k = 0$. Direct arrivals, first break refractions, and ground roll are all linear events that plot as straight lines to the right of signal (slower velocity). All of these may alias and cross signal in the higher frequency range. Where, and if, these events cross signal depends on group interval.

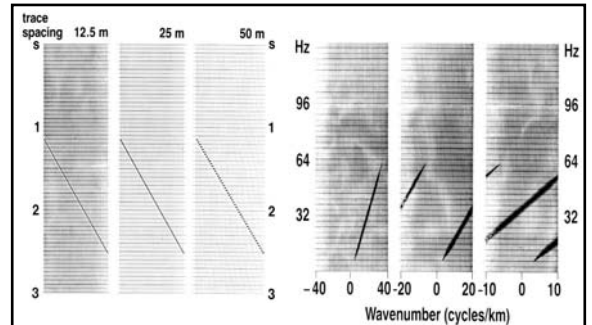


Fig. 3-62 Effect of Group Interval on Spatial Aliasing

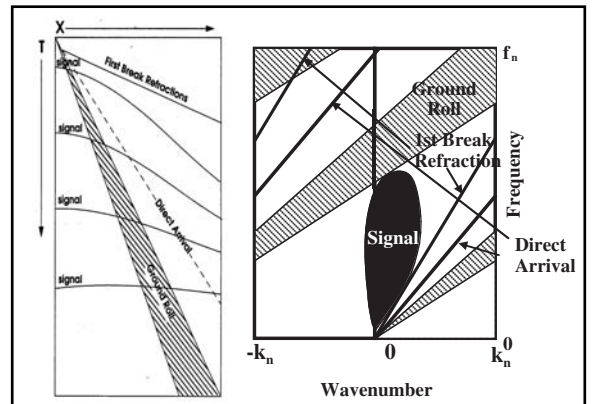


Fig. 3-63 Separation of Signal and Noise in F-K

The Z-transform

The *Z-transform* is another mathematical operation used in seismic exploration. It transforms a time series into a power series, allowing simple algebra to be used when working with time series.

Given the time series $\{x_t\} = \{x_0, x_1, x_2, x_3, x_N\}$, its Z-transform is:

$$Z\{x_t\} = x_0 + x_1 z + x_2 z^2 + x_3 z^3 + \dots + x_N z^N \quad (3.37)$$

The Z-transform is related to the Fourier transform because $z = e^{-i2\pi fT}$.

Given the two time series $\{xt\} = \{2, -1\}$ and $\{yt\} = \{3, 2, -1\}$, we saw earlier that the convolution of $\{xt\}$ and $\{yt\}$ was $w(t) = \{6, 1, -4, 1\}$. Taking the Z-transforms of the two time series gives $X(z) = 2 - z$ and $Y(z) = 3 + 2z - z^2$.

Multiplying $X(z)$ and $Y(z)$ gives $X(z)Y(z) = 6 + 4z - 2z^2 - 3z - 2z^2 + z^3 = 6 + z - 4z^2 + z^3$. The inverse Z-transform is $Z^{-1}(6 + z - 4z^2 + z^3) = \{6, 1, -4, 1\}$. That is, the coefficient of each power of z is the corresponding value of the time series, with the power of z determining the delay in sample periods. The product of the two Z-transforms is the Z-transform of the convolution, so it is possible to obtain a convolution with a simple algebraic operation.

Remembering that the cross-correlation of $\{yt\}$ with $\{xt\}$ is:

$$\{fxy\} = \{xt\} * \{y-t\} \text{ and } \{y-t\} = \{-1, 2, 3\}$$

then

$$\begin{aligned} Z\{y-t\} &= -z-2 + 2z-1 + 3 \\ Z\{\phi xy\} &= (2 - z)(-z^2 + 2z^1 + 3) = -2z^2 + 4z^1 + 6 + z^1 - 2 - 3z \\ &= -2z^2 + 5z^1 + 4 - 3 \end{aligned}$$

Taking the inverse Z-transform yields: $\{\phi xy\} = \{-2, 5, 4, -3\}$, which agrees with the earlier result.

Another useful application of the Z-transform is the factoring of a power series into doublets.

$$\begin{aligned} X(z) &= x_0 + x_1z + x_2z^2 + x_3z^3 + \dots + x_Nz^N \\ &= (a_1+b_1z)(a_2+b_2z)(a_3+b_3z)\dots(a_N+b_Nz) \end{aligned}$$

If $|a_n| > |b_n|$, then the doublet is minimum phase, and if $|a_n| < |b_n|$, then the doublet is maximum phase. A time series of any length is minimum phase only if all the doublets into which it is factored are minimum phase.

Multiplication by z^n is equivalent to delaying the time series by n sample periods. For example $\{x_t\} = \{4, -2, 1\}$, so $X(z) = 4 - 2z + z^2$. Let $W(z) = zX(z) = 4z - 2z^2 + z^3$. The inverse of $W(z) = \{wt\} = \{0, 4, -2, 1\}$. Note that while $\{xt\}$ is minimum phase, $\{wt\}$ is mixed phase because the delay makes one of the roots of $\{w_t\}$ equal to zero.

It is often desired to find the inverse of a wavelet, etc. Given the wavelet $w(t)$, its inverse $w^{-1}(t)$, is defined by:

$$w(t) * w^{-1}(t) = \delta(t) \quad (3.38)$$

where $\delta(t)$ is the Dirac delta function. What we call a spike is described mathematically as $A\delta(t)$, where A is the amplitude of the spike.

$$Z\{w(t)\} = W(z), Z\{w^{-1}(t)\} = W^{-1}(z), \text{ and } Z\{_(t)\} = 1.$$

Thus, in the Z-domain, $W(z) W^{-1}(z) = 1$, which gives $W^{-1}(z) = 1/W(z)$. Given the time series $\{2, -1\}$, its Z-transform is $2 - z$ and the Z-transform of its inverse is $W^{-1}(z) = 1/(2 - z) = 1/2 + z/4 + z^2/8 + z^3/16 + \dots$. The inverse is infinitely long but it is a converging series because the input is minimum phase ($2 > |-1|$). If we use a truncated version of the inverse, $H(z) = 1/2 + z/4 + z^2/8$, then $W(z) H(z) = 1 - z^3/8$ and the inverse is $(1, 0, 0, -1/8)$. Since the desired output is $\{1, 0, 0, 0\}$, the error is $-1/8$ in the fourth sample. Increasing the length (number of samples) of the inverse will, if it is minimum phase, decrease the error but never eliminate it. A better way to estimate an inverse will be presented in the seismic data processing section.

The Radon transform

The *Radon Transform* transforms data from the T - X domain into the t - p domain where p is the ray parameter, $p = \Delta t / \Delta x$, and $\tau = t - px$. Figure 3-64 illustrates the ray parameter, which is the constant in Snell's Law.

The Radon transform (also called slant stack) is calculated as follows:

- Determine the minimum moveout (ΔT_{min}) and maximum moveout (ΔT_{max}) on the trace that will include all desired events. The maximum moveout will probably be for the shallowest reflection and the minimum movement will probably be on the deepest reflection of interest.

- Calculate the number of p-traces (N_p) from

$$N_p = (\Delta T_{max} - \Delta T_{min}) / \Delta T$$

where ΔT is the sample interval.

Alternately, the number of p-traces can be specified.

- For the first p-trace, apply a linear moveout correction to every trace of the CMP gather

$$\Delta T_n = (x_n / x_{max}) \Delta T_{max}$$

where:

ΔT_n = moveout correction applied to nth trace

x_n = offset corresponding to nth trace

x_{max} = maximum offset in gather

ΔT_{max} = maximum movement

- Stack all traces. The output is the first p-trace.

- Decrement ΔT_{max} by ΔT (sample interval) to obtain the linear moveout correction for the second p-trace.

- Apply the revised linear moveout and stack to obtain the second p-trace.

- Repeat steps 5 and 6 until all p-traces are generated.

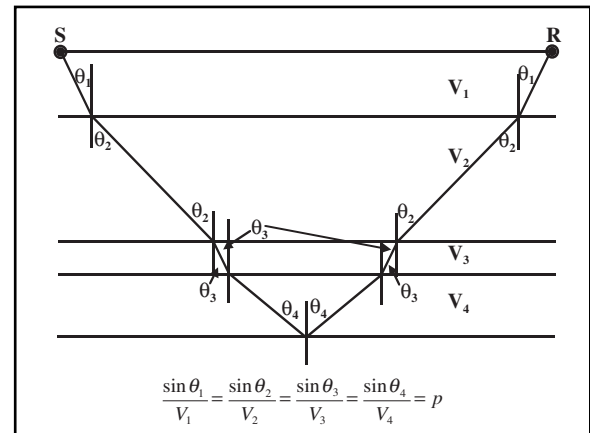


Fig. 3-64 Definition of the Ray Parameter

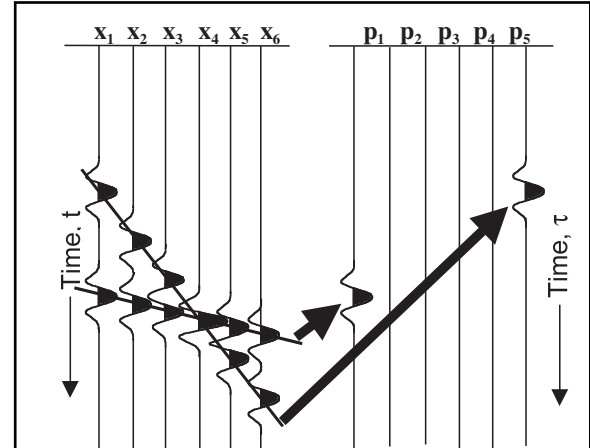


Fig. 3-65 The Radon Transform

Figure 3-65 illustrates the Radon Transform with a simple example. The record in the T - X domain has two dipping events. The shallower dip is designated ΔT_{min} and the steeper dip is designated ΔT_{max} .

Six values of p are selected, so $\Delta T = (\Delta T_{max} - \Delta T_{min})/5$ with $p_1 = \Delta T_{min}$ and $p_6 = \Delta T_{max}$. Ideally, the two dipping events in T - X will map into single wavelets on the p_1 and p_6 traces in t - p .

Figure 3-66 provides a schematic representation of how events in T - X map into t - p . Table 3-6 summarizes the mapping in terms of event shapes in each domain.

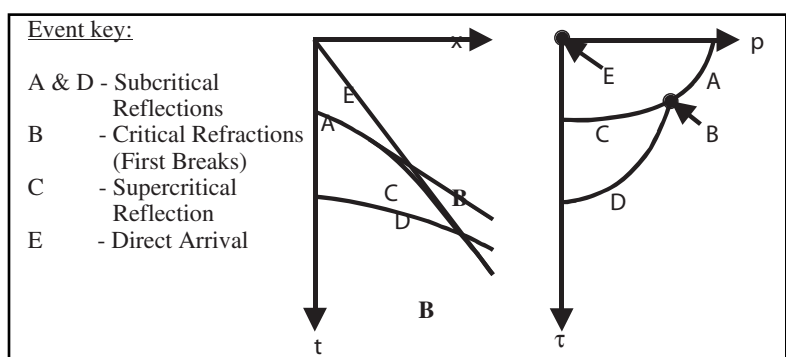


Fig. 3-66 Event Mapping between T - X and t - p Domains

Table 3-6 *T-X and t-p Relationships*

T-X	τ -p
Hyperbola	Ellipse
$t^2 = t^2 + (x/V)^2$	$\tau^2 = t^2 (1 - V^2 p^2)$
Line	Point
Point	Line

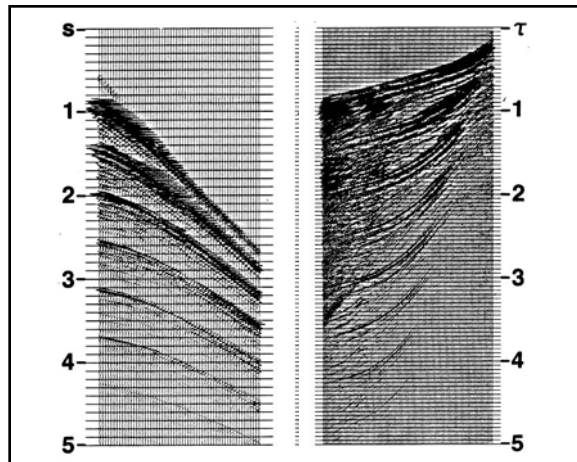
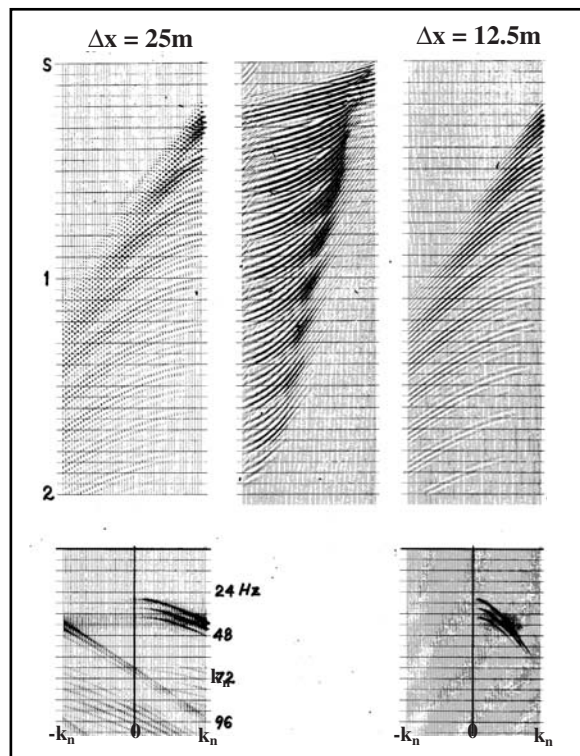
**Fig. 3-67** *CMP Record in T-X Domain and t-p Domain***Fig. 3-68** *Trace Interpolation with the Radon Transform*

Figure 3-67 shows a CMP record in the T - X and t - p domains. Note that the hyperbolic reflection events in T - X become elliptical in t - p .

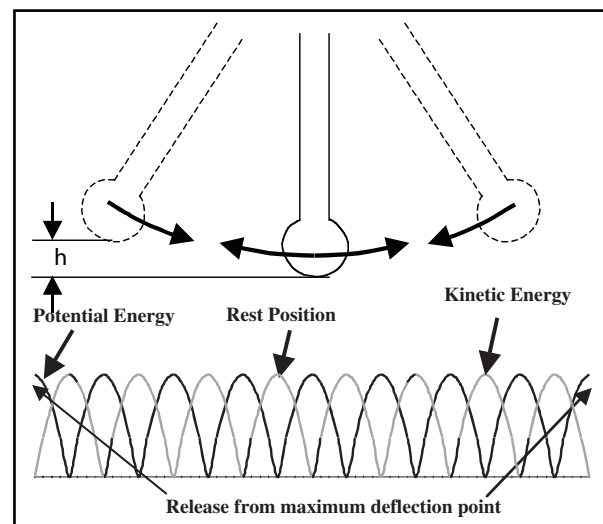
Radon transform applications include:

- multiple suppression
- time-variant dip filtering
- trace interpolation
- refraction inversion
- velocity analysis
- migration before stack

Figure 3-68 illustrates trace interpolation using the Radon Transform. In this example, the data are transformed into the τ - p domain with a trace interval of 25 m and twice as many traces are output with a trace interval of 12.5 m. In this way, spatial aliasing can be avoided without having to acquire the data at 12.5 m trace intervals.

The complex trace

Seismic detectors record motion and, thus, only measure kinetic energy. In a dynamic system total energy is the sum of kinetic and potential energy. For example, as a clock pendulum swings back and forth, it has its maximum velocity at the rest position and at that point all of its energy is kinetic energy ($KE = \frac{1}{2} mv^2$). At its maximum deflection points on each side, its velocity is zero, but it is at a height h above its rest position and all energy is potential energy ($PE = mgh$). See Fig. 3-69. In between these two extremes, the total energy is the sum of kinetic and potential energy.

**Fig. 3-69** *A Clock Pendulum and Its Energy Cycle*

The *complex* trace, or *analytic signal*, attempts to show total energy in seismic wave propagation. The analytic signal, $u(t)$, is defined as:

$$u(t) = x(t) + iy(t)$$

where

$x(t)$ = recorded seismic trace and

$y(t)$ = *quadrature trace*

$$= H\{x(t)\} = \frac{1}{\pi t} x(t) \quad (3.39)$$

$H(t)$ = *Hilbert Transform*

$$\therefore u(t) = [\delta((t) + \frac{i}{m})] \cdot x(t) \quad (3.40)$$

The imaginary part of a complex number or variable is usually considered to be orthogonal to the real part. So the complex trace shows the total energy at any one time as the vector sum of the real and imaginary or quadrature trace.

Complex trace analysis makes use of the real trace and the quadrature trace along with three derived quantities—instantaneous amplitude, instantaneous phase, and instantaneous frequency.

Instantaneous Amplitude:

$$R(t) = [x(t)]^2 + [y(t)]^2 \quad (3.41)$$

Instantaneous Frequency:

$$\phi(t) = \tan^{-1} \left[\frac{x(t)}{y(t)} \right] \quad (3.42)$$

Instantaneous Phase:

$$w(t) = \frac{d\phi(t)}{dt} \quad (3.43)$$

Figure 3-70 illustrates these quantities.

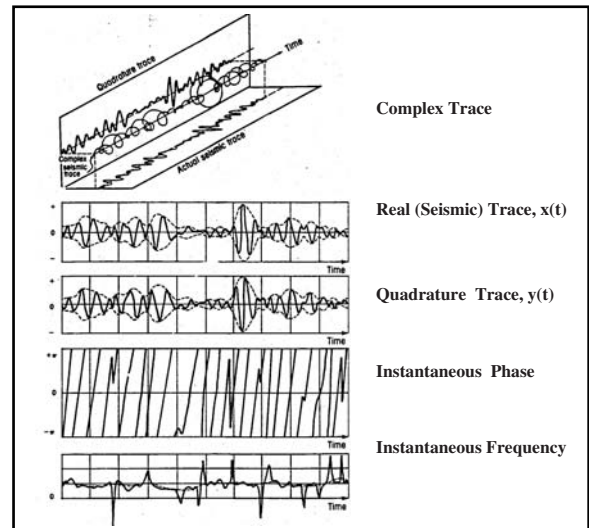


Fig. 3-70 Complex Trace Analysis

Workshop

1. Match the list of properties with the wave types by writing the appropriate letter(s) after the wave type.

- A Particle motion in the direction of propagation.
- B Particle motion orthogonal to direction of propagation.
- C Particle motion describes retrograde ellipse.
- D Propagates through body of medium.
- E Propagates along surface of medium.
- F Propagates in solids.
- G Propagates in fluids.

P-wave: _____.

S-wave: _____.

Rayleigh wave: _____.

Love wave: _____.

2. P-waves always propagate faster than S-waves in the same medium. True or False?

3. A P-wave that is propagating in a medium having a velocity of 2000 m/s is incident on a medium having a velocity of 2500 m/s at an angle of 15 degrees from the normal to the interface. Determine the angles at which all resulting waves propagate in both media.

4. What are the values of the reflected amplitude, A_1 , and the transmitted amplitude, A_2 , in Figure 3-71?

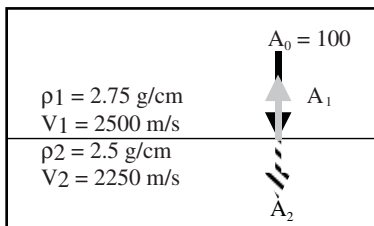


Fig. 3-71

5. Complete Table 3-7 by determining the output frequencies for each input frequency and sample period.

Table 3-7 Output Frequencies for Various Sample Periods

Input Frequency (Hz)	Frequency Output (Hz)	Frequency Output (Hz)	Frequency Output (Hz)	Frequency Output (Hz)
60				
120				
180				
240				
300				

6. Given the impulse response of a system shown in Figure 3-72, what is the output when the input is as shown in the following?

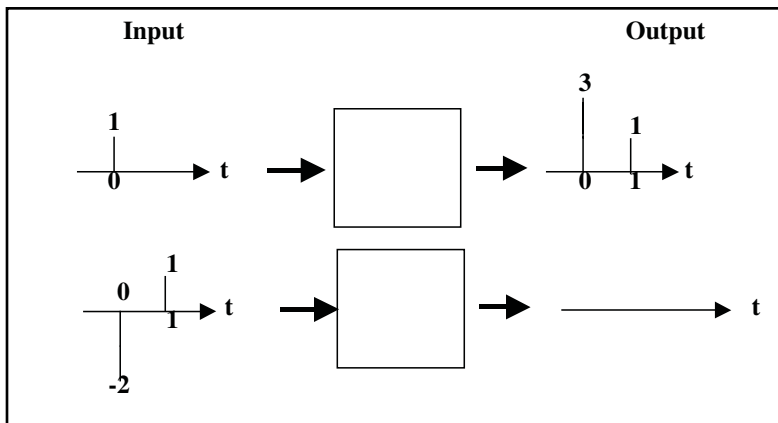


Fig. 3-72

7. Given wavelet $a = \{5, -2\}$ and wavelet $b = \{-3, 1\}$, calculate the cross-correlations, ϕ_{ab} and ϕ_{ba} .
8. Calculate the autocorrelation of wavelet a in exercise 7.
9. Which of the following are minimum-phase wavelets? The first value in each case is at time zero.
- 6, -1, -2
 - 3, 4, -4
 - 0, 12, -1, -6
 - 2, 5, -2
 - 28, -27, 5

10. Identify the phase of the wavelets shown in Figure 3-73 as zero phase, linear phase, $+90^\circ$ phase and -90° phase.

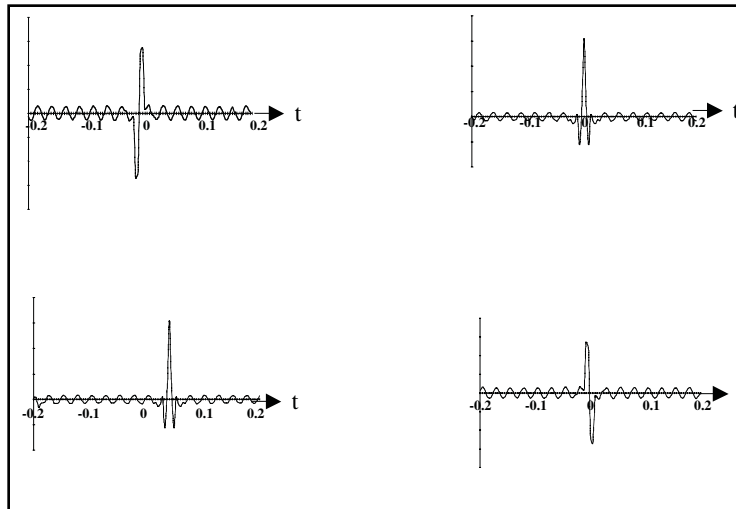


Fig. 3-73

11. Which wavelet has the larger bandwidth, *A* or *B*?

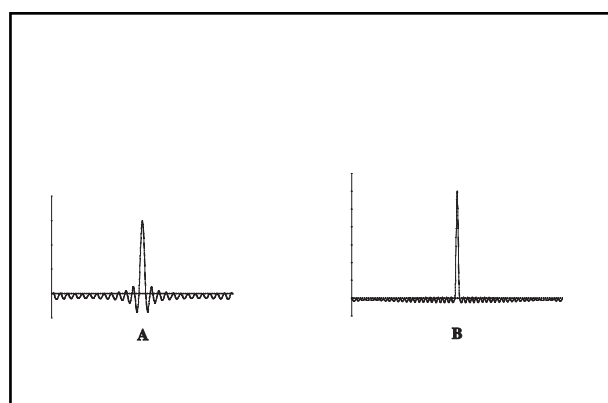


Fig. 3-74

12. The velocity in the target zone is expected to be in the range of 3200 m/s to 3600 m/s at times of 2.7 s to 3.0 s.

a. What maximum frequency is required to give a vertical resolution of 25 m?

b. What maximum frequency is required to give a horizontal resolution of 25 m?

13. It is desired to have frequencies up to 50 Hz in the target zone. If the velocity and maximum dip are expected to be 3600 m/s and 35° , respectively, what is the largest group interval that will assure having the desired frequency?
14. Use the Z-transform method to calculate the convolution of wavelets a and b of exercise 7.
15. Determine the inverse of wavelet a in exercise 7.
16. Shown in Figure 3-75 is a schematic representation of a shot record. Sketch in the indicated spaces, the appearance of this record in the F - K and t - p domains.

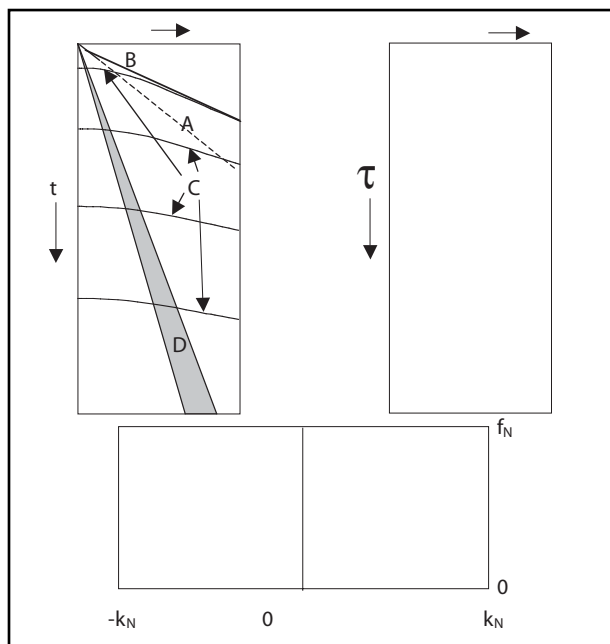


Fig. 3-75



4

Seismic Refraction Exploration

Introduction

A variety of seismic refraction techniques, differing mostly in the geometry of source and receiver configurations, have been used. Inline shooting calls for *shot point* (the position at which the charges are detonated) and detectors laid out along a straight line, arc, or fan shooting involves detectors laid out along an arc of a circle with the shot-point position at the center of the circle, and broadside shooting calls for detectors laid out in a straight line with the shot point offset perpendicular from the center of the line of detectors.

Inline geophone spreads may have as many as 1024 *stations*—location for one or the center of a group of detectors. Spacing between successive detectors or groups ranges from around 50 ft to more than 600 ft in a few cases. Also varying considerably, and in many cases not constant throughout the survey, is the distance from the shot point and the nearest detector position, called *offset distance*. Offset distances of 20 to 30 miles are not uncommon.

Refraction Methods

Inline shooting methods. Figure 4-1 illustrates a layout for *intensive inline refraction* shooting along a 48,000-ft north-south line. The numbers 1 through 6 denote positions of 6 shot points equally spaced along the line. A spread of 24 geophone groups with 400-ft spacing is laid out symmetrically between two successive shot

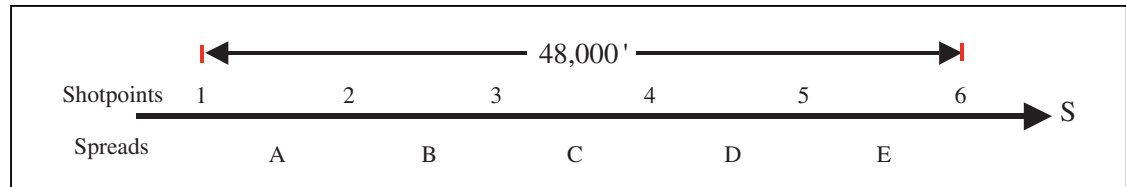


Fig. 4-1 Layout for Intensive Refraction Shooting

points. With the spread at *A*, shots are fired at each shot point in succession and records made. Then, the spread is moved to positions *B*, *C*, *D*, and *E*, with the same shooting procedure. Thirty records are thereby obtained. This procedure gives complete subsurface coverage but involves a great deal of work and many workers.

At least two shooting and drilling crews should be used to attain good efficiency, and two recording crews might also be used to improve speed of operation further. Thus, considering the number of workers involved, the equipment necessary, and the amount of explosives detonated (perhaps hundreds of pounds at some shot points), this would be an expensive operation—particularly if continued along this or other lines.

A modification of this procedure, called *simple inline forward-and-reverse coverage*, dispenses with shot points two, three, four, and five. The spread is moved as previously described, but shots are fired into the spread from only the two end shot points.

The savings in cost, time, and personnel may be sufficient to offset the loss in completeness, particularly if the geology is rather simple. Timing the first arrivals, or the times at which more or less abrupt trace deflections are first noted, begins interpretation of the 10 records obtained. Times picked for each trace must be corrected for variations in surface elevation and in the near-surface, low-velocity zone. An additional time correction is usually applied to correct to a reference surface such as sea level.

Corrected times are plotted on what is commonly called a *T-X* plot. The vertical scale of the plot is corrected refraction time, and the horizontal scale is the distance between shot and receiver corresponding to the trace from which the time was read. For each such distance, there will be two times corresponding to refraction times from the north and the south ends of the profile.

As shown in Figure 4-2, straight lines are usually fitted to the plotted points. Note that the points normally do not fit exactly to a straight line, but that the best line in a least-square error sense is fitted to appropriate segments of each set of points. It can be seen that if the refractor and surface are both plane and parallel, then refraction time between successive detectors is equal to the separation between the detectors divided by the refraction velocity. Hence, the straight lines shown in Figure 4-2 have slopes that are the reciprocals of refraction velocities.

Inspection of Figure 4-2 reveals that the velocities obtained for the second and third refractor differ according to whether refraction paths run from north to south or from south to north. The interpretation of this situation is that the refractors are not horizontal but dipping. Relationships between dip angle, apparent velocities, and actual velocities allow us to compute dip angles, and actual velocities values obtained for the second refractor are a 40° dip to the south and a velocity of 9000 ft per second (fps). For the third refractor, we compute a 70° dip to the south (with respect to the surface) and a velocity of 15,000 fps.

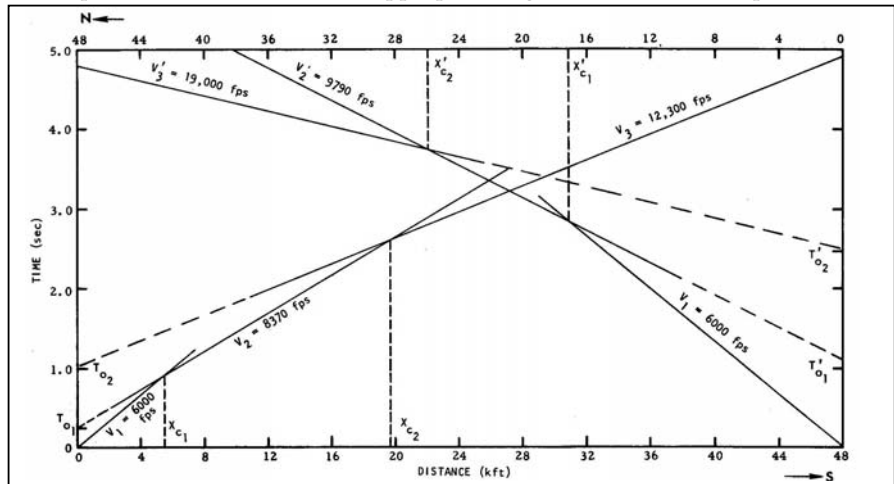


Fig. 4-2 T-X Plot for Inline Refraction Shooting

Layer thickness can be computed from either of two sets of data obtained from the *T-X* plot of Figure 4-2—the first set being the intercept times T_{o1} , T_{o1}' , T_{o2} , and T_{o2}' that are found by projecting the straight line fits back to zero distance axes and the second set being the critical distances X_{o1} , X_{o1}' , X_{o2} , and X_{o2}' .

Using these derived data, we construct the model shown in Figure 4–3. Note that this model, which assumes plane refractors, is the simplest one fitting the observations. A more detailed model would likely show more irregular refractors, such as the subsurface relief of each horizon. A refraction profile should also be run at right angles to the one described to obtain true dip of the refractors since the maximum dip may be in a direction other than south.

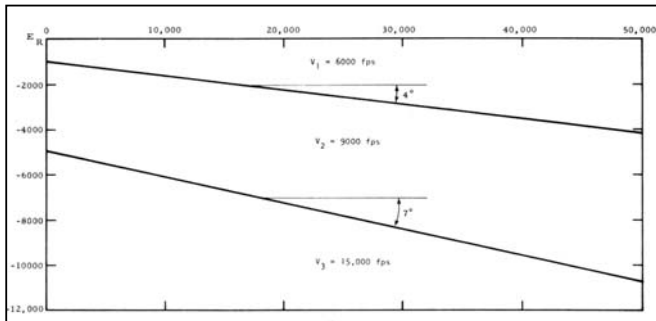


Fig. 4-3 Simplified Earth Model Based on Data from Figure 4-2

only first arrivals are picked at each distance range, no points corresponding to this layer will be plotted, or the number plotted may be insufficient to show clearly the existence of the layer.

A number of other approaches for inline refraction surveys have been used, most resulting in further reduction of required personnel, materials, and equipment but creating losses in the completeness of the data and the data interpretation. Also, in some cases, there is need for additional assumptions regarding subsurface variations. Consequently, applications of such procedures are limited to geologically simple areas and to reconnaissance of new areas.

Other refraction shooting methods. *Fan* or *arc* shooting, seen in Figure 4–4, has been quite successful in locating relatively shallow salt domes and plugs in areas where seismic velocity is normally rather low. Ideally, all shot-to-detector distances in fan shooting are kept equal. Hence; refractions that travel through the higher-velocity salt reach detectors ahead of those that do not.

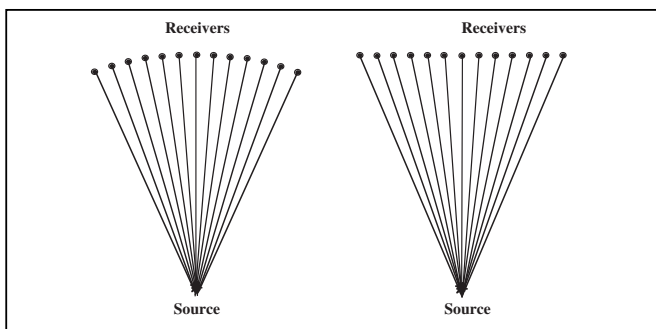


Fig. 4-4 Arc and Broadside Shooting

interpreted as variations in refractor depth. By interspersing inline shots, a calibration of sorts is provided for mapping the subsurface along a straight line if spreads overlap sufficiently. Compared with most other methods, broadside shooting results in relatively low cost-per-mile subsurface coverage.

Advantages and disadvantages of the refraction method. Advantages of the refraction method of exploration are that it obtains velocity information directly, can be faster and often cheaper than reflection methods in terms of cost-per-mile of coverage, and, in a few cases, yields results where reflection methods fail. Refraction methods are especially useful for large-scale reconnaissance of new areas and for detailing intrusives such as salt domes and their flanks.

Disadvantages include interpretational ambiguities, cumbersome computations, possibly complex field operations, and the need for a higher degree of surveying accuracy and skill. Several surveying, shooting, and drilling crews may be required to keep pace with the recording crew so a large capital outlay may be needed for equipment and explosives.

See Appendix A for the derivation of calculations used in analysis and interpretation of refraction data.

Another point concerning the interpretation of refraction data is that there are situations in which the method breaks down unless accounted for beforehand from prior information. One situation is the existence of a layer or layers in which the seismic velocity is less than in the overlying layer. Critical refraction cannot occur in this situation, so no refractions are received from this layer for use in estimating layer thickness and velocity. Thickness of other layers and depths to lower ones will be in error due to the *velocity inversion*.

Another situation resulting in incomplete data is the presence of one or more layers, with thickness such that the refraction from the deeper layer arrives at the surface first. If

refractions from the shallower layer are plotted, they will be in error due to the *velocity inversion*.

By shooting in mutually perpendicular directions across the salt mass, data are obtained from which the position and a rough outline of the salt mass can be determined. A general idea of the *normal structure*—away from salt intrusion—and locations of salt masses are needed to make the method feasible. Extensive fan shooting in the 1930s led to the discovery of nearly all relatively shallow salt domes in the Gulf Coast area of the United States.

Broadside shooting is well adapted to the mapping of subsurface relief of a particular refractor if the *overburden*—material between the surface and refractor—is reasonably well known. After adjustment for differences in shot-to-detector distances, refraction-time variations from trace to trace are

Workshop

1. Use the $T-X$ plot shown in Figure 4–5 to determine the dip angle j , the critical angle qc , and the true velocity of the second layer V_1 .

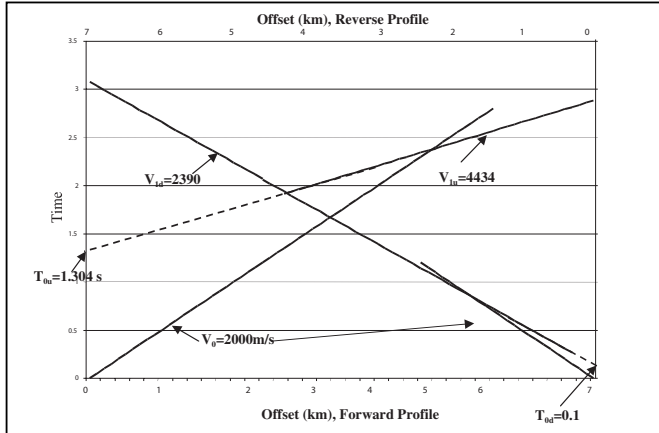


Fig. 4–5



5

Seismic Reflection Data Acquisition

Introduction

The functions required in any seismic reflection data acquisition program are the same, as seen in the following notes.

Permitting—Permission must be obtained from all owners or authorities prior to entering and working in the area. *Positioning*—Precise locations of source and receiver positions must be known. *Signal Generation*—Seismic waves with appropriate amplitudes and frequency spectra must be generated. *Recording*—Seismic waves must be detected and converted to electrical signals. Electrical signals must be transmitted to the recording system with minimum attenuation and distortion. The way and the order in which these functions are performed depend to a great extent on the environment.

Land acquisition tends to be sequential. Positioning, usually called *surveying* on land, commences as soon as permitting has progressed sufficiently. If explosives are used for signal generation (energy source), then drilling and loading of holes precedes recording activities. If vibrators are used as the energy source, then signal generation and recording are performed simultaneously.

In marine acquisition, the source, receivers, and recording system are all constantly moving. The navigation system must determine the position of the vessel, sources, and receivers while recording data.

In transition zones between land and marine and in shallow water marine surveys, elements of both land and marine techniques are employed.

Land seismic surveys are conducted in many parts of the world with tremendous variations in topography, weather, surface conditions, population densities, and many other factors. There is usually little functional difference in how these surveys are conducted, but the kinds of equipment and instrumentation varies a great deal.

Another factor that causes variations in how seismic surveys are conducted is whether the survey is 2-D or 3-D. Up until the 1970s, all seismic surveys were 2-D. This means that lines of survey were on the order of one mile apart, and sources were usually in line with the receivers. A tacit assumption in 2-D surveys is that all subsurface reflection points lie in a vertical plane through the line of survey.

In 3-D seismic surveys, the sources and receivers are not all in line with each other. Receivers that record from a single source are laid out over an area instead of along a relatively straight line. Also, receiver lines are much more closely spaced in 3-D than in 2-D. This provides much denser sampling of the subsurface.

Permitting

The problems presented in permitting an area for seismic data acquisition differ considerably between land and marine and between those conducted in the United States and in other countries. In marine surveys, the property owners are nations or political subdivisions of them (states or provinces). For land surveys conducted in the United States, one must consider not only owners of the surface but also the subsurface. It is not uncommon in this country for a piece of land to be occupied by a person who leases it from the owner of the surface but does not own the mineral rights. In most, if not all, other countries the government owns all mineral rights, but the surface land may be owned privately.

Initial planning for a seismic acquisition program is done from maps. Before surveying or recording can begin, permission to enter the area must be obtained. Perhaps the most important thing for the permit agent to do is to plan ahead and start early. Neither a client nor a contractor can afford to have seismic surveying activities delayed as a result of not having secured required permits.

Identify all owners, whether private or government agencies. Failure to do this can result in lawsuits, skips in coverage, or even confrontations between field personnel and irate property owners. Once the owners are identified, contact the person or governmental agency responsible for granting permission to resolve any questions or clarify any uncertainty with respect to permit requirements.

International permitting presents special problems. Each country has its own unique set of permitting challenges. Import/export agents, who specialize in expediting the importation of seismic survey equipment and personnel, can aid in identifying permit issues for a particular country. Typically, the oil company requesting seismic services will be familiar with permitting requirements for the countries in which it operates.

Items to consider in international permitting are

- governmental permits
- environmental regulation and permits
- governmental import/export fees
- notification of military or coastal patrol authorities
- territorial water disputes
- requirements for use of local labor

The oil company contracting for seismic services is frequently in the best position to negotiate for and secure governmental permission.

In land operations, the permit agent is usually the first person to see the area of survey. The permit agent should inform the project manager and other interested parties about potential problems with access or obstructions that may require lines to be deviated or moved.

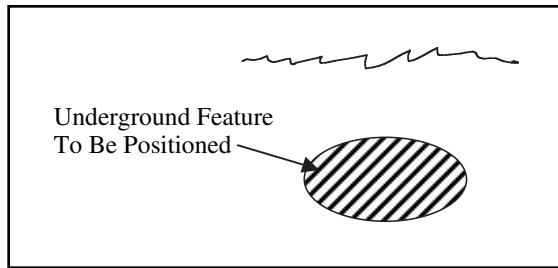


Fig. 5-1 Target Reference

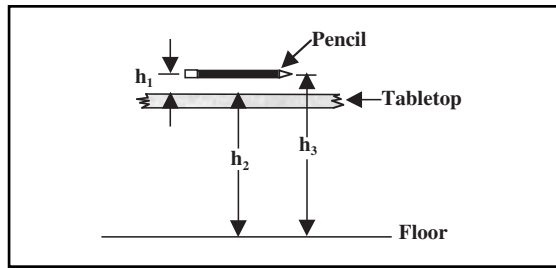


Fig. 5-2 Simple Example of Vertical Reference Datum

Positioning

Good seismic positioning provides accurate horizontal and vertical positions for the entire underground feature within the time that the client has allotted. One question that must be asked is to what will the positions be referred? (Fig. 5-1)

Datum is a very important concept in positioning. A datum is a well-defined reference surface to which measurements are referred. For example, assume you want to know the elevation of a pencil. To answer that question, the elevation must be defined. We can determine where the pencil lies in relation to the table it is on or in relation to its height from the floor. Figure 5-2 shows the situation. We can specify the height of the pencil above the tabletop (h_1) and the level of the floor below the tabletop (h_1). In this case, the tabletop is the datum. Alternatively, we could make the floor our datum and reference the heights of both the tabletop and the pencil to the floor. The height of the pencil depends on the datum—the height-above-the-tabletop datum is less than the height-above-the-floor datum. This is a simplified example of a *vertical reference datum*.

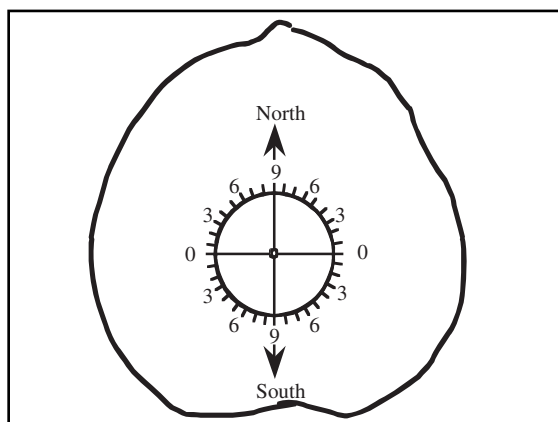


Fig. 5–3 *Geoid*

Unfortunately, the Earth is not flat! Therefore, surfaces that are close to spherical tend to be used to model the Earth's size and shape. One such surface is known as the *geoid*. The geoid is a vertical reference surface, and it is usually very close to mean sea level (MSL). See Figure 5–3. It must be noted that there are a number of different vertical reference datums, each with its particular strengths and weaknesses for a given region. Examples include GEOID '96 and OSU91.

Since the geoid is usable for heights only, we must introduce the concept of a *horizontal reference datum*. Consider this example—your house is the origin of a two-dimensional coordinate system. As you move away from your house, the relative positions of you and your car will change horizontally. Figure 5-4 shows a simple representation of a *two-dimensional horizontal datum* with its origin at your house. This datum does not take into account the fact that the Earth's surface is curved. A satisfactory horizontal datum for use in seismic exploration must recognize the Earth's curvature. *Geodetic latitude* (Fig. 5-5) is an angular measure of position. It is measured from the equator and reaches +90° at the North Pole and -90° at the South Pole.

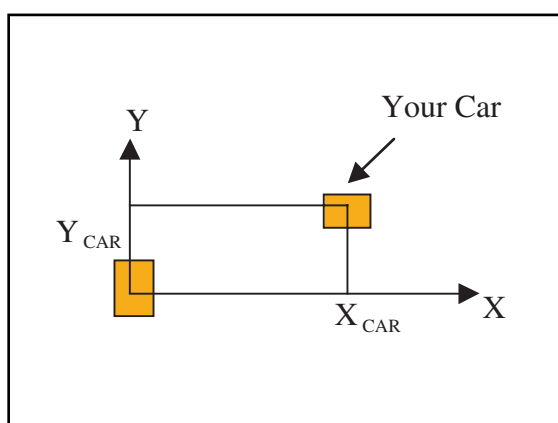


Fig. 5-4 Horizontal Reference Datum Example

Geodetic longitude (Fig. 5–6) is also an angular measure of position. It is measured in the equatorial plane. It is positive east of the Greenwich, England, Meridian of Longitude and negative west of the Greenwich, England, Meridian of Longitude. Note that the latitude (ϕ_G) and longitude (λ) values depend on the parameters of the reference ellipsoid.

Given the latitude, longitude, and ellipsoidal height, it is possible to calculate the X , Y , and Z Cartesian coordinates of a point.

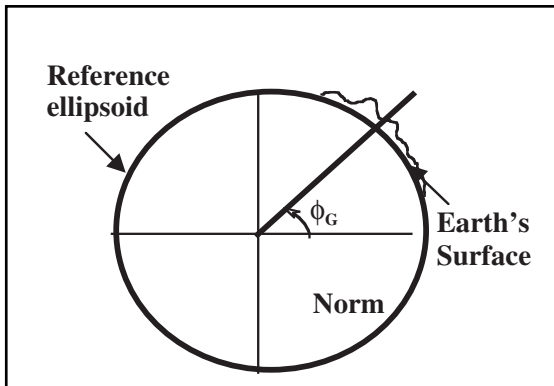


Fig. 5-5 Geodetic Latitude

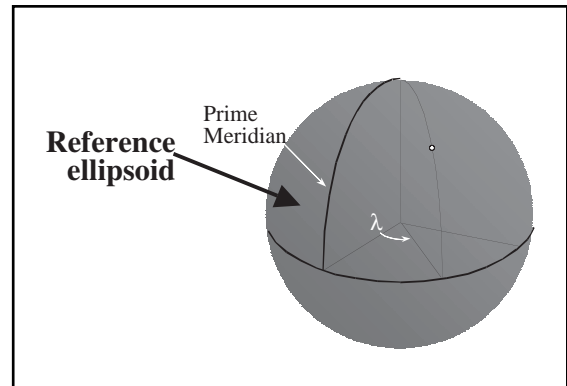


Fig. 5-6 Longitude Measurement

As implied previously, there is more than one kind of ellipsoid (Fig. 5-7). Geocentric ellipsoids are centered at the Earth's center of mass, while regional ellipsoids (such as Clarke 1866 or International) are not (Fig. 5-8). These differences (among others) lead to the need for datum transformations.

In Figure 5-9, Datum 2 is the *local* or *survey datum*, such as might be used in a marine seismic survey. It is desired to change from Datum 2 to Datum 1. The most complete datum transformation requires seven parameters. These are

- DX —datum shift in the X direction
- DY —datum shift in the Y direction
- DZ —datum shift in the Z direction
- e_x —rotation about the X axis
- e_y —rotation about the Y axis
- e_z —rotation about the Z axis
- δS —scale difference in parts per million

The critical thing is that these transformation parameters are entered into the survey system with the proper magnitude and sign.

Many clients will want the local datum positions of the subsurface feature to be expressed in a map projection. A map projection takes the latitude and longitude of a point and converts them into linear units of *northing* (N) and *easting* (E). Consider the simple example in Figure 5-10.

Begin at the origin and go due north for 1000.000 meters on the ellipsoid. This is about 33.3" of latitude. This will be at a northing of 999.6 meters. This northing would, of course, be much different on a different type of map projection.

Among the more common map projection types are the Lambert Conical and Universal Transverse Mercator. Each has its own particular parameters that the surveyor must carefully check to avoid costly positioning errors.

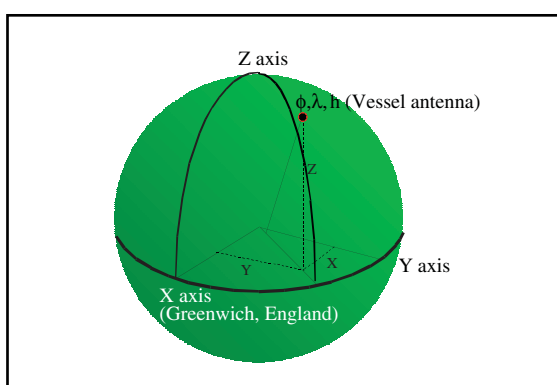


Fig. 5-7 Horizontal Reference Datum

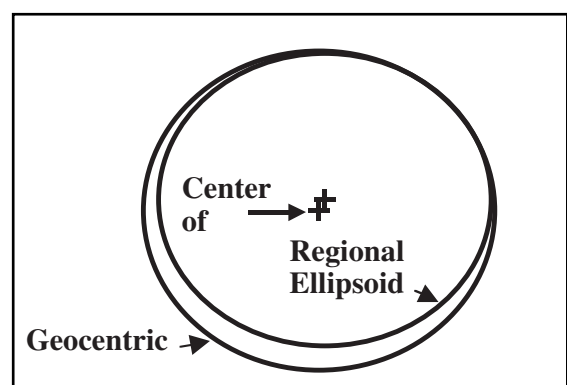


Fig. 5-8 Geocentric and Non-Geocentric Ellipsoids

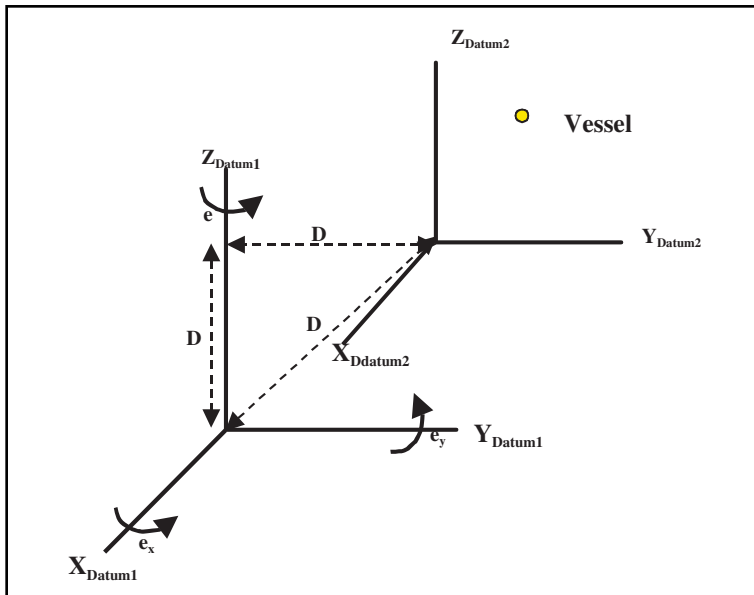


Fig. 5–9 Datum Transformation

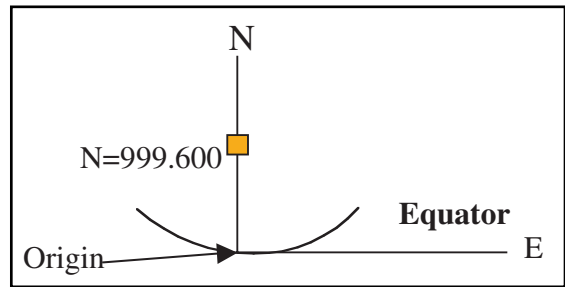


Fig. 5–10 Map Projection

Marine navigation. From a geophysical standpoint, the vessel is only located as an intermediate step in determining the location of the energy source array and seismic detectors. From a safety standpoint, accurate positioning and steering of the vessel is a necessity. The vessel is where all of the people are—this includes the clients and contractors. Except in rare cases, there are numerous hazards (surface facilities, buoys, reefs, shoals, and international boundaries) that must be avoided in order to execute a safe, incident-free marine 3-D survey. The vessel position is also used as a geodetic anchor point for vessel relative positioning systems such as laser or acoustic tracking systems.

Vessel navigation requires absolute positioning in order to relate the position of the vessel to other features (coastlines, platforms, shoals, or reefs) on the surface of the earth. All forms of absolute positioning commonly used in 3-D seismic survey rely on the observation of radio waves to determine the vessel position relative to precisely known reference positions known as *base stations*. There are two main types of radio positioning systems—surface-based and satellite-based systems. Surface-based systems rely on fixed-base stations located on the surface of the earth in the vicinity of the prospect site. Satellite-based systems use orbiting satellites as the base stations. The base stations may be *static* (*geosynchronous*) or *dynamic*. Table 5–1 provides a summary of surface-based positioning systems used in marine seismic acquisition programs.

Table 5–1 Surface-based Navigation Systems

System	Frequency	Geometry	Usable Range	Accuracy
Mini Ranger	5.4–5.9 GHz	Circular	25–50 km	5–20 m
Trisponder	8.8–9.5 GHz	Circular	25–50 km	3–12 m
Syledis	420–450 MHz	Circular	60–110 km	5–15 m
Maxiran	420–450 MHz	Circular	60–150 km	10–50 m
UF Transponder	430–440 MHz	Circular	60–80 km	5–15 m
ARGO	1.6–2.0 MHz	Circular	150–700 km	8–25 m
Microphase	1.6–2.0 MHz	Circular	150–700 km	10–30 m
SPOT	1.6–2.0 MHz	Circular	800–1000 km	10–500 m
Hyperfix	1.6–3.4 MHz	Circular	150–700 km	10–30 m
Geoloc	2.0 MHz	Circular	800–1000 km	10–50 m
Loran C	100 kHz	Hyperbolic	300–1500	50–500 m
Pulse/8	100 kHz	Hyperbolic	300–800 km	30–500 m

The basic concept of radio positioning systems is that radio signal transit times or phase measurements may be converted to equivalent distances by scaling by the propagation velocity of electromagnetic energy. Phase measurements have a cyclic ambiguity of an integer number of wavelengths.

Two primary positioning geometries for surface-based positioning are circular and hyperbolic. Circular systems measure the transit time or phase of a radio signal from a known

location, called the *base station*, to the remote receiver resulting in a *circular line of position* (LOP), as seen in Figure 5–11. Hyperbolic systems measure the transit time difference or phase difference between radio signals sent from two known locations—master and slave base stations—to the remote receiver resulting in a hyperbolic line of position.

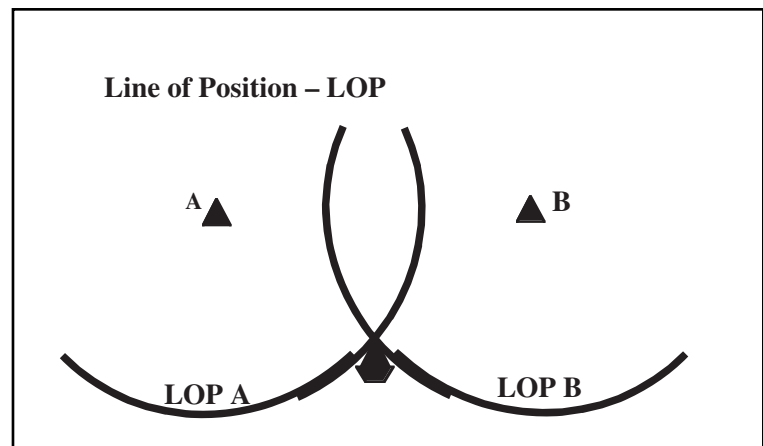


Fig. 5-11 Range-Range LOPs

Radio frequencies used in surface-based radio positioning systems are classified as:

- SHF (Super High Frequencies), 5 – 10 GHz
- UHF (Ultra High Frequency), 400 – 450 MHz
- MF (Medium Frequency), 1 – 4 MHz
- LF (Low Frequency), 100 kHz

In general, the higher the frequency, the greater the accuracy potential, and the lower the frequency, the greater the range potential.

Several satellite-based systems have been developed. The Transit or Navy Navigation Satellite System (NNSS) was developed by the U.S. Department of Defense. It is based on measurement of Doppler shift of transmitted frequency and uses hyperbolic geometry. It has been more or less superseded by the Global Positioning System (GPS). The Navstar GPS was also developed by Department of Defense. It is a ranging system that measures transit time of signal and uses spherical geometry. Starfix is a commercial system that uses geosynchronous communication satellites.

The wide acceptance of GPS positioning technologies, and in particular the wide application of differential GPS positioning techniques for high accuracy positioning, has transformed navigation and positioning in the seismic industry. Surface-based radio navigation systems have largely been superseded by differential GPS or similar satellite-based technologies on the basis of cost, accuracy, and simplified logistical considerations

The GPS is a satellite-based positioning system that can be used night and day from virtually all corners of this planet. The benefits of GPS in seismic work follow:

- all-weather operation
- extremely good accuracy over long distances
- 24-hour per day availability virtually everywhere
- very good reliability
- much faster than conventional surveying techniques in many situations

There are currently 27 satellites in orbit around the world. These are mainly BLOCKII and BLOCK IIR satellites. GPS is made up of three segments:

- the space segment (the satellite hardware and software)
- the control segment (controls the quality of the space segment)
- the user segment (all of the users of GPS)

There are two types of measurements in GPS:

- **Pseudo-range:** measure an unambiguous range to the satellite.
- **Carrier phase:** an ambiguous measurement that has the benefit of higher resolution than the pseudo-range.

The satellite positions must be known to be able to position an object on the Earth's surface. The satellite positions are calculated from an ephemeris, which the user uses to calculate the satellite positions. Table 5-2 provides an overview of GPS systems.

Table 5-2 Basic GPS Overview

	Number of Reference Stations	Accuracy Positions	Minimum Satellites for 3-D	Accuracy Depends on	Accurate Enough for Seismic Work?
Stand-alone Position Non-Differential Point Position	None	100 m	4	Number of satellites	No
Differential Position or Relative Position	At least 1	Generally 1–5 m	4 (5 for some systems)	Number of satellites & distance from base station, etc.	Under proper conditions

In this context, a *reference station* is a GPS base station that is located on a very accurate survey point—not to be confused with the reference stations that the GPS control segment uses. There are several types of differential positions, each with its advantages and disadvantages in terms of accuracy, reliability, and cost.

GPS receivers are used to track the GPS satellites. These receivers do not send signals to the satellites; they receive radio waves from them. The GPS antenna receives the signals from the satellites. The receiver decodes these signals, calculates a position, and provides output (usually RS-232) to other systems (Fig. 5-12).

Every satellite sends out two carriers—*L1* at 1575.42 MHz and *L2* at 1227.6 MHz. The advantage is low noise. The disadvantage is an unknown number of cycles, which means range cannot be directly measured.

Both *L1* and *L2* carriers have a series of ones and zeroes modulated onto them. These are the pseudorandom codes. *L1* has the civilian access (C/A) and precise (P) code. The P code is also encrypted to form the Y code. Civilians can directly access the C/A code, but with only 100 meter accuracy. This effect is known as selective availability (S/A). S/A is thought to be caused by clock dithering in the satellites. This is the GPS standard positioning service. Only the military can directly access the P-code with special receivers. However there are some recent breakthroughs that simulate using the P-code with non-military receivers. *L2* has only the P-code.

Survey accuracy can be considered to have two components—absolute and relative. Absolute is important for interpretation, drilling etc. Relative is important for processing algorithms, frequency preservation, imaging, and more. Errors in absolute positioning accuracy are most commonly caused by incorrect datum transformations. The relative positioning accuracy necessary to preserve the required signal frequencies depends on application. For a *bin size* selected to preserve two samples per wavelength on steepest dips, a positioning error of $\frac{1}{8}$ group interval or $\frac{1}{8}$ of the bin dimension is required. (Bins are discussed further later in this chapter.)

Common Mid-Points (CMP) are an accounting tool used by geophysicists. It is important to know the positions of the sources and receivers. It is not important to have the locations in exact multiples of the group intervals to ensure that midpoints of traces are at bin centers

Absolute positioning accuracy is required for determining drilling locations, reservoir monitoring/depletion studies, and survey extensions. Relative positioning accuracy for vessels, sources, and streamers is required for binning (fold and offsets), imaging, normal move out correction (NMO), dip move out (DMO), pre-stack migration, and location corrections.

Maximum error tolerance for land 3-D is $\frac{1}{8}$ of the surface group interval (on surface). If this were extended to marine operations, it would imply 3 m accuracy for a 25 m group interval or line spacing, 1.5 m for 12.5 m group interval or line spacing, and 0.75 m for 6.25 m group interval or line spacing. None of these are fully realizable with today's technology.

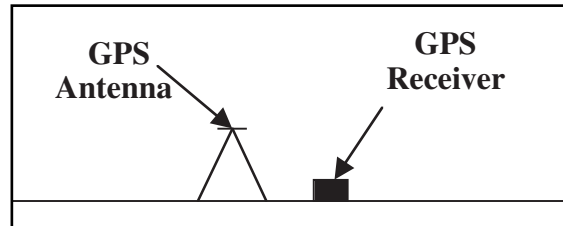


Fig. 5-12 GPS Receivers and Antenna

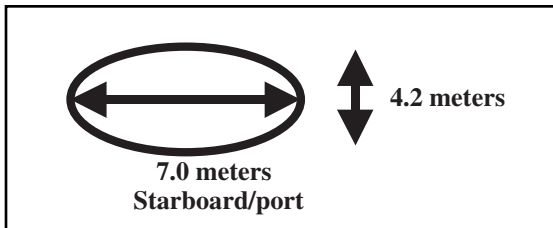


Fig. 5-13 Antenna Motion

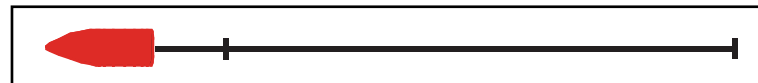


Fig. 5-14 Source and Receiver Assumptions for 2-D Recording

For any radio positioning system, the antenna position is what is actually determined. Typically, this antenna position is not coincident with the points of interest—vessel stern, center of source array, or center of near offset receiver group. Offset application errors, both for vessel positions and navigation buoy positions, are responsible for a surprisingly large number of major positioning busts. These are caused by offsets being ignored or not applied, offsets applied with wrong sign convention, offsets assumed to be the same as previous or incorrectly measured.

Antenna motion can introduce large positioning errors unless the antenna location is corrected for vessel pitch and roll using inclinometer data. For example (Fig. 5-13), for an antenna height of 20 m, if a vessel rolls 10 degrees to either side and pitches 6 degrees fore and aft, then the implied antenna movement is: *starboard/port* (right/left) = $\pm 20 \text{ m} \times \sin 10^\circ = \pm 3.5 \text{ m}$, *fore/aft* (front/back) movement = $\pm 20 \text{ m} \times \sin 6^\circ = \pm 2.1 \text{ m}$.

Relative positions of all elements of a marine acquisition system must be determined. Since some segments of the total system are below the water surface, in-water positioning devices are required. Vessel and platform attitude sensors include the gyrocompass, the *inclinometer* to measure pitch and roll, and the GPS vector systems. Remote target relative positioning systems include a short baseline (SBL) acoustics system, an ultra-short baseline (USBL) acoustics system, and laser ranging systems. Navigation head and tail buoys—radio navigation or GPS—provide remote target absolute positioning systems. Magnetic cable compasses—rotary card or flux gate—are streamer heading sensors. There are inter-cable, source, and vessel acoustics as well as ancillary devices like the velocimeter, cable tension, and depth indicators.

In 2-D recording, the streamer is assumed to be straight and that source and streamer follow boat track. Geometry is often assigned based on shot point and receiver group intervals without use of navigation data (Fig. 5-14).

These assumptions are rarely, if ever, satisfied. Sea currents, tides, and wind usually cause the streamer(s) to deviate from a straight line behind the vessel or *feather*. Figure 5-15 illustrates a simple example of feathering and defines the feathering angle. Feathering angle, α , is used to measure cable deflection due to crosscurrents. Cross-line cable deflection = cable length $\times \sin (\alpha)$ For a 6000 m streamer:

$$1^\circ = 105 \text{ m}$$

$$2^\circ = 209 \text{ m}$$

$$3^\circ = 314 \text{ m}$$

$$4^\circ = 418 \text{ m} = 1/4 \text{ mile}$$

$$8^\circ = 835 \text{ m} = 1/2 \text{ mile}$$

$$16^\circ = 1654 \text{ m} = 1 \text{ mile}$$

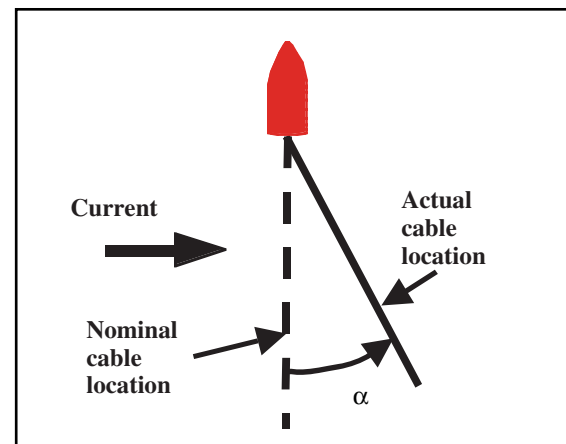


Fig. 5-15 Cable Feathering

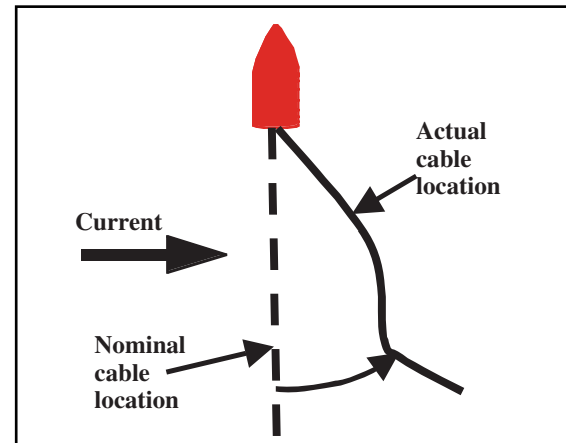


Fig. 5-16 Streamer Curvature

Variations in boat steering and currents result in the cable shape departing from simple assumptions of linearity. An example of streamer curvature caused by feathering is shown in Figure 5-16.

From about 1975 to 1977, the simple assumptions of Figure 5–14 were used in marine 3-D surveys. That is, the streamer shape was straight or a very simple curve, the source and streamer front end followed the boat track, and there was a constant streamer feather angle. Offsets from source to receiver were determined by measurement of deployed lengths of rope, hoses, and other towed equipment.

From 1977 to 1985, the streamer shape was defined by a curve fit to the cable compass readings. The tow fixture angle was used to define the departure angle of the streamer from the vessel. It was also assumed that the source followed the boat track or the gyrocompass.

By 1985, multiple streamers were standard. Up until 1991, streamer shapes continued to be defined by a curve fit to the cable compass readings. The near-vessel targets (source arrays and near detector group) were located using laser tracking or acoustic measurements. Radio navigation tail buoys at the end of the streamers augmented the cable compass measurements.

After 1991, the number of streamers being pulled continued to increase. Positioning measurements are made from a variety of sensors, including cable compasses, acoustic ranges, laser measurements, and navigation buoy positions. All are combined to form an integrated positioning network. Positioning accuracy indicators are now output along with coordinate estimates. Figure 5–17 illustrates such a network and identifies its components.

The vessel attitude sensors are the gyrocompass, the inclinometer, and the GPS vector system. A *gyrocompass* is an inertial device that measures ship's *heading*, the direction the vessel is pointing, as opposed to vessel *track* or *course made good*, which is the direction the vessel is traveling, with respect to true north. Unfortunately, gyrocompasses are subject to a number of errors that are speed, course, and latitude dependent. Overall accuracy for most systems is on the order of 0.5 to 0.7 degrees. An *inclinometer* is also an inertial device. It measures the ship's pitch and roll—along-axis and cross-axis vertical rotation—with respect to vertical.

Multiple GPS antennae are mounted on the vessel. GPS observations of these are used to solve for vectors between antennae. The vectors are, in turn, resolved into pitch, roll, and *yaw*—heading. Because carrier phase and carrier phase difference observations are used, this relative vector is an extremely accurate representation of vessel attitude. This is called the GPS vector system.

Figure 5–18 defines some vessel heading terms. The vessel track or course made good t is the direction that the ship is traveling. The vessel heading h is the direction that the ship is pointing. In general, vessel heading and vessel track are not equivalent because of wind and currents. Vessel heading is usually measured with a gyrocompass. The crab angle c is the angular difference between the direction the vessel is heading and the direction the vessel is traveling.

The remote target positioning system uses relative positioning sensors. The short baseline acoustics—Sonardyne SIPS, Syntron Multitrak, or DigiCOURSE Digirange—use acoustic travel time measurements to compute position fixes for remote targets. Ultra-short baseline acoustics—Simrad HPR or Ferranti ORE Trackpoint—use a phased array approach to measure distance and bearing to remote targets. Laser systems—MARS or LaserTrack—use laser range and angle measurements to locate remote targets. All relative positioning sensors measure the location of remote targets with respect to known points on the vessel and are strongly dependent on gyrocompass measurements to compute absolute positions. Consequently, the accuracy of these systems degrades as the distance from the vessel to the target increases.

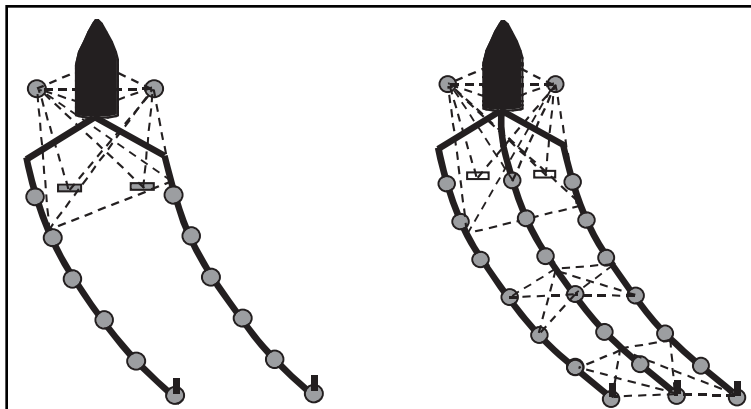


Fig. 5–17 Source and Receiver Positioning, 1985–1991 and Current

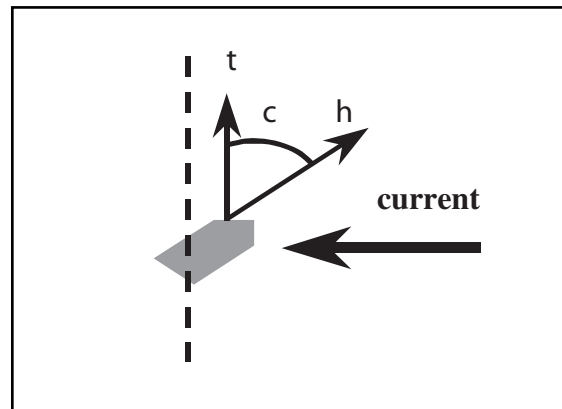


Fig. 5–18 Vessel Heading Terms

Acoustic systems have the advantage of being located beneath the water surface where the sources and receivers are. Acoustic systems also have high resolution. However, the signals they receive can follow multiple paths between sources and receivers, and the path followed may not be known. There is also some uncertainty in the velocity of water that can lead to error in distance computations.

All calculations are relative to the gyrocompass and, thus, include any errors in the gyrocompass reading. Pitch and roll of the vessel influence results obtained, and offsets to position of interest may be large. Geometry of the sensors may not be optimum.

The principal advantage of laser systems is their accuracy, with range at ± 1 m and angle accuracy of ± 0.1 . On the other hand, its surface location is a disadvantage. *Target acquisition* (locating the target) and *target discrimination* (differentiating among multiple targets) may be a problem, particularly in bad weather with fog or rain. The laser system locations are also relative to the gyrocompass.

Absolute positioning sensors used in remote target positioning include navigation tail and head buoys plus a GPS vector system. Navigation tail and head buoys may use either surface-based or satellite-based (GPS) radio positioning. Navigation tail buoys close the magnetic traverse at the end of the streamers and probably have the largest overall impact in improving positioning accuracy at the tail end of the streamers. Navigation head buoys are used to augment the front-end network by removing dependency on gyrocompass measurements associated with relative positioning systems. GPS-based vector systems that use GPS observations to compute vectors from a known location on the vessel to remote targets are NOT dependent on gyrocompass measurements to calculate absolute target coordinates. Unfortunately, navigation buoys measure surface, not subsurface, positions.

Streamer heading sensors (magnetic cable compasses) are of two types—rotary card and fluxgate magnetometer. Rotary card cable compasses have permanent magnets attached to a card that is gimbal-mounted and allowed to align with Earth's magnetic field. A *fluxgate magnetometer* is a toroid with two vertical coils placed orthogonally to measure the component of Earth's magnetic field in each horizontal axis. Cable compasses measure the *magnetic azimuth* of the streamer—the angle with respect to magnetic north. The difference between true or geographic north and magnetic north depends on declination. There are also deviations caused by local effects such as nearby magnetic bodies.

Declination is the difference between magnetic north and true north. Mathematical models of Earth's magnetic field and nautical charts are typically used to estimate true north. The Earth's magnetic field changes as a function of both position and time, so it is important to use a contemporary magnetic field model. Direction of magnetic north is determined by the horizontal component of Earth's magnetic field. The horizontal component of the magnetic field is a maximum at the equator and zero at the magnetic poles. The vertical component of Earth's magnetic field is zero at the equator and a maximum at the magnetic poles.

Most modern cable compasses are housed as a component in an integrated compass/depth controller unit. Note that depth controllers are often referred to as *birds* (Fig. 5–19), so the integrated units are often termed *compass/birds*. These are typically spaced in 300 m or 400 m intervals along each streamer.

Compass data can be adversely affected by the sea state, which can translate rapid accelerations to the compass unit, thereby causing it to depart from a purely horizontal orientation. Magnetic compasses sense the total magnetic field, not just the Earth's field. Consequently, large metal objects (such as platforms or vessels) can adversely impact compass performance.

A fifth-order polynomial fit is used for cable shape determination. Typically, up to 20 compasses may be used for each cable (Fig. 5–20). Compass calibration values can be used or zeroed. Real-time displays of cable shape and data are available. Multiple streamers use laser tracking data and acoustic data for front-end positions. Active navigation buoys are used to determine magnetic variation anomalies.



Fig. 5–19 Bird/Compass on Test Rig

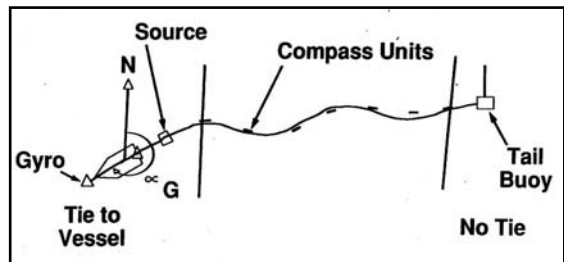


Fig. 5–20 Traditional Applications—Cable Shaping

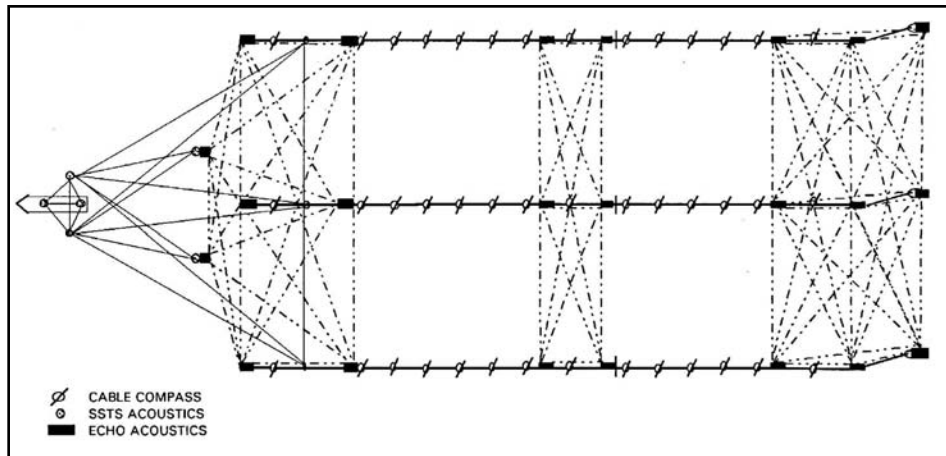


Fig. 5–21 Acoustic Configuration Diagram

The same or similar system used for remote target positioning is used for near vessel tracking of source arrays and near offset receiver groups as relative positioning targets. Acoustic devices are typically arranged in a braced quadrilateral arrangement with diagonal ranges included to measure streamer skew (Fig. 5–21). Acoustic devices tend to be distributed in sub-networks at the head, middle, and tail of the streamers. The cable head network is almost always coupled to the source arrays or a navigation head buoy or both, while the cable tail network is typically coupled to navigation tail buoys. Typical acoustic ranges are on the order of 500 m or less.

The speed of sound in water must be accurately estimated in order to convert measured acoustic travel times into corresponding distance measurements. The speed of sound in seawater depends on temperature, salinity, and pressure. It also varies as a function of depth, geographic location, and time. Devices used to measure water velocity include the *velocimeter* and the *expendable bathythermograph* (XBT). The velocimeter continuously measures speed of sound in water over a very short baseline. The XBT measures temperature as a function of depth in order to compute a sound velocity versus depth profile. Baseline measurements compute velocity from acoustic travel time measurements over known distances—along vessel hull transducers or streamer cable.

Depth indicators (DI) are typically deployed along the streamer as well as at the source array. All compass/bird units contain a depth indicator, which is used as a feedback mechanism to ensure that the streamer is at its target depth. In addition, some streamers have internal depth indicators. Depth indicators are also placed on each gun string in the seismic array. Typically, there is more than one depth indicator per gun string. Depth indicators function by sensing the ambient pressure and relating this pressure to depth.

Cable tension measurements can be used to estimate the amount of streamer stretch or elongation. Cable tension is also very useful in measuring the stresses the streamer cable is subject to during data acquisition.

Energy source location can be done several ways. *Stepback* methods apply nominal offsets from a known position on the vessel to the center of source array along an assumed azimuth—gyrocompass, vessel track, or nearest cable compass. This is extremely crude because the absence of any measurements to substantiate the selected offset and azimuth. It essentially amounts to guessing rather than measuring. *Vessel-relative* positioning methods measure distance and azimuth from vessel to energy source using laser or acoustic measurements. It still requires a smaller stepback from the measured position on the array to the center of the source. *Absolute* positioning methods employ a radio navigation receiver on or near the source array. This relaxes gyrocompass dependency, thereby improving position accuracy. In the *acoustically coupled* method, source position acoustic measurements are used to couple source array to relative or (preferably) absolute surface positions. This is the most accurate means of source positioning, short of a full network solution.

Various methods have been used for cable shaping. Piecewise linear is a simple but extremely crude method. It is not suitable for receiver locations. Curve fits include circular arc, polynomial fit, cubic spline, and streamer offset and arc length. Polynomial (fifth-order) fits are commonly used today.

Integrated positioning networks (Fig. 5–22) provide a comprehensive, integrated solution that fully uses all positioning measurements (absolute positions, relative positions, relative range and bearing, compass bearings, and cable arc length constraints) to derive optimum coordinate estimates for each network node.

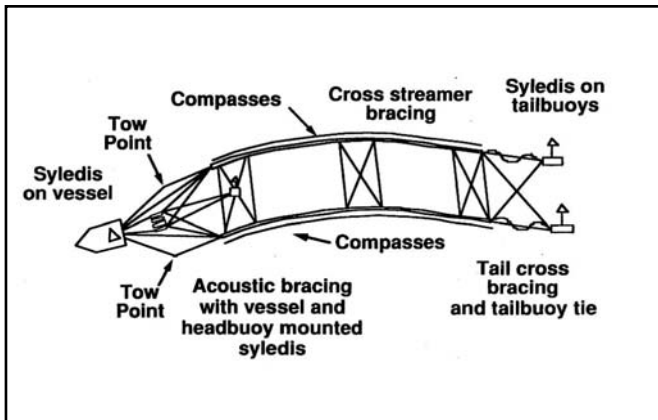


Fig. 5-22 An Integrated Solution

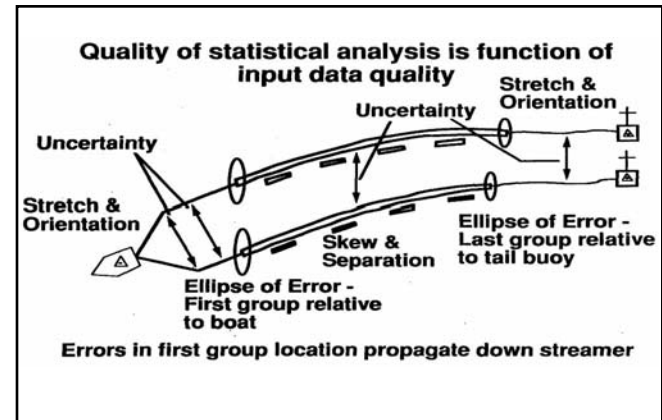


Fig. 5-23 Statistical Analysis

Redundant measurements can be exploited to improve coordinate reliability and to reduce statistical uncertainty. In addition to coordinates, integrated network solutions compute the coordinate uncertainties, which are vital for assessing positioning accuracy (Fig. 5-23). Most network algorithms are implemented as a *Kalman filter*. The Kalman filter can be thought of as a sequential implementation of a traditional least squares network adjustment algorithm that has been modified to predict future states of the network based on past behavior and a dynamic model.

Land surveying. Before any lines are laid out, a system must be developed for numbering source points, receiver points, and midpoints. The numbering system should work for all phases of operation—survey, data acquisition, data processing, and interpretation.

Some systems do not handle non-integers. For example, numbers assigned to source lines between receiver lines and/or receiver lines between source lines must usually be integers. Some systems expect regular Cartesian coordinates. Unique line numbers and point numbers work well for most systems except for Cartesian coordinates. Unique numbers make it easier to manage recovery shots. No two points should have the same number.

The surveyor is responsible not only for locating all source and receiver positions but also for laying out annotated markers on the ground to their locations. The surveyor must ensure that correct transformations are made between survey datums. This is the most frequent source of error.

The surveyor must provide x and y coordinates and elevations for all source and receiver positions. He or she must be aware of terrain limitations of crew equipment and permit restrictions—offsets from wells, springs and other similar elements. The surveyor must also under guidance from project manager, client, or geophysicist locate recovery shots to acquire the required subsurface coverage when source or receiver positions cannot be occupied.

The surveyor must also provide detailed maps for each line, swath, loop, or patch showing source and receiver locations, skips or offset source locations, safety hazards, permit problem areas, fences and drive-arounds, access routes to and from lines, and any wells (oil or water).

Surveyors use many of the same instruments as are used in marine navigation, particularly GPS. Electronic distance measuring devices are also frequently used. Conventional surveying instruments, such as transit and chain, still have a place in land surveying.

Surveying is done in *loops*—the surveyor returns to a particular starting point or previously located position. The difference between the first and second location of this point is called a *mistie*. The client company usually specifies the maximum error or mistie. There will be a maximum allowable error in both horizontal position and elevation. If the error is within the allowed amount, then it may be distributed around the loop followed by the surveyor.

Positioning summary

The final product for land and marine seismic surveys is an accurate three-dimensional position for the subsurface feature. To achieve this, the surveyor must check the following geodetic quantities carefully:

- a. datums to be used
- b. datum transformation parameters
- c. ellipsoid parameters
- d. map projection parameters
- e. geoid model or incline plane

Survey quality control is an important aspect of positioning. For minimum GPS performance verification:

- take a position and record it at known location at start of the day
- take a position and record it at a different known location at the end of the day
- check positions against known locations

Conventional survey equipment should be checked for calibration on a regular basis, typically weekly, whenever possible damage has occurred, after instrument repair, whenever anomalous locations are detected, and whenever excessive misties and/or loop closures are observed. Good documentation of all instrument calibrations and checks should be maintained.

Despite modern positioning systems, errors can still occur. To prevent or minimize these, take special care with datum transformations. Use automated electronic data transfer whenever possible to reduce risk of errors. Surveyed positions plotted on maps should be checked against theoretical positions on program maps. Source and receiver position numbers for key locations (starts and ends of lines or wells) should also be checked against theoretical positions on program maps. Any differences should be checked and verified.

Final survey products include the following items.

- Source and receiver coordinates and elevations in a standard electronic format such as UKOOA or SEG P1. These are sent to the client and to the field crew seismologist for inclusion in files used in the data initialization stage of data processing.
- Post-plot maps showing source and receiver coordinates including key topographical features like coastlines, rivers, and lakes; survey benchmarks; and any wells, roads, or similar items that were surveyed.
- A final report that should include a description of personnel involved in the survey, method(s) and equipment used, datum transformations, and closure errors or misties.

Signal generation

Seismic energy sources must have these characteristics:

- adequate strength for penetration to geologic targets
- broadband signature rich in both low and high frequencies
- balanced, flat spectrum—tuned source
- stable, repeatable signature
- mechanically and electrically reliable

For 3-D operations, energy sources should also have:

- compact spatial extent to minimize array effects
- spatial symmetry to minimize asymmetric array response in the in-line and cross-line dimensions

Air guns, water guns, and several others are or have been used as marine energy sources. Air guns are, by far, the most used for marine operations. In the transition zone, dynamite is used in shot holes or marine-type sources, depending on water depth and environment. Land energy sources include dynamite in shot holes, and Vibroseis. Source selection is usually based on availability, the ability to generate seismic energy required to image primary objective, cost effectiveness, and accessibility.

Airguns. Requirements for marine energy sources are

- produce a powerful pulse
- have capability of rapid firing (approximately 10 sec intervals)
- are simple to operate, consistent, and trouble-free
- remain at constant depth and have minimum drag when towed
- cause no injury to marine life
- minimize *bubble effect* (repeated expansions and contractions of volume of gas)

Airgun arrays satisfy all of these. Explosives satisfy all but one critical requirement—they do cause damage to marine life. Consequently, explosives have not been used in deepwater marine surveys for many years. Only in very shallow water, where holes can be easily dug, are explosives used in marine work.

Basic airgun operation is as follows (Fig. 5–24). Airguns of various sizes are combined to form arrays. The compressor on the back deck supplies compressed air. The navigation system sends a signal to the Airgun Controller when the source point is reached. The Airgun Controller fires each gun in the array and sends a signal to recording instruments to start recording.

Figure 5–25 illustrates major components of airguns and airgun operation. The solenoid valve is electrically connected to the airgun controller, and hoses to the compressor connect the air intake. Compressors operate at a pressure of 2000 psi. Pressures up to 4000 psi have been used in experiments, but it was found that the danger was too great to use in a production mode.

In the *charged* condition the solenoid is positioned to close the *firing line* and open the *fill passage*. Air is introduced through the air intake valve and the fill passage and enters the chamber via the *chamber fill orifice*. The airgun is *fired* when the pressure in the chamber reaches 2000 psi. On a signal from the airgun controller, the solenoid valve position is changed to open the firing line and airflows into the *firing chamber*. The pressure in the firing chamber causes the sleeve to move up and air begins *exhausting* into the water via the *exhaust ports*. The movement of the sleeve compresses the air in the *spring chamber* even further. As air exhausts from the chamber into the water, the pressure in the spring chamber becomes able to push the sleeve down, closing the exhaust ports and the air gun is now *exhausted*. The cycle can now begin again.

A single airgun is a poor energy source because of its bubble effect. This is shown in Figure 5–26. When the compressed air is introduced into the water, it creates an air bubble that rapidly expands, and the pressure in the bubble becomes less than the surrounding water pressure. As a result, the bubble contracts. However, the contraction goes too far and air

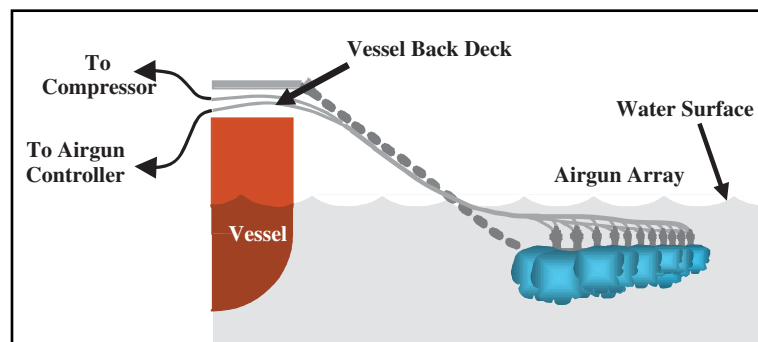


Fig. 5–24 The Airgun Technique

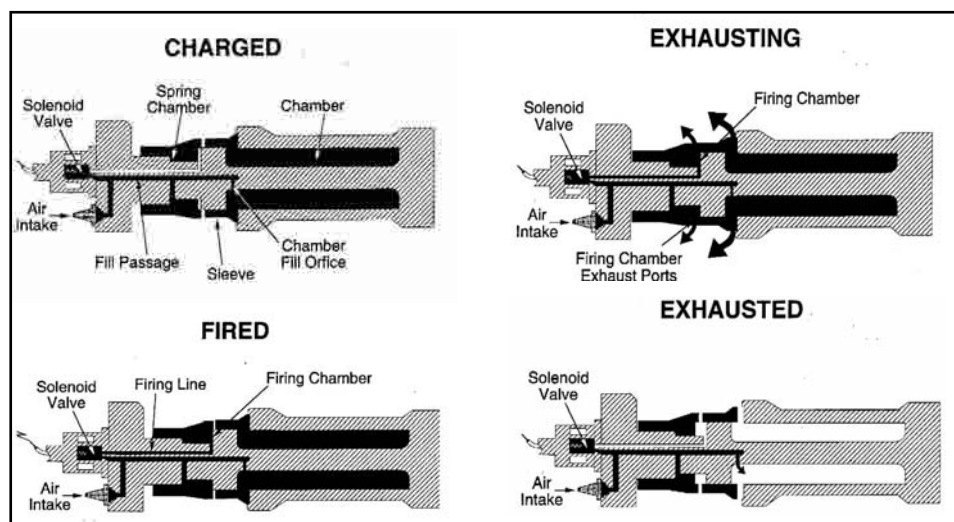


Fig. 5–25 Airgun Operation

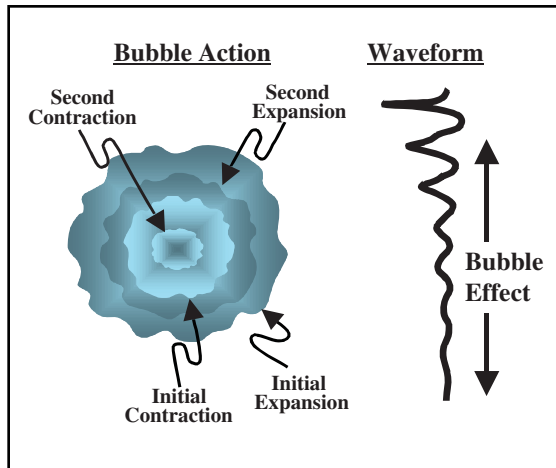


Fig. 5-26 The Bubble Effect

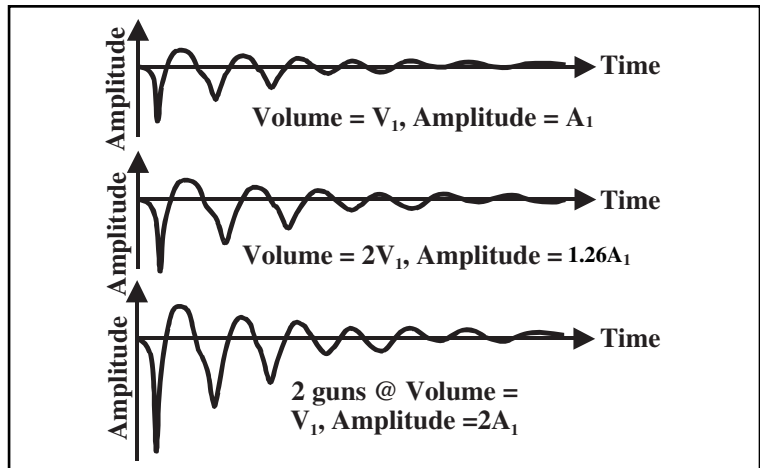


Fig. 5-27 Airgun Pressure-Volume Relationship

pressure is once again higher than water pressure and a second, although smaller, expansion occurs. Repeated contractions and expansions occur until all the energy is dissipated. Figure 5-26 illustrates this and the waveform produced by the bubble effect.

Pressure produced by a single airgun is proportional to the cube root of *gun volume*—the total space in the airgun occupied by air. Signal amplitudes are proportional to pressure, so amplitude is also proportional to $V^{1/3}$. So, as shown in Figure 5-27, increasing the volume of a single airgun gives only 26% larger amplitude. However, using two airguns of the same volume placed closely together produces twice the amplitude.

Airguns are used in arrays for two reasons—to increase signal amplitudes and to minimize the bubble effect. The latter is illustrated in Figure 5-28. In this very simple array, three different size guns (different volumes) are used—one large gun, three medium size guns, and three small guns. The guns of the same size are grouped closely together (clustered). Spacing between the one large gun and the two clusters is such that the bubbles interfere destructively except at the initial expansion. Note that the airguns in the array do not fire simultaneously. The smaller guns are delayed because their bubbles achieve maximum expansion earlier than the larger guns. Note also the lower frequency content of the larger guns. Large numbers of airguns of various sizes are grouped together to form tuned arrays. With proper spacing of single guns and gun clusters (array design), virtually any desired signal waveform can be achieved.

The two main objectives of airgun array design are to obtain adequate energy source strength and sufficiently broad frequency bandwidth. The best way to determine a source strength requirement is to conduct a field experiment using different strength sources to record a 2-D line and then process and analyze the results. For the obvious reasons (time and cost), this is almost never done. A review of previously acquired 2-D or 3-D data can aid in determining adequate source strength requirements. Amplitude decay analysis and time variant spectral analysis of previously gathered 2-D or 3-D data can help determine the depth (recording time) of penetration of useful seismic energy. It is possible to *overshoot* an area by using an energy source that is too strong.

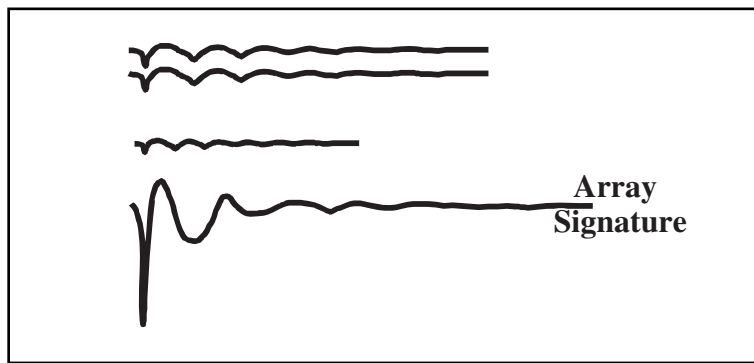


Fig. 5-28 Waveform Synthesis by Airgun Arrays

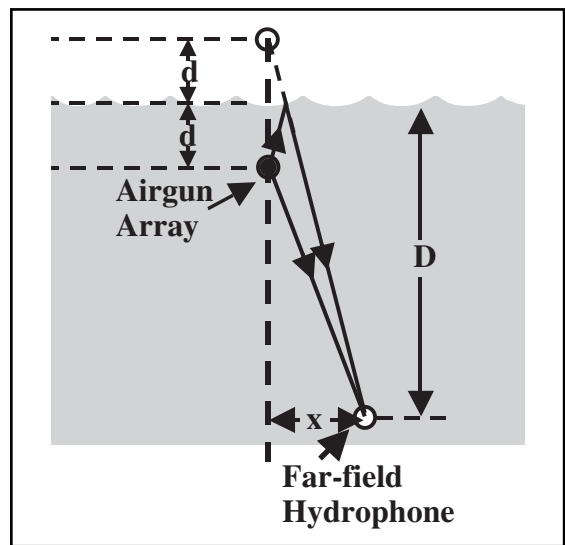


Fig. 5-29 Measurement of the Far-field Signature

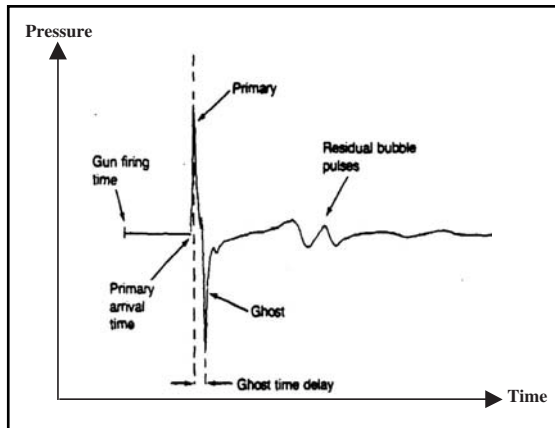


Fig. 5-30 Time Domain Attributes

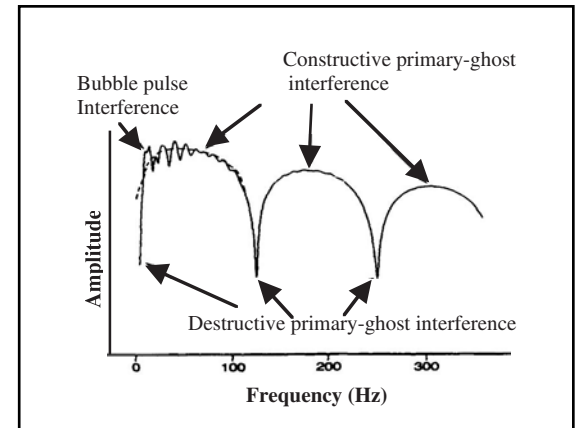


Fig. 5-31 Airgun Frequency Domain Attributes

Airgun arrays are towed below the water surface, usually at depths of around 10 m. As a consequence, upward-traveling energy from the airgun array is reflected at the surface and interferes with the downward-traveling energy to produce ghosts. In Figure 5-29 a hydrophone is shown at a depth D (usually about 100 m below the airgun array) below the water surface and displaced slightly behind the array. The airgun array is at depth d below the surface. When the array is fired, energy travels out in all directions. The ghost, produced by reflection at the water surface, appears to come from a source placed d above the water surface.

The angles of incidence of concern at the water surface are small enough that we can use the vertical incidence reflection coefficient from Equation 3.11 of Chapter 3.

$$R_{12} = \frac{\rho_2 V_2 - \rho_1 V_1}{\rho_2 V_2 + \rho_1 V_1} = \frac{\frac{\rho_2 V_2}{\rho_1 V_1} - 1}{\frac{\rho_2 V_2}{\rho_1 V_1} + 1}$$

In this case, medium 1 is water and medium 2 is air. The velocity of sound in water is about three times that of sound in air and the density of water is hundreds of times larger than that of air. So, with very little error, the ratio $\frac{\rho_2 V_2}{\rho_1 V_1}$ and $R_{12} \approx -1$. The ghost is thus seen to be an inverted and delayed version of the primary signal, as shown in Figure 5-30.

Figure 5-31 shows the frequency domain attributes of an airgun array signature. In the frequency domain, ghosts appear as notches or zero points in the amplitude spectrum. The frequency at which the notches occur depends on depth of the airgun array and water velocity.

$$f = \frac{V_W}{2d} \quad (5.1)$$

where

f is the notch frequency

V_W is the water velocity

d is the source depth

Airgun array specifications, also called specs, may be given in the time domain or frequency domain. Time domain specs are strongly dependent on signature filtering and bandwidth. *Peak-to-peak strength (PTP)* measures, in bar-meters, the signature strength, and *primary-to-bubble ratio (PBR)*, a dimensionless quantity, measures signature shape. See Figure 5-32.

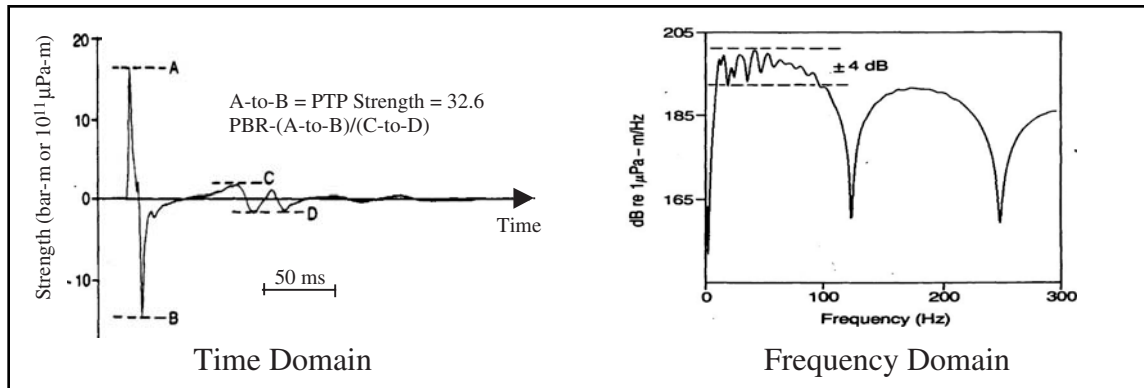


Fig. 5-32 Airgun Array Signatures and Parameters

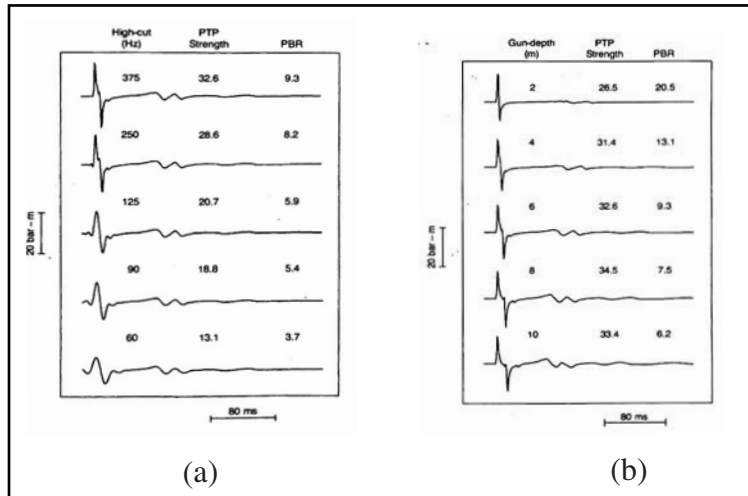


Fig. 5-33 Signature Variation with Frequency and Depth

specifications are influenced by array depth (Fig. 5-33b). Low-cut instrumentation filters and high-cut anti-alias filters affect the time domain specs of an airgun array. The best way to compare the performance of different energy source arrays is by using calibrated amplitude spectra. Table 5-3 summarizes the effects of various array parameters on airgun specs.

The total volume of an airgun array is not, by itself, a good indicator of an energy source's strength. Source strength is roughly proportional to the *cube root* of the array volume. An airgun array's strength is roughly proportional to the number of elements (single guns or clustered guns) in the array.

Table 5-3 Airgun Specs and Array Parameters

Parameter	Strength	Peak-to-Bubble Ratio
Number of Elements	Proportional to the number of elements	No direct relationship
Element Volume	Proportional to the cube root of volume	Increases as volume increases
Element Depth	Increases initially, then decreases with increase in depth	Decreases as depth increases
Firing Pressure	Increases as firing pressure increases	Increases as firing increases
Port Area	Proportional to square root of port area	Increases as port area increases
Port Closure Pressure	No effect if closure pressure is < 0.5 of firing pressure	Decreases as port closure pressure increases
Synchronization	Decreases as spread in firing times increase	Decreases as spread in firing times increase
Horizontal Element Spacing	Decreases as elements move closer together	Increases when bubbles coalesce

Frequency domain specs are always preferred over time domain specs, since calibrated amplitude spectra provide absolute frequency-by-frequency strength information. *Spectral amplitude* (dB referenced to 1 micropascal-m/Hz) measures signature strength. *Spectral flatness* (dB); measures signature shape. Low and high cut filter effects are clearly evident and calibrated amplitude spectra also give a direct insight into ghost notch effects.

There are pitfalls in using time domain specs. The peak-to-peak strength and primary-to-bubble ratio of an airgun array signature are strongly dependent on the frequency bandwidth. Unless the bandwidth of a signature is known, it is impossible to validly compare time domain specifications for different source arrays. Because the depth of a source array has a profound effect on the frequency bandwidth of the array signature, time domain

Array parameters that depend on the type of airguns used in an array (firing pressure, port area, and port closure pressure) affect the fundamental characteristics of array signatures only weakly. An airgun array can be tuned to have a high primary-to-bubble ratio by towing the array at a shallow depth, but a shallow array has a much weaker low-frequency response than an array at a conventional depth.

Air guns in use today are the type called *sleeve guns*. Figure 5–34 shows a variety of sleeve guns.

Since airguns are used in arrays, some method must be used to assemble the array, maintain the separation between elements, and tow it as a unit at a fixed depth. Figure 5–35 shows a side view of a typical sub-array. The top part floats on the water surface and is attached to the boat by a tow cable or chain. The bottom frame is suspended by cables of a fixed length, according to the desired firing depth. Hoses and electrical connections run between the assembly and the back deck. Fittings allow airguns to be suspended by chains at any desired spacing.

Figure 5–36 shows a plan (top) view of dual airgun array. Each sub-array (heavy black lines indicated by numbers one through eight) has guns with a total volume of 750 cubic inches. The sub-arrays are 21.05 ft long and are six feet apart in each array. Location of other components (acoustic pods, GPS, MARS) used in source location are also shown in Figure 5–36.

Paravanes or other diverters are used to maintain the separation between the two arrays. It is important not only to maintain the desired separation between elements of the sub-arrays but also to maintain the required separation between sub-arrays. If this is not done, then the array response will not be as designed.

The depth at which the source array is towed determines the frequency of the ghost notches and affects the ghost response. Figures 5–37 shows the ghost responses for a 6 m and a 10 m source depth. Figure 5–38 gives the ratio, in dB, of the response at 10 m depth to that at the 6 m depth. Note that the comparison ends at the notch frequency for the 10 m depth.

Compact, symmetrical arrays are preferred to minimize filtering of seismic energy reflected from steeply dipping interfaces due to non-vertical arrival. Any filtering effects due to the spatial extent of the array will be uniform in both the in-line and cross-line directions. Wide or long source arrays, which are spatially extended in either the cross-line or in-line direction, are detrimental to high fidelity recording of steeply dipping energy in the direction of maximum spatial extent. Figure 5–39 illustrates energy transmission from compact and wide arrays. Compact is desirable for 3-D surveys and wide for 2-D surveys.



Fig. 5-34 A Single Sleeve Gun, a Disassembled Sleeve Gun, a Sleeve Gun with a Mounting Harness, and a Family of Sleeve Guns

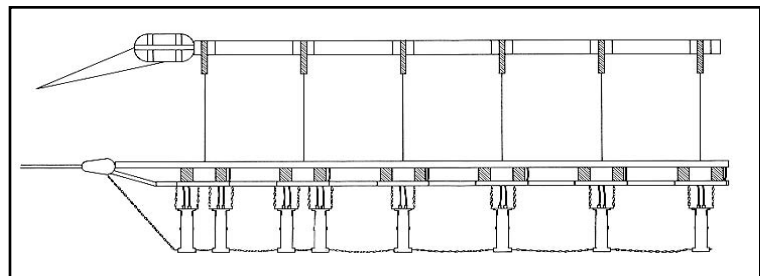


Fig. 5-35 Side View of a Typical Sub-array Configuration

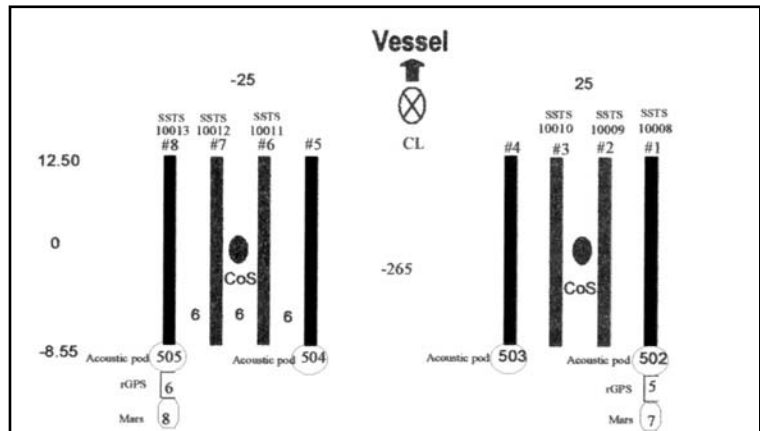


Fig. 5-36 Plan View of a Typical Source Array

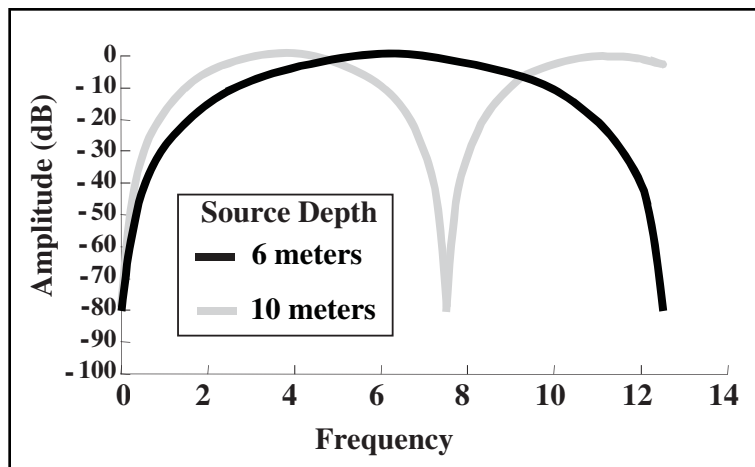


Fig. 5-37 Streamer and Source Depth Ghost Notches

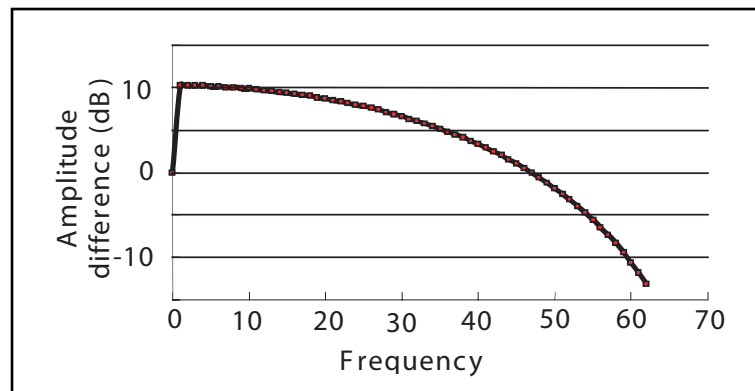


Fig. 5-38 Ghost Response at 5 and 10 m

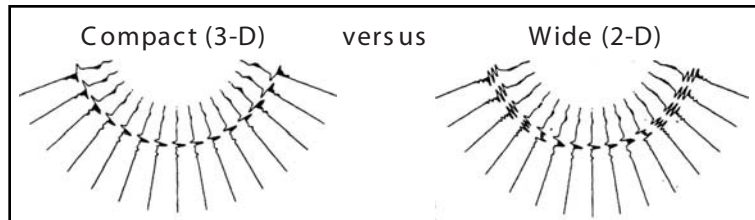


Fig. 5-39 Source Array Effects

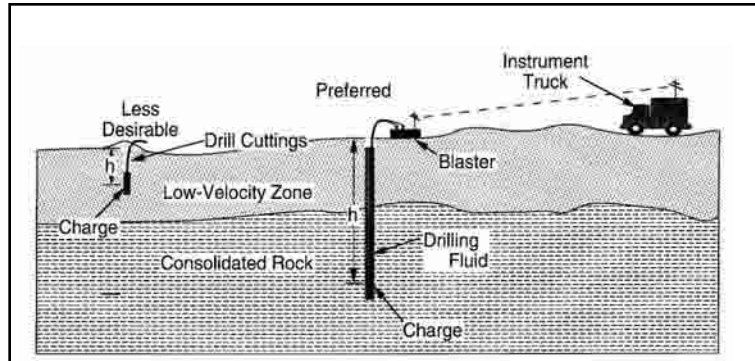


Fig. 5-40 The Explosive Technique

Explosives. Normally, on land the choice is between vibrators and explosives. The choice depends upon suitability to terrain, surface conditions, ease of drilling, availability of personnel and equipment, environmental and governmental regulations, cost comparisons, and other factors. Explosives are not usually used in offshore data acquisition because of environmental regulations or in densely populated or industrial areas because of possible damage and permitting problems.

Explosives are an *impulsive* energy source because they transfer seismic energy into the ground in the form of a short duration impulse. Explosives are usually loaded and shot in drilled holes. However, some use has been made of explosive cord that is buried very shallowly in, usually, linear patterns. Further discussion follows that on explosives in drilled holes.

When loading explosives in drilled holes, it is desirable to drill deep enough to ensure that the explosive charge is below the base of the weathered layer. This gives the best signal level and bandwidth while minimizing shot-generated noise. Other factors to consider in the determination of hole depth follow.

- Is there a formation in which energy transfer is optimized?
- Can the surface ghost be used to reinforce the primary wavelet in the earth-air interface where the reflection coefficient equals -1?
- Should single deep holes be used or should multiple shallow holes be drilled in an array or pattern to cancel coherent noise?

The preferred technique (Fig. 5-40) is to load a charge or charges in a hole or holes drilled through the low-velocity zone (weathering). The charge may be dynamite, nitro-carbo-nitrate or ammonium nitrate fertilizer mixed with diesel fuel. The size of charge depends on depth h and shot medium. Principal advantages are that time through the low-velocity zone can be measured directly (via an up-hole geophone), surface wave generation is minimal, and having only one pass through the low-velocity zone reduces attenuation. In some cases, the time and cost of drilling dictate drilling shallow holes. When this is done, an array of several holes is drilled to enhance the signal and attenuate surface waves at the source.

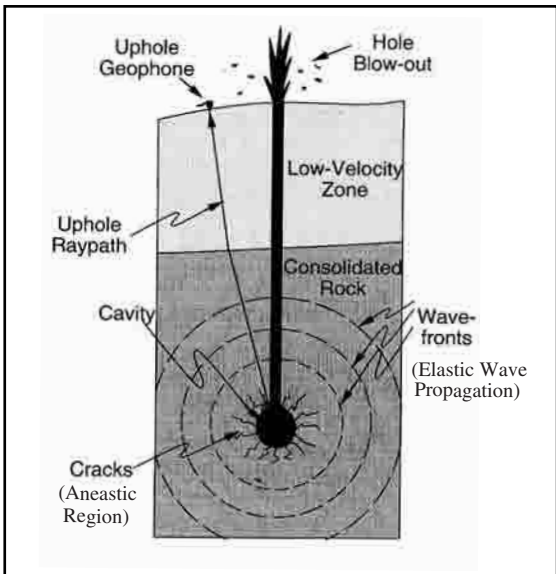


Fig. 5-41 Explosive Source Operation

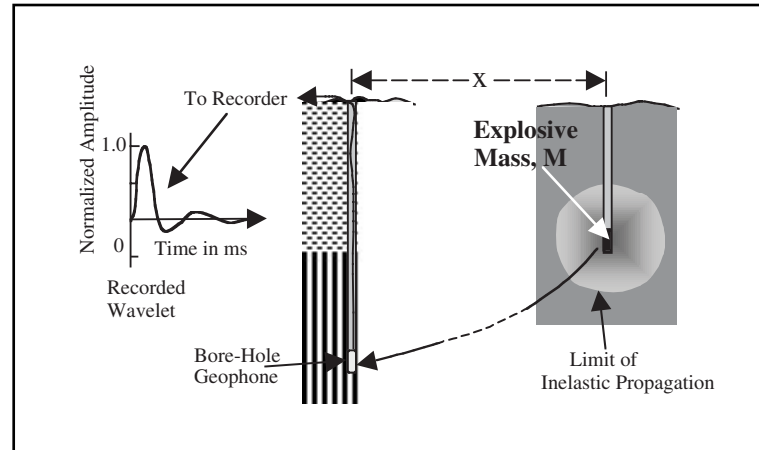


Fig. 5-42 Measuring the Far-field Signature of an Explosive Source

Figure 5-41 illustrates explosive source operation. A high-voltage pulse is applied to a blasting cap by a blaster. Heat from the cap initiates rapid combustion of the charge (explosive mass). Combustion produces a large volume of hot gas that expands at a very fast rate. Pressure against the hole walls is transmitted as seismic (elastic) waves in approximately spherical wave fronts radiating out in all directions. Some of this energy reaches the up-hole geophone via a minimum time path. Part of the energy produced by explosion may be expended in blowing out material (drilling mud, rocks) from the hole. This is called *hole blowout*. Some of the energy produces permanent deformation in the form of a cavity and cracks in the medium around the shot (an elastic zone).

Figure 5-42 shows a method of measuring the far-field signature of an explosive source, assuming a homogeneous medium. Two holes are drilled 100 m or so apart. A charge is loaded at the bottom of the shallower hole and a geophone (detector) connected to a recorder is placed at the bottom of the deeper hole. The charge is fired, and the signal received directly from the charge is recorded. The left side of Figure 5-42 indicates the shape of the recorded wavelet. The amplitude is *normalized*—amplitudes are divided by the maximum amplitude.

The amplitude, duration, bandwidth, and spectral amplitude of the pulse produced by an explosive source depend on charge size. Figure 5-43 shows wavelets and their amplitude spectra for two charges, one of mass M and one of mass $M/8$. The amplitude, duration, and bandwidth are proportional to the cube root of the charge mass. The amplitude of the spectrum is proportional to charge mass raised to the $2/3$ power.

The medium surrounding the charge also affects signal. Drilling deeper may place charges in a more favorable shot medium, producing higher amplitudes and wider bandwidth. However,

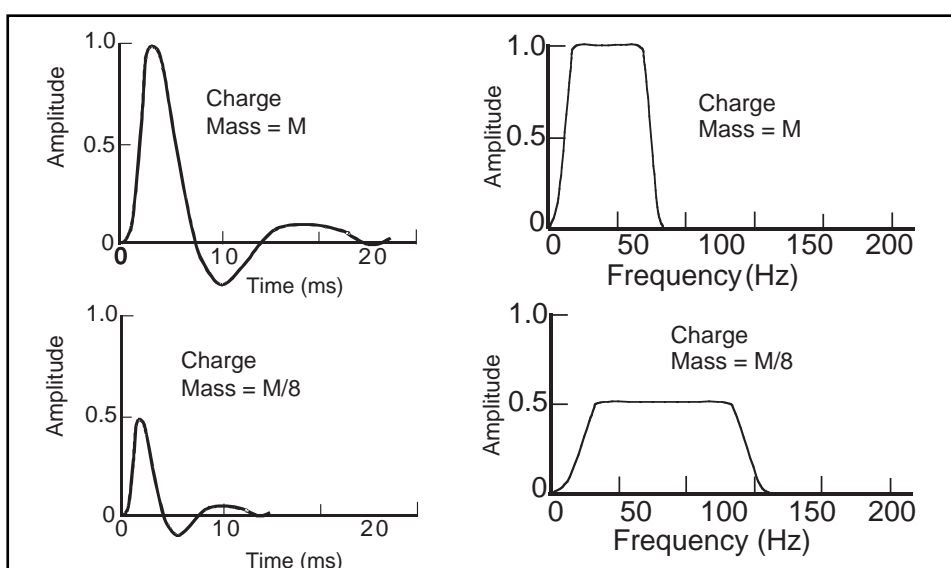


Fig. 5-43 Effect of Charge Size

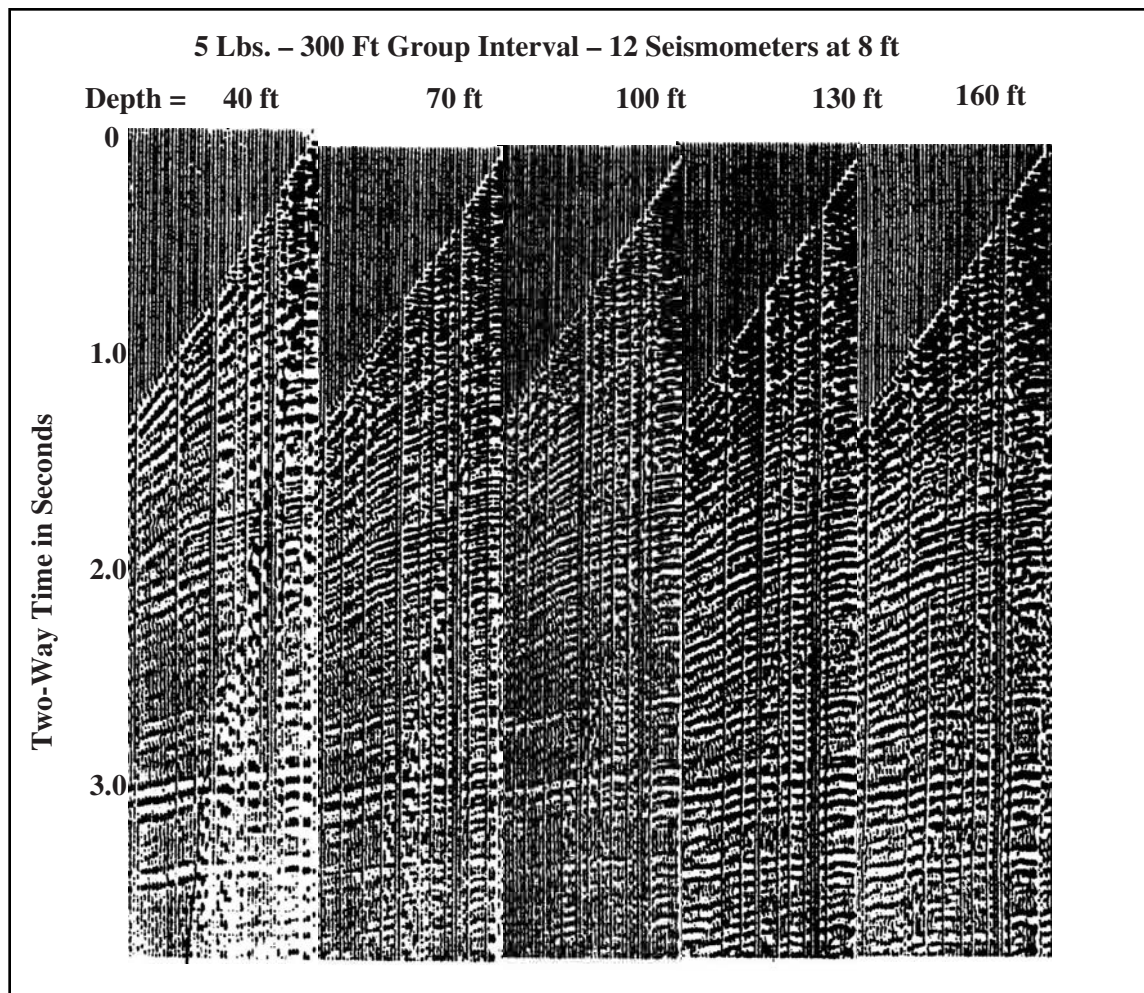


Fig. 5-44 Charge Depth Test

increasing either charge size or shot depth would not only increase cost but could adversely affect data quality. Increasing the number of holes would seem the best choice, but this would at least double the cost of drilling and the budget may not allow it. Field-testing is used to indicate an optimum charge size and shot depth.

Figure 5-44 shows the results of such a test. Usually, a hole is dug to a greater depth than that anticipated being used, and a constant charge size is shot at various depths, starting at the bottom of the hole. Once the optimum depth is determined, experiments with charge size are used to determine optimum charge.

Geoflex and *Primacord* are two commercial names for explosive cord. When used as a seismic energy source, cord is inserted into the ground with a tractor-mounted plow. As the plow turns over the soil to a depth of about 18 inches, the explosive cord is fed out of the rear of the tractor into the furrow. The cord is buried as the soil collapses over it. Usually, two or more lines of explosive cord are used. The lines are around 200 ft long and spaced about 15 ft apart. See Figure 5-45.

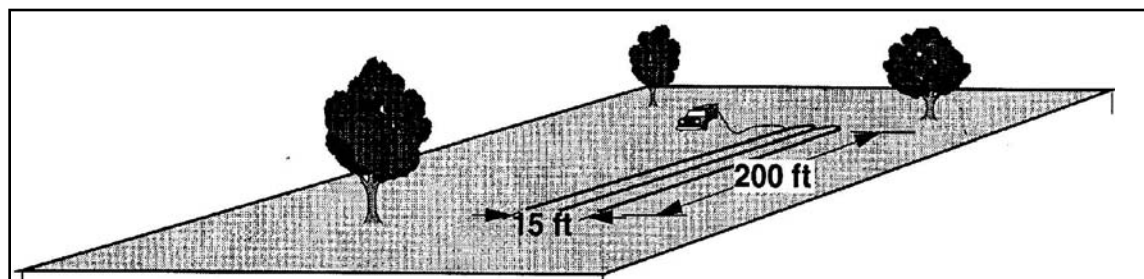


Fig. 5-45 Explosive Cord as a Seismic Energy Source

The cord detonates at 21,000 ft/sec, and being laid out in lines has some directivity in the energy propagation and attenuates horizontal noise. The advantages are that:

- charges are small but very efficient.
- it is cheap and fast because no drilling is required

It must be noted, however, that a soft surface is required for the method to be practical.

Vibrators. The vibrator (trade name Vibroseis) was developed by Conoco. A vibrator is a vehicle-mounted energy source that produces a vibratory or swept-frequency signal of relatively long duration (2 to 32 sec). Principal components of a vibrator system are illustrated in Figure 5–46, courtesy of WesternGeco. Major elements of a vibrator system include

- diesel engine
- converts fuel into mechanical energy
- propels vehicle and powers hydraulic system (single engine)
- hydraulic pump
- converts mechanical energy to hydraulic energy
- compensates for pressure by providing flow necessary to maintain desired pressure
- hydraulic supply system
- provides pulsation reduction
- stores hydraulic energy on a duty cycle basis
- filters and distributes hydraulic fluid
- vibrator control electronics
- generates electrical signals to control vibratory system
- servovalve
- modulates hydraulic flow to yield desired acoustic output under the electrical control of vibrator control electronics
- reaction mass
- acts as an inertial element in actuator assembly for force to push or react against and is typically 4000 to 10,000 lb. in weight (Hold-down force holds the baseplate in contact with ground. It is sum of actuator assembly and vehicle weight applied through isolation spring.)
- base plate
- applies generated vibratory force to ground
- isolation springs
- decouples vibratory motion of base plate from vehicle—usually an air bag
- vibrator actuator
- houses piston rod and servovalve
- acts as inertial element
- ported for oil passages
- stilts
- provides mounting structure for vibrator actuator
- delivers vibratory force to base plate
- straddles vehicle drive line in some conventional truck mounts
- radius rods
- provides lateral stability for isolation system
- accelerometer
- measures phase and amplitude of base plate and/or reaction mass motion

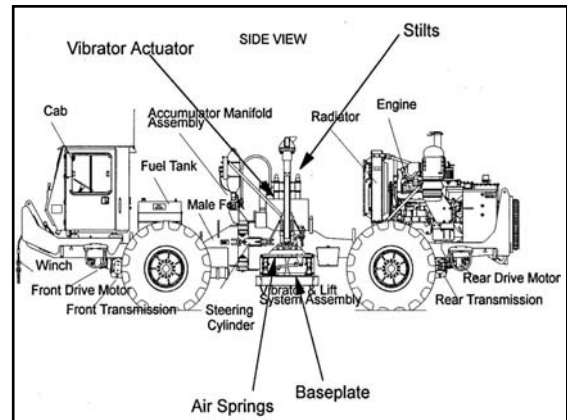


Fig. 5–46 Truck-mounted Vibrator Components



Fig. 5-47 Side View of a Truck-mounted Vibrator

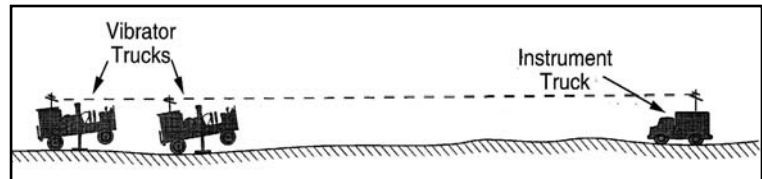


Fig. 5-48 Vibrator Operation

Figure 5-47 is a photograph, courtesy of WesternGeco, of a vibrator used in West Texas.

Vibrator operation is as follows (Fig. 5-48):

1. Two or more vibrator trucks are positioned at source points within a source array (VP).
2. The base plates are lowered to the ground and the trucks are jacked-up to place additional weight on the base plates, providing reactive mass.
3. An encoded swept-frequency signal (pilot sweep) is transmitted from the vibrator control unit in the instrument truck to similar units in each vibrator truck.
4. All vibrators input the prescribed signal into the ground and instruments begin recording simultaneously.
5. Recording continues for the length of the sweep plus the listen time.
6. All records obtained at a single source point are vertically stacked (summed) into one record.
7. Records are cross-correlated with the filtered pilot sweep to produce a record as long as the listen time.

Consider the following example. Reflections are recorded at times of 0.7 s, 1.2 s, 1.95 s, 2.2 s, 2.86 s, 3.17 s, and 4.006 s. Sweep length is 10 s. The first reflection will be recorded from 0.7 s to 10.7 s, the second from 1.2 s to 11.2 s, the third from 1.95 s to 11.95 s, etc. As can be seen, there is considerable overlap among the reflections. In fact, the overlap is so great that raw vibrator records are unintelligible. This is why cross-correlation with the pilot sweep is required. An uncorrelated vibrator (Vibroseis) record using a 10 s sweep, and the corresponding correlated vibrator record is shown in Fig. 6-12.

Cross-correlation measures the similarity between two time series. In this case, the two time series are the pilot sweep that has had the instrument filters applied to it (*filtered pilot sweep*) and the raw vibrator record, which had the same filters applied while it was being recorded. In the frequency domain, cross-correlation is the product of the two amplitude spectra and the difference in phase spectra. Since the raw vibrator record has had the instrument filters applied to it, the filtered pilot must be used to cancel out the phase response of the recording instrument filters.

Noise spikes (static, parity) must be suppressed (*De-spiking* applied) prior to correlation. Since correlation can be expressed as convolution of one time series with a time-reversed second time series, cross-correlation with a spike produces an inverted sweep that is combined with the output record. Figure 5-49 shows the effect of a single high-amplitude spike in an uncorrelated record. The amplitude is 1000 times larger than trace samples.

Figure 5-50 illustrates vibrator correlation, assuming an earth response with four primary reflections. The raw record is the convolution of the vibrator sweep and the earth response. Only the start of the first reflection can be determined.

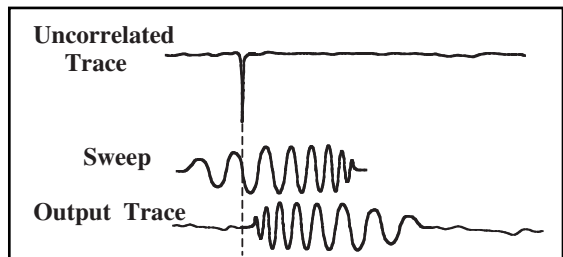


Fig. 5-49 Effect of Spike on Vibrator Cross-correlations

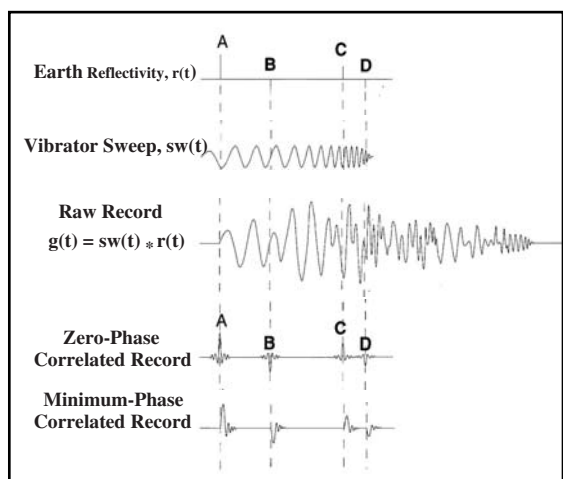


Fig. 5-50 Vibroseis Correlation

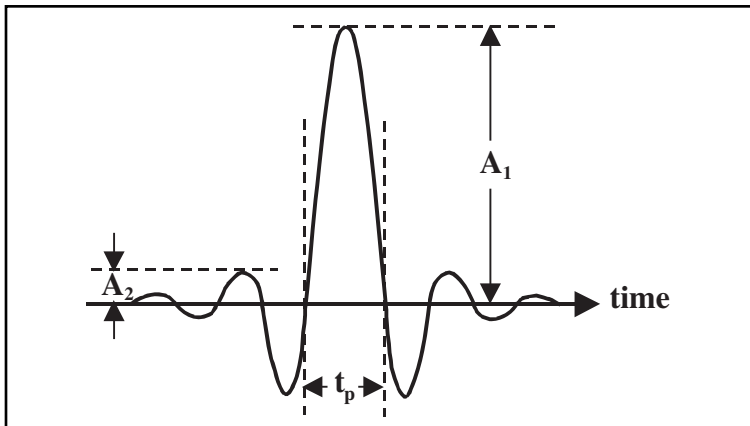


Fig. 5-51 Klauder Wavelet and Resolution

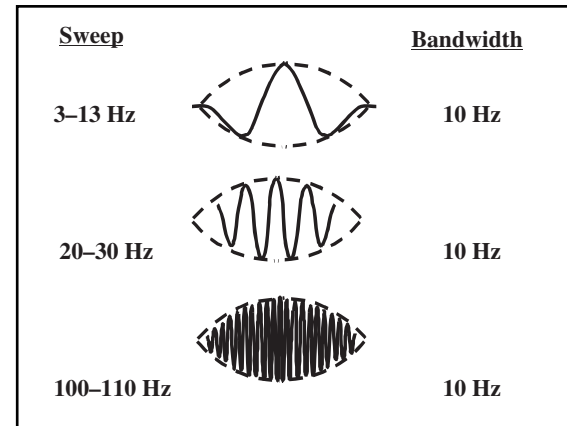


Fig. 5-52 Width

Since each reflection signal is the vibrator sweep scaled by the reflection coefficient, conventional cross-correlation produces a scaled version of the pilot sweep's autocorrelation, which is symmetrical and zero-phase. This is called *zero-phase correlation*. In many cases, *Weiner-type deconvolution* is applied in processing. This deconvolution assumes a minimum phase input. To provide for this, the option of minimum phase correlation is provided. Actually, *minimum phase correlation* uses an inverse filter technique to add the minimum-phase spectrum to the zero-phase correlation output. The difference between zero-phase and minimum-phase correlation is shown at the bottom of Figure 5-50.

The *Klauder wavelet* (Fig. 5-51) is used to represent the reflection wavelet produced by zero-phase correlation. The characteristics of a Klauder wavelet are described by definition, resolution, and width. *Resolution* may be thought of as the width of the peak (or trough) at the crossover point. In Figure 5-51, t_p = resolution. This assumes that all frequencies in a sweep are of the same amplitude and the sweep is linear. *Definition* may be thought of as the ratio of the amplitude of the largest peak (trough) to the amplitude of either adjacent peak (trough). This corresponds to the ratio A_1/A_2 , in Figure 5-51.

The width is a measure of the wavelet's duration as measured in time units. It is inversely proportional to cycles of bandwidth and may be computed from $2/(\text{bandwidth in Hz})$. Note that all three wavelets in Figure 5-52 have 10 Hz bandwidths, and, thus, the same width despite the differences in frequency content. As resolution and width get smaller and definition gets larger, the resemblance of the Klauder wavelet to a spike increases.

Good resolution depends more on bandwidth in octaves than in Hz. This is shown in Figure 5-53, where wavelets with zero through four octave bandwidths but different frequency ranges are compared. Infinite bandwidth gives a true spike or impulse function.

Parameters for vibrators are

- sweep type
- sweep length
- start and stop frequencies
- taper length
- number of vibrators
- number of sweeps/vibrator

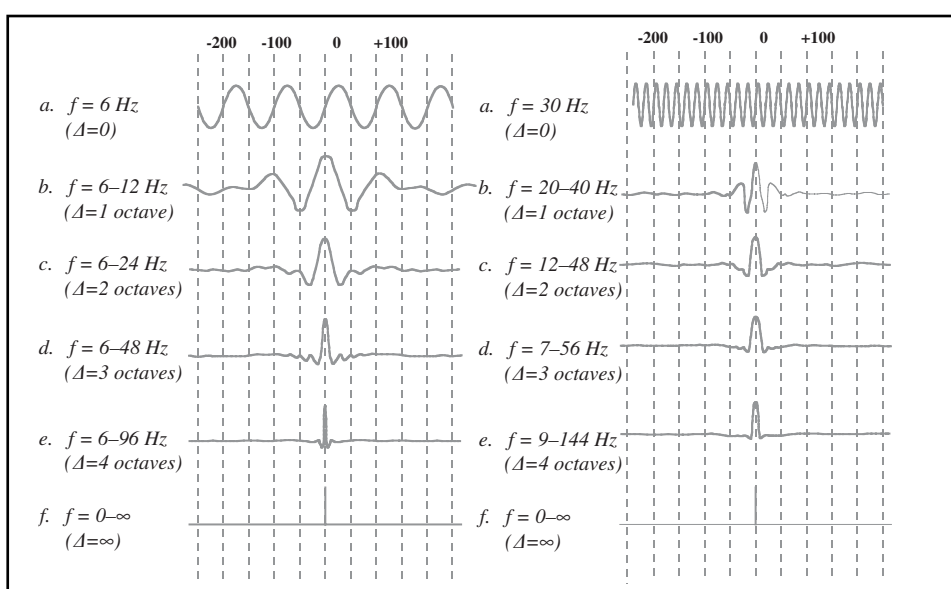


Fig. 5-53 Resolution versus Sweep Bandwidth

Listen time depends on desired output record length.

A wide variety of sweep types are available. The original sweep was linear and frequency was a linear function of time. Other sweep types include T^n (usually $0.3 < n < 3$), exponential, and logarithmic. Figure 5–54 illustrates the change in sweep frequency with time for linear, $T^{0.3}$, T^3 , logarithmic, and exponential sweeps. In each case, the start frequency is 10 Hz and the stop frequency is 80 Hz. Sweep length is 5 s in each case.

Of the five sweeps shown in Figure 5–54, the $T^{0.3}$ sweeps longest at the higher frequencies. This results in more high-frequency energy that is desirable to compensate for inelastic attenuation. The T^3 sweeps longest at the lower frequencies. This is desirable for penetration, since the lower frequencies are less affected by inelastic attenuation. The linear sweep is intermediate between the other two. The logarithmic sweeps slightly more in the higher frequencies than the linear, and the exponential sweeps slightly less in the lower frequencies than the T^3 .

Figure 5–55 shows the pilot sweeps corresponding to Figure 5–54. It is clear that the $T^{0.3}$ sweep has more high-frequency content than the others. Likewise, it is clear that the T^3 sweep has more low-frequency content than the others. The logarithmic sweep has an appearance closer to the linear sweep than to the $T^{0.3}$ sweep, and the exponential sweep has an appearance closer to the T^3 sweep than to the linear sweep.

The number of sweeps and sweep length are selected based on acceptable signal-to-noise ratio (S/N). Both the number of sweeps and sweep length affect the production rate. Fewer long sweeps may result in better data and an increase in production if reduction in the number of sweeps/pattern results. A larger move-up distance between sweeps (a larger separation between source points in the source array or more groups between source arrays for lower fold) makes it more difficult to maintain source array configuration and increases time between sweeps.

The time between sweeps is equal to sweep time + listen time + move-up time (time required to move a vibrator from one source point to the next). The current tendency is to move vibrators during listen time, but moving during listen time causes coherent noise on receiver spread.

Signal-to-Noise ratio (S/N) for vibrators is proportional to:

- square root of number of sweeps, $\sqrt{N_S}$
- square root of number of receivers, $\sqrt{N_R}$
- square root of sweep length in seconds, \sqrt{L}
- number of vibrators, N_V

Hence, $S/N \propto (N_V) \propto (N_S \times L)^{1/2}$

The number of sweeps to compensate for lost vibrators N_{S2} is given by:

$$N_{S2} = (N_{V1}/N_{V2})^2 \times N_{S1} \quad (5.2)$$

where

N_{V1} = original number of vibrators

N_{V2} = number of vibrators remaining after loss

N_{S1} = original number of sweeps

The change in sweep length to compensate for lost vibrators L_2 is given by:

$$L_2 = (N_{V1}/N_{V2})^2 \times L_1 \quad (5.3)$$

where

L_1 = original sweep length

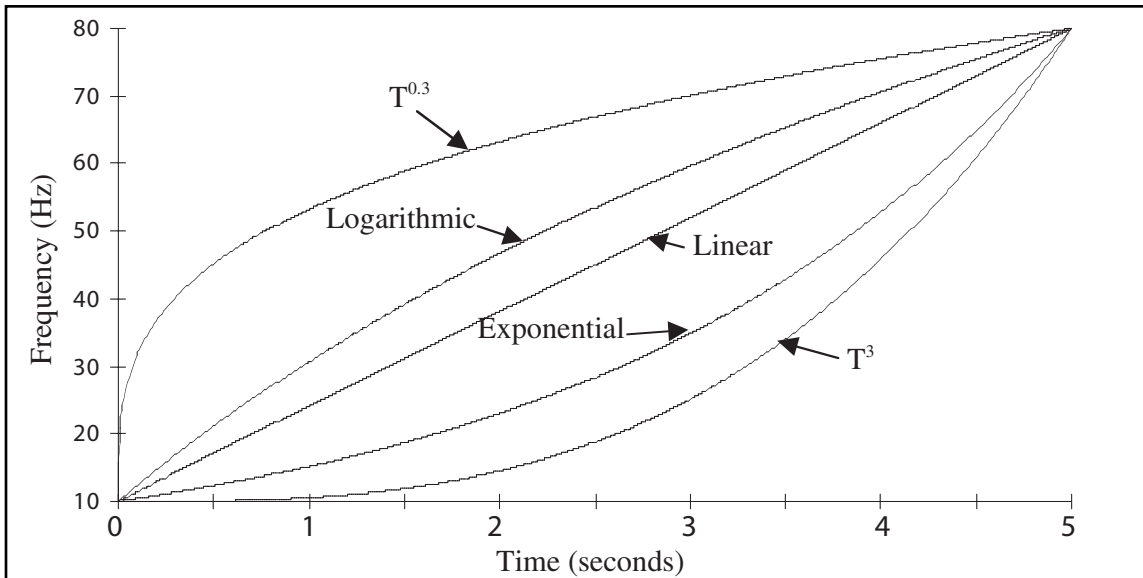


Fig. 5-54 Frequency versus time for Various Sweep Types

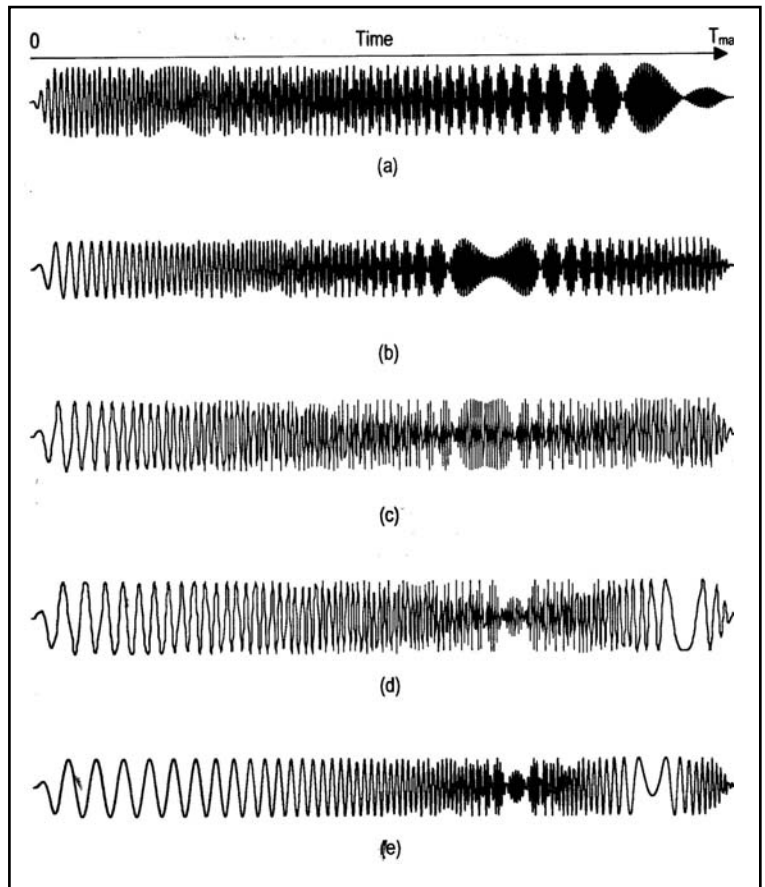


Fig. 5-55 Pilot Sweeps for $T^{0.3}$, Logarithmic, Linear, Exponential, and T^3

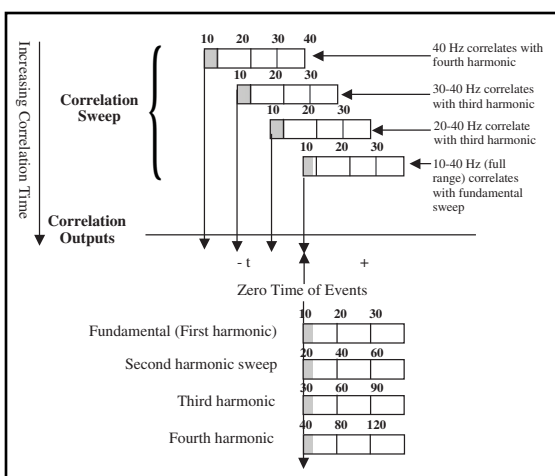


Fig. 5-56 Vibroseis Correlation Ghosts

Both the number of sweeps and the sweep length can be changed to compensate for lost vibrators, as indicated here.

$$N_{S2} \times L_2 = (N_{V1}/N_{V2})^2 \times N_{S1} \times L_{1V} \quad (5.4)$$

It follows from the preceding that doubling the amplitude of a vibrator signal requires increasing the number of vibrators by two, the number of sweeps by four, the sweep length by four, or the number of sweeps *and* the sweep length by two.

The bandwidth of a vibrator is established by initial and final frequency values for the sweep. The bandwidth, in turn, depends on the required resolution to solve the particular geophysical problem presented by the survey. The start frequency may depend on the type of surface material encountered. Hard surface material results in production of higher amplitude harmonics.

Harmonics are always produced when vibrators sweep. Only the amplitudes vary. One effect of vibrator harmonics is the generation of *Vibroseis correlation ghosts*—a type of noise on correlated vibrator records. Figure 5–56 demonstrates the generation of harmonics for an *upsweep*—start frequency lower than stop frequency.

The top part of the figure illustrates how the pilot sweep is moved past the sweep recorded at the start of a reflection event. The bottom part of the figure illustrates the position of the fundamental (pilot) sweep plus the second, third and fourth harmonics. When the pilot sweep first encounters the signal, the only correlation is the 40-Hz component of the pilot sweep with the 40-Hz component of the fourth harmonic.

The vertical arrow drawn from the left of this position indicates the time of this correlation is earlier than the event actually occurs. As the pilot moves through the recorded event to the time of the 30-Hz component, the 30–40-Hz range of the pilot correlates with the same frequencies in the third harmonic. The vertical arrow from this position also indicates the correlation occurs earlier than the event actually occurs. Next is shown the shift position at the time of the 30-Hz component of the pilot. Now the 20–40-Hz range of the pilot correlates with the same frequencies in the second harmonic. This also occurs earlier than the event actually occurs.

The last position is where the start of the sweep is aligned with the start of the reflection event. Here the full range, 20–40 Hz, correlates only with the fundamental sweep and is coincidental with the event time.

The duration of any ghost is, of course, the difference between highest and lowest frequency arrival times. For a down-sweep, these times are given by:

$$t_1 = \frac{T(f_1 n - f_1)}{\Delta} \text{ and } t_2 = \frac{T(f_2 n - f_2)}{\Delta} \quad (5.5)$$

For an up-sweep, these times are given by:

$$t_1 = \frac{T(f_1 - f_1 n)}{\Delta} \text{ and } t_2 = \frac{T(f_2 - f_2 n)}{\Delta} \quad (5.6)$$

where

t_1 = arrival time of lowest ghost frequency

t_2 = arrival time of highest ghost frequency

T = sweep length

Δ = sweep bandwidth ($f_1 - f_2$)

n = order of harmonic (second = 2, third = 3, etc.)

It follows from Equation 5.5 that for a down-sweep, times t_1 and t_2 are positive, while from Equation 5.6, it can be seen that times are negative for an up-sweep. This is the reason up-sweeps are generally preferred over down-sweeps.

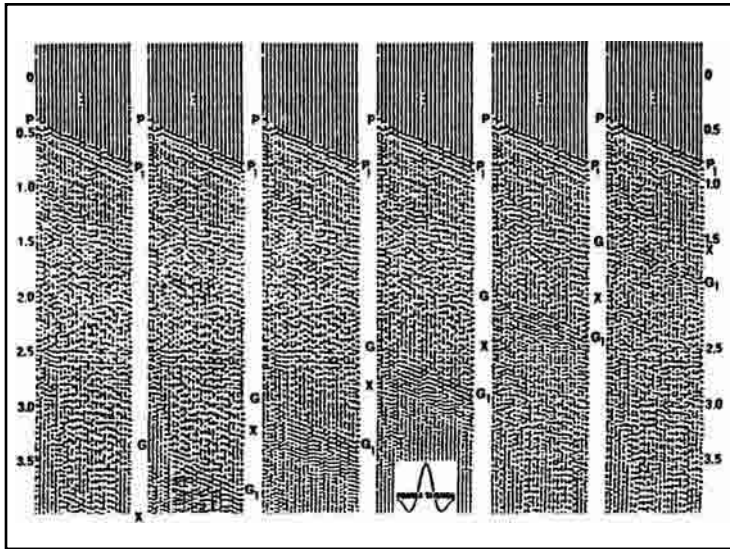


Fig. 5-57 Vibroseis Correlation Ghost Examples

Figure 5-57 shows a set of correlated vibrator records with sweep length, T , ranging from 7 seconds to 2 seconds. The sweep is from 35 Hz to 10 Hz, making the bandwidth, Δ , 25 Hz. The first break refraction is labeled PP_1 and the correlation ghosts are labeled GG_1 , on each record.

Table 5-4 lists the start and stop times of each harmonic relative to PP_1 . The worst problems occur for short sweeps and lower order harmonics.

Table 5-4 Correlation Ghost Start and Stop Times

$T(s)$	Second Harmonic		Third Harmonic		Fourth Harmonic	
	$t_1(s)$	$t_2(s)$	$t_1(s)$	$t_2(s)$	$t_1(s)$	$t_2(s)$
7	9.8	2.8	19.6	5.6	29.4	8.4
6	8.4	2.4	16.8	4.8	25.2	7.2
5	7	2	14	4	21	6
4	5.6	1.6	11.2	3.2	16.8	4.8
3	4.2	1.2	8.4	2.4	12.6	3.6
2	2.8	0.8	5.6	1.6	8.4	2.4

Figure 5-58 illustrates the effect of surface material on the generation of harmonics. Figure 5-58a is the autocorrelation of a 50-Hz to 10-Hz sweep that is 1 second long. Figures 5-58b and 5-58c are crosscorrelations between the fundamental and models—shown at right of crosscorrelations—for second harmonics at locations A and B. Location A has a hard rock surface, and location B has an alluvium surface. Note the lower level of harmonic generation at the softer surface.

Another parameter affecting vibrator correlation waveforms is the end taper. This is usually a cosine ramp function of the form:

$$s_s(t) = 1/2 [1 - \cos(\pi t / t_t)] \text{ for } 0 = t = t_1 \quad (5.7)$$

and

$$s_s(t) = 1/2 [1 - \cos(\pi [T - t] / t_t)] \text{ for } T - t_1 = t = T$$

where

t_t = the taper length in seconds

T = the sweep length in seconds

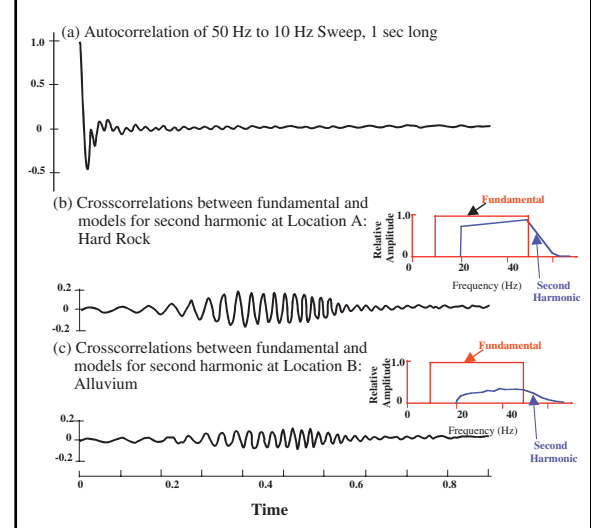


Fig. 5-58 Effect of Surface Material

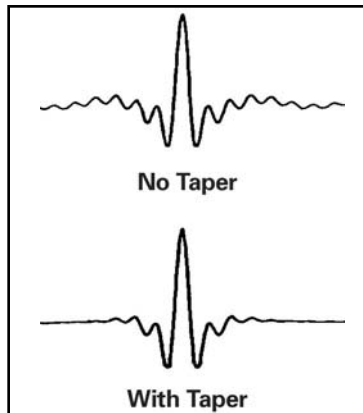


Fig. 5–59 Effect of Taper on Pilot Autocorrelation

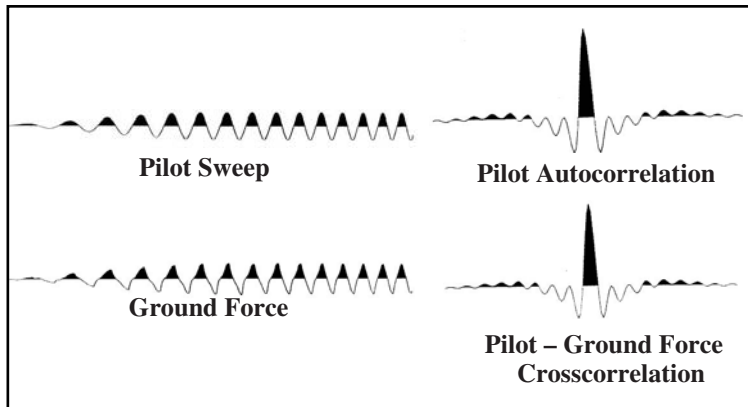


Fig. 5–60 Attenuation of Sweep Distortion by Crosscorrelation

The effect of the taper on the sweep can be seen in Figure 5–59. Figure 5–60 shows the effect of the taper by comparing pilot autocorrelations. With no taper, the side lobes have much higher amplitudes.

Even though the sweep put into the ground may be considerably distorted, the crosscorrelation between the filtered pilot and the sweep will not necessarily show this distortion. Remember that crosscorrelation behaves as a filter, and its output can contain no frequency components not in the pilot. The distortion seen on sweeps is usually at higher frequencies than in the pilot sweep and, thus, do not appear on the correlated sweep. The early part of a 5–65 Hz, 8 s pilot sweep is shown at the top left of Figure 5–60. At the top right is the autocorrelation of this sweep. The measured sweep put into the ground (ground force) is shown at the lower left, and to its right is the cross-correlation between the two sweeps. Note the strong similarity between the autocorrelation and the cross-correlation in Figure 5–60.

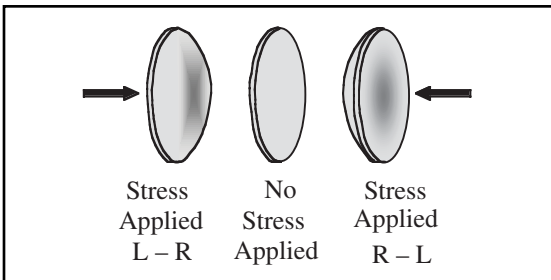
In summary, vibrators produce a controlled frequency-content signal, the only source that does so. Maximum frequency range is from about 5 Hz to 511 Hz. Maximum sweep length is 32 seconds. A wide variety of sweep types are available: linear, T^n , logarithmic, exponential, and others. Sweeps may be up (increasing frequency) or down (decreasing frequency). A cosine taper is applied at each end of a sweep to limit side-lobe amplitudes. A vibrator signal is low *power* but not low *energy*. Cross-correlation of output record with pilot sweep collapses long duration signals into impulsive-appearing signals and increases signal power. Two or more (usually more) vibrator units are used together. This increases cost but speeds operation. Multiple sweeps per shot point increase signal levels and signal-to-noise ratios. Vibrators can be used anywhere heavy vehicles can operate, including towns and cities, but cannot be used in marshy or mountainous areas or in jungles. Very hard surfaces may limit vibrators' effectiveness, as this type of surface tends to distort signals.

Recording

The seismic waves generated by the seismic energy sources propagate as mechanical energy. Recording of seismic waves presents the following problems.

1. Ground motion on land and changes in water pressure in the marine environment, resulting from seismic waves generated by the source, must be detected.
2. The detected seismic energy must be converted to a form that can be stored, displayed, and manipulated in such a way as to allow optimum information extraction from the data.
3. Implemented such that fidelity and precision are maximized, distortion is minimized, and retrieval of the stored information for processing and analysis can be readily accomplished.

Seismic detectors are special forms of *electro-mechanical transducers*—devices that convert mechanical energy into electrical energy. This is necessary because seismic energy is a form of mechanical energy. Mechanical methods of detecting and storing the amplitude and arrival time of seismic events are difficult and imprecise, and computer processing requires an electrical input.



5-61 Piezoelectric Crystals

More than one type of detector is required since in land exploration, both P- and S-waves are detected as motion of the earth's surface while in marine exploration, P-waves are detected as pressure changes in the water. No single detector type can detect both ground motion and pressure change. In the marine environment detectors called *hydrophones* are used. On land, *geophones* are used.

Hydrophones. Most hydrophones make use of the *piezoelectric effect*, which is that the application of stress to the surface, in some materials, causes a flow of electrons in the direction of the stress. Change in pressure is the stress for marine operations. Figure 5-61 illustrates the reaction of piezoelectric crystals to applied stress. Since current is the flow of charge, a current is produced proportional to the applied stress. Current across a load produces a voltage. The voltages so produced are then input to a seismic recording system.

Most hydrophones used today are transformer-coupled, piezoelectric hydrophones. An equivalent circuit (simplified) for a generic hydrophone group is shown in Figure 5-62. Here, the hydrophones are represented as a voltage source in series with a capacitor. There are usually 14 or 16 crystals in a bank. R_p and L_p are the resistance and inductance, respectively, of the transformer primary. R_s and L_s are the resistance and inductance, respectively, of the transformer secondary. R_d represents the damping resistance.

A modern transformer-coupled hydrophone used for geophysical prospecting has an amplitude frequency response represented by the following (simplified) equation, which is based on the equivalent circuit of Figure 5-62.

$$H_{Bd}(F) = H_{Bo} \left[\frac{\frac{R_d}{R_d + R_z}}{\sqrt{\left[\left(\frac{F_n}{F} \right)^2 + 1 \right]^2 + \left[2b_t \left(\frac{F_n}{F} \right) \right]^2}} \right] \quad (5.8)$$

where:

$H_{Bd}(F)$ is the sensitivity of the damped hydrophone at the test frequency F in Volts/Bar

H_{Bo} is the open circuit sensitivity of the hydrophone, measured unloaded at two or three octaves above resonance in Volts/Bar

R_d is the total effective damping resistance, which includes the influence of the acquisition system in ohms

R_z is the output impedance of the phone in ohms

F_n is the natural frequency of the phone, based on the input inductance of the transformer and the capacitance of the sensor bank in Hz

F is the test frequency in Hz

b_t is the total damping—the sum of the open circuit damping and the damping due to the damping resistor—expressed as a decimal fraction

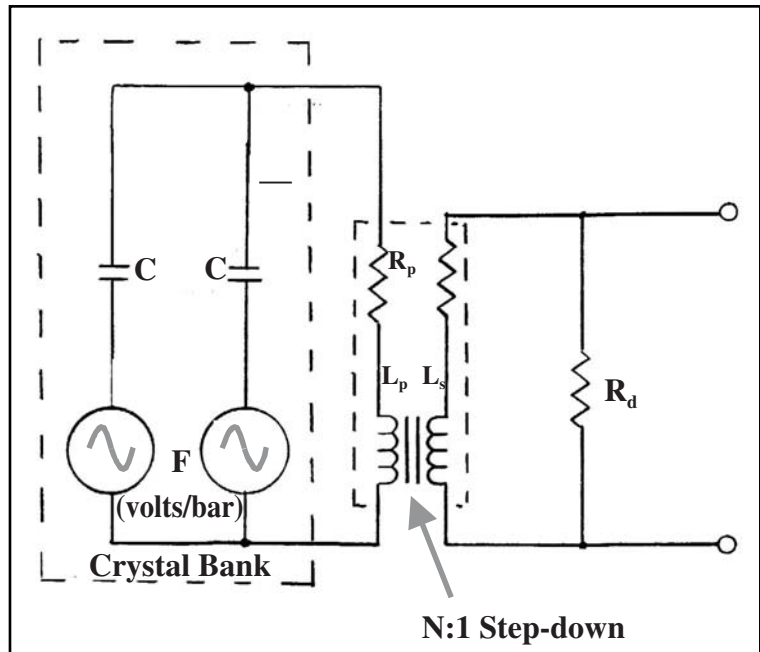


Fig. 5-62 Hydrophone Equivalent Circuit

The circuit diagram shows a 'Crystal Bank' connected to a bridge circuit. The bridge consists of two capacitors (C) in series with two voltage sources (F, in Volts/Bar). The outputs of the bridge are connected to the primary (L_p, R_p) and secondary (L_s, R_s) windings of a transformer. The secondary side is connected to a load resistor (R_d). An arrow points to the text 'N:1 Step-down' below the diagram.

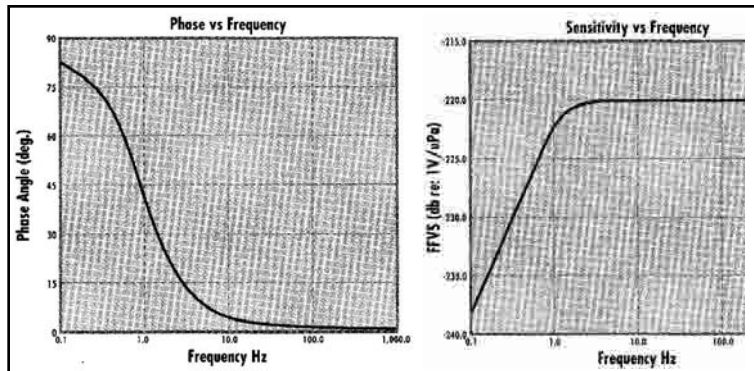


Fig. 5–63 Input/Output Model 2522 Near-field Hydrophone

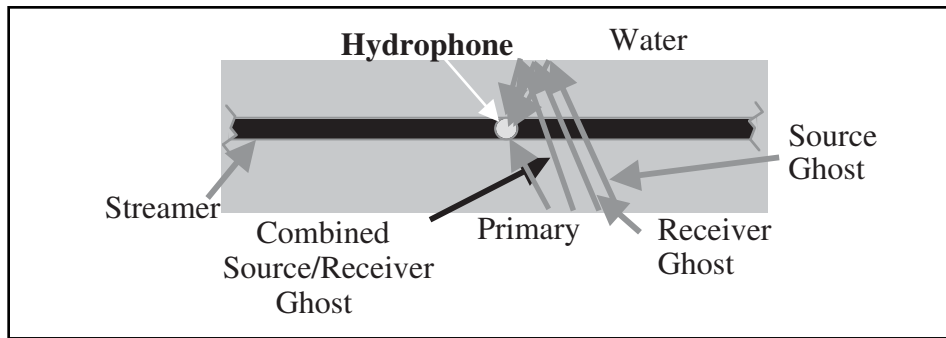


Fig. 5–64 Hydrophone Ghosts

Note that *resonance* and *damping* will be discussed later in this chapter.

Equation 5.8 is valid as long as the RMS amplitude of the differential pressure signal source is constant, and the frequencies of interest are within normal geophysical limits. Additional terms must be added to the equation to account for the high frequency characteristics of the transformer and the sensing crystals, as well as any frequency-dependent characteristics of the mechanical housing. The phase versus frequency response for a constant pressure drive is defined by the following equation.

$$\phi = \left[\frac{2b_t \frac{F_n}{F}}{\left(\frac{F_n}{F} \right)^2 + 1} \right] \quad (5.9)$$

Figure 5–63 shows the phase and amplitude response of an Input/Output Model 2522 near-field hydrophone. The response is flat from about 1 Hz.

Hydrophones in marine streamers are always used in closely spaced groups or arrays. This is because an individual hydrophone output is small. Current systems employ 14 to 16 hydrophones/group and group lengths are usually 6.25 m, 12.5 m, or 25 m.

Marine streamers are towed beneath the water surface. Shallower depths give higher frequencies but, usually, more noise. Greater depths give lower frequency but less noise. Also, as shown in Figure 5–64, the fact that the hydrophones and the source are towed beneath the surface allows energy to reach the hydrophones via undesired ray paths. Every reflection event is recorded four times.

- **Primary.** Energy travels from the source to the reflecting interface and then upward to the hydrophone group
- **Source ghost.** Initially upward-traveling energy is reflected down at the water surface to the reflecting interface and then up to the hydrophone group.
- **Receiver ghost.** Energy travels from the source to the reflecting interface and then up to the water surface where it is reflected down to the hydrophone group.
- **Combined source-receiver ghost.** Initially up-traveling energy is reflected down at the water surface to the reflecting interface and then up to the water surface where it is reflected down to the hydrophone group.

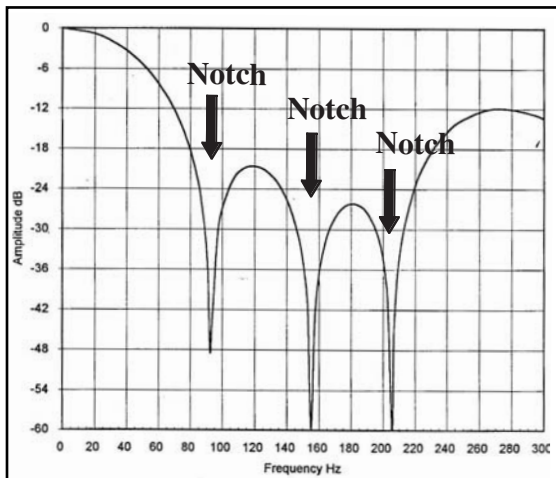


Fig. 5-65 Amplitude Response for 12.5 m Group, 14 Phone Array

Ghosts introduce notches in hydrophone group responses as shown in Figure 5-65.

Geophones. Seismic energy sources generate waves that travel mostly down, initially, and are returned to the surface by reflection and refraction. On land, these waves cause the earth's surface to move and this motion can be described in terms of ground particle displacement, velocity (speed), and acceleration. Of the three parameters of motion, the most readily measured is velocity, using moving coil seismometers.

Moving coil seismometers make use of the property that an electrical voltage is generated in a conductor moving through a magnetic field (Lenz' Law). Mathematically, this is written:

$$e = \frac{d\Phi}{dt} \quad (5.10)$$

where

e is the induced voltage

Φ is magnetic flux (lines of force)

Figure 5-66 is a simplified representation of an exploration seismometer, more commonly called a geophone. Principal components are

- case
- planting spike
- permanent magnet
- mass
- wire coil
- spring

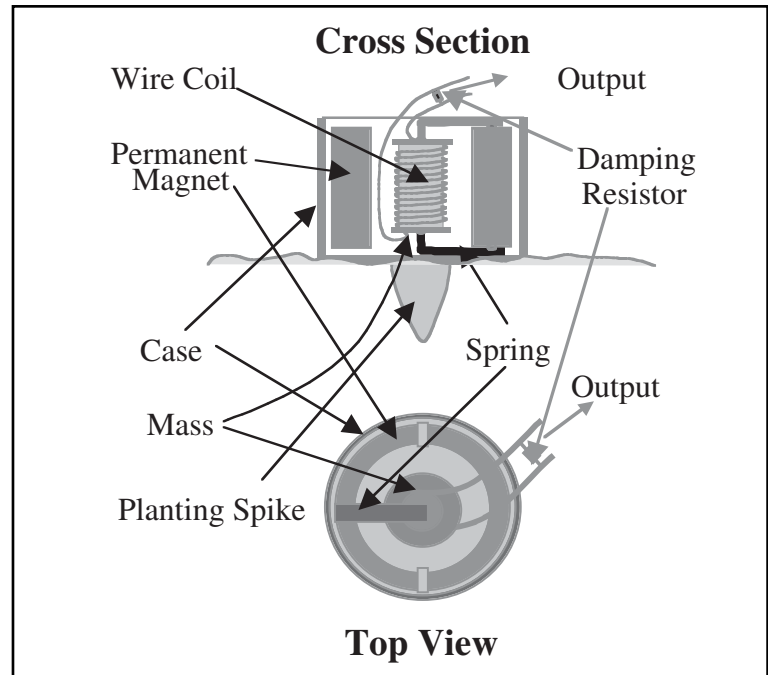


Fig. 5-66 Geophone Components

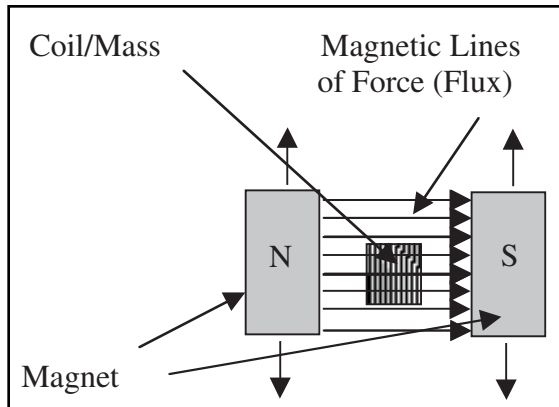


Fig. 5–67 Geophone Magnetic Field

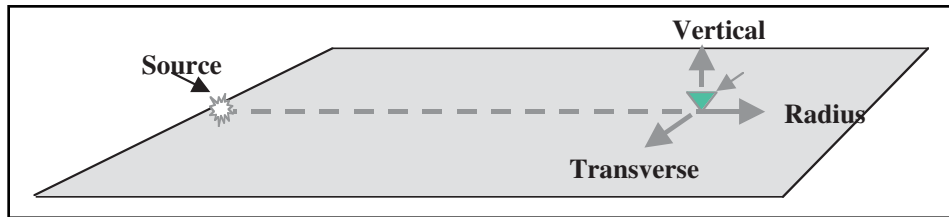


Fig. 5–68 Three-component Geophones

The planting spike couples the case to the ground, so that we can assume that the case faithfully follows the ground motion. The magnet is attached to the case and moves with it. The mass, with a wire coil wrapped around it, is suspended by a spring so that it remains fixed with regard to the earth as a whole. Seismic waves arriving at the geophone cause the case and magnet to move up and down.

The case and mass lie within the magnetic field of the permanent magnet, which is described by lines of force or flux, Φ (Fig. 5–67). The relative motion between mass and case causes the coil to be cut by lines of force. This is described by $d\Phi/dt$.

Magnetic flux can be defined by the flux density B and the area A through which the flux flows— $\Phi = BA$. Assuming a constant flux density, the change in flux with time is caused by a change in the total area across which lines of force flow through the coil.

$$e = -\frac{d\Phi}{dt} = -B \frac{dA}{dt} \quad (5.11)$$

The coil is assumed to be constrained to motion perpendicular to the magnetic field, and the change in area can be described by $dA = l ds$, where l = circumference of the coil and ds = instantaneous displacement of the case and magnet. Substituting for dA in the previous equation yields:

$$e = -B1 \frac{ds}{dt} \quad (5.12)$$

Since the case moves with the ground, $\frac{ds}{dt} = v$, where v = ground particle velocity. Thus, we have, finally:

$$e = -B1v \quad (5.13)$$

The previous series of equations shows that $e \propto v$ or that the voltage output by a geophone is directly proportional to the ground particle velocity.

Geophones can be made to respond to vertical, radial (in the direction of the receiver line) and transverse (orthogonal to the direction of the receiver line) motion of the ground by rotating the mounting of all active elements of the geophone 90° from the vertical position. Three-component geophone systems (Fig. 5–68) can be used to record both P- and S-waves. This procedure allows more information to be extracted from seismic data but adds to the expense in both data acquisition and processing.

Damping is used in geophones to retard the tendency to oscillate at the natural frequency that depends on mass and spring constant. Damping used to be accomplished with some fluid, such as oil, being placed within the case. Damping, today, is accomplished by placing shunt resistors across the output of a phone that provides a back electromotive force (emf)—an opposing emf field.

The parameter h is used to describe damping, with $h = 1$ corresponding to *critical damping*, $h < 1$ meaning the geophone is *under damped*, and $h > 1$ meaning the geophone is *over damped*. For the case of no damping, $h = 0$, the geophone oscillates continuously but, in practice, gravity and air friction would eventually bring the mass to rest (Figure 5-69).

For seismic exploration, geophysicists require as short a signal as possible. Hence, some damping is required. Critical damping means that after the case is displaced, it returns to the rest position with no oscillations and no over-swing. Normal damping for geophones is 0.7 (70% of critical). This gives a slight (only 5%) over-swing past the zero position. It is a compromise between considerations of over-swing, output amplitude, and phase shift.

For no damping, $h = 0$, the amplitude peaks at the resonance or natural frequency. Low frequencies are preferred to extend width—a low resonant frequency is desirable. This can be accomplished through design with a heavier mass or a stiffer spring. High geophone sensitivity is desirable. (Geophone sensitivity or transduction is measured in volts/inch/second.) Heavy damping provides a shorter impulse but at the cost of reduced sensitivity. Light damping tends to promote oscillations and enhance low frequencies such as those at which ground roll occurs. Typical resonant frequencies for reflection work are 14 Hz and 10 Hz. These choices are sometimes made in lieu of low-cut system filters.

The geophone behaves as a filter since it attenuates frequencies lower than its natural frequency. With 70% damping, the geophone acts as a low-cut filter with cutoff equal to the natural frequency and a slope of 12 dB/octave. The geophone also introduces phase shifts between the input and output signal. *Input* is the physical up and down movement of the geophone. A phase shift of 90° always occurs at the natural frequency regardless of the degree of damping. Phase shift below the natural frequency is greater than 90°. Above the natural frequency the phase shift is less than 90°. See Figure 5-70.

A geophone is a mechanical system designed to allow a single degree of freedom in the vertical direction. Also, a geophone has other *vibrational resonances* that couple loosely into its primary motional mode, including a horizontal oscillatory mode in which the mass behaves as though it were attached to the case via a horizontal spring. This produces a *spurious resonance*,

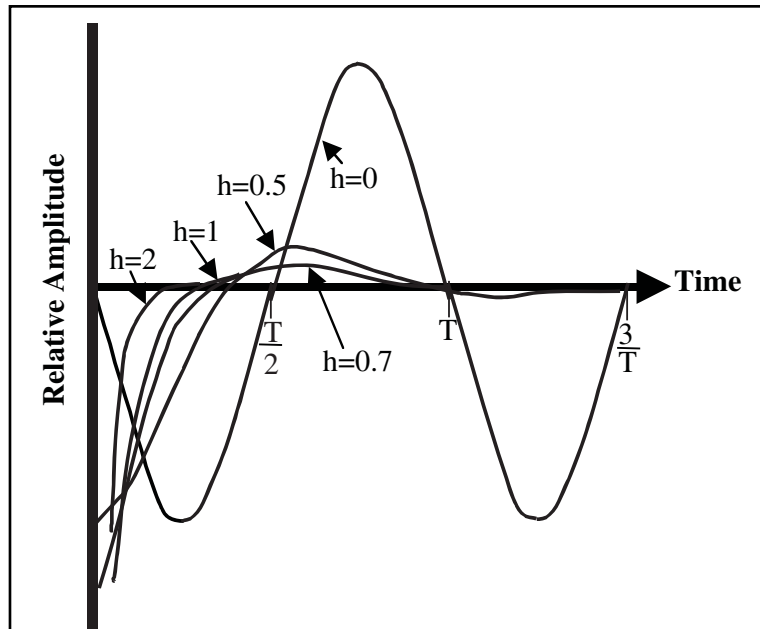


Fig. 5-69 Geophone Damping

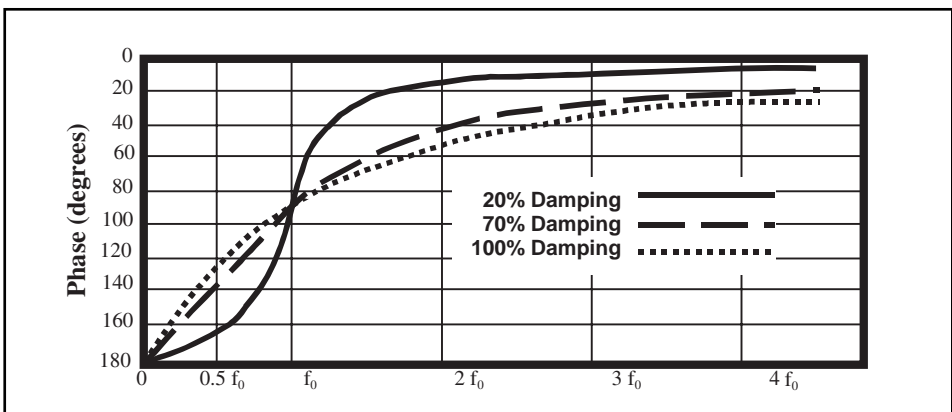


Fig. 5-70 Geophone Phase Response

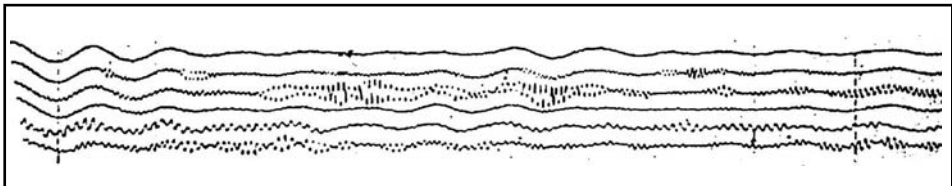


Fig. 5-71 Spurious Resonance or Parasitics

or *parasitic*. Figure 5–71 is a recording of parasitic resonances on a single-geophone-per-trace spread of Geospace's GSC 11D, 8-Hz geophones at distances of 180 ft to 415 ft from a 1-lb. Nitramon charge. While the noise has rather high amplitude, it can be easily recognized because it is much higher frequency than the nearby ambient noise.

Geophone parameters that can be varied are natural or resonant frequency, open circuit damping (some damping is always present), and coil resistance. Table 5–5 provides some guidelines in selecting these parameter values.

Table 5–5 Selecting Geophone Parameter Values

Parameter	Goal	Approach
Natural Frequency	Reduce low frequency signal or ground roll	Select a higher natural frequency detector to suppress low frequencies (28 to 30 Hz or higher)
	Enhance the high frequency data for higher resolution	
	Enhance low frequency signals	Select a low natural frequency (8 to 14 Hz)
Open Circuit Damping	Have total damping equal to 0.6	Select a seismometer with an open circuit damping approaching but not greater than 0.6
	Maintain high sensitivity under load	
Coil Resistance	Increase sensitivity	Choose large coil resistance
	Decrease noise pickup	Choose low coil resistance
	Reduce effect of load impedance	

The normal assumption is that geophone case motion is a replica of ground velocity. However, this assumption is invalid in loose soil. Since the soil is elastic, geophone amplitude and phase are distorted. These effects can reduce within seismic frequencies by increasing the mass, increasing the radius of the geophone, using longer spikes to provide firmer contact with compacted soil, or using buried phones for better plants in compact soil. These solutions are expensive and require careful consideration. Small phones are generally more economical and all that is required is a good vertical plant in compact soil. If compact soil is not available, the cost of burying has to be considered.

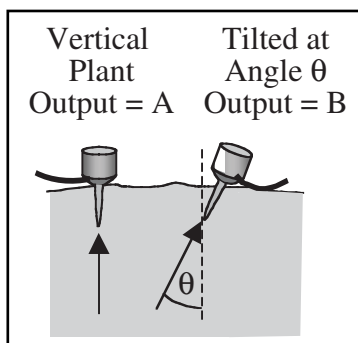


Fig. 5–72 Geophone Tilt

Geophones are directional, sensing only the vertical component of motion. If a geophone is planted (placed in the ground) at an angle θ , then amplitude is proportional to $\cos\theta$. See Figure 5–72. If the geophone is at an angle of $\pm 20^\circ$ from the vertical, then there is a loss of 5% in amplitude. Far offsets add an angle of emergence to a tilted or poorly planted phone. For example, an emergence angle of 30° adds to the geophone tilt of 20° . The amplitude is now proportional to $\cos(20^\circ + 30^\circ)$ giving a 35% loss in amplitude. Geophones are generally rated as operational within ± 20 degrees. Spurious harmonics may also contaminate the signal within the seismic bandwidth outside this angle.

It is not only important that geophones be planted vertically but also firmly in contact with the ground. Figure 5–73 shows four planting conditions that rate from best to poor with regard to earth coupling. The best plant is either buried (Fig. 5–73a) or a geophone with its 5½-inch planting spike solidly placed in firm ground with all loose soil first scraped away (Fig. 5–73b). A geophone with its 3-inch planting spike solidly placed in firm ground with all loose soil first scraped away (Fig. 5–73c) is a good plant. A geophone with its 3-inch planting spike solidly placed in firm ground with only vegetation, such as pine needles, brushed away is a fair plant. A geophone planted on top of vegetation, such as pine needles or very loose soil, is a poor plant. Figure 5–74 shows the effect of these planting conditions by displaying the amplitude and phase responses predicted from impulse response measurements.

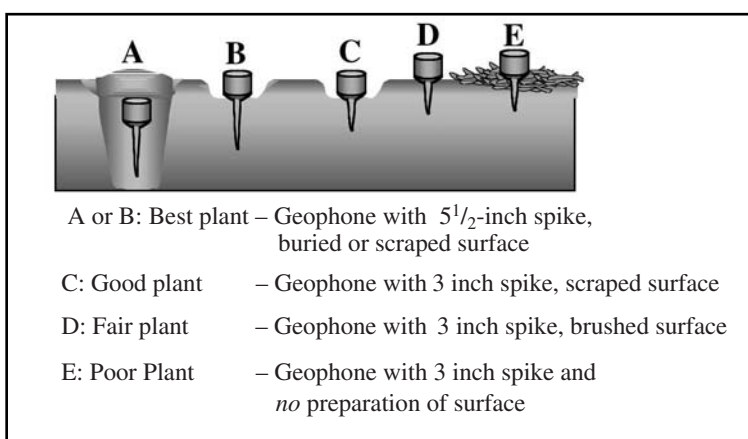


Fig. 5–73 Geophone Planting Conditions

Noise on a seismic record is, basically, anything you don't want to record. There are two general types of noise—ambient and source-generated. *Ambient noise* is naturally occurring (wind, rain, lightning,

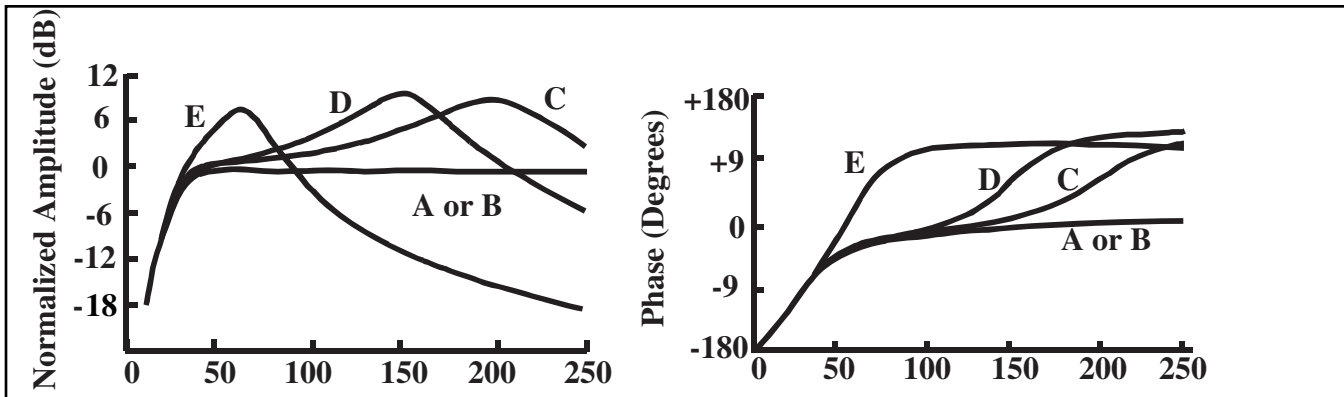


Fig. 5-74 Effect of Geophone Planting Conditions on Amplitude and Phase Responses

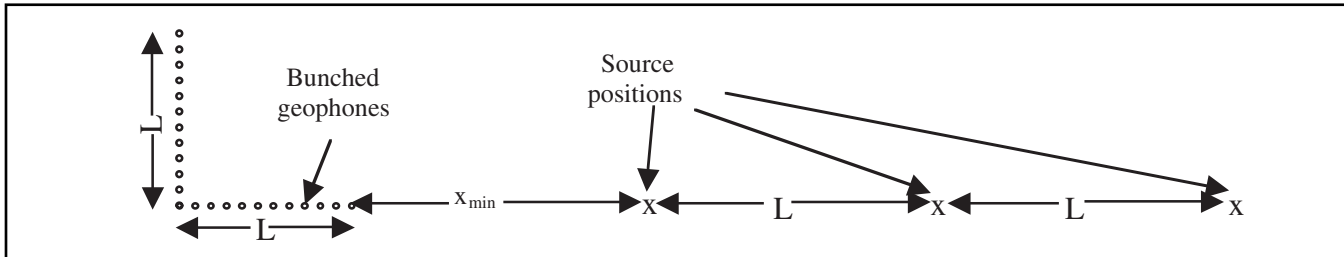


Fig. 5-75 Noise Spread and Shooting Procedures

thunder, surf, earthquakes) or cultural (vehicular and foot traffic, grazing animals, pumps). *Source-generated* noise includes ground roll, air blast, guided waves, and others. Since noise is undesirable, although unavoidable, measurement of noise characteristics (frequency, wavelength propagation velocity) aids in design of techniques to minimize noise recording. Such measurements are done in noise tests.

A useful method of conducting noise tests is to lay out about 12, or more, groups of several bunched geophones, with total length L , and a similar set of 11 geophones perpendicular to these. The length L should be equal to the planned group interval in the seismic survey. Figure 5-75 shows the suggested layout and shooting procedure. Shoot (or sweep) into these geophones starting at the minimum offset x_{\min} and continuing at intervals L as shown in Figure 5-75. The minimum offset should also be equal to that planned for the survey. One record is made at each source position. Offsets for the first record are x_{\min} to $x_{\min} + L$. Offsets for the second record are $x_{\min} + L$ to $x_{\min} + 2L$, etc. Records are combined with traces offset-ordered.

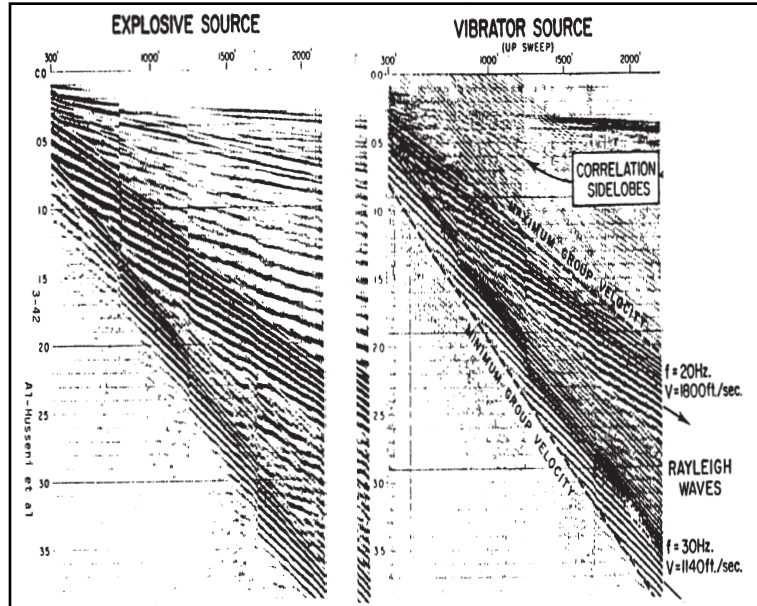


Fig. 5-76 Noise Test Example

Figure 5-76 is an example of a noise test record. It is important in conducting noise tests that the same source be used as in the seismic survey. While the same information is present in both the records shot with explosives and the records obtained from vibrator sweeps, there are some differences as well.

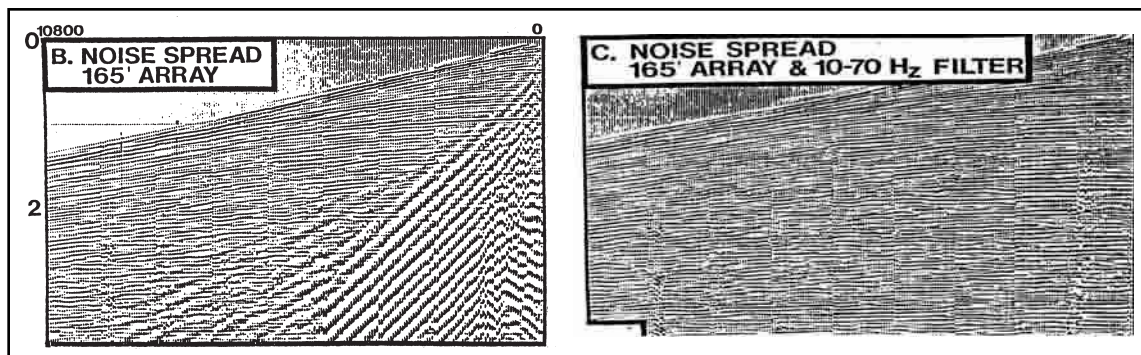


Fig. 5-77 Attenuation of Ground Roll with Band-pass Filter

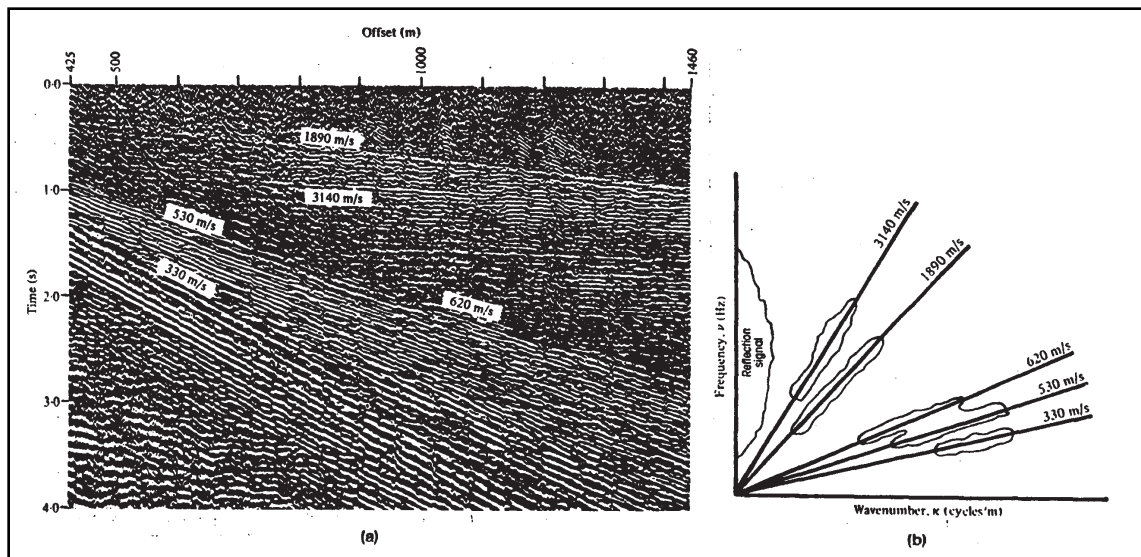


Fig. 5-78 Noise Analysis or Walk Away

The various noise types are recognized by velocity and frequency. Note that ground roll is not a single event but is, instead, a dispersed noise train. Ground roll normally contains all frequencies released by source, and it penetrates into earth as a function of wavelength. Low frequency equals long wavelength, which means deeper penetration into the surface layer. High frequency equals short wavelength, which means shallow penetration. Since velocity in earth normally increases with depth, the low frequency, long wavelength ground roll travels faster than shallower-penetrating high frequencies. This causes dispersion of ground roll. Velocity is a function of wavelength or frequency.

A variety of methods are available for attenuating noise. In many cases, ground roll has significant amplitudes only at frequencies lower than the signal. In such cases, a band-pass filter will provide adequate noise attenuation. Figure 5-77 illustrates this by showing a noise test record on the left and the same record after application of a 10 Hz low-cut filter. The filter essentially eliminates the ground roll.

Figure 5-78 shows a noise test record on the left and its *F-K* domain representation on the right. Noise is well separated from signal. A velocity or *F-K* filter should give good attenuation of the linear noise.

From measurements of noise wavelength λ and velocity V , calculate frequency f from $f = 1/T$ and wavelength λ from above relationship. Calculate wave number k for signal and noise from the relationship of $k = 1/\lambda$. Use these values to design the optimum receiver array, considering availability of geophones, cost, time, and difficulty of lay out.

In seismic exploration, arrays comprise two or more elements in a geometric pattern. The elements may be sources or receivers. In land exploration, arrays are used primarily to attenuate source-generated, horizontally propagating noise. In marine exploration, arrays are used primarily to increase signal levels. Arrays can be linear (usually in line with or parallel to the receiver lines) or areal (with both in-line and cross-line components).

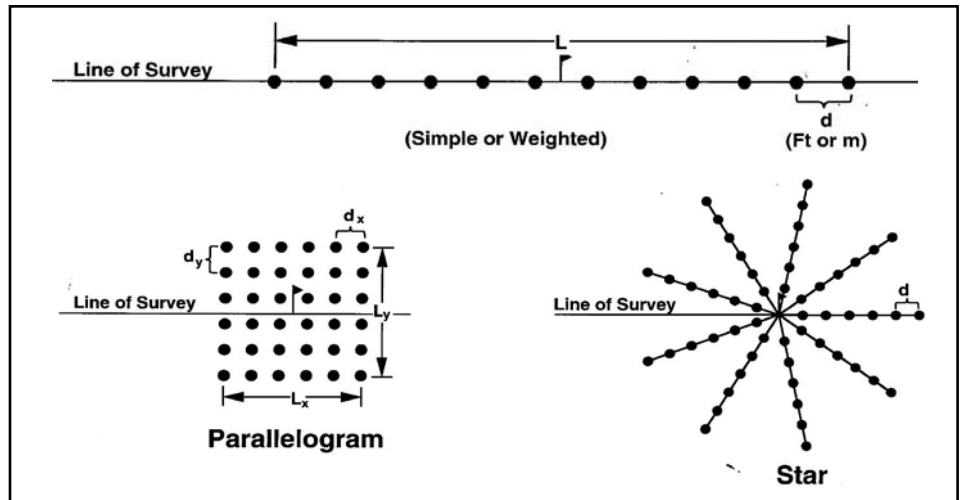


Fig. 5-79 Array Configurations

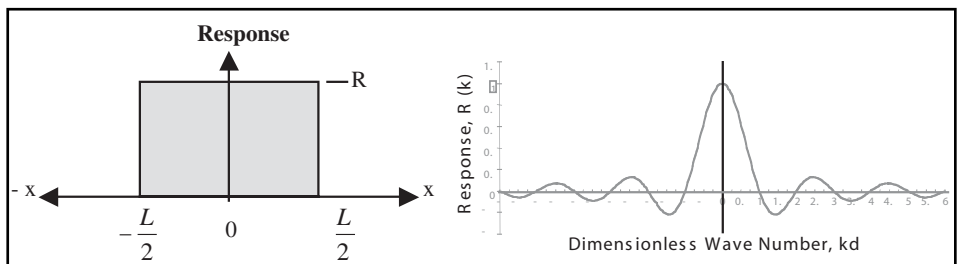
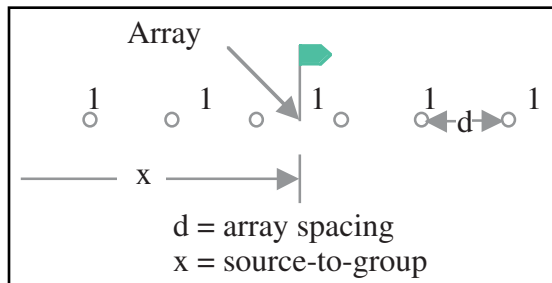
Fig. 5-80 Ideal Receiver Response for Space Domain x and Wave Number Domain K 

Fig. 5-81 Linear, Equally Spaced, Equally Weighted Array

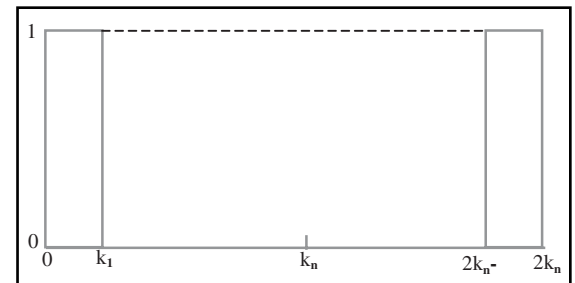


Fig. 5-82 Conventional Representation of Desired Response of Linear, Equally Weighted, Equally Spaced Array

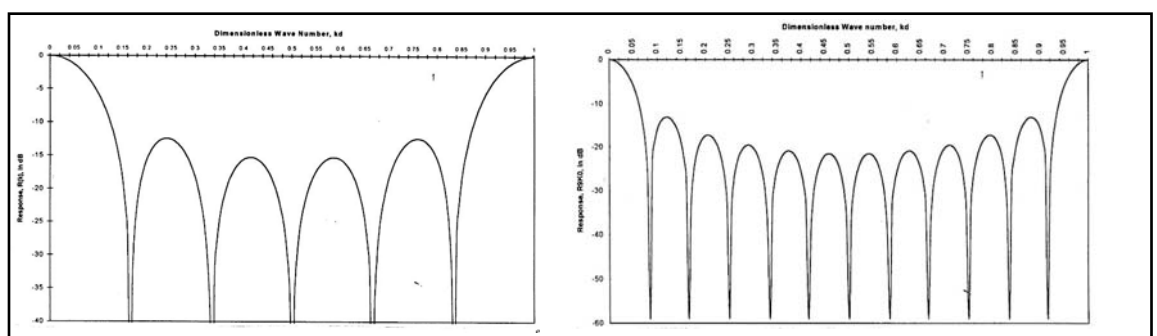


Fig. 5-83 Response of Linear, Equally Weighted, Equally Spaced Arrays, 6 Element and 12 Element

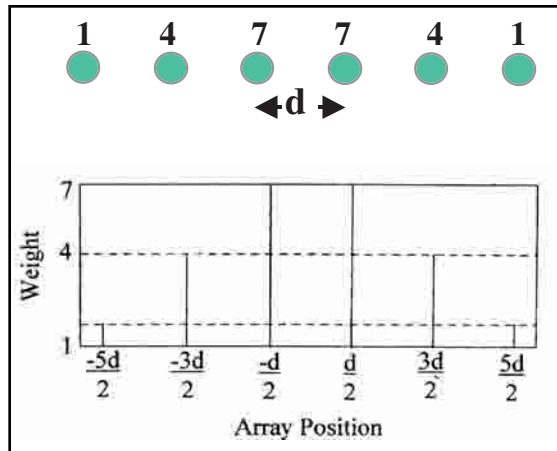


Fig. 5–84 Alternative Methods of Representing the Spatial Response of Linear, Unequally Weighted, Equally Spaced Arrays

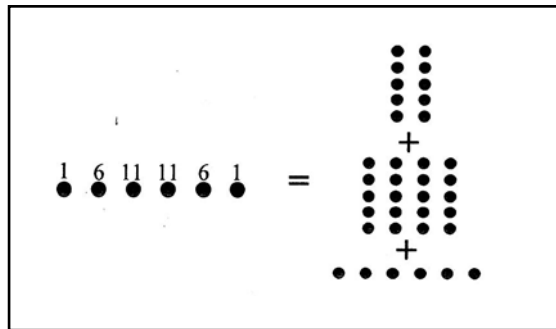


Fig. 5–85 Decomposing Linear, Unequally Weighted, Equally Spaced Arrays

There are different kinds of linear arrays—equal weights and equal spacing, variable weights and equal spacing, and equal weights and variable spacing. Areal arrays include rectangular, parallelogram, chevron, and star. See Figure 5–79.

Consider a theoretical receiver that responds continuously and equally along its length L . Figure 5–80 shows the response of this array in the space x and wave number k domains. However, seismic data are not recorded continuously but at discrete points. Therefore, seismic data are *space-sampled* data. Arrays are made of discrete elements, and thus they are discrete spatial filters. Figure 5–81 shows a 6-element, linear, equally spaced, equally weighted array. Spacing between elements is d , ft, or m.

If k_1 is the wave number at which the signal-to-noise ratio = 1, then the desired array response is as shown in Figure 5–82. Note that array responses are usually shown for the range $0 < k < 2k_n$ or $0 < kd < 1$. The response of an equally weighted, linear array having N equally spaced elements is given by:

$$R(k) = \frac{\sin(N\pi kd)}{\sin(\pi kd)} \quad (5.14)$$

Actual responses, thus, differ from the desired response as shown in the example of Figure 5–83.

Linear, variably weighted, equally spaced arrays can be used for both receiver and source arrays. Receiver arrays can be weighted by clustering geophones with the number of geophones per cluster determining the weight. Source arrays can be weighted by loading different charges or by varying number of sweeps. Array weights can be shown as numbers corresponding to weights, above array positions, or as lines whose heights represent weights and separations represent array spacing (Fig. 5–84).

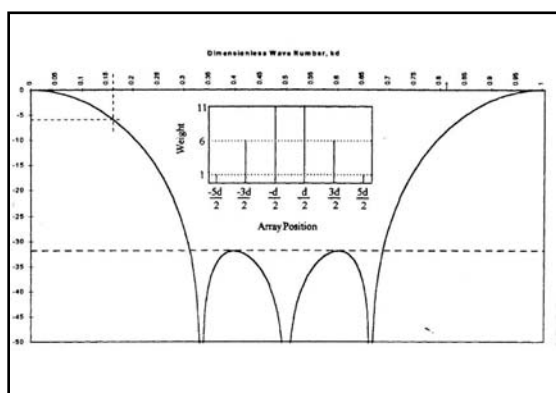


Fig. 5–86 Linear Array with Variable Weights

Responses of weighted arrays are found by decomposing them into equally weighted linear arrays. The array shown in Figure 5–85 is decomposed into one 6-element, five 4-element, and five 2-element arrays. The k -domain responses of each component is calculated from Equation 6.14 and summed. The result is shown in Figure 5–86. Note that w_i is the weight of each array element.

While arrays can be an effective tool for attenuating horizontally propagating noise, they can also be harmful to recording signal. One such situation is when there are large elevation changes over the area where the array is to be placed. It is generally accepted that the maximum elevation difference across an array should not exceed one-fourth of the smallest wavelength expected λ_{\min} . Since $V = f \lambda$, the signal having the smallest wavelength will have the highest frequency f_{\max} and the restriction on elevation difference can be written as:

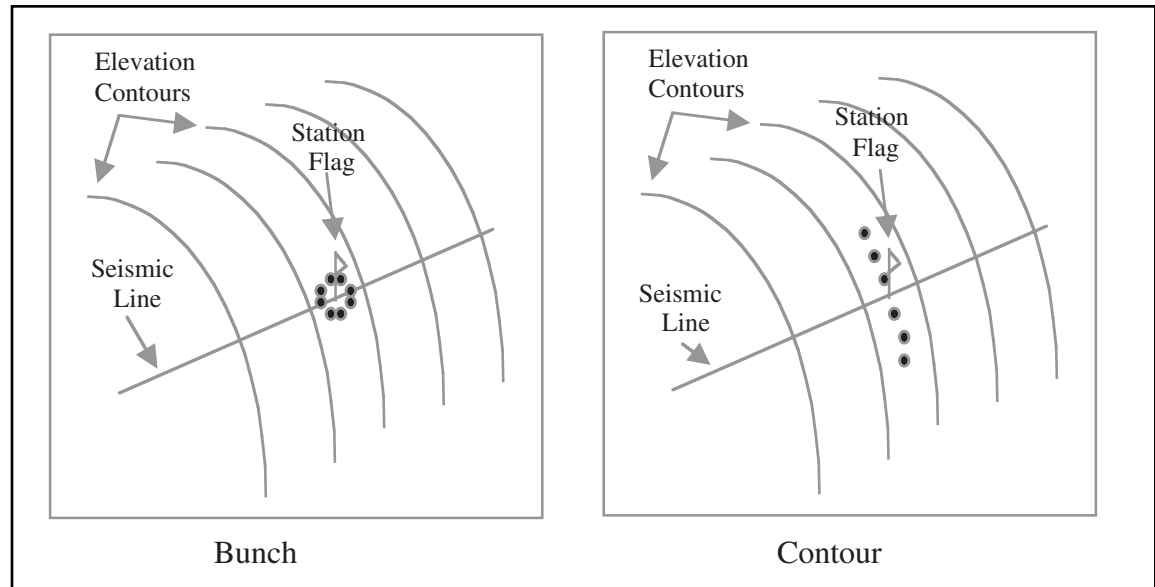


Fig. 5-87 Geophone Layouts in the Presence of Large Elevation Differences

$$x \leq \frac{V}{4f_{\max}} \quad (5.15)$$

On the other hand, given an elevation difference x , the highest frequency that can be recorded satisfactorily is given by:

$$f_{\max} \leq \frac{V}{4x}$$

Figure 5-87 shows alternative methods of laying out geophones in the presence of excessive elevation differences.

Recording systems. Seismic recording systems measure and record electrical inputs from detector groups with maximum fidelity and precision, minimum distortion, and the capability to be readily retrieved for subsequent processing and analysis. The environment under which this must be done is challenging.

First-break amplitudes are usually the largest inputs and may be 140 to 160 dB higher than amplitudes of the deepest reflections. Source-generated noise amplitudes are often considerably larger than signal received at the same time. Amplitudes of multiples and reverberations may also be larger than reflections that are recorded at about the same time. Amplitudes of the earliest reflections can be 100 dB or more—larger than those of the latest primary reflections. Ambient noise is usually about 70 to 80 dB below first-break amplitudes but larger than later reflection amplitudes. Amplitudes of signals and various noises received at the same time can cover a range of up to 100dB. All recording systems produce internal noise, and the level of this noise, expressed as an equivalent input noise, establishes a floor for signal recording. Figure 5-88 shows the situation graphically.

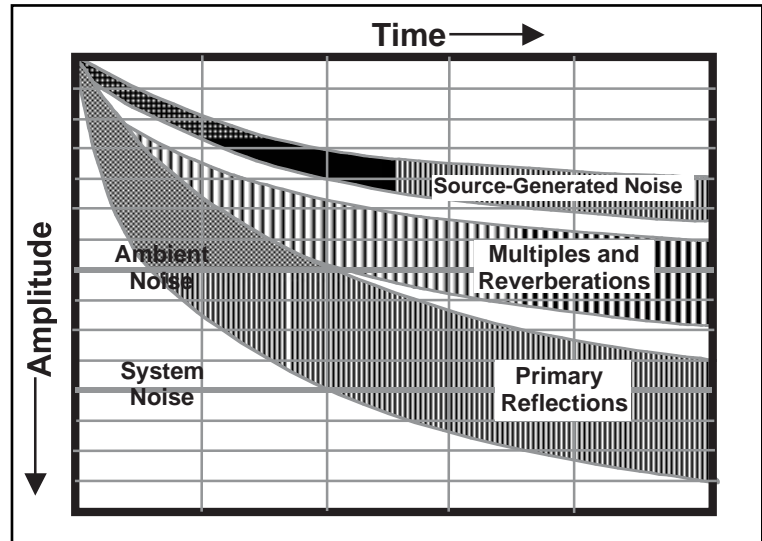


Fig. 5-88 Seismic Amplitudes

First-break amplitudes are usually the largest inputs and may be 140 to 160 dB higher than amplitudes of the deepest reflections. Source-generated noise amplitudes are often considerably larger than signal received at the same time. Amplitudes of multiples and reverberations may also be larger than reflections that are recorded at about the same time. Amplitudes of the earliest reflections can be 100 dB or more—larger than those of the latest primary reflections. Ambient noise is usually about 70 to 80 dB below first-break amplitudes but larger than later reflection amplitudes. Amplitudes of signals and various noises received at the same time can cover a range of up to 100dB. All recording systems produce internal noise, and the level of this noise, expressed as an equivalent input noise, establishes a floor for signal recording. Figure 5-88 shows the situation graphically.

System performance requirements include a large dynamic range, wide bandwidth, large amplitude range, low harmonic distortion, and minimal system noise. System operational requirements include:

- large channel capacity at all sampling rates
- multi-line/multi-streamer capacity
- large number of channels/line or channels/streamer
- large roll capacity
- adequate auxiliary channels
- wide range of group and line intervals
- correlation and stack capability (land)
- internal testing capability
- remote status monitoring
- long battery life (land)
- good status and QC displays

Modern seismic recording systems consist of two distinct parts—ground (land) or in-water (marine and OBC) systems and truck or onboard systems.

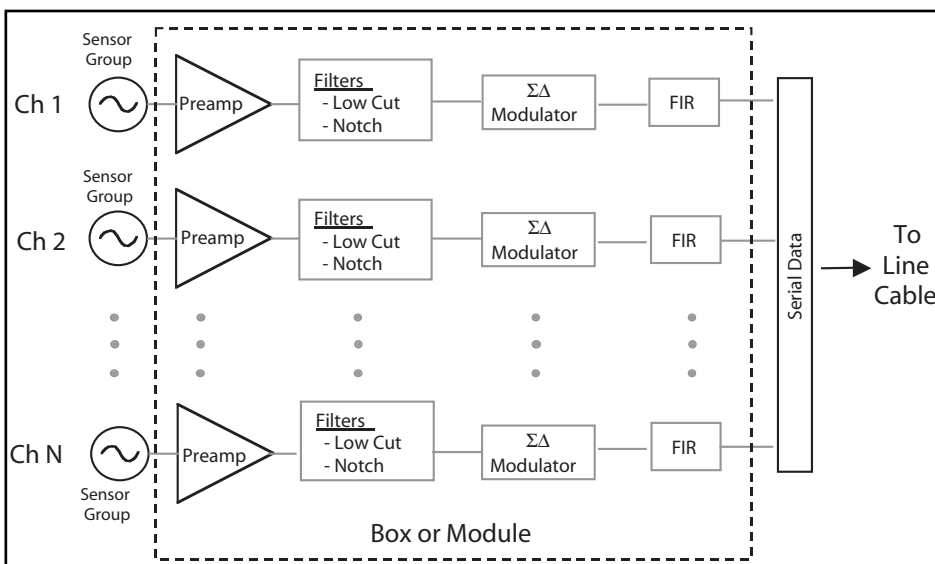
Ground and in-water system modules are located near detector groups. Major components are

- preamplifier (preamp)
- low-cut and notch filters
- sigma-delta modulator
- finite impulse response (FIR) module

Modules also include components for testing and status reporting. Figure 5–89 is a block diagram for a typical 24-bit module. The number of channels (N = number of geophone group inputs) varies considerably, ranging from one to eight. Each channel is identical up to the serial data bus.

Preamplifiers increase amplitude of seismic signal received from the cable by applying a constant gain. Usually, preamplifier gain can be selected as 0 dB (x1), 12 dB (x4), 24 dB (x16), 36 dB (x64), or 48 dB (x256). In some 3-D surveys, preamp gain may be set differently for different offset ranges to compensate for amplitude variation with distance. It is very important that preamplifiers operate with the least possible addition of noise and distortion.

The filters here are analog filters. Low-cut filters should be used with caution. Do not kill low-frequency noise with these filters if it damages data. Emphasis today is on preservation of signal rather than attenuation of noise. Notch filters can be used to attenuate highline noise but see the following discussion first. Note the absence of anti-alias filters. In 24-bit systems, they are not needed at this point because data are sampled at rates far above the seismic frequency range.



To minimize phase and amplitude distortion, use wide data band pass, avoid steep filter slopes, use notch filters only as last resort, and do not change recording filter settings once survey has begun, although playback filters can be changed as required. Amplitude distortion can only be partially corrected by seismic processing, but some signal amplitude information lost due to the S/N ratio of recorded seismic data. Phase distortion can theoretically be removed in seismic processing, but this requires the impulse response of the recording system, including filters used in data acquisition.

Fig. 5–89 24-Bit Electronics

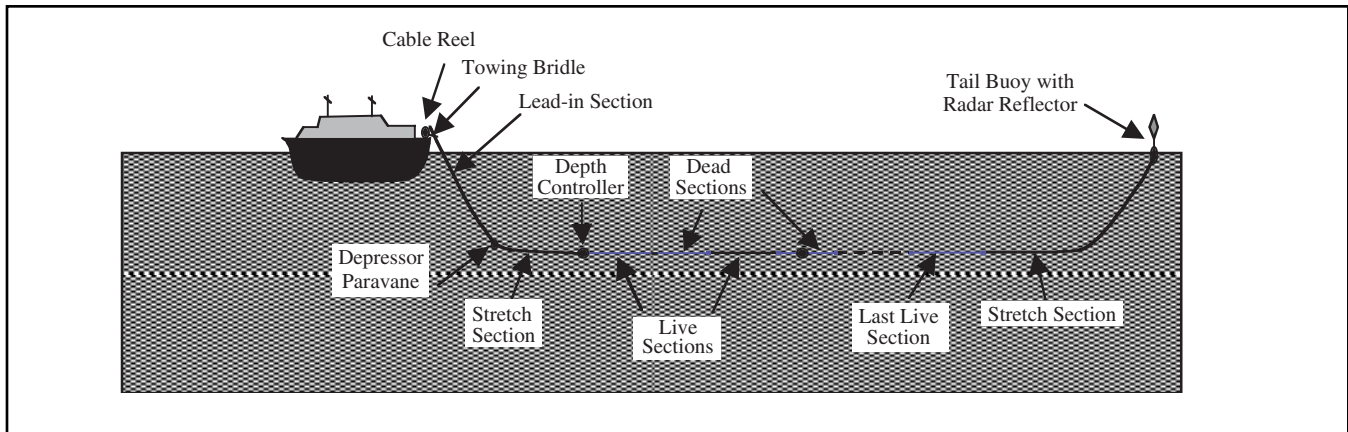


Fig. 5–90 Streamer Configuration

Practical limitations are imposed by the non-linear phase response at filter limits and steep cut-off filter slopes found in notch filters.

The sigma-delta modulator is a single-bit, analog-to-digital converter. That is, one bit—0 or 1—is output each sample period, which is on the order of 4 nsec ($1 \text{ nsec} = 10^{-9} \text{ seconds}$). The output stream of bits goes to the FIR where it goes through two stages of averaging and application of digital anti-alias filters appropriate to the selected output sample period (0.5, 1, 2, or 4 ms). The averaging process results in the final value being output as a 24-bit binary number.

Marine in-water recording systems. Marine recording systems have two parts—the in-water system and the onboard system. The in-water system consists of a set of streamers that are towed behind the vessel. Figure 5–90 shows a typical streamer configuration. Cable reels on the stern of the vessel are used to hold the streamers when not deployed. Electrical connection between the streamer electronics and the onboard system are made at these reels.

The physical connection between the vessel and the streamer proper is via the *towing bridle* and the *lead-in section*. Streamers are made in sections of various types. *Stretch sections* must be deployed at the front and tail ends of streamers being towed from lateral separation devices (diverters) in order to attenuate vibration attributable to the motion of the separation device and from tail buoy jerks. The depressor *paravane* acts as a vertical diverter to place the streamer at the required depth. Depth sensors and depth controllers are also put at various points in the streamer to maintain the streamer at a constant depth throughout. The balance of the streamer is composed of *live sections* and *dead sections*.

Live sections contain hydrophone groups and electronic components that apply filters to the data, convert the analog outputs of the hydrophone groups into digital signals, perform instrument tests, and monitor various aspects of the electronics modules' operation. Dead sections act as spacers. All sections from the last live section to the lead-in section have either twisted pair copper wires or optical fiber cables to carry data from the hydrophone groups to the onboard system and receive commands from the onboard system. Devices used by the positioning system are also in or on the streamers.

Live sections vary in length (Table 5–6). The group interval should be sufficiently small to ensure that data are adequately sampled in the common shot domain—that the data are not spatially aliased. Most systems allow selection of group intervals that are subintervals of section length. The group length, or length of the hydrophone array, should be as small as practical in order to minimize attenuation of high-frequency components of steeply dipping in-line reflection events. Ideally, the source array and receiver array lengths should be comparable.

Table 5–6 In-water Systems Comparison

Parameter	I/O System Two MSX	Syntron SYNTRAK 480-24 MSTS	Hydroscience CenturyMux
Section Length	100 m	75 m	100 m
Streamer OD	6.35 cm	5.6 or 6.2 cm	5.1 cm
Groups/Section	8	12, 6, 3	32, 16, 8, 4
Group Spacing	12.5 m	6.25, 12.5 or 25 m	3.125, 6.25, 12.5 or 25 m
Channels/Module	16	12	Distributed electronics
Max Length	12,000 m	7200 m expandable to 10,000 m	7900 m
Max Ch/Streamer	704 at 1 ms	480 at 1 ms	640 at 1 ms
Hydrophones/Group	14	16	16

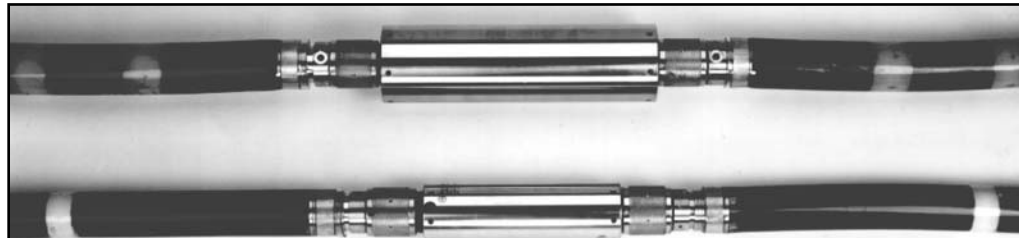
Streamer depth should be consistent with project bandwidth requirements in terms of the frequencies at which ghost notches occur. For shallow depths (< 8 m), noise specifications need to be relaxed due to the increased sea noise near the surface.

Table 5–6 lists significant parameter values for I/O System Two MSX, Syntron SYNTRAK 480-24 MSTS, and Hydroscience CenturyMux in-water systems.

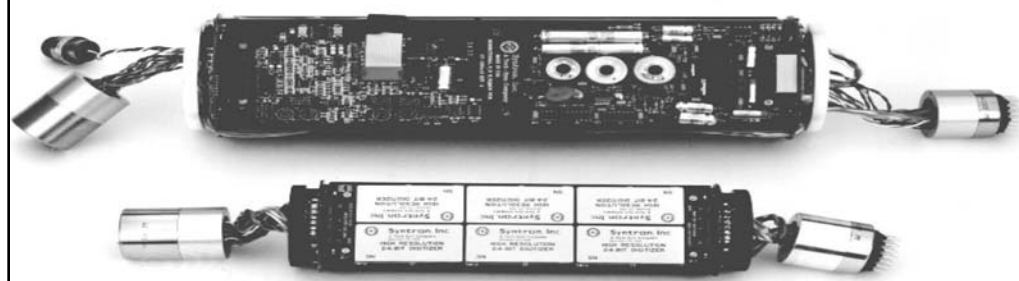
There have been many improvements in marine systems in recent years. Among these are an increase in number of channels per streamer, ability to tow and record from more streamers, reduction in streamer noise, lower instrument noise, less distortion, and improved dynamic range. Much of the improvement stems from conversion to 24-bit systems from 16-bit systems. Figure 5–91 compares Syntron 16-bit with 24-bit streamers and electronics.

Land ground systems. Land ground systems have similar components to marine in-water systems. Major components are

- electronics modules or boxes
- sectionalized line cables
- line interface modules
- jumper cables



(a) Old 16-bit (top) and new 24-bit streamers (bottom)



(a) Old 16-bit (top) and new 24-bit electronics (bottom)

Fig. 5–91 Comparison between 16-Bit and 24-Bit Systems

Every manufacturer has its own special names for these components, but all systems have the same basic configuration. Figure 5–92 shows the typical ground system configuration.

The boxes receive analog inputs from geophone groups. There are usually six or eight geophone groups, but Sercel has only one geophone group input per box. The boxes then convert these to digital signals and transmit these as data channels through the line cables, line interface module, and jumper cable to the truck-mounted system. Boxes also receive digital data from other boxes downstream from them and retransmit them at required voltage levels. They receive and process commands for configuration, testing, and status (conditions within the box); and transmit results of tests and status inquiries back to the truck-mounted system. For systems that use fiber optic cables to transmit data, boxes must also have optical-electric converters since data are transmitted as light but processed in the box as electrical signals.

Land sectionalized cables can be connected to boxes at each end. There will be as many connectors, called *takeouts*, for geophone groups as there are channels in the boxes. In the case of six- or eight-channel systems, half of the geophone inputs go to the box at one end of the cable and half to the other.

Line interface modules receive all geophone group inputs from a single receiver line, order them, and transmit them to the truck-mounted system. They also may receive and retransmit data from other line interface modules.

Jumper cables provide connections between line interface modules and from a line interface module to the truck-mounted system,

Onboard or truck-mounted systems. Major components include

- system control unit
- line/streamer interface modules
- correlator/stacker module
- operator console modules
- tape transports
- printers and/or cameras

Figure 5–93 shows these components as they appear in the recording on WesternGeco's marine vessel, the Western Monarch.

In marine operations, the system control unit interfaces with the navigation system and the airgun controller to assure that recording begins at the proper location and that this is coordinated with airgun array firing. The system control unit also controls the flow of data from the streamer interface modules and to the tape transport units as well as the functions of peripheral devices.

Streamer interface modules function much the same way as the line interface modules in land ground systems but are located onboard the vessel rather than in the streamers.

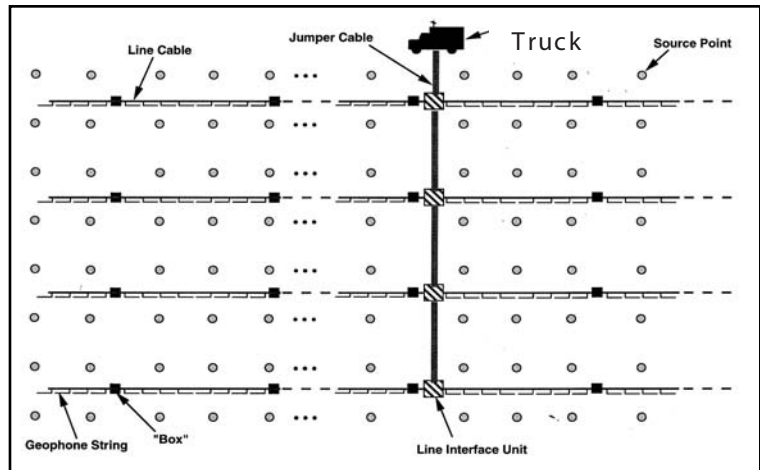


Fig. 5–92 Land Ground System Configuration



Fig. 5–93 Recording Room on the Western Monarch

The correlator/stacker module is optional land equipment used with vibrators. It is specially designed to perform cross-correlation between the filtered pilot sweep and the raw vibrator records and to do vertical stacking (including the diversity stack option).

The system operators use the operator console modules to configure and monitor the recording system. Tape transports, along with tape transport control units, format the data received from the system control unit and record it on magnetic tape. Printers and/or cameras are used to produce monitor records—hard copy or visual versions of data recorded on tape—status reports and other necessary records.

Some definitions of terms are required before continuing the discussion of recording.

Dynamic range is an amplitude ratio. It has the general definition of the ratio of the largest signal that can be recorded to rms instrument noise or the largest recoverable signal divided by the smallest recoverable signal.

Total dynamic range is the maximum system gain divided by the system noise level.

Instantaneous dynamic range is the ratio of the smallest signal that will cause a change in the presence of a larger signal. Instantaneous dynamic range is a function of the number of bits in either the A/D converter or the mantissa of the seismic word. (A 14-bit converter gives an instantaneous dynamic range of $20\log 2^{14}$ or 84 db). It controls amplitude capabilities of system's digital recording of seismic data.

All of these ranges are usually expressed as dB above system noise level.

Harmonic distortion is the ratio of the sum of the recorded amplitudes of second and higher-order harmonics to the amplitude of the input fundamental, which is usually stated in dB.

Cross-feed is the ratio of the amplitudes of electromagnetically induced signal in one channel to the amplitude of that input on another channel.

These parameters are used to evaluate recording system performance and capability.

Recorded data includes noise and signal superimposed on each other. Seismic processing may enhance data if the seismic signal is recorded within the precision of the A/D converter (instantaneous dynamic range - IDR). Seismic signals may have amplitude range of 120 dB or more when considering the amplitudes of direct arrivals and ground roll versus those of deep, faint reflections.

All recording systems have definable phase and amplitude (impulse) response for each component. The recording system fidelity is less than perfect because of amplitude, phase, and bandwidth distortion combined with the corruption of seismic wavelet with system noise. The recoverable dynamic range of seismic data is restricted by noise introduced by the recording system. Seismic recording systems have limited dynamic range. Signal and noise are superposed over the desired bandwidth, and a distorted wavelet is obtained because each component of the recording system tends to operate on or filter the seismic energy.

A magnetic tape is a strip of plastic coated with iron oxide particles. In magnetic tape recording, data are retained by magnetization of the iron oxide particles. In analog magnetic tape recording, data are represented by varying magnetization intensity along each *track*, with one track per *channel*. In digital magnetic tape recording, the direction of magnetization at small, discrete areas of tape indicates 0 or 1 values. There is no connection between channel number and track number.

Digital magnetic tape recording and related operations make use of number systems other than decimal. Data are actually recorded on tape using *binary* numbers. Some use has been made of *octal* numbers, and *hexadecimal* numbers are frequently used in tape dumps as well as in other applications of digital data. The top part of Table 5-7 shows the *radix*, or base, of these number systems and the digits used by each. Decimal numbers are included for reference. Note that the hexadecimal system requires six more digits than the decimal system has, so capitals *A* through *F* are used. The bottom part of Table 5-7 shows how to count from zero to decimal 15 in all four number systems. Note that three binary digits or bits are required to count from zero to decimal seven. This means that a single octal digit can represent a set of three bits. Four bits are required to count from zero to decimal 15. In hexadecimal, only one digit is required. Thus, a single hexadecimal digit is often used to represent sets of four bits.

Table 5–7 Number Systems

Name		Radix		Digits Used			
Hex.	Dec.	Oct.	Binary	Hex.	Dec.	Oct.	Binary
0	0	0	000	8	8	10	1000
1	1	1	001	9	9	11	1001
2	2	2	010	A	10	12	1010
3	3	3	011	B	11	13	1011
4	4	4	100	C	12	14	1100
5	5	5	101	D	13	15	1101
6	6	6	110	E	14	16	1110
7	7	7	111	F	15	17	1111

All the four of these number systems use positional representation. That is, the position of a digit in the number indicates its magnitude with regard to power of the radix. The following illustrates this.

$$\text{Hexadecimal} - 92D_{16} = 9 \times 16^2 + 2 \times 16^1 + D \times 16^0 = 2304 + 32 + 13 = 2349_{10}$$

$$\text{Decimal} - 2349_{10} = 2 \times 10^3 + 3 \times 10^2 + 4 \times 10^1 + 9 \times 10^0 = 2000 + 300 + 40 + 9$$

$$\text{Octal} - 4455_8 = 4 \times 8^3 + 4 \times 8^2 + 5 \times 8^1 + 5 \times 8^0 = 2048 + 256 + 40 + 5 = 2349_{10}$$

$$\text{Binary} - 100100101101_2 = 1 \times 2^{11} + 0 \times 2^{10} + 0 \times 2^9 + 1 \times 2^8 + 0 \times 2^7 + 0 \times 2^6$$

$$+ 1 \times 2^5 + 0 \times 2^4 + 1 \times 2^3 + 1 \times 2^2 + 0 \times 2^1 + 1 \times 2^0$$

$$= 2048 + 256 + 32 + 8 + 4 + 1 = 2349_{10}$$

This example shows how to write the same number in four different number systems.

The advantage of the binary system is that its two digits—0 and 1—can be represented by systems with only two states—off-on, up-down. In magnetic tape recording, the iron oxide particles can be magnetized in either of two directions, so one can represent 0 and the other 1.

Computers can be programmed to do many things but these many things are done with only a few operations. All logic operations are simply combinations of three basic logic operations—or, and, and not. (Not is also called *complementation*). These operations are summarized in the following example.

$$0 \text{ OR } 0 = 0 \quad 0 \text{ AND } 0 = 0 \quad \text{NOT } 0 = 1$$

$$0 \text{ OR } 1 = 1 \quad 0 \text{ AND } 1 = 0 \quad \text{NOT } 1 = 0$$

$$1 \text{ OR } 0 = 1 \quad 1 \text{ AND } 0 = 0$$

$$1 \text{ OR } 1 = 1 \quad 1 \text{ AND } 1 = 1$$

Note that there are no + and – signs in computers, so the first (from left to right) bit of binary numbers is the *sign bit*, with a 0 indicating a positive number and a 1 indicating a negative number. The second bit is the *most significant bit (MSB)* and the last bit is the *least significant bit (LSB)*.

Two methods of complementation are used in binary arithmetic—*one's complement* and *two's complement*. These are illustrated using the binary equivalent of decimal 872. The one's complement is formed by changing all 0s to 1s and vice versa. The two's complement is formed by adding a 1 to the least significant.

$$+872_{10} = 000001101101000$$

$$-872_{10} = 111110010010111 = \text{one's complement}$$

$$\underline{\quad} +1$$

$$= 111110010011000 = \text{two's complement.}$$

The only arithmetic operation a computer can perform is addition! Multiplication is done by repeated addition. Division is done by repeated subtraction. To subtract, add the *complement* of the number to be subtracted.

The following shows how a computer subtracts decimal 872 from decimal 872, using the one's complement.

$$872_{10} = 000001101101000$$

$$-872_{10} = +\underline{111110010010111}$$

$$= 0 = 111111111111111$$

The result is all 1s! This is sometimes called negative zero. Intuitively, this does not seem to be a correct answer. However, it works.

The following shows how a computer subtracts decimal 872 from decimal 872, using the two's complement.

$$872_{10} = 000001101101000$$

$$-872_{10} = +\underline{111110010011000}$$

$$= 0 = 1|000000000000000$$

In the above operation, a 16th bit is created by the carry of one in adding the two numbers. Since in this example, only 15 bits can be retained in the register, the 16th bit overflows and only the 15 zeros are present. This is a result with which we are, intuitively, more comfortable. Either complement yields valid results but it must always be stipulated which is being used.

Write heads in the tape transport unit do the writing of data on magnetic tape. *Write heads* are, basically, electric coils maintained in fixed position a very small distance above the magnetic tape. The magnetic tape passes under the write heads and current in the write heads causes the iron oxide particles to be magnetized in the up or down direction depending on direction of current through the head. As the magnetic tape moves, tracks of data are recorded along the length of the tape. For many years, the standard for magnetic tape recording was nine tracks. Now, magnetic tape cartridges commonly have 36 tracks.

A variety of methods have been used to encode data on magnetic tape. One of the earliest methods was called *non-return-to-zero* (NRZI). This is illustrated in Figure 5–94. Note that the data are being recorded along a single track (along the length of the tape, not across the tape). When a one is recorded, the direction of current in the write head changes and so does the direction of magnetization on tape. When a zero is recorded, the direction of current in the write head does not change and neither does the direction of magnetization on tape. When the tape is being read, changes of direction in tape magnetization cause changes in direction of current in the *read heads*.

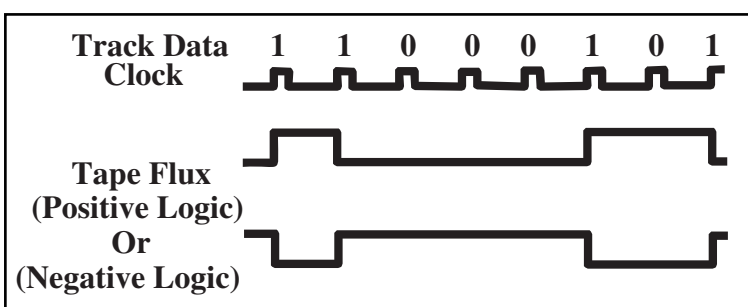


Fig. 5–94 Non-Return-to-Zero Encoding

A more recent and more often used method of encoding data on magnetic tape is called *group coded recording* (GCR). In GCR, data are initially encoded in NRZI with resynchronization bursts at 1600-bit intervals. Data are recorded as follows:

- track data are split into groups of seven bits—DDDDDDDD
- A horizontal parity *E* is added to form an 8-bit group—DDDDDDDDE
- the 8-bit group is split into two 4-bit subgroups—DDDD DDDE
- the 4-bit subgroup is translated into a standard 5-bit code

Translation table examples:

$$1000 \rightarrow 11010$$

$$1001 \rightarrow 01001$$

$$1111 \rightarrow 01111$$

$$0001 \rightarrow 11001$$

Table translation is a table look-up procedure, not application of an algorithm or formula.

- Two 5-bit subgroups are combined to form a 10-bit storage group.
- Then, 158 storage groups are written in NRZI followed by an all ones resynchronization group.

There are some tape format terms that need to be defined. Figure 5-95 provides a visual aid in understanding these terms. Near the beginning of a magnetic tape there is a physical, magnetic marker, called the *beginning of tape* (B.O.T.). The tape transport must sense the B.O.T. before recording can begin. At the end of the tape is a similar physical, magnetic marker, called the *end of tape* (E.O.T.). The tape transport looks ahead for the E.O.T. and, when it is detected, determines whether there is enough room on the tape to continue recording. If not, the tape is stopped, and the operator is informed that a tape change is required. A *magnetic tape record* is quite different from a seismic record. A magnetic tape record is a volume of data separated by an internal record gap (I.R.G.). A *file* is the largest division on tape, and is separated from other files by an end-of-file (E.O.F.) code that is all ones.

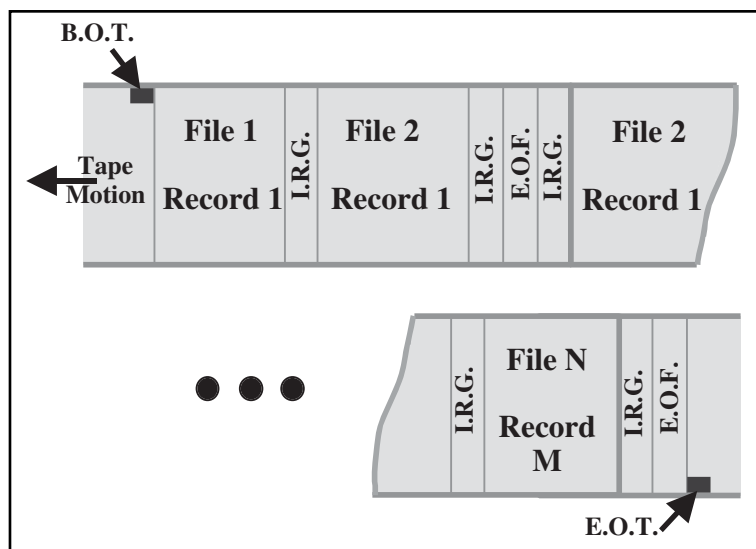


Fig. 5-95 Tape Schematic

A *byte* has eight data bits plus a parity bit. The byte is the basic index of tape format. A *parity* bit (*P*) is used for quality control in magnetic tape recording. One bit in a group is used to assure that the number of logical ones written on the tape is odd (*odd parity*) or even (*even parity*). Odd parity, illustrated here, is most used in seismic exploration.

Data Value: 0100110 (Three 1s)

Parity Bit Value: 0

Value Written to Tape: 0 1 0 0 1 1 0 0 0 (Three 1s)

Data Value: 0101 1001 (Four 1s)

Parity Bit Value: 1

S MSB
LSB PAR

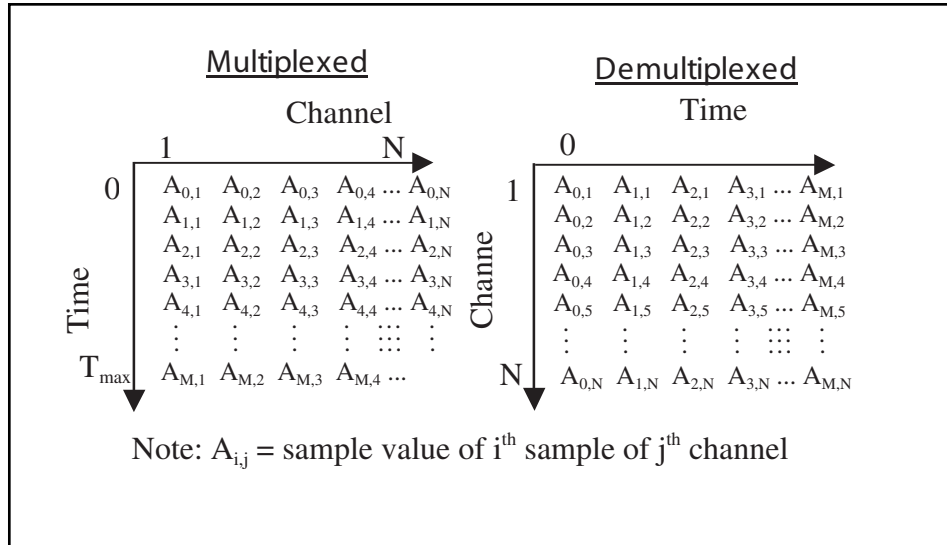


Fig. 5–96 Multiplexed and De-multiplexed Data

Value Written to Tape: 0 1 0 1 1 10 1 1 (Five 1s)

Here, S identifies sign bit, MSB is most significant bit, LSB is least significant bit and P is parity bit.

A *word* is, essentially, a computer term. It is important when interrogating tape by dumping. Dumps are indexed by words. Word size varies from computer to computer.

Multiplexed data are written on tape in sample order. That is, all samples obtained at the same time are written together in data channel order. *De-multiplexed data* are written in channel order. That is, all samples for the same channel are written together, ordered by sample times. See Figure 5–96.

At the beginning of digital recording in the early- to mid-1960s, a great variety of tape formats were in use by contractors and clients. To eliminate the chaos, the Society of Exploration Geophysicists (SEG) adopted standard formats. These were:

1967 — *SEG A* (field data, multiplexed, NRZI), *SEG B* (field data, multiplexed, NRZI), and *SEG X* (data exchange, de-multiplexed, NRZI)

1972 — *SEG C* (field data, multiplexed, NRZI or PE) introduced to accommodate IFP recorders

1975 — *SEG Y* (de multiplexed, NRZI or Phase Encoded) introduced as new data exchange format to accommodate computer field equipment and newer processing hardware

1980 — *SEG D* (multi-purpose, multiplexed or de-multiplexed, details in header) introduced to accommodate further advances in data acquisition and processing. SEG D was revised in 1994 to accommodate other developments including 24-bit recording

Details on tape formats are found in Appendix B.



6

Seismic Reflection Exploration Processing

Introduction

There are some variations in processing related to acquisition environment (land, marine, or ocean bottom cable) and source type. Land and ocean bottom cable (OBC) processing require *static corrections* but marine does not. Marine processing requires integration of navigation processing with initial seismic processing. OBC requires calculation of constants needed to sum hydrophone and geophone data. Land vibrator data must be *vertically stacked* and cross-correlated with the sweep.

Preliminary processing for vibrator data

Vertical stack is applied to vibrator data to attenuate coherent noise when sweeps are made at separate points in a source array and to attenuate random noise by \sqrt{N} , where N is the number of records stacked together. Vertical stack reduces data processing cost through reduction of data volume. Thus, vertical stack outputs fewer records with better signal-to-noise ratios. Modern recording systems integrate vertical stacking with acquisition.

Figure 6-1 illustrates the vertical stack process. In this example, sweeps are made at four locations in the source array resulting in four records, which are shown here schematically. The four records are summed (sample values at like times on like-numbered channels added together) and divided by four. Since each record was acquired from different effective source points, source-to-receiver offsets differ, and, thus, arrival times are different on each record. The time differences are much more

significant for the ground roll since its propagation velocity is much slower than that of primary reflections. Time differences translate into phase differences producing attenuation of the ground roll. Time differences between primary reflections are insignificant and no appreciable attenuation occurs.

In *simple* or *straight stack* (described previously) there is no scaling of traces before stack. In *diversity stack*, scalers that depend on trace power are applied before the traces are stacked. The same samples are stacked in each type of stack. Differences among the stacks are the way the amplitudes are scaled prior to stack.

Straight stack (Fig. 6-2) is used when signal and noise levels are about the same on all input records, and the noise level is equal to or less than signal level (S/N ratio ≥ 1). The figure uses synthetic traces to demonstrate straight stack, which is a two-step process.

1. Sum the samples at the same time on traces having the same number on records at the same shotpoints.

2. Divide the sum trace by the number of contributors to keep amplitudes within the dynamic range of the instruments and to maintain trace modulation.

Summarizing straight stack

- no scaling is applied before stack
- the output trace is the average of the input traces
- signal is coherent and stacks in phase are reinforced
- noise is random and stacks out of phase are attenuated
- signal-to-random noise improvement is \sqrt{N} where N is the number of contributing traces

Diversity stack (Fig. 6-3) is used when signal amplitudes are weak but are consistent from record to record and noise level is greater than signal level— S/N ratio < 1 . The condition that diversity stack best handles is when noise is not coherent but, instead, appears as noise bursts of limited time duration (city traffic, animals, line truck).

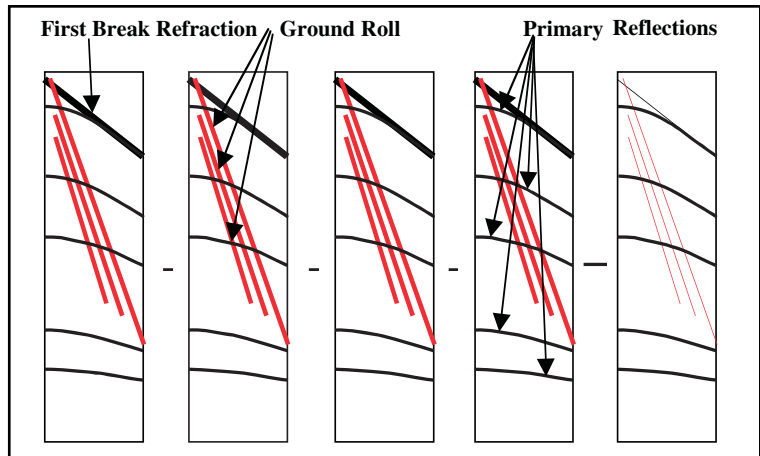


Fig. 6-1 Vertical Stack

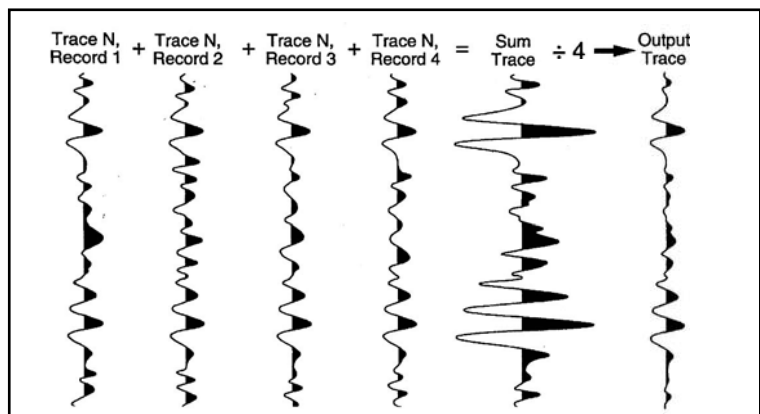


Fig. 6-2 Straight Stack

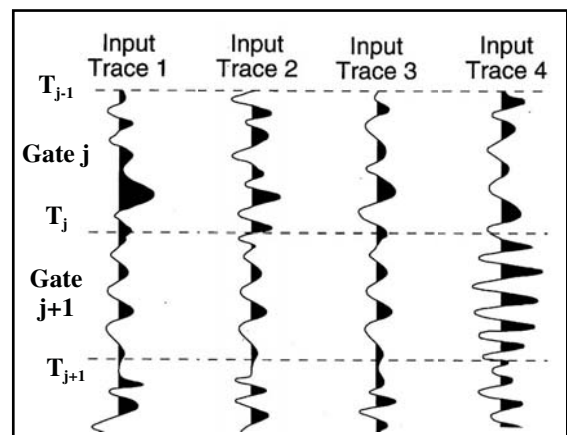


Fig. 6-3 Diversity Stack Time Gates

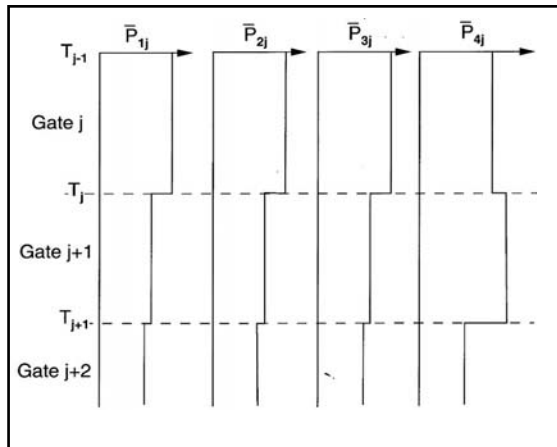


Fig. 6-4 Average Power of Each Trace in Each Gate

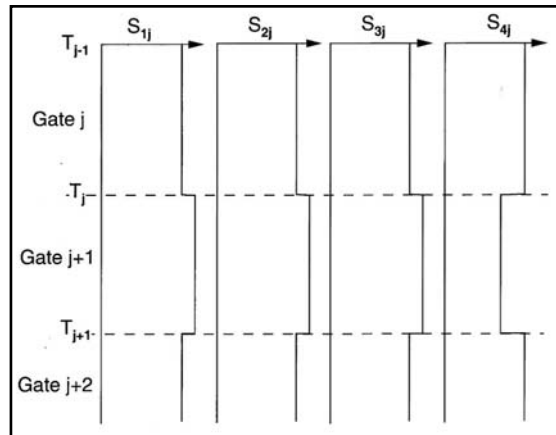


Fig. 6-5 Scalers for Each Gate

Application of diversity stack requires the following steps.

1. Divide traces into time gates. Gates should be no longer than noise bursts.
2. Compute average power in each gate of each trace.

Average power in j^{th} gate of i^{th} trace \bar{P}_{ij} is given by $\bar{P}_{ij} = \frac{1}{K} \sum_{j=1}^K A_{ijk}^2$

where

A_{ijk} is the amplitude of the k^{th} sample in the j^{th} gate of the i^{th} input trace

K is the number of samples in the gate (Fig. 6-4)

3. Compute scalers for each gate of each trace. To maintain correct amplitude balance, make scalers relative to average gate power for all traces in stack.

Average gate power, \bar{P}_j is given by:

$$\bar{P}_j = \frac{1}{N} \sum_{i=1}^N \bar{P}_{ij}$$

where

\bar{P}_{ij} is the average power of the in the j^{th} gate of the i^{th} input trace

N is the number of traces to be stacked

The scaler (Fig. 6-5) for the j^{th} gate of the i^{th} input trace S is given by:

$$S_{ij} = \frac{\bar{P}_j}{\bar{P}_{ij}}$$

4. Compute scaling function $S_j(t)$ for each trace by linear interpolation between gate center times (Fig. 6-6).
5. Apply scaling functions to traces (Fig. 6-7). $O_j(t) = A_j(t) \times S_j(t)$.
6. Stack scaled traces (Fig. 6-8).

$$O(t) = \frac{1}{N} \sum_{j=1}^K O_j(t)$$

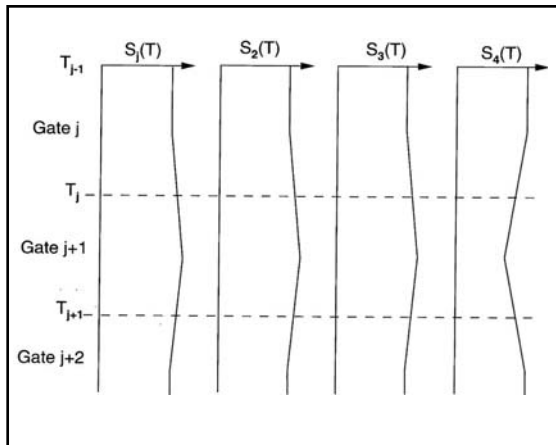


Fig. 6-6 Diversity Stack Scaling Functions

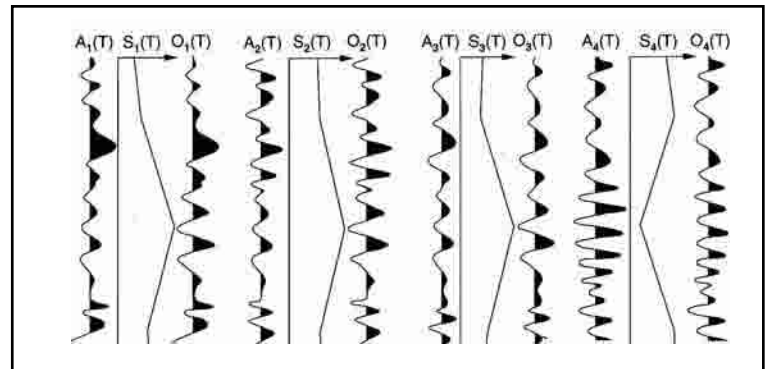


Fig. 6-7 Application of Diversity Scalers

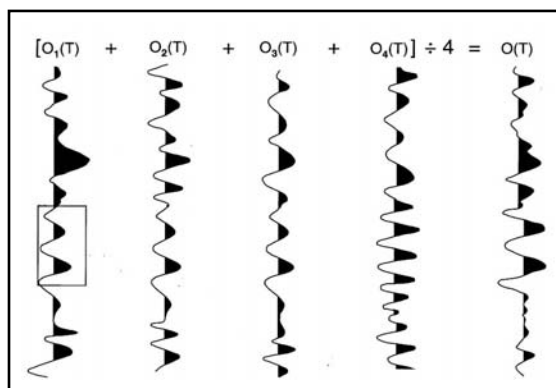


Fig. 6-8 Diversity Stack Output

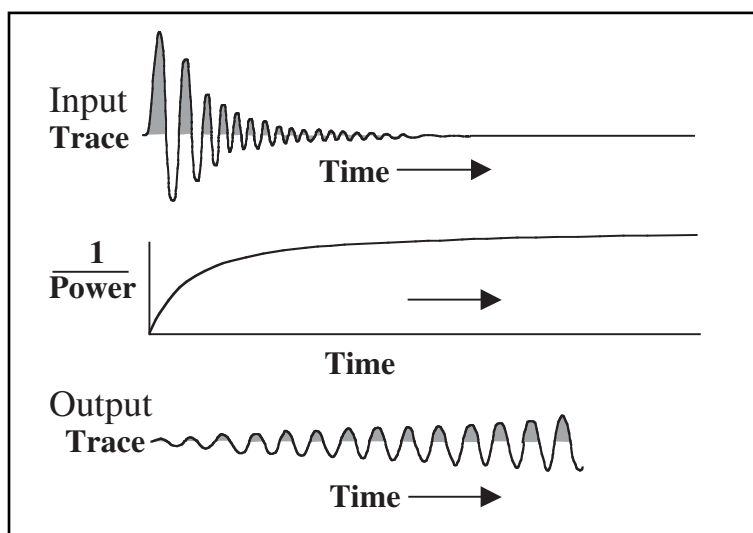


Fig. 6-10 Need for Scaler Normalization

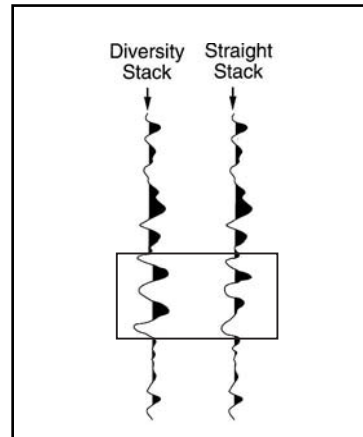


Fig. 6-9 Stack Comparison

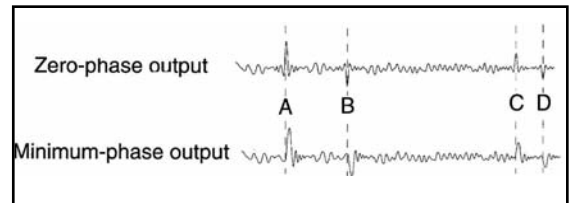


Fig. 6-11 Zero- and Minimum-phase Correlation

As shown by the synthetic trace example (Fig. 6–9), diversity stack, when used in proper conditions, is superior to straight stack. The boxed region of Figure 6–10 demonstrates the superiority of diversity stack in revealing signal in the presence of incoherent noise.

Since recorded amplitudes decay rapidly with time, scalers inversely proportional to power would increase rapidly with time, and scaling would make amplitudes increase with time. Thus, diversity stack scalers need to be normalized (Fig. 6–10).

A weak, noisy record (from an event such as a misfire) would be scaled very high and cause distortion in stack output. An amplitude threshold should be set and records with amplitudes below this threshold omitted from the stack to prevent this.

When vibrators are used as the energy source, the pilot sweep is recorded on a separate (auxiliary) trace of each record or on a special record as is the pilot sweep that has been passed through the analog filters in the recording. The sweep to use in correlation must be specified by the user, and the filtered sweep should always be specified so that the phase of the filters will be removed from the output wavelet. Otherwise, the output will not be zero phase.

Vibroseis correlation involves the following steps:

- align the pilot sweep and trace at time zero
- cross multiply pilot and trace sample values and sum the product
- store sum of products as output value at time zero
- shift the pilot sweep one sample period in the positive direction and repeat previous steps to obtain output value for next sample period
- continue the procedure until desired output record length (listen time) is obtained

This was shown by Figure 5–50, using a synthetic example. The input trace (top) is unintelligible. After the filtered pilot sweep is shifted past primary reflection A, a short duration, zero-phase wavelet can be seen. Subsequent shifts disclose the presence of primary reflections B, C, and D.

When the pilot sweep passes over a reflection event the output is, essentially, an autocorrelation scaled by the reflection coefficient, making the output wavelets zero-phase. Deconvolution, which is applied in later processing, usually requires a minimum-phase input for optimum results. Minimum-phase correlation output is an option in modern Vibroseis correlation programs. Zero-phase wavelets are converted to minimum phase by inverse filtering, and sweep frequencies are input to permit correct inverse filter design.

Figure 6–11 compares zero-phase and minimum-phase Vibroseis correlation. Note that the time for a reflection event is at the peak (or trough for a negative reflection coefficient) for zero-phase wavelets but is where the wavelet first breaks down, or up, for minimum phase wavelets.

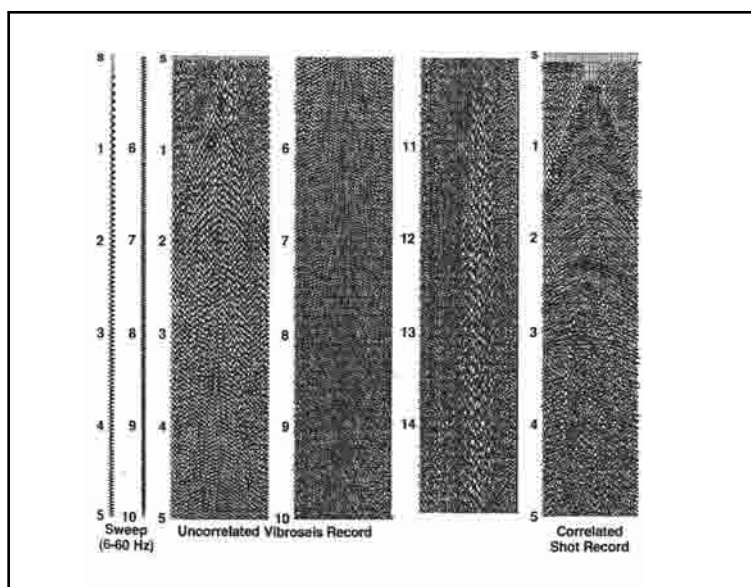


Fig. 6–12 Uncorrelated and Correlated Vibroseis Shot Records

In summary, Vibroseis correlation collapses a long-duration sweep into a short-duration wavelet similar to impulsive source wavelets. Either zero- or minimum-phase wavelets can be output as specified by the user. Record length is reduced by an amount equal to the duration of sweep.

Figure 6–12 shows a 10 second sweep, an uncorrelated Vibroseis record made with that sweep, and the correlated version of the same record. The uncorrelated record is 15 seconds long and the correlated record is five seconds long.

Seismic data processing sequences. The objective of seismic data processing is to produce an image of the subsurface target that is as accurate as possible. Inputs are field records on magnetic tape, survey /navigation data on magnetic tape, reports, and maps

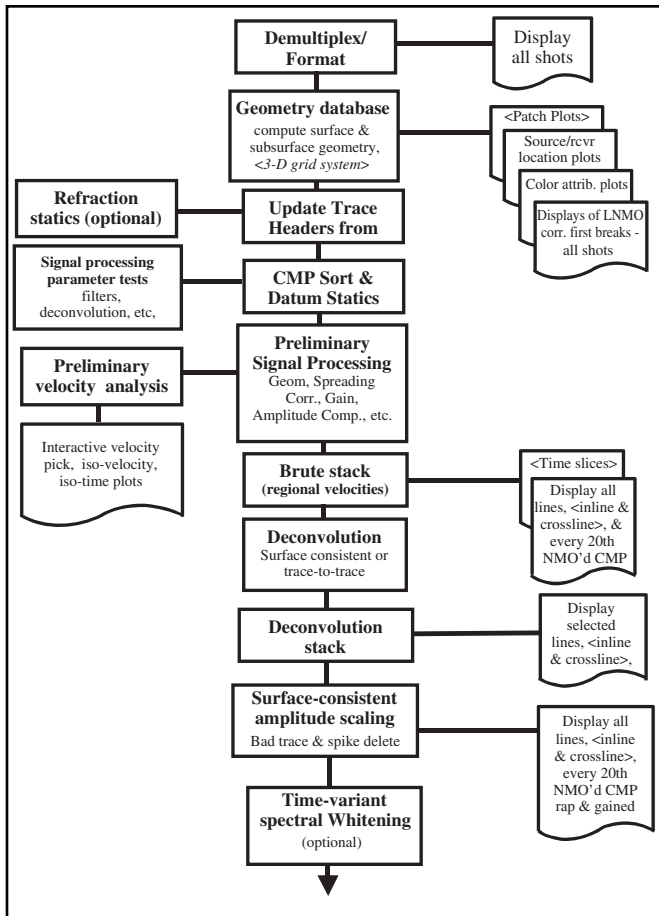


Fig. 6-13 Typical Processing Sequence

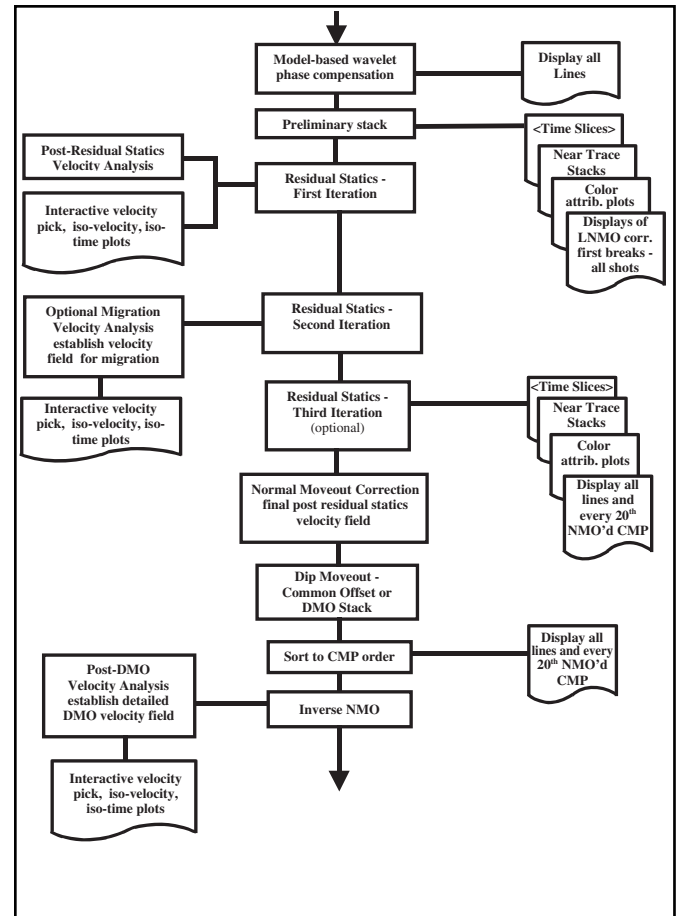


Fig. 6-14 Typical Processing Sequence (continued)

on a variety of media. Outputs are *seismic (cross) sections* with the same value displays and *iso-time* (amplitude variations over the data volume at constant times) displays. Iso-velocity displays (contours of equal velocities) are also produced and used to evaluate velocity picks.

The amplitude processing done to this point has had no effect on signal bandwidth. Usually, deconvolution of some sort is applied for this purpose. Note that Wiener type deconvolution is statistical in nature and should not be applied if AVO analysis is to be performed. Surface consistent deconvolution should be applied when AVO is planned.

The same basic processes are applied to both 2-D and 3-D data, but the nature of the 3-D data volume is such that some processes are applied only to 3-D data and other processes are applied quite differently in 3-D. Figures 6-13 through 6-15 comprise a flow chart for a typical processing sequence. Processes, displays, and other elements that apply only to 3-D are shown as <3-D only>.

Processing begins with data initialization. This is shown in the first three boxes of Figure 6-13. The first process shown, *demultiplex*, should only be necessary when reprocessing very old data. Modern seismic recording systems supply field data in *demultiplexed* form. These data will, however, be in one of the standard SEG formats and will have to be converted to the format specified by the processing system being used. It is best to display all shots at this stage to ensure data correspond to documentation and to identify problems in the data.

The *geometry database* is extremely important. All source and receiver positions must be assigned unique numbers and given coordinates in the *x-y* coordinate system adopted. Extensive and intensive quality control must be applied to assure that the geometry described by field documentation is correct and, if not, corrections made. Geometry errors can produce velocity

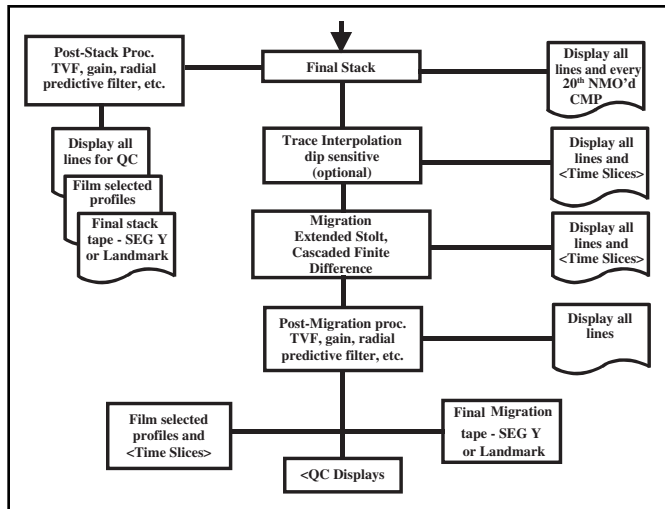


Fig. 6-15 Typical Processing Sequence (continued)

Geometrical spreading correction and some sort of *time-variant amplitude correction (gain)* are applied for this purpose. The output of this preliminary signal processing provides input to a *brute stack*, in which a *regional velocity function* is used for *NMO correction*. Brute stack sections for all lines are displayed. In 3-D processing, this means not only all the lines parallel to the receiver lines (in-lines) but also all lines created by selecting CMPs perpendicular to the receiver lines (cross-lines). *Horizontal sections*, or *time slices*, at times in the target zone are displayed as well.

CMP gathers with preliminary signal processing are used to perform an initial *velocity analysis*. Results of the analysis are interpreted via an interactive velocity picking process. The effect of velocity choices on CMP gathers and on temporal and spatial variation of the *velocity field* can be monitored in real time. *Iso-velocity* (contours or color-coding to show times at which the velocities have the same value) displays and *iso-time* (amplitude variations over the data volume at constant times) displays are also produced and used to evaluate velocity picks.

The amplitude processing done to this point has had no effect on signal bandwidth. Usually, deconvolution of some sort is applied for this purpose. After deconvolution is applied, data should be stacked using the same regional velocity function. If the velocities obtained in the initial velocity analysis are used changes caused by the differences in velocities cannot be separated from those caused by deconvolution.

Amplitude variations dependent on surface location of sources and receivers may still be present. Corrections for such amplitude variations should be determined and applied—*surface-consistent amplitude correction*. Amplitude thresholds (minimum and maximum) should be established and traces with rms amplitudes below the threshold (weak or dead traces) and those above the threshold (noisy traces) should be zeroed and not used in subsequent processing. Traces should be checked for *spikes*—abrupt, large positive or negative changes in amplitude—and any found should be removed. Since many processes are applied as convolutions, spikes will cause the impulse response of the process to be superimposed on the trace. Data should again be stacked and all lines displayed. In addition selected CMP gathers (every 20th gather, for example) should be displayed.

If data are not sufficiently *white*, a process called *time-variant spectral whitening* can be applied. This has the effect of making the amplitude spectrum flat over a desired bandwidth and does not attempt to increase amplitudes outside this bandwidth. If used, data should be stacked and all lines displayed for evaluation of process effect.

Model-based phase compensation (Fig. 6-14) can be applied to remove residual phase components and provide the desired zero-phase wavelets. Time-variant spectral whitening can be used as an alternative to statistical deconvolution when coupled with model-based phase compensation. Again, display all lines after a process is applied.

At this point, the velocities obtained in the initial velocity analysis are used for NMO corrections and a preliminary stack performed. Quality control displays at this stage consist not only of the stack sections for all lines but also time slices in the target zone, near trace stacks or gathers, color attribute (amplitude) displays, and selected CMP gathers (same set as previously selected). Comparison with stack sections from the previous process shows the effect of the new velocities.

and statics errors that cannot be removed except by geometry correction. The displays shown at the right of the geometry database box in Figure 6-13 are used for this purpose. The results of the geometry quality control (QC) are used to update the geometry database.

At this point, a sort into *common midpoint* (CMP) format is made for use in parameter testing and selection. In land processing, datum statics are also calculated and applied. If refraction statics are used, then calculations are performed separately for later use. The updated geometry database should provide data needed for both datum and refraction statics.

Since each trace in the final output is to be a representation of the earth impulse response at each midpoint position, amplitudes must be corrected for losses along the reflection ray paths.

In land processing, at least two iterations of *residual statics* are run, with a third iteration optional. The number of iterations depends on how quickly residual statics converge to a stable value. Each residual statics iteration is followed by a velocity analysis. The combinations of residual statics and velocity analyses better separate time variations in the near surface from those along reflection ray paths and those caused by geological structure variations.

In marine processing, no residual statics analysis is performed, and usually at least one less velocity analysis is done. However, in both land and marine processing, DMO is applied to remove the effect of dip from velocities and to move data to their true zero-offset position. This requires application of NMO corrections and, in some cases, sorting into the common offset domain. After the DMO correction is applied, the NMO correction is backed out—inverse NMO corrections are applied.

After this, a final stacking velocity field is obtained via velocity analysis and interactive velocity picking. This velocity field is used to apply NMO corrections to CMP traces and then do the final CMP stack. The usual QC displays are also produced. Post stack processes such as time-variant filtering (TVF), attenuation of residual multiple reflections, and attenuation of ambient noise are applied to produce a CMP stack with the best possible signal-to-noise ratio.

A variety of migration algorithms are available. The choice depends on cost, maximum dip, and frequency requirements. In 3-D, a choice must be made between one-pass and two-pass migration. One-pass migration is true 3-D migration while two-pass migration applies 2-D migration in-line followed by another 2-D migration cross-line. In Figure 6-15, two-pass migration using *extended Stolt migration* for the in-line migration and cascaded (multi-stage) *finite difference migration* for cross-line migration is indicated.

The final stack is then input to migration. It is usually best to input a stack that does not have TVF applied to it. Interpolation to a smaller spatial sampling interval may be advisable prior to migration to limit the harmful effect of spatial aliasing on migration. This is particularly the case in 3-D when the cross-line sampling interval is quite large compared to in-line. It may also be necessary to apply some sort of *multiple attenuation* processing other than deconvolution. Such processing can be done pre-stack, post-stack, or both. Multiple attenuation before the final velocity analysis can improve the quality of the velocity field.

Data initialization

Field tape processing has two basic functions—reformatting magnetic tape data and editing traces.

Reformatting magnetic tape may, but usually does not, involve demultiplexing. Most data, today, are recorded in demultiplex format. In earlier times, the conversion from multiplex to demultiplex (shown in Fig. 5-96) was the first process applied. However, data must be put in the format required by the processing software.

Trace editing includes *despiking* (elimination of high amplitude anomalies), *polarity reversal* (change to correct polarity), *trace zeroing* (set trace amplitudes to zero if average amplitude is outside amplitude thresholds), and *source/receiver coupling compensation* (correct trace amplitudes for poor coupling at specific surface locations).

After field tape processing is complete, geometry must be checked. This is usually done by applying *linear moveout* (LMO) corrections and displaying first breaks. Linear moveout corrections take the form:

$$T_c = T - \frac{x}{V_R} \quad (6.1)$$

where

T_c = first break time corrected for linear moveout

T = raw first break time

x = offset for trace being corrected

V_R = refraction velocity of first refractor

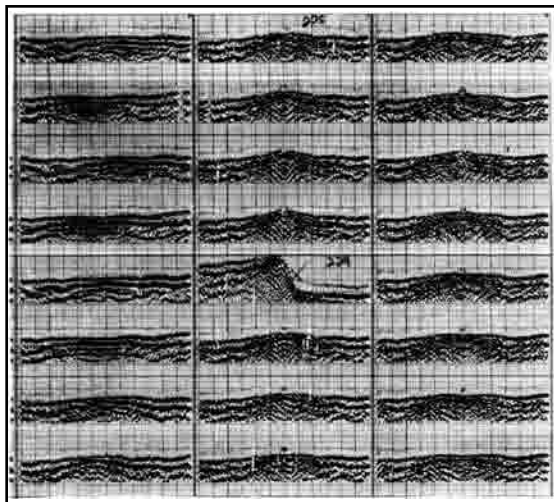


Fig. 6-16 LMO Traces Display

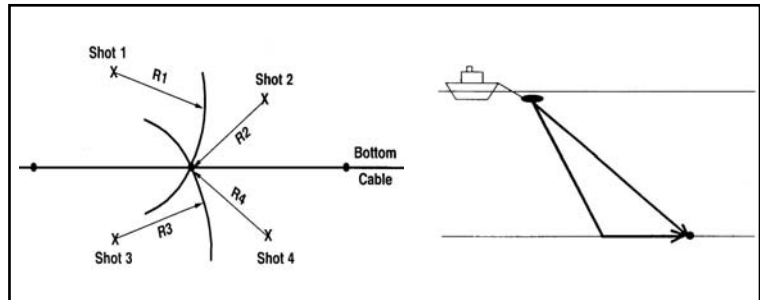


Fig. 6-17 OBC Receiver Location

If geometry is correct, traces corresponding to arrivals from the first refractor will have first breaks aligned. Short offset traces will be overcorrected if direct arrivals are first breaks. Far offset traces will be under corrected. This is shown in Figure 6-16. Most records appear to be normal, indicating geometry provided from the field is correct for these shots. However, shot number 329 (fifth record from top in the center) shows anomalous first breaks. Traces on the left are under corrected and traces on the right are overcorrected. This indicates that the shot point location is incorrect and should be moved to the right.

In OBC operations, receiver locations are not known precisely. Source positions are located using differential GPS positioning (GPS antenna on source array) and first arrivals from the seismic data are picked. For direct arrivals, the times picked multiplied by water velocity give the acoustic ranges or source-to-receiver distances. For first break refractions, calculate ranges by subtracting delay times from first break times and multiplying the difference by the refractor (sub-water layer) velocity. Since records are shot from multiple sources into the same receivers, receiver locations can be computed using a multi-range acoustic positioning method analogous to conventional radio positioning with the known source positions acting as base stations (Fig. 6-17).

Data are input as *shot* or *common source* records. After data initialization is completed, data are output in common midpoint or CMP format. Other applications require *common offset* or *common receiver* format. Reflection point or stacking diagrams, such as in Figure 6-18, facilitate collecting or gathering traces for various purposes. Depth points for each field record are shifted down, vertically, but are in correct horizontal positions.

Stacking diagrams form a trace matrix. Lines drawn through the matrix indicate which traces to collect for specific gathers, as shown in Figure 6-19. Vertical lines connect traces that have common midpoints. Horizontal lines connect traces that have common sources. A line drawn through the shortest offset traces connect traces in a *near-trace gather* (NTG). Lines parallel to the NTG line connect traces that have common offsets. Another set of slanting lines, with a steeper slope, connect traces that have common receivers.

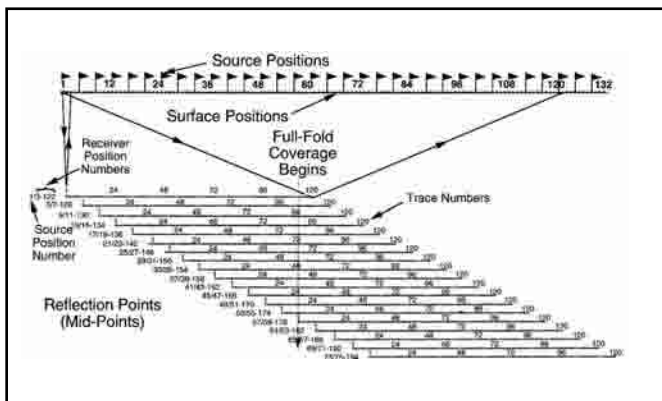


Fig. 6-18 A Stacking Diagram

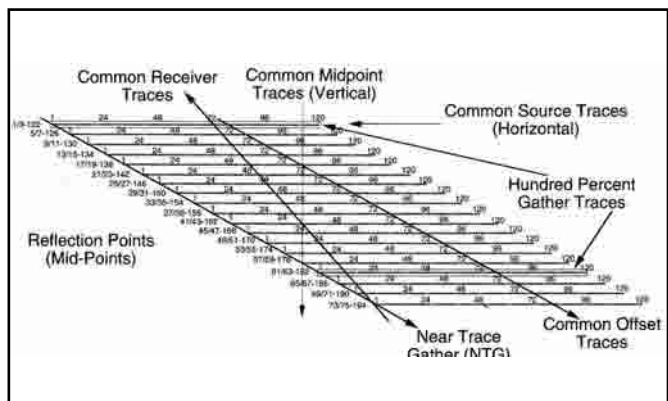


Fig. 6-19 Trace Gathers

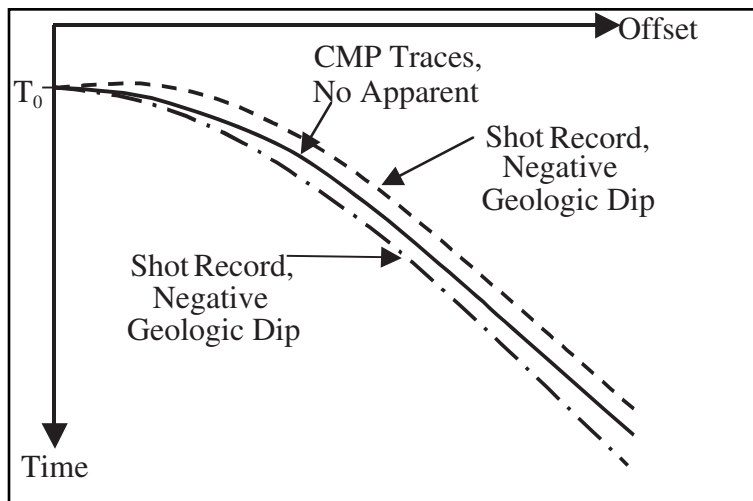


Fig. 6-20 Shot and CMP Traces with Geologic Dip

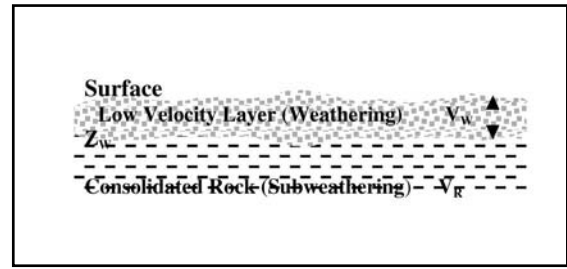


Fig. 6-21 Near-surface Model

Common source (shot) traces differ in moveout, offset, receivers, and may differ in dip. This is the format for input to amplitude recovery and velocity filtering. Common receiver traces differ in moveout, offset, sources, and may differ in dip. This format may be used in surface consistent processing. Common midpoint traces differ in moveout, offset (split spread shooting may result in duplicate offsets), receivers, and sources. This format is the input to velocity analysis and CMP Stack (after NMO/DMO and static corrections, if the latter are done). Independence from effect of dip on NMO curves is an important attribute for the just-mentioned processes.

Figure 6-20 shows moveout on CMP traces and common source (shot) traces. The moveout on each trace is the sum of NMO and geologic dip. If dip is negative, then reflection times initially decrease and minimum reflection time may not be at zero offset. If dip is positive, then moveout is greater than NMO alone at all offsets. On CMP traces however, the effect of dip on reflection times is negligible for dips up to about 10° .

Common offset traces differ in receivers, sources, and reflection points. Trace-to-trace time differences are caused by differences in dip and/or velocity. This is the format for input to DMO. It is also used to determine residual moveout in residual statics analysis and other special analyses.

An NTG is a set of common offset traces with minimum offset. It is used for QC and parameter determination. It is a good indicator of horizon times and dips. A 100% gather (HPC) is a collection of records that provide single-fold coverage of the subsurface. The HPC is obtained by selecting every N^{th} shot record, where $N = \text{maximum fold}$. It may be used in conjunction with the NTG to analyze spatial variation of velocity.

There is a layer of unconsolidated rock just below the surface in virtually all land areas. See Figure 6-21. This layer, or layers, has quite low and variable

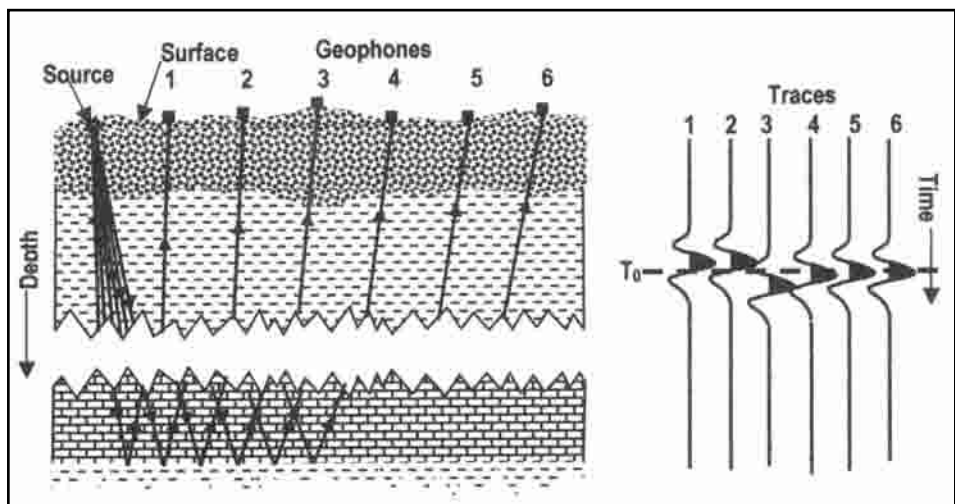


Fig. 6-22 Effect of Variable Near Surface

seismic velocities. It is sometimes called the *low-velocity layer* or *weathering*. The variable velocity and/or thickness produces trace-to-trace time differences which give false pictures of subsurface structure. The effect of variations in surface elevations and the near-surface thickness and velocity can readily be seen on a reflection from a flat reflector.

Ray paths from a source to a flat reflector and upward to six geophones through a variable near surface are shown on the left of Figure 6–22. On the right are the reflection events recorded at geophones one through six on traces one through six. If it were not for the variation in the near surface, all events would be recorded at time T_0 . A variable near surface causes reflection time variations that, if not properly accounted for, can give false impressions of geologic structure and/or seismic velocity.

Static corrections are applied to remove the effect of elevation and near-surface variations on reflection times. In effect, datum statics strip off the near surface and materials down to the datum, which is usually flat. This moves sources and receivers from the actual surface to a new reference plane underlain by material having a higher velocity V_R than weathering.

Datum static corrections are calculated separately for sources *SSC* and receivers *RSC*. The total static *DSC* for a particular trace is the sum of the source static and the receiver static.

$$DSC = SSC + RSC \quad (6.2)$$

There are two basic situations for datum statics computations. Case I, for a surface source, and Case II, for sources shot beneath the surface. Figure 6–23 shows Case I. The source static *SSC* is calculated from:

$$SSC = - \left[\frac{E_{ss} - E_{ws}}{V_w} + \frac{E_{ws} - E_R}{V_R} \right] \quad (6.3)$$

The receiver static *RSC* is calculated from:

$$RSC = - \left[\frac{E_{sr} - E_{wr}}{V_w} + \frac{E_{wr} - E_R}{V_R} \right] \quad (6.4)$$

where

E_{ss} = elevation of the surface at the source position

E_{sr} = elevation of the surface at the receiver position

E_{ws} = elevation of the base of the weathering at the source position

E_{wr} = elevation of the base of the weathering at the receiver position

E_R = elevation of the datum plane

V_w = velocity of the weathering

V_R = replacement velocity

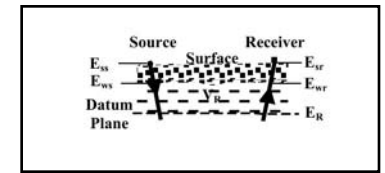


Fig. 6-23 Static Corrections,
Case I: Surface Source

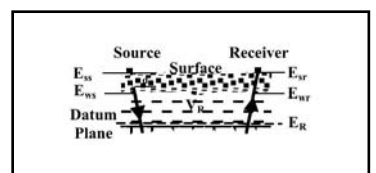


Fig. 6-24 Static Corrections,
Case IIa: Source in Weathering

Case II has two subclasses. The source, for Case IIa (Fig. 6–24), is within the weathering or near surface layer. In this case the source static correction is computed from Equation 6.5 or Equation 6.6.

$$SSC = - \left[\frac{E_{ss} - d - E_{ws}}{V_W} + \frac{E_{ws} - E_R}{V_R} \right] \quad (6.5)$$

$$SSC = - \left[\frac{E_{ss} - E_{ws}}{V_W} - T_{uh} + \frac{E_{ws} - E_R}{V_R} \right] \quad (6.6)$$

where

E_{ss} , E_{sr} , E_{ws} , E_{wr} , E_R , V_{ws} and V_R are as previously defined

d = depth of source

T_{uh} = up-hole time

Up-hole time is the time required for energy to travel from the source to a geophone at the surface near the top of the hole. The receiver static is calculated from Equation 6.4.

In Case IIb (Fig. 6–25), the hole is drilled through the weathering. The source static correction is calculated from Equation 6.7a or Equation 6.7b.

$$SSC = - \left[\frac{E_{ss} - d - E_R}{V_R} \right] \quad (6.7a)$$

$$SSC = - \left[\frac{E_{ss} - E_R}{V_R} - T_{uh} \right] \quad (6.7b)$$

Sometimes a less detailed approach, called elevation statics, is used. In this method, the base of the weathering is ignored and an average velocity to the datum V_{avd} is used. Computation of the source elevation static (SESC), the receiver elevation static (RESC), and the total elevation static (ESC) is shown below for Cases I and II.

Case I

$$SESC = - \frac{E_{ss} - E_R}{V_{avd}}$$

$$SESC = - \frac{E_{sr} - E_R}{V_{avd}}$$

Case II

$$SESC = - \frac{E_{ss} - E_R}{V_{avd}} + T_{uh} = - \frac{E_{ss} - d - E_R}{V_{avd}} \quad (6.8)$$

$$RESC = - \frac{E_{sr} - E_R}{V_{avdd}} \quad (6.9)$$

Datum statics, however they are calculated, are saved as separate source and receiver statics and total datum statics are added to trace headers.

Refraction static corrections are computed in a four-step process:

1. pick refraction travel times
2. decompose refraction times
3. construct refraction elevation model
4. compute static corrections

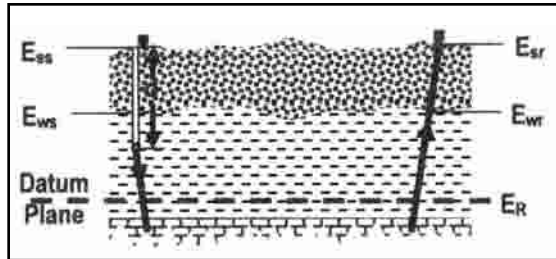


Fig. 6-25 Static Corrections, Case IIb: Source in Subweathering

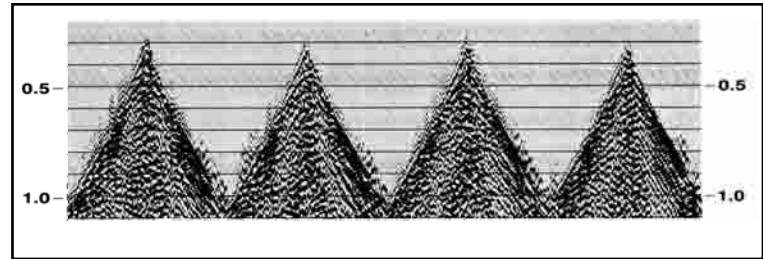


Fig. 6-26 First Breaks of Selected CMP Gathers

Figure 6-26 shows first breaks of a few CMP gathers. First break times are picked as the time at which the traces first break downward. The short offset times, in general, will correspond to direct arrivals. Later picks will be refraction arrivals from the base of the weathering or a deeper refractor. Figure 6-27 shows ray paths and a time-distance or *T-X* plot of first break times versus offset. Velocities V_0 , V_1 , and V_2 are calculated from the inverse slopes ($\Delta d/\Delta t$) of the lines fitted to the data in the *T-X* plot.

Refraction arrivals can be decomposed into three parts:

$$T_{ij} = t_i + t_{ij} + t_j \quad (6.10)$$

where

t_{ij} = refraction time from the source i to receiver j

t_i = time from the source down to the refractor

t_j = time along the refactor beneath the source to beneath the receiver

t_j = time from refractor up to the receiver

In Figure 6-28, $t_i = SP/V_0$, $t_{ij} = PQ/V_1$, and $t_j = SP/V_0$.

In multifold shooting, many estimates of t_i and t_j are obtained. For example, in Figure 6-29 traces are recorded at receiver group R_1 from sources S_1 , S_2 , S_3 , and S_4 . Similarly, traces are recorded at receiver groups R_A , R_B , R_C , and R_D from source S_4 . Folds much greater than four are common, and a particular source position is often also a receiver position. The redundancy of information about surface positions allows application of statistical methods to extract delay times of t_i and t_j .

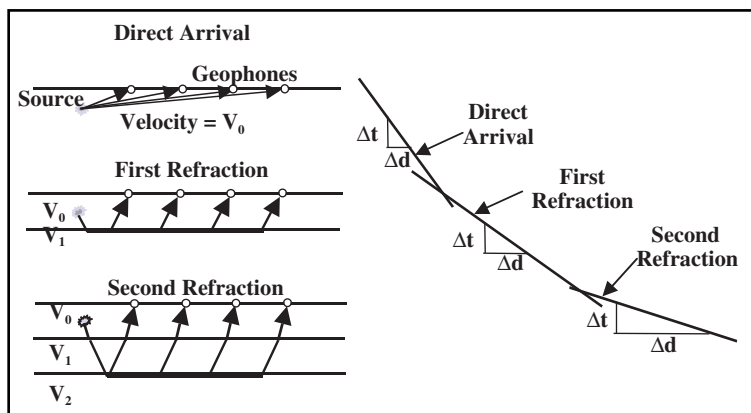


Fig. 6-27 First Break Ray Paths and T-X Plot

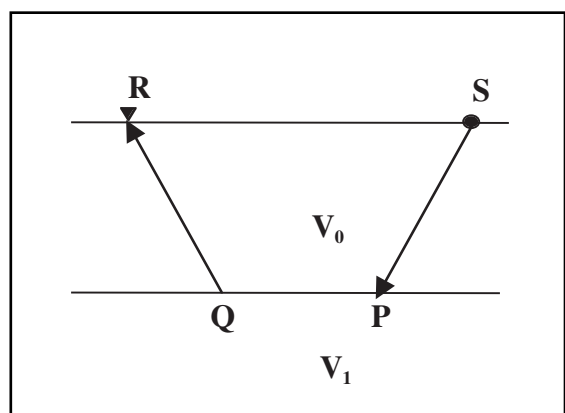


Fig. 6-28 Refraction Ray Path Segments

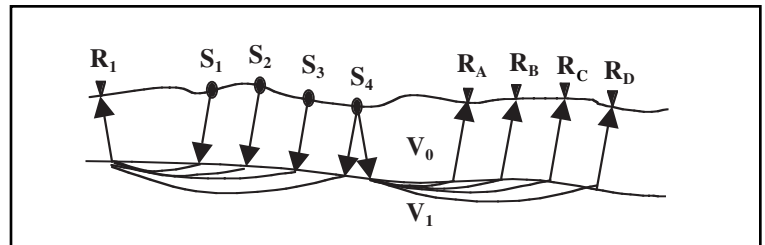


Fig. 6-29 Redundancy of Data in Refraction Statics Determination

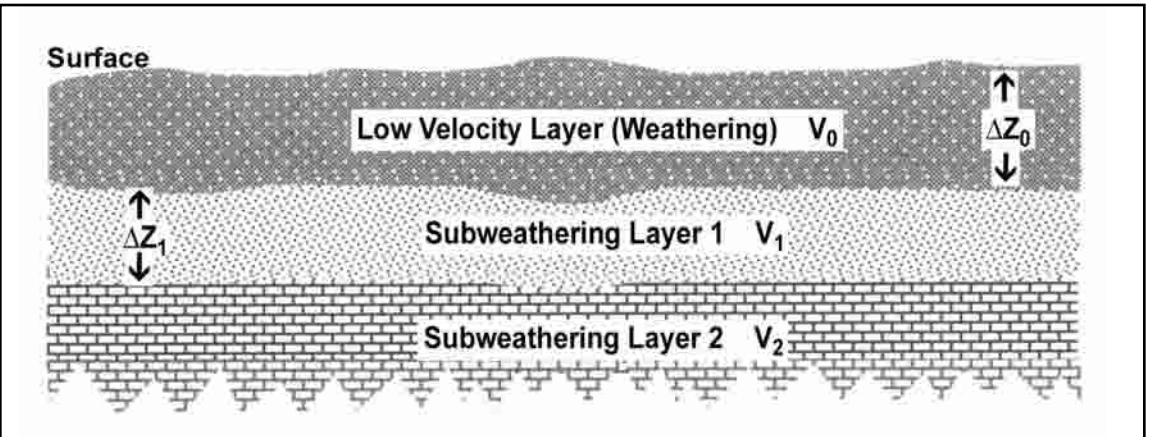


Fig. 6-30 Refraction Elevation Model

If the refraction velocity V_R is known, then the time along the refractor can be calculated from:

$$t_{ij} = \frac{x_{ij}}{V_R}$$

where

x_{ij} is the distance between source i and receiver j .

Substituting this into Equation 6.10 and solving for t_i yields:

$$t_i = T_{ij} - \frac{x_{ij}}{V_R} - t_j \quad (6.11)$$

The Gauss-Seidel method is an iterative method of obtaining surface consistent solutions from redundant data. In Equation 6.11, initial values of t_j factors (e.g. = 0) are selected and a least-square error estimate of t_j is obtained. The error is used to update the t_j factors and a second iteration, third, and more iterations are performed. The iterations are done very quickly and there is usually a rapid convergence to a particular value of t_j . The same approach is used to determine all t_i and t_j values.

Using the methods described in chapter 4, layer thicknesses ΔZ_0 and ΔZ_1 below the various surface positions (stations) can be calculated from the delay times t_i and known velocities V_0 , V_1 , and V_2 . This allows construction of a refraction elevation model, such as that shown in Figure 6-30. Datum statics can then be calculated from relevant Equations 6.4 through 6.9.

Preliminary signal processing

There are two main objectives in this stage of processing—eliminating amplitude variations caused by factors other than reflection coefficient variations and attenuating coherent noise.

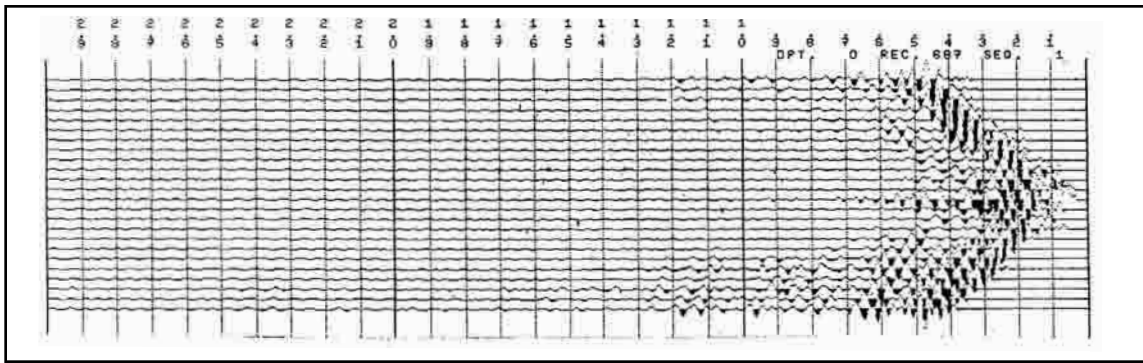


Fig. 6–31 Field Record with No Gain Applied

Amplitude processing. If a field record recorded by a 24-bit system or one recorded by an FTP system with gain removed is displayed, it has the appearance of the record of Figure 6–31. Amplitudes rapidly decay primarily due to geometrical spreading and inelastic attenuation.

Geometric spreading. In a constant velocity medium, energy spreads out from the source at the same rate in all directions. Wavefronts in such a medium are spherical. At a time t_1 , the surface area of the wavefront in a medium of velocity V is $\pi(Vt_1)^2$. At a later time t_2 , the surface area of the wavefront is $\pi(Vt_2)^2$. Amplitude is proportional to the square root of energy per unit area. Assume no energy is lost in propagation and the total energy is E . The amplitude at time t_1 is A_1 , and the amplitude at time t_2 is A_2 . The ratio of amplitudes is

$$\frac{A_1}{A_2} = \sqrt{\frac{E}{\pi(Vt_1)^2}} = \sqrt{\frac{E}{\pi(Vt_2)^2}} = \sqrt{\frac{t_1}{t_2}} \quad (6.12)$$

It follows from Equation 6.12 that $A_1 t_1 = A_2 t_2 = \text{constant}$. In the case of a constant velocity medium, amplitude losses caused by geometric spreading, also called *spherical divergence*, can be corrected by multiplication by time t .

In real cases, however, velocities are not constant. In fact, velocities usually increase with depth so actual wavefronts are not spherical, and their areas increase at a faster rate than in spherical divergence. This is illustrated in Figure 6–32.

To compensate for the faster increase in wavefront surface area when velocity increases with depth (and time), the geometric spreading correction is defined as $g(t) = (V/V_0)^2 t$ where V is a smoothed regional velocity function and V_0 is the initial velocity or velocity at time zero. Figure 6–33 shows the effect of the Geometric Spreading Correction.

Gain functions. The geometric spreading correction does not compensate for all amplitude losses. Usually the most severe losses are caused by inelastic attenuation—absorption and scattering—along the path. These losses depend on path length (and record time) plus the Q-factors of subsurface rocks through which the seismic waves propagate. A number of approaches (often called gain or scaling) are used to correct amplitudes for inelastic attenuation. These can be broadly classed as either *empirical* or *statistical*.

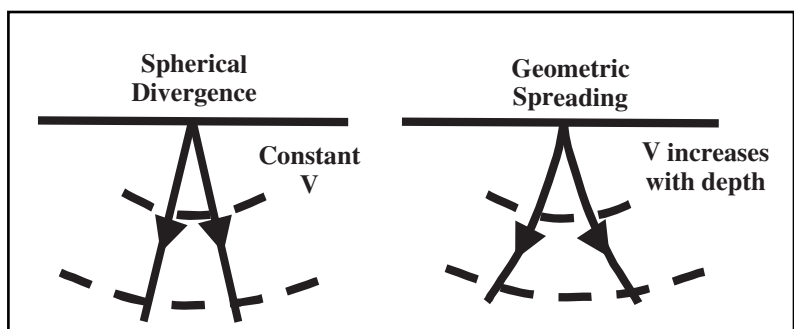


Fig. 6–32 Spherical Divergence and Geometric Spreading

Seismic reflection exploration processing involves several steps to analyze and interpret seismic data. One key step is amplitude processing, which includes applying gain to correct for geometric spreading and inelastic attenuation. Other steps include filtering, deconvolution, and velocity analysis to determine subsurface rock properties and structures.

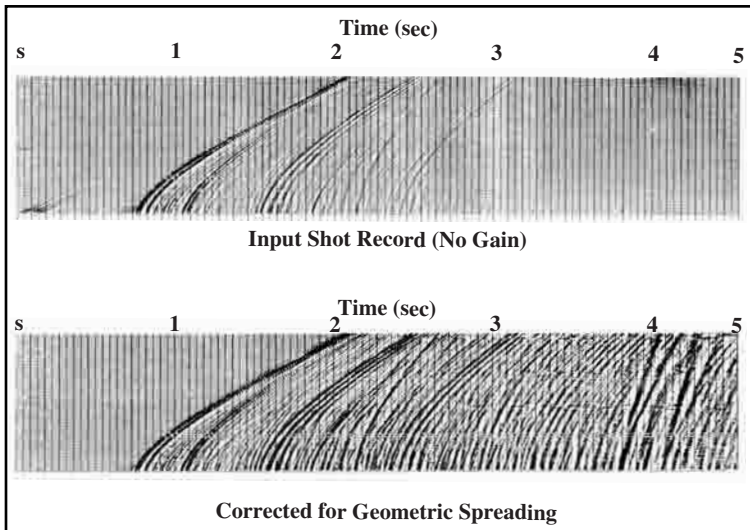


Fig. 6-33 Geometric Spreading Correction Example

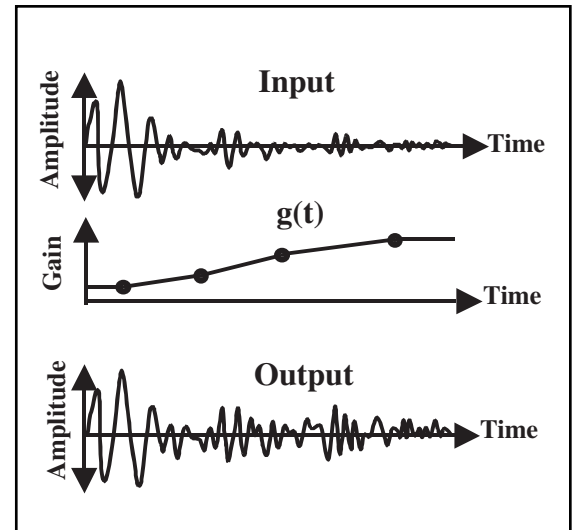


Fig. 6-34 Programmed Gain Control

Programmed gain control (PGC) is one of the empirical methods. It is a rather straightforward approach. One simply analyzes the data and selects two or more (usually more) pairs of times and gains. Gain is simply a number by which the input amplitudes are multiplied. Gain between the selected times is determined by linear interpolation. This is illustrated in Figure 6-34.

Designating $A_i(t)$ the input trace, $g(t)$ the PGC gain function, and $A_o(t)$ the output trace, input and output are related by:

$$A_o(t) = A_i(t)g(t) \quad (6.13)$$

Usually, a variety of functions are applied to representative CMP gathers. These outputs are then displayed and visually inspected to determine the best result. This evaluation is very qualitative since knowing what the result *should be* is required.

Another empirical approach is exponential scaling. This seems a good approach, intuitively, since it is known that inelastic attenuation is a type of exponential decay. The relation between input $A_i(t)$ and output $A_o(t)$ in this case is

$$A_o(t) = A_i(t)10^{at} \quad (6.14)$$

where a is a constant, usually expressed in dB/sec.

Similar to the procedure for PGC, various values of the constant a are used to apply exponential scaling to representative CMP gathers. These outputs are then displayed and visually inspected to determine the best result. Again, this evaluation is very qualitative since knowing what the result should be is required.

A frequently used method of amplitude processing is called automatic gain control (AGC). This is a statistical approach that is based on methods of volume control used in electronic audio systems. In such systems, a part of the output from an audio amplifier is fed back to the input. The effect is to maintain audio outputs within a narrow range, avoiding very loud or very faint volumes. Some electronic systems have fast AGC and others have slow AGC. In fast AGC the time between output and feedback action to limit output variation is very short. As a result, there is little variation in output sound volume. In slow AGC, the time between output and feedback action to limit output variation is longer and more variation in output sound volume is allowed.

One approach to AGC, called instantaneous AGC (IAGC), is as follows:

1. select a time gate or number of samples N
2. calculate the *average absolute amplitude* \bar{A} within the time gate

$$\bar{A} = \frac{1}{N} \sum |A_n| \quad (6.16)$$

where

$|A_n|$ = absolute value of amplitude samples in the time gate, $n = 1, 2, \dots, N$

3. determine the scaler from $S = \frac{A_{desired}}{\bar{A}}$, where $A_{desired}$ is the desired average absolute amplitude for the entire trace—A value of 1800 mv for $A_{desired}$ is frequently used
4. select the position within the gate at which the scaler will be applied
5. multiply the amplitude in the selected position by the scaler—this is the first output
6. move the gate down the trace one sample and repeat steps one through five
7. continue until all samples are used

The critical parameter is *gate length*. A very short gate is similar to fast AGC and results in elimination of almost all amplitude variation. Note that amplitude variations caused by subsurface geology must be preserved. A very long gate is similar to slow AGC and allows too much amplitude variation. Another negative effect of a long gate is a high-frequency filtering effect. The usual approach is to try different gate lengths and evaluate by visual inspection of CMP displays. Better results are sometimes obtained by allowing gate length to linearly increase. Signal-to-noise ratios decrease with record time so less gain variation is desirable at later times. Also, bandwidth decreases on the high side as record time increases, making high-frequency filtering less important.

Another AGC is *RMS AGC*. This is probably used more often than IAGC and may be the most-used form of amplitude processing. The method involves the following steps:

1. select a time gate or number of samples N
2. calculate the *root mean square (rms) amplitude* \hat{A} within the time gate

$$\hat{A} = \sqrt{\frac{1}{N} \sum_{n=1}^N A_n^2} \quad (6.16)$$

where

A_n = amplitude samples in the time gate, $n = 1, 2, \dots, N$

3. determine the scaler from $S = \frac{A_{desired}}{\hat{A}}$, where $A_{desired}$ is the desired rms amplitude for the entire trace—a value of 2000 mv for $A_{desired}$ is frequently used
4. assign this scaler to the center of the gate
5. move to the next gate down the trace and repeat steps one through four
6. continue until all samples are used
7. develop the RMS AGC function $g(t)$ by extrapolating the value of the first scaler back to start time, linearly interpolating between scalers up to the center of the last gate, and extrapolating the value of the last scaler forward to end of trace
8. multiply the input trace by the rms scaler function $g(t)$ as in Equation 6.13 and illustrated in Figure 6–34.

As with instantaneous AGC, gate length is the critical parameter in RMS AGC. However, gates do not overlap in RMS AGC so the AGC action is not so fast. Gate lengths increasing with time are very common in RMS AGC.

OBC scaling. Ocean bottom cables are used in relatively shallow water. A major problem in this type of seismic acquisition is the presence of multiple reflections in the water layer. In OBC operations, these are called *OBC ghosts*. Figure 6-35 shows ray paths for a primary, plus the first and second ghosts. A third ghost is produced by additional reflections within the water layer.

The first ghost has opposite polarity from the primary because the reflection coefficient at the surface equals -1. The ghost arrivals have alternating polarity and decreased amplitude because the reflection coefficient of the water bottom is less than 1. As a result, a long source wavelet is produced, as shown in Figure 6-36.

A wavelet such as that in Figure 6-36 is unacceptable. The ghosts must be attenuated so that wavelets are reduced to acceptable durations. The OBC method records data with both hydrophones and geophones and takes advantage of the differences in their responses to ghosts.

Figure 6-37 illustrates the generation of hydrophone ghosts. The numbers in the figure correspond to the following:

- the amplitude incident on the water bottom after reflection (primary reflection amplitude) = 1
- reflection coefficient of the water bottom = R
- reflection coefficient of the surface = -1
- the amplitude transmitted into the water from below = $1 + R$
- the amplitude reflected downward at the water surface = $-(1 + R)$
- the amplitude reflected upward at the water bottom = $-R(1 + R)$
- the amplitude reflected downward at the water surface = $R(1 + R)$

Continued reflection at water bottom and surface result in the amplitude of successive ghosts being $-R$ times that of the previous ghost.

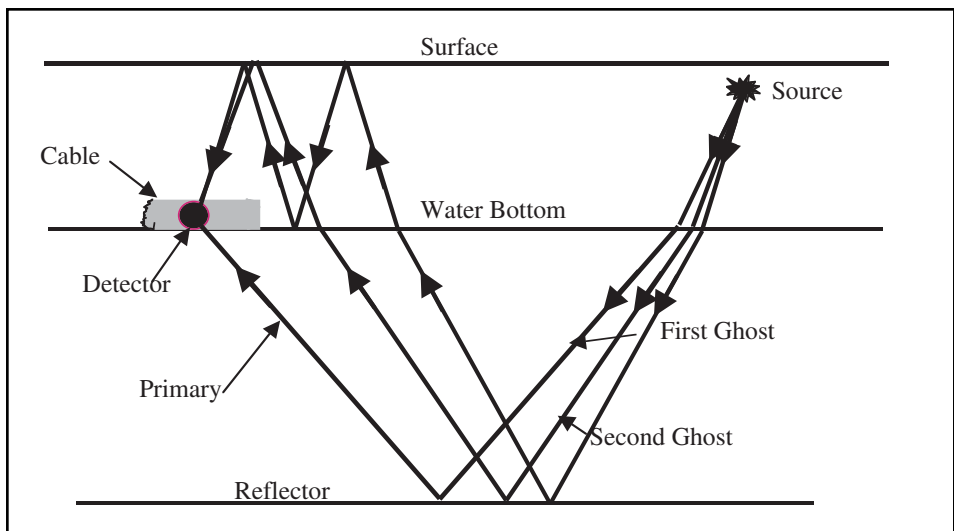


Fig. 6-35 Ray Paths of OBC Ghosts

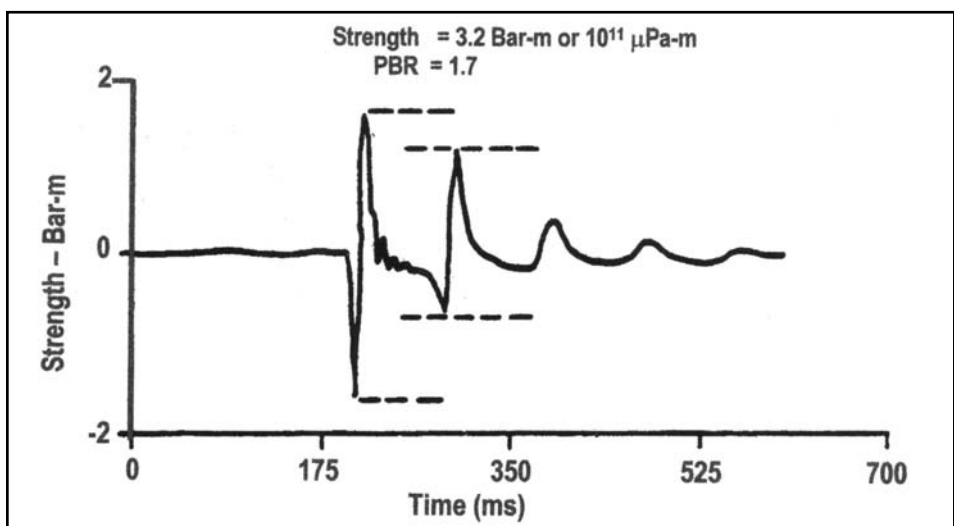


Fig. 6-36 OBC Primary Plus Ghosts

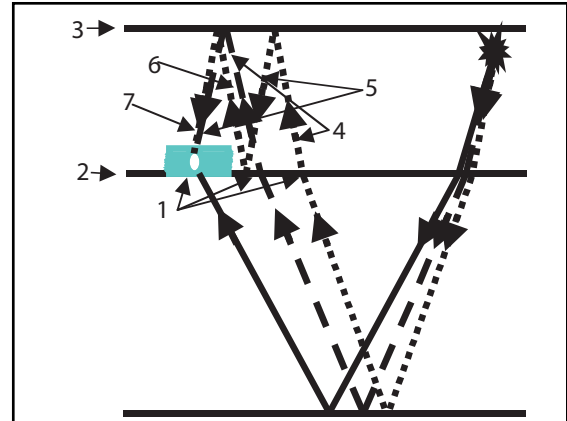


Fig. 6-37 Hydrophone Ghosting

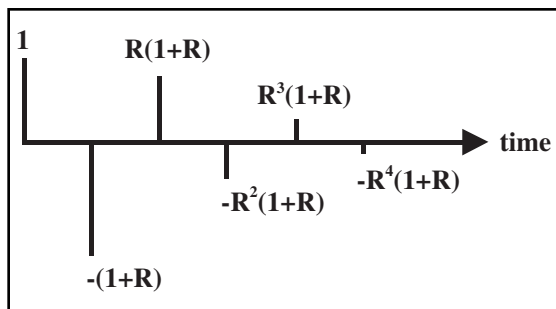


Fig. 6-38 Hydrophone Ghost Impulse Response

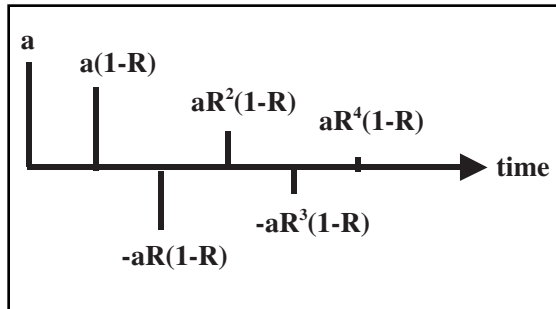


Fig. 6-40 Geophone Ghost Impulse Response

The effective wavelet for the hydrophone ghost is the convolution of the source wavelet with the hydrophone ghost impulse response, which is shown in Figure 6-38.

Outputs of geophones differ from those of hydrophones for two reasons:

- the polarity of hydrophone signals do not depend on the direction in which energy is incident on them but that of a geophone does
- the geophone sensitivity differs from that of the hydrophone

This means that the geophone ghost differs from the hydrophone ghost, as shown in Figures 6-39 and 6-40. The numbers in Figure 6-39 refer to the following explanations.

1. the amplitude incident on the water bottom after reflection (primary reflection amplitude) = 1
2. reflection coefficient of the water bottom = R
3. reflection coefficient of the surface = -1
4. the amplitude transmitted into the water from below = $1 - R$
5. the amplitude reflected downward at the water surface = $-(1 - R)$
6. the amplitude recorded by the geophone is $a(1-R)$ where a is the ratio between geophone and hydrophone sensitivity. The downward travel causes the change in signal polarity
7. the amplitude reflected up at the water bottom = $-R(1 + R)$
8. the amplitude reflected down at the water surface = $R(1 + R)$
9. the amplitude recorded by the geophone is $-a(1-R)$

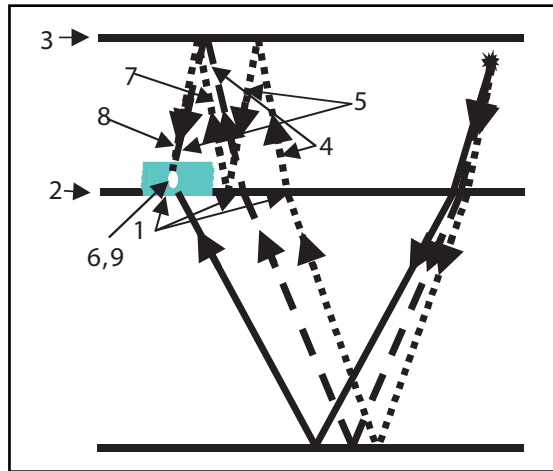


Fig. 6-39 Geophone Ghosting

Continued reflection at water bottom and surface result in the amplitude of successive ghosts being $-R$ times that of the previous ghost.

The effective wavelet for the hydrophone ghost is the convolution of the source wavelet with the hydrophone ghost impulse response that is shown in Figure 6-40.

The problem is to determine the scaling factor that will result in ghost cancellation when the scaled outputs are combined. The ratio of hydrophone ghost amplitude to geophone ghost amplitude is

$$\frac{(1+R)}{a(1-R)}$$

Since neither a nor R are known, some method of determining the proper scaling is needed. A frequently used method used is

1. do a common receiver sort
2. elect a window where both sensors have signal
3. balance the amplitudes in the windows of each sensor
4. guess at scale factor and apply to the geophone window
 - a. sum traces in the window
 - b. autocorrelate the summed traces
 - c. compute *varimax* over region where the side lobe due to ghost energy appears

The varimax is defined as follows:

Let $x_j, j = 1, 2, 3, \dots, N$ represent the digital samples of a trace, then

$$\text{Varimax} = \frac{x_1^4 + x_2^4 + x_3^4 + \dots + x_N^4}{(x_1^2 + x_2^2 + x_3^2 + \dots + x_N^2)^2} \quad (6.17)$$

5. increment the scale factor and go back to step four until the factor range is covered
6. select the scale factor that has the best varimax value
7. correct that factor for amplitude balance in step three
8. apply the corrected scale factor to the entire geophone gather and sum
9. repeat steps two through eight for each receiver gather
10. re-sort data to common shot gathers

Figure 6-41 illustrates the variation in the ratio $\frac{(1+R)}{(1-R)}$ across 360 receiver locations.

Dual sensor recording significantly reduces water column reverberations and the associated spectral ghost notches and increases the spectral bandwidth of the data.

Other methods of determining the appropriate scalars are based on different responses to S/N ratio and different responses to variation in water bottom reflection coefficient. Some people do not acknowledge reverberations at the source and use calibration shooting based on receiver ghosts only. Calibration shots are expensive to record.

Varimax scalars are very robust and work well for areas with small reflection coefficients at the water bottom. They are relatively insensitive to variations in signal-to-noise ratio.

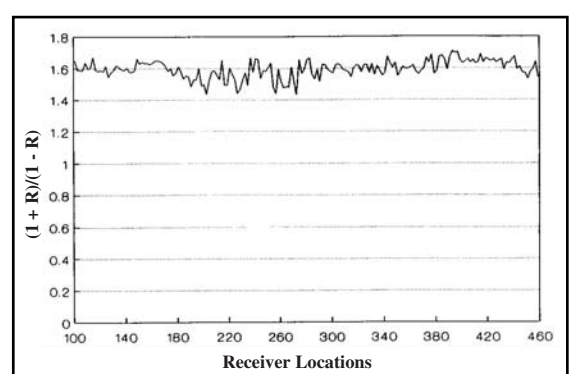


Fig. 6-41 A Plot of Scale Factor $(1+R)/(1-R)$ for 360 Receiver Locations

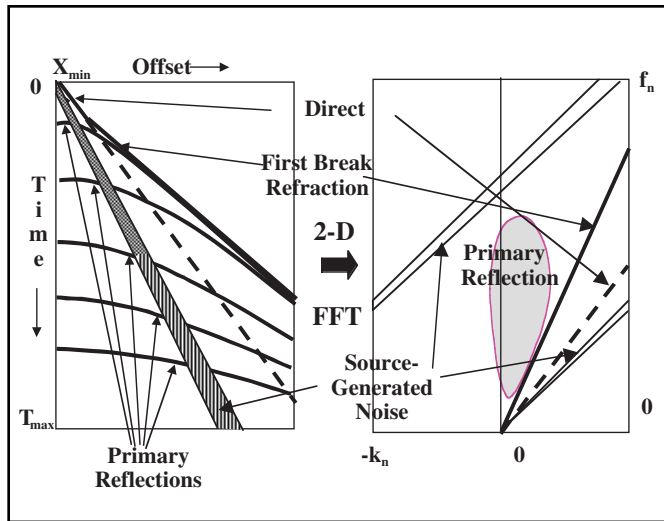


Fig. 6-42 Transformation from T-X to F-K Domain

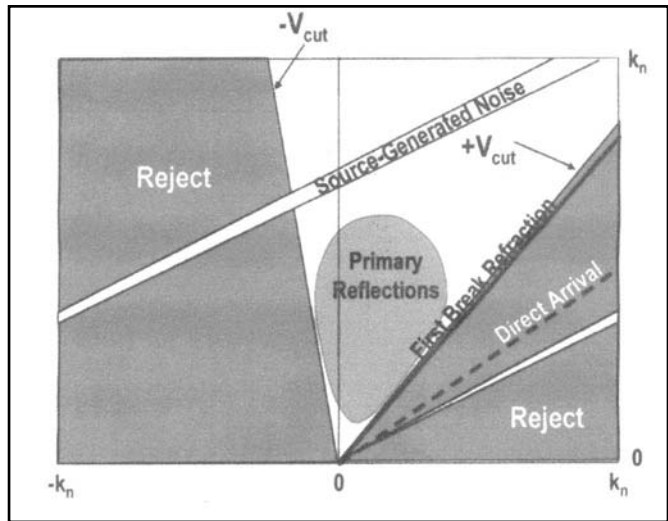


Fig. 6-43 Positive and Negative Cut Lines

Noise suppression

The position of noise suppression in the processing sequence is somewhat controversial. The controversy is over the order in which spiking deconvolution and noise suppression should be applied. The authors' opinion is that noise suppression should precede deconvolution in order that the source wavelet, which spiking deconvolution is to remove, can be more clearly seen and its inverse better designed. It is generally true that in deconvolution the noise amplitudes are often increased by the deconvolution filter, but the objectionable noise components can usually be removed by band pass filtering.

Velocity filtering. The objective of velocity filtering is to eliminate or, at least, significantly attenuate source-generated noise and other undesired linear events. The procedure for applying velocity filtering is as follows:

1. Transform field records from T-X to F-K domain, separating signal from noise on the basis of dip or apparent velocity differences (Fig. 6-42).
2. Define positive and negative velocity cut lines. Data between cut lines will be passed, and everything else will be rejected (Fig. 6-43).
3. Multiply data in the pass zone by 1 and in the reject zone by 0. Linearly increase multiplier from 0 to 1 in narrow ramp zones just outside the two cut lines (Fig. 6-44). Velocities are close to $+V_{cut}$ (Fig. 6-45).
4. Transform F-K domain back to T-X domain. The first-break refraction is still evident but attenuated. All other linear events are eliminated. Far offset part of early reflections may be partially attenuated because their velocities are close to $+V_{cut}$ (Fig. 6-45).

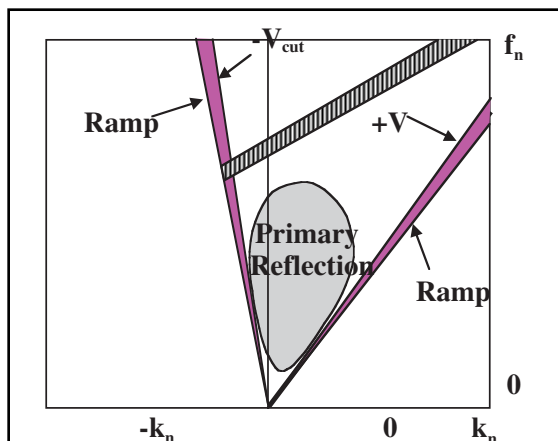


Fig. 6-44 Filtering in the F-K Plane

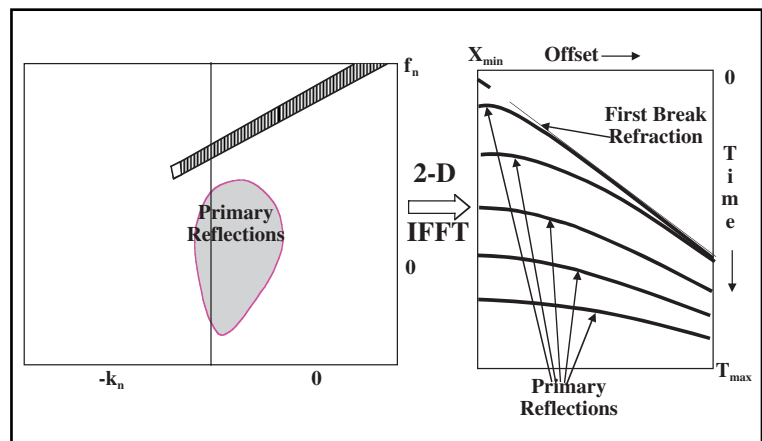


Fig. 6-45 Transformation of Filtered Record from F-K to T-X Domain

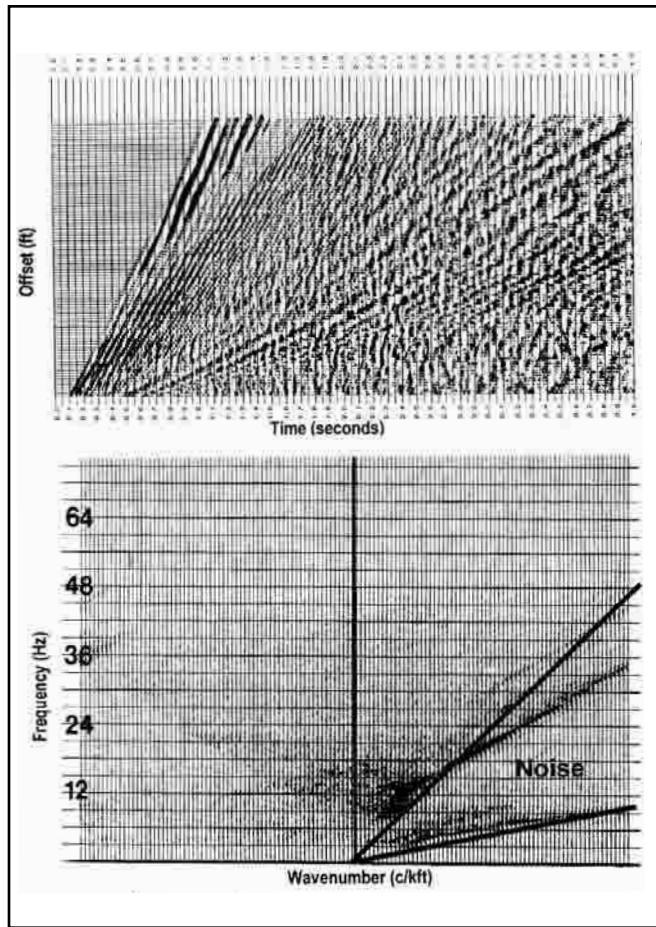


Fig. 6-46 Noise Record in the T-X Domain and the F-K Domain

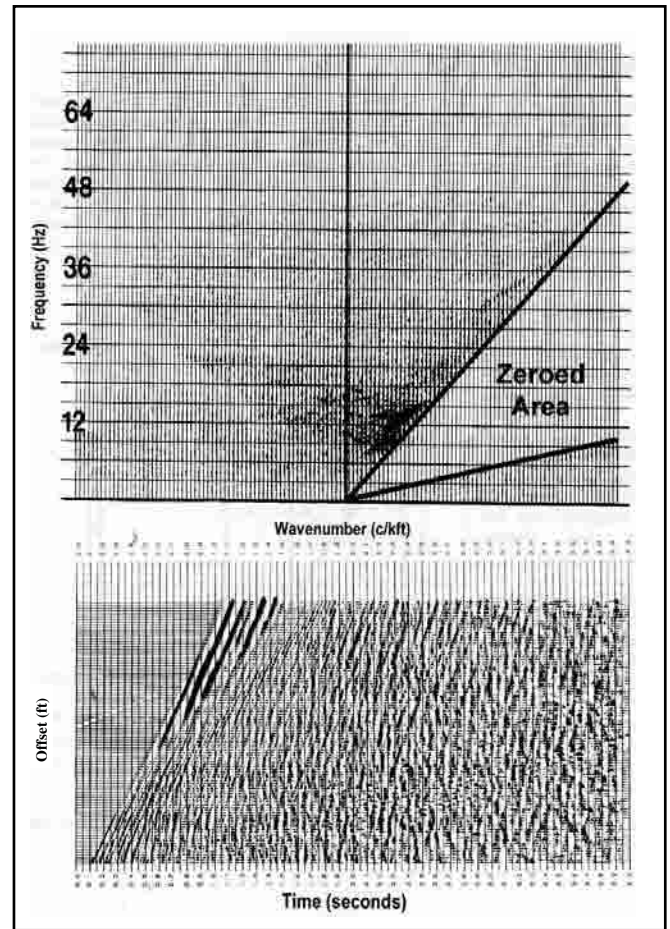


Fig. 6-47 Filtered Field Record in the F-K Domain and the T-X Domain

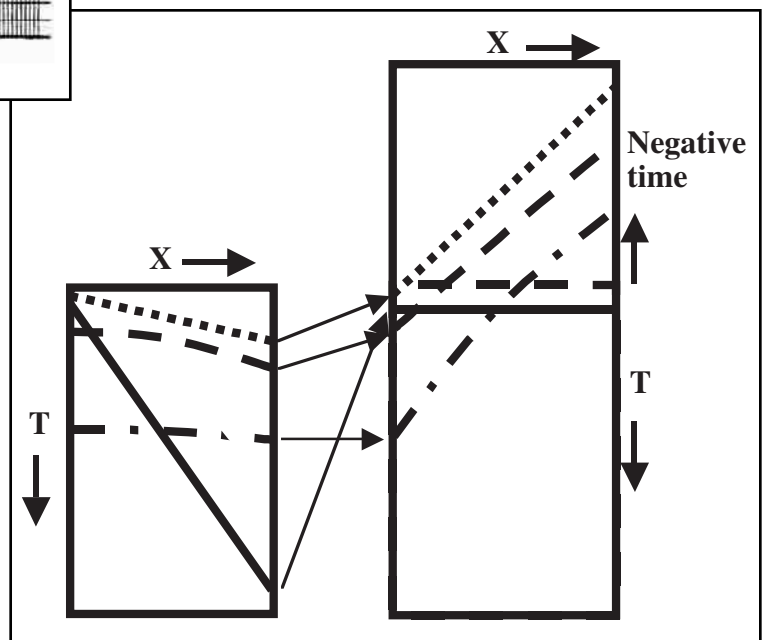


Fig. 6-48 Linear Moveout Applied to Linear Noise

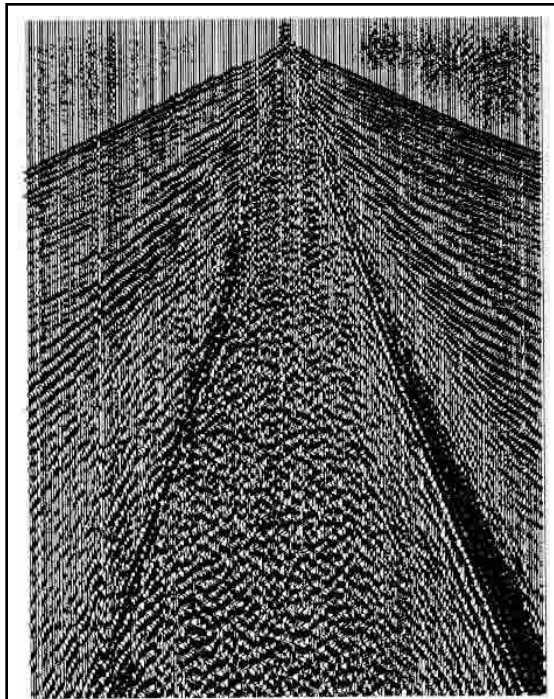


Fig. 6-49 Field Record Dominated by Linear Noise

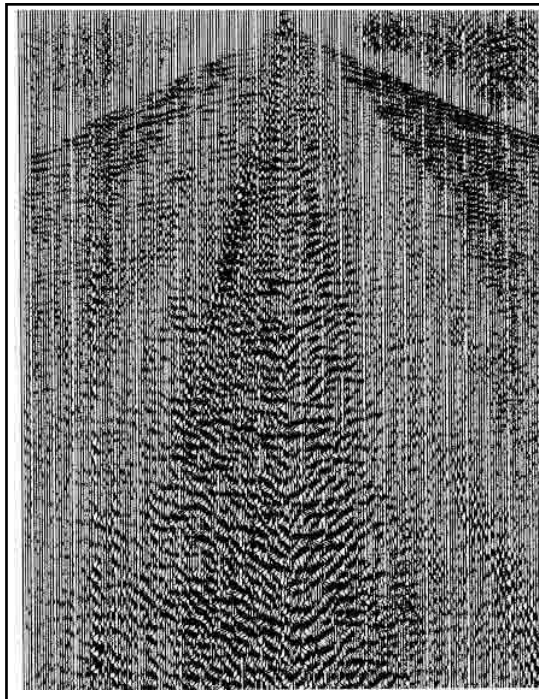


Fig. 6-50 Record of Fig. 6-49 after Six Passes of Linear Noise Attenuation

Figure 6-46 shows a noise record in both the T-X and F-K domains. In the F-K domain, lines are drawn that include the minimum and maximum noise velocities. These are used as the velocity cut lines for velocity filtering. The area inside these two lines is zeroed. Figure 6-47 shows the F-K domain after this is done and the inverse transform back into the T-X domain.

Linear noise attenuation. If noise is propagated with a constant velocity, it has linear moveout in the T-X domain. Applying a static shift equal to the offset divided by the velocity of the noise results in flattening the noise—occurs at the same time on all traces—but signal and other noise trains are not aligned. A simple time domain trace-to-trace filter can be applied by scaling then summing consecutive traces. For example, a three-trace filter is applied by multiplying the first and third traces in a set by -0.5 and the second by 1. The traces are then summed to output the trace at position two in the set. This is also called trace mixing. Note that negative record times need to be preserved in this operation because the time shifts applied are larger than moveout on first breaks and early reflections (Fig. 6-48).

For the method to be effective, noise amplitudes must be well balanced from trace to trace. Another problem is that signal must have sufficient negative moveout to prevent significant attenuation in the filtering process. This assumption is sometimes not adequately met, and signal does undergo significant attenuation.

Linear noise attenuation must be applied to every noise train that significantly interferes with signal. This may require a great many applications when noise trains at many different velocities are present.

Figure 6-49 is presented as an example of a record with many distinct noise trains. Noise propagating at 500 m/s, 666 m/s, 1000 m/s, 1500 m/s, 2100 m/s, and 2800 m/s can be identified. The combination of many noise trains with high amplitudes causes signal to be almost totally obscured.

Figure 6-50 shows the same record after the linear noise process has been applied for all six noise velocities.

Velocity analysis

Seismic velocity means, in general, the rate of seismic wave propagation—distance/time. It is usually measured in meters per second or feet per second. The term velocity rarely occurs alone in seismic exploration because there are so many *kinds* of seismic velocities, such as instantaneous velocity, interval velocity, average velocity, rms velocity, NMO velocity, stacking velocity, migration velocity, and apparent velocity.

Instantaneous velocity is the velocity at which a seismic wave propagates at a point within a medium. It varies with wave type or propagation mode. P-wave velocity V_p is always the fastest. S-wave velocity V_s is the second fastest. The ratio VP/VS is greater than or equal to $\sqrt{2}$. Rayleigh wave velocity is usually about 92% of S-wave velocity and Love wave velocity is slightly slower than Rayleigh wave velocity. Instantaneous velocity also depends on rock type, age, depth of burial, porosity, pore shape, pore fluid, confining pressure, and other elements.

The closest thing to instantaneous velocity measurement is the sonic log or *continuous velocity log* (CVL). This is done in a borehole using a special tool.

Interval velocity V_i is the average propagation velocity through a depth or time interval, and it equals the thickness of the depth interval divided by vertical time through the interval. Figure 6-51 shows a well log on the left and determination of interval velocity from the log on the right. It can be seen on the log that there are definite velocity trends. That is, over certain depth intervals, velocity tends to be about the same, and between these depth intervals velocity changes abruptly. Denote these depth intervals by Δz_i , $i = 1, 2, \dots, N$. The direct measurement by the CVL is μ s/ft. Summing these times over the indicated depth intervals gives the times Δt_i , $i = 1, 2, \dots, N$. Interval velocities are obtained from:

$$V_1 = \frac{\Delta z_1}{\Delta t_1} \quad (6.18)$$

Average velocity \bar{V} is total depth to a reflector Z_r divided by time to the reflector or twice the depth to the reflector divided by two-way, zero-offset reflection time T_i .

$$\bar{V} = \frac{2Z_r}{T_i} \quad (6.19)$$

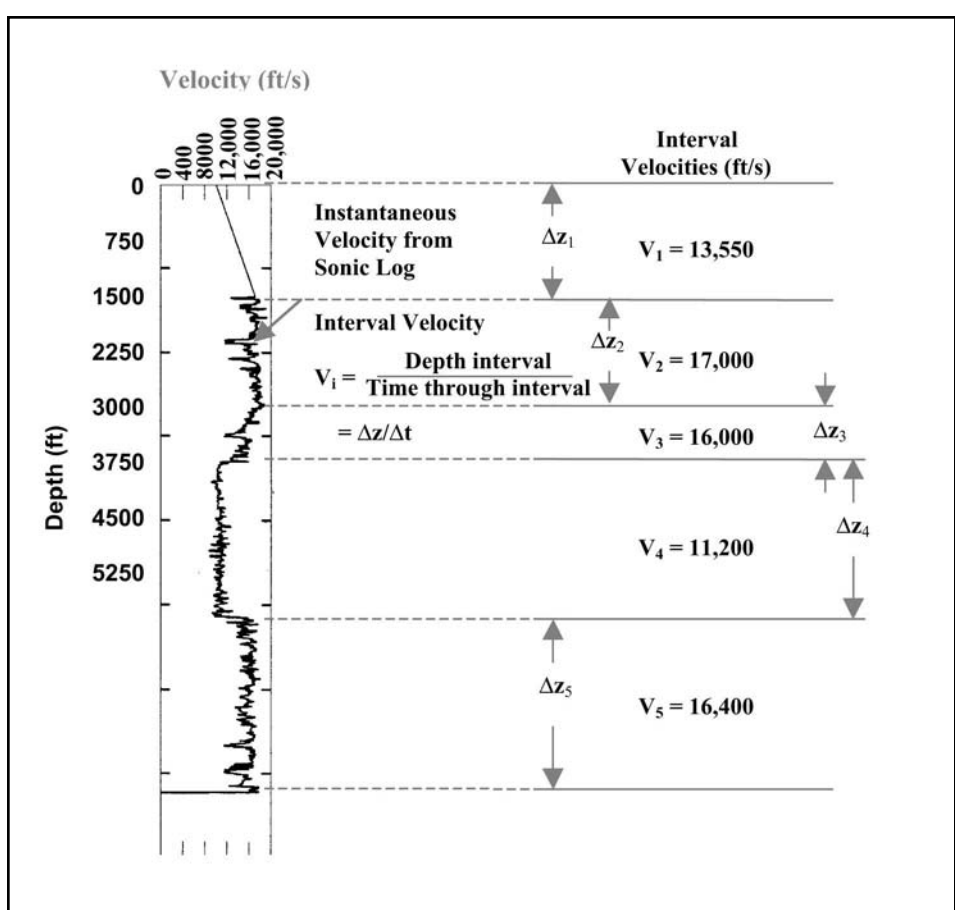


Fig. 6-51 Instantaneous and Interval Velocities

Average velocity can be calculated from interval velocities using:

$$\bar{V}_n = \frac{\sum_{i=1}^n V_i \Delta t_i}{\sum_{i=1}^n \Delta t_i} \quad (6.20)$$

Root mean square velocity \tilde{V} is the square root of the average squared velocity and is calculated from:

$$\tilde{V}_n = \sqrt{\frac{\sum_{i=1}^n V_i^2 \Delta t_i}{\sum_{i=1}^n \Delta t_i}} \quad (6.21)$$

NMO velocity is the velocity used to correct for NMO—to make primary reflections on CMP gather records occur at the same time on all traces. For plane horizontal or gently dipping layers, NMO velocity is equal to the RMS velocity.

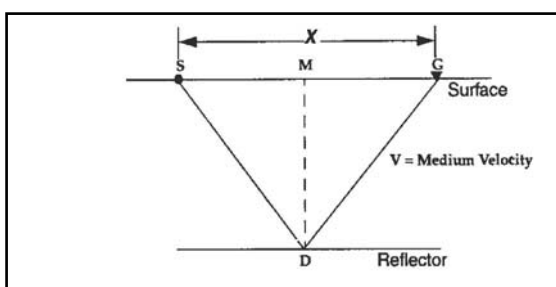
Stacking velocity is the velocity that gives the optimum CMP stack output when used for NMO corrections.

Migration velocity is the velocity that optimizes the output of a migration algorithm—repositioning of the reflected energy to the correct locations.

Apparent velocity is the velocity at which seismic waves appear to propagate along the surface of the earth.

Velocities of most concern, usually, are stacking velocity, migration velocity, and average velocity—used to convert from time to depth. Sonic logs, when available, give direct measures of interval velocities from which the desired velocities can sometimes be calculated but this can only be done where wells exist and must be interpolated between wells or extrapolated beyond wells. Sonic logs measure vertical velocity that, because of anisotropy, may differ from horizontal velocity and also uses higher frequency signals than surface seismic surveys that may give different velocities

Normal moveout. In most cases, it is necessary to determine the required velocities from the data that are to be processed. In one way or another, this is done from measurements of *moveout*—the change in reflection time across a set of CMP traces. In general moveout is the algebraic sum of NMO and geologic dip.



6-52 Single Horizontal Layer

NMO is the extra time required for energy to travel from a seismic energy source to a seismic receiver group at some distance from the source via reflection from a subsurface reflector. This is illustrated in Figure 6-52.

In Figure 6-52 the source is at *S* and the receiver is at *G*. Since the reflector is horizontal and the velocity *V* is constant, reflection occurs at point *D*, vertically below *M*, the midpoint between *S* and *G*. The time from *S* to *D* to *G* is:

$$t_x = \frac{(SD + DG)}{V}$$

The time from *M* to *D* and back to *M* (zero-offset time) is:

$$t_0 = \frac{2MD}{V}$$

From the above, $SD = DG = \frac{Vt_x}{2}$ and $MD = \frac{Vt_0}{2}$. Applying the Pythagorean theorem yields:

$$\left[\frac{V_{NMO}t_x}{2} \right]^2 = \left(\frac{x}{2} \right)^2 + \left[\frac{V_{NMO}t_0}{2} \right]^2 \quad (6.22)$$

Solving Equation 6.22 for t_x :

$$t_x = \sqrt{\left[\frac{x}{V_{NMO}} \right]^2 + [t_0]^2} \quad (6.23)$$

NMO DtNMO is the difference between the zero offset time t_0 and the reflection time t_x .

$$\Delta t_{NMO} = t_x - t_0 = t_0 \left\{ \sqrt{\left[\frac{x}{V_{NMO}t_0} \right]^2 + 1} - 1 \right\} \quad (6.24)$$

It can be seen from Equation (6.24) that Δt_{NMO} increases as offset x increases and decreases as V_{NMO} and/or t_0 increase. This is also shown in Table 6-1. Equation 6.22 is actually the equation of a hyperbola, and Figure 6-53 shows that reflection events have hyperbolic shapes.

Table 6-1 Variation of DtNMO with Time, Velocity, and Offset

Time (s)	Velocity (m/s)	Δt_{NMO} for offset $x =$	
		1000 m	2000 m
0.25	2000	0.309	0.780
0.5	3500	0.140	0.443
1.0	3000	0.054	0.201
2.0	3500	0.020	0.080
4.0	4000	0.008	0.031

to zero offset. The time for each sample is set equal to T_0 , and T_x is calculated for a given offset for that trace and velocity for that time. The sample value at the calculated T_x is moved up to T_0 by subtracting Δt_{NMO} . See Figure 6-54.

Figure 6-55 gives a more detailed picture of the NMO correction process for a particular trace for an offset x . On the left is shown that the NMO velocity is different for each sample. It actually increases with time. In the center is a table representing sample amplitudes versus sample time on the input, shot-organized record before NMO. On the right is shown the sample values that have been shifted up in time. In the figure, Δt_{NMO} = integral multiples of sample period Δt .

Note that Figure 6-55 assumes that the NMO corrections are integral multiples of the sample period. When this is not the case (the usual situation), there is no valid sample amplitude to shift. The solution is to interpolate between known values using an interpolation filter. This is shown in Figure 6-56, where Δt_{NMO} = nonintegral multiples of sample period Δt .

Reflection events will be *flattened*—arrive at same time on all

NMO correction is usually done trace by trace. Each sample is mapped from a particular trace offset

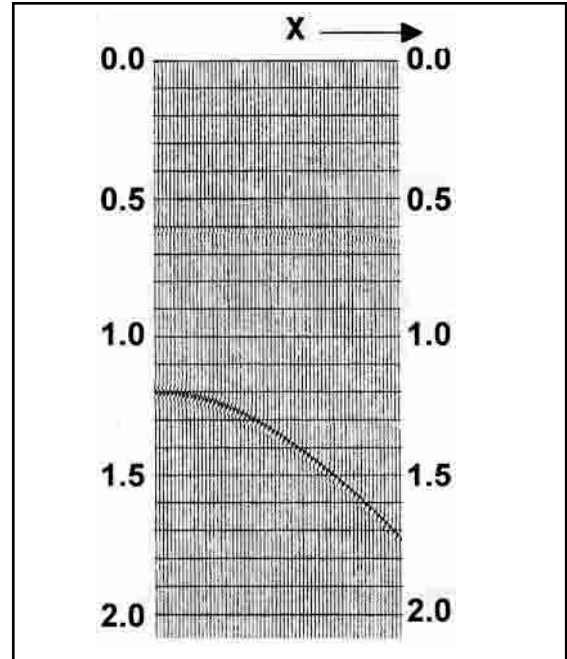


Fig. 6-53 Reflection with Normal Moveout

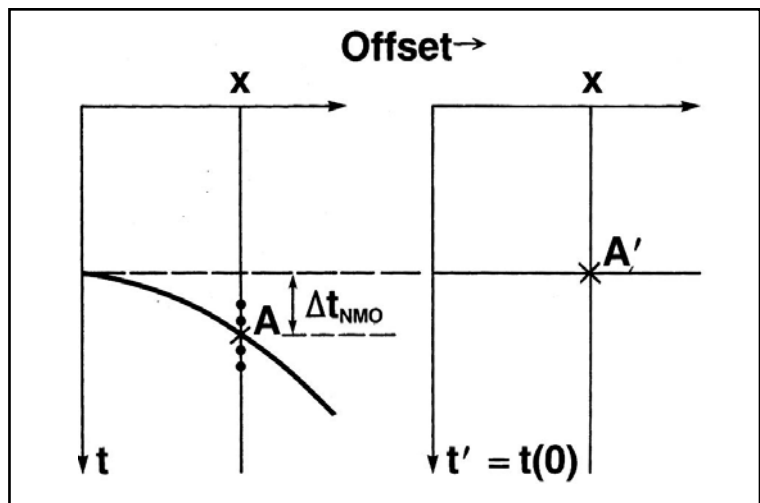


Fig. 6-54 NMO Correction

Offset = x		Before NMO		After NMO	
Time = t(0)	Velocity	Time = t(0)	Amplitude	Time = t(0)	Amplitude
0	V(0)	⋮	⋮	⋮	⋮
ΔT	V(ΔT)	⋮	⋮	⋮	⋮
2ΔT	V(2ΔT)	nΔT	A(nΔT)	nΔT	A[(n+k)ΔT]
3ΔT	V(3ΔT)	⋮	⋮	⋮	⋮
⋮	⋮	⋮	⋮	⋮	⋮
nΔT	V(nΔT)	(n+k)ΔT	A[(n+k)ΔT]	(n+k)ΔT	A[(n+p)ΔT]
⋮	⋮	⋮	⋮	⋮	⋮
(n+p)ΔT	A[(n+p)ΔT]	⋮	⋮	⋮	⋮
⋮	⋮	⋮	⋮	⋮	⋮

n, k and p are integers

Fig. 6-55 The NMO Correction Process

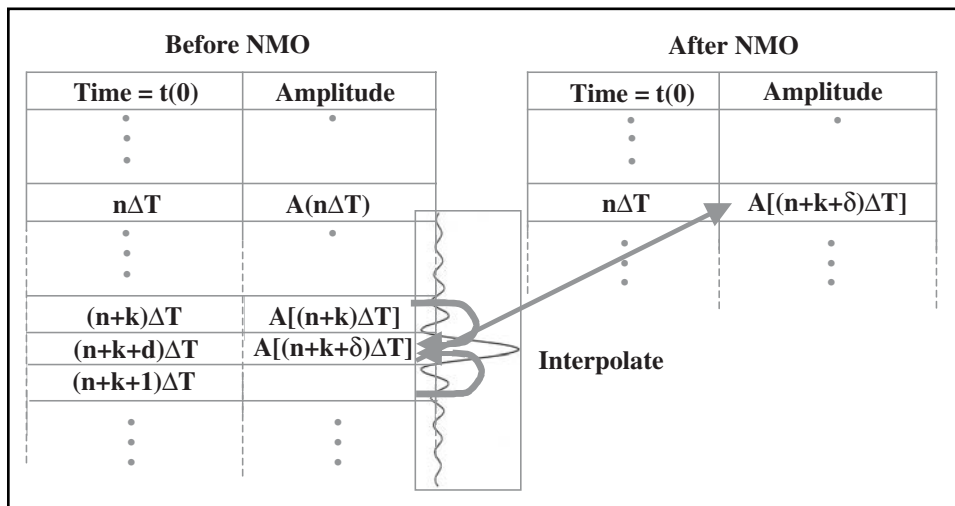


Fig. 6-56 The NMO Correction Process

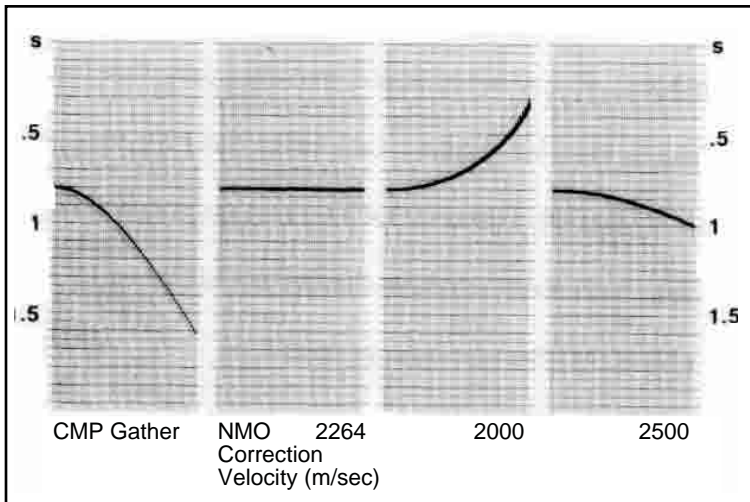


Fig. 6-57 Effect of Velocity on NMO Correction

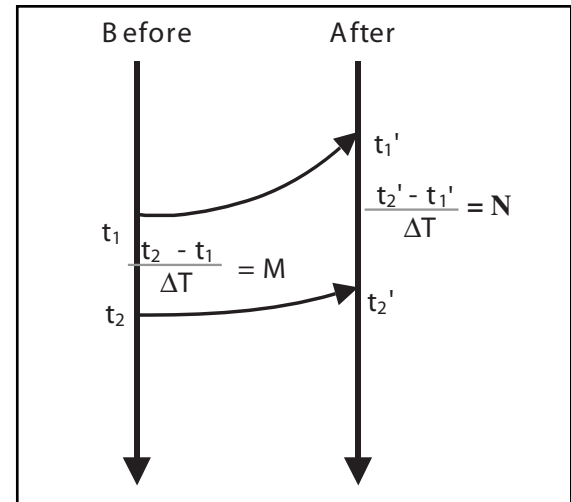


Fig. 6-58 NMO Stretch

traces of a CMP record—only if the correct NMO velocity is used. The effect of using incorrect velocities is shown in Figure 6-57. On the left of the figure is the input gather record indicated by a single hyperbolic event. Using the correct velocity of $V_{NMO} = 2264$ m/s results in a flat event. Using a velocity of 2000 m/s—slower than V_{NMO} —results in the event being *overcorrected*. The correction exceeds NMO and the event curves upward. Using a velocity of 2500 m/s—faster than V_{NMO} —the event is *under-corrected*. Not all of the NMO has been removed.

NMO correction is done sample by sample. Each sample time is used as t_0 in the NMO equation and the velocity at that time used for V_{NMO} . As previously noted, V_{NMO} increases as t_0 increases. As a result, NMO corrections decrease as t_0 and V_{NMO} increase. Thus, the mapping process places output samples farther apart than they were on the input, causing an apparent increase in wavelet duration or decrease in frequency. This effect, called *NMO stretch*, is greatest at early times and long offsets.

Figure 6-58 demonstrates this. Before the NMO corrections are applied, there are M samples at a sample interval ΔT , between times of t_1 and t_2 . The sample at time t_1 maps into t_1' and time t_2 maps into t_2' . Between a time of t_1' and t_2' , there are N samples at a sample interval ΔT . The amount of stretch is indicated by the increase in the number of samples N compared to the original M samples. Data are muted (zeroed) at times and offsets where the stretch exceeds the maximum allowable. The allowed stretch is some-times measured by the ratio $N:M$. In which case, a maximum ratio of 2:1 is the usual default value.

Mute schedules are specified by input of time-offset pairs. Mute times between time-offset pairs are determined by linear interpolation. Data earlier than mute times are zeroed. Note, also that the mutes are applied with a ramp so that trace amplitudes do not change abruptly from zero to some large value. Such abrupt amplitude changes are interpreted as “spikes” and can have unwanted effects when some other processes are applied.

Mute times should be picked by inspection rather than using a default. Figures 6-59 and 6-60 show why this is so. Figure 6-59 shows three CMPs as they appear on input, after NMO correction (note the heavy distortion at early times and near offsets caused by NMO stretch), and after default NMO mutes are applied. Figure 6-60a shows the center NMO-corrected record of Figure 6-59. Figure 6-60b is the stack of the two near traces of the original gather record. The dotted line is the hand-picked mute schedule. Figure 6-60c is the full-fold stack obtained from the original gather with a poor mute choice based on picks from the original gather. The mutes in Figure 6-60b are preferred over those in Figure 6-60c because more data are preserved. Muting is necessary to remove data overly distorted

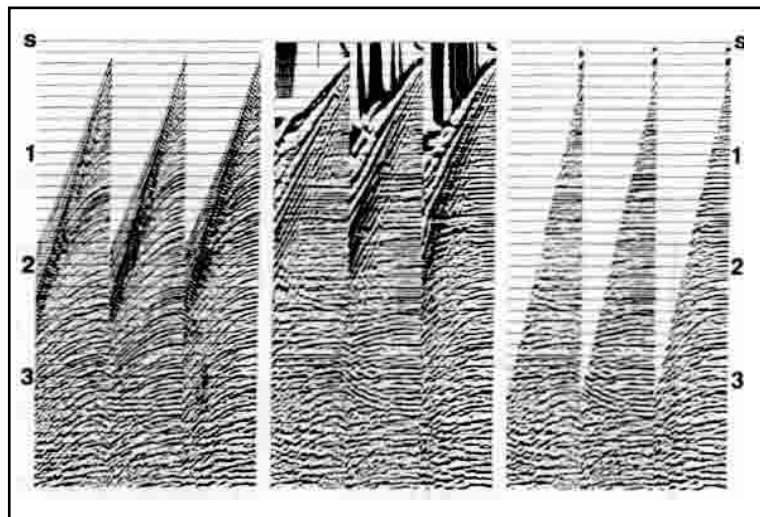


Fig. 6-59 Input CMP Records, the Same Records after NMO Correction, and after NMO Mute

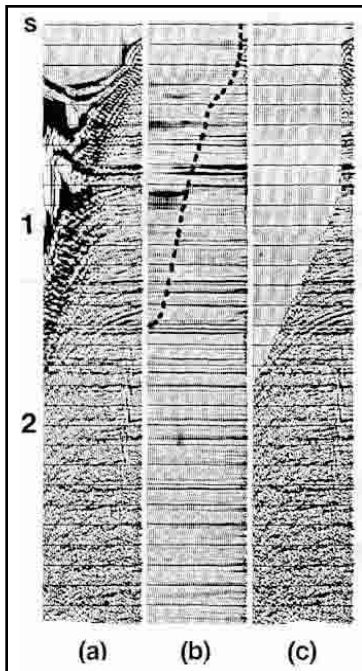


Fig. 6-60 Picked Versus Default Mutes

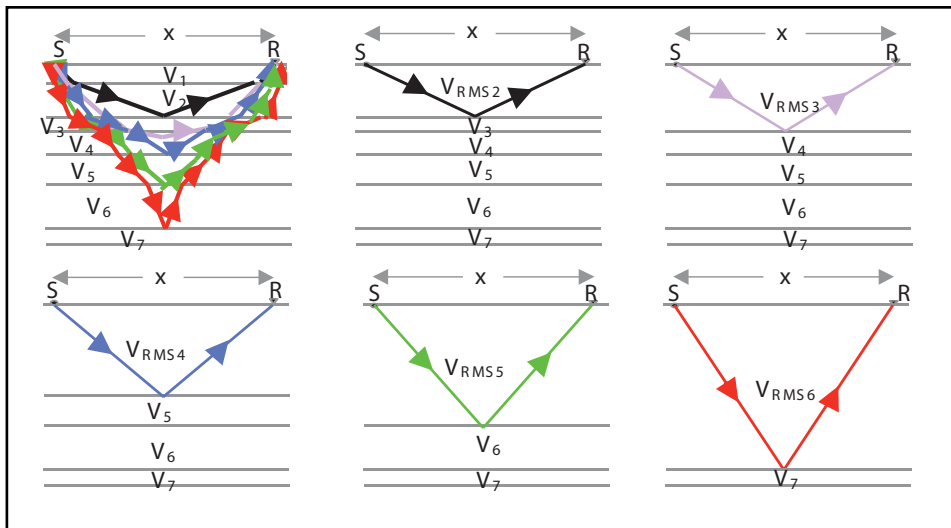


Fig. 6-61 RMS Velocity as the Replacement Velocity in the Multi-layer Situation

by NMO correction, but, it must be remembered, muting also reduces fold at early record times. The choice of mutes is, thus, a compromise between optimizing fold and minimizing the effect of distortion caused by NMO correction.

The NMO equations, Equations 6.21 and 6.22, assume a constant velocity and a horizontal reflector. This is not the situation encountered in seismic exploration. Instead, there are multiple layers with different velocities. The solution is to "scrape off" the layers one at a time and replace these layers with a single layer and a constant velocity. If the reflectors are flat or gently dipping, then the RMS velocity can be used.

Figure 6-61 illustrates this approach to NMO correction. The top left drawing shows ray paths for reflections from the bottoms of layers two through six. For a reflection from layer one, velocity V_1 is used for NMO correction. For a reflection from the base of layer two, layers one and two are replaced by a single layer with the RMS velocity V_{RMS2} . The remaining drawings in Figure 6-61 show how the pattern continues for subsequent reflections. For NMO calculation purposes, all layers above the reflecting interfaces are replaced by a single layer having the appropriate RMS velocity.

The use of the RMS velocity is subject to some restrictions:

- reflecting interfaces must be horizontal or gently dipping
- trace offset must be less than or equal to reflector depth

Figure 6-62 shows the effect of offset on the applicability of RMS velocity to NMO calculation by comparing NMO obtained from the earth model and by use of RMS velocity in equation (6.21). Note that the errors between model times and NMO times calculated by using V_{RMS} are no more than 1 ms when the offset x is less than reflector depth Z . Even at an offset of 11,000 ft and depth of 5500 ft, $x = 2Z$, the error is only 0.014 s, which is less than 1%.

Earth Model		$Z = 5500$ ft		$Z=8875$ ft	
$V_1 = 6000$ ft/s	$Z_1 = 1500$ ft	Offset (ft)	T_{model}	T_{VRMS}	T_{model}
		0	1.300	1.300	2.050
		1000	1.305	1.305	2.053
		3000	1.345	1.345	2.078
		5000	1.421	1.422	2.127
		7000	1.527	1.530	2.198
		9000	1.655	1.663	2.290
$V_2 = 10,000$ ft/s $Z_2 = 4000$ ft		11,000	1.801	1.815	2.398
$V_3 = 9000$ ft/s	$Z_3 = 3375$ ft				2.401

Fig. 6-62 NMO for Plane, Horizontal, and Iso-Velocity Layers

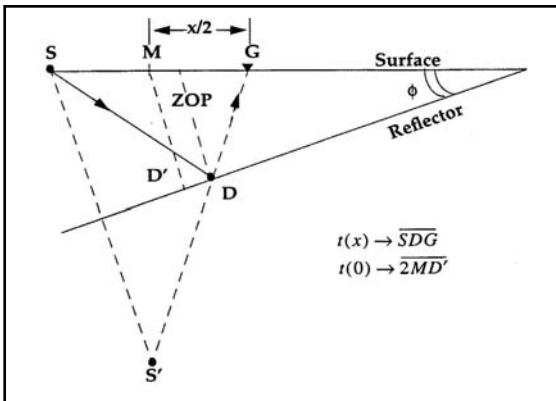


Fig. 6-63 Reflection from a Dipping Reflector

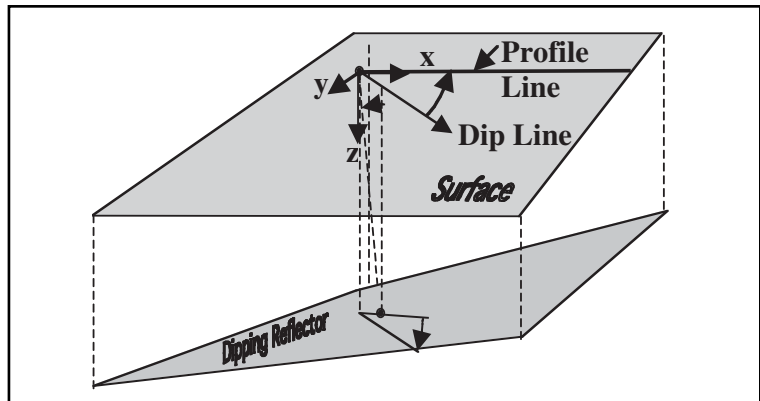


Fig. 6-64 A Dipping Reflector in 3-D

Of greater interest to petroleum exploration are dipping layers. Figure 6-63 shows a single layer with the reflector dipping at angle ϕ . The reflection ray path from source S to receiver G reflects at point D on the dipping reflector. The midpoint between source and receiver is at M but a line from M perpendicular to the reflector intersects the reflector at D' not D . Thus for the dipping case, the midpoint is not the zero offset position (ZOP) for the reflection.

In Figure 6-63, S' is the image point of the source S . From triangle SGS' :

$$V^2 t_x^2 = V^2 t_0^2 + x^2 \cos^2 \phi$$

Dividing by V^2 gives:

$$\begin{aligned} t_x^2 &= t_0^2 + \frac{x^2 \cos^2 \phi}{V^2} \\ &= t_0^2 + \frac{x^2}{(V/\cos\phi)^2} = t_0^2 + \frac{x^2}{V_{DIP}^2} \end{aligned} \quad (6.25)$$

where

$$V_{DIP} = \frac{V}{\cos\phi}$$

For CMP gathers with a dipping reflector, the velocity needed to correct for NMO is always greater than the RMS velocity or that used for flat reflectors. Also, as dip increases, the velocity required to flatten data increases and the amount of NMO decreases. Dip decreases travel time from source to receiver because of the shorter path from source to receiver.

In 3-D operations, the azimuth between source and receiver must also be considered. Figure 6-64 shows a reflector dipping at angle ϕ , but the receiver line is at an angle ϕ' —the azimuth—from the dip direction. In this situation:

$$V_{MNO} = \frac{V}{\sqrt{1 - \sin^2\phi + \cos^2\theta}} \quad (6.26a)$$

or

$$V_{MNO} = \frac{V}{\cos\phi'} \quad (6.26b)$$

where

$$\cos \phi' = \sqrt{1 - \sin^2\phi + \cos^2\theta}$$

Table 6–2 NMO Velocities

Model	NMO Velocity
Single horizontal layer	Layer Velocity
Horizontally stratified	RMS velocity if small spread layers assumption is valid
Single dipping layer	Layer velocity/ $\cos(\text{dip angle})$
Multi-layered with arbitrary dips	RMS velocity if small spread and small dip assumptions are valid

If shooting is along the on dip azimuth, then $\theta = 0^\circ$, and apparent dip equals true dip. If shooting is in the strike direction azimuth, then $\theta = 90^\circ$, and apparent dip equals 0° . That is, the reflector appears to be flat with no dip! At intermediate azimuths, the apparent dip is less than true dip.

Stacking velocities do not tie at line intersections for dipping reflectors. This is because the lines are shot at different azimuths, causing differences in apparent dip angle and, hence, different velocities and different NMO calculations.

Table 6–2 summarizes the choices of NMO velocity for various subsurface situations. With regard to Table 6–2, the small-spread assumption is that offset is less than reflector depth. The small-dip assumption is that dip angles are less than 10° .

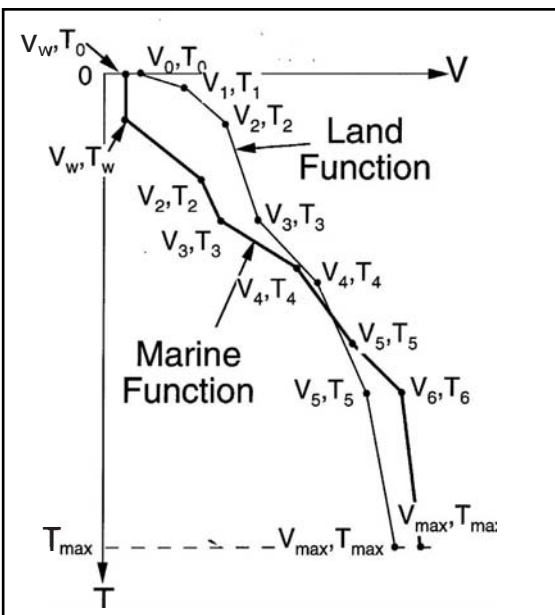
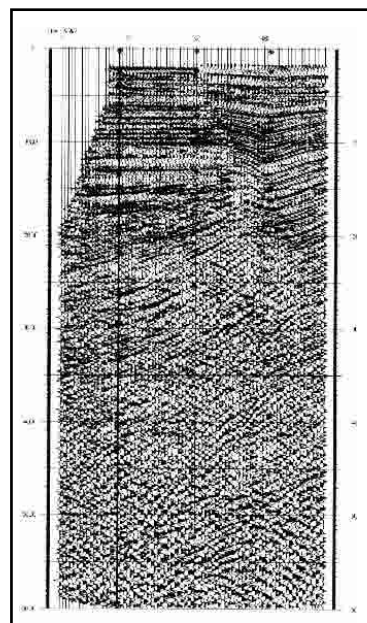
Velocity analysis techniques. The purpose of velocity analysis is to determine stacking velocity, called *velocity functions* and seen in Figure 6–65, that, when used to implement NMO corrections, yield the optimum stack. In general, approaches to this problem include the following:

- time-velocity space restricted to velocity values that can be reasonably expected
- NMO correction evaluated statistically, using small time gates and many estimates of stacking velocity
- both time and velocity adequately sampled
- results of velocity calculations displayed in forms that allow accurate velocity interpretation

The initial result of velocity analysis is a set of velocity functions determined at specific points within the survey. Velocity functions are sets of time and velocity pairs that define velocities for every sample in the CMP traces. Interpolation between and extrapolation from these functions yields a *velocity field* that defines a velocity for every sample in the data volume.

Velocity analysis requires the following:

- selection of velocity analysis locations
- this is often done by regular sampling (such as every 20th CMP) of every seismic line
- locations should be chosen to comprehend structural variation in areas of greater structural variation—Figure 6–66 shows a portion of a seismic section and the CMP selected for the velocity analysis example that follows
- determination of the velocity sweep, which is defined by a low velocity trend and a high velocity trend that depends on the area as seen in Figure 6–67
- a constant velocity stack (CVS) display is sometimes used to generate the velocity trend. (*Constant velocity stack* is a process in which a set of constant velocities, equally incremented between the lowest and highest velocities expected, is used to apply NMO corrections and then stack the CMPs.) In Figure 6–70, the open diamonds indicate picks made for the trend function
- a velocity fan consisting of this trend function plus three to five slower and three to five faster functions may also be generated

**Fig. 6–65 Velocity Functions****Fig. 6–66 Velocity Analysis Location Used for Example**

- within the velocity sweep, a total of 40 to 60 velocities are used to calculate and apply NMO corrections. Seven to 11 CMPs (center CMP plus 3 to 5 on either side) are used in each analysis
- selection of time gate width
- time gates should contain at least four to five samples
- they usually overlap
- choice of statistical parameter used to determine the velocities that provide the best stack
- *semblance* is frequently used for this purpose. Semblance is determined by dividing the square of summed stack amplitudes by total gate power. Semblances that are plotted in velocity displays are often smoothed in time and velocity

Figure 6–68 is a semblance plot in gray scale—the darker the gray, the higher the semblance value. The central velocity trend is shown as a heavy broken line, and the four lower and higher velocities are on each side. Figure 6–69 shows the stack of CMPs used in this analysis for each of the nine velocity functions of Figure 6–68.

Figure 6–70 is a CVS display used to generate the velocity trend for the IVP session. In CVS, NMO corrections are made using a single constant velocity at all times for each trace in the CMP, then stacked together. Stack response is the criterion for velocity picks. The open diamonds indicate picks made for the trend function

Usually, velocity analysis and interpretation are done interactively. Primary interpretation is based on the semblance display but other displays such as the center CMP before and after NMO correction can be viewed to confirm picks of velocity and time pairs. Figures 6–71 through 6–76 illustrate interactive velocity processing.

Figure 6–71 is the semblance plot generated from the input velocity fan. The white circles are the picks (time and velocity pairs) selected from the CVS display. The event at 1729 ms (indicated by the white arrow) is used to demonstrate the effect of interactive velocity picks.

Shown at the left in Figure 6–72 is CMP 61 corrected for NMO using the velocity function shown in white on the semblance plot. The right display is a stack panel with CMP 61 at the center. It can be seen that the event at about 1729 ms—see black double arrow—has a doubled appearance.

Figure 6–73 is the semblance plot with a slower velocity picked for the event at 1729 ms, as indicated by the white arrow. Figure 6–74 is the same as Figure 6–72 except that CMP 61 corrected for NMO using the modified velocity function (too slow at 1729 ms) shown in white on the semblance plot of Figure 6–73. The stack panel with CMP 61 at the center shows the event at about 1729 ms—see black double arrow—has lost its doubled appearance.

Figure 6–75 is the semblance plot with a faster velocity picked for the event at 1729 ms, as indicated by the white arrow. Figure 6–76 shows CMP 61 corrected for NMO using the second modified velocity function (too fast at 1729 ms) shown in white on the semblance plot of Figure 6–75. The stack panel with CMP 61 at the center shows the event at about 1729 ms—see the black double arrow—has, again, lost its doubled appearance.

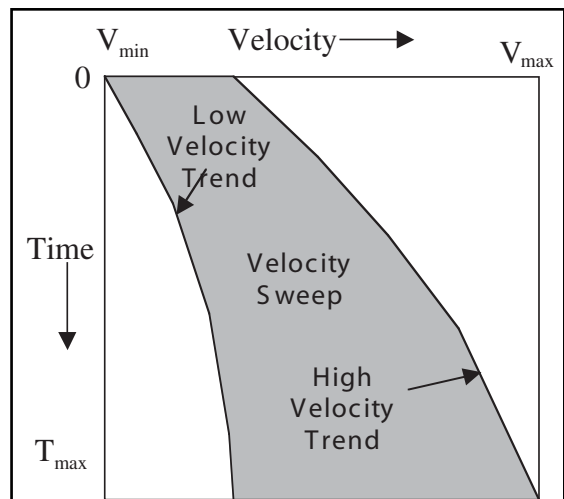


Fig. 6–67 The Velocity Sweep

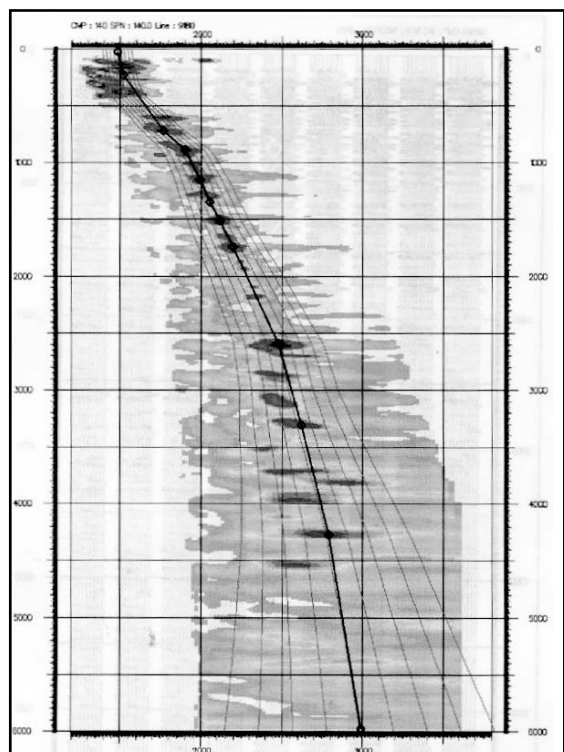


Fig. 6–68 Semblance Plot

The stack panel with CMP 61 at the center shows the event at about 1729 ms—see black double arrow—has lost its doubled appearance.

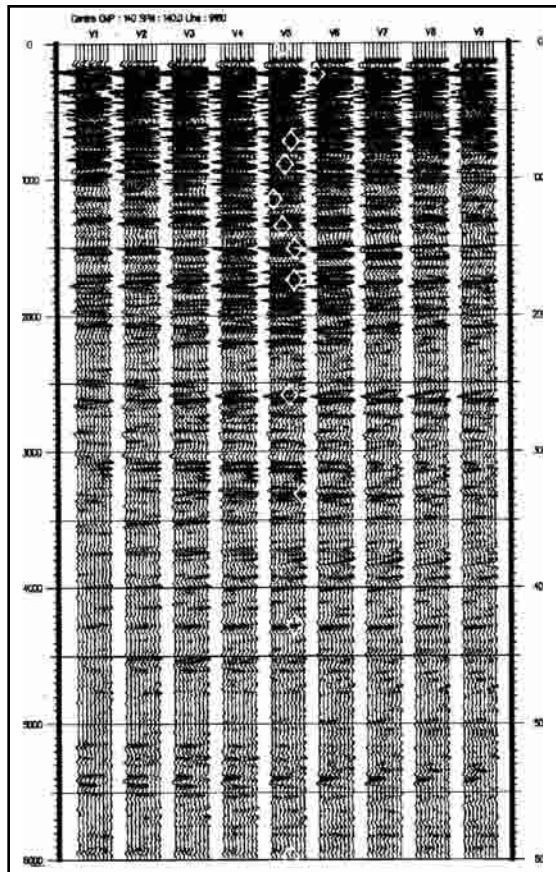


Fig. 6-69 Stack of CMPs Using the Nine Velocity Functions of Figure 6-68

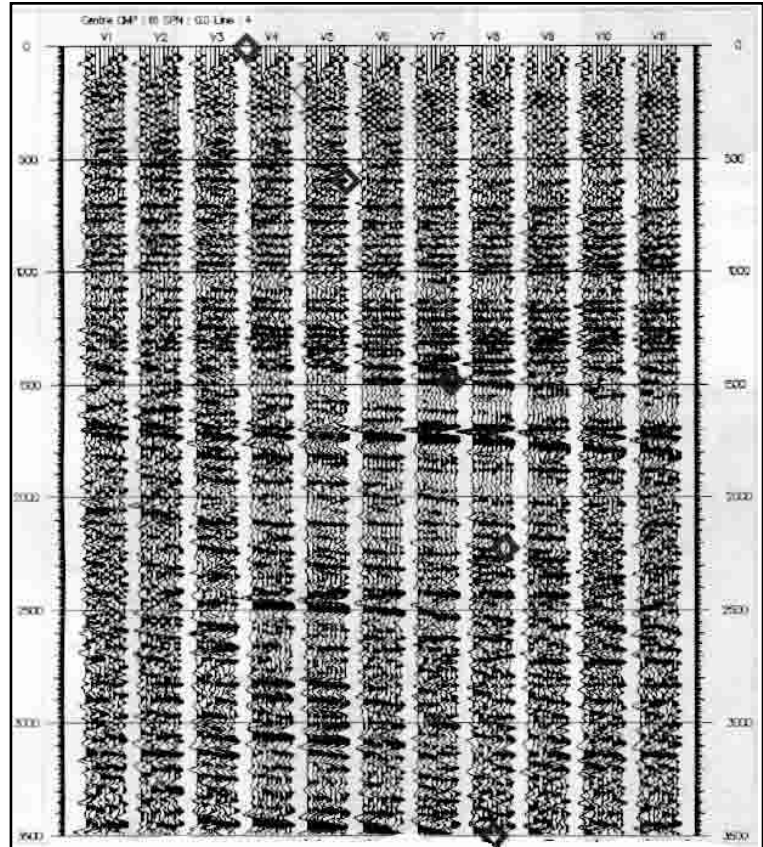


Fig. 6-70 CVS Display Used to Generate the Velocity Trend for the IVP Session

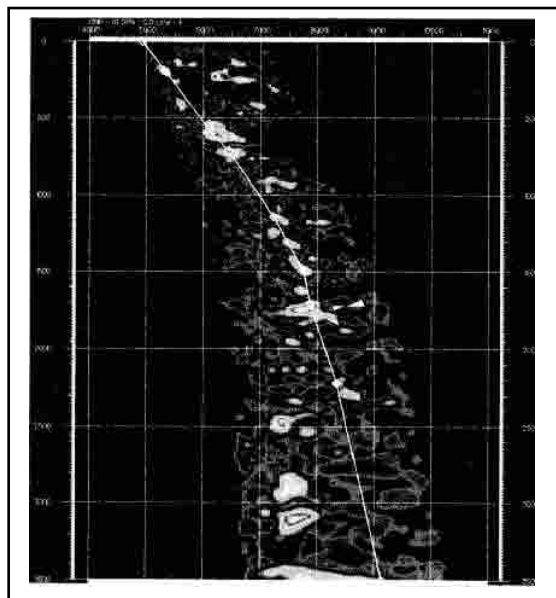


Fig. 6-71 Semblance Plot Generated from the Input Velocity Fan

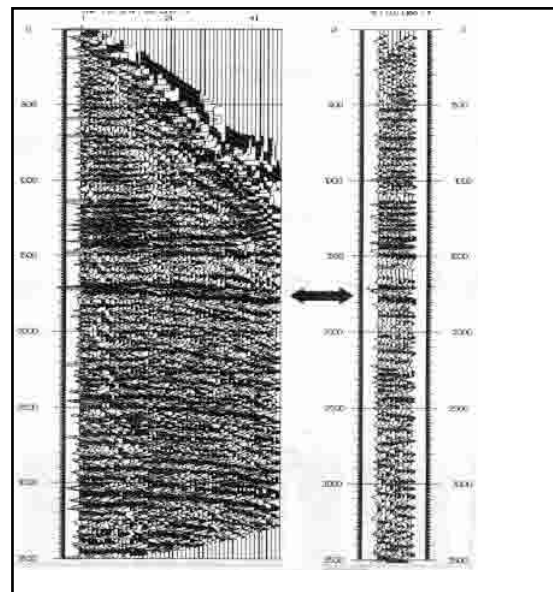


Fig. 6-72 CMP 61 Corrected for NMO Using Velocity Function

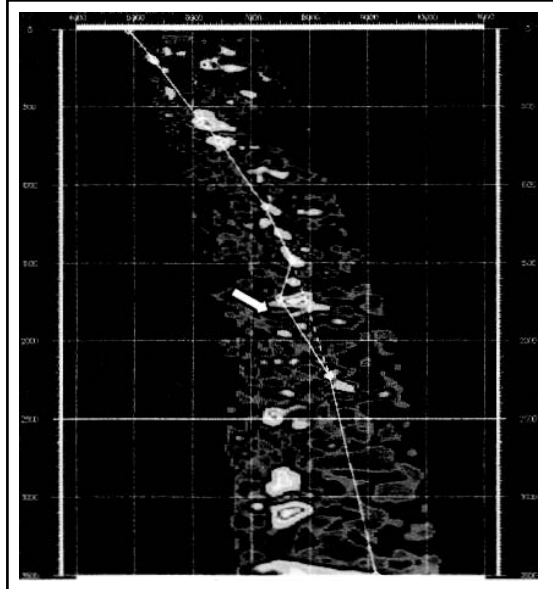


Fig. 6-73 Semblance Plot with a Slower Velocity Picked for Event at 1729 ms

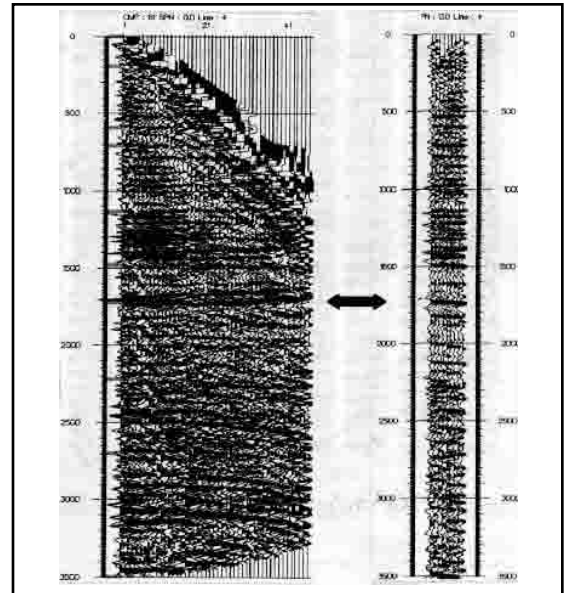


Fig. 6-74 Same as Figure 6-72 Except CMP 61 is Corrected for NMO Using the Modified Velocity Function

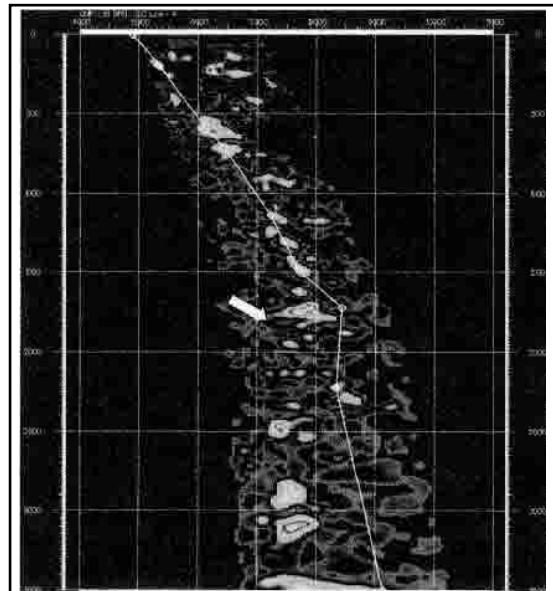


Fig. 6-75 Semblance Plot with a Faster Velocity Picked for Event at 1729 ms

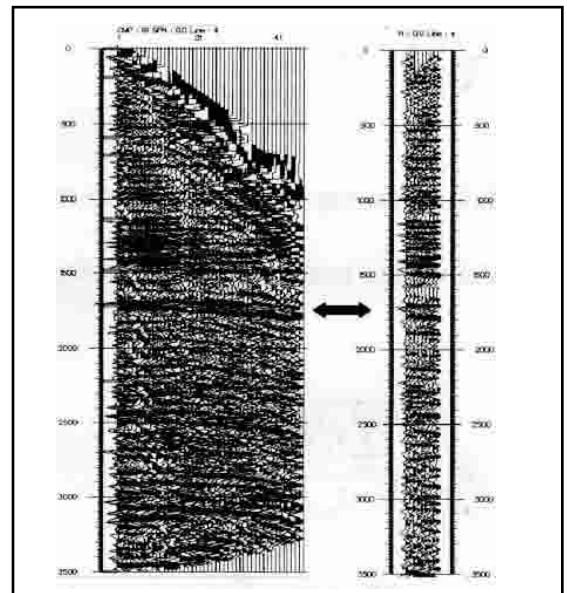


Fig. 6-76 Same as Figure 6-72 Except CMP 61 is Corrected for NMO Using the Modified Velocity Function

When the too slow and too fast picks of the event at 1729 ms were made in Figures 6–73 and 6–75, a *velocity inversion* of the stacking velocity resulted—the stacking velocity decreased from one pick to the next. This is never a valid interpretation of a velocity analysis.

Velocity inversions for interval velocities are expected because of changes in lithology of sedimentary strata. The *Dix Equation* can be used to show that stacking velocities must always increase with time. The Dix equation can be derived from Equation 6.21. To do that, substitute $T_n = \sum_{i=1}^n \Delta t_i$ into that equation, to give:

$$\tilde{V}_n = \sqrt{\frac{\sum_{i=1}^n V_i^2 \Delta t_i}{T_n}} \quad (6.27)$$

where

T_n is the two-way reflection time for the n^{th} event picked in the velocity interpretation

\tilde{V}_n is the RMS velocity, here equated to the stacking velocity.

The $n+1^{th}$ stacking velocity pick is thus

$$\tilde{V}_{n+1} = \sqrt{\frac{\sum_{i=1}^{n+1} V_i^2 \Delta t_i}{T_{n+1}}} \quad (6.28)$$

From Equation 6.27, $\tilde{V}_n^2 T_n = \sum_{i=1}^n V_i^2 \Delta t_i$. Substituting this into Equation 6.28 yields:

$$\tilde{V}_{n+1} = \sqrt{\frac{V_n^2 T_n + V_{n+1}^2 \Delta t_{n+1}}{T_{n+1}}}$$

Solving this equation for V_{n+1} , the implied interval velocity between the reflection times T_n and T_{n+1} , gives the Dix equation:

$$V_{n+1} = \sqrt{\frac{\tilde{V}_{n+1}^2 T_{n+1} - \tilde{V}_n^2 T_n}{T_{n+1}}} \quad (6.29)$$

If $\tilde{V}_n > \tilde{V}_{n+1}$, which is the case for a stacking velocity inversion, the quantity inside the square root sign is likely to be either negative or too small to give a realistic value for the interval velocity \tilde{V}_{n+1} .

An example will further illustrate the point. Let $\tilde{V}_n = 2800\text{m/s}$, $\tilde{V}_{n+1} = 2500\text{m/s}$, $T_n = 2\text{ s}$, and $T_{n+1} = 2.25\text{ s}$. This means that $\Delta T_{n+1} = 0.25\text{ s}$. Substituting these values into Equation 6.29 gives:

$$V_{n+1} = \sqrt{\frac{2500^2 \times 2.25 - 2800^2 \times 2}{0.25}} = \sqrt{\frac{14962500 - 15680000}{0.25}} = \sqrt{-2870000}$$

So, our example gives an imaginary number for interval velocity, and the pick at 2.25 s is too slow or the pick at 2 s is too fast!

- **Computational procedures.** In performing velocity analysis, it should be kept in mind that the velocity field is the only output of velocity analysis. Processes and computational procedures can be employed that enhance the accuracy and resolution of the velocities but are not passed on to later stages of processing. There are two basic aspects of this—reduction of data quantity and enhancement of signal.

Data reduction. The obvious thing in the first category is to resample to a larger sample period—from 2 ms to 4 ms or even from 4 ms to 8 ms. This results in about a 50% reduction in data to be processed. The anti-alias filter must be applied, but usually the trend of the low frequency part of signal is the most significant.

Partial stacking—adding together a selected number of adjacent offsets in CMP gather—is another approach to data reduction. By adding traces corresponding to four offsets, 64-fold data is reduced to 16 fold.

Calculate coherences for each gather individually and average coherence for multiple CMP gathers or calculate coherence for the sum of CMP gathers. Remember to sum CMPs in the presence of dip with great caution—the time dip across the CMPs stacked must be less than one-fourth of the dominant period for CMPs in the sum. When summing adjacent CMP gathers, the sum should have every possible shot-to-receiver offset!

Use a preliminary stack mute to remove data outside the NMO stretch mute, but be conservative, and do not mute too much. Use different velocities with different mutes.

Use only as high velocity values as absolutely necessary. High velocities are difficult to resolve because residual moveout is very small and very high velocities are rarely encountered.

Signal enhancement. Apply differential NMO before stacking. Too much summation causes deterioration of velocity resolution. Time dip between adjacent CMPs limits the number of adjacent CMPs that can be summed.

Apply band pass filtering to restrict data to those frequencies having the best signal-to-noise ratios. As noted previously, only the low frequency velocity trend is required for most processing.

AGC decreases high amplitude noise, such as ground roll and multiples, relative to data, improving ability to pick correct velocities.

Velocity problems. A number of things can be and are encountered that affect velocity analysis negatively. Among these are

- dip
- offsets
- near-surface anomalies (statics)
- multiple reflections

Dip-related problems. Stacking velocities do not tie at line intersections for dipping reflectors. This is because the lines are shot at different azimuths, causing differences in apparent dip angle and, hence, different velocities and different NMO calculations. The solution for this problem is the application of DMO. The DMO process will be discussed later in this chapter.

Offset-related problems. Offsets that do not satisfy the short spread requirement— $X \leq Z$ —can produce problems. This is demonstrated in Figure 6–77. Here the reflection times are those observed for a flat layered earth model with the maximum offset of $x_{\max} > Z$, where Z is the depth of the reflector. As offset increases, the calculated NMO diverges further from the actual moveout.

Velocity analysis is, basically, the fitting of NMO curves to observed moveout. Figure 6–78a shows a best fit to the observed moveout of Figure 6–77 and Figure 6–78b shows the NMO-corrected event using this best fit hyperbola. The event is not flattened, resulting in a less than optimum stack, and the zero-offset time T^0 is too early.

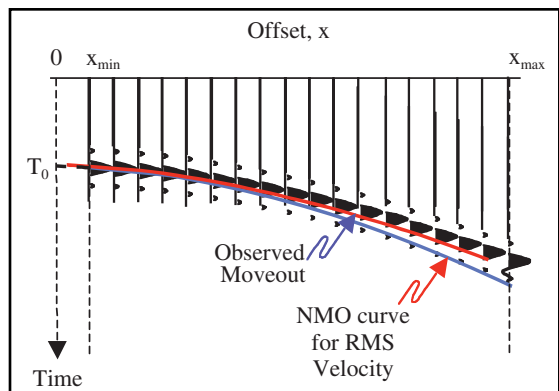


Fig. 6–77 Observed Moveout versus NMO for a Flat Layered Earth

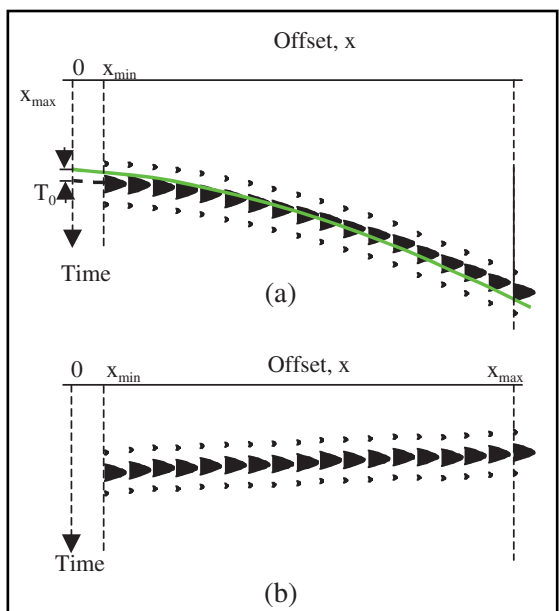


Fig. 6–78 Best Fit Hyperbola to Observed Moveout, NMO-Corrected Traces Using Velocity Obtained from Best Fit Hyperbola

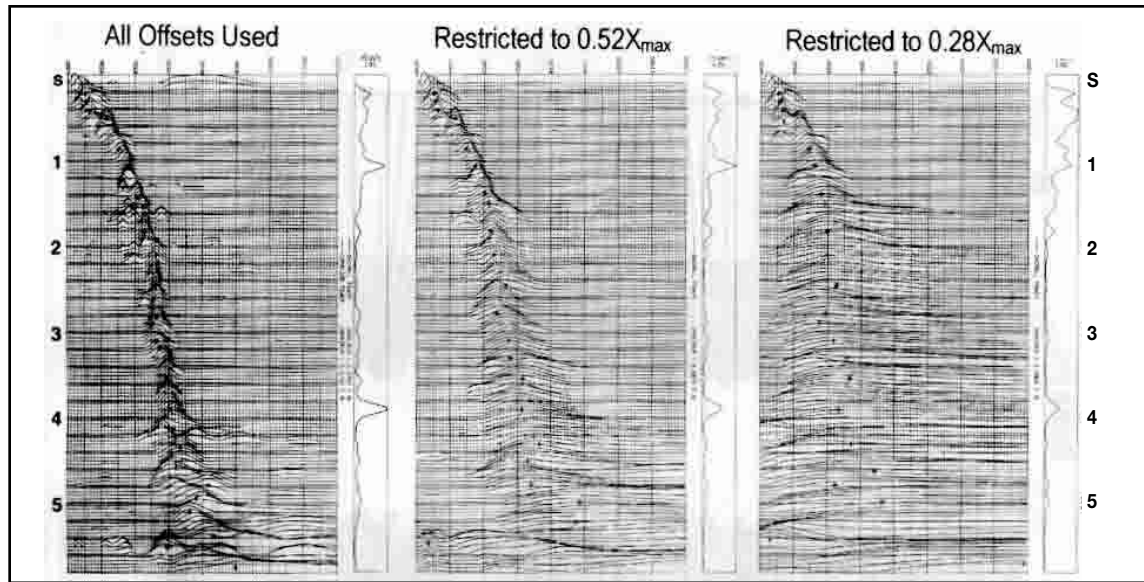


Fig. 6-79 Effect of Restricting Offsets on Velocity Analysis

Not using a full range of both long and short offset traces can also have a very negative effect on velocity analysis. This is demonstrated in Figure 6-79. In this figure, coherence is plotted as a wiggly trace with amplitude indicating coherence values. It is desirable to have the velocity trend defined by large coherence maxima with small breadth. The display on the left of Figure 6-79 satisfies this requirement. The center display shows what happens when traces are restricted to those corresponding to 52% of the maximum offset. Clearly, velocity resolution has decreased. The display on the right shows the effect of further offset restriction. Here it is only out to 28% of the maximum offset. The velocity trend is very difficult to see.

Effect of near-surface anomalies on velocities. Near-surface anomalies produce erroneous velocities if proper account of them is not taken. Figure 6-80 presents an earth model with a near-surface anomaly.

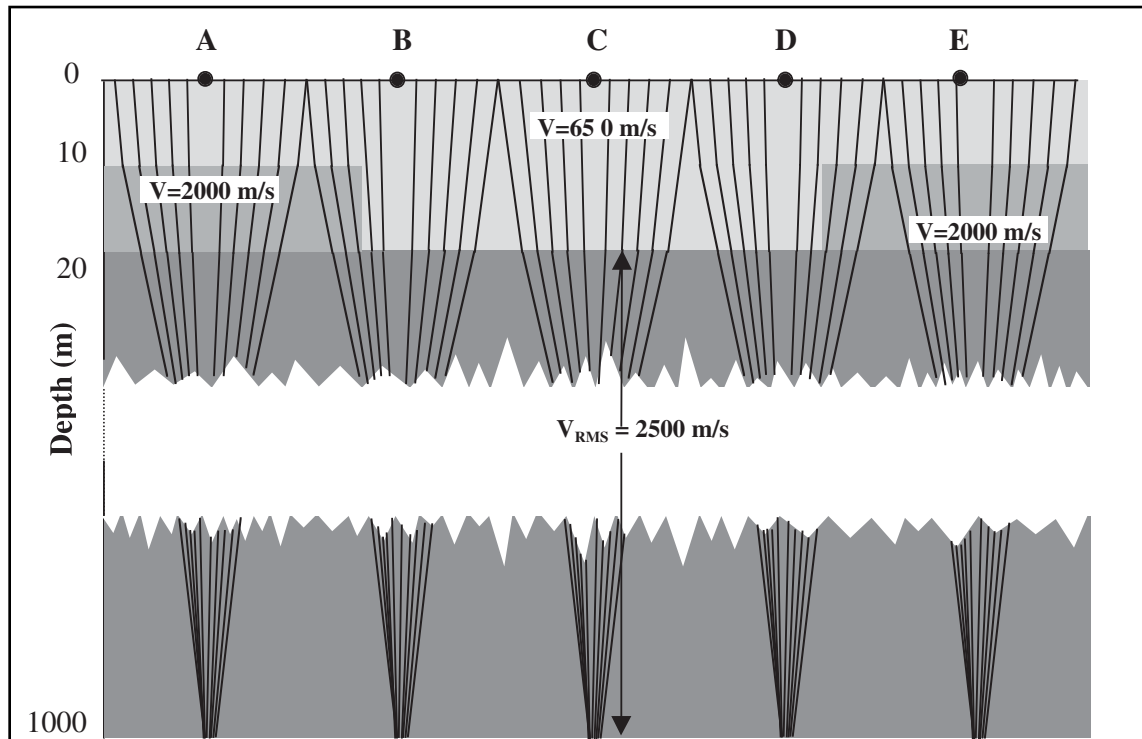


Fig. 6-80 Earth Model with Near-surface Anomaly

In this model, the unconsolidated rock extends to a depth of 10 m, abruptly increases to 20 m depth, then abruptly returns to the 10 m depth. Velocity of the unconsolidated rock is 650 m/s. The 10 m depth sections of the near-surface are underlain by 10 m layers of consolidated rock having a velocity of 2000 m/s. From a depth of 20 m, there are layers of consolidated rock with an RMS velocity of 2500 m/s.

Five CMPs, designated A, B, C, D, and E, and five ray paths corresponding to offsets of 200 m, 400 m, 600 m, 800 m, and 1000 m for each CMP are shown. Because of the near-surface anomaly some ray paths go through the 2000 m/s layer and others do not. Figure 6-81 shows the effect of this by displaying simulated recordings of the reflection from 1000 m deep reflector at CMPs A through E.

The events at CMPs A, C, and E show hyperbolic moveout, although the hyperbola at C differs from those at A and E. Events at B and D do not exhibit hyperbolic moveout, but best fit hyperbolas are shown for both events.

The model of Figure 6-80 was used to calculate arrival times for CMPs at 100 m intervals. From these arrival times, velocities were determined. Figure 6-82 displays the results of these calculations. Note that the variation in apparent stacking velocity across the model does not exactly follow the near surface anomaly. At the edges of the anomaly, velocities rapidly decrease, increase, then again decrease to a stable value where the all ray paths of the CMPs are in the thick portion of the unconsolidated rock.

Figure 6-83 is a simulated CMP stack for the model of Figure 6-80. While the reflector is actually flat, the near-surface anomaly has produced apparent structure.

Problems caused by multiple reflections. When multiple reflections are present in the data, semblance maxima are produced for both primary and multiple reflections. In some cases, the two sets of semblance maxima can be easily distinguished with the multiples showing a lower velocity trend than the primaries. In other cases, multiple amplitudes are so strong that maxima for primary reflections are obscured.

An example of the latter situation is shown in Figure 6-84. The center CMPs at locations 224 and 684—the coherence displays for velocity analyses at these locations—are shown before (left) and after (right) multiple attenuation is accomplished. Note that before multiple attenuation, the primary velocity trend at times later than about 3 seconds cannot be discerned. After multiple attenuation, the primary velocity trend becomes obvious.

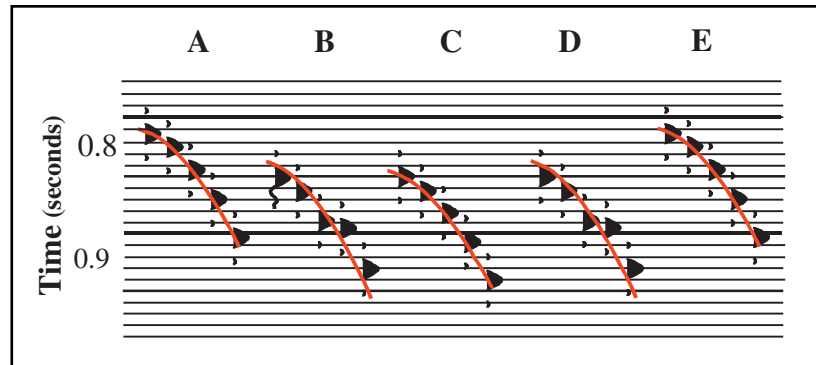


Fig. 6-81 Synthetic Traces Based on Model of Figure 6-80

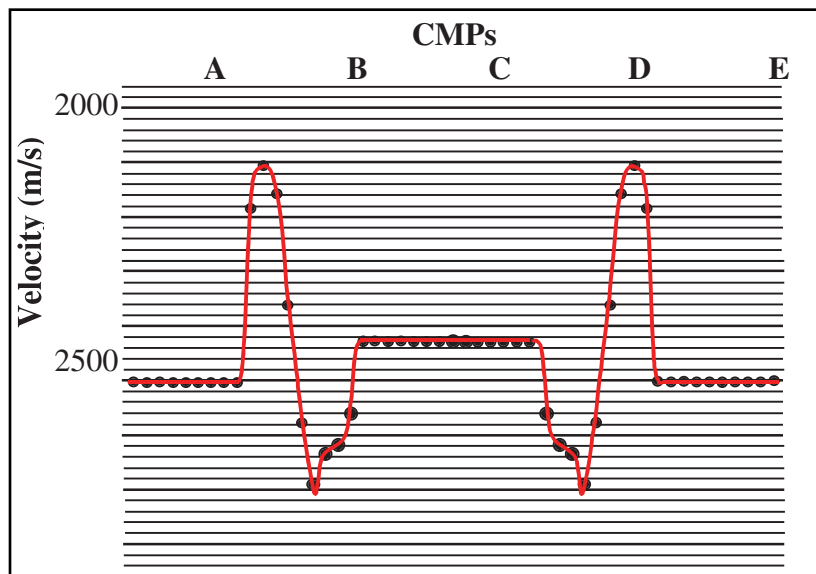


Fig. 6-82 Variations in Stacking Velocity Caused by Near-surface Anomaly

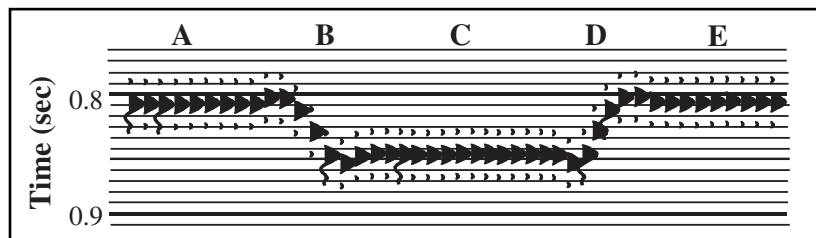


Fig. 6-83 Stack of Synthetic Traces Based on Model of Figure 6-80 and Velocities of Figure 6-82

7

Seismic Reflection Data Interpretation

Introduction

A seismic trace is regarded as the superposition of reflections from many subsurface interfaces where the acoustic impedance (product of velocity and density) changes. This superposition concept describes a seismic wavelet being reflected back at each change of acoustic impedance, with the sign and amplitude of the reflection being proportional to the sign and fractional change of the acoustic impedance. The seismic trace is represented simply by the mathematical operation of convolving (filtering) the wavelet with the Earth's reflectivity. It is a log of acoustic impedance as a function of two-way travel time of the seismic energy.

In conventional seismic interpretation, it is assumed that the acoustic impedance changes are parallel to the bedding planes so that mapping the arrival times of reflections gives the structural picture. Any discontinuity of the reflections is assumed to indicate faulting or some other structural or stratigraphic feature.

For many decades, seismic reflection interpretation involved the arrival times of the markers with little attention given to the amplitude, frequency, and wave-shape variations. Seismic reflection was used mainly in the interpretation of the structural aspects of the hydrocarbon traps with little emphasis on the stratigraphic aspects. Most of the stratigraphic traps found were serendipitous—discovered during the search for something else.

Stratigraphic interpretation of seismic data requires good data quality and involves some art as well as science. The effects of structural complications may overwhelm the effects of stratigraphic variations in a good record area. However, in many areas, seismic stratigraphy can add important geological information and enhance the understanding of the depositional environments, which may help in the understanding the origin, accumulation, and trapping mechanisms of the hydrocarbon deposits.

The seismic traces are trying to tell us the details about the subsurface, but their voices cannot be heard because they speak in a very high-noise environment. With better techniques in field data acquisition and great advancements in data processing, we can have better quality data. This makes it more feasible to extract stratigraphy from the seismic record and makes us believe in the geological significance of the seismic signature of stratigraphic sequence analysis.

Without understanding the basics, it is difficult for one to comprehend the physical meaning of the seismic signature and to relate it to stratigraphy—first in regional aspect, second in local aspect, and finally in individual reflection characteristics. Understanding the basics will help us to identify lithology, depositional environments, and direct hydrocarbon indicators.

The reliability of this information is dependent on the quality of the seismic data. Good-quality data depends on proper field acquisition, careful data processing flow, and a high degree of quality control in order to preserve the frequencies and amplitudes of the reflectors.

In the previous chapters of this text, we discussed data processing techniques necessary to generate a geologically sound seismic section that reveals reliable and meaningful stratigraphic information. Migration was discussed to give a better understanding of the proper imaging of the subsurface. Lateral and vertical resolution of seismic data was considered for better understanding of the limitations of seismic data. At this point, we are prepared to review stratigraphy, stratigraphic traps, depositional environments, facies, geometry of traps, and seismic signature.

Part of this text is devoted to the discussion of forward and inverse modeling approaches and their applications to stratigraphic sequence analysis. The last part of the text is devoted to modern geophysical applications and techniques such as *vertical seismic profiling* (VSP), *amplitude versus offset* (AVO), high-resolution seismic data, shear-wave applications in seismic stratigraphy, and 4-D technology.

Finally, we discuss current research and future developments in borehole measurements, advancements in subsurface imaging, and their role in enhancing the stratigraphic interpretation of seismic data.

Modeling

Introduction. Models are representations of some physical situation used to explain observations or to confirm hypotheses. Physical models are constructed to scale and experiments performed on them, often in an attempt to duplicate observed data. Mathematical models are more often used, usually in conjunction with computers. In seismic exploration, such models most often are used to test or develop interpretations of seismic data.

Geologists have used various models, including plate tectonics models of earth movement, to test theory. Paleontological studies are used to model the reservoir conditions of an area. Surface geologic features and available subsurface geology are used to the model subsurface targets of interest.

Geophysicists also use models to represent the subsurface. Resistivity logs, density logs, and interval transit time logs obtained from borehole measurements provide data for models that are most useful for interpolating between drilled wells. There are various methods of checking these models. The most common of these devices are magnetic anomaly mapping, gravity anomaly mapping, and the seismic refraction and reflection mapping schemes. The seismic reflection method is the most detailed of these since it has better resolution and fewer ambiguities than the others. Unfortunately, seismic reflection exploration does have its distortion mechanisms. The following paragraphs investigate seismic reflection exploration measurements, inferences made or calculated from the measurements, and how these may distort the image of the modeled subsurface geology.

Seismic exploration measures the Earth's response to mechanical energy injected into the ground or water. This energy may be impulsive (explosives or airguns) or vibratory (the swept frequency signal of the Vibroseis system). The direct measurements are amplitude as a function of time.

At each interface between subsurface materials differing in velocity and or density, some energy is reflected and some transmitted or refracted. The amplitude of the reflected pressure wave at a given interface, relative to the incident amplitude, is described by the reflection coefficient for that interface. The reflection coefficient depends on the contrast between velocity and density plus the angle of incidence. The Zoeppritz equations are a relatively complex set of four equations that can be used to determine amplitudes of all wave types produced by an incident P- or S-wave. In most seismic reflection applications, a simpler expression (actually valid only for incidence normal to the interface but applicable for small angles usually encountered) can be used. This is:

$$R_v = \frac{\rho_2 v_2 - \rho_1 v_1}{\rho_2 v_2 + \rho_1 v_1} \quad (7.1)$$

where

ρ = density

v = interval velocity

The subscripts denote the Earth layers involved in the reflection process. Units for density and velocity are not important as long as the same units are used in layers 1 and 2.

The response that seismic reflection exploration seeks to measure is the two-way reflection time to interfaces of interest and the reflection coefficients of those interfaces.

Equation 7.1 combined with derived average velocities allows modeling depth of burial, formation thickness, lateral extents, and, in some cases, porosity and hydrocarbon presence. However, it is also necessary to recognize and compensate for distortions from the true subsurface model that the seismic method produces.

Seismic distortions. There are three categories of seismic distortions as follows:

1. errors in position with events displaced laterally and vertically
2. apparent bedding changes caused by reflection response differences
3. noise or unwanted information that interferes with and masks desired information

Historically, the last item—noise—has received the most attention in seismic acquisition and processing. Improvement of the signal-to-noise ratio is a paramount goal in both acquisition and processing. Methods used for this purpose include

1. source/geophone arrays
2. offset distance selection
3. vertical and horizontal stacking
4. frequency filtering
5. velocity filtering
6. deconvolution

Figure 7-1 shows a typical exploration sequence. A prospect is identified by geologists and a seismic program is initiated. The interpreter sees the distorted view of the sub-surface on the cross-sections produced by the seismic effort. He must test the validity of the geologists' initial model, which requires study of and compensation for distortion mechanisms. If this is not done, chances of finding oil or gas are poor. All distortions should be examined to determine methods to eliminate them.

Only flat, parallel bedding is correctly represented on CMP stack sections. Irregular and dipping beds are distorted. For example, an anticline (Fig. 7-2) appears larger than its true dimensions because the energy fans out of from the convex surface reflecting it. Figure 7-2 also illustrates the concept of focusing from a syncline or low structure.

Diffraction occurs when there are discontinuities in the seismic events such as faults, folds, and changes in lithology. In the case of a deep-seated syncline, another phenomenon is observed—two intersecting events with an apparent anticline beneath them. In fact it resembles a bow tie. This phenomenon is explained in the chapter 3 and is referred to as Fermat's principle

Figure 7-3 shows curved reflecting surfaces (synclines and anticlines).

a) In Figure 7-3a, the zero offset stack shows three synclines and one anticline. Note the bow tie effect shows as the two deep-seated synclines. Diffractions are observed from the anticline D-E. In Figure 7-3b, the process of migration removes the distortion in the stacked section.

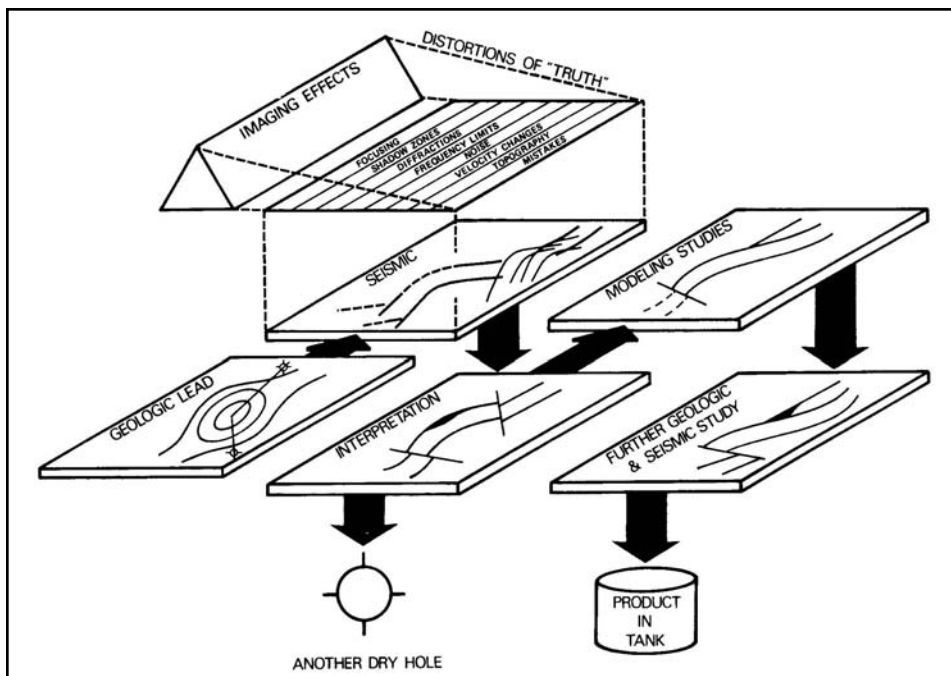


Fig. 7-1 Typical Exploration Sequence

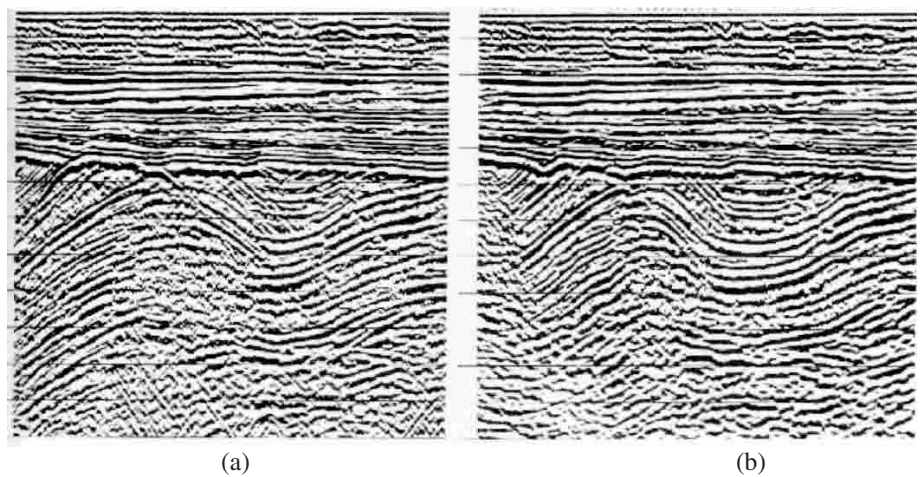


Fig. 7-2 Focusing in Anticlines and Synclines

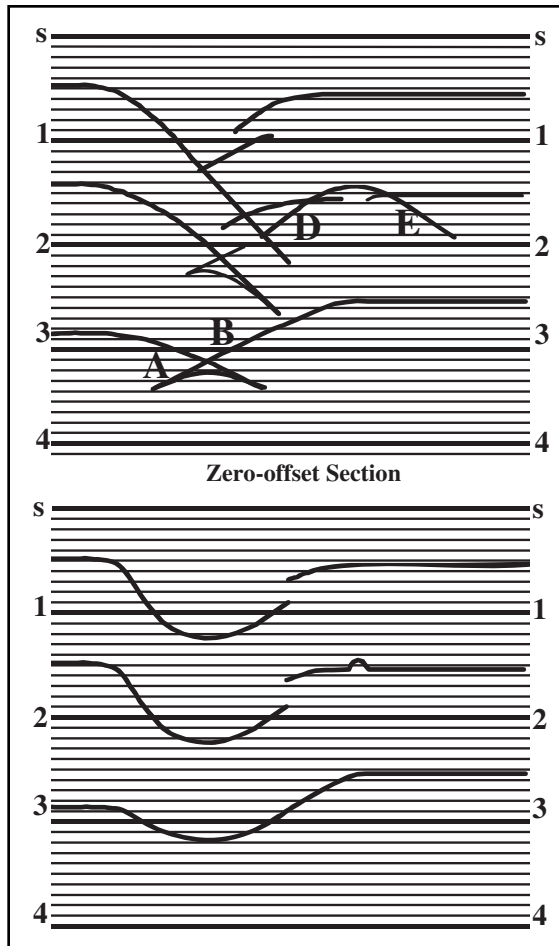


Fig. 7-3 Bow Tie Effect of Buried Focus

The bow ties were untied and reveal the true subsurface structure as synclines. The anticline is reduced in size of the after the diffraction is collapsed by the migration process. Figure 7-4 is another example of the bow tie effect and its resolution by migration.

In Figure 7-5, there are areas with no energy returning (dead areas). These are commonly referred to as *shadow zones*. Shadow zones are common near faults and other discontinuous areas in the subsurface. Here, energy has been focused on other receivers and does not show reflectors in their true positions.

Diffractions occur at discontinuities in the subsurface. Faults and velocity discontinuities, as seen at bright spot terminations, are examples.

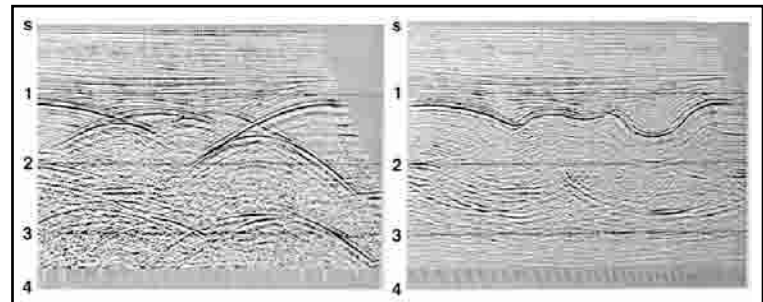


Fig. 7-4 The Zero-offset Stack Shows the Focusing of the Narrow, Deep-seated Syncline and the Migrated Stack Shows the Bow Tie Untied

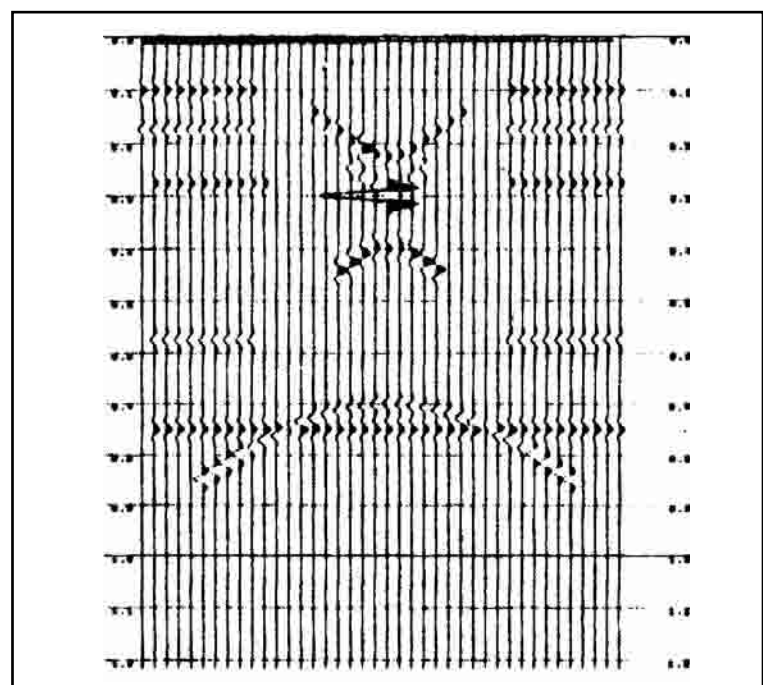


Fig. 7-5 Shadow Zones

In Figure 7–6, a CMP stack section for a seismic line across a large horst block, diffractions mask the fault plane on the left of the section. Figure 7–7, a normal incidence ray path model of this feature without diffractions, shows the fault zone more clearly. A shadow zone in the fault vicinity can also be seen.

The seismic reflection method uses only the lower end of the acoustic spectrum. This is because the earth attenuates high frequencies much faster than low frequencies. Under normal petroleum exploration conditions, the usable frequency range rarely exceeds 80 Hz. Often, in any one area, closer limits are imposed. Since ground roll and wind noise may cover the lower and higher frequencies in the 5–80 Hz range, the signal frequency band is more often on the order of 20–60 Hz.

The limits on bandwidth carry with them limits on resolution. When layering thickness becomes thin with respect to wavelength—about 100 ft—the wavelets are longer than the time between them, and they interfere with one another. This results in a wavelet complex with amplitude and phase dependent on the convolution of the layering with the band-pass filtering. At very thin layering, the reflections become so close together that the interference becomes so severe that no reflection is present or one strong reflection is present as in Figure 7–8.

With the most advanced software programs and hardware equipments, the acquisition and processing of seismic data is carried out in an optimum manner and residual noise will mask the subsurface to some extent. Examples of noise are

- random noise
- residual coherent noise
- out of plane reflections
- multiples
- ghosts

This interfering energy can cause apparent reflection changes in time (pseudo faults), frequency (pseudo stratification change), amplitude (apparent change in reflection coefficient), or phase (structure or stratigraphic anomaly).

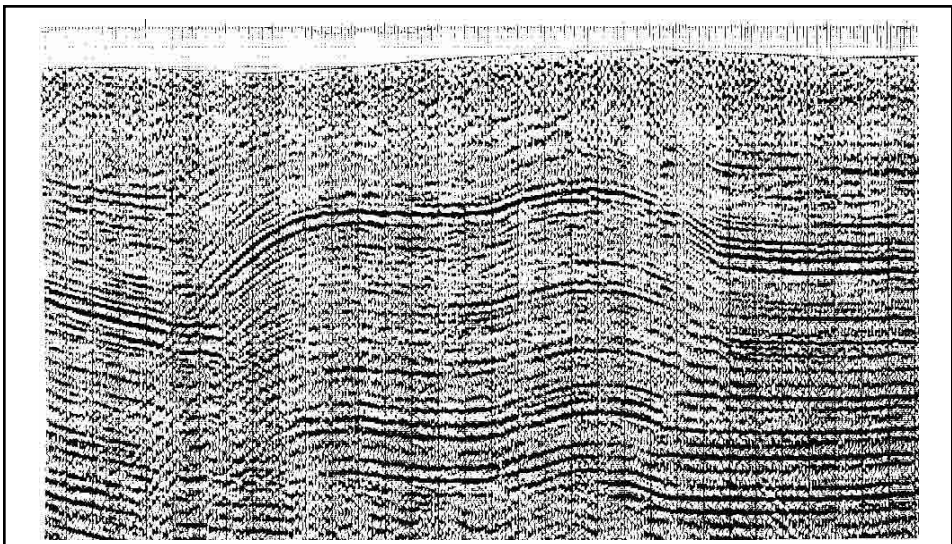


Fig. 7-6 Zero-Offset Section of Horst Block

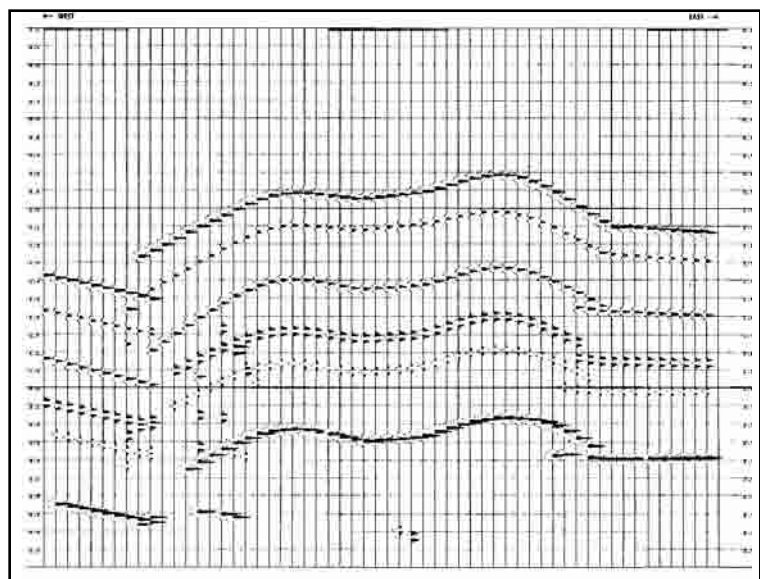


Fig. 7-7 Normal Incidence Ray Path Model of Horst Block

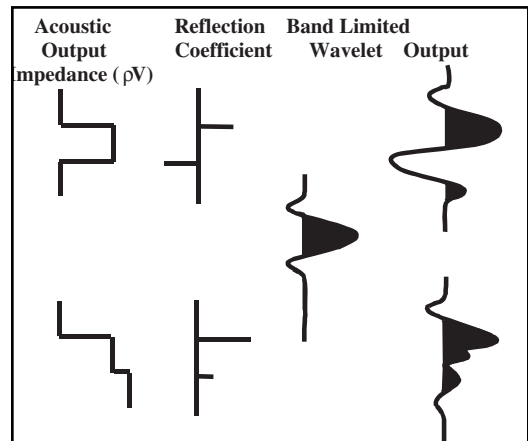


Fig. 7-8 Thin Bed Response

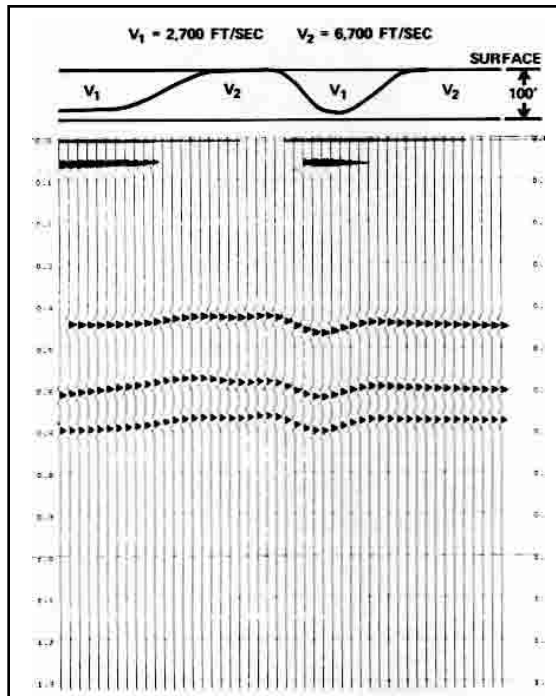


Fig. 7-9 Distortion in the Seismic Data because Of Lateral Near Surface Velocity Variation

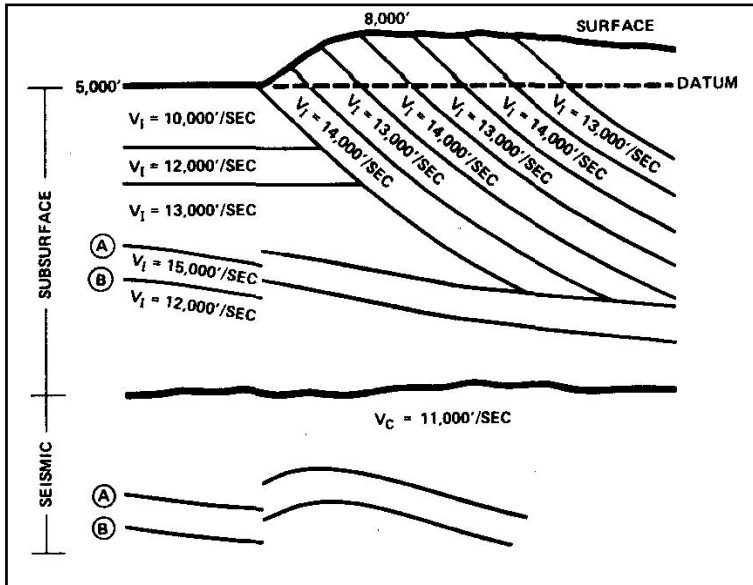


Fig. 7-10 Distortion in the Deep Structure because of False Turnover against the Fault Plane

Variations in the surface and near surface are frequent sources of seismic distortion. Surface material changes cause source and receiver response variations that affect reflection quality. Variations in thickness and velocity of the near surface, laterally and vertically, cause event times for traces to indicate false structure. Figure 7-9 shows the effects of a varying near surface velocity the subsurface. Note, in this model, the deep reflector is a flat calibration horizon and shows the distortion directly. Figure 7-10 is a case showing how elevation and near surface velocity causes an apparent turnover into a fault when it really doesn't exist.

Automatic statics programs and other static correction methods attempt to remove these time shifts before stacking data. Gradual variations in a near-surface layer defy the ability of software programs to eliminate the time variations they cause. Some areas are so complex that the correction velocity to datum needs to vary as the line progresses.

Without changes in velocity variations in the subsurface, there would be no reflections. Velocity variation can, however, cause distortions that distort the view of the subsurface. Some examples of distortions caused by velocity variations are

1. false structure caused by velocity pull-up from shallower beds (Fig. 7-11)
2. apparent thickness changes (Figs. 7-12 and 7-13)
3. pseudo-faults from overlaying anomalies (Figs. 7-14, 7-15, and 7-16)
4. over-pressure shale zones (Figs. 7-17 and 7-18)

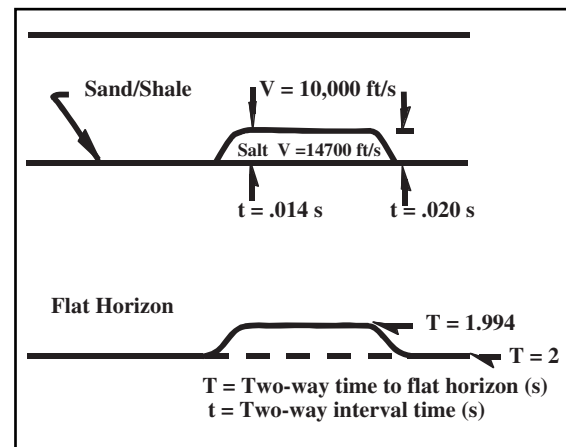


Fig. 7-11 Velocity Pull-up

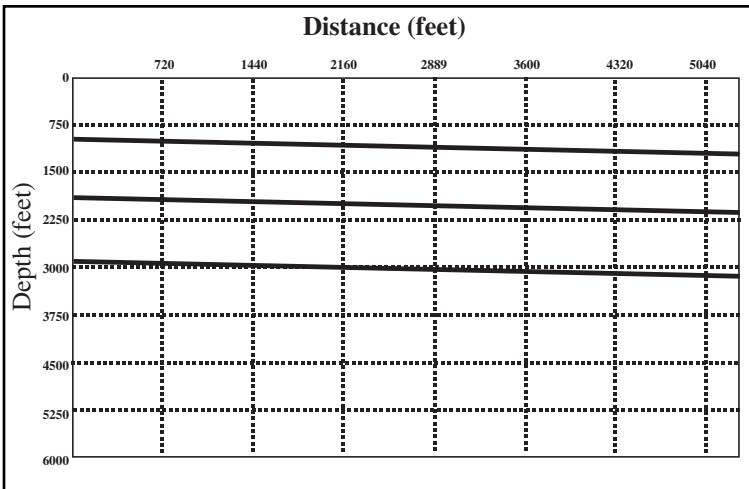


Fig. 7-12 Subsurface Section—Basinward Thinning

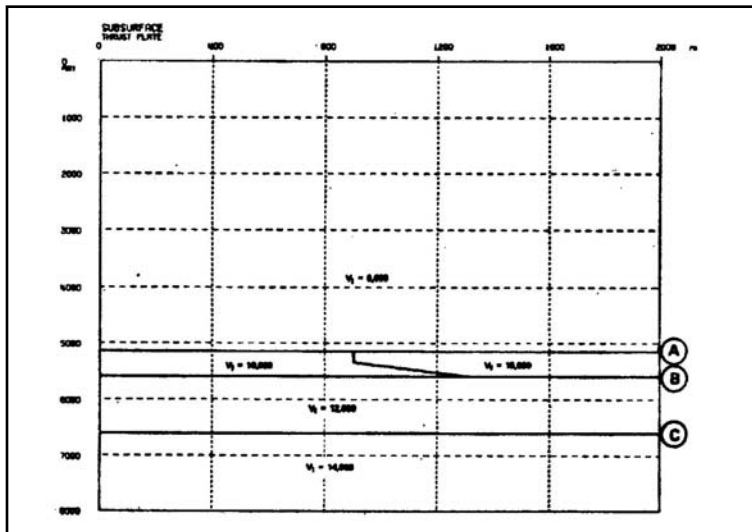


Fig. 7-14 Subsurface Pseudo Fault Model

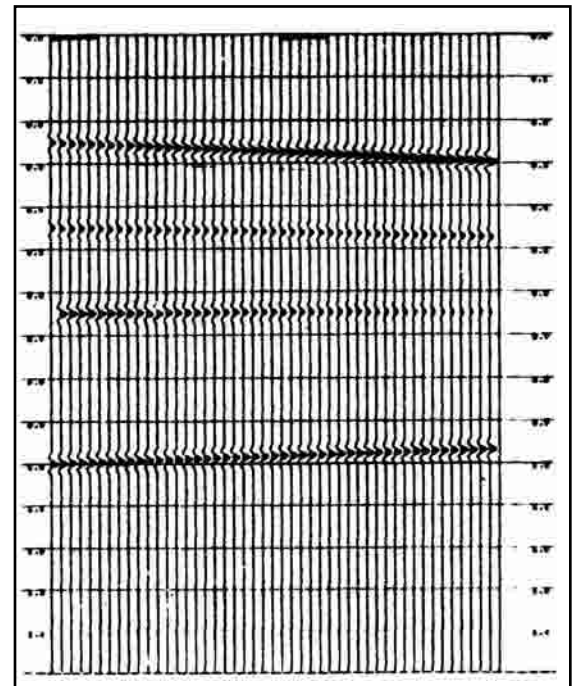


Fig. 7-13 Seismic Model—Basinward Thinning

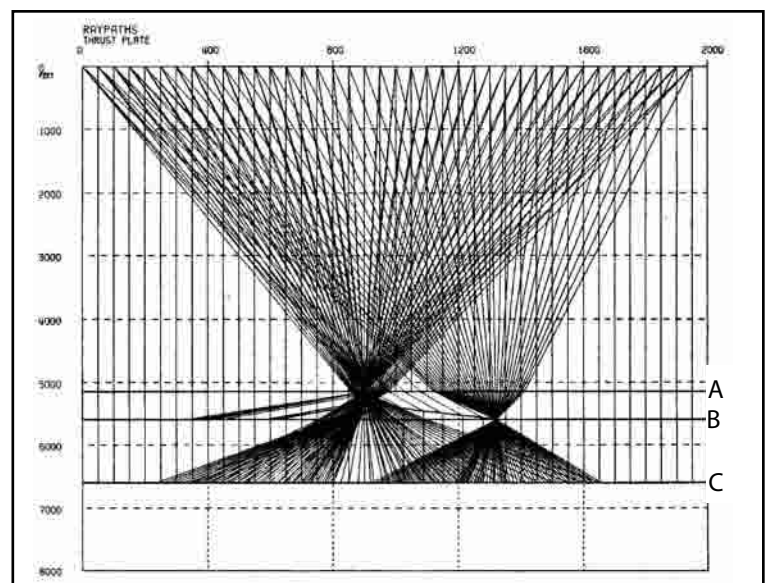


Fig. 7-15 Ray Tracing For the Subsurface Model of Figure 7-14

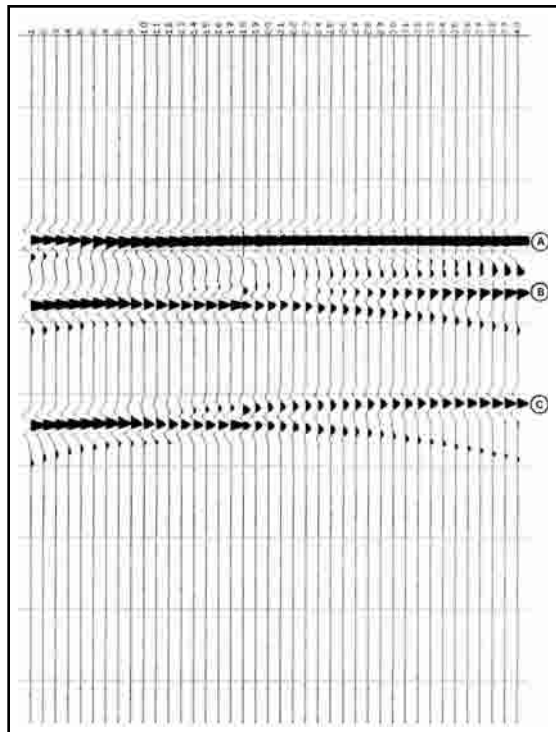


Fig. 7-16 Seismic Model For the Pseudo Fault

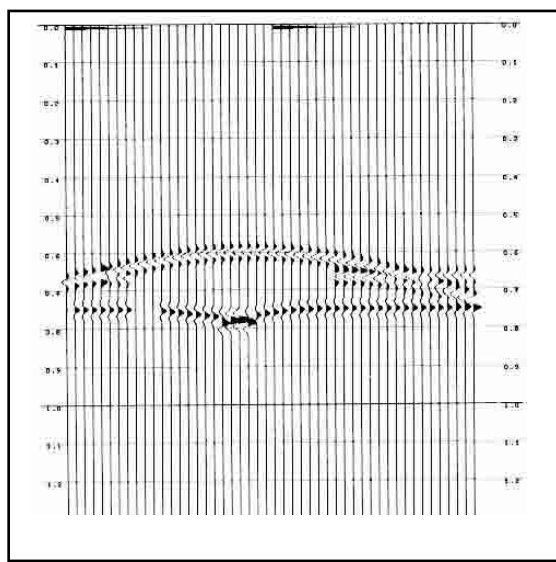


Fig. 7-18 Seismic Model of Over-pressure Shale

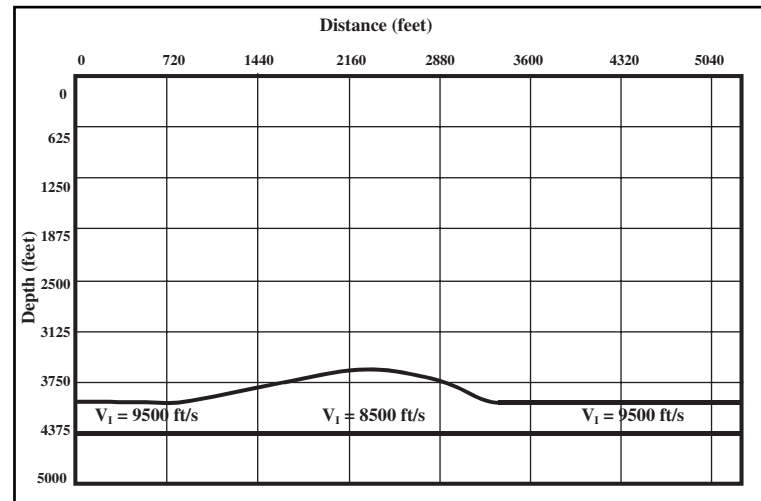


Fig. 7-17 Over-pressure Shale Model

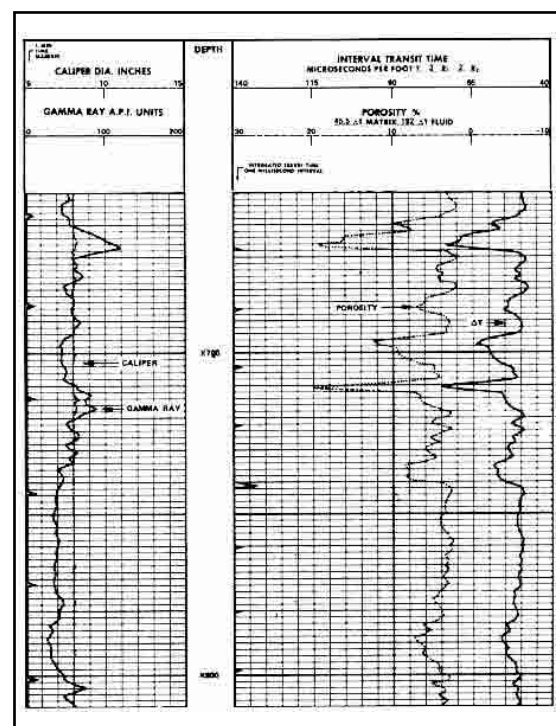


Fig. 7-19 Interval Transit Time Log

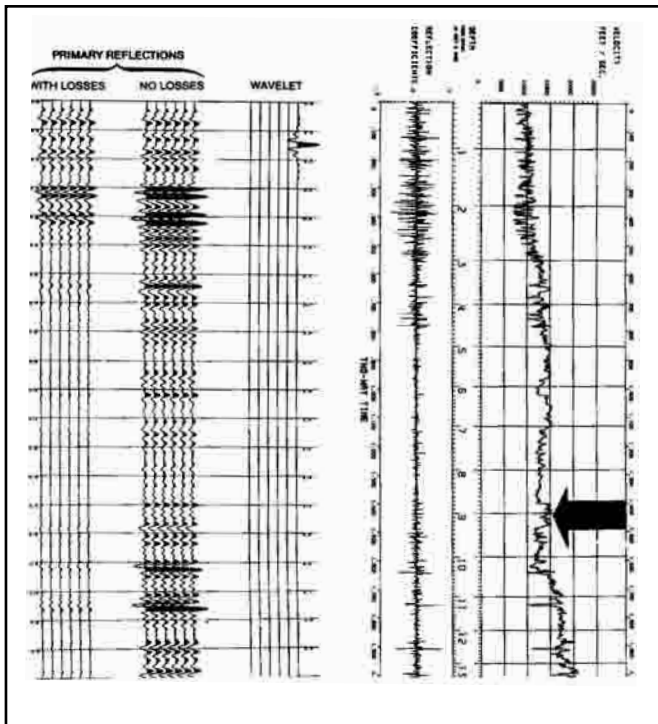


Fig. 7-20 Primary Reflection Synthetic without Modeling

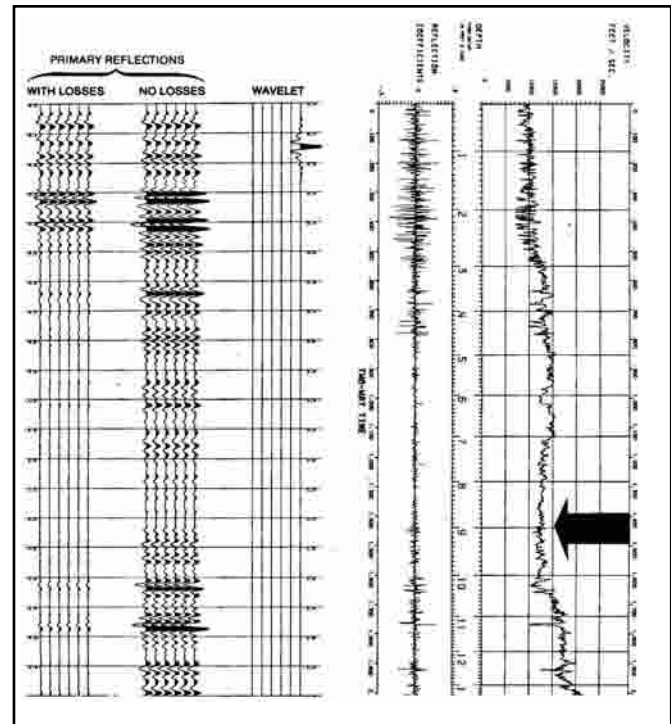


Fig. 7-21 Primary Reflection Synthetic with Velocity Modified between 8700 and 9350 Ft

The previous figures are a few of the distortion mechanisms in seismic exploration that must be recognized and the effects of which must be removed to the extent possible. The modeling process is one way of doing this.

Geophysicists perform modeling on an ongoing basis. Some digital processing techniques—velocity spectra, amplitude analysis, post stack velocity analysis, wavelet processing, and migration—help with this modeling. Modeling programs have been written for direct use in model construction.

Seismic modeling is an important step in upgrading the quality of the play or it may condemn it and save dry hole money.

1-D modeling. Synthetic seismograms are one-dimensional models. They are produced from interval transit time logs or continuous velocity logs (Fig. 7-19).

The method of calculating synthetics is as follows:

1. develop a velocity log (velocity versus depth series)
2. integrate this log to produce a depth versus time curve
3. the log can be combined with a density log, and a reflection coefficient versus time log can be calculated using Equation 7.1.

$$R_v = \frac{\rho_2 v_2 - \rho_1 v_1}{\rho_2 v_2 + \rho_1 v_1}$$

4. calculate auxiliary functions as desired
 - a. transmission losses ($1 - R_v^2$)
 - b. multiples (first order or all multiples)
 - c. ghosts
 - d. reverberations
5. convolve reflection coefficient logs with a pre-selected wavelet to obtain the synthetic seismogram

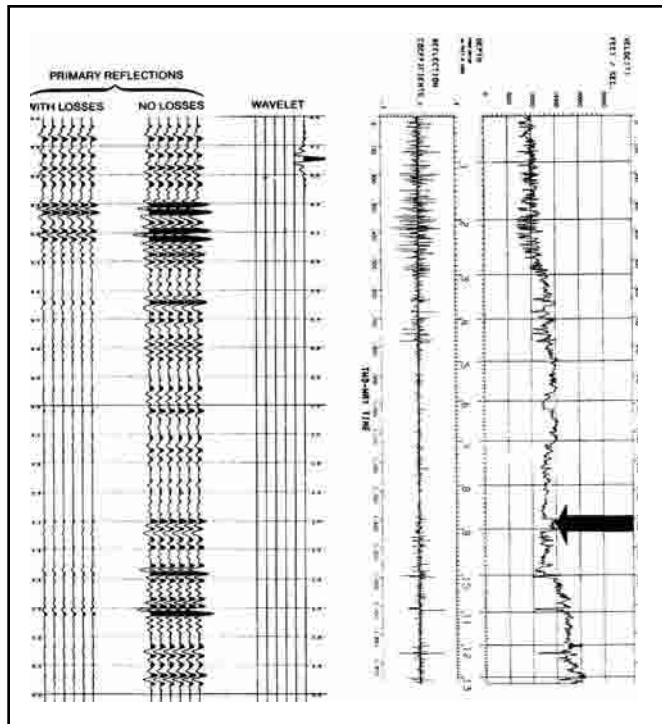


Fig. 7-22 Primary Reflection Synthetic with Depth Modification at 8700 Ft Bed Thickness Reduced from 430 to 312 Ft

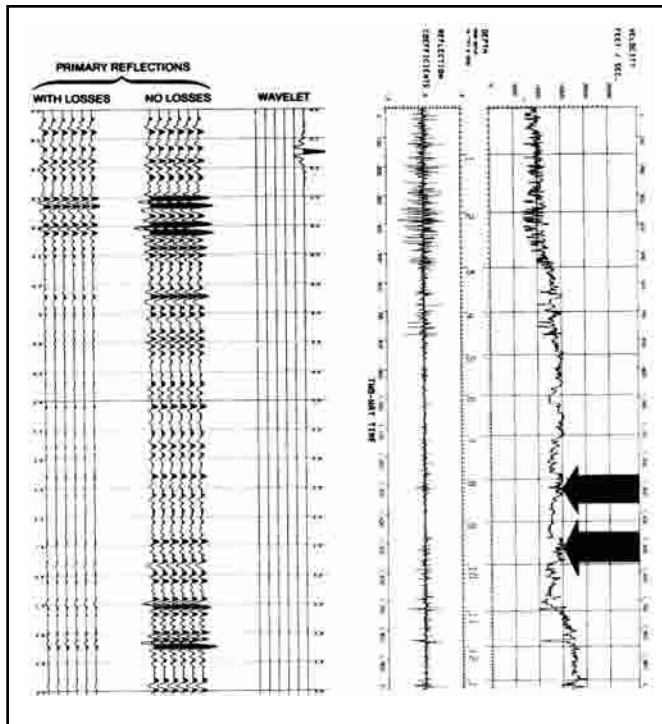


Fig. 7-23 Primary Reflection Synthetic with Repeat Section to Simulate Thrust Faulting

This results in the development of a model taken from a well log, which closely resembles a seismic trace taken at the same location.

Geophysicists compare the synthetic to their data and correlate their sections to geologic markers, which are easily seen on the log. A synthetic seismogram is shown in Figure 7-20. Synthetics can also be used to help select acquisition and processing procedures, which will best preserve data most important to the prospect.

Further studies of the subsurface can be done by making assumptions regarding the effect of changes in the geologic section. Changes can be made (modeled) in the synthetic to test the validity of the assumptions. Synthetics may be modeled by the following:

1. changing a bed thickness
2. change bed velocity
3. change bed density
4. merge logs
5. include slabs or ramps of velocity or density in logs

Figures 7-21 through 7-23 demonstrate some of these modeling techniques. The arrow indicates the part of the log that will be modified in these figures.

Further applications of synthetic seismogram uses are shown in Figures 7-24 and 7-25. Five wells have been collected for geologic and geophysical studies. Figure 7-24 shows the interval velocity logs for the five wells plotted against time. The logs have been time shifted so that horizon D is flat, simulating an ancient seabed condition. The high-speed sandstone formation B-C is shown as it was deposited. This is a deltaic deposition where most of the material is near shore to the right. Figure 7-25 is the synthetic seismogram traces for the same wells. Notice the amplitude and phase distortion throughout the pinch-out zone of B-C.

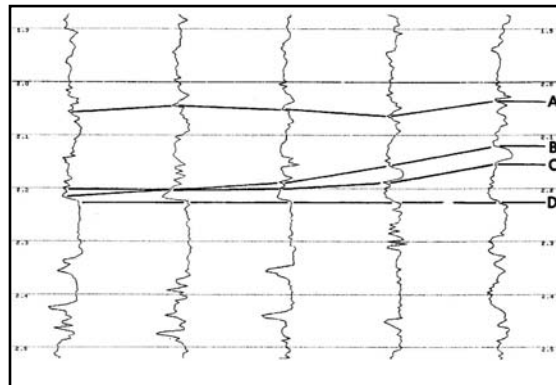


Fig. 7-24 Model Cross-section Showing Interval Velocity Versus Time

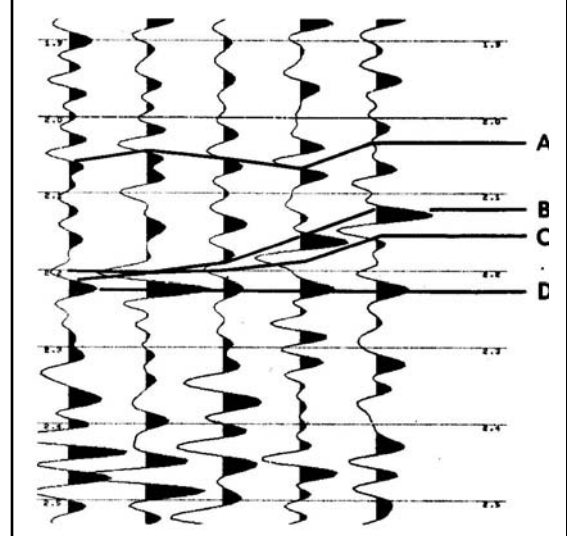


Fig. 7-25 Model Cross-section of Primary Reflection

2-D modeling. The one-dimensional modeling techniques can be used to study a few points on a subsurface to resolve detailed changes in a localized area. However, where there are lateral variations between points, focusing, shadow zones, or diffractions, two-dimensional modeling is used. Two-dimensional models range from simple to complex. A list of model types, in increasing order of complexity, is shown in Table 7-1.

Table 7-1 2-D Models

Type	Description	Restrictions
Normal incidence straight path	Uses average velocity for times and position	Limited accuracy in focusing diffractions and shadow zones
Vertical path no diffractions	Interpolated one dimensional	No focusing, no shadow zones,
Normal incidence	Snell's law	Poor resolution of tightly folded structure ray tracing (less than a wavelength)
Wave equation	Finite differences, Huygen's principle	Most complete solution, very expensive
CMP ray tracing	Offset rays by Snell's law	Most useful in testing processing parameters, very costly

Interpreters use two-dimensional modeling to test assumed geologic sections against seismic data to confirm or reject the assumptions. The complexity of the modeling scheme depends on the complexity of the subsurface. This, in turn, determines the cost of the modeling. Normal incidence ray tracing is the most widely used modeling technique because it gives the desired accuracy for most problems at a reasonable cost.

Steps in ray-trace modeling include the following:

- make a scaled model of the assumed subsurface geology that includes bedding geometry, interval velocities, and densities if available (Fig. 7-26)
- input the model into a computer in the form required by the software being used
- do the ray-tracing calculations (Fig. 7-27)
- calculate vertical incidence reflection and transmission coefficients for every interface in the model
- use a unit impulse to generate a seismic section (Fig. 7-28a)
- select a source wavelet and convolve it with the section just completed (Fig. 7-28b)
- add random noise if this seems appropriate to the problem (Fig. 7-29)

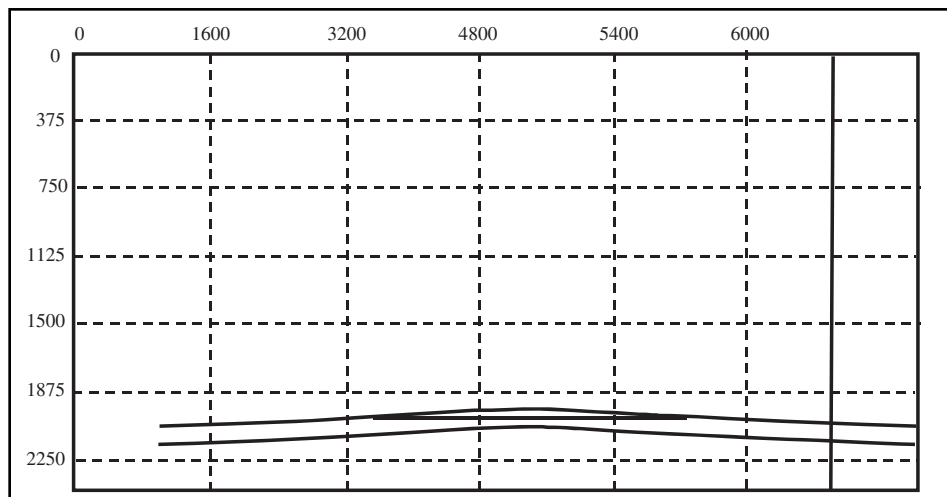


Fig. 7-26 Subsurface Depth Model

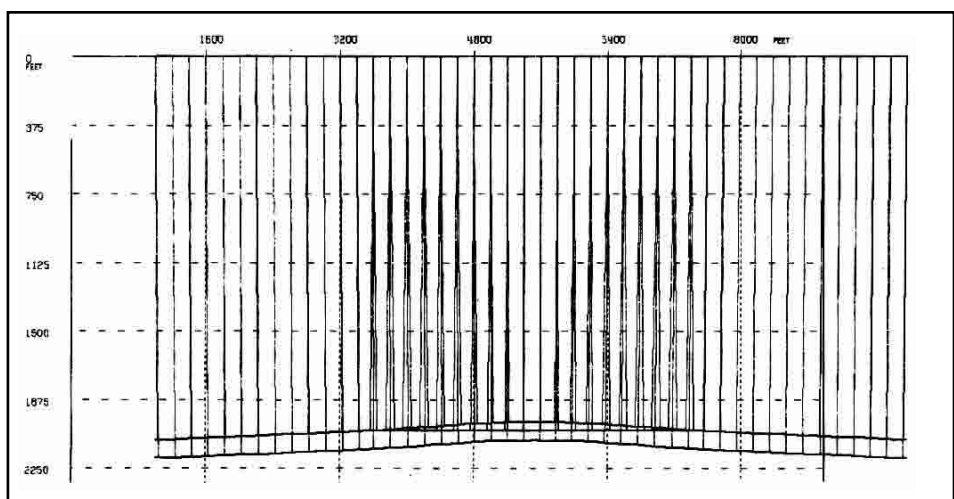


Fig. 7-27 Ray Tracing of the Model

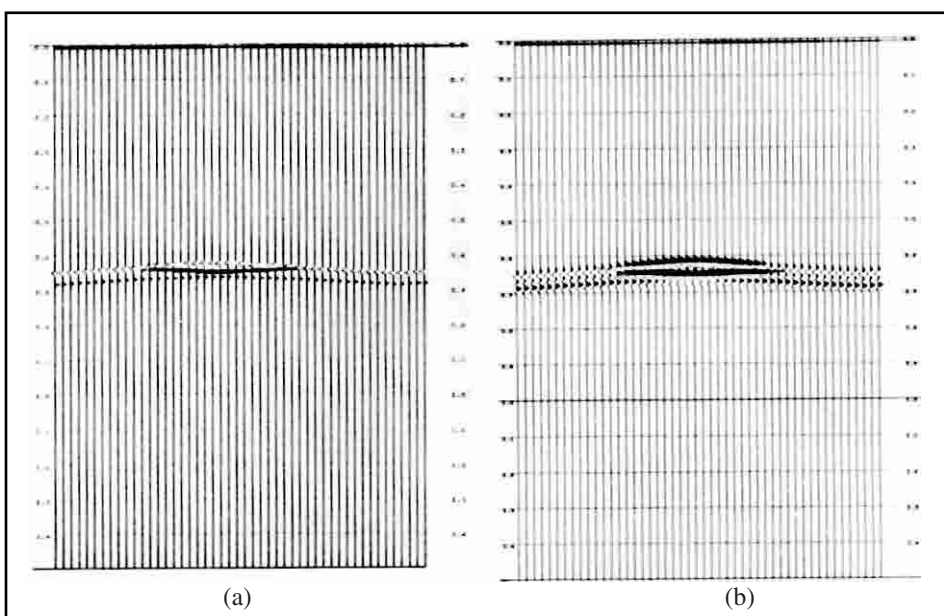


Fig. 7-28 Spike Seismogram and Wavelet Seismogram from the Model

The model is then iteratively altered to agree with the seismic section while keeping parameters confined to the local physical limits.

Inverse modeling. This is building a geologic depth model section from seismic time data observed in the field. Ideally, it would approach the function of an interpreter. Inversion is used in a wide application of the exploration, exploitation, and development fields with a great success. For example, in a best-guess velocity model where a first approximation to the depth section is developed then iteratively altered to conform to the physical acquired data.

3-D modeling. Since the subsurface is a three-dimensional solid, two-dimensional assumptions limit the interpreter's analysis. Currently, the seismic industry is using 3-D acquisition and processing, and as it becomes the standard method, modeling will be done in three dimensions also. Some 3-D modeling is now performed, as the computer technology is developed to apply and improve these techniques.

Conclusions. The seismic exploration method attempts to accurately define subsurface geologic structures and stratigraphy. The seismic sections output from seismic data processing can be thought of as seismic or acoustic models of the subsurface. The modeling process uses assumptions regarding the geologic structure and stratigraphy that produced the acoustic model and tests the model against physical constraints and the real data.

There are three advantages in building models.

- Modeling forces a closer look at mechanisms causing seismic distortion.
- Modeling costs much less than relying on the drill to test an interpretation.
- Modeling is the best method available for geophysicists to develop the insights required for data interpretation.

Seismic inversion and wavelet processing

A new technique in signal data processing called *wavelet processing* has been developed to help obtain the better resolution for the detection of thin layers and to provide improved data for stratigraphic interpretation. The objective of wavelet processing is to optimize the shape of the seismic pulse and make it a symmetrical or zero-phase wavelet, which is the simplest form and the one the interpreter desires.

The seismic trace is often described as the convolution of a waveform with the reflectivity series. It can be expressed by the equation:

$$f(t) = c(t) * p(t) + n(t) \quad (7.2)$$

where

$f(t)$ = the seismic trace

$c(t)$ = random reflection coefficient series

$p(t)$ = pulse waveform

$n(t)$ = additive random noise

* = the convolution notation

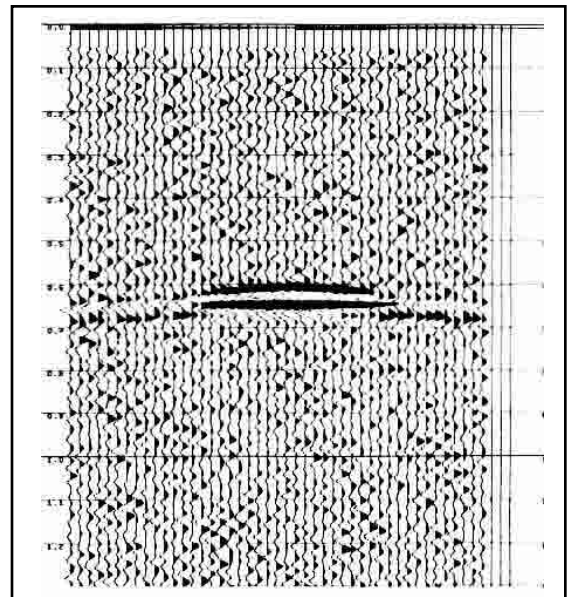


Fig. 7-29 Random Noise Added to the Wavelet Seismogram

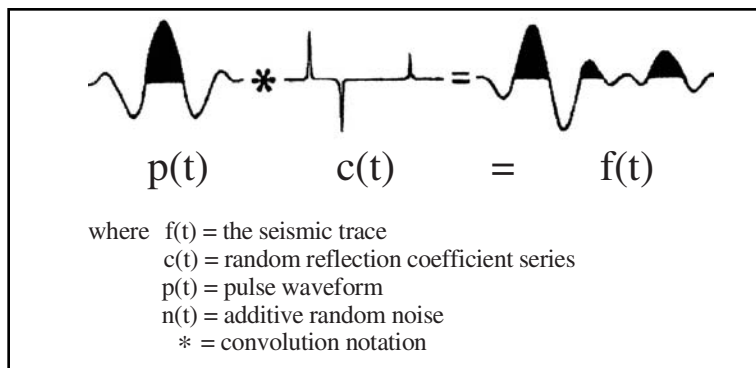


Fig. 7-30 The Seismic Trace

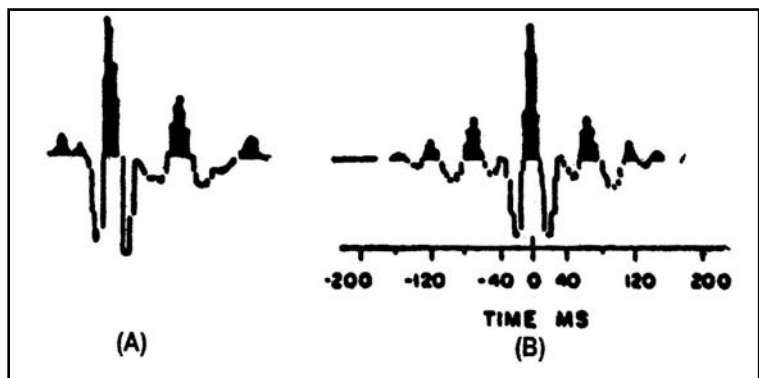


Fig. 7-31 Direct Measurement of Seismic Waveform

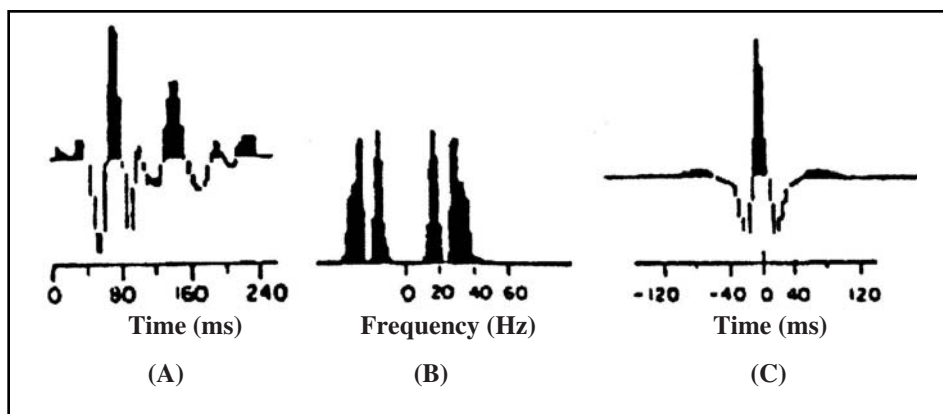


Fig. 7-32 Deterministic Measurement of Seismic Waveform

reflectivity series are log measurements or from reasonable geological parameters. A common approach is to assume that the water-bottom reflection event, which is free of refraction arrival events, emulates a good approximation to a single reflection event. This method is shown in Figure 7-32.

The primary assumption for $c(t)$ is that it is a random and unpredictable series. Figure 7-30 illustrates Equation 7.2.

Wavelet extraction. Interest in wavelet estimation has generated several methods for extracting the wavelet from the seismic data. Included in these methods are

- direct measurements of seismic waveform
- deterministic wavelet extraction
- statistical estimation of the wavelet

Each of these methods has its merits and its drawbacks.

Direct measurement of noise-free seismic waveforms can be made only in the deep-water environment. Measurements made close to the source are termed *near-field* source signatures, while those made at a distance comparable to that of reflected events are called *far-field* source signature. The effect of the ghost reflections, source arrays, instrumentation filters, and the cable must be accounted for in order to produce a valid representation of the waveform found on the seismic trace. Figure 7-31a is a measured near-field waveform derived from an airgun signature. Corrections were applied for surface reflection, so this waveform should match the far-field wavelet that propagates along the surface. Wavelet processing with this wavelet will give a zero-phase symmetrical waveform as shown in Figure 7-31b.

A basic assumption in deterministic wavelet extraction is that in a noise-free, multiple-free seismic trace, the trace may be regarded as a convolution of the reflectivity series with the wavelet. If the reflectivity series is determined, then it can be removed to reveal the estimate of the basic wavelet. Sources of the

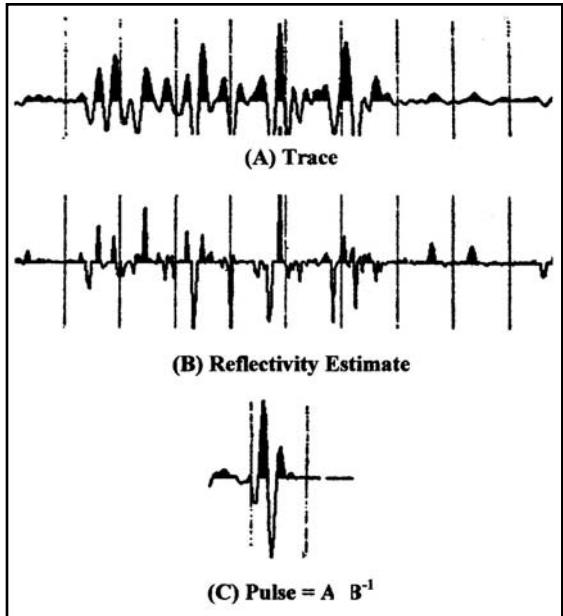


Fig. 7-33 Statistical Estimation of Wavelet

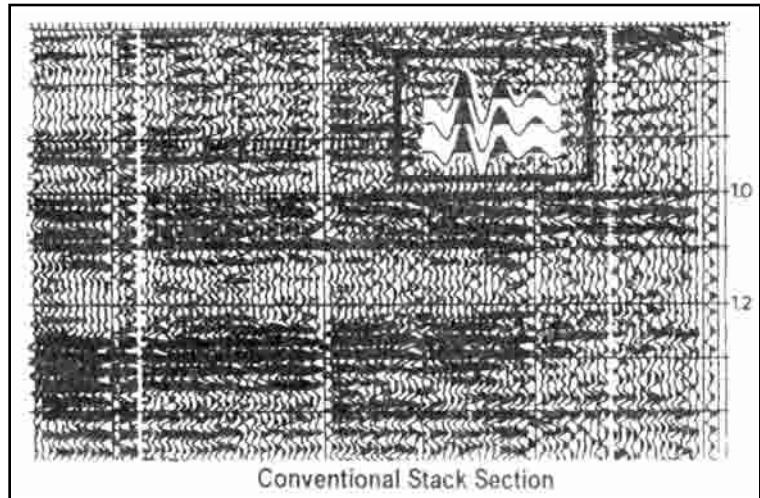


Fig. 7-34 Statistical Method of Wavelet Processing with 12 Traces

If the two previous approaches fail in estimating the waveform, then a statistical approach can be applied. One method in this category is *spiking deconvolution* to estimate the reflection coefficient. This approach must reflect the assumption of the earth model (Fig. 7-33).

Other methods of waveform estimation include *homomorphic filters* and *structural deconvolution*. Discussion of these methods is beyond the scope of this book.

Estimates of signal waveforms allow the design of filters that optimize the amplitude and phase spectrum within the recorded bandwidth.

Equation 7.3 provides a means to design a unique operator for each seismic trace.

$$h(t) = \frac{\hat{p}(t)}{p(t)} \quad (7.3)$$

where

$h(t)$ = shaping filter

$p(t)$ = estimated pulse

$P(t)$ = autocorrelation of $p(t)$

\wedge Denotes time reversal

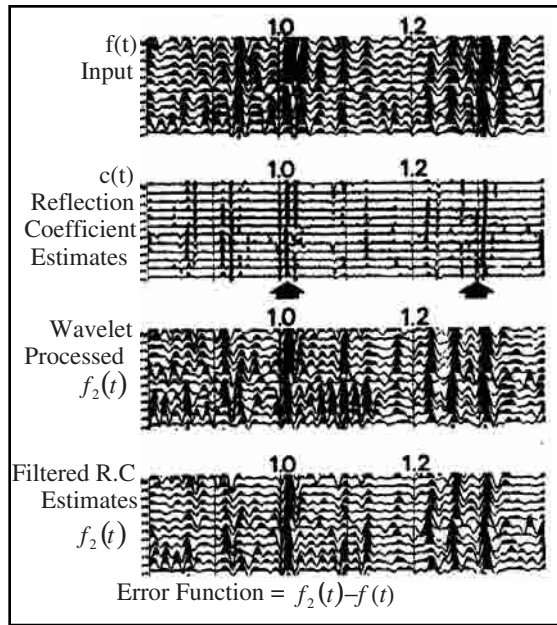


Fig. 7-35 Statistical Method of Wavelet Processing

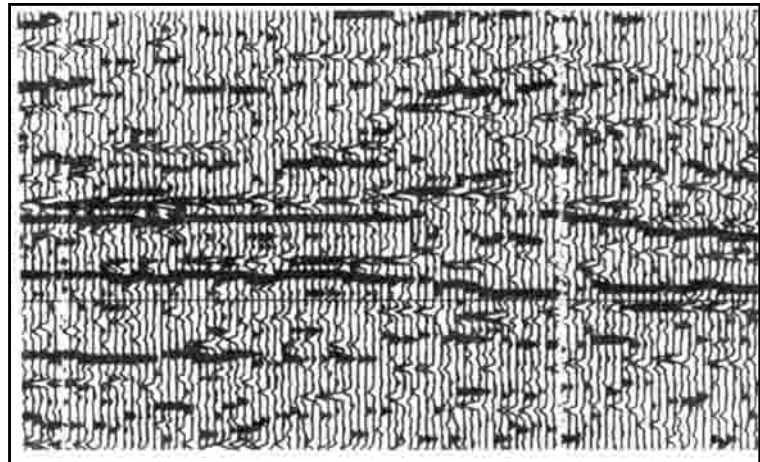


Fig. 7-36 Estimated Reflection Coefficients

Division by the autocorrelation levels the frequency spectrum and then corrects the phase spectrum to zero phases. This design is more effective than the standard deconvolution filters. No assumption of the phase is needed, and band limiting of the method suppresses high-frequency noise. Pioneers of this approach include Robinson (1963) and Treitel and Peacock (1969). Stone, et al. (1977) proposed that method for extracting the wavelet from the seismic trace using reflection coefficient estimates. The procedure for estimating, evaluating, and correcting the seismic reflection coefficient from seismic data is summarized as follows:

1. estimate the reflection coefficients by applying a multi-channel, predictive error, adaptive operator (Burg 1975)
2. use the estimates to extract and apply a wavelet that shapes the trace wavelet to zero phase
3. filter the estimates with a zero-phase band pass filter and compare to the wavelet-processed data
4. compute the difference between the filter spike estimates and the wavelet-processed data to create an error function
5. analyze the error function for correction to the estimates

Addition of the corrections to the estimates gives the seismic reflection coefficients. Figures 7-34 and 7-35 illustrate these steps.

Wavelet processing and stratigraphic interpretation. Wavelet processing can solve many stratigraphic interpretation problems. These include removing instrumental filters and establishing correct polarity and arrival time. As a result:

- a symmetrical waveform is assured and resolution of closely spaced layers is optimal for the bandwidth
- well log synthetics can be easily related to the seismic data, as both have a symmetrical waveform
- lines recorded with different sources, methods, and instruments can be made to tie
- look-alike anomalies can be located by lateral correlation on the wavelet section displays

Estimated reflection coefficients can be displayed by using a large plotting scale for a close look and to investigate a particular zone of interest. See Figure 7-36.

A popular way to display reflection coefficient estimates is to integrate them:

$$V_{i+1} = \frac{V_i(1+R)}{(1-R)} \quad (7.4)$$

where

V_{i+1} = the i^{th} interval velocity, in unit distance per second

R_i = reflection coefficient

This transforms the reflection coefficient estimates to interval velocities. Such integration often reveals more unnoticed anomalies.

Advantages of using the acoustic impedance log display include

- the interval velocity displays are easier to correlate with well log data
- they are handy and clearly show lateral variations
- zones of exceptional porosity are often detectable

Such a display, devised by Lindeth (1977) from strongly spiked deconvolution of seismic data was called a *seislog*.

Wavelet processing techniques. Figure 7-37 illustrates the sequence of wavelet processing techniques using the statistical method of estimating the reflection coefficient series from the seismic data. Figure 7-37a represents a final stack section, normally of mixed phase. It is easier for the interpreter to work with a simple wavelet shape. Through wavelet processing, the section will be converted to a zero-phase stack. The part of the section inside the rectangle is used to observe effect of the processing sequence.

Figure 7-37b shows the raw reflection coefficient estimates, using the Burg algorithm, which is a predictive, adaptive solution of structural deconvolution. Figure 7-37c is the wavelet-processed, zero phase stack. Figure 7-37d is the refined estimates. Figure 7-37e shows the filtered reflection coefficient with zero-phase wavelet. Note the similarity of c and e, which gives confidence that this statistical approach is a reliable method to correct the phase of the seismic data to zero-phase pulse.

Figure 7-38a is a seismic section on which arrows indicate two geologic markers. The upper marker is a discrete—well-separated—reflector that is present throughout but not very well defined. The lower one is a limestone layer 85 feet thick. Encased in shale, the top of the limestone should give a strong, positive response followed by a strong negative. There is no indication of this signature in the section. Figure 7-38b is the estimated reflection coefficient. The discrete reflector is clearly separated. Top and bottom of the limestone layer are crisply defined. Interpretation of thin layers can be

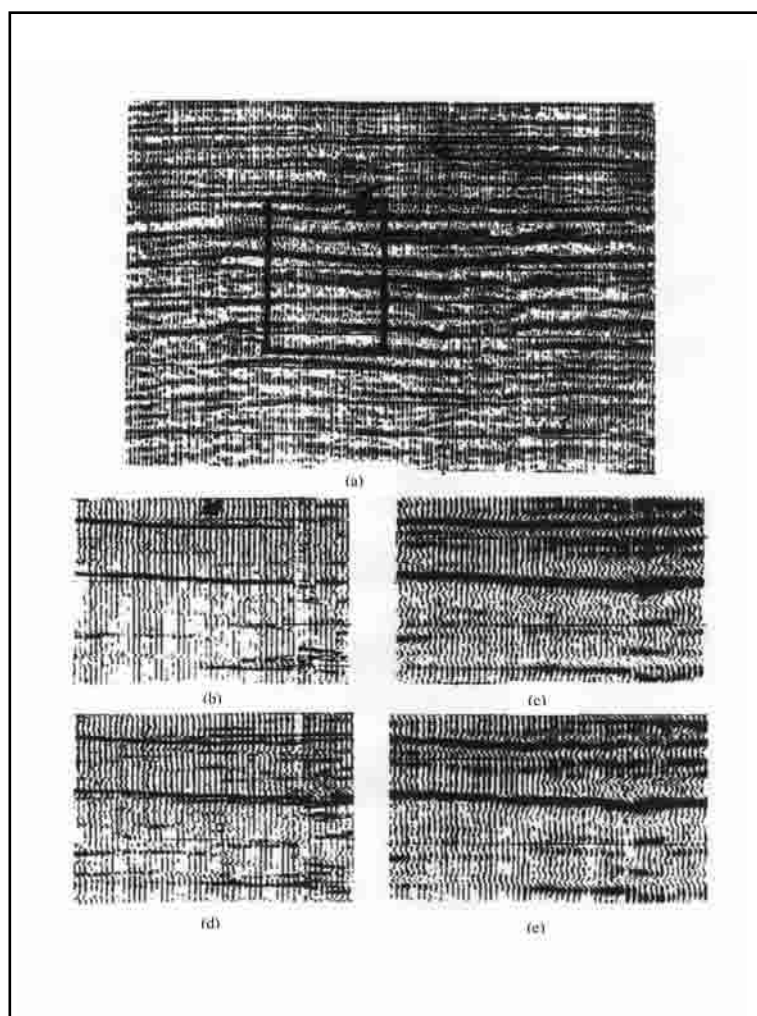


Fig. 7-37 Sequence of Wavelet Processing Technique

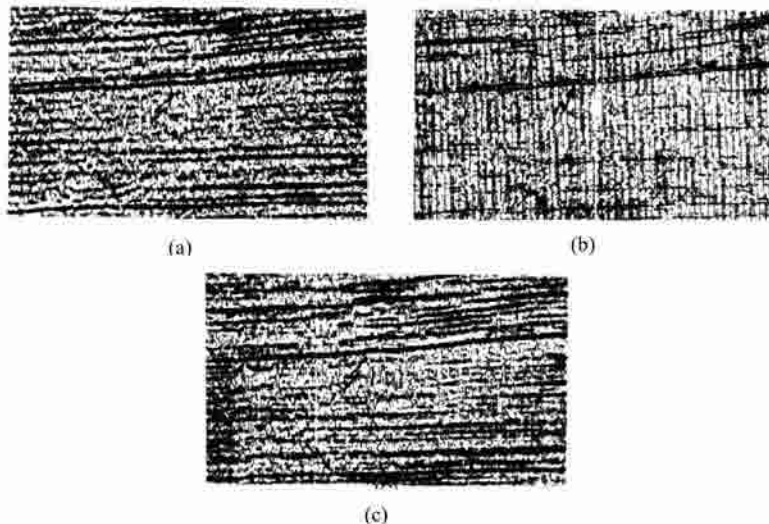


Fig. 7-38 Enhanced Interpretation from Wavelet Processing

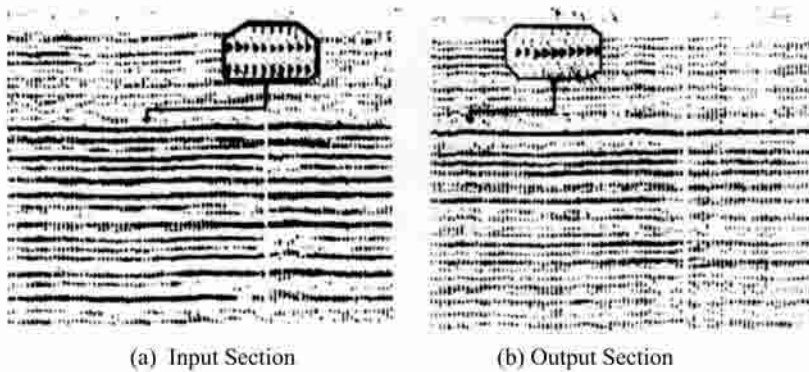


Fig. 7-39 Wavelet Processing and Better Interpretation

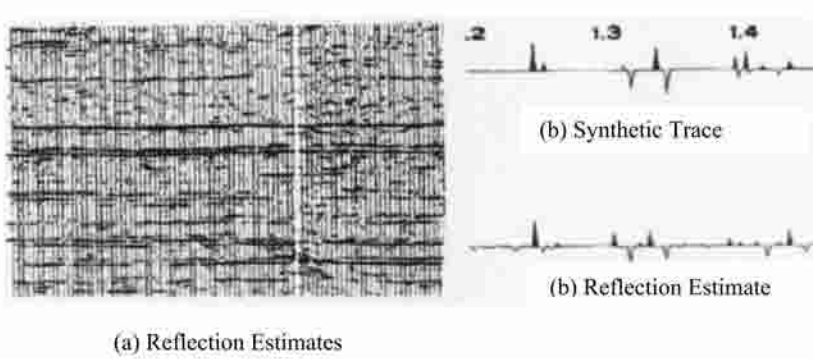


Fig. 7-40 Reflection Estimates

Low-frequency data can obscure small faults and make their delineation difficult. Even rather sizeable faults can be less obvious. In Figure 7-42a, the arrow at 1 marks a layer that appears to be continuous, although there is a possible amplitude anomaly just below the arrow at 2. The apparent time sag on the deeper event reinforces the initial interpretation.

attempted on an expanded-scale display of the estimated reflection coefficient. In Figure 7-38c the estimated reflection coefficient was used to derive the basic wavelet, and the wavelet was applied to correct the phase to zero-phase. The limestone is indicated by the expected narrow-band response of a positive followed by a negative.

Figure 7-39 is another illustration of enhanced interpretation through wavelet processing of seismic data. Figure 7-39a shows the top of a chalk marker with overlying shale. The response is not clear; a strong positive reflection coefficient would be expected. Figure 7-39b is the wavelet-processed section. The top and bottom of the chalk are clearly defined, and surface effects resulting in low frequency zone are removed.

Figure 7-40a shows the reflection coefficient estimates. The sharp definition of the reflectors is clearly seen. Figure 7-33b is a synthetic trace and Figure 7-26c is the corresponding reflection estimate. Comparing the reflectivity series derived from well logs and reflection coefficient estimates from seismic data shows a good match, which supports the validity of this approach. Also, note the detection of the transition zone going into the chalk.

Figure 7-41 compares the wavelet-processed portion of a stacked section with a synthetic seismogram that was generated by convolving the reflectivity series from the well log data with a zero-phase wavelet. A very good match is obtained. The blank portion of the synthetic seismogram is due to the lack of data below total depth of the well. Note the good match above this point.

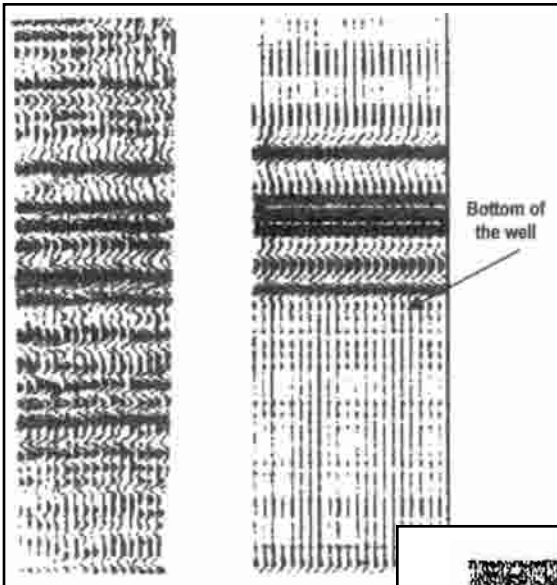


Fig. 7-41 Synthetic Seismograms and Wavelet Processing

Figure 7-42b gives a very different impression from the reflectivity estimates of Figure 7-42a. The simplification of the response reveals discontinuities and amplitude contrast. This increased discrimination shows that the structure is a graben fault.

Stratigraphic application. An objective of wavelet processing is to improve the ability to interpret subtle stratigraphic targets. Small reefs are among the most difficult of these targets. Reef signatures are dim, rather than bright, and the structural evidence is very slight. Figure 7-43a is an example of a section over such a target. An arrow indicates the reef-bearing reflection group. Apparent thickening and a reflection discontinuity detect the reef.

Figure 7-43b shows the reflection coefficient estimates. There is a considerable improvement in the lateral character consistency and resolution. The expanded scale in Figure 7-44 shows several reflection layers, which can help in better interpretation of the reef boundaries. Figure 7-43c shows a wavelet-processed stack. Note that the correlation on each side of the reef is more definite as the section becomes zero-phase with simple wavelet shape. Figure 7-43d is the acoustic impedance log. It shows a relative decrease of the velocity (deflection to the left) that is an indication of porosity. This is a qualitative analysis, and can be used to locate similar anomalies.

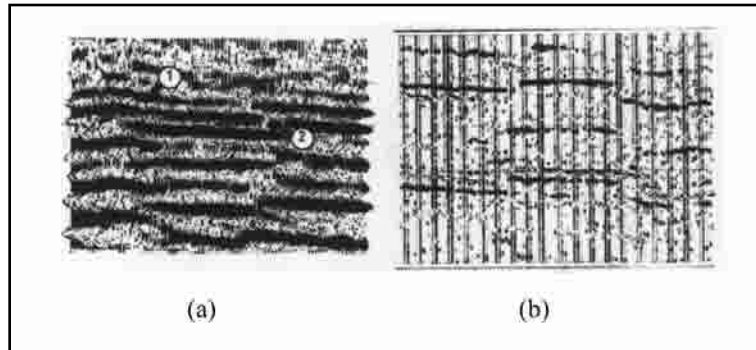


Fig. 7-42 Fault Detection from Estimated Reflection Coefficient

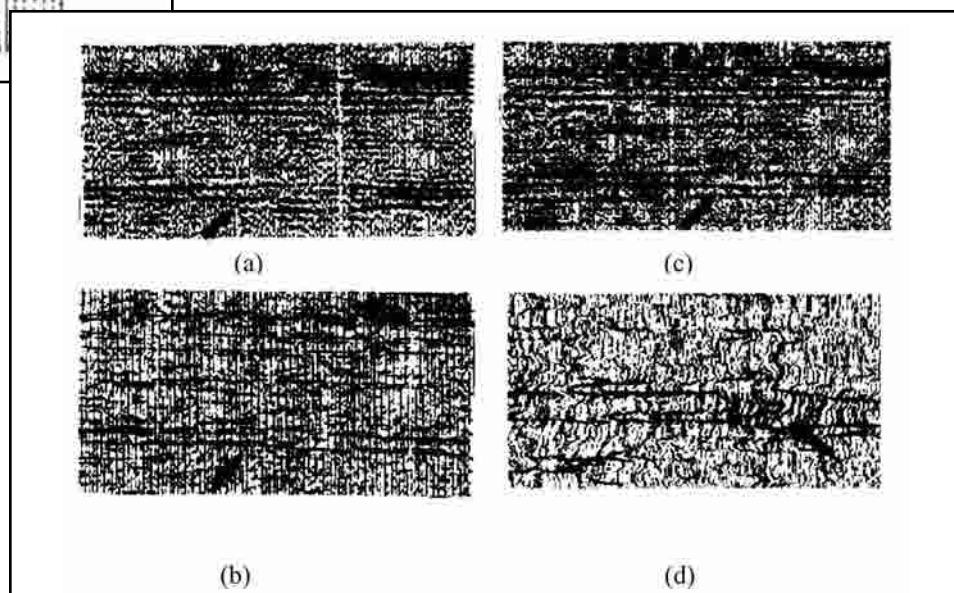


Fig. 7-43 Stratigraphic Application: Reef Showing (a) Final Stacked Section, (b) Estimated Reflection Coefficient, (c) Wavelet Processed Stack, and (d) Interval Velocity Log

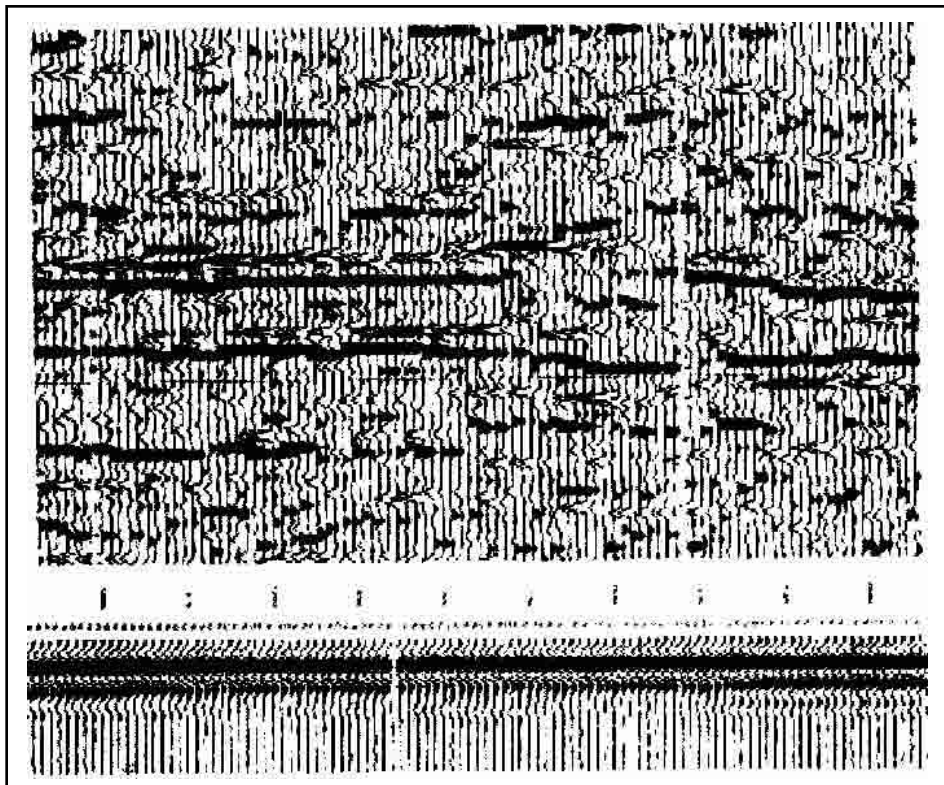


Fig. 7-44 Stratigraphic Application Using Wavelet Processing

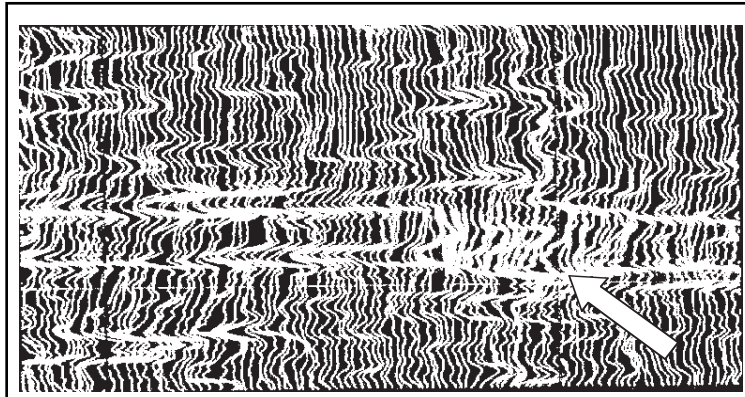


Fig. 7-45 Interval Velocities on the Reef Example

The top part of Figure 7-44 is an expanded-scale version of the reflection coefficient of Figure 7-43c and the bottom part is a set of extracted wavelets from every trace on the seismic section. The inverse will be applied to make the stack traces zero phase. Figure 7-45a is an expanded-scale version of the acoustic impedance log of Figure 7-43d. The heavy line is a synthetic log, derived from the integration of the sonic and density logs and inserted in the seismically derived acoustic impedance log. A decent match is evident.

Reflection coefficients can be converted to an interval velocity log. If density is incorporated with interval velocity from logs, then an acoustic impedance log can be obtained as shown below. The heavy wiggle is the synthetic seismogram. There is a good match with the seismic acoustic impedance log. Interval velocity or acoustic impedance decrease around the reef is observed. This is a qualitative measure, and can be used to locate similar anomalies along the seismic profile.

Summary. Estimating the reflectivity series provides information needed to optimize the basic wavelet in the seismic data.

There are several methods for wavelet estimations. A technique suited to seismic data is predictive and adaptive deconvolution, known as the *Burg algorithm*. It provides an estimate of the reflectivity series from the seismic trace. An estimated wavelet will be applied to yield a zero-phase seismic section. Some of the benefits that may result from successful wavelet estimation are

- better correlation with well logs, improved resolution of thin layers
- delineation of small fault patterns
- removal of near-surface effects on subtle stratigraphic traps

Caption and Courtesy List

Fig. 1-1	Seismic Waves from Big Bertha's Firing
Fig. 1-2	Dip Shooting
Fig. 1-3	Typical 2-D Seismic Geometry
Fig. 1-4	Continuous or Single-fold Subsurface Coverage
Fig. 1-5	CMP Shooting
Fig. 1-6	Multi-fold Shooting
Fig. 1-7	Meandering Stream Channel
Fig. 1-8	3-D Prospect Layout
Fig. 2-1	A Fossil Sequence
Fig. 2-2	Dating Rocks from Fossils
Fig. 2-3	Internal Structure of the Earth
Fig. 2-4	The Lithosphere
Fig. 2-5	Mountains, Ridges, and Rises of the World
Fig. 2-6	Seafloor Spreading
Fig. 2-7	Mantle Convection Currents
Fig. 2-8	Tectonic Plate Boundaries
Fig. 2-9	Tectonic Plate Model
Fig. 2-10	Pangea, the Universal Continent, about 200 Million Years Ago
	(modified from R.S. Dietz and J.C. Holden, <i>Scientific American</i> , 1970)
Fig. 2-11	The Continents in Their Present Positions and Their Projected Positions 50 Million Years from Now
	(After R.S. Dietz and J.C. Holden, <i>Scientific American</i> , 1970)
Fig. 2-12	Top Part of the Earth's Crust
Fig. 2-13	Formation of Igneous Rocks
Fig. 2-14	The Rock Cycle
Fig. 2-15	Sorting
Fig. 2-16	Prevalent Sedimentary Rock Types
Fig. 2-17	The East Texas Oil Field
Fig. 2-18	Strike and Dip
Fig. 2-19	Strike, Dip, and Plunge
Fig. 2-20	Stress-strain Relationship
Fig. 2-21	Types of Stress
Fig. 2-22	Folding of Rocks
Fig. 2-23	Monoclines, Synclines, and Anticlines
Fig. 2-24	Terms Describing Anticlines
Fig. 2-25	Symmetric and Asymmetric Folds
Fig. 2-26	Anticlinal Dome, Overhead View
Fig. 2-27	Eroded Folds
Fig. 2-28	An Eroded, Plunging Syncline in Northwest Africa (<i>Photo by U.S. Air Force</i>)
	and an Eroded, Plunging Anticline in the Zagros Mountains of Iran
	(<i>Photo by Aerofilms, Ltd., through courtesy of John S. Shelton</i>)
Fig. 2-29	Joints
Fig. 2-30	Fault Motion
Fig. 2-31	Dip Slip Faults
Fig. 2-32	Well Bores through Normal and Reverse Faults
Fig. 2-33	Fault Displacement along the Great Glen Fault
Fig. 2-34	Horsts and Grabens
Fig. 2-35	Rollover Anticline
Fig. 2-36	The Fuel Cycle
Fig. 2-37	Molecular Forms of Petroleum
Fig. 2-38	Migration of Hydrocarbons
Fig. 2-39	Components of Clastic Sedimentary Rocks
Fig. 2-40	The Oil Window
Fig. 2-41	Effect of Grain Size on Porosity and Permeability
Fig. 2-42	Geothermal Gradient in Sedimentary Basins

Fig. 2–43	Hydrostatic Pressure Gradient
Fig. 2–44	Anticline Trap
Fig. 2–45	Reservoir Spill Point
Fig. 2–46	Reservoir Fluid Types
Fig. 2–47	Asymmetrical Anticline Trap
Fig. 2–48	Fault Trap
Fig. 2–49	Growth Fault or Down-to-the-Basin Fault
Fig. 2–50	Fault Cutting Reservoir into Separate Accumulations
Fig. 2–51	Fault Trap with Multi-Level Production
Fig. 2–52	Western Overthrust Belt
Fig. 2–53	The Stratford Field
Fig. 2–54	Oil Fields Formed by Angular Unconformities
Fig. 2–55	Production from Sands Above Angular Unconformity, and Cross Section through the Bolivar Coastal Fields in Lake Maracaibo, Venezuela
Fig. 2–56	Reef Facies
Fig. 2–57	Reef Configurations
Fig. 2–58	The Alberta Reef Trend and the Redwater Oil Field
Fig. 2–59	Michigan Basin Silurian Reef Trend
Fig. 2–60	Lenticular Sand Shapes and Origins
Fig. 2–61	Bush City Pool
Fig. 2–62	Coastal Sand Pinch-outs
Fig. 2–63	Giant Oil Fields Formed by Salt Domes
Fig. 2–64	Fractured Reservoir Rock
Fig. 2–65	Granite Wash
Fig. 2–66	(workshop)
Fig. 2–67	(workshop)
Fig. 2–68	(workshop)
Fig. 2–69	(workshop)
Fig. 2–70	(workshop)
Fig. 2–71	(workshop)
Fig. 2–72	(workshop)
Fig. 2–73	(workshop)
Fig. 2–74	(workshop)
Fig. 2–75	(workshop)
Fig. 2–76	(workshop)
Table 2–1	Divisions of Geologic Time
Table 2–2	Clastic Grain Size Classification
Table 2–3	Chemical Composition of Petroleum
Table 2–4	Reservoir Rock Porosity
Table 2–5	Reservoir Rock Permeability
Table 2–6	Rock Grid
Fig. 3–1	Basic Elastic Moduli and Poisson's Ratio
Fig. 3–2	P- and S-waves
Fig. 3–3	SV and SH Waves
Fig. 3–4	Rayleigh Waves
Fig. 3–5	Love Waves
Fig. 3–6	Basic Wave Parameters
Fig. 3–7	Fermat's Principle
Fig. 3–8	Snell's Law
Fig. 3–9	Critical Refraction and Head Waves
Fig. 3–10	Wavefronts and Rays
Fig. 3–11	Wavefronts from a Point Energy Source
Fig. 3–12	Huygen's Principle
Fig. 3–13	P- and SV-wave Reflection Coefficients
Fig. 3–14	P-wave Normal Incidence Reflection and Transmission
Fig. 3–15	Earth Reflectivity Function
Fig. 3–16	Noise-Free Seismic Trace Derived from Earth Reflectivity Function

Fig. 3-17	Direct Waves and Shallow Reflections
Fig. 3-18	Reverberations or Water Bottom Multiple Reflections
Fig. 3-19	Multiple Reflections
Fig. 3-20	Guided Waves
Fig. 3-21	Diffractions
Fig. 3-22	Effect of Ambient Noise on Seismic Trace
Fig. 3-23	Schematic Land Seismic Record
Fig. 3-24	A Seismic Shot Record
Fig. 3-25	Digital Recording
Fig. 3-26	Effect of Sample Period
Fig. 3-27	Aliasing
Fig. 3-28	Measuring the Earth's Impulse Response
Fig. 3-29	Convolution
Fig. 3-30	Cross-correlation of $\{y_p\}$ onto $\{x_m\}$
Fig. 3-31	Cross-correlation of $\{x_m\}$ onto $\{y_p\}$
Fig. 3-32	Autocorrelation of $\{x_m\}$
Fig. 3-33	Single Frequency Sinusoids
Fig. 3-34	Amplitude and Phase Spectra for Single-frequency Sinusoids
Fig. 3-35	Signal Synthesis and Decomposition
Fig. 3-36	Time and Frequency Domains
Fig. 3-37	Effect of Time Reversal
Fig. 3-38	Frequency Filter Types
Fig. 3-39	Band-pass Filtering
Fig. 3-40	Anti-alias Filters
Fig. 3-41	Phase Definitions
Fig. 3-42	Effect of Adding 90° to Phase Spectrum
Fig. 3-43	Changes in Waveform with Successive Additions of 90° Phase
Fig. 3-44	Effect of Adding Linear Phase-to-phase Spectrum
Fig. 3-45	Linear Phase Slope and Time Shift
Fig. 3-46	Phase and Wavelet Shape
Fig. 3-47	Minimum-, Maximum-, and Mixed-phase Wavelets
Fig. 3-48	Effect of Bandwidth
Fig. 3-49	Bandwidth and Vertical Resolution
Fig. 3-50	A Wedge or Pinch-out
Fig. 3-51	Phase and Resolution
Fig. 3-52	Horizontal Resolution and Fault Displacement
Fig. 3-53	The Fresnel Zone
Fig. 3-54	Spatial Sampling
Fig. 3-55	A Seismic Record as a Two-dimensional Array
Fig. 3-56	The F-K Plane
Fig. 3-57	Noise Record in T-X and F-K Domains
Fig. 3-58	Plane Wave Incident on Surface
Fig. 3-59	Spatial Aliasing as a Function of Dip and Frequency
Fig. 3-60	Linear Events in T-X and F-K
Fig. 3-61	Linear Dipping Events
Fig. 3-62	Effect of Group Interval on Spatial Aliasing
Fig. 3-63	Separation of Signal and Noise in F-K
Fig. 3-64	Definition of the Ray Parameter
Fig. 3-65	The Radon Transform
Fig. 3-66	Event Mapping between T-X and τ -p Domains
Fig. 3-67	CMP Record in T-X Domain and τ -p Domain
Fig. 3-68	Trace Interpolation with the Radon Transform
Fig. 3-69	A Clock Pendulum and Its Energy Cycle
Fig. 3-70	Complex Trace Analysis
Fig. 3-71	(workshop)
Fig. 3-72	(workshop)
Fig. 3-73	(workshop)
Fig. 3-74	(workshop)
Fig. 3-75	(workshop)

Table 3-1	Source-Generated Noise
Table 3-2	Ambient Noise
Table 3-3	Nyquist Frequency
Table 3-4	Vertical Resolution
Table 3-5	Variation of the Fresnel Zone with Time and Frequency
Table 3-6	T-X and t-p Relationships
Table 3-7	Output Frequencies for Various Sample Periods
Fig. 4-1	Layout for Intensive Refraction Shooting
Fig. 4-2	T-X Plot for Inline Refraction Shooting
Fig. 4-3	Simplified Earth Model based on Data from Figure 4-2
Fig. 4-4	Arc and Broadside Shooting
Fig. 4-5	(workshop)
Fig. 5-1	Target Reference
Fig. 5-2	Simple Example of Vertical Reference Datum
Fig. 5-3	Geoid
Fig. 5-4	Horizontal Reference Datum Example
Fig. 5-5	Geodetic Latitude
Fig. 5-6	Longitude Measurement
Fig. 5-7	Horizontal Reference Datum
Fig. 5-8	Geocentric and Non-Geocentric Ellipsoids
Fig. 5-9	Datum Transformation
Fig. 5-10	Map Projection
Fig. 5-11	Range-Range LOPs
Fig. 5-12	GPS Receivers and Antenna
Fig. 5-13	Antenna Motion
Fig. 5-14	Source and Receiver Assumptions for 2-D Recording
Fig. 5-15	Cable Feathering
Fig. 5-16	Streamer Curvature
Fig. 5-17	Source and Receiver Positioning, 1985–1991 and Current
Fig. 5-18	Vessel Heading Terms
Fig. 5-19	Bird/Compass on Test Rig (<i>courtesy WesternGeco</i>)
Fig. 5-20	Traditional Applications—Cable Shaping
Fig. 5-21	Acoustic Configuration Diagram (<i>courtesy WesternGeco</i>)
Fig. 5-22	An Integrated Solution
Fig. 5-23	Statistical Analysis
Fig. 5-24	The Airgun Technique
Fig. 5-25	Airgun Operation
Fig. 5-26	The Bubble Effect
Fig. 5-27	Airgun Pressure—Volume Relationship
Fig. 5-28	Waveform Synthesis by Airgun Arrays
Fig. 5-29	Measurement of the Far-field Signature
Fig. 5-30	Time Domain Attributes
Fig. 5-31	Airgun Frequency Domain Attributes
Fig. 5-32	Airgun Array Signatures and Parameters
Fig. 5-33	Signature Variation with Frequency and Depth
Fig. 5-34	A Single Sleeve Gun, a Disassembled Sleeve Gun, a Sleeve Gun with a Mounting Harness, and a Family of Sleeve Guns (<i>courtesy WesternGeco</i>)
Fig. 5-35	Side View of a Typical Sub-array Configuration
Fig. 5-36	Plan View of a Typical Source Array
Fig. 5-37	Streamer and Source Depth Ghost Notches
Fig. 5-38	Ghost Response at 5 and 10 m
Fig. 5-39	Source Array Effects
Fig. 5-40	The Explosive Technique
Fig. 5-41	Explosive Source Operation
Fig. 5-42	Measuring the Far-Field Signature of an Explosive Source
Fig. 5-43	Effect of Charge Size
Fig. 5-44	Charge Depth Test (<i>After M.R. Hewitt, Seismic Data Acquisition Co., 1980</i>)

Fig. 5–45	Explosive Cord as a Seismic Energy Source
Fig. 5–46	Truck-Mounted Vibrator Components (<i>courtesy WesternGeco</i>)
Fig. 5–47	Side View of a Truck-Mounted Vibrator (<i>courtesy WesternGeco</i>)
Fig. 5–48	Vibrator Operation
Fig. 5–49	Effect of Spike on Vibrator Cross-Correlations
Fig. 5–50	Vibroseis Correlation
Fig. 5–51	Klauder Wavelet and Resolution
Fig. 5–52	Width
Fig. 5–53	Resolution Versus Sweep Bandwidth <i>(Waveforms adapted from Catalog of Klauder Wavelets by Robert L. Geyer, Seismograph Services Corp.)</i>
Fig. 5–54	Frequency Versus Time for Various Sweep Types
Fig. 5–55	Pilot Sweeps for $T^{0.3}$, Logarithmic, Linear, Exponential, and T^3
Fig. 5–56	Vibroseis Correlation Ghosts
Fig. 5–57	Vibroseis Correlation Ghost Examples (<i>courtesy WesternGeco</i>)
Fig. 5–58	Effect of Surface Material
Fig. 5–59	Effect of Taper on Pilot Autocorrelation
Fig. 5–60	Attenuation of Sweep Distortion by Cross-Correlation
Fig. 5–61	Piezoelectric Crystals
Fig. 5–62	Hydrophone Equivalent Circuit
Fig. 5–63	Input/Output Model 2522 Near-field Hydrophone
Fig. 5–64	Hydrophone Ghosts
Fig. 5–65	Amplitude Response for 12.5 m Group, 14 Phone Array
Fig. 5–66	Geophone Components
Fig. 5–67	Geophone Magnetic Field
Fig. 5–68	Three-Component Geophones
Fig. 5–69	Geophone Damping
Fig. 5–70	Geophone Phase Response
Fig. 5–71	Spurious Resonance or Parasitics (<i>courtesy WesternGeco</i>)
Fig. 5–72	Geophone Tilt
Fig. 5–73	Geophone Planting Conditions
Fig. 5–74	Effect of Geophone Planting Conditions on Amplitude and Phase Responses
Fig. 5–75	Noise Spread and Shooting Procedures
Fig. 5–76	Noise Test Example (<i>courtesy WesternGeco</i>)
Fig. 5–77	Attenuation of Ground Roll with Band-pass Filter (<i>courtesy WesternGeco</i>)
Fig. 5–78	Noise Analysis or Walk Away (<i>from Encyclopedia of Exploration Geophysics, R.E. Sheriff, 1991</i>)
Fig. 5–79	Array Configurations
Fig. 5–80	Ideal Receiver Response for Space Domain x and Wave Number Domain K
Fig. 5–81	Linear, Equally Spaced, Equally Weighted Array
Fig. 5–82	Conventional Representation of Desired Response of Linear, Equally Weighted, Equally Spaced Array
Fig. 5–83	Response of Linear, Equally Weighted, Equally Spaced Arrays, 6 Element and 12 Element
Fig. 5–84	Alternative Methods of Representing the Spatial Response of Linear, Unequally Weighted, Equally Spaced Arrays
Fig. 5–85	Decomposing Linear, Unequally Weighted, Equally Spaced Arrays
Fig. 5–86	Linear Array with Variable Weights
Fig. 5–87	Geophone Layouts in the Presence of Large Elevation Differences
Fig. 5–88	Seismic Amplitudes
Fig. 5–89	24-Bit Electronics
Fig. 5–90	Streamer Configuration
Fig. 5–91	Comparison between 16-Bit and 24-Bit Systems
Fig. 5–92	Land Ground System Configuration
Fig. 5–93	Recording Room on the Western Monarch (<i>courtesy WesternGeco</i>)
Fig. 5–94	Non-Return-to-Zero Encoding
Fig. 5–95	Tape Schematic
Fig. 5–96	Multiplexed and De-multiplexed Data
Fig. 5–97	Typical 2-D Geometry
Fig. 5–98	Maximum and Minimum Offset Requirements
Fig. 5–99	Maximum and Minimum Offset Requirements for Refracted Arrivals

Fig. 5–100	Off-End Spread
Fig. 5–101	Symmetric Split Spread
Fig. 5–102	Up-dip or Down-dip?
Fig. 5–103	Start-of-Line Procedures, Normal Shooting
Fig. 5–104	Start-of-Line Procedures, Fast Ramp On to Full Fold
Fig. 5–105	Obstacle Avoidance at the Source Array
Fig. 5–106	Recovery Shots
Fig. 5–107	Typical 3-D Geometry
Fig. 5–108	Migration Aperture from Dip for Constant Velocity (Straight Ray Paths)
Fig. 5–109	Migration Aperture from Dip for Constant Velocity (Straight Ray Paths) Using Geologic Depth
Fig. 5–110	Migration Aperture from Curved and Straight Ray Paths
Fig. 5–111	Migration Aperture from Fresnel Zone
Fig. 5–112	Distribution of Diffraction Energy (<i>Diffraction energy distribution according to Claerbout</i>)
Fig. 5–113	Determining Total Migration Aperture
Fig. 5–114	Total Survey Area Required to Correctly Image Target
Fig. 5–115	Bins or Cells
Fig. 5–116	Bin Shapes
Fig. 5–117	Subsurface Coverage in Marine Surveys
Fig. 5–118	Static Binning
Fig. 5–119	Overlapping or Wide Binning
Fig. 5–120	Effect of Multiple Streamers and Multiple Sources on Data Acquisition
Fig. 5–121	Conventional Straight Line or Racetrack Shooting
Fig. 5–122	Circle Shooting
Fig. 5–123	Approaches to Salt Dome Shooting
Fig. 5–124	Azimuthal Variation in Conventional One-boat Operation and Two-boat Undershoot Operations
Fig. 5–125	Obstacle Avoidance, One-boat Operation and Two-boat Undershoot
Fig. 5–126	Obstacle Avoidance with Two Boats
Fig. 5–127	Acquisition Template
Fig. 5–128	Swath Layout Method, Swath Shooting Method
Fig. 5–129	Shot Index
Fig. 5–130	Offset and Azimuth Variation in a Bin (<i>after M. Galbraith, 3-D Survey Design by Computer, 1994</i>)
Fig. 5–131	A Star Array and Its Polar Response
Fig. 5–132	Straight Line Method (<i>after M. Galbraith, 3-D Survey Design by Computer, 1994</i>)
Fig. 5–133	Another Type of Swath Shooting (<i>after M. Galbraith, 3-D Survey Design by Computer, 1994</i>)
Fig. 5–134	The Brick Pattern (<i>after M. Galbraith, 3-D Survey Design by Computer, 1994</i>)
Fig. 5–135	Odds and Evens (<i>after M. Galbraith, 3-D Survey Design by Computer, 1994</i>)
Fig. 5–136	The Zig-zag and Double Zig-zag Patterns (<i>after M. Galbraith, 3-D Survey Design by Computer, 1994</i>)
Fig. 5–137	The Non-orthogonal Pattern (<i>after M. Galbraith, 3-D Survey Design by Computer, 1994</i>)
Fig. 5–138	Bin Fractionation Method (<i>after M. Galbraith, 3-D Survey Design by Computer, 1994</i>)
Fig. 5–139	The Button Patch Method (<i>after M. Galbraith, 3-D Survey Design by Computer, 1994</i>)
Fig. 5–140	Recovery Shots with In-line Shift
Fig. 5–141	Recovery Shots with Cross-line Shifts
Fig. 5–142	(workshop)
Fig. 5–143	(workshop)
Fig. 5–144	(workshop)
Fig. 5–145	(workshop)
Fig. 5–146	(workshop)
Table 5–1	Surface-Based Navigation Systems
Table 5–2	Basic GPS Overview
Table 5–3	Airgun Specs and Array Parameters
Table 5–4	Correlation Ghost Start and Stop Times
Table 5–5	Selecting Geophone Parameter Values
Table 5–6	In-Water Systems Comparison
Table 5–7	Number Systems
Table 5–8	Pros And Cons Of Various Layout Strategies
	<i>(Source: M. Galbraith, 3-D Survey Design by Computer, 1994)</i>
Fig. 6–1	Vertical Stack

Fig. 6-2	Straight Stack
Fig. 6-3	Diversity Stack Time Gates
Fig. 6-4	Average Power of Each Trace in Each Gate
Fig. 6-5	Scalers for Each Gate
Fig. 6-6	Diversity Stack Scaling Functions
Fig. 6-7	Application of Diversity Scalers
Fig. 6-8	Diversity Stack Output
Fig. 6-9	Stack Comparison
Fig. 6-10	Need for Scaler Normalization
Fig. 6-11	Zero- and Minimum-phase Correlation
Fig. 6-12	Uncorrelated and Correlated Vibroseis Shot Records
Fig. 6-13	Typical Processing Sequence
Fig. 6-14	Typical Processing Sequence (continued)
Fig. 6-15	Typical Processing Sequence (continued)
Fig. 6-16	LMO Traces Display (<i>courtesy WesternGeco</i>)
Fig. 6-17	OBC Receiver Location
Fig. 6-18	A Stacking Diagram
Fig. 6-19	Trace Gathers
Fig. 6-20	Shot and CMP Traces with Geologic Dip
Fig. 6-21	Near-surface Model
Fig. 6-22	Effect of Variable Near Surface
Fig. 6-23	Static Corrections, Case I: Surface Source
Fig. 6-24	Static Corrections, Case IIa: Source in Weathering
Fig. 6-25	Static Corrections, Case IIb: Source in Subweathering
Fig. 6-26	First Breaks of Selected CMP Gathers (<i>courtesy WesternGeco</i>)
Fig. 6-27	First Break Ray Paths and T-X Plot
Fig. 6-28	Refraction Ray Path Segments
Fig. 6-29	Redundancy of Data in Refraction Statics Determination
Fig. 6-30	Refraction Elevation Model
Fig. 6-31	Field Record with No Gain Applied
Fig. 6-32	Spherical Divergence and Spherical Spreading
Fig. 6-33	Geometric Spreading Correction Example (<i>courtesy WesternGeco</i>)
Fig. 6-34	Programmed Gain Control
Fig. 6-35	Ray Paths of OBC Ghosts
Fig. 6-36	OBC Primary Plus Ghosts
Fig. 6-37	Hydrophone Ghosting
Fig. 6-38	Hydrophone Ghost Impulse Response
Fig. 6-39	Geophone Ghosting
Fig. 6-40	Geophone Ghost Impulse Response
Fig. 6-41	A Plot of Scale Factor $(1+R)/(1-R)$ for 360 Receiver Locations
Fig. 6-42	Transformation from T-X to F-K Domain
Fig. 6-43	Positive and Negative Cut Lines
Fig. 6-44	Filtering in the F-K Plane
Fig. 6-45	Transformation of Filtered Record from F-K to T-X Domain
Fig. 6-46	Noise Record in the T-X Domain and the F-K Domain (<i>courtesy WesternGeco</i>)
Fig. 6-47	Filtered Field Record in the F-K Domain and the T-X Domain (<i>courtesy WesternGeco</i>)
Fig. 6-48	Linear Moveout Applied to Linear Noise
Fig. 6-49	Field Record Dominated by Linear Noise (<i>courtesy WesternGeco</i>)
Fig. 6-50	Record of Figure 6-49 After Six Passes of Linear Noise Attenuation (<i>courtesy WesternGeco</i>)
Fig. 6-51	Instantaneous and Interval Velocities
Fig. 6-52	Single Horizontal Layer
Fig. 6-53	Reflection with Normal Moveout
Fig. 6-54	NMO Correction
Fig. 6-55	The NMO Correction Process
Fig. 6-56	The NMO Correction Process
Fig. 6-57	Effect of Velocity on NMO Correction
Fig. 6-58	NMO Stretch

Fig. 6-59	Input CMP Records, the Same Records after NMO Correction, and after NMO Mute
(courtesy WesternGeco)	
Fig. 6-60	Picked Versus Default Mutes (<i>courtesy WesternGeco</i>)
Fig. 6-61	RMS Velocity as the Replacement Velocity in the Multi-layer Situation
Fig. 6-62	NMO for Plane, Horizontal, and Iso-Velocity Layers
Fig. 6-63	Reflection from a Dipping Reflector
Fig. 6-64	A Dipping Reflector in 3-D
Fig. 6-65	Velocity Functions
Fig. 6-66	Velocity Analysis Location Used for Example
Fig. 6-67	The Velocity Sweep
Fig. 6-68	Semblance Plot
Fig. 6-69	Stack of CMPs Using the Nine Velocity Functions of Figure 6-68 (<i>courtesy WesternGeco</i>)
Fig. 6-70	CVS Display Used to Generate the Velocity Trend for the IVP Session (<i>courtesy WesternGeco</i>)
Fig. 6-71	Semblance Plot Generated from the Input Velocity Fan (<i>courtesy WesternGeco</i>)
Fig. 6-72	CMP 61 Corrected for NMO Using Velocity Function (<i>courtesy WesternGeco</i>)
Fig. 6-73	Semblance Plot with a Slower Velocity Picked for Event at 1729 ms (<i>courtesy WesternGeco</i>)
Fig. 6-74	Same as Figure 6-72 Except CMP 61 is Corrected for NMO Using the Modified Velocity Function (<i>courtesy WesternGeco</i>)
Fig. 6-75	Semblance Plot with a Faster Velocity Picked for Event at 1729 ms
(courtesy WesternGeco)	
Fig. 6-76	Same as Figure 6-72 Except CMP 61 is Corrected for NMO Using the Modified Velocity Function
(courtesy WesternGeco)	
Fig. 6-77	Observed Moveout versus NMO for a Flat Layered Earth
Fig. 6-78	Best Fit Hyperbola to Observed Moveout, NMO-corrected Traces
	Using Velocity Obtained from Best Fit Hyperbola
Fig. 6-79	Effect of Restricting Offsets on Velocity Analysis (<i>courtesy WesternGeco</i>)
Fig. 6-80	Earth Model with Near-Surface Anomaly
Fig. 6-81	Synthetic Traces Based on Model of Figure 6-80
Fig. 6-82	Variations in Stacking Velocity Caused by Near-Surface Anomaly
Fig. 6-83	Stack of Synthetic Traces Based on Model of Figure 6-80 and Velocities of Figure 6-82
Fig. 6-84	Velocity Analysis Before and After Multiple Attenuation
Fig. 6-85	Deconvolution Objectives
Fig. 6-86	Information in a Correlogram
Fig. 6-87	Whitening Deconvolution Representation in the Frequency Domain
Fig. 6-88	Effect of Adding White Noise to the Input Amplitude Spectrum
Fig. 6-89	Adding White Noise by Increasing Zero-lag Value of the Input Autocorrelation
Fig. 6-90	Input Autocorrelation and the Information It Contains
Fig. 6-91	Representation of Gapped Deconvolution Representation in the Frequency Domain
Fig. 6-92	Comparison of Whitening and Gapped Deconvolution
Fig. 6-93	Wavelet Shapes at Early, Middle, and Late Record Times
Fig. 6-94	Design and Application Gates for Time-Variant Deconvolution
Fig. 6-95	Effect of Filter Length on Deconvolution of Trace with Five Reflections (<i>courtesy WesternGeco</i>)
Fig. 6-96	Data Used to Illustrate TVD Parameter Testing (<i>courtesy WesternGeco</i>)
Fig. 6-97	Autocorrelation Window Selection
Fig. 6-98	Operator Length Tests
Fig. 6-99	Prediction Length Tests
Fig. 6-100	White Noise Tests
Fig. 6-101	Example of TVD
Fig. 6-102	Trace Decomposition
Fig. 6-103	Source and Receiver Amplitude Spectra Extracted from Trace Decomposition
Fig. 6-104	Only Geometric Spreading Applied and Same Record after Application of
	Surface Consistent Amplitude Correction (<i>courtesy WesternGeco</i>)
Fig. 6-105	TVSW Flow Chart
Fig. 6-106	Automatic Filter Design in TVSW
Fig. 6-107	User-Defined Filters for TVSW
Fig. 6-108	Three-Filter TVSW Example
Fig. 6-109	Filter Output, Gain Output
Fig. 6-110	Effect of Number of TVSW Filters on CMP Stack (<i>courtesy WesternGeco</i>)

Fig. 6-111	Effect of Number of TVSW Filters on Amplitude Spectra (<i>courtesy WesternGeco</i>)
Fig. 6-112	MBWP Models for Vibrator Records
Fig. 6-113	MBWP Models for Dynamite Records
Fig. 6-114	Absorption and Scattering
Fig. 6-115	Representative Q Values
Fig. 6-116	Evaluation of Q
Fig. 6-117	Transition Zone Example of MBWP Application
Fig. 6-118	Data of Figure 6-117 after MBWP (<i>courtesy WesternGeco</i>)
Fig. 6-119	Wavelets After Decon but Before MBWP and After Both Decon and MBWP
Fig. 6-120	Effects of Absorption
Fig. 6-121	Effect of Noise on Deconvolution
Fig. 6-122	The Forward Q-Filter and Deconvolution
Fig. 6-123	Phase Compensation
Fig. 6-124	Cascaded Amplitude Compensation
Fig. 6-125	Amplitude Compensation
Fig. 6-126	Inverse-Q Example
Fig. 6-127	Illustration of Residual Statics
Fig. 6-128	Residual NMO and Residual Statics
Fig. 6-129	Three CMPs with Residual Statics
Fig. 6-130	The Reflection Residual Statics Method
Fig. 6-131	Defining Windows for Residual Statics Analysis
Fig. 6-132	Definition of Quality Factors Q_{jh} and Δt_{jh}
Fig. 6-133	Surface Consistent Travel Time Model
Fig. 6-134	Decomposition of Residual Statics into Long, Medium, and Short Wavelength Statics
Fig. 6-135	Reflection-Based and Refraction-Based Residual Statics (<i>courtesy WesternGeco</i>)
Fig. 6-136	Increase in Dip of Multiples
Fig. 6-137	Change in Multiple Period with Offset
Fig. 6-138	Synthetic Example (<i>courtesy WesternGeco</i>)
Fig. 6-139	Autocorrelation of Data in Figure 6-138 (<i>courtesy WesternGeco</i>)
Fig. 6-140	Radon Transform of the Data in Figure 6-138
Fig. 6-141	Autocorrelation of Data in Figure 6-140 (<i>courtesy WesternGeco</i>)
Fig. 6-142	Data of Figure 6-140 after Gapped Deconvolution (<i>courtesy WesternGeco</i>)
Fig. 6-143	Autocorrelation of Data in Figure 6-142 (<i>courtesy WesternGeco</i>)
Fig. 6-144	Inverse Radon Transform of the Data in Figure 6-142 (<i>courtesy WesternGeco</i>)
Fig. 6-145	Reverberation Sampling by Receivers
Fig. 6-146	Modeling of Water Bottom Multiple Sequence from Previous Occurrence
Fig. 6-147	Approximating the Water Bottom by a Straight Line
Fig. 6-148	Model Used to Generate Synthetic Data (<i>courtesy WesternGeco</i>)
Fig. 6-149	Synthetic Data Produced from Model of Figure 6-148 by Ray Tracing (<i>courtesy WesternGeco</i>)
Fig. 6-150	The Data of Figure 6-149 after Forward Extrapolation of One Round Trip
	Through the Water Layer (<i>courtesy WesternGeco</i>)
Fig. 6-151	Reflectivity Operators Designed for Seven Different Gates of Data in Figure 6-149
	(<i>courtesy WesternGeco</i>)
Fig. 6-152	Result of Subtracting Predicted Multiples from Data of Figure 6-149 (<i>courtesy WesternGeco</i>)
Fig. 6-153	A CMP Stack Showing Strong Multiples (<i>courtesy WesternGeco</i>)
Fig. 6-154	CMP Stack Section of Fig. 6-153 after Application of WEMA (<i>courtesy WesternGeco</i>)
Fig. 6-155	Source-Generated and Receiver-Generated Reverberations for Peg-Leg Multiples
Fig. 6-156	Input Record and Corrected Record for NMO Using Reverberation Velocity
Fig. 6-157	NMO-Corrected Record of Figure 6-156 and Record Transformed into F-K Domain
Fig. 6-158	F-K Record of Figure 6-157 After Velocity Filter Applied and Record Transformed into T-X Domain
Fig. 6-159	The T-X Domain Record of Figure 6-158 and Record After Inverse NMO Corrections
Fig. 6-160	Synthetic Data Used to Illustrate F-K Multiple Attenuation (<i>courtesy WesternGeco</i>)
Fig. 6-161	Multiple Attenuation from CMP Stack
Fig. 6-162	F-K Multiple Attenuation Using an Intermediate Velocity Function
Fig. 6-163	F-K Multiple Attenuation Example (<i>courtesy WesternGeco</i>)
Fig. 6-164	Synthetic Data Used to Illustrate Radon Transform Filtering (<i>courtesy WesternGeco</i>)
Fig. 6-165	Data of Figure 6-164 Transformed into τ -p Domain
Fig. 6-166	Data of Figure 6-165 after Velocity Mutes Are Applied (<i>courtesy WesternGeco</i>)

Fig. 6-167	Inverse Radon transform of Data of Figure 6-166 (<i>courtesy WesternGeco</i>)
Fig. 6-168	Reflection from a Dipping Horizon
Fig. 6-169	Conflicting Dips
Fig. 6-170	Moveout from Conflicting Dips
Fig. 6-171	Conflicting Dips
Fig. 6-172	Zero-Offset Ray Paths for a Synclinal Reflector and Appearance on CMP Stack
Fig. 6-173	Conventional Processing (<i>courtesy WesternGeco</i>)
Fig. 6-174	Locus of Non-zero Reflection Points
Fig. 6-175	Pre-Stack Migration of a Spike Showing Input and Proper Migration
Fig. 6-176	Three-step Imaging
Fig. 6-177	Post-stack and Pre-stack Migration
Fig. 6-178	Kirchhoff Impulse Response (<i>after S.M. Deregowski</i> , First Break)
Fig. 6-179	DMO in the Common Offset Domain
Fig. 6-180	The DMO Process
Fig. 6-181	Depth Model of Six Point Scatterers Buried in a Constant Velocity
Fig. 6-182	DMO Example Using Synthetic Data Derived from Model of Figure 6-181 (<i>courtesy WesternGeco</i>)
Fig. 6-183	Zero-offset Section Associated with the Depth Model in Figure 6-181 (<i>courtesy WesternGeco</i>)
Fig. 6-184	DMO Processing Stages for Synthetic Data of Figure 6-181(<i>courtesy WesternGeco</i>)
Fig. 6-185	CMP Gathers without DMO and with Kirchhoff DMO (<i>courtesy WesternGeco</i>)
Fig. 6-186	Velocity Analysis Displays with and without DMO
Fig. 6-187	Data Acquired Near a Major Fault, Conventional CMP Stack, and Post-stack Migration (<i>courtesy WesternGeco</i>)
Fig. 6-188	Velocity Analysis Displays Contoured in Correlation Coefficients
Fig. 6-189	Data of Figure 6-187 after DMO (<i>courtesy WesternGeco</i>)
Fig. 6-190	Data of Figure 6-187 After DMO, CMP Stack, Post-stack Migration, and Pre-stack Migration
Fig. 6-191	Effect of Event Alignment on CMP Stack
Fig. 6-192	Enlarged View of Time Scans Shown in Table 6-3 (<i>courtesy WesternGeco</i>)
Fig. 6-193	Two-Sum Median Stack (<i>courtesy WesternGeco</i>)
Fig. 6-194	Eight-Sum Median Stack (<i>courtesy WesternGeco</i>)
Fig. 6-195	Partial Stack to 12-fold Then Two-sum Median Stack
Fig. 6-196	Comparison of Conventional CMP Stack and Median Stack
Fig. 6-197	CMP Traces before NMO Correction and Stack—Flat Reflector and CMP Traces before NMO Correction and Stack
Fig. 6-198	CMP Traces before NMO Correction and Stack—Dipping Reflector and CMP Traces before NMO Correction and Stack
Fig. 6-199	Dipping Reflector in True Position and as Seen on CMP Stack Section
Fig. 6-200	A Buried Focus or Syncline in Its True Perspective and a Bow Tie
Fig. 6-201	Anticlinal Reflector and Its Appearance on CMP Stack
Fig. 6-202	Geology and CMP Stack
Fig. 6-203	Dipping Reflector as Seen on CMP Stack Section and After Migration
Fig. 6-204	Stack and Migration
Fig. 6-205	Imaging Hierarchy
Fig. 6-206	Circular Migration
Fig. 6-207	Hyperbolic Migration
Fig. 6-208	Distortion Caused by Refraction of Light
Fig. 6-209	Representation of a Point Aperture and the Diffraction Hyperbola Produced from It
Fig. 6-210	Set of Closely Spaced Point Apertures and Resultant of Diffraction Hyperbolas Produced from Them
Fig. 6-211	Summation of Amplitudes along the Hyperbola
Fig. 6-212	Downward Continuation
Fig. 6-213	Downward Continuation Migration with Depth Slices at Different Layers
Fig. 6-214	Fit of Parabola to Hyperbola—Low Order Explicit
Fig. 6-215	Fit of Parabola to Hyperbola—High Order Explicit
Fig. 6-216	Constant Velocity Stolt Migration Flow Chart
Fig. 6-217	Reduction of Bandwidth in Migration
Fig. 6-218	Stolt Migration Example—Multi-Dip Model (<i>courtesy WesternGeco</i>)
Fig. 6-219	Gazdag's Phase Shift Migration Flow Chart
Fig. 6-220	Comparison of Kirchhoff and Downward Continuation Migration Approaches
Fig. 6-221	Effect of Phase and Bandwidth on Migration of Diffraction (<i>courtesy WesternGeco</i>)

Fig. 6-222	Diffraction in T-X and F-K
Fig. 6-223	A Spike in the T-X and F-K Domains
Fig. 6-224	Data Wrap Around
Fig. 6-225	Preventing Wrap-around Effects
Fig. 6-226	Truncated Diffractions
Fig. 6-227	Migration Wave-fronting
Fig. 6-228	Migration of Multi-dip Model with 6 to 36 Hz Bandwidth (<i>courtesy WesternGeco</i>)
Fig. 6-229	Migration of Multi-dip Model with 6 to 90 Hz Bandwidth (<i>courtesy WesternGeco</i>)
Fig. 6-230	Effect of Spatial Sampling on Migration (<i>courtesy WesternGeco</i>)
Fig. 6-231	Spatial Aliasing and Migration—The Role of Interpolation
Fig. 6-232	Kirchhoff Impulse Response (<i>courtesy WesternGeco</i>)
Fig. 6-233	Chatter on the Limbs of the Kirchhoff Impulse Response
Fig. 6-234	Finite Difference Impulse Response
Fig. 6-235	Stolt Impulse Response When W = 1 and 0.5 (<i>courtesy WesternGeco</i>)
Fig. 6-236	Aperture Width Test, Multi-dip Model
Fig. 6-237	Aperture Width Test, Diffraction Migration (<i>courtesy WesternGeco</i>)
Fig. 6-238	Aperture Width Test, Field Data (<i>courtesy WesternGeco</i>)
Fig. 6-239	Aperture Width and Random Noise (<i>courtesy WesternGeco</i>)
Fig. 6-240	Maximum Dip Test, Multi-dip Model
Fig. 6-241	Maximum Dip Test, Field Data With Aperture Width of 384 Traces (<i>courtesy WesternGeco</i>)
Fig. 6-242	Effect of Velocity Errors on Kirchhoff Migration (<i>courtesy WesternGeco</i>)
Fig. 6-243	Depth Step Test, Implicit Finite Difference With a Sample Period of 4 ms
Fig. 6-244	The Zig-zag Effect
Fig. 6-245	Depth Step Test, Implicit Finite Difference Migration of Diffractions (<i>courtesy WesternGeco</i>)
Fig. 6-246	A CMP Stack Section and Sketch Highlighting Salient Features of the Stack (<i>courtesy WesternGeco</i>)
Fig. 6-247	Implicit Finite Difference Migration of the CMP Stack Section of Figure 6-246
	Using a Depth Step of 40 ms and a Sketch Pointing Out Significant Aspects of the Migration (<i>courtesy WesternGeco</i>)
Fig. 6-248	Implicit Finite Difference Migration of the CMP Stack Section of Figure 6-246
	Using A Depth Step Of 20 ms and a Sketch Pointing Out Significant Aspects of the Migration (<i>courtesy WesternGeco</i>)
Fig. 6-249	Comparison of Parabolic and Hyperbolic Time Shifts
Fig. 6-250	Velocity Test, Implicit Finite Difference Migration, Depth Step of 20 ms (<i>courtesy WesternGeco</i>)
Fig. 6-251	Comparison of Finite Difference Algorithms, Multi-dip Model
Fig. 6-252	Comparison of Finite Difference Algorithms, Three-point Aperture Model
Fig. 6-253	Parameter Test for Stretch Factor W in Stolt Migration (<i>courtesy WesternGeco</i>)
Fig. 6-254	Depth Step Test, Phase Shift Migration, Multi-dip Model
Fig. 6-255	Depth Step Test, Phase Shift Migration, Field Data
Fig. 6-256	Effect of Velocity Errors on Phase-Shift Migration (<i>courtesy WesternGeco</i>)
Fig. 6-257	Salt Model Used to Demonstrate Extended Stolt Migration
Fig. 6-258	Stolt Migration of Salt Model, Field Data W = 0.3, and Velocity Error (<i>courtesy WesternGeco</i>)
Fig. 6-259	Stolt Migration of Salt Model, Field Data W = 0.5, and Velocity Error (<i>courtesy WesternGeco</i>)
Fig. 6-260	Velocity Data Used to Develop Velocities for the Four-Stage Stolt Migration of Figure 6-259
Fig. 6-261	Four-Stage Stolt Migration at W = 0.9 of Model and Field Data (<i>courtesy WesternGeco</i>)
Fig. 6-262	Phase-Shift Migration of Model and Field Data (<i>courtesy WesternGeco</i>)
Fig. 6-263	Point Scatterer Geometry
Fig. 6-264	Kirchhoff Pre-Stack Time Migration
Fig. 6-265	Conceptual View of Pre-stack Depth Migration
Fig. 6-266	Pre-Stack Depth Migration—Velocity and Focusing
Fig. 6-267	Up- and Down-going Waves (<i>after Claerbout, 1985</i>)
Fig. 6-268	Overthrust Model
Fig. 6-269	Synthetic Data from Overthrust Model Processed with Kirchhoff DMO, CMP Stack, and Steep-dip, Post-Stack Migration (<i>courtesy WesternGeco</i>)
Fig. 6-270	Pre-stack Depth Migration of Synthetic Data
Fig. 6-271	Shot-geophone Sinking Depth Migration Flow Chart
Fig. 6-272	Amplitude Spectrum of Migrated Trace
Fig. 6-273	Band-pass Filter Response and Corner Frequencies
Fig. 6-274	Filter Scan

Fig. 6-275	Filter Scan Interpretation
Fig. 6-276	Interpolation and Extrapolation of Band-pass Filter Application Times
Fig. 6-277	Time-to-depth Conversion
Fig. 6-278	Trace Display Modes
Fig. 6-279	Display Gain
Fig. 6-280	Variations in Horizontal Scale
Fig. 6-281	Variations in Vertical Scale
Fig. 6-282	Color Display Options (<i>from AAPG Memoir 42</i>)
Fig. 6-283	Line Orientations
Fig. 6-284	Migrated Cross-Line Profiles for Lines Designated by D in Figure 6-283
Fig. 6-285	Migrated In-Line Profiles for Lines Designated by D in Figure 6-283
Fig. 6-286	3-D Migrated Profile for Diagonal Line in Figure 6-283
Fig. 6-287	Constructing Structure Maps from Time Slices (<i>AAPG Memoir 42</i>)
Fig. 6-288	Time Slice Through a Salt Dome (<i>AAPG Memoir 42</i>)
Fig. 6-289	(<i>workshop</i>)
Fig. 6-290	(<i>workshop</i>)
Fig. 6-291	(<i>workshop</i>)
Fig. 6-292	(<i>workshop</i>)
Fig. 6-293	(<i>workshop</i>)
Fig. 6-294	(<i>workshop</i>)
Fig. 6-295	(<i>workshop</i>)
Fig. 6-296	(<i>workshop</i>)
Table 6-1	Variation of Δt_{NMO} with Time, Velocity, and Offset
Table 6-2	NMO Velocities
Table 6-3	Sorted Trace Amplitudes—Median and Average Values
Table 6-4	Post-stack Migration Summary
Table 6-5	Relative Processing Speeds of Migration Algorithm
Table 6-6	Pre-stack Time and Depth Migration Types
Table 6-7	Processes and Effect
Fig. 7-1	Typical Exploration Sequence (<i>after Morrison, Seismograph Services Corp.</i>)
Fig. 7-2	Focusing in Anticlines and Synclines (<i>courtesy WesternGeco</i>)
Fig. 7-3	Bow Tie Effect of Buried Focus
Fig. 7-4	The Zero-offset Stack Shows the Focusing of the Narrow, Deep-seated Syncline and the Migrated Stack Shows the Bow Tie Untied (<i>courtesy WesternGeco</i>)
Fig. 7-5	Shadow Zones (<i>courtesy Seismograph Service Corp.</i>)
Fig. 7-6	Zero-offset Section of Horst Block (<i>courtesy Seismograph Service Corp.</i>)
Fig. 7-7	Normal Incidence Ray Path Model of Horst Block
Fig. 7-8	Thin Bed Response
Fig. 7-9	Distortion In The Seismic Data Because Of Lateral Near Surface Velocity Variation (<i>courtesy Seismograph Service Corp.</i>)
Fig. 7-10	Distortion in the Deep Structure because of False Turnover Against the Fault Plane (<i>courtesy Seismograph Service Corp.</i>)
Fig. 7-11	Velocity Pull-up (<i>courtesy Seismograph Service Corp.</i>)
Fig. 7-12	Subsurface Section—Basinward Thinning (<i>courtesy Seismograph Service Corp.</i>)
Fig. 7-13	Seismic Model—Basinward Thinning (<i>courtesy Seismograph Service Corp.</i>)
Fig. 7-14	Subsurface Pseudo Fault Model (<i>courtesy Seismograph Service Corp.</i>)
Fig. 7-15	Ray Tracing For the Subsurface Model of Figure 7-14 (<i>courtesy Seismograph Service Corp.</i>)
Fig. 7-16	Seismic Model For the Pseudo Fault (<i>courtesy Seismograph Service Corp.</i>)
Fig. 7-17	Over-Pressured Shale Model (<i>courtesy Seismograph Service Corp.</i>)
Fig. 7-18	Seismic Model of Over-pressured Shale (<i>courtesy Seismograph Service Corp.</i>)
Fig. 7-19	Interval Transit Time Log (<i>courtesy Seismograph Service Corp.</i>)
Fig. 7-20	Primary Reflection Synthetic without Modeling (<i>courtesy Seismograph Service Corp.</i>)
Fig. 7-21	Primary Reflection Synthetic With Velocity Modified Between 8700 and 9350 ft (<i>courtesy Seismograph Service Corp.</i>)
Fig. 7-22	Primary Reflection Synthetic With Depth Modification at 8700 ft Bed Thickness Reduced from 430 to 312 ft (<i>courtesy Seismograph Service Corp.</i>)
Fig. 7-23	Primary Reflection Synthetic With Repeat Section to Simulate Thrust Faulting (<i>courtesy Seismograph Service Corp.</i>)

- Fig. 7-24 Model Cross-section Showing Interval Velocity Versus Time (*courtesy Seismograph Service Corp.*)
- Fig. 7-25 Model Cross-section of Primary Reflection (*courtesy Seismograph Service Corp.*)
- Fig. 7-26 Subsurface Depth Model (*courtesy Seismograph Service Corp.*)
- Fig. 7-27 Ray Tracing of the Model (*courtesy Seismograph Service Corp.*)
- Fig. 7-28 Spike Seismogram and Wavelet Seismogram from the Model (*courtesy Seismograph Service Corp.*)
- Fig. 7-29 Random Noise Added to the Wavelet Seismogram (*courtesy Seismograph Service Corp.*)
- Fig. 7-30 The Seismic Trace (*courtesy Seismograph Service Corp.*)
- Fig. 7-31 Direct Measurement of Seismic Waveform (*after Neidell, courtesy SEG*)
- Fig. 7-32 Deterministic Measurement Of Seismic Waveform (*after Neidell, courtesy SEG*)
- Fig. 7-33 Statistical Estimation Of Wavelet (*after Stone, courtesy Seismograph Service Corp.*)
- Fig. 7-34 Statistical Method of Wavelet Processing With 12 Traces (*courtesy Seismograph Service Corp.*)
- Fig. 7-35 Statistical Method of Wavelet Processing (*after Stone, courtesy Seismograph Service Corp.*)
- Fig. 7-36 Estimated Reflection Coefficients (*after Stone, courtesy Seismograph Service Corp.*)
- Fig. 7-37 Sequence Of Wavelet Processing Technique (*courtesy Seismograph Service Corp.*)
- Fig. 7-38 Enhanced Interpretation from Wavelet Processing (*courtesy Seismograph Service Corp.*)
- Fig. 7-39 Wavelet Processing and Better Interpretation (*after Stone, courtesy Seismograph Service Corp.*)
- Fig. 7-40 Reflection Estimates (*after Stone, courtesy Seismograph Service Corp.*)
- Fig. 7-41 Synthetic Seismograms and Wavelet Processing (*courtesy Seismograph Service Corp.*)
- Fig. 7-42 Fault Detection from Estimated Reflection Coefficient (*courtesy Seismograph Service Corp.*)
- Fig. 7-43 Stratigraphic Application: Reef Showing (a) Final Stacked Section, (b) Estimated Reflection Coefficient, (c) Wavelet Processed Stack, and (d) Interval Velocity Log (*courtesy Seismograph Service Corp.*)
- Fig. 7-44 Stratigraphic Application Using Wavelet Processing (*after Stone, 1982*)
- Fig. 7-45 Interval Velocities on the Reef Example (*after Stone, 1982*)
- Fig. 7-46 Seismic Section from the Baltimore Canyon Trough (*courtesy Western Geco*)
- Fig. 7-47 Stratigraphic Cross-section from Well Log Data Showing Stratal Surfaces
- (*after Vail et al, AAPG, 1977*)
- Fig. 7-48 Seismic Velocity for Tertiary Example (*after Vail et al, AAPG, 1977*)
- Fig. 7-49 Seismic Reflections at Stratal Surfaces with a Change in the Acoustic Impedance
- (*after Schramm et al, AAPG, 1977*)
- Fig. 7-50 Discontinuity Surfaces Caused by Erosion and Depositional Hiatus Unconformities
- Fig. 7-51 Terminology Proposed for Reflection Terminations (*after Mitchum et al, AAPG, 1977*)
- Fig. 7-52 Seismic Reflection Parameters used in Seismic Stratigraphy and Their Geologic Significance
- (*after Mitchum et al, AAPG, 1977*)
- Fig. 7-53 Parallel, Subparallel, and Divergent Seismic Reflection Configuration
- (*after Mitchum et al, AAPG, 1977*)
- Fig. 7-54 Stratified Simple and Complex Facies (*after Mitchum et al, AAPG, 1977*)
- Fig. 7-55 Fill Facies Units (*after Mitchum et al, AAPG, 1977*)
- Fig. 7-56 Seismic Facies of Carbonate (*after Mitchum et al, AAPG, 1977*)
- Fig. 7-57 Modified Seismic Reflections (*after Mitchum et al, AAPG, 1977*)
- Fig. 7-58 External Geometry of Some Facies Units (*after Mitchum et al, AAPG, 1977*)
- Fig. 7-59 Geologic Interpretation of Seismic Facies Parameters (*after Mitchum et al, AAPG, 1977*)
- Fig. 7-60 Stratal Terminations at Upper Boundary (*after Mitchum et al, AAPG, 1977*)
- Fig. 7-61 Generalized Stratigraphic Section on a Sequence and Generalized Chronostratigraphic Section of the Sequence (*after Mitchum et al, AAPG, 1977*)
- Fig. 7-62 Coastal On-lap (*after Vail, Mitchum, Thompson, AAPG, 1977*)
- Fig. 7-63 Coastal On-lap as a Function of Eustatic Level Change, Subsidence, and Sediment Supply
- (*after Vail, Mitchum, Thompson, AAPG, 1977*)
- Fig. 7-64 Three Scenarios during Coastal On-lap (*after Vail, Mitchum, Thompson, AAPG, 1977*)
- Fig. 7-65 Coastal On-lap Indicates a Relative Still Stand of Sea Level
- (*after Vail, Mitchum, Thompson, AAPG, 1977*)
- Fig. 7-66 Downward Shift in Coastal On-lap (*after Vail, Mitchum, Thompson, AAPG, 1977*)
- Fig. 7-67 Method for Calculating the Amount of Coastal On-lap and Downward Shift
- as a Measurement of Relative Fall of Sea Level (*after Vail, Mitchum, Thompson, AAPG, 1977*)
- Fig. 7-68 Continental Margin Clinoform Analysis (*after Vail, Mitchum, Thompson, AAPG, 1977*)
- Fig. 7-69 Downward Shift in Coastal On-lap in San Joaquin, California
- (*after Vail, Mitchum, Thompson, AAPG, 1977*)
- Fig. 7-70 Progradational and Marine On-lap Cycles, Tertiary, North Sea
- (*after Vail, Mitchum, Thompson, AAPG, 1977*)

Fig. 7-71	Relative Changes in Sea Level, Concepts of Paracycles, Cycles, and Super Cycles <i>(after Vail, Mitchum, Thompson, AAPG, 1977)</i>
Fig. 7-72	Correlation of Regional Cycles of Relative Sea-level Change and Averaging to Construct Global Cycles <i>(after Vail, Mitchum, Thompson, AAPG, 1977)</i>
Fig. 7-73	Estimation of Eustatic Change from Jurassic to Holocene <i>(after Vail, Mitchum, Thompson, AAPG, 1977)</i>
Fig. 7-74	First- and Second-order Global Cycles of Relative Sea-Level Change <i>(after Vail, Mitchum, Thompson, AAPG, 1977)</i>
Fig. 7-75	Global Cycle of Sea-level Changes, Jurassic to Tertiary <i>(after Vail, Mitchum, Thompson, AAPG, 1977)</i>
Fig. 7-76	Control of Sedimentation and Depositional System <i>(after Bally, 1987)</i>
Fig. 7-77	Reflection Terminations Patterns and Types of Discontinuity <i>(after Posamentier et al, SEPM, 1988)</i>
Fig. 7-78	Reflection Termination Patterns Types of Discontinuities That Define Cyclic Sequences <i>(after Posamentier et al, SEPM, 1988)</i>
Fig. 7-79	Accommodation Envelope as a Function of Eustacy and Subsidence <i>(after Posamentier et al, SEPM, 1988)</i>
Fig. 7-80	Eustacy, Relative Sea Level, Water Depth as a Function of Sea Surface, Water Bottom and Datum Position <i>(after Posamentier et al, SEPM, 1988)</i>
Fig. 7-81	Accommodation as a Function of Eustacy and Subsidence <i>(after Posamentier et al, SEPM, 1988)</i>
Fig. 7-82	Relative Sea Level as a Function of Eustacy and Subsidence <i>(after Posamentier et al, SEPM, 1988)</i>
Fig. 7-83	Response of Relative Sea Level to Differential Tectonic Thermal Subsidence <i>(after Posamentier et al, SEPM, 1988)</i>
Fig. 7-84	Effect of Relative Sea Level Rise on Coastline Position <i>(after Posamentier et al, SEPM, 1988)</i>
Fig. 7-85	Type 1 Unconformity <i>(after Posamentier and Vail, SEPM, 1988)</i>
Fig. 7-86	Response of Sedimentation on an Interval of Rapid Eustatic Fall <i>(after Posamentier et al, SEPM, 1988)</i>
Fig. 7-87	Distribution Of Low-stand Wedge Deposits Along The Outer Shelf/Upper Slope <i>(after Posamentier et al, SEPM, 1988)</i>
Fig. 7-88	New Space Added During an Interval of Constant Rate of Relative Sea Level Rise Following Type 1 Unconformity <i>(after Posamentier et al, SEPM, 1988)</i>
Fig. 7-89	Bayline Position and Low-stand Deposits During Rapid Short- and Long-period Eustatic Fall <i>(after Posamentier et al, SEPM, 1988)</i>
Fig. 7-90	Elements of Coastal Onlap Curve <i>(after Posamentier et al, SEPM, 1988)</i>
Fig. 7-91	Type 2 Unconformity <i>(after Posamentier et al, SEPM, 1988)</i>
Fig. 7-92	Effect of Equilibrium Point Migration on Fluvial Deposition in Prograding Environment <i>(after Posamentier et al, SEPM, 1988)</i>
Fig. 7-93	Effect of Shifting Equilibrium Point on Fluvial Deposition <i>(after Posamentier et al, SEPM, 1988)</i>
Fig. 7-94	Response of the Topset Bed Thickness to Eustatic Fall <i>(after Posamentier et al, SEPM, 1988)</i>
Fig. 7-95	Relationship Between Eustatic Sea Level and Phases of Erosion and System Track Deposition <i>(after Posamentier et al, SEPM, 1988)</i>
Fig. 7-96	Types Of Parasequence Sets <i>(after Van Wagoner et al, SEPM, 1988)</i>
Fig. 7-97	Recognizing and Dating Unconformities <i>(after Vail et al, AAPG, 1984)</i>
Fig. 7-98	Unconformity Types <i>(after Vail et al, AAPG, 1984)</i>
Fig. 7-99	Type 1 Erosion
Fig. 7-100	Relation between Transgression or Regression and Eustatic Sea Level <i>(after Vail, Mitchum, Thompson, AAPG, 1977)</i>
Fig. 7-101	A Deposition Sequence in Depth and Time and Its Relation to Marine Condensed Section, Coastal Onlap, Shoreline, and Eustatic Sea Level <i>(Jervey, AAPG, 1977)</i>
Fig. 7-102	Relationship of Sequence to Relative Changes of Coastal Onlap, Types and Ages of Unconformities, Condensed Intervals/Ages, and Inferred Eustatic Sea-Level Changes <i>(after Vail, AAPG, 1984)</i>
Fig. 7-103	Estimation of Worldwide Hydrocarbon Reserve in Clastic Depositional Sequences
Fig. 7-104	Diagrammatic Seismic Section Showing Common Stratigraphic Geometries and Terminations <i>(after Vail, AAPG, 1984)</i>
Fig. 7-105	Seismic Section Showing System Tracts and Other Elements of Depositional Sequences <i>(after Vail, Mitchum, Thompson, AAPG, 1977)</i>

Fig. 7-106	An Idealized Siliciclastic Depositional Sequence Showing Depositional System Tracts and Their Bounding Surface (<i>after Haq et al, SEPM, 1988</i>)
Fig. 7-107	Schematic Diagram of Carbonate Lithofacies Distribution in a Sequence (<i>after Sarg et al, SEPM, 1987</i>)
Fig. 7-108	Carbonate Facies Belts With Representative Textural Types (<i>after Sarg, SEPM, 1988</i>)
Fig. 7-109	Diagrammatic Mixed Carbonate and Clastic Sequence Showing Lithologies and Sequence-Stratigraphic Elements (<i>after Vail et al, AAPG, 1987</i>)
Fig. 7-110	Highstand Systems Tract (<i>after Posamentier et al, SEPM, 1988</i>)
Fig. 7-111	Carbonate Highstand Deposition (<i>after Sarg, SEPM, 1988</i>)
Fig. 7-112	Low-stand System Tract Basin Floor Fan and Siliciclastic Low-stand Systems Tract
	During Basin Floor Fan Deposition (<i>Posamentier et al, SEPM, 1988</i>)
Fig. 7-113	Low-stand Systems Tract Slope Fan and Siliciclastic Low-stand Systems Tract
	During Slope Fan Deposition (<i>after Vail and Sangree, AAPG, 1987</i>)
Fig. 7-114	Low-stand Systems Tract Prograding Wedge and Siliciclastic Low-stand Systems Tract
	During Prograding Wedge Deposition (<i>Posamentier et al, SEPM, 1988</i>)
Fig. 7-115	Different Settings for Low-stand Tract Deposition (<i>after Vail et al, AAPG, 1987</i>)
Fig. 7-116	Type 1 Carbonate and Carbonate Early Lowstand Systems Tract (<i>after Sarg, SEPM, 1988</i>)
Fig. 7-117	Transgressive Systems Tract and Siliciclastic Transgressive System Tracts
Fig. 7-118	Carbonate Late Low-stand and Transgressive System Tracts (<i>after Sarg, SEPM, 1988</i>)
Fig. 7-119	Sediments Accommodations Potential and Its Relationship to the Marine Condensed Sediments (<i>after Loutit et al, SEPM, 1988</i>)
Fig. 7-120	The Stratigraphic Relationship of Marine Condensed Sections to Others Depositional Systems Tracts
	(<i>after Loutit et al, SEPM, 1988</i>)
Fig. 7-121	Marine Condensed Sections and Their Relationship with the Stratigraphic Succession
	(<i>after Loutit et al, SEPM, 1988</i>)
Fig. 7-122	Depth and Time Sections Showing the Marine Condensed Sections Within the Sequence Frame Work
	(<i>after Loutit et al, SEPM, 1988</i>)
Fig. 7-123	Siliciclastic Lithofacies and Siliciclastic Shelf-margin Systems Tract
	(<i>Posamentier et al, SEPM, 1988</i>)
Fig. 7-124	Type 2 Carbonate Sequence Diagram Showing a Slow Fall of the Sea Level
	Interpreted as a Type 2 Sequence (<i>after Sarg, SEPM, 1988</i>)
Fig. 7-125	Sequence Stratigraphy Depositional Model Showing Carbonate and Evaporite Lithofacies,
	Distribution of Carbonate and Evaporite Lithofacies Within the Deposition Sequence Framework (<i>after Sarg, SEPM, 1988</i>)
Fig. 7-126	Stratal Pattern in Type 1 Sequence—Stratal Pattern in Type 1 Sequence Deposited in the Basin
	With Shelf Break (<i>after J. C. Van Wagoner et al, SEPM, 1988</i>)
Fig. 7-127	Stratal Pattern in Type 1 Sequence Deposited in a Basin with Ramp Margin
	(<i>after J. C. Van Wagoner et al, SEPM, 1988</i>)
Fig. 7-128	Type 2 Sequence Boundary (<i>after J. C. Van Wagoner et al, SEPM, 1988</i>)
Fig. 7-129	Possible Reservoir Quality Sand in Siliciclastic Sequence (<i>after Vail et al, AAPG, 1987</i>)
Fig. 7-130	Summary of Factors Affecting the Hydrocarbon-play Potential of Siliciclastic Deposition Systems Tracts (<i>after Sangree and Vail, AAPG, 1989</i>)
Fig. 7-131	Summary of Factor Affecting the Hydrocarbon-play Potential of Siliciclastic Deposition Systems Tracts (<i>after Vail et al, AAPG, 1987</i>)
Fig. 7-132	Systems Tracts in the Gulf Coast Basin (<i>after Sangree and Vail, AAPG, 1989</i>)
Fig. 7-133	Systems Tracts Within Depositional Sequences Deposited Basinward
	of USA Gulf Coast Contemporaneous Growth Faults (<i>Greenlee and Moore, SEPM, 1988</i>)
Fig. 7-134	Triassic Chronostratigraphic and Eustatic-cycle Chart (<i>after Haq et al, AAPG, 1989</i>)
Fig. 7-135	Jurassic Chronostratigraphic and Eustatic-cycle Chart (<i>after Haq et al, AAPG, 1989</i>)
Fig. 7-136	Cretaceous Chronostratigraphic and Eustatic-cycle Chart (<i>after Haq et al, AAPG, 1989</i>)
Fig. 7-137	Cenozoic Chronostratigraphic and Eustatic-cycle Chart (<i>after Haq et al, AAPG, 1989</i>)
Fig. 7-138	High-resolution Seismic Recording Using Vibroseis (<i>courtesy AAPG</i>)
Fig. 7-139	High-resolution Seismic Section (<i>courtesy Seismograph Service Corp.</i>)
Fig. 7-140	High-frequency Marine Seismic Section (<i>courtesy AAPG</i>)
Fig. 7-141	Vertical Seismic Profiling Concepts
Fig. 7-142	Upgoing and Downgoing Events
Fig. 7-143	Raw, Upgoing and Downgoing Events (<i>courtesy Seismograph Service Corp.</i>)
Fig. 7-144	Identification of Seismic Reflectors (<i>modified from Black et al, 1981</i>)

Fig. 7-145	Separation of Up- and Downgoing Events in F-K Space
Fig. 7-146	Comparison of VSP with Synthetic Seismogram (<i>after Hardage, 1983</i>)
Fig. 7-147	Predicting Interval Velocity Ahead of the Bit (<i>after Hardage, 1983</i>)
Fig. 7-148	Predicting Depth of a Seismic Reflector (<i>after Hardage, 1983</i>)
Fig. 7-149	Looking Ahead of the Bit (<i>after Hardage, 1983</i>)
Fig. 7-150	Increase in Angle of Incidence With Offset
Fig. 7-151	AVO Classes (<i>courtesy WesternGeco</i>)
Fig. 7-152	Angle Gathers (<i>courtesy WesternGeco</i>)
Fig. 7-153	Two-term AVO Inversion (<i>courtesy WesternGeco</i>)
Fig. 7-154	Portion of a CMP Stack Section Showing a Bright Spot, P-wave Intercept Section, Pseudo S-wave Section, and Poisson's Ratio Section (<i>courtesy Seismograph Service Corp.</i>)
Fig. 7-155	Orientation of P- and S-wave Particle Motion
Fig. 7-156	Mode Conversion of Ray Paths
Fig. 7-157	Schematic Representation of Three-Component Records
Fig. 7-158	F-K Domain Representation of Vertical Component Record in Figure 7-157
Fig. 7-159	Vertical Component Record of Figure 7-157 after NMO Corrections Using S-wave Velocities
Fig. 7-160	Vertical Component Record of Figure 7-157
Fig. 7-161	The Near Surface as Seen by P- and S-waves
Fig. 7-162	Comparison of P-P and P-SV Ray Paths
Fig. 7-163	Ray Paths of CRP Traces for P-SV
Fig. 7-164	Representative P-P, P-SV, and SH-SH Traces
Fig. 7-165	Traces of Figure 7-164 after Time Scaling to Enhance Event Correlation
Fig. 7-166	Shear-wave and P-wave Sections (<i>courtesy CGG</i>)
Fig. 7-167	Unpaired Reflections (<i>adapted from K.H. Waters, 1987</i>)
Fig. 7-168	Rock Velocities Versus Lithology from Well Logs (<i>after Castagna et al, SEG, 1984</i>)
Fig. 7-169	Rock Velocity Versus Lithology from Laboratory Examples (<i>after Castagna et al, SEG, 1984</i>)
Fig. 7-170	Flowchart for a 4-D Project
Fig. 7-171	Wedge Model with Gas Cap (<i>from Huang et al, 2001</i>)
Fig. 7-172	Relationships among Reservoir Thickness, Gas Saturation, and Amplitude Change (<i>from Huang et al, 2001</i>)
Fig. 7-173	Raw Difference after Applying Global Equalization with a Single Scaler (<i>from Huang et al, 2001</i>)
Fig. 7-174	Difference after Global Phase and Amplitude Match (<i>from Huang et al, 2001</i>)
Fig. 7-175	Difference after Time- and Space-variant Cross-equalization (<i>from Huang et al, 2001</i>)
Fig. 7-176	Difference along the Reservoir Horizon after Global Equalization (<i>from Huang et al, 2001</i>)
Fig. 7-177	Difference along the Reservoir Horizon after Local Equalization (<i>from Huang et al, 2001</i>)
Fig. 7-178	Seismic Difference after Matching with Cumulative Production (<i>from Huang et al, 2001</i>)
Fig. 7-179	Residual Gas Saturation Map after Material Balance Matching and Calibration (<i>from Huang et al, 2001</i>)
Fig. 7-180	Perspective View of the Sand Structure Containing the Currently Producing 4500 ft Reservoir (<i>from Pennington et al, 2001</i>)
Fig. 7-181	Smoothed Production History of the 4500 ft Reservoir (<i>from Pennington et al, 2001</i>)
Fig. 7-182	Inverted Legacy Data Volume Showing Acoustic Impedance 12 ms below the Top of the Tracked 4500 ft Horizon (<i>from Pennington et al, 2001</i>)
Fig. 7-183	Time-Lapse Difference Mapped on the 4500 ft Reservoir (<i>from Pennington et al, 2001</i>)
Fig. 7-184	Changes in P-wave velocity, Poisson's Ratio, and Acoustic Impedance with Time of Production (<i>provided by Wayne D. Pennington and Horacio Acevedo</i>)
Fig. 7-185	Amplitudes Extracted from Partial-offset Stacked P-wave Data for the 4500 ft Reservoir from Phases I and II (<i>from Pennington et al, 2001</i>)
Fig. 7-186	Amplitudes Extracted from Partial-offset Stacked P-wave Data for the Little Neighbor Reservoir from Phases I and II (<i>from Pennington et al, 2001</i>)
Fig. 7-187	Amplitudes extracted from Partial-offset (Unmigrated) Stacked P-wave Data for the Little Neighbor Reservoir from Phases I and II (<i>from Pennington et al, 2001</i>)
Table 7-1	2-D Models
Table 7-2	P-P and P-SV CRP Trace Attribute Comparisons
Table 7-3	Acoustic Impedance Change Caused by Gas Saturation Change

List of Figures

1-1	Seismic Waves from Big Bertha's Firing
1-2	Dip Shooting
1-3	Typical 2-D Seismic Geometry
1-4	Continuous or Single-fold Subsurface Coverage
1-5	CMP Shooting
1-6	Multi-fold Shooting
1-7	Meandering Stream Channel
1-8	3-D Prospect Layout
2-1	A Fossil Sequence
2-2	Dating Rocks from Fossils
2-3	Internal Structure of the Earth
2-4	The Lithosphere
2-5	Mountains, Ridges, and Rises of the World
2-6	Seafloor Spreading
2-7	Mantle Convection Currents
2-8	Tectonic Plate Boundaries
2-9	Tectonic Plate Model
2-10	Pangea, The Universal Continent, About 200 Million Years Before the Present
2-11	The Continents in Their Present Positions and Their Projected Positions 50 Million Years from Now
2-12	Top Part of the Earth's Crust
2-13	Formation of Igneous Rocks
2-14	The Rock Cycle
2-15	Sorting
2-16	Prevalent Sedimentary Rock Types
2-17	The East Texas Oil Field
2-18	Strike and Dip
2-19	Strike, Dip, and Plunge
2-20	Stress-strain Relationship
2-21	Types of Stress
2-22	Folding of Rocks
2-23	Monoclines, Synclines, and Anticlines
2-24	Terms Describing Anticlines
2-25	Symmetric and Asymmetric Folds
2-26	Anticlinal Dome, Overhead View
2-27	Eroded Folds
2-28	An Eroded, Plunging Syncline in Northwest Africa and an Eroded, Plunging Anticline in the Zagros Mountains of Iran
2-29	Joints
2-30	Fault Motion
2-31	Dip Slip Faults
2-32	Well Bores through Normal and Reverse Faults
2-33	Fault Displacement along the Great Glen Fault
2-34	Horsts and Grabens
2-35	Rollover Anticline
2-36	The Fuel Cycle
2-37	Molecular Forms of Petroleum
2-38	Migration of Hydrocarbons
2-39	Components of Clastic Sedimentary Rocks
2-40	The Oil Window
2-41	Effect of Grain Size on Porosity and Permeability
2-42	Geothermal Gradient in Sedimentary Basins
2-43	Hydrostatic Pressure Gradient
2-44	Anticline Trap
2-45	Reservoir Spill Point

2-46	Reservoir Fluid Types
2-47	Asymmetrical Anticline Trap
2-48	Fault Trap
2-49	Growth Fault or Down-to-the-basin Fault
2-50	Fault Cutting Reservoir into Separate Accumulations
2-51	Fault Trap with Multi-level Production
2-52	Western Overthrust Belt
2-53	The Stratford Field
2-54	Oil Fields Formed by Angular Unconformities
2-55	Production from Sands above and Angular Unconformity and Cross Section through the Bolivar Coastal Fields in Lake Maracaibo, Venezuela
2-56	Reef Facies
2-57	Reef Configurations
2-58	The Alberta Reef Trend and the Redwater Oil Field
2-59	Michigan Basin Silurian Reef Trend
2-60	Lenticular Sand Shapes and Origins
2-61	Bush City Pool
2-62	Coastal Sand Pinch-outs
2-63	Giant Oil Fields Formed by Salt Domes
2-64	Fractured Reservoir Rock
2-65	Granite Wash
2-66	Workshop
2-67	Workshop
2-68	Workshop
2-69	Workshop
2-70	Workshop
2-71	Workshop
2-72	Workshop
2-73	Workshop
2-74	Workshop
2-75	Workshop
2-76	Workshop
3-1	Basic Elastic Moduli and Poisson's Ratio
3-2	P- and S-waves
3-3	SV and SH Waves
3-4	Rayleigh Waves
3-5	Love Waves
3-6	Basic Wave Parameters
3-7	Fermat's Principle
3-8	Snell's Law
3-9	Critical Refraction and Head Waves
3-10	Wavefronts and Rays
3-11	Wavefronts from a Point Energy Source
3-12	Huygen's Principle
3-13	P- and SV-wave Reflection Coefficients
3-14	P-wave Normal Incidence Reflection and Transmission
3-15	Earth Reflectivity Function
3-16	Noise-free Seismic Trace Derived from Earth Reflectivity Function
3-17	Direct Waves and Shallow Reflections
3-18	Reverberations or Water Bottom Multiple Reflections
3-19	Multiple Reflections
3-20	Guided Waves
3-21	Diffractions
3-22	Effect of Ambient Noise on Seismic Trace
3-23	Schematic Land Seismic Record
3-24	A Seismic Shot Record
3-25	Digital Recording
3-26	Effect of Sample Period

3-27	Aliasing
3-28	Measuring the Earth's Impulse Response
3-29	Convolution
3-30	Crosscorrelation of $\{y_p\}$ onto $\{x_m\}$
3-31	Crosscorrelation of $\{x_m\}$ onto $\{y_p\}$
3-32	Autocorrelation of $\{x_m\}$
3-33	Single Frequency Sinusoids
3-34	Amplitude and Phase Spectra for Single Frequency Sinusoids
3-35	Signal Synthesis and Decomposition
3-36	Time and Frequency Domains
3-37	Effect of Time Reversal
3-38	Frequency Filter Types
3-39	Band-pass Filtering
3-40	Anti-alias Filters
3-41	Phase Definitions
3-42	Effect of Adding 90° to Phase Spectrum
3-43	Changes in Waveform with Successive Additions of 90° Phase
3-44	Effect of Adding Linear Phase-to-phase Spectrum
3-45	Linear Phase Slope and Time Shift
3-46	Phase and Wavelet Shape
3-47	Minimum-, Maximum-, and Mixed-phase Wavelets
3-48	Effect of Bandwidth
3-49	Bandwidth and Vertical Resolution
3-50	A Wedge or Pinch-out
3-51	Phase and Resolution
3-52	Horizontal Resolution and Fault Displacement
3-53	The Fresnel Zone
3-54	Spatial Sampling
3-55	A Seismic Record as a Two-dimensional Array
3-56	The F-K Plane
3-57	Noise Record in T-X and F-K Domains
3-58	Plane Wave Incident on Surface
3-59	Spatial Aliasing as a Function of Dip and Frequency
3-60	Linear Events in T-X and F-K
3-61	Linear Dipping Events
3-62	Effect of Group Interval on Spatial Aliasing
3-63	Separation of Signal and Noise in F-K
3-64	Definition of the Ray Parameter
3-65	The Radon Transform
3-66	Event Mapping between T-X and τ -p Domains
3-67	CMP Record in T-X Domain and τ -p Domain
3-68	Trace Interpolation with the Radon Transform
3-69	A Clock Pendulum and Its Energy Cycle
3-70	Complex Trace Analysis
3-71	Workshop
3-72	Workshop
3-73	Workshop
3-74	Workshop
3-75	Workshop
4-1	Layout for Intensive Refraction Shooting
4-2	T-X Plot for Inline Refraction Shooting
4-3	Simplified Earth Model Based on Data from Figure 4-2
4-4	Arc and Broadside Shooting
4-5	Workshop

5-1	Target Reference
5-2	Simple Example of Vertical Reference Datum
5-3	Geoid
5-4	Horizontal Reference Datum Example
5-5	Geodetic Latitude
5-6	Longitude Measurement
5-7	Horizontal Reference Datum
5-8	Geocentric and Non-geocentric Ellipsoids
5-9	Datum Transformation
5-10	Map Projection
5-11	Range-Range LOPs
5-12	GPS Receivers and Antenna
5-13	Antenna Motion
5-14	Source and Receiver Assumptions for 2-D Recording
5-15	Cable Feathering
5-16	Streamer Curvature
5-17	Source and Receiver Positioning, 1985–1991 and Current
5-18	Vessel Heading Terms
5-19	Bird/Compass on Test Rig
5-20	Traditional Applications—Cable Shaping
5-21	Acoustic Configuration Diagram
5-22	An Integrated Solution
5-23	Statistical Analysis
5-24	The Airgun Technique
5-25	Airgun Operation
5-26	The Bubble Effect
5-27	Airgun Pressure–Volume Relationship
5-28	Waveform Synthesis by Airgun Arrays
5-29	Measurement of the Far Field Signature
5-30	Time Domain Attributes
5-31	Airgun Frequency Domain Attributes
5-32	Airgun Array Signatures and Parameters
5-33	Signature Variation with Frequency and Depth
5-34	A Single Sleeve Gun, a Disassembled Sleeve Gun, a Sleeve Gun with a Mounting Harness, and a Family of Sleeve Guns
5-35	Side View of a Typical Sub-array Configuration
5-36	Plan View of a Typical Source Array
5-37	Streamer and Source Depth Ghost Notches
5-38	Ghost Response at 5 and 10 m
5-39	Source Array Effects
5-40	The Explosive Technique
5-41	Explosive Source Operation
5-42	Measuring the Far-field Signature of an Explosive Source
5-43	Effect of Charge Size
5-44	Charge Depth Test
5-45	Explosive Cord as a Seismic Energy Source
5-46	Truck-mounted Vibrator Components
5-47	Side View of a Truck-mounted Vibrator
5-48	Vibrator Operation
5-49	Effect of Spike on Vibrator Cross-correlations
5-50	Vibroseis Correlation
5-51	Klauder Wavelet and Resolution
5-52	Width
5-53	Resolution Versus Sweep Bandwidth
5-54	Frequency Versus Time for Various Sweep Types
5-55	Pilot Sweeps for $T^{0.3}$, Logarithmic, Linear, Exponential, and T^3
5-56	Vibroseis Correlation Ghosts
5-57	Vibroseis Correlation Ghost Examples

5-58	Effect of Surface Material
5-59	Effect of Taper on Pilot Autocorrelation
5-60	Attenuation of Sweep Distortion by Cross-correlation
5-61	Piezoelectric Crystals
5-62	Hydrophone Equivalent Circuit
5-63	Input/Output Model 2522 Near-field Hydrophone
5-64	Hydrophone Ghosts
5-65	Amplitude Response for 12.5 m Group, 14 Phone Array
5-66	Geophone Components
5-67	Geophone Magnetic Field
5-68	Three-component Geophones
5-69	Geophone Damping
5-70	Geophone Phase Response
5-71	Spurious Resonance or Parasitics
5-72	Geophone Tilt
5-73	Geophone Planting Conditions
5-74	Effect of Geophone Planting Conditions on Amplitude and Phase Responses
5-75	Noise Spread and Shooting Procedures
5-76	Noise Test Example
5-77	Attenuation of Ground Roll with Band-pass Filter
5-78	Noise Analysis or Walk Away
5-79	Array Configurations
5-80	Ideal Receiver Response for Space Domain x and Wave Number Domain K
5-81	Linear, Equally Spaced, Equally Weighted Array
5-82	Conventional Representation of Desired Response of Linear, Equally Weighted, Equally Spaced Array
5-83	Response of Linear, Equally Weighted, Equally Spaced Arrays, 6 Element and 12 Element
5-84	Alternative Methods of Representing the Spatial Response of Linear, Unequally Weighted, Equally Spaced Arrays
5-85	Decomposing Linear, Unequally Weighted, Equally Spaced Arrays
5-86	Linear Array with Variable Weights
5-87	Geophone Layouts in the Presence of Large Elevation Differences
5-88	Seismic Amplitudes
5-89	24-Bit Electronics
5-90	Streamer Configuration
5-91	Comparison between 16-Bit and 24-Bit Systems
5-92	Land Ground System Configuration
5-93	Recording Room on the Western Monarch
5-94	Non-Return-to-Zero Encoding
5-95	Tape Schematic
5-96	Multiplexed and De-multiplexed Data
5-97	Typical 2-D Geometry
5-98	Maximum and Minimum Offset Requirements
5-99	Maximum and Minimum Offset Requirements for Refracted Arrivals
5-100	Off End Spread
5-101	Symmetric Split Spread
5-102	Up-dip or Down-dip?
5-103	Start-of-line Procedures, Normal Shooting
5-104	Start-of-line Procedures, Fast Ramp On to Full Fold
5-105	Obstacle Avoidance at the Source Array
5-106	Recovery Shots
5-107	Typical 3-D Geometry
5-108	Migration Aperture from Dip for Constant Velocity (Straight Ray Paths)
5-109	Migration Aperture from Dip for Constant Velocity (Straight Ray Paths)
	Using Geologic Depth
5-110	Migration Aperture from Curved and Straight Ray Paths
5-111	Migration Aperture from Fresnel Zone
5-112	Distribution of Diffraction Energy
5-113	Determining Total Migration Aperture

5-114	Total Survey Area Required to Correctly Image Target
5-115	Bins or Cells
5-116	Bin Shapes
5-117	Subsurface Coverage in Marine Surveys
5-118	Static Binning
5-119	Overlapping or Wide Binning
5-120	Effect of Multiple Streamers and Multiple Sources on Data Acquisition
5-121	Conventional Straight Line or Racetrack Shooting
5-122	Circle Shooting
5-123	Approaches to Salt Dome Shooting
5-124	Azimuthal Variation in Conventional One-boat Operation and Two-boat Undershoot Operations
5-125	Obstacle Avoidance, One-boat Operation and Two-boat Undershoot
5-126	Obstacle Avoidance with Two Boats
5-127	Acquisition Template
5-128	Swath Layout Method, Swath Shooting Method
5-129	Shot Index
5-130	Offset and Azimuth Variation in a Bin
5-131	A Star Array and Its Polar Response
5-132	Straight Line Method
5-133	Another Type of Swath Shooting
5-134	The Brick Pattern
5-135	Odds and Evens
5-136	The Zig-zag and Double Zig-zag Patterns
5-137	The Non-Orthogonal Pattern
5-138	Bin Fractionation Method
5-139	The Button Patch Method
5-140	Recovery Shots with In-line Shift
5-141	Recovery Shots with Cross-line Shifts
5-142	Workshop
5-143	Workshop
5-144	Workshop
5-145	Workshop
5-146	Workshop
6-1	Vertical Stack
6-2	Straight Stack
6-3	Diversity Stack Time Gates
6-4	Average Power of Each Trace in Each Gate
6-5	Scalers for Each Gate
6-6	Diversity Stack Scaling Functions
6-7	Application of Diversity Scalers
6-8	Diversity Stack Output
6-9	Stack Comparison
6-10	Need for Scaler Normalization
6-11	Zero- and Minimum-phase Correlation
6-12	Uncorrelated and Correlated Vibroseis Shot Records
6-13	Typical Processing Sequence
6-14	Typical Processing Sequence (continued)
6-15	Typical Processing Sequence (continued)
6-16	LMO Traces Display
6-17	OBC Receiver Location
6-18	A Stacking Diagram
6-19	Trace Gathers
6-20	Shot and CMP Traces with Geologic Dip
6-21	Near-surface Model
6-22	Effect of Variable Near Surface
6-23	Static Corrections, Case I: Surface Source
6-24	Static Corrections, Case IIa: Source in Weathering
6-25	Static Corrections, Case IIa: Source in Subweathering

6-26	First Breaks of Selected CMP Gathers
6-27	First Break Ray Paths and T-X Plot
6-28	Refraction Ray Path Segments
6-29	Redundancy of Data in Refraction Statics Determination
6-30	Refraction Elevation Model
6-31	Field Record with No Gain Applied
6-32	Spherical Divergence and Spherical Spreading
6-33	Geometric Spreading Correction Example
6-34	Programmed Gain Control
6-35	Ray Paths of OBC Ghosts
6-36	OBC Primary Plus Ghosts
6-37	Hydrophone Ghosting
6-38	Hydrophone Ghost Impulse Response
6-39	Geophone Ghosting
6-40	Geophone Ghost Impulse Response
6-41	A Plot of Scale Factor $(1+R)/(1-R)$ for 360 Receiver Locations
6-42	Transformation from T-X to F-K Domain
6-43	Positive and Negative Cut Lines
6-44	Filtering in the F-K Plane
6-45	Transformation of Filtered Record from F-K to T-X Domain
6-46	Noise Record in the T-X Domain and the F-K Domain
6-47	Filtered Field Record in the F-K Domain and the T-X Domain
6-48	Linear Move Out Applied to Linear Noise
6-49	Field Record Dominated by Linear Noise
6-50	Record of 6-49 after Six Passes of Linear Noise Attenuation
6-51	Instantaneous and Interval Velocities
6-52	Single Horizontal Layer
6-53	Reflection with Normal Move Out
6-54	NMO Correction
6-55	The NMO Correction Process
6-56	The NMO Correction Process
6-57	Effect of Velocity on NMO Correction
6-58	NMO Stretch
6-59	Input CMP Records, Same Records after NMO Correction, and after NMO Mute
6-60	Picked Vs. Default Mutes
6-61	RMS Velocity as the Replacement Velocity in the Multi-layer Situation
6-62	NMO for Plane, Horizontal, and Iso-velocity Layers
6-63	Reflection from a Dipping Reflector
6-64	A Dipping Reflector in 3-D
6-65	Velocity Functions
6-66	Velocity Analysis Location Used for Example
6-67	The Velocity Sweep
6-68	Semblance Plot
6-69	Stack of CMPs Using the Nine Velocity Functions of Figure 6-68
6-70	CVS Display Used to Generate the Velocity Trend for the IVP Session
6-71	Semblance Plot Generated from the Input Velocity Fan
6-72	CMP 61 Corrected for NMO Using the Velocity Function Shown in White on the Semblance Plot
6-73	Semblance Plot with a Slower Velocity Picked for Event at 1729 ms
6-74	CMP 61 Corrected for NMO
6-75	Using the Modified Velocity Function
6-76	Semblance Plot with a Faster Velocity Picked for Event at 1729 ms
6-77	CMP 61 Corrected for NMO
6-78	Using the Modified Velocity Function
6-79	Observed Move Out versus NMO for a Flat Layered Earth
6-80	Best Fit Hyperbola to Observed Move Out, NMO-corrected Traces
6-81	Using Velocity Obtained from Best Fit Hyperbola
6-82	Effect of Restricting Offsets on Velocity Analysis
6-83	Earth Model with Near-Surface Anomaly

6-81	Synthetic Traces Based on Model of Figure 6-80
6-82	Variations in Stacking Velocity Caused by Near-Surface Anomaly
6-83	Stack of Synthetic Traces Based on Model of Figure 6-80 and Velocities of Figure 6-82
6-84	Velocity Analysis before and after Multiple Attenuation
6-85	Deconvolution Objectives
6-86	Information in a Correlogram
6-87	Whitening Deconvolution Representation in the Frequency Domain
6-88	Effect of Adding White Noise to the Input Amplitude Spectrum
6-89	Adding White Noise by Increasing Zero-lag Value of the Input Autocorrelation
6-90	Input Autocorrelation and the Information It Contains
6-91	Representation of Gapped Deconvolution Representation in the Frequency Domain
6-92	Comparison of Whitening and Gapped Deconvolution
6-93	Wavelet Shapes at Early, Middle, and Late Record Times
6-94	Design and Application Gates for Time-variant Deconvolution
6-95	Effect of Filter Length on Deconvolution of Trace with Five Reflections
6-96	Data Used to Illustrate TVD Parameter Testing
6-97	Autocorrelation Window Selection
6-98	Operator Length Tests
6-99	Prediction Length Tests
6-100	White Noise Tests
6-101	Example of TVD
6-102	Trace Decomposition
6-103	Source and Receiver Amplitude Spectra Extracted from Trace Decomposition
6-104	Only Geometric Spreading Applied and Same Record after Application
	of Surface Consistent Amplitude Correction
6-105	TVSW Flow Chart
6-106	Automatic Filter Design in TVSW
6-107	User-Defined Filters for TVSW
6-108	Three-Filter TVSW Example
6-109	Filter Output, Gain Output
6-110	Effect of Number of TVSW Filters on CMP Stack
6-111	Effect of Number of TVSW Filters on Amplitude Spectra
6-112	MBWP Models for Vibrator Records
6-113	MBWP Models for Dynamite Records
6-114	Absorption and Scattering
6-115	Representative Q Values
6-116	Evaluation of Q
6-117	Transition Zone Example of MBWP Application
6-118	Data of Figure 6-117 after MBWP
6-119	Wavelets after Decon but before MBWP and after Both Decon and MBWP
6-120	Effects of Absorption
6-121	Effect of Noise on Deconvolution
6-122	The Forward Q-Filter and Deconvolution
6-123	Phase Compensation
6-124	Cascaded Amplitude Compensation
6-125	Amplitude Compensation
6-126	Inverse-Q Example
6-127	Illustration of Residual Statics
6-128	Residual NMO and Residual Statics
6-129	Three CMPs with Residual Statics
6-130	The Reflection Residual Statics Method
6-131	Defining Windows for Residual Statics Analysis
6-132	Definition of Quality Factors Q_{ijh} and Δ_{ijh}
6-133	Surface Consistent Travel Time Model
6-134	Decomposition of Residual Statics into Long, Medium, and Short Wavelength Statics
6-135	Reflection-based and Refraction-based Residual Statics
6-136	Increase in Dip of Multiples
6-137	Change in Multiple Period with Offset

6-138	Synthetic Example
6-139	Autocorrelation of Data in Figure 6-138
6-140	Radon Transform of the Data in Figure 6-138
6-141	Autocorrelation of Data in Figure 6-140
6-142	Data of Figure 6-140 After Gapped Deconvolution
6-143	Autocorrelation of Data in Figure 6-142
6-144	Inverse Radon Transform of the Data in Figure 6-142
6-145	Reverberation Sampling by Receivers
6-146	Modeling of Water Bottom Multiple Sequence from Previous Occurrence
6-147	Approximating the Water Bottom by a Straight Line
6-148	Model Used to Generate Synthetic Data
6-149	Synthetic Data Produced from Model of Figure 6-148
6-150	The Data of Figure 6-149 after Forward Extrapolation of One Round Trip through the Water Layer
6-151	Reflectivity Operators Designed for Seven Different Gates of Data in Figure 6-149
6-152	Result of Subtracting Predicted Multiples from Data of Figure 6-149
6-153	A CMP Stack Showing Strong Multiples
6-154	CMP Stack Section of Figure 6-153 after Application of WEMA
6-155	Source-generated and Receiver-generated Reverberations for Peg-leg Multiples
6-156	Input Record and Corrected Record for NMO Using Reverberation Velocity
6-157	NMO-Corrected Record of Figure 6-156 and Record Transformed into F-K Domain
6-158	F-K Record of Figure 6-157 after Velocity Filter Applied and Record Transformed into T-X Domain
6-159	The T-X Domain Record of Figure 6-158 and Record after Inverse NMO Corrections
6-160	Synthetic Data Used to Illustrate F-K Multiple Attenuation
6-161	Multiple Attenuation from CMP Stack
6-162	F-K Multiple Attenuation Using an Intermediate Velocity Function
6-163	F-K Multiple Attenuation Example
6-164	Synthetic Data Used to Illustrate Radon Transform Filtering
6-165	Data of Figure 6-164 Transformed into τ -p Domain
6-166	Data of Figure 6-165 after Velocity Mutes Are Applied
6-167	Inverse Radon Transform of Data of Figure 6-166
6-168	Reflection from a Dipping Horizon
6-169	Conflicting Dips
6-170	Move Out from Conflicting Dips
6-171	Depth Point Smear in the Presence of Dip
6-172	Zero-offset Ray Paths for a Synclinal Reflector and Appearance on CMP Stack
6-173	Conventional Processing
6-174	Locus of Non-zero Reflection Points
6-175	Pre-stack Migration of a Spike Showing Input and Proper Migration
6-176	Three-step Imaging
6-177	Post-stack and Pre-stack Migration
6-178	Kirchhoff Impulse Response
6-179	DMO in the Common Offset Domain
6-180	The DMO Process
6-181	Depth Model of Six Point Scatterers Buried in a Constant Velocity
6-182	DMO Example Using Synthetic Data Derived from Model of Figure 6-181
6-183	Zero-offset Section Associated with the Depth Model in Figure 6-181
6-184	DMO Processing Stages for Synthetic Data of Figure 6-181
6-185	Using Incorrect Velocity for NMO Correction
6-186	CMP Gathers without DMO and with Kirchhoff DMO
6-187	Velocity Analysis Displays with and without DMO
6-188	Data Acquired Near a Major Fault, Conventional CMP Stack, and Post-Stack Migration
6-189	Velocity Analysis Displays Contoured in Correlation Coefficients
6-190	Data of Figure 6-187 after DMO
6-191	Data of Figure 6-187 after DMO, CMP Stack, Post-Stack Migration, and Pre-Stack Migration
6-192	Effect of Event Alignment on CMP Stack
6-193	Enlarged View of Time Scans Shown in Table 6-3
6-194	Two-sum Median Stack
6-194	Eight-sum Median Stack

6-195	Partial Stack to 12-fold Then Two-sum Median Stack
6-196	Comparison of Conventional CMP Stack and Median Stack
6-197	CMP Traces before NMO Correction and Stack-flat Reflector and CMP Traces
	before NMO Correction and Stack
6-198	CMP Traces before NMO Correction and Stack-Dipping Reflector and CMP Traces
	before NMO Correction and Stack
6-199	Dipping Reflector in True Position and as Seen on CMP Stack Section
6-200	A Buried Focus or Syncline in Its True Perspective and a Bowtie
6-201	Anticlinal Reflector and Its Appearance on CMP Stack
6-202	Geology and CMP Stack
6-203	Dipping Reflector as Seen on CMP Stack Section and after Migration
6-204	Stack and Migration
6-205	Imaging Hierarchy
6-206	Circular Migration
6-207	Hyperbolic Migration
6-208	Distortion Caused by Refraction of Light
6-209	Representation of a Point Aperture and the Diffraction Hyperbola Produced from It
6-210	Set of Closely Spaced Point Apertures and Resultant of Diffraction Hyperbolas Produced from Them
6-211	Summation of Amplitudes along the Hyperbola
6-212	Downward Continuation
6-213	Downward Continuation Migration with Depth Slices at Different Layers
6-214	Fit of Parabola to Hyperbola, Low Order Explicit
6-215	Fit of Parabola to Hyperbola, High Order Explicit
6-216	Constant Velocity Stolt Migration Flow Chart
6-217	Reduction of Bandwidth in Migration
6-218	Stolt Migration Example, Multi-dip Model
6-219	Gazdag's Phase Shift Migration Flow Chart
6-220	Comparison of Kirchhoff and Downward Continuation Migration Approaches
6-221	Effect of Phase and Bandwidth on Migration of Diffraction
6-222	Diffraction in T-X and F-K
6-223	A Spike in the T-X and F-K Domains
6-224	Data Wrap Around
6-225	Preventing Wrap-Around Effects
6-226	Truncated Diffractions
6-227	Migration Wave-fronting
6-228	Migration of Multi-dip Model with 6 to 36 Hz Bandwidth
6-229	Migration of Multi-dip Model with 6 to 90 Hz Bandwidth
6-230	Effect of Spatial Sampling on Migration
6-231	Spatial Aliasing and Migration—the Role of Interpolation
6-232	Kirchhoff Impulse Response
6-233	Chatter on the Limbs of the Kirchhoff Impulse Response
6-234	Finite Difference Impulse Response
6-235	Stolt Impulse Response When $W = 1$ and 0.5
6-236	Aperture Width Test, Multi-Dip Model
6-237	Aperture Width Test, Diffraction Migration
6-238	Aperture Width Test, Field Data
6-239	Aperture Width and Random Noise
6-240	Maximum Dip Test, Multi-dip Model
6-241	Maximum Dip Test, Field Data with Aperture Width of 384 Traces
6-242	Effect of Velocity Errors on Kirchhoff Migration
6-243	Depth Step Test, Implicit Finite Difference with a Sample Period of 4 ms
6-244	The Zig-zag Effect
6-245	Depth Step Test, Implicit Finite Difference Migration of Diffractions
6-246	A CMP Stack Section and Sketch Highlighting Salient Features of the Stack
6-247	Implicit Finite Difference Migration of the CMP Stack Section of Figure 6-246
	Using a Depth Step of 40 ms and a Sketch Pointing Out Significant Aspects of the Migration
6-248	Implicit Finite Difference Migration of the CMP Stack Section of Figure 6-246
	Using a Depth Step Of 20 ms and a Sketch Pointing Out Significant Aspects of the Migration

6-249	Comparison of Parabolic and Hyperbolic Time Shifts
6-250	Velocity Test, Implicit Finite Difference Migration, Depth Step of 20 ms
6-251	Comparison of Finite Difference Algorithms, Multi-dip Model
6-252	Comparison of Finite Difference Algorithms, Three-point Aperture Model
6-253	Parameter Test for Stretch Factor W in Stolt Migration
6-254	Depth Step Test, Phase Shift Migration, and Multi-dip Model
6-255	Depth Step Test, Phase Shift Migration, and Field Data
6-256	Effect of Velocity Errors on Phase-shift Migration
6-257	Salt Model Used to Demonstrate Extended Stolt Migration
6-258	Stolt Migration of Salt Model, Field Data W = 0.3, and Velocity Error
6-259	Stolt Migration of Salt Model, Field Data W = 0.5, and Velocity Error
6-260	Velocity Data Used to Develop Velocities for the Four-stage Stolt Migration of Figure 6-259
6-261	Four-stage Stolt Migration at W = 0.9 of Model and Field Data
6-262	Phase-shift Migration of Model and Field Data
6-263	Point Scatterer Geometry
6-264	Kirchhoff Pre-stack Time Migration
6-265	Conceptual View of Pre-stack Depth Migration
6-266	Pre-stack Depth Migration—Velocity and Focusing
6-267	Up- and Down-going Waves
6-268	Overthrust Model
6-269	Synthetic Data from Overthrust Model Processed with Kirchhoff DMO, CMP Stack, and Steep-dip, Post-Stack Migration
6-270	Pre-stack Depth Migration of Synthetic Data
6-271	Shot-geophone Sinking Depth Migration Flow Chart
6-272	Amplitude Spectrum of Migrated Trace
6-273	Band-pass Filter Response and Corner Frequencies
6-274	Filter Scan
6-275	Filter Scan Interpretation
6-276	Interpolation and Extrapolation of Band-pass Filter Application Times
6-277	Time-to-depth Conversion
6-278	Trace Display Modes
6-279	Display Gain
6-280	Variations in Horizontal Scale
6-281	Variations in Vertical Scale
6-282	Color Display Options
6-283	Line Orientations
6-284	Migrated Cross-line Profiles for Lines Designated by D in Figure 6-283
6-285	Migrated In-line Profiles for Lines Designated by D in Figure 6-283
6-286	3-D Migrated Profile for Diagonal Line in Figure 6-283
6-287	Constructing Structure Maps from Time Slices
6-288	Time Slice through a Salt Dome
6-289	Bright Spots on Vertical and Horizontal Sections
6-290	Workshop
6-291	Workshop
6-292	Workshop
6-293	Workshop
6-294	Workshop
6-295	Workshop
6-296	Workshop
6-297a	Workshop
6-297b	Workshop
7-1	Typical Exploration Sequence
7-2	Focusing in Anticlines and Synclines
7-3	Bow Tie Effect of Buried Focus
7-4	The Zero-offset Stack Shows the Focusing of the Narrow, Deep-seated Syncline and the Migrated Stack Shows the Bow Tie Untied
7-5	Shadow Zones
7-6	Zero-offset Section of Horst Block

7-7	Normal Incidence Ray Path Model of Horst Block
7-8	Thin Bed Response
7-9	Distortion in the Seismic Data because of Lateral Near Surface Velocity Variation
7-10	Distortion in the Deep Structure because of False Turnover against the Fault Plane
7-11	Velocity Pull-up
7-12	Subsurface Section—Basinward Thinning
7-13	Seismic Model—Basinward Thinning
7-14	Subsurface Pseudo Fault Model
7-15	Ray Tracing For the Subsurface Model of Figure 7-14
7-16	Seismic Model For the Pseudo Fault
7-17	Over-pressured Shale Model
7-18	Seismic Model of Over-pressured Shale
7-19	Interval Transit Time Log
7-20	Primary Reflection Synthetic without Modeling
7-21	Primary Reflection Synthetic with Velocity Modified Between 8700 and 9350 ft
7-22	Primary Reflection Synthetic with Depth Modification at 8700 ft Bed Thickness Reduced from 430 to 312 ft
7-23	Primary Reflection Synthetic with Repeat Section to Simulate Thrust Faulting
7-24	Model Cross-section Showing Interval Velocity versus Time
7-25	Model Cross-section of Primary Reflection
7-26	Subsurface Depth Model
7-27	Ray Tracing of the Model
7-28	Spike Seismogram and Wavelet Seismogram from the Model
7-29	Random Noise Added to the Wavelet Seismogram
7-30	The Seismic Trace
7-31	Direct Measurement of Seismic Waveform
7-32	Deterministic Measurement Of Seismic Waveform
7-33	Statistical Estimation Of Wavelet
7-34	Statistical Method of Wavelet Processing with 12 Traces
7-35	Statistical Method of Wavelet Processing
7-36	Estimated Reflection Coefficients
7-37	Sequence of Wavelet Processing Technique
7-38	Enhanced Interpretation from Wavelet Processing
7-39	Wavelet Processing and Better Interpretation
7-40	Reflection Estimates
7-41	Synthetic Seismograms and Wavelet Processing
7-42	Fault Detection from Estimated Reflection Coefficient
7-43	Stratigraphic Application: Reef Including the Final Stacked Section, Estimated Reflection Coefficient, Wavelet-processed Stack, and Interval Velocity Log
7-44	Stratigraphic Application Using Wavelet Processing
7-45	Interval Velocities on the Reef Example
7-46	Seismic Section from the Baltimore Canyon Trough
7-47	Stratigraphic Cross-section from Well Log Data Showing Stratigraphic Surfaces
7-48	Seismic Velocity for Tertiary Example
7-49	Seismic Reflections at Stratigraphic Surfaces with a Change in the Acoustic Impedance
7-50	Discontinuity Surfaces Caused by Erosion and Depositional Hiatus Unconformities
7-51	Terminology Proposed for Reflection Terminations
7-52	Seismic Reflection Parameters Used in Seismic Stratigraphy and Their Geologic Significance
7-53	Parallel, Subparallel, and Divergent Seismic Reflection Configuration
7-54	Stratified Simple and Complex Facies
7-55	Fill Facies Units
7-56	Seismic Facies of Carbonate
7-57	Modified Seismic Reflections
7-58	External Geometry of Some Facies Units
7-59	Geologic Interpretation of Seismic Facies Parameters
7-60	Stratal Terminations at Upper Boundary
7-61	Generalized Stratigraphic Section on a Sequence and Generalized Chronostratigraphic Section of the Sequence
7-62	Coastal Onlap

7-63	Coastal On-lap as a Function of Eustatic Level Change, Subsidence, and Sediment Supply
7-64	Three Scenarios during Coastal On-lap
7-65	Coastal On-lap Indicates a Relative Still Stand of Sea Level
7-66	Downward Shift in Coastal On-lap
7-67	Method for Calculating the Amount of Coastal On-lap and Downward Shift
	as a Measurement of Relative Fall of Sea Level
7-68	Continental Margin Cliniform Analysis
7-69	Downward Shift in Coastal On-lap in San Joaquin, California
7-70	Progradational and Marine On-lap Cycles, Tertiary, North Sea
7-71	Relative Changes in Sea Level, Concepts of Paracycles, Cycles, and Super Cycles
7-72	Correlation of Regional Cycles of Relative Sea-level Change and Averaging to Construct Global Cycles
7-73	Estimation of Eustatic Change from Jurassic to Holocene
7-74	First- and Second-order Global Cycles of Relative Sea-level Change
7-75	Global Cycle of Sea-level Changes, Jurassic to Tertiary
7-76	Control of Sedimentation and Depositional System
7-77	Reflection Terminations Patterns and Types of Discontinuity
7-78	Reflection Termination Patterns Types of Discontinuities That Define Cyclic Sequences
7-79	Accommodation Envelope as a Function of Eustacy and Subsidence
7-80	Eustacy, Relative Sea Level, Water Depth as a Function of Sea Surface, Water Bottom and Datum Position
7-81	Accommodation as a Function of Eustacy and Subsidence
7-82	Relative Sea Level as a Function of Eustacy and Subsidence
7-83	Response of Relative Sea Level to Differential Tectonic Thermal Subsidence
7-84	Effect of Relative Sea Level Rise on Coastline Position
7-85	Type 1 Unconformity
7-86	Response of Sedimentation on an Interval of Rapid Eustatic Fall
7-87	Distribution Of Low Stand Wedge Deposits Along The Outer Shelf/Upper Slope
7-88	New Space Added During an Interval of Constant Rate of Relative Sea Level Rise
	Following Type 1 Unconformity
7-89	Bayline Position and Low Stand Deposits During Rapid Short- and Long-period Eustatic Fall
7-90	Elements of Coastal On-lap Curve
7-91	Type 2 Unconformity
7-92	Effect of Equilibrium Point Migration on Fluvial Deposition in Prograding Environment
7-93	Effect of Shifting Equilibrium Point on Fluvial Deposition
7-94	Response of the Topset Bed Thickness to Eustatic Fall
7-95	Relationship Between Eustatic Sea Level and Phases of Erosion and System Track Deposition
7-96	Types Of Parasequence Sets
7-97	Recognizing and Dating Unconformities
7-98	Unconformity Types
7-99	Type 1 Erosion
7-100	Relation between Transgression or Regression and Eustatic Sea Level
7-101	A Deposition Sequence in Depth and Time and Its Relation to Marine Condensed Section,
	Coastal On-lap, Shoreline, and Eustatic Sea Level
7-102	Relationship of Sequence to Relative Changes of Coastal On-lap, Types and Ages of Unconformities,
	Condensed Intervals/Ages, and Inferred Eustatic Sea-level Changes
7-103	Estimation of Worldwide Hydrocarbon Reserve in Clastic Depositional Sequences
7-104	Diagrammatic Seismic Section Showing Common Stratigraphic Geometries and Terminations
7-105	Seismic Section Showing System Tracts and Other Elements of Depositional Sequences
7-106	An Idealized Siliciclastic Depositional Sequence Showing Depositional System Tracts
	and Their Bounding Surface
7-107	Schematic Diagram of Carbonate Lithofacies Distribution in a Sequence
7-108	Carbonate Facies Belts with Representative Textural Types
7-109	Diagrammatic Mixed Carbonate and Clastic Sequence Showing Lithologies
	and Sequence-stratigraphic Elements
7-110	High-stand Systems Tract
7-111	Carbonate High-stand Deposition
7-112	Low-stand System Tract Basin Floor Fan and Siliciclastic Low-stand Systems Tract
	during Basin Floor Fan Deposition

7-113	Low-stand Systems Tract Slope Fan and Siliciclastic Low-stand Systems Tract
7-114	during Slope Fan Deposition
7-114	Low-stand Systems Tract Prograding Wedge and Siliciclastic Low-Stand Systems Tract
7-114	during Prograding Wedge Deposition
7-115	Different Settings for Low-stand Tract Deposition
7-116	Type 1 Carbonate and Carbonate Early Low-stand Systems Tract
7-117	Transgressive Systems Tract and Siliciclastic Transgressive System Tracts
7-118	Carbonate Late Low-stand and Transgressive System Tracts
7-119	Sediments Accommodations Potential and Its Relationship to the Marine-condensed Sediments
7-120	The Stratigraphic Relationship of Marine Condensed Sections to Others Depositional Systems Tracts
7-121	Marine Condensed Sections and Their Relationship with the Stratigraphic Succession
7-122	Depth and Time Sections Showing the Marine Condensed Sections within the Sequence Frame Work
7-123	Siliciclastic Lithofacies and Siliciclastic Shelf-margin Systems Tract
7-124	Type 2 Carbonate Sequence Diagram Showing a Slow Fall of the Sea Level
	Interpreted as a Type 2 Sequence
7-125	Sequence Stratigraphy Depositional Model Showing Carbonate and Evaporite Lithofacies,
	Distribution of Carbonate and Evaporite Lithofacies within the Deposition Sequence Framework
7-126	Stratal Pattern in Type 1 Sequence—Stratal Pattern in Type 1 Sequence
	Deposited in the Basin with Shelf Break
7-127	Stratal Pattern in Type 1 Sequence Deposited in a Basin with Ramp Margin
7-128	Type 2 Sequence Boundary
7-129	Possible Reservoir Quality Sand in Siliciclastic Sequence
7-130	Summary of Factors Affecting the Hydrocarbon-play Potential of Siliciclastic Deposition Systems Tracts
7-131	Summary of Factor Affecting the Hydrocarbon-play Potential of Siliciclastic Deposition Systems Tracts
7-132	Systems Tracts in the Gulf Coast Basin
7-133	Systems Tracts within Depositional Sequences Deposited Basinward of USA Gulf Coast
	Contemporaneous Growth Faults
7-134	Triassic Chronostratigraphic and Eustatic-cycle Chart
7-135	Jurassic Chronostratigraphic and Eustatic-cycle Chart
7-136	Cretaceous Chronostratigraphic and Eustatic-cycle Chart
7-137	Cenozoic Chronostratigraphic and Eustatic-cycle Chart
7-138	High-resolution Seismic Recording Using Vibroseis
7-139	High-resolution Seismic Section
7-140	High-frequency Marine Seismic Section
7-141	Vertical Seismic Profiling Concepts
7-142	Up- and Downgoing Events
7-143	Raw, Up-going and Down-going Events
7-144	Identification of Seismic Reflectors
7-145	Separation of Up- and Downgoing Events in F-K Space
7-146	Comparison of VSP with Synthetic Seismogram
7-147	Predicting Interval Velocity Ahead of the Bit
7-148	Predicting Depth of a Seismic Reflector
7-149	Looking Ahead of the Bit
7-150	Increase in Angle of Incidence with Offset
7-151	AVO Classes
7-152	Angle Gathers
7-153	Two-term AVO Inversion
7-154	Portion of a CMP Stack Section Showing a Bright Spot, P-wave Intercept Section,
	Pseudo S-wave Section, and Poisson's Ratio Section
7-155	Orientation of P- and S-wave Particle Motion
7-156	Mode Conversion of Ray Paths
7-157	Schematic Representation of Three-component Records
7-158	F-K Domain Representation of Vertical Component Record in Figure 7-157
7-159	Vertical Component Record of Figure 7-157 after NMO Corrections Using S-wave Velocities
7-160	Vertical Component Record of Figure 7-157
7-161	The Near Surface as Seen by P- and S-waves
7-162	Comparison of P-P and P-SV Ray Paths
7-163	Ray Paths of CRP Traces for P-SV

7-164	Representative P-P, P-SV, and SH-SH Traces
7-165	Traces of Figure 7-164 after Time Scaling to Enhance Event Correlation
7-166	Shear-Wave and P-Wave Sections
7-167	Unpaired Reflections
7-168	Rock Velocities Versus Lithology from Well Logs
7-169	Rock Velocity Versus Lithology from Laboratory Examples
7-170	Flowchart for a 4-D Project
7-171	Wedge Model with Gas Cap
7-172	Relationships among Reservoir Thickness, Gas Saturation, and Amplitude Change
7-173	Raw Difference after Applying Global Equalization with a Single Scaler
7-174	Difference after Global Phase and Amplitude Match
7-175	Difference after Time- and Space-variant Cross-equalization
7-176	Difference along the Reservoir Horizon after Global Equalization
7-177	Difference along the Reservoir Horizon after Local Equalization
7-178	Seismic Difference after Matching with Cumulative Production
7-179	Residual Gas Saturation Map after Material Balance Matching and Calibration
7-180	Perspective View of the Sand Structure Containing the Currently Producing 4500 ft Reservoir
7-181	Smoothed Production History of the 4500 ft Reservoir
7-182	Inverted Legacy Data Volume Showing Acoustic Impedance
	12 ms below the Top of the Tracked 4500 ft Horizon
7-183	Time-lapse Difference Mapped on the 4500 ft Reservoir
7-184	Changes in P-wave Velocity, Poisson's Ratio, and Acoustic Impedance with Time of Production
7-185	Amplitudes Extracted from Partial-offset Stacked P-wave Data for the 4500 ft Reservoir
	from Phases I and II
7-186	Amplitudes Extracted from Partial-offset Stacked P-wave Data for the Little Neighbor Reservoir
	from Phases I and II
A-1	Earth Model for a Single Horizontal Layer
A-2	Two Horizontal Layers Earth Model
A-3	Earth Model for a Single Dipping Layer
A-4	Two Dipping Layers Earth Model
B-1	Data Input Card
B-2	Track/Bit Conventions
B-3	SEG A and B Formats—Header Block
B-4	SEG A and B Formats—Header Block (continued)
B-5	SEG A Format—Data Block
B-6	SEG B Format—Data Block
B-7	SEG B Format—Data Block (continued)
B-8	SEG X Format
B-9	SEG C Format—Data Block
B-10	SEG Y Format
B-11	SEG Y Format, Reel Identification Header—EBCDIC Image Block
B-12	SEG Y Format, Reel Identification Header—Binary Coded Block
B-13	SEG Y Format, Trace Data Block
B-14	SEG Y Format, Trace Identification Header Written in Binary Code
B-15	SEG Y Format, Trace Identification Header Written in Binary Code (continued)
B-16	SEG D Format
B-17	SEG D Format, General Header
B-18	SEG D Format, Channel Set Descriptor
B-19	SEG D Format, Channel Set Examples
B-20	SEG D Format, Start of Scan and Timing Word
B-21	SEG D Format, Demultiplexed Trace Header
B-22	Format Codes
B-23	SEG D Format, Data Recording Method, 2½ Byte Binary Exponent-multiplexed
B-24	SEG D Format, Data Recording Method, 2½ Byte Binary Exponent-demultiplexed
B-25	SEG D Format, Data Recording Method, Four Byte Hexadecimal Exponent - Multiplexed
B-26	SEG D Format, Data Recording Method, 32-Bit IEEE Format

C-1	Heave and Throw in a Normal Fault
C-2	Designation of Trap Types
C-3	Incident, Reflected, and Refracted Rays
C-4	T-X Plot with Velocities and Delay Times Labeled
C-5	Vector Diagram
C-6	Answer to Question 3
C-7	Receiver and Source Array Responses and Combined Source and Receiver Response
C-8	Wiggle Trace (left) and Variable Area (right) Trace Displays
C-9	Optimum Value for Maximum Correlation Shift
C-10	(a) CMP Stack, (b) Migrated Stack, and (c) Sketch
C-11	Optimum Migration Velocity
C-12	Four CMP Stacks of Same Data with Different Trace Spacings
C-13	Phase Shift Migrations of the Stacks Shown in Figure C-12

List of Tables

2-1	Divisions of Geologic Time
2-2	Clastic Grain Size Classification
2-3	Chemical Composition of Petroleum
2-4	Reservoir Rock Porosity
2-5	Reservoir Rock Permeability
2-6	Rock Grid
3-1	Source-generated Noise
3-2	Ambient Noise
3-3	Nyquist Frequency
3-4	Vertical Resolution
3-5	Variation of the Fresnel Zone with Time Frequency
3-6	T-X and τ -p Relationships
3-7	Frequency Table
5-1	Surface-based Navigation Systems
5-2	Basic GPS Overview
5-3	Airgun Specs and Array Parameters
5-4	Correlation Ghost Start and Stop Times
5-5	Selecting Geophone Parameter Values
5-6	In-water Systems Comparisons
5-7	Number Systems
5-8	Pros and Cons of Various Layout Strategies
6-1	Variation of Δt_{NMO} with Time, Velocity, and Offset
6-2	NMO Velocities
6-3	Sorted Trace Amplitudes, Median, and Average Values
6-4	Post-stack Migration Summary
6-5	Relative Processing Speeds of Migration Algorithms
6-6	Pre-stack Time and Depth Migration Types
6-7	Processes and Effect
7-1	2-D Models
7-2	P-P and P-SV CRP Trace Attribute Comparisons
7-3	Acoustic Impedance Change Caused by Gas Saturation Change
C-1	Output Frequencies

Contents

1 Overview and Summary
Introduction
Seismic Refraction Exploration Overview
Seismic Reflection Exploration Overview
2 Geological Background
Introduction
Geologic Time Scale
Internal Structure of the Earth
Rocks in the Earth's Crust
Deformation of Crustal Rocks
The Nature of Petroleum
Oil and Gas Accumulation
Hydrocarbon Traps
Workshop
3 Geophysical and Mathematical Background
Basic Geophysical Theory
Wave propagation
Seismic amplitudes
The seismic record
Mathematical Theory and Concepts
Sampled data
Convolution and Correlation
Time and Frequency Domains
Phase and Its Effect on Waveforms
Effect of Bandwidth
The F-K Domain
The Z-transform
The Radon transform
The Complex Trace
Workshop
4 Seismic Refraction Exploration
Introduction
Refraction Methods
5 Seismic Reflection Data Acquisition
Introduction
Permitting
Positioning
Positioning Summary
Signal Generation
Recording
Seismic Detectors
Noise
Recording Systems
2-D Acquisition Parameters and Operations
3-D Acquisition Parameters and Operations
Workshop

6 Seismic Reflection Data Processing
Introduction
Data Initialization
Preliminary Signal Processing
Noise Suppression
Velocity Analysis
Brute Stack
Deconvolution
Surface-consistent Scaling
Time-variant Spectral Whitening (TVSW)
Model-based Wavelet Processing (MBWP)
Inverse-Q Filtering
Residual Statics
Pre-stack Multiple Attenuation
CMP Stack
Post-stack Multiple Attenuation
Migration
Band-pass filtering
Time-to-Depth Conversion
Display
Seismic Data Processing Summary
Workshop
7 Seismic Reflection Data Interpretation
Introduction
Modeling
Seismic Inversion and Wavelet Processing
Seismic Stratigraphy
Modern Techniques and Future Applications of Sequence Stratigraphy
High resolution seismic data acquisition
Vertical Seismic Profiling (VSP)
Amplitude versus offset (AVO)
Shear waves and seismic stratigraphy
4-D Seismic Technology
Appendix A: Refraction Calculations
Single Horizontal Layer, V ₁ > V ₀
Two Horizontal Layers, V ₂ > V ₁ > V ₀
N Horizontal Layers, V ₀ < V ₁ < V ₂ < . . . < V _N
Single Dipping Layer, V ₁ > V ₀
Two Dipping Layers, V ₂ > V ₁ > V ₀
Appendix B: SEG Tape Formats
Introduction
Comments and Notes
Standard Tape Formats
Appendix C: Workshop Answers
Geological Background Workshop Answers
Geophysical and Mathematical Background Workshop Answers
Seismic Refraction Exploration Workshop Answers
Seismic Reflection Data Acquisition Workshop Answers
Seismic Reflection Data Processing Workshop Answers
Bibliography



Index

- 1-D modeling (data interpretation), 306–308
- 2-D modeling (data interpretation), 308–310
- 2-D seismic survey, 4, 6, 72, 119–125: parameters/operations, 72, 119–125
- 3-D modeling (data interpretation), 310
- 3-D seismic survey, 4–6, 72, 125–141: parameters/operations, 72, 125–141; marine, 130–135; land, 135–141
- 4-D seismic technology (stratigraphy), 298, 385–392: time-lapse seismic, 298, 385–392
- 16-bit electronics, 112–113
- 24-bit electronics, 111
- 1970s concepts (seismic stratigraphy), 319

A

- Absolute age, 8
- Accommodation space, 333, 432
- Accumulation (oil and gas), 21–23: requirements, 21–22; generation, 22–23; migration, 22–23; deposit, 22–23
- Acoustic impedance, 39, 297, 314, 368, 387, 443–444
- Acoustics system, 78–81: travel time measurement, 79; positioning method, 81; configuration diagram, 81
- Acquisition parameters/operations (seismic reflection data), 72, 119–141: 2-D, 72, 119–125; 3-D, 72, 125–141
- Aggradation, 337

- Airgun (seismic energy source), 84–89, 365:
operation, 84;
pressure-volume relationship, 85;
array specification, 86–88;
signature, 86–87
- Airwave, 40, 56
- Alberta Reef trend, 27
- Aliasing, 43, 50, 55, 57–58:
anti-alias filter, 50
- Alluvial phase, 327
- Ambient noise, 40–42, 105
- Amplitude (wave), 6, 36, 38–39,
46–50, 59, 62, 85, 87, 90, 115, 153,
160–162, 199–201, 210, 242, 298,
318, 323, 369–374, 388–392,
442–444:
amplitude versus offset, 6, 298,
369–374;
spectrum, 38–39, 46–50, 59, 87;
spike, 59;
instantaneous, 62;
signal, 85;
normalized, 90;
response, 115;
processing, 153, 160–162;
correction, 153, 199–201;
compensation, 210;
trace, 242;
reflection, 323;
difference/change, 388–392,
442–444;
time lapse difference, 443
- Amplitude versus offset (AVO), 6,
298, 369–374:
two-term inversion, 371–373;
three-term inversion, 373;
data processing, 373–374;
applications, 374;
summary, 374
- Analog recording, 42–43
- Analytic signal, 62
- Angle of incidence, 37, 39
- Angular unconformity, 14, 26, 321
- Anisotropic medium, 34
- Antenna, 78–79:
position/motion, 78
- Anti-alias filter, 50
- Anticline fold, 15–16
- Anticline trap, 16, 18, 24–25:
asymmetric, 25
- Anticline, 15–16, 18–19, 24–25,
246–247, 300:
fold, 15–16;
limb, 16;
trap, 16, 18, 24–25;
dome, 16;
rollover, 18–19
- Aperture width (migration), 262–264
- Apparent truncation, 322
- Appendices, 393–399, 401–444:
refraction calculations, 393–399;
SEG standard tape formats,
401–412;
workshop answers, 413–426;
color plates, 427–444
- Arc/fan shooting, 69
- Aromatics, 20
- Asphalts, 20
- Asthenosphere, 10
- Atlantic ridge, 10
- Attenuation rate (wave), 49
- Autocorrelation, 45–46, 49, 189,
217–219, 294–295, 313
- Automatic gain control (AGC),
162–163:
instantaneous, 163
- Axis (anticline), 16
- Azimuth, 80, 127, 137, 176–177:
distribution, 127
- B**
- Backward propagation, 209
- Band-pass filtering, 50, 52, 182,
279–281:
pass band, 50, 52;
time-variant filter, 280–281
- Bandwidth effect (resolution), 52–54,
94:
vertical, 52–53;
horizontal, 53–54
- Bandwidth loss (migration), 254–255
- Bandwidth, 52–54, 94, 97, 254–255,
302:
effect, 52–54, 94;
loss, 254–255
- Base station (geosynchronous), 75
- Base-lap, 322
- Basement rock, 12
- Basin deposit, 440
- Basin subsidence, 332
- Basin-floor fan, 354–355
- Basinward thinning, 304
- Bathythermography, 81
- Bayline, 334, 435
- Bed thickness, 299, 303, 307, 338,
436
- Beginning of tape (BOT), 17
- Bibliography, 445–453
- Big Bertha, 2
- Bin fractionation method, 139–140
- Bin/binning (data), 130–132,
139–140:
fractionation, 139–140
- Binary number, 115
- Biochronostratigraphy, 358
- Biogenic gas, 22
- Bird (depth controller), 80
- Body wave, 34
- Bolivar coastal oil fields, 26
- Bow tie effect, 301
- Brachistochrone, 36
- Brick pattern shooting, 138, 140
- Bright spot, 432
- Broadside shooting, 69
- Brute stack (data processing), 185,
215
- Bubble effect, 84–85
- Bulk density, 34
- Bulk modulus, 34
- Burg algorithm, 314, 317
- Bush City trend, 27–28
- Butane, 20
- Button patch method, 139–140
- Byte (index unit), 118
- C**
- Cable. *See Streamers.*
- Cambrian era, 8
- Cap rock, 28
- Carbon dioxide, 20

- Carbonate deposit/deposition, 343–348, 350, 354, 357, 439; lithofacies distribution, 343–344; catch-up deposition, 344–345, 348; keep-up deposition, 345, 348
- Card image (SEG format), 402
- Carrier phase measurement (GPS), 76
- Cascaded finite difference (migration), 154, 270–273
- Cascaded T-X domain (migration), 270–273
- Catch-up carbonate deposition, 344–345, 348
- Cell (data). *See* Bin/binning.
- Cement/cementation (rock), 13, 21
- Cenozoic cycle, 8, 358, 361
- Cenozoic era, 8
- Chamber fill orifice, 84
- Channel (magnetic tape), 115
- Chaotic shooting, 140
- Charge depth test, 91
- Charge size effect, 90
- Charged condition (airgun), 84
- Chemical rock, 12
- Chronostratigraphy (depositional sequence), 358–362; biochronostratigraphy, 358
- Circle shooting, 133–134, 140; concentric, 134
- Circular line of position, 75–76
- Circular migration, 249
- Classical mechanics, 33
- Clastic deposit/deposition, 12–14, 21, 342–344, 358
- Climate, 332, 347–348, 350
- Clipping (data), 119
- Clock pendulum, 61
- Closure (trap), 24
- Coastline position, 433, 435
- Coil resistance, 104–105
- Color plates, 427–444
- Combination trap (strati-structural), 24, 27–28
- Common depth point (CDP), 130
- Common midpoint (CMP) stack, 4, 61, 77, 121–123, 127, 130–132, 136, 153, 156, 159, 174, 177–178, 182, 184–185, 211–214, 216, 223–225, 237–239, 241, 246, 302, 370; pre-stack multiple attenuation, 225; seismic reflection data processing, 241
- Common offset format, 155–156
- Common receiver format, 155
- Common reflection point (CRP), 379–380
- Common source record, 155–156
- Compass data, 80
- Compass/birds unit, 80
- Complementation, 116
- Complex trace, 61–62; analysis, 61–62
- Compressive stress, 15–16
- Computation (velocity analysis), 181
- Concentric circle shooting, 134
- Concordant stratal surface, 318
- Condensate, 20
- Conflicting dips, 232
- Constant velocity stack (CVS), 177–179; display, 177–179
- Continental crust, 9
- Continental drift, 10
- Continental margin, 328
- Continuous shooting, 3, 429
- Continuous velocity log (CVL), 170
- Control points, 212
- Convolution, 44–46, 49; method, 44; correlation, 44–46, 49
- Convolution method, 44
- Core (Earth), 9
- Correlation, 44–46, 49, 59, 93–94, 189, 212–213, 217–219, 294–295, 313; convolution, 44–46, 49; autocorrelation, 45–46, 49, 189, 217–219, 294–295, 313; cross-correlation, 45, 59, 93, 213; zero-phase, 93–94; minimum-phase, 94; window selection (residual statics), 212
- Course made good (vessel), 79
- Cratonic basin, 346–347
- Creekology, 1
- Crest (anticline), 16
- Cretaceous cycle, 8, 358, 360
- Cretaceous period, 8
- Cross-correlation, 45, 59, 93, 213; vibrator, 93; model trace building, 213
- Cross-feed, 114
- Cross-line fold, 126
- Cross-line shift (source), 140–141
- Crude oil, 19–20, 22
- Crust (Earth), 9–10, 12–19; oceanic, 9; continental, 9; rock, 12–19
- Crustal rock, 12–19; deformation, 14–19; folding, 15–19
- Cutoff frequency, 49
- Cuttings (drilling), 9
- Cycles and paracycles (seismic stratigraphy), 337–339
- Cyclic redundancy check, 402
- Cyclic sequence stratigraphy, 331–334; concepts and principles, 331–334

D

- Damping (wave), 100, 103–104
- Data acquisition (seismic reflection), 3–6, 39–43, 55, 71–146, 298, 362–363, 401–412, 418–421; overview, 3–6; recording, 3–4, 39–43, 55, 71, 99–118, 401; digital, 42–43, 401; filtering, 43; introduction, 71–72; permitting, 71–72; positioning, 71–83; signal generation, 71, 83–99; 2-D parameters/operations, 119–125;

- 3D parameters/operations, 125–141;
workshop, 142–146, 418–421;
high-resolution, 298, 362–363;
SEG standard tape formats, 401–412
- Data block (SEG format), 402
- Data initialization (data processing), 152, 154–160
- Data interpretation (seismic reflection), 6, 297–392:
introduction, 297–298;
modeling, 298–310;
seismic inversion and wavelet processing, 310–317;
seismic stratigraphy, 318–362;
modern techniques and future applications of sequence stratigraphy, 361–392
- Data processing (seismic reflection), 6, 147–295, 421–426:
introduction, 147–154;
vibrator data, 147–154;
data initialization, 152, 154–160;
signal, 160–166;
noise suppression, 167–169;
velocity analysis, 170–185;
brute stack, 185;
deconvolution, 186–199;
surface-consistent scaling, 199–201;
time-variant spectral whitening, 201–204;
model-based wavelet processing, 204–208;
inverse-Q filtering, 208–210;
residual statics, 211–215;
pre-stack multiple attenuation, 216–240;
common midpoint stack, 241;
post-stack multiple attenuation, 242–245;
migration, 246–279;
bandpass filtering, 279–281;
time-to-depth conversion, 282;
display, 282–285;
summary, 285–286;
workshop, 287–295, 421–426
- Data reduction (velocity analysis), 182
- Data wrap around, 257
- Datum concept, 73
- Datum position, 432
- Datum statics, 157–160:
correction, 157–158
- Datum transformation, 74–75, 83
- Dead section, 112
- Decibel (dB), 49
- Declination, 80
- Deconvolution (seismic reflection data processing), 94, 153, 185–199, 209, 216–220, 312:
Wiener, 94, 192–193;
signature, 186–187;
time domain, 186;
time-variant, 186–197;
whitening, 186–192, 194, 196–197, 216;
gapped, 192, 216, 218–219;
surface-consistent, 198–199;
spiking, 209, 312;
 τ - p domain, 216–220
- Deformation (rock), 14–19
- Demultiplex/demultiplexing, 152, 154
- Deposition (rock), 8, 12–14, 21, 298, 318–361, 432–439:
deposition process, 12–14;
clastic, 12–14, 21, 342–344, 358;
depositional environment, 298;
depositional sequence, 318–361;
depositional system, 318–361, 432–439;
depositional system tract, 318–361, 432–439;
eustacy, 326, 329, 332–341, 343, 358–361, 432–436;
fluvial, 337;
carbonate, 343–348, 350, 354, 357, 439;
siliciclastic, 343, 345–349, 353–354;
depositional model, 350;
evaporite, 351–351
- Depositional environment, 298
- Depositional model, 350
- Depositional sequence, 318–361:
seismic stratigraphy, 339–343;
redefined, 339–343;
chronostratigraphy, 358–362
- Depositional system, 318–361, 432–439:
analysis, 318;
tract, 318–361, 432–439
- Depositional system tract (seismic stratigraphy), 318–361, 432–439:
deposition, 318–361, 432–439;
eustacy, 326, 329, 332–341, 343, 358–361, 432–436;
- highstand, 335–337, 342–348, 357–358, 437;
transgressive, 335, 342, 347–348, 355–357;
fluvial, 337;
lowstand, 342, 345–346, 435, 438–439;
shelf margin, 342, 349, 351, 357–358, 439;
clastic, 342–344, 358;
hydrocarbon play, 353–354;
Gulf Coast Basin, 354–356;
carbonate, 343–348, 350, 354, 357, 439;
siliciclastic, 343, 345–349, 353–354;
evaporite, 351–351
- Depth (reservoir), 21–23
- Depth controller, 80
- Depth indicator, 81
- Depth migration, 249–253, 256, 260, 273–274, 431
- Depth point smear, 232
- Depth slice, 284
- Depth step (Gazdag's phase shift migration), 269
- Despiking, 93, 154
- Detector location, 67
- Devonian period, 8
- Differential tectonic thermal subsidence, 334, 433
- Diffraction (wave), 41–42, 54, 129, 256–258, 273, 301, 319, 322:
energy, 129;
summation, 273
- DigiCOURSE Digrange, 79
- Digital recording, 42–43, 401
- Dip (rock), 3, 15, 17, 56–58, 60, 126–127, 134, 154, 156, 176, 182, 231–240, 246–248, 263–264
- Dip moveout (DMO), 126–127, 134, 154, 182, 231–240:
pre-stack multiple attenuation, 182, 231–241;
dipping reflector, 231–233;
conflicting dips, 232
- Dip moveout (pre-stack multiple attenuation), 182, 231–241:
moveout for dipping reflector, 231–233;

- data processing, 233–235;
synthetic example, 236–237;
field data examples, 238–240
- Dip plot, 3, 17, 57–58
- Dip shooting, 3
- Dip slip fault, 17
- Dipping reflector, 156, 176, 231–233, 246–248:
moveout, 231–233
- Dip-related problem (velocity analysis), 182
- Dirac delta function, 59
- Direct wave, 40
- Disconformity, 321
- Discontinuity surface, 320
- Discontinuity, 320, 332, 341–342:
surface, 320
- Displacement, 299
- Display (data processing), 282–285
- Distortion (seismic), 99, 114, 299–306:
harmonic, 114;
model, 299–306
- Diversity stack process, 148–151
- Dix equation, 181
- Dome, 16, 28, 134:
anticline, 16;
salt, 28, 134;
salt diapir, 28
- Doppler shift, 76
- Doublet, 59
- Downlap surface (DLS), 340
- Downlap, 322, 340, 343:
base-lap, 322;
surface, 340
- Down-to-the-basin fault, 25
- Downward continuation migration (data processing), 249–253, 256, 260, 273–274, 431:
time and depth, 251–252, 431
- Drag fold, 25
- Drilling (well), 1–2
- Dry gas, 20, 22–23
- Dynamic base station, 75
- Dynamic range, 114:
instantaneous, 114
- Dynamite (energy source), 364
- E**
- Earth crust, 9–10, 12–19:
oceanic, 9;
continental, 9;
rock, 12–19
- Earth impulse response, 44
- Earth model (refraction calculations), 393–399:
single horizontal case, 393–395;
two horizontal layers case, 393, 395–396;
single dipping layer case, 393, 397–398;
two-dipping layers case, 393, 399;
N horizontal layers case, 396–397
- Earth model, 69, 183, 393–399:
refraction calculations, 393–399
- Earth reflectivity function, 44
- Earth structure (internal), 9–11, 429
- Earthquake activity, 11
- East Texas oil field, 14, 26
- Economic viability, 5
- Editing (trace), 154
- Effective fold, 126
- Elastic medium, 33–34
- Elastic moduli, 34
- Electric field, 9
- Electromechanical transducer, 99
- Electromotive force, 103
- Electronic data transfer, 83
- Elevation statics, 158
- Ellipsoid, 74
- Empirical approach (amplitude processing), 161–162
- End of tape (EOT), 117
- Energy source (vertical seismic profiling), 81, 364–365:
location, 81;
dynamite, 364;
other impulsive sources, 365;
vibrator, 365;
airgun, 365
- Enhanced recovery, 20
- Eocene epoch, 8
- Epoch (Earth history), 8–9
- Equilibrium point, 334, 336–337, 343:
migration, 337
- Era (Earth history), 8
- Eroded fold, 16–17
- Erosion (rock), 12, 14, 16–17, 334, 338–340, 347, 351:
process, 12, 14;
fold, 16–17
- Ethane, 20
- Eustacy, 326, 329, 332–341, 343, 358–361, 432–436
- Evaporite lithofacies, 350–351:
deposition, 350–351
- Exhaust port, 84
- Expendable bathythermography, 81
- Explicit finite difference, 253
- Exploding reflector model (seismic reflection data processing), 251
- Exploration method, 2–6:
well surveying, 2;
magnetic anomaly, 2;
gravitational anomaly, 2;
seismology, 2–6;
seismic refraction method, 2;
seismic reflection method, 2–6
- Exploration sequence, 300
- Explosive (seismic energy source), 89–92:
operation, 90;
cord, 91–92
- Explosive cord, 91–92
- Extended Stolt migration, 154
- Extensional stress, 15
- External geometry, 318
- F**
- Facies change, 26
- Fan/arc shooting, 69
- Far-field signature, 85, 90
- Fast/finite Fourier transform (FFT), 48
- Fault cutting reservoir, 25
- Fault/faulting (rock), 15, 17–18, 25–26, 54, 246–247, 303–304:
normal, 17–18;
motion, 17;
plane, 17–18;

- oblique slip, 17;
dip slip, 17;
strike slip, 17–18;
reverse, 17–18;
growth, 18, 25;
thrust, 18, 25–26;
displacement, 18, 54;
down-to-the-basement, 25;
fault cutting reservoir, 25;
trap, 25;
pseudo, 303–304
- Fermat's principle, 36
- Ferranti ORE Trackpoint, 79
- File (tape division), 117
- Fill passage, 84
- Filter scan, 279–281
- Filter/filtering, 43, 49–52, 82, 104, 111, 154, 167–169, 182, 187–189, 192–193, 201–206, 208–210, 216, 225–232, 279–281, 297, 312:
data, 43;
frequency, 49–50;
band-pass, 50, 52, 182, 279–281;
anti-alias, 50;
time variant, 154, 280–381;
velocity, 167–169, 216;
inverse-Q, 208–210;
F-K, 216, 225–229;
radon transform, 230–232;
scan, 279–281;
homomorphic, 312
- F-inflection point, 333–335
- Finite difference migration (data processing), 154, 252–253, 258–259, 261–262, 265–268, 270–273:
cascaded, 154, 270–273;
explicit, 253;
implicit, 253, 265–268;
T-X domain, 261–262;
input parameters, 265–267;
migration velocity errors, 267–268
- Finite impulse response (FIR), 111
- Firing chamber, 84
- Firing line, 84
- First break, 38, 192:
refraction, 38
- F-K domain, 55–58, 216, 225–229, 235, 262, 268:
plane, 56;
filtering, 216, 225–229;
Stolt migration, 262;
migration parameters, 268
- F-K filtering (pre-stack multiple attenuation), 216, 225–229
- F-K migration parameters, 268
- F-K plane, 56
- Flexibin/bin shooting, 140
- Flooding surface, 320, 337
- Fluvial deposition, 337
- Fluxgate magnetometer, 80
- Fold/folding (rock), 15–19, 25, 125–126, 135–136:
monocline, 15–16;
anticline, 15–16;
syncline, 15–16;
old, 16;
nose, 16;
symmetric/asymmetric, 16;
planeplaned, 16;
plunging, 16–17;
eroded, 16–17;
drag, 25;
in-line, 125;
maximum, 125;
effective, 126;
taper, 136
- Footwall, 17–18
- Fore/aft antenna movement, 78
- Formation gas, 20
- Formation volume factor (FVF), 20
- Fossil mold, 22
- Fossil, 9, 22
- Fourier transform (FT), 47–48, 55, 58
- Fracture (rock), 17, 28
- Free gas cap, 24
- Frequency domain, 46–50, 86–87:
time domain, 46–50
- Frequency filter types, 49–50
- Frequency spectrum, 48, 62:
instantaneous, 62
- Fresnel zone, 54, 128–129
- Full swath roll, 137
- Full-fold coverage, 123
- G**
- Gain control, 161–163
- Gain function, 161–163
- Gapped deconvolution, 192, 216, 218–219
- Gardener equation, 383
- Gas cap, 24, 442
- Gas hydrate, 321
- Gas only pool, 24
- Gas saturation, 442
- Gas-to-oil ratio (GOR), 20
- Gate length, 163
- Gauss-Seidel method, 160, 199–200
- Gazdag's phase shift migration, 255, 269:
depth step, 269;
velocity errors, 269
- Geocentric ellipsoid, 74
- Geodesy, 73–74, 83:
parameter, 83
- Geodetic latitude/longitude, 73–74
- Geoflex (explosive cord), 91
- Geoid model, 83
- Geoid, 73, 83
- Geologic image/model, 6
- Geologic marker, 314–315
- Geologic objective, 5
- Geologic time scale, 8–9
- Geological background, 7–31, 413–415:
uniformitarianism, 7;
law of superposition, 7–8;
law of horizontality, 8;
geologic time scale, 8–9;
internal earth structure, 9–11;
crustal rock, 12–14;
crustal rock deformation, 14–19;
nature of petroleum, 19–20;
oil and gas accumulation, 21–23;
hydrocarbon trap, 24–28;
workshop, 29–31, 413–415
- Geometric spreading, 4, 67–68, 121–122, 153, 161–162, 201, 286:
coverage, 4, 68;
correction, 153, 286
- Geometry database, 152–153
- Geophone (recorder), 99, 101–110, 164–165, 278:
over-damped, 103;
noise, 105–110;
array, 105–110;
tilt, 105
- Geophysical and mathematical background, 33–66, 416–417:

basic geophysical theory, 33–42; mathematical theory and concepts, 42–62; workshop, 63–66, 416–417

Geophysical image/model, 6

Geophysical theory, 33–42: seismic wave propagation, 34–38; seismic wave amplitude, 38–39; seismic data record, 39–42

Geosynchronous base station, 75

Geothermal gradient, 23

Ghost/ghosting (OBC), 97–98, 101–102, 164–166, 306: vibroseis, 97–98; source, 101; receiver, 101; combined source-receiver, 101

Global cycle (relative sea level), 328–331

Global positioning system (GPS), 76–80, 83, 155: pseudo-range measurement, 76

Goat trail shooting, 140

Graben, 18

Grain size (rock), 13, 23

Granite wash, 28

Gravitational anomaly, 2

Gravity fault, 17–18

Ground motion, 99

Ground roll, 35, 40, 56, 105–107

Ground water, 23

Group coded recording, 117

Group interval effect, 58

Growth fault, 18, 25

Guided wave, 41–42, 46

Gulf Coast Basin system tract (seismic stratigraphy), 354–356

Gulf of Mexico, 19

Gun volume, 85

Gyrocompass, 79–80

H

Hanging wall, 17–18

Harmonic distortion, 114

Harmonics (vibrator), 97–98, 114: distortion, 114

Head buoy, 80

Head wave, 38, 40, 42

Header block (SEG format), 402

Heading (ship), 79

Heave, 17–18

Helium, 20

Hemipelagic facies, 321

Hexadecimal number, 115

Hexagonal patch shooting, 140

High-resolution data (sequence stratigraphy), 298, 362–363: acquisition, 362–363

Highstand system tract (seismic stratigraphy), 335–337, 342–348, 357–358, 437: deposition, 335–337; shelf margin system, 357–358

Historical geology, 8

Holocene epoch, 8

Holocene/Pleistocene models (seismic stratigraphy), 351–352

Homogeneous medium, 33–34

Homomorphic filter, 312

Horizontal migration (oil and gas), 23

Horizontal reference datum, 73

Horizontal resolution, 53–54

Horizontal section, 153

Horizontality, 8

Horst, 18, 302

Hugoton gas field, 27–28

Huygen's principle, 38

Hydrocarbon (nature of) 19–20: petroleum, 19–20; chemical elements, 19

Hydrocarbon play (seismic stratigraphy), 353–354: depositional system tract, 353–354

Hydrocarbon potential, 14, 16, 18, 21, 24–28, 298, 318–362

Hydrocarbon trap, 14, 16, 18, 21, 24–28, 298, 342–343, 353, 356: sedimentary rock, 24; pinch-out, 24, 27–28; structural, 24; stratigraphic, 24; strati-structural/combination, 24, 27–28; anticline, 24–25; tilting, 24;

closure, 24; reservoir spill point, 24; free gas cap, 24; mature hydrocarbon, 24; saturated pool, 24; undersaturated pool, 24; gas only pool, 24; pay zone, 25; fault, 25; growth/down-to-the-basin fault, 25; fault cutting reservoir, 25; thrust fault, 25–26; drag fold, 25; overthrust belt, 25–26; Western Overthrust Belt, 25–26; Painter Reservoir field, 25–26; up-dip facies change, 26; Statfjord field, 26; angular unconformity, 26; East Texas oil field, 26; Prudhoe Bay oil field, 26; Bolivar coastal oil fields, 26; reefs, 26–27; Alberta Reef trend, 27; Redwater oil field, 27; Michigan Basin Silurian reef trend, 27; pinnacle reef, 27; lenticular sandstone reservoir, 27–28; Bush City trend, 27–28; Hugoton gas field, 27–28; salt dome, 28; salt diapir, 28; cap rock, 28; fractured reservoir, 28; granite wash, 28; geometry, 298

Hydrogen sulfide, 20

Hydrophone (recorder), 99–102, 164–166: equivalent circuit, 100; near-field, 101; array, 101

Hydrostatic pressure gradient, 23

Hyperbolic line of position, 75–76

Hyperbolic migration, 249

I

Igneous rock, 12

Imaging, 6, 94, 233, 248–249, 298, 385: resolution, 52–54, 94, 298

Impedance (acoustic), 39, 297, 314, 368, 387, 443–444
 Implicit finite difference, 253, 265–268:
 input errors, 265–267
 Impulse response, 44, 234
 Impulsive energy source, 89, 299, 364–365
 Inclinometer, 78–79
 Inhomogeneous medium, 34
 In-line fold, 125
 In-line shift (source), 140–141
 Inline shooting (seismic refraction exploration), 67–69:
 intensive, 67–68
 Instantaneous amplitude, 62
 Instantaneous automatic gain control, 163
 Instantaneous dynamic range, 114
 Instantaneous frequency, 62
 Instantaneous phase, 62
 Instantaneous velocity, 170
 Integrated positioning network, 81–82
 Interbed multiple (reflection), 41
 Interference, 241
 Intergranular void, 21
 Internal convergence, 321
 Internal Earth structure, 9–11, 429
 Internal record gap, 117
 Interpolation, 258–260
 Interval velocity, 170, 323
 Intragranular void, 21–22
 Inverse fast/finite Fourier transform (IFFT), 47–48, 227
 Inverse modeling (seismic reflection data interpretation), 310
 Inverse-Q filtering (seismic reflection data processing), 208–210
 Inversion approach, 6
 Inverted legacy data volume, 443
 Irreducible water saturation, 23
 Irregular shooting, 140
 Isochronous paleodepositional surface, 318

Isostasy, 15
 Iso-time, 153
 Isotropic medium, 33–34
 Iso-velocity, 153

J

Joint (rock), 17
 Jumper cable, 113
 Jurassic cycle, 8, 358–359
 Jurassic period, 8

K

Kalman filter, 82
 Karcher, Clarence, 3
 Keep-up carbonate deposition, 345, 348
 Kinetic energy, 61
 Kirchhoff impulse response, 234–235, 260–261
 Kirkchhoff migration (seismic reflection data processing), 234–235, 250–251, 256, 258–262, 273–277:
 impulse response, 234–235, 260–261;
 T-X domain, 260–261;
 input parameters, 262
 Klauder wavelet, 94

L

Lambert conical mercator, 74
 Land ground recording system, 113–118
 Land seismic record, 42
 Land surveying (positioning), 42, 71–72, 82, 113–118:
 seismic record, 42;
 land ground recording system, 113–118
 Lapout surface, 318
 Laser range/angle measurement, 79
 LaserTrack system, 79
 Law of horizontality, 8
 Law of reflection, 37
 Law of refraction, 37

Law of superposition, 7–8
 Layer thickness, 68
 Leaching, 13
 Lead-in section, 111
 Least significant bit (LSB), 116
 Least time path, 36
 Lenticular sandstone reservoir, 27–28
 Limb (anticline), 16
 Line of position (LOP), 75–76
 Line orientation, 431
 Linear event, 46
 Linear moveout (LMO) correction, 154–155
 Linear noise attenuation (suppression), 169
 Listen time, 94
 Lithofacies, 321
 Lithogenetic sequence, 352
 Lithology, 384
 Lithosphere, 10
 Live section, 112
 Local datum, 74
 Long period statics, 215
 Long wavelength statics, 214–215
 Longitude measurement, 430
 Loop (survey), 82
 Love wave, 35
 Low frequency (radio), 76
 Lowstand system tract (seismic stratigraphy), 342, 345–346, 435, 438–439
 Lowstand wedge, 335, 438
 Low-velocity layer, 156

M

Magnetic anomaly, 2, 80
 Magnetic field, 2, 9–10, 80, 102–103:
 anomaly, 2, 80;
 polarization, 10
 Magnetic polarization, 10
 Magnetic tape record, 117, 154:
 data reformatting, 154
 Magnetostratigraphy, 358

- Mantle (Earth), 9–11; convection current, 10–11
- Mantle convection current, 10–11
- Map/mapping, 74–75, 83; map projection, 74–75
- Marine condensed section (MCS), 340–341, 347–351
- Marine in-water recording system, 111–113
- Marine navigation (positioning), 71–72, 75–82
- MARS system, 79
- Mathematical theory and concepts, 42–62; sampled data, 42–43; convolution and correlation, 44–46; time and frequency domains, 46–50; phase effect on waveforms, 50–52; bandwidth effect, 52–54; F-K domain, 55–58; Z-transform, 58–59; radon transform, 60–61; complex trace, 61–62
- Mature hydrocarbon, 24
- Maximum correlation shift, 212
- Maximum dip (migration), 263–264
- Maximum error tolerance, 77
- Maximum fold, 125
- Maximum offset, 135–136; maximum minimum, 135
- Maximum-delay wavelet, 51–52
- Maximum-phase wavelet, 51–52
- Mean sea level, 73
- Meanderbelt, 357
- Meandering stream channel, 5
- Median stack (post-stack multiple attenuation), 216, 242–244
- Medium frequency (radio), 76
- Mesozoic era, 8
- Metamorphic rock, 12
- Methane, 19–20, 22
- Michigan Basin Silurian reef trend, 27
- Migration (oil and gas), 21–23; migration path, 21; horizontal, 23
- Migration (data processing), 127–130, 134, 136, 171, 231, 233–234, 239–241, 246–279, 337, 431; aperture/halo, 127–130, 136; zero offset, 134; cascaded finite difference, 154, 270–273; velocity, 171, 265, 267–269, 271; pre-stack, 231, 233, 240–241, 274–279; post-stack, 234, 239, 241, 273–274; problem, 246–248; solution, 248–249; algorithms, 249–250, 258–279; time and depth, 249–253, 260, 273, 431; hyperbolic, 249; circular, 249; Kirchhoff, 250–251, 256, 260–262; exploding reflector model, 251; downward continuation, 250–252, 256, 274, 431; finite difference, 252–253, 261–262, 265–268, 270–273; Stolt F-K, 254–255, 262; bandwidth loss, 254–255; Gazdag's phase shift, 255, 269; phase shift, 255, 269, 273; limitations, 256–258; multi-dip model, 258; conclusion, 258–260; Kirchhoff T-X domain, 260–261; finite difference T-X domain, 261–262; input parameters, 262–269, 271; aperture width, 262–264; maximum dip, 263–264; velocity errors, 265, 267–269, 271; F-K parameters, 268; Stolt stretch factor, 268; stages, 270; equilibrium point, 337
- Migration algorithms, 249–250, 258–279; processing speed, 273–274
- Migration aperture/halo, 127–130, 136
- Migration bandwidth loss, 254–255
- Migration in stages, 270
- Migration input parameters (data processing), 262–269, 271; Kirchhoff migration, 262; aperture width, 262–264; maximum dip, 263–264; velocity errors, 265, 267–268, 271; finite difference, 265–267; F-K parameters, 268; stretch factor, 268
- Migration to zero offset (MZO), 134
- Migration velocity, 171, 265, 267–269, 271; errors, 265, 267–269, 271
- Mineral, 12
- Minimum-delay wavelet, 51–52
- Minimum-phase correlation, 94
- Minimum-phase wavelet, 51–52
- Miocene epoch, 8
- Mississippian period, 8
- Mistie (location difference), 82
- Model trace building (residual statics), 212–214; cross-correlation, 213
- Model-based phase compensation, 153
- Model-based wavelet processing (data processing), 204–208; summary, 208
- Modeling (data interpretation), 298–310; introduction, 298–299; seismic distortion, 299–306; 1-D, 306–308; 2-D, 308–310; 3-D, 310; inverse, 310; conclusions, 310
- Modeling, 6, 11, 153, 156, 186–187, 204–208, 212–214, 251, 258, 276–277, 298–310, 332, 350–352, 442; geologic model, 6; geophysical model, 6; plate tectonics model, 11, 298; phase compensation model, 153; near-surface model, 156; trace model, 186–187; wavelet processing model, 204–208; trace-building model, 212–214; travel time model, 214; exploding reflector model, 251; multi-dip migration model, 258; overthrust model, 276–277; seismic reflection data interpretation, 298–310; distortion model, 299–306; seismic model, 304–310; normal incidence model, 308;

- ray trace model, 308–310;
inverse model, 310;
quantitative model, 332;
depositional model, 350;
Pleistocene/Holocene models,
351–352;
wedge model, 442
- M**odulus of elasticity, 34
- Mohorovicic discontinuity (Moho),
9–10
- Monocline fold, 15–16
- Most significant bit (MSB), 116
- Moveout, 60, 126–127, 134, 154–155,
171–185, 216–240:
moveout/velocity dip methods,
216–240
- Moveout/velocity dip methods
(pre-stack multiple attenuation),
216–240:
common midpoint stack, 225;
F-K filtering, 225–229;
radon transform (τ - p domain)
filtering, 230–231;
dip moveout, 231–240;
dipping reflector, 231–233
- Multi-dip model (migration), 258
- Multifold shooting, 4, 159
- Multiple attenuation (data
processing), 185, 216–240:
velocity analysis, 185;
predictability methods, 216–225;
moveout/velocity/dip methods,
216–240;
wave equation, 216, 220–225;
amplitude methods, 216
- Multiple attenuation (velocity
analysis), 185
- Multiple reflection, 40–42, 184–185,
220–221, 225, 319, 429, 432:
water bottom, 41, 220–221, 225,
432;
interbed, 41;
velocity analysis, 184–185
- Multiple streamer effect, 132, 134
- Multiplexed data, 118
- N**
- Naphthenes, 20
- Natural frequency, 104–105
- Natural gas, 19–20, 22
- Navigation (vessel), 75–82:
navigation system, 75;
vessel-relative positioning method,
81
- Navigation processing, 147
- Navy Navigation Satellite System
(NNSS), 76
- Near-field hydrophone, 101
- Near-surface anomaly effect (velocity
analysis), 183–184
- Near-surface model, 156
- Near-trace gather (NTG), 155–156
- Near-vessel tracking, 81–82
- Nigeria, 19
- Nitrogen, 20
- NMO correction, 153, 172–174,
177–180, 182, 185, 211, 225,
233–234, 246
- Noise suppression (data processing),
167–169:
velocity filtering, 167–169;
linear noise attenuation, 169
- Noise test, 106–107
- Noise, 40–42, 44, 55–56, 93, 95,
105–110, 122, 124, 151, 167–169,
208–210, 299, 302, 310, 313:
noise-free seismic trace, 40–42, 44;
ambient, 40–42, 105;
source-generated, 40–41, 105, 124;
spike, 93;
signal-to-noise ratio, 95, 122, 208;
spread, 106;
test, 106–107;
suppression, 167–169;
deconvolution, 208–210;
random, 310
- Noise-free seismic trace, 40–42, 44
- Non-depositional hiatus, 321
- Non-geocentric ellipsoid, 74
- Non-orthogonal pattern shooting,
139–140
- Non-return-to-zero, 117
- Non-zero reflection, 233
- Normal fault, 17–18
- Normal incidence model, 308
- Normal incidence, 39, 308:
model, 308
- Normal moveout (NMO), 77,
119–122, 126, 153–154, 171–180,
182, 185, 211, 214, 225, 233–234,
246:
correction, 153, 172–174, 177–180,
182, 185, 211, 225, 233–234,
246;
velocity, 171–173, 177;
stretch, 174;
mute time/schedule, 174–175;
residual, 211, 214
- Normal structure, 69
- Normalized amplitude, 90
- Nose (folding), 16
- Number system, 115:
radix/base, 115
- Numbering system (land surveying),
82
- Nyquist frequency, 43, 55
- O**
- Oblique progradation, 326
- Oblique slip fault, 17
- Obstacle avoidance (shooting),
124–125, 134–136, 140
- Ocean bottom cable (OBC)
operations, 147, 155, 164–166:
scaling, 164–166
- Oceanic crust, 9
- Octal number, 115
- Octave, 49
- Odds and evens shooting, 138, 140
- Offset (data), 67, 119–121, 135–136,
155–156, 182–183, 216–217, 444:
velocity analysis, 182–183;
restricting, 183;
periodicity, 216–217;
partial offset, 444
- Offset (shooting), 67, 135–137
- Offset-related problems (velocity
analysis), 182–183
- Oil and gas accumulation, 14, 19–23:
habitat, 14;
nature of petroleum, 19–20;
crude oil, 19–20, 22;
natural gas, 19–20, 22;
gas-to-oil ratio, 20;
oil in place, 20;
requirements, 21–22;
oil window, 22;

generation, 22–23;
migration, 22–23;
deposit, 22–23
Oil in place, 20
Oil window, 22
Old fold, 16
Onlap, 322, 325–328, 336, 341, 435:
 base-lap, 322
Open basin, 346
Optical recording, 42
Ordovician period, 8
Organic matter, 22
Organic rock, 12
Orogeny, 8
Overburden, 15, 69
Overlap, 4
Overpressured shale, 303, 305
Overshoot, 85
Overthrust belt, 25–26, 276–277:
 model, 276–277
Overthrust model, 276–277
Ownership, 72

P

Painter Reservoir field, 25–26
Paleocene epoch, 8
Paleontology, 9
Paleosol, 339
Paleozoic era, 8
Pangea, 11
Paracycles and cycles (seismic stratigraphy), 337–339
Paraffins, 20
Parasequence set, 338–339, 437:
 type, 437
Parasitic resonance, 104
Paravane/diverter, 88, 111–112
Parity bit, 118
Parity/quality check (SEG format),
 402
Partial stacking, 182
Partial-offset data, 444
Pass band, 50, 52
Patch (stations), 135

Patch shooting, 140
Pattern (shooting), 137–140
Pay zone, 25
Peak-to-peak strength measures,
 86–87
Peg-leg multiple (reflection), 41, 225
Pennsylvanian period, 8
Period (Earth history), 8–9
Periodicity (offset), 216–217
Perm plug, 22
Permeability (rock), 13–14, 21–23
Permian period, 8
Permitting (data acquisition), 71–72
Petroleum (nature of), 19–20:
 hydrocarbons, 19–20;
 chemical elements, 19
Petroleum exploration history, 1–6:
 surface seepage, 1;
 drilling, 1–2;
 creekology, 1;
 trendology, 1;
 scientific theory, 2;
 surface geology, 2;
 exploration method, 2;
 well surveying, 2;
 magnetic anomaly, 2;
 gravitational anomaly, 2;
 seismology, 2;
 seismic refraction method, 2;
 seismic reflection method, 2–6
Petroleum geology, 8
Petroleum habitat, 14
Phase compensation, 153, 209:
 model-based, 153
Phase definition (angle), 50
Phase effect (waveform), 50–52
Phase lead/lag, 50
Phase response, 104, 115
Phase shape, 51
Phase shift, 51, 255, 269, 272–273:
 migration, 255, 269, 273;
 velocity errors, 269
Phase spectrum, 47–48, 50–51
Phased array distance measurement,
 79
Phase-shift migration, 269, 273:
 velocity errors, 269
Piezoelectric effect, 100
Pinch-out, 24, 27–28, 53
Pinnacle reef, 27
Plane wave, 56–57
Planting (geophone), 105–106
Plate tectonics model, 11, 298
Plate tectonics, 10–11, 15, 298, 334,
 433:
 theory, 10–11;
 model, 11, 298;
 boundary, 11;
 subsidence, 334, 433
Pleistocene epoch, 8
Pleistocene/Holocene models
 (seismic stratigraphy), 351–352
Pleneplaned fold, 16
Pliocene epoch, 8
Plunge (rock), 15
Plunging fold, 16–17
Poisson's ratio, 34, 383, 444
Polar response, 137
Polarity reversal, 154
Pore/porosity (rock), 21–23:
 primary, 22;
 secondary, 22
Positioning (data acquisition), 4–5,
 71–83, 119–141:
 design, 4–5;
 marine navigation, 71–72, 75–82;
 land surveying, 71–72, 82;
 equipment, 73–83;
 datum, 74;
 positioning system, 75;
 geometry, 75, 119–141;
 accuracy analysis, 82;
 summary, 83
Positioning datum, 74
Positioning design, 4–5
Positioning equipment, 73–83:
 surface-based positioning system,
 75
Positioning geometry, 75, 119–141:
 2-D, 119–125;
 3-D, 125–141
Positioning system (surface-based),
 75
Post-stack migration, 234, 239, 241,
 273–274

Post-stack multiple attenuation (data processing), 242–245:
 median stack, 242–244;
 optimum trace-weighted stack, 245

Power series, 58

Precambrian era, 8

Predictability methods (pre-stack multiple attenuation), 216–225:
 time-variant deconvolution, 216–217;
 τ - p domain deconvolution, 217–220;
 wave equation multiple attenuation, 220–225

Preliminary processing (vibrator data), 147–154:
 seismic data processing sequences, 151–154

Preliminary signal processing (seismic reflection data), 160–166:
 amplitude processing, 160–161;
 geometric spreading, 161–162;
 gain functions, 161–163;
 ocean bottom cable scaling, 164–166

Pre-planning (project), 5

Pressure gradient, 23

Pressure wave, 34–39, 444

Pre-stack migration, 231, 233, 240–241, 274–279

Pre-stack multiple attenuation (data processing), 216–240:
 predictability methods, 216–225;
 moveout/velocity/dip methods, 216–240;
 amplitude methods, 216

Primacord (explosive cord), 91

Primary porosity, 22

Primary reflection synthetic, 306

Primary reflection, 39, 41, 101, 306:
 synthetic, 306

Primary-to-bubble ratio, 86–87

Primus/first wave, 34

Progradation, 326, 328, 337, 343–345, 356

Programmed gain control (PGC), 162

Project coordination, 4–5

Propane, 20

Prudhoe Bay oil field, 14, 26

Pseudo fault, 303–304

Pseudo-range measurement (GPS), 76

Pulling/pushing the spread, 121

P-wave and S-wave orientation (seismic stratigraphy), 375

P-wave versus S-wave seismic section (seismic stratigraphy), 376–377

P-wave, 34–39, 375–377, 444:
 S-wave, 375–377

Q

Q-factor (rock), 206–208

Quality control (positioning), 83

Quantitative modeling, 332

Quaternary period, 8

R

Racetrack shooting, 133

Radial shooting, 134

Radio frequency, 76

Radio positioning system, 75–76, 80

Radix/base (number system), 115

Radon transform (τ - p) filtering, 230–232:
 pre-stack multiple attenuation, 230–231

Radon transform, 60–61, 217–220, 230–232:
 filtering, 230–232

Ramp margin, 440

Random noise, 310

Ray path, 36, 38, 60, 157, 159, 164, 232, 302, 304, 308–310, 376, 379–380:
 theory, 36, 38, 60;
 trace modeling, 308–310

Ray theory, 36, 38, 60:
 parameter, 60

Ray trace modeling, 308–310

Rayleigh wave, 35, 40

Read head (tape), 117

Receiver elevation static, 158

Recording (data acquisition), 3–4, 39–43, 55, 71, 75–79, 99–118, 401:
 data record, 3–4, 39–43, 55;
 digital, 42–43, 401;

source and receiver, 75–79;
 recording system, 99–118;
 detector, 99;
 hydrophone, 100–102;
 geophone, 101–110;
 noise, 105–110;
 recording system types, 110–118

Recording system (data acquisition), 99–118:
 detector, 99;
 hydrophone, 100–102;
 geophone, 101–110;
 noise, 105–110;
 recording system types, 110–118

Recording system types, 110–118:
 marine in-water system, 111–112;
 land ground system, 113–118

Recovery shot, 124–125

Redefined depositional sequence (seismic stratigraphy), 339–343

Redwater oil field, 27

Reef/reef trend, 26–27, 316

Reference station, 77

Reflection amplitude/frequency, 323

Reflection coefficient, 38–40, 313–317

Reflection configuration, 318, 323

Reflection continuity, 318, 323

Reflection estimate, 315

Reflection flattening, 172

Reflection geometry, 323

Reflection significance (seismic stratigraphy), 319–320

Reflection termination terminology (seismic stratigraphy), 322

Reflection time, 40, 53, 171

Reflection, 37–42, 44, 53–54, 101, 171–172, 184–185, 209, 211–212, 215, 233, 251, 297, 299, 306, 313–320, 322–323, 429:
 law of reflection, 37;
 coefficient, 38–40, 313–317;
 signal, 39;
 reflectivity, 39–40, 44, 209, 297, 299;

primary, 39, 41, 101, 306;
 multiple, 40–42, 184–185, 319, 429;
 time, 40, 53, 171;
 interbed multiple, 41;
 reflector termination, 53–54;

- flattening, 172;
residual statics, 211–212, 215;
non-zero, 233;
exploding reflector model, 251;
synthetic, 306;
estimate, 315;
configuration, 318, 323;
continuity, 318, 323;
sideswipe, 319;
significance, 319–320;
termination terminology, 322;
amplitude/frequency, 323;
geometry, 323
- Reflection-based residual statics, 211–212, 215:
method, 211–212
- Reflectivity coefficient, 209
- Reflectivity function, 39–40
- Reflectivity, 39–40, 44, 209, 297, 299:
function, 39–40, 44;
coefficient, 209
- Reflector, 53–54, 251:
termination, 53–54;
exploding, 251
- Reformatting (data), 154
- Refraction calculation, 393–399:
single horizontal case, 393–395;
two horizontal layers case, 393,
395–396;
single dipping layer case, 393,
397–398;
two dipping layers case, 393, 399;
N horizontal layers case, 396–397
- Refraction exploration method, 2,
67–70, 393–399, 417–418:
inline shooting, 67–69;
other methods, 69;
advantages/disadvantages, 69;
workshop, 70, 417–418;
calculation, 393–399
- Refraction, 2, 37–38, 56, 67–70,
158–160, 215, 299–300, 393–399,
417–418:
exploration method, 2, 67–70,
393–399, 417–418;
law of refraction, 37;
refractor, 67–70, 417–418;
statics, 158–160, 215;
calculation, 393–399
- Refraction-based residual statics,
158–160, 215
- Refractor, 67–70, 417–418
- Regional ellipsoid, 74
- Regional velocity function, 153
- Relative positioning, 79, 81:
sensor, 79;
target, 81
- Relative sea level (seismic
stratigraphy), 325–345, 350–351,
432–433:
change, 325–345;
cycle, 328–331
- Requirements (oil and gas
accumulation), 21–22
- Reservoir analysis (shear wave),
384–385
- Reservoir rock, 21
- Reservoir spill point, 24
- Reservoir thickness, 442
- Residual statics (data processing),
154, 208, 211–215, 430:
conventional reflection-based
statics, 211–212;
correlation window selection, 212;
model trace building, 212–214;
cross-correlate traces, 213;
long and short wavelength statics,
214–215;
summary, 215;
analysis, 430
- Residual velocity, 271
- Residual water saturation, 23
- Resolution (image), 52–54, 94, 298:
bandwidth effect, 52–54, 94;
vertical, 52–53;
horizontal, 53–54
- Resolution (wavelet), 94
- Resonance (wave), 100, 104–105
- Resonant frequency, 104–105
- Restricting offset, 183
- Retrogradation, 336, 347
- Reverberation, 41, 220
- Reverse fault, 17–18
- R-inflection point, 336
- Rock cycle, 12
- Rock deformation, 14–19
- Rock matrix, 21
- Rock stress, 15
- Rock type, 13–14
- Rollover anticline, 18–19
- Root mean square automatic gain
control, 163
- Root mean square velocity, 171,
175–176, 181
- Rotary card compass, 80
- R-reflection point, 333–334
- Rugosity (rock), 364
- S**
- Salinity, 23
- Salt diapir, 28
- Salt dome shooting, 134
- Salt dome, 28, 134
- Sample increment, 43
- Sample period, 43
- Sampled data, 42–43
- Sampling theorem, 43
- Sand structure, 443
- Sandstone matrix, 21
- Sandstone reservoir, 27–28
- Satellite-based system, 76–80
- Saturated pool, 24
- Scaler normalization, 150
- Scan (multiplexed data record), 402:
SEG format, 402
- Scientific theory (petroleum
exploration), 2
- Sea level (seismic stratigraphy),
325–345, 350–351, 432–433:
change, 325–345, 350–351;
cycle, 328–331
- Sea state, 80
- Seafloor spreading theory, 10
- Seal (geological). *See* Trap
(hydrocarbon).
- Second wave, 35
- Secondary porosity, 22
- Sediment supply, 332–333, 345, 348
- Sedimentary basin, 13, 36
- Sedimentary rock, 12–14, 24, 36:
basin, 13, 36;
types, 13–14
- Sedimentation response, 434
- Sedimentation, 332, 334–335, 434

- Seepage (petroleum), 1
- SEG standard tape formats, 401–412: introduction, 401; comments and notes, 402; formats, 402–412
- Seismic data acquisition (overview), 3–6: data recording, 3–4; project coordination, 4–5; pre-planning, 5; geologic objective, 5; parameters, 6. *See also* Seismic reflection data acquisition.
- Seismic data recording (acquisition), 3–4, 39–43, 55, 71, 75–79, 99–118, 401: data record, 3–4, 39–43, 55; digital, 42–43, 401; source and receiver, 75–79; recording system, 99–118; detector, 99; hydrophone, 100–102; geophone, 101–110; noise, 105–110; recording system types, 110–118
- Seismic difference after production, 442
- Seismic distortion, 99, 114, 299–306: harmonic, 114; model, 299–306
- Seismic energy conversion, 99
- Seismic energy source, 83–99, 147–154, 299, 365: airgun, 84–89, 365; explosive, 89–92; vibrator, 89, 92–99, 147–154, 299, 365
- Seismic facies (seismic stratigraphy), 318, 322–325, 331
- Seismic geometry, 3
- Seismic inversion and wavelet processing (data interpretation), 310–317: wavelet extraction, 311–313; wavelet processing and stratigraphic interpretation, 313–314; wavelet processing techniques, 314–316; stratigraphic application, 316–317; summary, 317
- Seismic model, 304–310: 1-D, 306–308; 2-D, 308–310; 3-D, 310
- Seismic recording system, 99–118: performance requirements, 99; types, 110–118; components, 111; marine in-water system, 111–113; land ground system, 113–118
- Seismic reflection data acquisition, 3–6, 39–43, 55, 71–146, 362, 401–412, 418–421: overview, 3–6; recording, 3–4, 39–43, 55, 71, 99–118, 401; filtering, 43; introduction, 71–72; permitting, 71–72; positioning, 71–83; signal generation, 71, 83–99; 2-D acquisition parameters and operations, 72, 119–125; 3D acquisition parameters and operations, 72, 125–141; workshop, 142–146, 418–421; sequence stratigraphy, 362; SEG standard tape formats, 401–412
- Seismic reflection data interpretation, 6, 297–392: introduction, 297–298; modeling, 298–310; seismic inversion and wavelet processing, 310–317; seismic stratigraphy, 318–362; modern techniques and future applications of sequence stratigraphy, 361–392
- Seismic reflection data processing, 6, 147–295, 421–426: introduction, 147–154; preliminary processing for vibrator data, 147–154; processing sequences, 151–154; data initialization, 154–160; preliminary signal processing, 160–166; noise suppression, 167–169; velocity analysis, 170–185; brute stack, 185; deconvolution, 186–199; surface-consistent scaling, 199–201; time-variant spectral whitening, 201–204;
- model-based wavelet processing, 204–208; inverse-Q filtering, 208–210; residual statics, 211–215; pre-stack multiple attenuation, 216–240; common midpoint stack, 241; post-stack multiple attenuation, 242–245; migration, 246–279; band-pass filtering, 279–281; time-to-depth conversion, 282; display, 282–285; summary, 285–286; workshop, 287–295, 421–426
- Seismic reflection exploration, 2–6, 42–43, 71–295, 297–392, 401–412, 418–426: overview, 2–6; data acquisition, 3–6, 42–43, 71–146, 401–412, 418–421; data processing, 6, 147–295, 421–426; data interpretation, 6, 297–392
- Seismic reflection method (overview), 2–6: seismic wave, 2–6; history, 3; seismic wave generation, 3; seismic data acquisition, 3–6; project coordination, 4–5; pre-planning, 5; geologic objective, 5; data acquisition parameters, 6; data processing, 6; data interpretation, 6
- Seismic refraction exploration, 2, 67–70, 393–399, 417–418: overview, 2; velocity inversion, 2; refraction methods, 2, 67–69, 393–399, 417–418; workshop, 70, 417–418; calculation, 393–399
- Seismic refraction method (overview), 2: velocity inversion, 2
- Seismic stratigraphy (data interpretation), 6, 297–298, 318–362, 374–375: introduction, 318; acknowledgments, 318–319; 1970s concepts, 319; significance of reflections, 319–320; unconformable surfaces, 320–322;

- reflection termination terminology, 322; seismic facies, 322–325; relative sea level changes, 325–328; global cycles of relative sea level, 328–331; cyclic sequence stratigraphy, 331–334; basic concepts and principles, 331–334; erosion, 334–337; cycles and paracycles, 337–339; redefined depositional sequence, 339–343; highstand system tracts, 343–348, 357–358; marine-condensed sections, 348–35; Pleistocene and Holocene models, 351–352; depositional system tracts and hydrocarbon plays, 353–354; system tracts in Gulf Coast Basin, 354–356; transgressive system tracts, 356–357; highstand and shelf-margin system tracts, 357–358; chronostratigraphy of depositional sequences, 358–362
- Seismic trace, 40–42, 44, 61–62, 154–155, 186–187, 199, 212–214, 242, 245, 282–285, 297–298, 310–311
- Seismic velocity, 170
- Seismic wave recording, 3–4, 39–43, 55, 71, 99–118, 401: data record, 3–4, 39–43, 55; digital, 42–43, 401; recording system, 99–118; detector, 99; hydrophone, 100–102; geophone, 101–110; noise, 105–110; recording system types, 110–118
- Seismic wave, 2–6, 33–43, 55, 71, 99–118, 401: seismic data, 2–6; generation/propagation, 3, 34–38; amplitude, 38–39; data recording, 3–4, 39–43, 55, 71, 99–118, 401
- Seismology, 2–6: seismic refraction method, 2; seismic reflection method, 2–6
- Seismometer. *See* Geophone.
- Semblance plot, 178–180
- Sensitivity, 104
- Sequence stratigraphy, 318–392: concepts and principles, 331–334; techniques/applications, 361–392
- Sequence stratigraphy techniques/applications (data interpretation), 361–392: high-resolution seismic data acquisition, 362; vertical seismic profiling, 362–369; amplitude versus offset analysis, 369–374; shear waves and seismic stratigraphy, 374–375; S-wave and P-wave orientation, 375; shear wave generation, 375–376; S-wave versus P-wave seismic section, 376–377; processing S-wave data, 377–384; future of shear waves in reservoir analysis, 384–385; 4-D seismic technology, 385–392; summary/conclusions, 392
- Shadow zone, 301–302
- Shale matrix, 21
- Shaliness factor, 383
- Shear modulus, 34
- Shear stress, 15
- Shear wave generation (seismic stratigraphy), 375–376
- Shear wave, 35, 298, 374–376, 384–385: seismic stratigraphy, 374–375; generation, 375–376; reservoir analysis, 384–385
- Shear waves (reservoir analysis), 384–385
- Shelf break, 440
- Shelf margin system tract (seismic stratigraphy), 342, 349, 351, 357–358, 439: highstand system tract, 357–358
- Shooting through the spread, 123
- Short baseline acoustics system, 78–79
- Short period statics, 215
- Short spatial wavelength, 199
- Short wavelength statics, 214–215
- Shot index, 136
- Shot point, 67
- Shot record, 41–42, 155–156
- Shot-geophone sinking, 278
- Shrinkage factor, 20
- SH-wave, 35
- Sideswipe reflection, 319
- Sign bit, 116
- Signal amplitude, 85
- Signal enhancement (velocity analysis), 182, 286
- Signal generation (data acquisition), 71, 83–99: airgun, 84–89; explosive, 89–92; vibrator, 92–99
- Signal reflection, 39
- Signal/signaling, 39, 58, 62, 71, 83–99, 109, 122, 182, 208, 286: reflection, 39; signal-noise separation, 58; generation, 71, 83–99; amplitude, 85; signal-to-noise ratio, 95, 122, 208; enhancement, 182, 286
- Signal-noise separation, 58
- Signal-to-noise ratio, 95, 122, 208
- Signature deconvolution, 186–187
- Signature, 86–87, 90, 186–187, 298: airgun array, 86–87; far-field, 85, 90; deconvolution, 186–187
- Siliciclastic deposit/deposition, 343, 345–349, 353–354: lowstand system tract, 345–346; transgressive system tract, 347–348; shelf-margin system tract, 349
- Silurian period, 8
- Simple inline forward/reverse coverage, 68
- Simple multiple (reflection), 41
- Simple stack process, 148
- Simrad HPR, 79
- Single frequency sinusoid, 46–47
- Single-fold shooting, 3, 429
- Sinusoid, 46–47
- Slant stack transform, 60
- Sleeve gun, 88
- Snell's law, 36–37, 60

- Society of Exploration Geophysicists (SEG), 118, 401–412:
standard tape formats, 401–412
- Software, 302
- Solar wind, 9
- Sonardyne SIPS, 79
- Sound wave, 34
- Sour gas, 20
- Source and receiver (data recording), 75–79, 154:
coupling compensation, 154
- Source array, 86–89
- Source elevation static, 158
- Source point, 124
- Source rock, 21–23
- Source/receiver coupling compensation, 154
- Source-generated noise, 40–41, 105, 124
- Space-sampled data, 107–108
- Spatial aliasing, 57–58
- Spatial sampling, 55, 258–259
- Spectral amplitude, 38–39, 46–50, 59, 87:
spike, 59
- Spectral flatness, 87
- Spectral whitening (time-variant), 153, 201–204
- Spike (amplitude), 59
- Spike (noise), 93
- Spiking deconvolution, 209, 312
- Spread (geometric), 4, 67–68, 121–122, 153, 161–162, 201, 286:
coverage, 4, 68;
correction, 153, 286
- Spring chamber, 84
- Spurious resonance, 104
- Stack/stacking, 153, 155, 171, 181, 184
- Stacking diagram, 155
- Stacking velocity, 171, 181, 184
- Star array, 137
- Starboard/port antenna movement, 78
- Start-of-line procedures, 123–124
- Statfjord field, 26
- Static correction, 147, 157, 286
- Static/geosynchronous base station, 75
- Station (detector), 67
- Statistical analysis (positioning), 82
- Statistical approach (amplitude processing), 161–162
- Statistical communication theory, 42
- Statistical method (wavelet processing), 312–313
- Stepback method, 81
- Stock tank barrel, 20
- Stolt migration, 154, 225, 254, 258–259, 262, 268, 271–273:
extended, 154;
generalized, 254;
F-K domain, 262;
stretch factor, 268
- Straight-line shooting, 133, 137–138
- Straight stack process, 148
- Strain (rock), 15, 33–34
- Stratal geometry, 342
- Stratal layout, 322
- Stratal pattern, 350, 352, 440
- Stratal surface, 318–320:
concordant, 318
- Stratal termination, 342
- Stratfjord field, 26
- Stratigraphic application (seismic inversion and wavelet processing), 316–317
- Stratigraphic interpretation (seismic inversion and wavelet processing), 313–314
- Stratigraphic section, 325
- Stratigraphic trap, 24, 298
- Strati-structural trap, 24, 27–28
- Streamers, 78–81, 132, 134:
deviation, 78;
curvature, 78–79;
feathering, 78–79;
shape/shaping, 78–81;
position, 80;
heading sensor, 80;
tension, 81;
multiple, 132, 134
- Stress (definition), 33
- Stress-strain relationship (rock), 15
- Stretch factor (Stolt migration), 268
- Stretch section, 111
- Strike and dip, 15
- Strike slip fault, 17–18
- Structural deconvolution, 312
- Structural geology, 8
- Structural trap, 24, 27–28
- Sub-array configuration (airgun), 88
- Subsidence, 332–334, 340, 433:
basin, 332;
tectonic, 334, 433
- Super high frequency (radio), 76
- Superposition, 7–8, 273:
law of superposition, 7–8
- Surface geology, 2
- Surface wave, 35
- Surface-based navigation system, 75
- Surface-consistent amplitude correction, 153
- Surface-consistent deconvolution, 198–199:
summary, 199
- Surface-consistent scaling (data processing), 199–201
- Survey datum, 74
- Survey design, 4–5
- Survey equipment, 73–83:
surface-based surveying system, 75
- Survey geometry, 75, 119–141:
2-D, 119–125;
3-D, 125–141
- Surveying (data acquisition), 4–5, 71–83, 119–141:
design, 4–5;
marine navigation, 71–72, 75–82;
land surveying, 71–72, 82;
equipment, 73–83;
datum, 74;
surveying system, 75;
geometry, 75, 119–141;
accuracy analysis, 82;
summary, 83
- Surveying system (surface-based), 75
- SV-wave, 35
- Swath layout/shooting, 135, 138, 140
- S-wave and P-wave orientation (seismic stratigraphy), 375
- S-wave data processing (seismic stratigraphy), 377–384

S-wave versus P-wave seismic section (seismic stratigraphy), 376–377
 S-wave, 34–39, 375–384
 Sweep (vibrator), 92–99:
 distortion, 99
 Sweep distortion, 99
 Symmetric split spread, 121–122
 Symmetric/asymmetric folding, 16
 Syncline fold, 15–16
 Syncline, 15–16, 246–247, 300:
 fold, 15–16
 Synsedimentary tectonics, 356
 Synthetic seismogram, 305–308,
 315–316, 367
 Synthetic trace, 184
 Syntron Multitrak, 79
 System tract (seismic stratigraphy),
 318–361, 432–439:
 deposition, 318–361, 432–439;
 eustacy, 326, 329, 332–341, 343,
 358–361, 432–436;
 highstand, 335–337, 342–348,
 357–358, 437;
 transgressive, 335, 342, 347–348,
 355–357;
 fluvial, 337;
 lowstand, 342, 345–346, 435,
 438–439;
 shelf margin, 342, 349, 351,
 357–358, 439;
 clastic, 342–344, 358;
 siliciclastic, 343, 345–349,
 353–354;
 hydrocarbon play, 353–354;
 Gulf Coast Basin, 354–356;
 carbonate, 343–348, 350, 354,
 357, 439;
 evaporite, 350–351

T

τ -p domain, 60–61, 216–220:
 pre-stack multiple attenuation
 deconvolution, 216–220
 Tail buoy, 80
 Takeout/connector, 113
 Tape format (SEG), 118, 401–412
 Tape schematic, 117
 Taper (vibroseis), 98–99
 Target acquisition, 80

Target discrimination, 80
 Target positioning system, 73, 75–83:
 reference, 73;
 acquisition, 80;
 discrimination, 80
 Target reference, 73
 Tectonic plate, 10–11, 15, 298, 334,
 356, 433:
 theory, 10–11;
 model, 11, 298;
 boundary, 11;
 subsidence, 334, 433
 Tectonic subsidence, 334, 433
 Template (patch plus points), 135
 Tertiary period, 8
 Thermal gas, 22
 Thermal subsidence, 334, 433
 Thin bed response, 302
 Third-order cycle, 358
 Three-dimensional position (feature),
 83
 Three-term AVO inversion, 373
 Throw, 17–18
 Thrust fault, 18, 25–26
 Tilting (trap), 24
 Time and depth downward
 continuation (migration), 249–253,
 256, 260, 273–274, 431
 Time dating (rock/rock group), 8
 Time domain deconvolution, 186
 Time domain, 46–50, 86–87, 186,
 216:
 frequency domain, 46–50;
 deconvolution, 186
 Time migration, 249–253, 256, 260,
 273–374, 431
 Time reversal, 48–49
 Time rock group, 9
 Time series, 45–46, 48, 58
 Time slice, 153, 284–285, 431:
 salt dome, 431
 Time-lapse difference (amplitude),
 443
 Time-lapse seismic (4-D), 298,
 385–392
 Time-to-depth conversion (data
 processing), 282
 Time-variant amplitude correction
 (gain), 153
 Time-variant deconvolution (TVD),
 186–197, 216–217:
 parameter selection/testing,
 194–196;
 summary, 196–197
 Time-variant filter, 154, 280–281
 Time-variant spectral whitening (data
 processing), 153, 201–204:
 summary, 204
 Tomography, 385
 Toplap, 322, 325–326, 328
 Topset bed thickness, 436
 Total dynamic range, 114
 Towing bridle, 111
 Trace analysis, 40–42, 44, 61–62,
 154–155, 184, 186–187, 199,
 212–214, 242, 245, 282–285,
 297–298, 310–311:
 interpolation, 61;
 complex, 61–62;
 editing, 154;
 zeroing, 154;
 gather, 155;
 synthetic trace, 184;
 trace model, 186–187;
 decomposition, 199;
 trace-building model, 212–214;
 amplitude, 242;
 trace-weighted stack, 245;
 display, 282–285
 Trace model, 186–187
 Trace-building model (residual
 statics), 212–214:
 cross-correlation of traces, 213
 Trace-weighted stack (post-stack
 multiple attenuation), 245
 Track (magnetic tape), 115
 Track (vessel), 79
 Track/bit conventions (SEG format),
 402
 Transduction, 104
 Transformer-coupled hydrophone, 100
 Transgressive system tract (seismic
 stratigraphy), 335, 342, 347–348,
 355–357
 Transit satellite system, 76
 Transit time log, 305

Transmission coefficient, 39
 Transverse isotropy, 34
 Trap (hydrocarbon), 14, 16, 18, 21, 24–28, 298, 342–343, 353, 356: anticline, 16, 18, 24–25; sedimentary rock, 24; pinch-out, 24, 27–28; structural, 24, 27–28; stratigraphic, 24, 27–28; strati-structural/combination, 24, 27–28; tilting, 24; closure, 24; reservoir spill point, 24; free gas cap, 24; mature hydrocarbon, 24; saturated pool, 24; undersaturated pool, 24; gas only pool, 24; pay zone, 25; fault, 25; growth/down-to-the-basin fault, 25; fault cutting reservoir, 25; thrust fault, 25–26; drag fold, 25; overthrust belt, 25–26; Western Overthrust Belt, 25–26; Painter Reservoir field, 25–26; up-dip facies change, 26; Statfjord field, 26; angular unconformity, 26; East Texas oil field, 26; Prudhoe Bay oil field, 26; Bolivar coastal oil fields, 26; reefs, 26–27; Alberta Reef trend, 27; Redwater oil field, 27; Michigan Basin Silurian reef trend, 27; pinnacle reef, 27; lenticular sandstone reservoir, 27–28; Bush City trend, 27–28; Hugoton gas field, 27–28; salt dome, 28; salt diapir, 28; cap rock, 28; fractured reservoir, 28; granite wash, 28; geometry, 298
 Trap geometry, 298
 Travel time, 79, 214: measurement, 79; model, 214
 Travel time model, 214

Trendology, 1
 Triassic cycle, 8, 358
 Triassic period, 8
 Truck-mounted vibrator, 92–99
 Two-dimensional array, 55
 Two-dimensional horizontal datum, 73
 Two-fold shooting, 4
 Two-point wavelet/doublet, 52
 Two-term AVO inversion, 371–373
 Two-way reflection time, 40
 T-X domain (finite difference migration), 55–58, 60–61, 68, 226–227, 229, 260–262, 270–273: T-X plot, 68; cascaded, 270–273
 Type 1 carbonate, 439
 Type 1 sequence, 350, 352, 439–440
 Type 2 sequence, 2, 352, 441

U

Ultra-high frequency (radio), 76
 Ultra-short baseline acoustics system, 78–79
 Unconformable surface (seismic stratigraphy), 320–322
 Unconformity, 14, 26, 318, 320–322, 334, 336, 338–339, 341, 434, 436
 Under-damped geophone, 103
 Undersaturated pool, 24
 Undershooting, 134, 136
 Uniformitarianism, 7
 Universal continent, 11
 Universal transverse mercator, 74
 Up-/down-going event, 441
 Up-dip facies change, 26
 Up-dip/down-dip, 122
 Upgoing/downgoing event, 365–366
 Upsweep (vibrator), 97

V

Variable area display, 282
 Variable near surface, 156
 Vector system (GPS), 79–80

Velocimeter, 81
 Velocity analysis (data processing), 170–185, 234, 238, 286: normal moveout, 171–177; analysis techniques, 177–181; computation procedures, 181; data reduction, 182; signal enhancement, 182, 286; velocity problem, 182; dip-related problems, 182; offset-related problems, 182–183; near-surface anomaly effect, 183–184; multiple reflection problems, 184–185; summary, 185; displays, 238
 Velocity analysis displays, 238
 Velocity error (migration), 265, 267–269, 271: implicit finite difference, 267–268; phase shift, 269
 Velocity field, 153, 177
 Velocity filtering, 167–169, 216: noise suppression, 167–169; τ - p domain, 216
 Velocity function, 177–180
 Velocity inversion, 2, 181: refraction, 2
 Velocity log, 170–171, 306–308, 316–317: average velocity, 170–171; apparent velocity, 171
 Velocity pull-up, 303
 Velocity sweep, 178
 Velocity variation, 303
 Vertical component record, 378
 Vertical reference datum, 73
 Vertical resolution, 52–53
 Vertical seismic profiling (VSP), 6, 298, 362–369: concept, 363; data acquisition, 364; energy sources, 364–365; data processing, 365–366; applications, 366–369
 Vertical stack process, 147–148
 Vessel navigation, 75–82: navigation system, 75; positioning method, 81

Vessel-relative positioning method, 81
 Vibrational resonance, 104–105
 Vibrator (seismic energy source), 89, 92–99, 147–154, 299, 365:
 operation, 93;
 cross-correlation, 93;
 data processing, 147–154
 Vibrator cross-correlation, 93
 Vibrator data (preliminary processing), 147–154
 Vibroseis correlation, 93–99, 151:
 ghost, 97–98
 Vibroseis record, 93–99, 151:
 correlation, 93–99, 151
 Vibroseis, 93–99, 151, 299, 362:
 record, 93–99, 151;
 correlation, 93–99, 151

W

Water bottom multiple reflection, 41, 220–221, 225, 432
 Water depth, 432
 Water saturation, 23
 Water set, 23
 Wave amplitude, 6, 36, 38–39, 46–50, 59, 62, 85, 87, 90, 115, 153, 160–162, 199–201, 210, 242, 298–299, 318, 323, 369–374, 388–392, 442–444:
 amplitude versus offset, 6, 298, 369–374
 Wave attenuation, 50
 Wave cycle, 36
 Wave damping, 100, 103–104
 Wave diffraction, 41–42, 54, 129, 256–258, 273, 301, 319, 322:
 energy, 129;
 summation, 273
 Wave equation multiple attenuation (WEMA), 216, 220–225:
 synthetic data example, 221–223;
 field data example, 223–224;
 processing considerations, 224–225;
 summary/conclusions, 225
 Wave equation, 33, 216, 220–225:
 multiple attenuation, 216, 220–225
 Wave field, 33, 36, 55

Wave frequency, 36, 40, 56–57
 Wave motion components, 35
 Wave number, 36, 55
 Wave orientation, 375
 Wave parameter, 36
 Wave period, 36, 215:
 statics, 215
 Wave propagation, 34–38
 Wave reflection, 39–40
 Wave resonance, 100, 104–105
 Wave train, 40
 Wave transmission, 39
 Wave velocity, 35, 40, 57, 382–383
 Waveform, 50–52, 85, 208, 311–312:
 phase effect, 50–52;
 synthesis, 85;
 stationarity, 208
 Wavefront, 38, 55–56
 Wavelength, 34, 36, 40, 199, 214–215:
 statics, 214–215
 Wavelet extraction (seismic inversion and wavelet processing), 311–313
 Wavelet processing and seismic inversion (data interpretation), 204–208, 310–317:
 model-based, 204–208;
 wavelet extraction, 311–313;
 statistical method, 312–313;
 stratigraphic interpretation, 313–314;
 wavelet processing techniques, 314–316;
 stratigraphic application, 316–317;
 summary, 317
 Wavelet, 40, 46–48, 50–52, 53, 94, 310–317, 364:
 shape, 51, 364;
 maximum/minimum delay, 51–52;
 maximum/minimum phase, 51–52;
 mixed-phase, 51–52;
 type, 53;
 width, 94;
 resolution, 94;
 processing, 310–317;
 extraction, 311–313
 Weathering (rock), 156
 Weathering process, 12, 14
 Wedge model (gas cap), 442
 Wedge/pinchout, 53
 Wegener, Alfred, 10
 Well logging, 298
 Well surveying, 2
 Western Overthrust Belt, 25–26
 Wet gas, 20, 22
 Wetting fluid, 23
 Whitening deconvolution, 186–192, 194, 196–197, 216
 Wiener deconvolution, 94, 192–193
 Wiggle trace/variable density display, 282
 Window definition, 430
 Window selection (residual statics), 212
 Word (computer), 118
 Workshop answers, 413–426
 Workshops, 29–31, 63–66, 70, 142–146, 287–295, 413–426:
 geological background, 29–31, 413–415;
 geophysical and mathematical background, 63–66, 416–417;
 seismic refraction exploration, 70, 417–418;
 seismic reflection data acquisition, 142–146, 418–421;
 seismic reflection data processing, 287–295, 421–426
 Write head (tape), 116

Y

Yoshimura equation, 383
 Young fold, 16
 Young's modulus, 34

Z

Zero offset, 134, 176, 233–234, 237, 249, 300–302:
 zero offset position, 176
 Zero-phase correlation, 93–94
 Zig-zag/double zig-zag shooting, 139–140
 Zoeppritz equations, 38, 299
 Z-transform, 58–59



Appendix A

Refraction Calculations

Calculating layer thickness, dip, and velocity can be very tedious when many layers are involved. Properly programmed computers can, of course, relieve much of this, but the calculations still require a lot of input. The following is presented to show how inline seismic refraction data are interpreted. Cases presented are

- single horizontal layer
- two horizontal layers
- single dipping layer
- two dipping layers

Single horizontal layer $V_1 > V_0$

Figure A-1 shows the model and notation used in the derivations that follow.

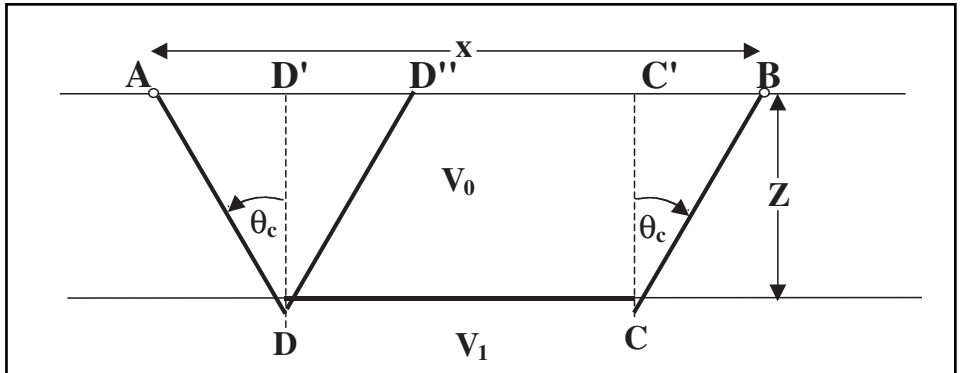


Fig. A-1 Earth Model for a Single Horizontal Layer

Assume a source is at A and a receiver at B . The refraction path is from A to D to C to B . Propagation from A to D and from C to B is at velocity V_0 . From D to C propagation is at velocity V_1 . It follows then that refraction time T can calculated from:

$$T = \frac{\overline{AD}}{V_0} + \frac{\overline{CD}}{V_1} + \frac{\overline{BC}}{V_0}$$

From Figure A-1 it can be seen that:

$$\overline{AD} = \overline{BC} = \frac{Z}{\cos\theta_c} \text{ and } \overline{CD} = x - (\overline{AD}' = \overline{CB}) = x - 2Z\tan\theta_c$$

where

Z = thickness of layer 1 = depth to refractor

θ_c = critical angle

Substituting in the original equation gives:

$$T = \frac{Z}{V_0\tan\theta_c} + \frac{x-2Z\tan\theta_c}{V_1} + \frac{Z}{V_0\cos\theta_c} = \frac{x}{V_1} + 2Z \left[\frac{1}{V_0\cos\theta_c} - \frac{\tan\theta_c}{V_1} \right]$$

Noting that $\tan\theta_c = \frac{\sin\theta_c}{\cos\theta_c}$,

$$T = \frac{x}{V_1} + \frac{2Z}{V_0\cos\theta_c} \left(1 - \frac{V_0\sin\theta_c}{V_1} \right)$$

But $\sin\theta_c = V_0/V_1$, so substituting in the previous equation:

$$T = \frac{x}{V_1} + \frac{2Z}{V_0\cos\theta_c} (1 - \sin^2\theta_c) = \frac{x}{V_1} + \frac{2Z\cos\theta_c}{V_0} = \frac{x}{V_1} + T_0 \quad (A.1)$$

where

$$T_0 = \text{delay time} = \frac{2Z\cos\theta_c}{V_0} \quad (A.2)$$

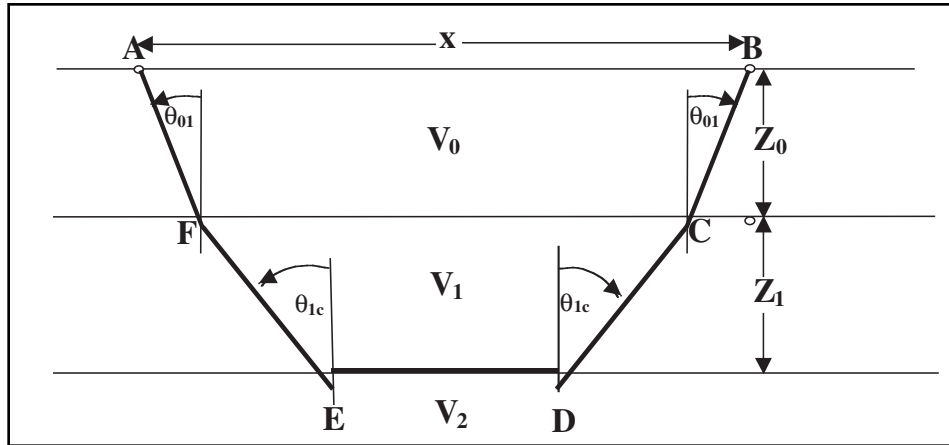


Fig. A-2 Two Horizontal Layers Earth Model

It follows that depth Z can be calculated from:

$$Z = \frac{V_0 T_0}{2 \cos \theta_c} \quad (\text{A.3})$$

Another parameter used in refraction is the *critical distance* or the distance at which the reflection at the critical angle occurs. This is also the minimum distance at which the refraction can be observed. From Figure A-1 the critical distance can be calculated as follows:

$$x_c = 2Z \tan \theta_c = 2Z \left(\frac{\sin \theta_c}{\cos \theta_c} \right) = 2Z \left(\frac{\sin \theta_c}{\sqrt{1 - \sin^2 \theta_c}} \right) = 2Z \left(\frac{\frac{V_0}{V_1}}{\sqrt{1 - \frac{V_0^2}{V_1^2}}} \right) = 2Z \left(\frac{V_0}{\sqrt{V_1^2 - V_0^2}} \right) \quad (\text{A.4})$$

Two horizontal layers $V_2 > V_1 > V_0$

Figure A-2 shows the model and notation used in the derivations that follow.

Assume a source is at A and a receiver at B . The refraction path is from A to D to C to B . Propagation from A to D and from C to B is at velocity V_0 . From D to C , propagation is at velocity V_1 . It follows, then that refraction time T can be calculated from:

$$T_2 = \frac{\overline{AF}}{V_0} + \frac{\overline{EF}}{V_1} + \frac{\overline{DE}}{V_2} + \frac{\overline{CD}}{V_1} + \frac{\overline{BC}}{V_0}$$

$$\overline{AD} = \overline{BC} = \frac{Z_0}{\cos \theta_{01}}, \overline{EF} = \overline{CD} = \frac{Z_1}{\cos \theta_{lc}}, \overline{DE} = x - 2Z_0 \tan \theta_{01} - 2Z_1 \tan \theta_{lc}$$

Substituting into the first equation, above:

$$T_2 = \frac{Z_0}{V_0 \cos \theta_{01}} + \frac{Z_1}{V_1 \cos \theta_{lc}} + \frac{x - 2Z_0 \tan \theta_{01} - 2Z_1 \tan \theta_{lc}}{V_2} + \frac{Z}{V_1 \cos \theta_{lc}} + \frac{Z_0}{V_0 \cos \theta_{01}}$$

$$\begin{aligned}
&= \frac{x}{V_2} + 2Z_0 \left(\frac{1}{V_0 \cos \theta_{01}} - \frac{\tan \theta_{01}}{V_2} \right) + 2Z_1 \left(\frac{1}{V_0 \cos \theta_{01}} - \frac{\tan \theta_{lc}}{V_2} \right) \\
&= \frac{x}{V_2} + \frac{2Z_0}{V_0 \cos \theta_{01}} \left(1 - \frac{V_0 \sin \theta_{01}}{V_2} \right) + \frac{2Z_1}{V_1 \cos \theta_{lc}} \left(1 - \frac{V_1 \sin \theta_{lc}}{V_2} \right)
\end{aligned}$$

Since $\frac{\sin \theta_{01}}{V_0} = \frac{\sin \theta_{lc}}{V_1} = \frac{1}{V_2}$

$$T_2 = \frac{x}{V_2} + \frac{2Z_0 \cos \theta_{01}}{V_0} + \frac{2Z_1 \cos \theta_{lc}}{V_1} = \frac{x}{V_2} + T_{01} + T_{02} \quad (\text{A.5})$$

where

$$T_{01} = \text{first delay time} = \frac{2Z_0 \cos \theta_{01}}{V_0} \text{ and} \quad (\text{A.6a})$$

$$T_{02} = \text{second delay time} = \frac{2Z_1 \cos \theta_{lc}}{V_1} \quad (\text{A.6b})$$

The critical distance for this case is given by:

$$x_c = 2Z_0 \tan \theta_{01} + 2Z_1 \tan \theta_{lc}$$

$$= 2Z_0 \left(\frac{V_0}{\sqrt{V_2^2 - V_0^2}} \right) + 2Z_1 \left(\frac{V_1}{\sqrt{V_2^2 - V_1^2}} \right) \quad (\text{A.7})$$

N Horizontal Layers $V_0 < V_1 < V_2 < \dots < V_N$

Using the model of Figure A-3 and extrapolating from the two layer case, the expression for the time of a refraction from the N^{th} refractor is:

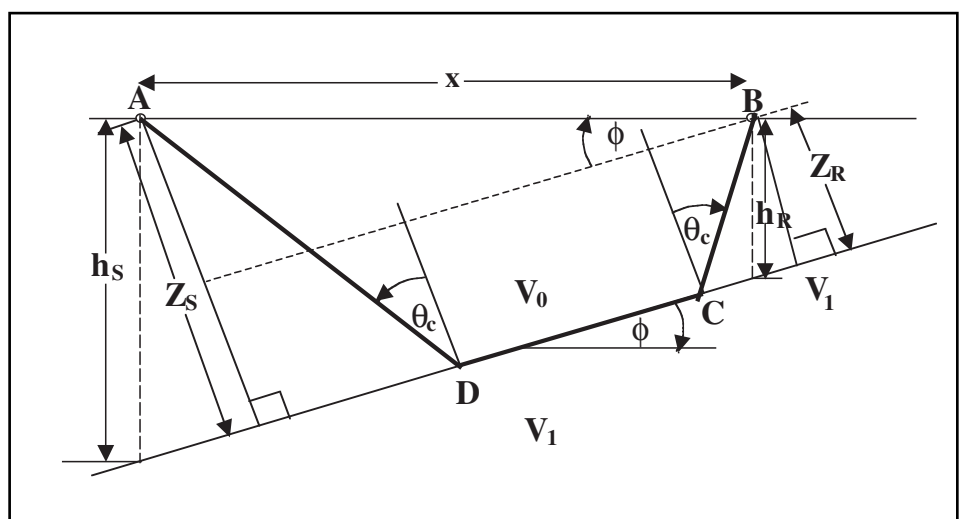


Fig. A-3 Earth Model for a Single Dipping Layer

$$T_1 = \frac{x}{V_N} + \sum_{n=1}^N T_{0n} \quad (\text{A.8})$$

where

$$T_{0n} = \frac{2Z_{n-1}\cos\theta_{n-1,n}}{V_{n-1}} \quad (\text{A.9})$$

Single dipping layer $V_1 > V_0$

Figure A-3 provides an Earth model and shows annotation used in the following derivations. As shown in the T-X plot of Figure 4-2, when the refractor dips, the refraction velocity in the up-dip direction appears to be different from that in the down-dip direction. From Figure A-3 the refraction time from A to B is:

$$T_1 = \frac{\overline{AD}}{V_0} + \frac{\overline{CD}}{V_1} + \frac{\overline{BC}}{V_0}$$

$$\overline{AD} = \frac{Z_S}{\cos\theta_c}, \overline{BC} = \frac{Z_R}{\cos\theta_c}, \text{ and } \overline{CD} = x\cos\phi - (Z_S - Z_R)\tan\theta_c$$

Substituting this information into the starting equation:

$$\begin{aligned} T_1 &= \frac{Z_S}{V_0\cos\theta_c} + \frac{Z_R}{V_0\cos\theta_c} + \frac{x\cos\phi - (Z_S - Z_R)\tan\theta_c}{V_1} \\ &= \frac{x\cos\phi}{V_1} + (Z_S - Z_R) \left(\frac{1}{V_0\cos\theta_c} - \frac{(Z_S - Z_R)\tan\theta_c}{V_1} \right) = \frac{x\cos\phi}{V_1} + \frac{(Z_S + Z_R)}{V_0\cos\theta_c} \left(1 - \frac{V_0\sin\theta_c}{V_1} \right) \\ &= \frac{x\cos\phi}{V_1} + \frac{(Z_S - Z_R)\cos\theta_c}{V_0} \end{aligned}$$

Shooting up-dip (from A to B), substitute $Z_R = Z_S - x\sin\phi$.

$$\begin{aligned} T_{lu} &= \frac{x\cos\phi}{V_1} + \frac{(2Z_S - x\cos\phi)\cos\theta_c}{V_0} = x \left(\frac{\cos\phi}{V_1} - \frac{\sin\phi\cos\theta_c}{V_0} \right) + \frac{2Z_S\cos\theta_c}{V_0} \\ &= x \left(\frac{\sin\theta_c\cos\phi}{V_0} - \frac{\sin\phi\cos\theta_c}{V_0} \right) + \frac{2Z_S\cos\theta_c}{V_0} = \frac{x \sin(\theta_c - \phi)}{V_0} + \frac{2Z_S\cos\theta_c}{V_0} \end{aligned}$$

Let $V_{lu} = V_0/\cos(\theta_c - \phi)$ and $Z_S = h_S\cos\phi$. Substituting these into the last equation gives:

$$T_{lu} = \frac{x}{V_{lu}} + \frac{h_S\cos\theta_c\cos\phi}{V_0} = \frac{x}{V_{lu}} + T_{0lu} \quad (\text{A.10})$$

Shooting down-dip (from B to A), substitute $Z_S = Z_R + x\sin\phi$.

$$T_{ld} = \frac{x\cos\phi}{V_1} + \frac{(2Z_R + x\sin\phi)\cos\theta_c}{V_0} = x \left(\frac{\cos\phi}{V_1} - \frac{\sin\phi\cos\theta_c}{V_0} \right) + \frac{2Z_S\cos\theta_c}{V_0}$$

$$= x \left(\frac{\sin\theta_c \cos\phi}{V_0} - \frac{\sin\phi \cos\theta_c}{V_0} \right) + \frac{2Z_S \cos\theta_c}{V_0} = \frac{x \sin(\theta_c - \phi)}{V_0} + \frac{2Z_S \cos\theta_c}{V_0}$$

Let $V_{lu} = V_0/\cos(\theta_c + \phi)$ and $Z_R = h_R \cos\phi$. Substituting these into the last equation gives:

$$T_{ld} = \frac{x}{V_{ld}} + \frac{h_s \cos\theta_c \cos\phi}{V_0} = \frac{x}{V_{ld}} + T_{old} \quad (\text{A.11})$$

Different *apparent* velocities are obtained when shooting up-dip [$V_{lu} = \frac{V_0}{\sin(\theta_c - \phi)}$]

and down-dip [$V_{ld} = \frac{V_0}{\sin(\theta_c + \phi)}$]. Solving for $\sin(\theta_c - \phi)$ and $\sin(\theta_c + \phi)$ gives

$$\sin(\theta_c - \phi) = \frac{V_0}{V_{lu}} \text{ and } \sin(\theta_c + \phi) = \frac{V_0}{V_{ld}}.$$

But $\sin(\theta_c - \phi) + \sin(\theta_c + \phi) = \sin\theta_c \cos\phi - \cos\theta_c \sin\phi + \sin\theta_c \cos\phi + \cos\theta_c \sin\phi = 2\sin\theta_c \cos\phi = \frac{V_0}{V_{lu}} + \frac{V_0}{V_{ld}} = V_0 \left(\frac{1}{V_{lu}} + \frac{1}{V_{ld}} \right)$

The true velocity, V_1 is given by:

$$V_1 = \frac{V_0}{\sin\theta_c} = 2\cos\phi \left(\frac{1}{\frac{1}{V_{lu}} + \frac{1}{V_{ld}}} \right) = 2\cos\phi \left(\frac{V_{lu} V_{ld}}{V_{lu} + V_{ld}} \right) \quad (\text{A.12})$$

$$\text{Also, } \theta_c = \frac{1}{2} [\sin^{-1}(\theta_c - \phi) + \sin^{-1}(\theta_c + \phi)] = \frac{1}{2} \left[\sin^{-1}\left(\frac{V_0}{V_{ld}}\right) + \sin^{-1}\left(\frac{V_0}{V_{lu}}\right) \right] \quad (\text{A.13})$$

$$\text{and } \phi = \frac{1}{2} [\sin^{-1}(\theta_c - \phi) - \sin^{-1}(\theta_c + \phi)] = \frac{1}{2} \left[\sin^{-1}\left(\frac{V_0}{V_{ld}}\right) - \sin^{-1}\left(\frac{V_0}{V_{lu}}\right) \right] \quad (\text{A.14})$$

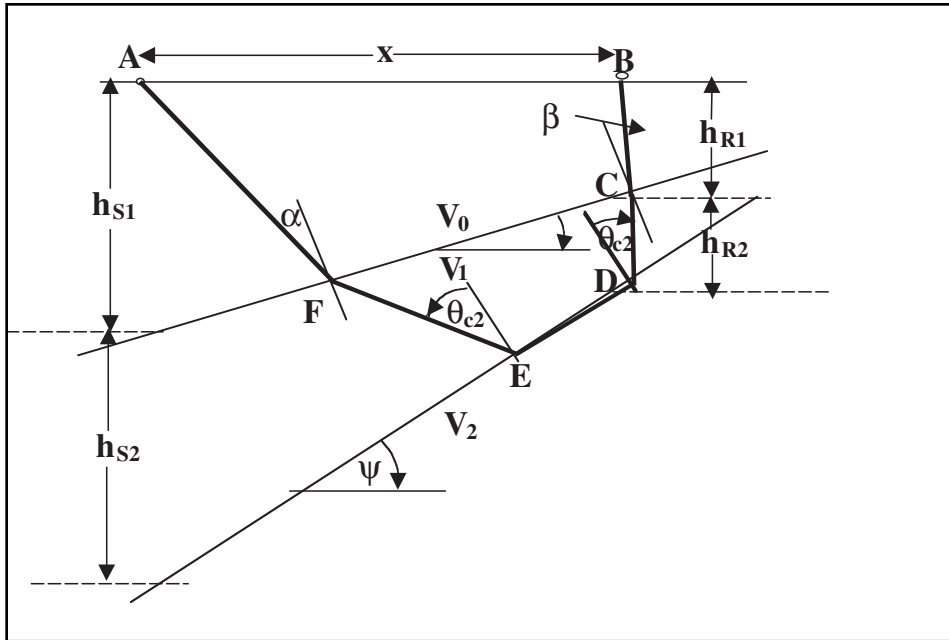


Fig. A-4 Two Dipping Layers Earth Model

Two dipping layers $V_2 > V_1 > V_0$

Derivation is similar to the one-layer dipping case. (See Fig. A-4. Up-dip is relative to layer 1.)

$$T_{2u} = \frac{x}{V_{2u}} + \frac{h_{S1}[\cos(\alpha + \phi) + \cos(\beta - \phi)] + 2h_{S2} \sin\theta_{cl} \cos\theta_{c2} \cos\psi}{V_0} + \frac{x}{V_{2u}} + T_{01u} \quad (\text{A.15})$$

$$T_{2d} = \frac{x}{V_{2d}} + \frac{h_{R1}[\cos(\alpha + \phi) + \cos(\beta - \phi)] + 2h_{R2} \sin\theta_{cl} \cos\theta_{c2} \cos\psi}{V_0} + \frac{x}{V_{2u}} + T_{01u} \quad (\text{A.16})$$

$$\text{where } V_{2u} = \frac{V_0}{\sin(\beta - \phi)} \text{ and } V_{2d} = \frac{V_0}{\sin(\alpha - \phi)} \quad (\text{A.17})$$

Interpretation of seismic refraction data is done one layer at a time. Single layer equations are used for the first layer, two layer equations for the second, etc.



Bibliography

Al-Sadi, H. N. *Seismic Exploration: Technique and Processing*. Birkhauser Verlag, 1982.

Angeleri, G. P. and Loinger, E. "Amplitude and Phase Distortions Due to Absorption in Seismograms and VSP." Paper presented at 44th annual meeting of EAE, 1982.

Anstey, N. A. "Attacking the Problems of the Synthetic Seismogram." *Geophysical Prospecting*, Vol. 8, 242–260.

Arya, V. K. and H. D. Holden. *A Geophysical Application: Deconvolution of Seismic Data*. Digital Signal Processing. N. Hollywood, CA, Western Periodicals, 1979, 324–338.

Backus, M. M. "The Reflection Seismogram in a Layered Earth." *AAPG Bulletin*, 1983, Vol. 67, 416–417.

Balch, A. H. and M. W. Lee. "Some Considerations on the Use of Downhole Sources in Vertical Seismic Profiles." Paper presented at 35th Annual SEG Midwestern Exploration Meeting, 1982.

Balch, A. H., M. W. Lee, J. J. Miller and R. T. Ryder. "The Use of Vertical Seismic Profiles in Seismic Investigations of the Earth." *Geophysics*, Vol. 47, 906–918.

Baranov, V. "Film Synthétique Avec Réflexions Multiples—Théorie et Calcul Pratique." *Geophysical Prospecting*. Vol. 8, 315–325.

- Baranov, V. *Synthetic Seismograms With and Without Multiple Reflections*. AFTP, July 1959.
- Barry, K. and T. R. Shugart. "Zero-Phase Seismic Sections." SEG preprint, Tulsa: SEG, 1975.
- Barton, D. C. "The Seismic Method of Mapping Geologic Structure." *Geophysical Prospecting* (American Institute of Mining and Materials Engineering), Vol. 1, 572–624.
- Berg, O. R. "Seismic Detection and Evaluation of Delta and Turbidite Sequences: Their Application to Exploration for the Subtle Trap." *AAPG Bulletin*, Vol. 66, 1271–1288.
- Bernard, H. A., R. J. LeBlanc, and C. F. Major. "Recent and Pleistocene Geology of Southeast Texas." *Geology of the Gulf Coast and Central Texas and Guidebook of Excursions*. Houston Geological Society, 1962, 175–205.
- Berryman, J. G. "Long-Wave Elastic Anisotropy in Transversely Isotropic Media." *Geophysics*, Vol. 44, 896–917.
- Biot, M. A. "Propagation of Elastic Waves in a Cylindrical Bore Containing a Fluid." *Journal of Applied Physics*, Vol. 23, 997–1005.
- Blair, D. P. "Dynamic Modeling of In-Hole Mounts for Seismic Detectors." *Geophysics Journal of the Royal Astronomical Society*, Vol. 69, 803–817.
- Bois, P., M. Laporte, M. Laverne, and G. Thomas. "Well-to-Well Seismic Measurements." *Geophysics*, Vol. 37, 471–480.
- Brewer, H. L. and J. Holtzscherer. "Results of Subsurface Investigations Using Seismic Detectors and Deep Bore Holes." *Geophysical Prospecting*, Vol. 6, 81–100.
- Brown, A. R. "Interpretation of Three-Dimensional Seismic Data." Second Edition. *AAPG Memoir* 42, Tulsa, 1988.
- Brown, L. F. Jr. and W. L. Fisher. "Seismic Stratigraphic Interpretation and Petroleum Exploration." AAPG, Continuing Education Course Note Series, No. 16, 1980.
- Burg, J. P. *Maximum Entropy Spectrum Analysis*. PhD dissertation, Stanford University, Stanford, CA, 1975.
- Busch, D. A. and Link, D. A. *Exploration Methods for Sandstone Reservoirs*. Tulsa: OGCI Publications, 1985.
- Butler, D. K. and J. R. Curro. "Crosshole Seismic Testing—Procedures and Pitfalls." *Geophysics*, Vol. 46, 23–29.
- Chapman, W. L., G. L. Brown, and D. W. Fair. "The Vibroseis System, a High Frequency Tool." *Geophysics*, Vol. 46, 1657–1666.
- Cheng, C. H. and M. N. Toksoz. "Elastic Wave Propagation in a Fluid-Filled Borehole and Synthetic Acoustic Logs." *Geophysics*, Vol. 46, 1042–1053.
- Cheng, C. H. and M. N. Toksoz. "Generation, Propagation and Analysis of Tube Waves in a Borehole." Paper P, Trans. SPWLA 23rd Annual Logging Symposium, Vol. I., 1982.
- Cheng, C. H. and M. N. Toksoz. "Tube Wave Propagation and Attenuation in a Borehole." Paper presented at Massachusetts Institute of Technology Industrial Liaison Program Symposium, Houston, 1981.
- Cherry, J. T. and K. H. Waters. "Shear-wave Recording Using Continuous Signal Methods." *Geophysics*, Vol. 33, 229–239.
- Chun, J., D. G. Stone, and C. A. Jacewitz. "Extrapolation and Interpolation of VSP Data." Tulsa: Seismograph Service Companies Report, 1982.
- Claerbout, J. F. *Fundamentals of Geophysical Data Processing*. McGraw-Hill, 1976, pp 136, 143, 157–159.
- Claerbout, J. F. *Imaging the Earth's Interior*, Blackwell Scientific Publication, 1985.
- Collins, F. and C. C. Lee. "Seismic Wave Attenuation Characteristics from Pulse Experiment." *Geophysics*, Vol. 21, 16–40.

- Courtier, W. H. and H. L. Mendenhall. "Experiences with Multiple Coverage Seismic Methods." *Geophysics*, Vol. 32, 230–258.
- Cramer, P. W., "Reservoir Development Using Offset VSP Techniques in the Denver-Julesburg Basin." *Journal of Petrochemical Technology*, February 1988, 197–205.
- Crampin, S. "A Review of Wave Motion in Anisotropic and Cracked Elastic Media." *Wave Motion*, Vol. 3, 343–391.
- Crampin, S. "Evaluation of Anisotropy by Shear-wave Splitting." *Geophysics*, Vol. 50, 142–152.
- Crawford, J. M., W. E. N. Doty, and M.R. Lee. "Continuous Signal Seismograph." *Geophysics*, Vol. 25, 95–105.
- Danborn, S. H. and S. N. Domenico. *Shear-wave Exploration*, Society of Exploration Geophysicists, 1987.
- Delaplanche, J., R. F. Hagemann, and P. G. C. Bolland. "An Example of the Use of Synthetic Seismograms." *Geophysics*, Vol. 28, 842–854.
- Dalley, R. M. et al. "Dip and Azimuth Displays for 3D Seismic Interpretation." *First Break*, March 1989, 86–95.
- Dennison, A. T. "An Introduction to Synthetic Seismogram Techniques." *Geophysical Prospecting*, Vol. 8, 231–241.
- DeVoogd, N. and H. Den Rooijen. "Thin Layer Response and Spectral Bandwidth." *Geophysics*, Vol. 48, 12–18.
- DiSiena, J. P. and J. E. Gaizer. "Marine Vertical Seismic Profiling." Paper OTC 4541, Offshore Technology Conference, 1983, 245–252.
- Dix, C. H. "Seismic Velocities from Surface Measurements." *Geophysics*, Vol. 20, 68–86.
- Dobrin, M. B. *Introduction to Geophysical Prospecting*. New York: McGraw-Hill International, 1960.
- Domenico, S. N. "Elastic Properties of Unconsolidated Porous Sand Reservoirs." *Geophysics*, Vol. 42, 1339–1369.
- Douze, E. J. "Signal and Noise in Deep Wells." *Geophysics*, Vol. 29, 721–732.
- Dunkin, J. W. and F. K. Levin. "Isochrons for a Three-dimensional System." *Geophysics*, Vol. 36, 1099–1137.
- Durschner, H. "Synthetic Seismograms from Continuous Velocity Logs." *Geophysical Prospecting*, Vol. 6, 272–284.
- Edelman, H. A. K. "Shover-shear-wave Generation by Vibration Orthogonal to the Polarization." *Geophysical Prospecting*, Vol. 29, 541–549.
- Faust, L. Y. "A Velocity Function Including Lithologic Variation." *Geophysics*, Vol. 18, 271–288.
- Fisher, W. L. and L. F. Brown. "Clastic Depositional Systems—A Generic Approach to Facies Analysis: An Annotated Outline and Bibliography." The University of Texas at Austin Bureau of Economic Geology, 1972.
- Fontaine, J. M., R. Cussey, J. Lacase, and L. Yapaudjia. "Seismic Interpretation of Carbonate Depositional Environments." *AAPG Bulletin*, 1987, 281–297.
- Futterman, W. I. "Dispersive Body Waves." *Journal of Geophysical Research*, Vol. 67, 5279–5291.
- Gaizer, J. E. and J. P. DiSiena. "VSP Fundamentals that Improve CDP Data Interpretation." Paper S12.2, 52nd Annual International Meeting of SEG, Technical Program Abstracts, 1982, 154–156.
- Galperin, E. I. "Vertical Seismic Profiling." SEG, *Special Publ.* No. 12, Tulsa, 1974.
- Gardner, D. H. "Measurement of Relative Ground Motion in Reflection Recording." *Geophysics*, Vol. 3, 40–45.

- Gardner, G. H. F., L. W. Gardner, and A. R. Gregory. "Formation Velocity and Density—The Diagnostic Basics for Stratigraphic Traps." *Geophysics*, Vol. 39, 770–780.
- Gary, M., R. McAfee, Jr., and C. L. Wolf. *Glossary of Geology*, American Geological Institute, Washington: 1987.
- Gassaway, G. S. and H. J. Richgels. "SAMPLE, Seismic Amplitude Measurement for Primary Lithology Estimation," 53rd SEG Meeting, Las Vegas, 1983, 610–613.
- Gelfand, V., P. Ng, and K. Larner. "Seismic Lithologic Modeling of Amplitude-versus-offset Data," 56th SEG Meeting, Houston, 1986, 332–334.
- Gerritsma, P. H. A. "Time to Depth Conversion in the Presence of Structure." *Geophysics*, Vol. 42, 760–772.
- Geyer, R. L. and S. T. Martner. "SH-waves from Explosive Source." *Geophysics*, Vol. 34, 893–905.
- Giles, B. F. "Pneumatic Acoustic Energy Source." *Geophysical Prospecting*, Vol. 16, 21–53.
- Godfrey, L. M., J. D. Stewart, and F. Schweiger. "Application of Dinoiseis in Canada." *Geophysics*, Vol. 33, 65–77.
- Goupillaud, P. L. "An Approach to Inverse Filtering of Near-surface Layer Effects from Seismic Records." *Geophysics*, Vol. 26, 754–760.
- Greaves, R. J. and T. J. Flup. "Three-dimensional Seismic Monitoring of an Enhanced Oil Recovery Process." *Geophysics*, Vol. 52, 1175–1187.
- Griffiths, D. H. and R. F. King. *Applied Geophysics for Engineers and Geologists*. London: Pergamon, 1965.
- Haq, B. U., J. Hardenbol, and P. R. Vail. "Chronology of Fluctuating Sea Levels Since the Triassic. *Science*, V. 235, 1156–1166.
- Hardage, B. A. "A New Direction in Exploration Seismology is Down." *The Leading Edge*, Vol. 2, No. 6, 49–52.
- Hardage, B. A. "An Examination of Tube Wave Noise in Vertical Seismic Profiling Data." *Geophysics*, Vol. 46, 892–903.
- Haskey, P., P. Duke, and J. Fargher. "Which 3-D?" 2nd Latin American Congress on Hydrocarbons, Rio de Janeiro, 1988.
- Hill, N. R. and I. Lerche "Acoustic Reflections from Undulating Surfaces." *Geophysics*, Vol. 51, 2160–2161.
- Hilterman, F. J. "Amplitudes of Seismic Waves—A Quick Look." *Geophysics*, Vol. 40, 745–762.
- Hilterman, F. J. "Three-Dimensional Seismic Modeling." *Geophysics*, Vol. 35, 1020–1037.
- Hindlet, F. "Thin Layer Analysis Using Offset/Amplitude Data." 56th SEG Meeting, Houston, Expanded Abstracts, 1986, 332–334.
- Huang, X., R. Will, M. Khan, and L. Stanley. "Integration of Time-lapse Seismic and Production Data in a Gulf of Mexico Gas Field." *The Leading Edge*, Vol. 20, 278–289.
- Jervey, M. T. *Quantitative Geological Modeling of Siliciclastic Rock Sequences and Their Seismic Expression*. 1988.
- Jolly, R. N. "Deep-hole Geophone Study in Garvin County, OK." *Geophysics*, Vol. 18, 662–670.
- Jolly, R. N. "Investigation of Shear Waves." *Geophysics*, Vol. 21, 905–938.
- Kearney, P. and M. Brooks. *An Introduction to Geophysical Exploration*. Blackwell Scientific Publication. 1984.
- Kelly, K. R., R. W. Ward., S. Treitel, and R. M. Alford. "Synthetic Seismograms: A Finite Difference Approach." *Geophysics*, Vol. 41, 2–27.

- Kennett, P., R. L. Ireson, and P. J. Conn. "Vertical Seismic Profiles—Their Applications in Exploration Geophysics." *Geophysical Prospecting*, Vol. 28, 676–699.
- Kluesner, D. F. "Champion Field: Role of Three-dimensional Seismic in Development of a Complex Giant Oilfield." *AAPG Bulletin*, 1988, 72, 207.
- Koefoed, O. and N. DeVoogd. "The Linear Properties of Thin Layers, with an Application to Synthetic Seismograms over Coal Seams." *Geophysics*, Vol. 45, 1254–1268.
- Lang, D. G. "Downhole Seismic Combination of Techniques Sees Nearby Features." *Oil and Gas Journal*, Vol. 77, No. 29, 63–66.
- Lang, D. G. "Downhole Seismic Technique Expands Borehole Data." *Oil and Gas Journal*, Vol. 77, No. 28, 139–142.
- Lash, C. C. "Investigation of Multiple Reflections and Wave Conversions by Means of Vertical Wave Test (Vertical Seismic Profiling) in Southern Mississippi." *Geophysics*, Vol. 47, 977–1000.
- Lavergne, M. and C. Willm. "Inversion of Seismograms and Pseudo Velocity Logs." *Geophysics*, Vol. 25, 231–250.
- LeBlanc, R. L. "Significant Studies of Modern and Ancient Deltaic Sediments." Broussard, M. L. (Ed), *Deltas, Models for Exploration*, Houston Geol. Soc., 1975, 13–85.
- Lee, M. W. and A. H. Balch "Computer Processing of Vertical Seismic Profile Data." *Geophysics*, Vol. 48, 272–287.
- Lee, M. W. and A. H. Balch. "Theoretical Seismic Wave Radiation from a Fluid-filled Borehole." *Geophysics*, Vol. 47, 1308–1314.
- Levin, F. K., J. F. Bayhi, J. W. Dunkin, J. D. Lea, D. B. Moore, R. K. Warren, and G. H. Webster. "Developments in Exploration Geophysics 1969–1974." *Geophysics*, Vol. 41, 209–218.
- Levin, F. K. and R. D. Lynn. "Deep Hole Geophone Studies." *Geophysics*, Vol. 23, 639–664.
- Lidz, B. H. (Ed). "Sea-Level Change—An Integrated Approach." SEPM, No. 42, 71–108.
- Lindseth, R. O. "The Seislog, A New Formation Logging Method." *AAPG-SEG Pacific Section*, Bakersfield, 1977.
- Lindsey, P., N. Neidell, and F. Hilterman. *Interpretive Uses of Seismic Modeling with Emphasis on Stratigraphy and Seismic Resolution*. Tulsa: SEG, 1975.
- Loutit, T. S., J. Hardenbol, P. R. Vail, and G. R. Baum. "Condensed Sections, The Key to Age Dating and Correlation of Continental Margin Sequences." Lidz, B. H., (Ed) *Sea-level change—an integrated approach*, SEPM, No. 42, 1988, 71–108.
- Marr, J. D. and E. F. Zagst. "Exploration Horizons from New Seismic Concepts of CDP and Digital Processing." *Geophysics*, Vol. 32, 207–224.
- Mayne, W. H. "Common Reflection Point Horizontal Stacking Techniques." *Geophysics*, Vol. 27, 927–938.
- Mayne, W. H. "Practical Considerations in the Use of Common Reflection Point Technique." *Geophysics*, Vol. 32, 225–229.
- Mayne, W. H. and R. G. Quay. "Seismic Signatures of Large Air Guns." *Geophysics*, Vol. 36, 1162–1173.
- McCollum, B. and W. W. Larue. "Utilization of Existing Wells in Seismograph Work." Early Geophysical Papers, Vol. 12, 119–127. Also, *AAPG Bulletin*, Vol. 15, 1409–1417.
- McQuillin, R., M. Bacon, and W. Barclay. *An Introduction to Seismic Interpretation*. Houston: Gulf Publishing Co., 1984.
- Meissner, R. and M. A. Hegazy. "The Ratio of the PP- to SS-reflection Coefficient as a Possible Future Method to Estimate Oil and Gas Reservoirs." *Geophysical Prospecting*, Vol. 29, 533–540.

- Mitchum, R. M. Jr. "Seismic Stratigraphic Expression of Submarine Fans." Berg, O. R. and E. G. Woolverton (Eds), *Seismic Stratigraphy II: An Integrated Approach: AAPG Memoir 39*, 1985, 117–138.
- Mitchum, R. M. Jr. and P. R. Vail. "Seismic Stratigraphy and Global Changes in Sea Level, Part 7: Seismic Stratigraphic Interpretation Procedure." Payton, C. E. (Ed), *Seismic Stratigraphy—Applications to Hydrocarbon Exploration: AAPG Memoir 26*, 1977, 135–143.
- Mitchum, R. M. Jr., P. R. Vail, and J. B. Sangree. "Seismic Stratigraphy and Global Changes in Sea Level, Part 6: Stratigraphic Interpretation of Seismic Reflection Patterns in Depositional Sequence." Payton, C. E. (Ed), *Seismic Stratigraphy—Applications to Hydrocarbon Exploration: AAPG Memoir 26*, 1977, 117–133.
- Mitchum, R. M. Jr., P. R. Vail, and S. Thompson, III. "Seismic Stratigraphy and Global Changes in Sea Level, Part 2: The Depositional Sequence as a Basic Unit for Seismic Stratigraphic Analyses." Payton, C. E. (Ed), *Seismic Stratigraphy—Applications to Hydrocarbon Exploration: AAPG Memoir 26*, 1977, 53–62.
- Neitzel, E. B. "Seismic Reflection Records Obtained by Dropping a Weight." *Geophysics*, Vol. 23, 58–80.
- Nettleton, L. L. *Geophysical Prospecting for Oil*. New York: McGraw-Hill, 1940.
- Ostrander, W. J. "Plane Wave Reflection Coefficients for Gas Sands at Non-normal Angles of Incidence." *Geophysics*, Vol. 49, 1637–1648.
- Parr, J. O. Jr. and W. H. Mayne. "A New Method of Pattern Shooting." *Geophysics*, Vol. 20, 539–564.
- Peacock, R. B. and D. M. Nash, Jr. "Thumping Technique Using Full Spread of Geophones." *Geophysics*, Vol. 27, 952–965.
- Pennington, W. D., H. Acevedo, J. L. Haataja, and A. Minaeva. "Seismic Time-lapse Surprise at Teal South, That Little Neighbor Reservoir is Leaking." *The Leading Edge*, Vol. 20, 1172–1175.
- Peterson, R. A., W. R. Fillipone, and F. B. Coker. "The Synthesis of Seismograms from Well Log Data." *Geophysics*, Vol. 20, 516–538.
- Pittmen, W. C. III. "Relationship Between Eustacy and the Stratigraphic Sequences of Passive Margins." *Geol. Soc. Am. Bulletin*, V. 89, 1389–1403.
- Posamentier, H. W., M. T. Jervey, and P. R. Vail. "Eustatic Controls on Clastic Deposition I." Lidz, B. H. (Ed), *Sea-level Changes—An Integrated Approach: SEPM*, No. 42, 125–154.
- Posamentier, H. W., M. T. Jervey, and P. R. Vail. "Eustatic Controls on Clastic Deposition II." Lidz, B. H. (Ed), *Sea-level Changes—An Integrated Approach: SEPM*, No. 42, 125–154.
- Poulter, T. C. "The Poulter Seismic Method of Geophysical Exploration." *Geophysics*, Vol. 15, 181–207.
- Pullin, N., L. Matthews, and K. Hirsche. "Techniques Applied to Obtain Very High Resolution 3-D Seismic Imaging at a Athabasca Tar Sands Thermal Pilot." *The Leading Edge*, Vol. 6, 10–15.
- Quarles, M. "Vertical Seismic Profiling—A New Seismic Exploration Technique." Paper presented at the 48th Annual International Meeting of SEG, 1978.
- Rascoe, B. "Regional Stratigraphic Analysis of Pennsylvanian and Permian Rock in Western Mid-Continent, Colorado, Kansas, Oklahoma, and Texas." *AAPG Bulletin*, 1962, No. 8, 1345–1370.
- Rice, R. B., et al. "Developments in Exploration Geophysics 1975–1980." *Geophysics*, Vol. 46, 1088–1099.
- Rich J. L. "Three Critical Environments of Deposition and Criteria for Recognition of Rocks Deposited in Each of Them." *Geol. Soc. Am. Bulletin* (1951), V. 62, 1–20.
- Riggs, E. D. "Seismic Wave Types in a Borehole." *Geophysics*, Vol. 20, 53–60.

- Ritchie, W. "Role of the 3D Seismic Technique in Improving Oilfield Economics." *Journal of Petrochemical Technology*, July 1986, 777–786.
- Robertson, J. D. "Reservoir Management Using 3D Seismic Data." *Journal of Petrochemical Technology*, 1986, 663–667.
- Robinson, E. A. *Migration of Geophysical Data*. Boston: IHRDC, 1983.
- Robinson, E. A. *Robinson-Treitel Reader*. Tulsa: Seismograph Service Corp., 1969.
- Robinson, E. A. *Seismic Velocity Analysis and the Convolutional Model*. Boston: IHRDC, 1983.
- Robinson, E. A. *Structural Properties of Stochastic Processes*. New York: John Wiley and Sons, 1963.
- Sangree, J. B., P. R. Vail, and R. M. Sneider. "Evolution of Facies Interpretation of the Shelf-Slope: Application of the New Eustatic Framework in the Gulf of Mexico." Offshore Technology Conference, 1988, 133–144.
- Sangree, J. B., D. C. Waylett, D. E. Frazier, G. B. Amerry, and W. J. Fennesey. "Recognition of Continental-Slope Facies, Offshore Texas-Louisiana." Bouma, A. H., G. T. Moore, and J. M. Coleman. (Eds), *Framework, Facies, and Oil-trapping Characteristics of the Upper Continental Margin*: AAPG Studies in Geology, No. 7, 87–116.
- Sangree, J. B. and J. M. Widmier. "Interpretation of Depositional Facies from Seismic Data." *Geophysics*, Vol. 44, No. 2, and 131–160.
- Sangree, J. B. and J. M. Widmier. "Seismic Stratigraphy and Global Changes in Sea Level, Part 9: Seismic Interpretation of Clastic Depositional Facies." C. E. (Ed), *Seismic Stratigraphy—Applications to Hydrocarbon Exploration: AAPG Memoir 26*, 1977, 165–184.
- Sarg, J. F. "Carbonate Sequence Stratigraphy." Lidz, B. H. (Ed) *Sea-level Change—An Integrated Approach*. SEPM, No. 42, 1988, 155–181.
- Schoenberger, M. and F. K. Levin, "Reflected and Transmitted Filter Functions for Simple Subsurface Geometries." *Geophysics*, Vol. 41, 1305–1317.
- Sengbush, R. L., P. L. Laurence, and F. J. McDonal, "Interpretation of Synthetic Seismograms." *Geophysics*, Vol. 26, 138–157.
- Sheriff, R. E. *Encyclopedic Dictionary of Exploration Geophysics*. Society of Exploration Geophysicists, Tulsa: 1961.
- Sheriff, R. E. "Factors Affecting Amplitudes—A Review of Physical Principles in Lithology and Direct Detection of Hydrocarbons Using Geophysical Methods." Symposium of the Geophysical Society of Houston, 1973. Also, *Geophysical Prospecting*, Vol. 25, 125–138.
- Shuey, R. T. "A Simplification of Zoeppritz Equations." *Geophysics*, Vol. 50, 609–614.
- Shultz-Gatterman, R. "Physical Aspects of the Air Pulser as a Seismic Energy Source." *Geophysical Prospecting*, Vol. 20, 155–192.
- Sloss, L. L. "Sequences in the Cratonic Interior of North America." *Geological Society of America Bulletin*, Vol. 74, 93–113.
- Stephens, R. B. and P. Sheng. "Acoustic Reflections from Complex Strata." *Geophysics*, 1100–1107.
- Stewart, R. R., R. M. Turpening, and M. N. Toksoz. "Study of a Subsurface Fracture Zone by Vertical Seismic Profiling." *Geophy. Res. Lett.*, Vol. 9, 1132–1135.
- Stone, D. G. *Estimation of Reflection Coefficients from Seismic Data*. Tulsa: SEG, 1977.
- Stone, D. G. *Robust Wavelet Estimation by Structural Deconvolution*. Tulsa: SEG, 1973.

- Stone, D. G. "VSP—The Missing Link." Paper presented at the VSP short course sponsored by the SE Geophysicists Society in New Orleans, 1981.
- Stone, D. G. and J. L. Atherton. *Decomposition of Seismic Trace*. Tulsa: SEG preprint, 1979.
- Tatham, R. H. "V_p/V_s and Lithology." *Geophysics*, Vol. 47, 336.
- Tatham, R. H. and M. D. McCormack. *Multicomponent Seismology in Petroleum Exploration*, SEG, 1991.
- Tatham, R. H. and P. L. Stoffa. "V_p/V_s—A Potential Hydrocarbon Indicator." *Geophysics*, Vol. 41, 837–849.
- Treitel, S. "Seismic Wave Propagation in Layered Media in Terms of Communication Theory." *Geophysics*, Vol. 31, 17–32.
- Treitel, S. and K. Peacock. "Predictive Deconvolution: Theory and Practice." *Geophysics*, Vol. 34, 155–169.
- Trorey, A. W. "Theoretical Seismograms with Frequency and Depth Dependent Absorption." *Geophysics*, Vol. 27, 766–785.
- Vail, P. R., J. N. Bubb, W. G. Hatlelid, R. M. Mitchum, J. B. Sangree, S. Thompson III, R. G. Todd, and J. M. Widmier. "Seismic Stratigraphy and Global Changes of Sea Level, Parts 1–11." Payton, C. E. (Ed), *Seismic Stratigraphy—Application to Hydrocarbon Exploration: AAPG Memoir 26*, 1977, 49–212.
- Vail, P. R., J. Hardenbol, and R. G. Todd. "Jurassic Unconformities, Chronostratigraphy, and Sea-level Changes from Seismic Stratigraphy and Biostratigraphy." Schlee, J. S. (Ed), *Inter-regional Unconformities and Hydrocarbon Accumulation: AAPG Memoir 36*, 1984, 129–144.
- Vail, P. R., R. M. Mitchum, Jr., and S. Thompson III. "Seismic Stratigraphy and Global Changes of Sea Level, Part 3: Relative Changes of Sea Level from Coastal Onlap." Payton, C. E. (Ed), *Seismic Stratigraphy—Application to Hydrocarbon Exploration: AAPG Memoir 26*, 1977, 49–212.
- Vail, P. R., R. M. Mitchum, Jr. and S. Thompson III. "Seismic Stratigraphy and Global Changes of Sea Level, Part 4: Global Cycles of Relative Changes of Sea Level." Payton, C. E. (Ed), *Seismic Stratigraphy—Application to Hydrocarbon Exploration: AAPG Memoir 26*, 1977, 83–97.
- Vail, P. R. and J. B. Sangree. "Sequence Stratigraphy Interpretation of Seismic, Well, and Outcrop Data Workbook." Short Course, Bureau of Economic Geology, Austin, Texas, April 8–9, 1988.
- Vail, P. R. and R. G. Todd. "North Sea Jurassic Unconformities, Chronostratigraphy, and Sea Level Changes from Seismic Stratigraphy." Proceedings of the Petroleum Geology of the Continental Shelf, Northwest Europe, 1981, 216–235.
- Vail, P. R., R. G. Todd, and J. B. Sangree. "Seismic Stratigraphy and Global Changes of Sea Level, Part 5: Chronostratigraphic Significance of Reflections." Payton, C. E. (Ed), *Seismic Stratigraphy—Application to Hydrocarbon Exploration: AAPG Memoir 26*, 1977, 99–116.
- van Sandt, D. R. and F. K. Levin. "A Study of Cased and Open Holes for Deep Seismic Detection." *Geophysics*, Vol. 28, 8–13.
- Van Wagoner, J. C., R. M. Mitchum Jr., H. W. Posamentier and P. R. Vail. "Key Definitions of Seismic Stratigraphy." Bally, A. W. (Ed), *Atlas of Seismic Stratigraphy*, Vol. 1, AAPG, 11–14.
- Walton, G. G. "Three-dimensional Seismic Method." *Geophysics*, Vol. 37, 417–430.
- Water, K. H. *Reflection Seismology, A Tool for Energy Resource Exploration*. New York: John Wiley and Sons, 1987.
- Wayland, R. J. and D. Lee. "Seismic Mapping of EOR Processes." *The Leading Edge*, 1986, 36–40.
- White, R. E. and P. N. S. O'Brien. "Estimation of the Primary Seismic Pulse." *Geophysical Prospecting*, Vol. 22, 627–651.
- Widess, M. B. "How Thin is a Thin Bed?" *Geophysics*, V. 38, 1976.

- Wright, J. "Reflection Coefficients at Pore-fluid Contacts as a Function of Offset." *Geophysics*, Vol. 51, 1858–1860.
- Wuenschel, P. C. "Seismogram Synthesis Including Multiples and Transmission Coefficients." *Geophysics*, Vol. 25, 106–219.
- Wyatt, K. D. "Synthetic Vertical Seismic Profile." *Geophysics*, Vol. 46, 880–991.
- Wyatt, S. B. "The Propagation of Elastic Waves Along a Fluid-filled Annular Region." Master of Science Thesis, University of Tulsa, 1979.
- Yilmaz, O. and R. Chambers. "Migration Velocity Analysis by Wave Field Extrapolation." *Geophysics*, Vol. 49, 1664–1674.
- Yilmaz, O. *Seismic Data Processing*. SEG, 1987.
- Yoshimura, M., S. Fujii, K. Tanaka, and K. Morita. "On the Relationship Between P- and S-wave Velocities in Soft Rock." Paper given at SEG annual international meeting, Dallas, 1982.
- Young, G. B. and L. W. Braile. "A Computer Program for the Application of Zoeppritz's Amplitude Equations and Knott's Energy Equations." *Bulletin of the Seismological Society of America*, Vol. 66 (6), 1881–1885.
- Yu, G. "Offset-amplitude Variation and Controlled-amplitude Processing." *Geophysics*, Vol. 50, 2697–2708.